Smart Sensors, Measurement and Instrumentation 21

Ignacio R. Matias
Satoshi Ikezawa
Jesus Corres *Editors*

Fiber Optic Sensors

Current Status and Future Possibilities

Springer

Smart Sensors, Measurement and Instrumentation

Volume 21

Series editor

Subhas Chandra Mukhopadhyay
Department of Engineering, Faculty of Science and Engineering
Macquarie University
Sydney, NSW
Australia
e-mail: S.C.Mukhopadhyay@massey.ac.nz

More information about this series at http://www.springer.com/series/10617

Ignacio R. Matias · Satoshi Ikezawa
Jesus Corres
Editors

Fiber Optic Sensors

Current Status and Future Possibilities

Springer

Editors
Ignacio R. Matias
Public University of Navarra
Pamplona
Spain

Jesus Corres
Public University of Navarra
Pamplona
Spain

Satoshi Ikezawa
Waseda University
Kitakyushu, Fukuoka
Japan

ISSN 2194-8402 ISSN 2194-8410 (electronic)
Smart Sensors, Measurement and Instrumentation
ISBN 978-3-319-42624-2 ISBN 978-3-319-42625-9 (eBook)
DOI 10.1007/978-3-319-42625-9

Library of Congress Control Number: 2016946313

© Springer International Publishing Switzerland 2017
This work is subject to copyright. All rights are reserved by the Publisher, whether the whole or part of the material is concerned, specifically the rights of translation, reprinting, reuse of illustrations, recitation, broadcasting, reproduction on microfilms or in any other physical way, and transmission or information storage and retrieval, electronic adaptation, computer software, or by similar or dissimilar methodology now known or hereafter developed.
The use of general descriptive names, registered names, trademarks, service marks, etc. in this publication does not imply, even in the absence of a specific statement, that such names are exempt from the relevant protective laws and regulations and therefore free for general use.
The publisher, the authors and the editors are safe to assume that the advice and information in this book are believed to be true and accurate at the date of publication. Neither the publisher nor the authors or the editors give a warranty, express or implied, with respect to the material contained herein or for any errors or omissions that may have been made.

Printed on acid-free paper

This Springer imprint is published by Springer Nature
The registered company is Springer International Publishing AG Switzerland

Preface

Fiber optic sensing technology is perfectly established nowadays and provides a range of solutions for an increasing gamut of applications in the areas ranging from structural health monitoring to biophotonic sensing, to name a few. New variety of fibers together with the development of nanostructured materials and the scientific advances in physics and chemistry have led us to discover new phenomenon stimulating new sensor developments.

In this book, we will see more interdisciplinary topics, an engineering maturity and novel technologies as even before induced by the diversity of applications. New ideas and concepts are proposed and tested, not only for various traditional parameters such as strain, temperature, or pressure, but also for new concepts, applications, and phenomenon.

Among the concepts, extended infrared sensors are making its appearance, and we have included a couple of chapters such as THz and Photonic Crystal Structures based sensing in this regard.

Another important aspect is the resonance generated when using thin films together with optical fibers. We are talking about surface plasmon resonances, lossy mode resonances, long-range surface exciton polariton, etc. These new phenomena for sensing purposes have an enormous potential.

We have tried to cover the main application subjects, such as power engineering, chemical engineering, bioengineering, environmental measurements, etc. Almost certainly, the application fields of optical fiber sensors will be extended and more commercial successes will be obtained in the near future.

Taking into account the geographic representation of the selected authors, with the underlying benefits in terms of different viewpoints, different ways of understanding, etc, we believe this will enrich the reading much more. In any case, we hope that the readers will find this book useful and interesting for their research works.

We would not like to finish without thanking all the authors for their effort and brilliant contribution to this book.

Pamplona, Spain — Ignacio R. Matias

Contents

Fiber Optic Sensors Based on Nano-Films 1
Minghong Yang, Jiankun Peng, Gaopeng Wang and Jixiang Dai

Lossy Mode Resonance Based Fiber Optic Sensors 31
Nidhi Paliwal and Joseph John

Plasmonics-Based Fiber Optic Sensors 51
Anuj K. Sharma

POF Biosensors Based on Refractive Index and Immunocapture Effect 69
Marcelo Werneck, Rafaela Lopes, Greice Costa, Domingos Rodrigues, Ariadny Arcas, Fabio Dutra, Vanessa Queiroz and Regina Allil

Plasma-Based Deposition and Processing Techniques for Optical Fiber Sensing 95
M. Dominik, M. Koba, R. Bogdanowicz, W.J. Bock and M. Śmietana

Trends in Fibre-Optic Uses for Personal Healthcare and Clinical Diagnostics 115
A.B. Socorro and S. Díaz

Optical Fibres for Radiation Dosimetry 149
S. O'Keeffe

Photonic Bandgap Fibre Based Gas Sensing: Current Status and Future Possibilities 167
J. Pawlat, X. Li, T. Sugiyama, J. Liang, Y. Zimin, L. Zimin, S. Ikezawa and T. Ueda

Structural Health Monitoring Fiber Optic Sensors 185
K. Loupos and A. Amditis

Brillouin Distributed Temperature Sensor Using Optical Time Domain Reflectometry Techniques 207
Himansu Shekhar Pradhan, P.K. Sahu, D. Ghosh and S. Mahapatra

Optical Sensing Based on Photonic Crystal Structures 223
J. Sevilla and A. Andueza

Long Period Grating Based Fibre Optic Chemical Sensors 241
Sergiy Korposh, Seung-Woo Lee and Stephen James

Magnetic Field Sensors Based on Optical Fiber 269
J. Ascorbe and J.M. Corres

Sensing at Terahertz Frequencies 301
P. Rodríguez-Ulibarri and M. Beruete

Multimode Interference Fiber Sensors for the Monitoring of Gasoline/Ethanol Blends 329
A.J. Rodriguez-Rodriguez, D.A. May-Arrioja, I. Hernandez-Romano and Ignacio R. Matías

Fiber Optic Sensors Based on Multicore Structures 347
D.A. May-Arrioja and J.R. Guzman-Sepulveda

Index 373

Fiber Optic Sensors Based on Nano-Films

Minghong Yang, Jiankun Peng, Gaopeng Wang and Jixiang Dai

Abstract The combination of fiber optics with sensitive nano-films offers great potential for the realization of novel sensing concepts. Miniatured optical fiber sensors with thin films as sensitive elements could enable new fields of optical fiber sensor applications. Thin films work as sensitive elements and transducer to get response and feedback from environments, while optical fibers are employed to work as signal carrier. In this chapter fiber optic sensors based on nano-films are reviewed.

1 Introduction

In optical engineering of sensing technology, recently the most important enabling technologies are based on structuring of fibres, either longitudinally or transversely. Bragg gratings are typical examples of longitudinally structuring of fibers, while micro-structured fibres (e.g. photonic crystal fibres) are the promising enabling technologies in terms of transversely structuring of fibers. Microstructured fibres, provide materials with dispersion characteristics unattainable with conventional materials, as well as otherwise unfeasible physical characteristics that can be controlled and realized for specific sensing applications.

Integration of novel functional material with fiber optic components is one of the new trends in the field of novel sensing technologies. The combination of fiber optics with functional materials offers great potential for the realization of novel sensors. Typically the in optical fibre sensing technology, fibre itself acts as sensing elements and also transmitting elements, such as fiber Bragg grating (FBG) [1], Brillouin or Raman Optical Time Domain Reflectometer (OTDR) [2, 3]. However such sensing components can only detect limited physical parameters such as temperature or strain based on its principle of characteristic wavelength drifts. While the idea of optical fiber sensing technology with nano-films is quite different

M. Yang (✉) · J. Peng · G. Wang · J. Dai
Wuhan University of Technology, Wuhan, People's Republic of China
e-mail: minghong.yang@whut.edu.cn

© Springer International Publishing Switzerland 2017

I.R. Matias et al. (eds.), *Fiber Optic Sensors*, Smart Sensors,
Measurement and Instrumentation 21, DOI 10.1007/978-3-319-42625-9_1

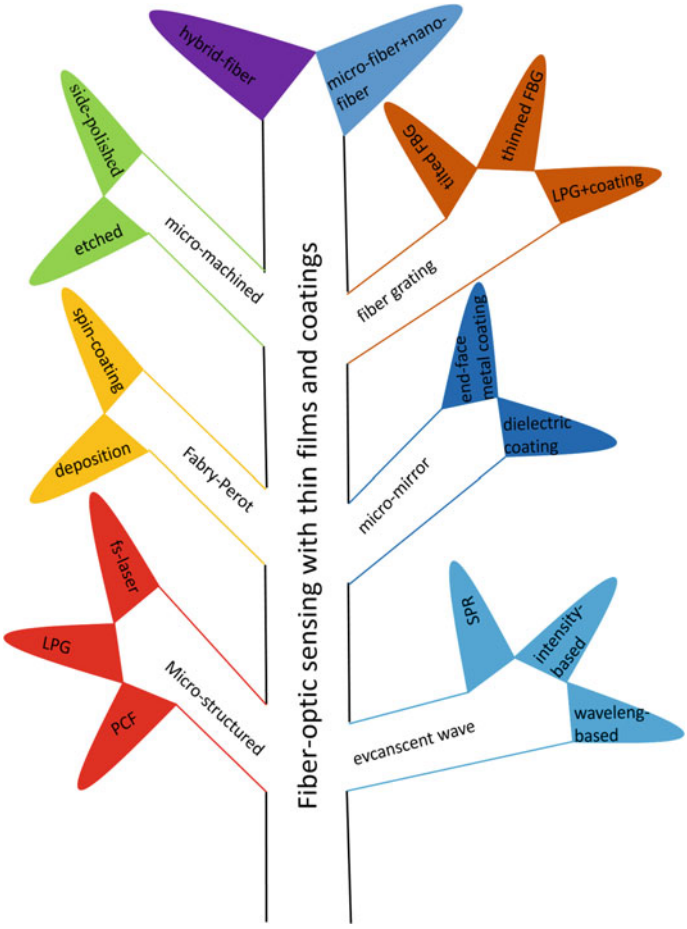

Fig. 1 Fiber-optic sensors based on thin films and coatings

with the traditional technology, nano-films can be employed as sensing component, therefore many parameters, including chemical or biological parameters, can be detected dependant on the design of different sensing films. When compared to the common fiber sensing technologies such as FBG and OTDR, fiber optic sensors based on nano-films show advantages on the diversity of measurement parameters. However, nano-films can be realized by many techniques including e-beam evaporation [4], magnetron sputtering [5], spin-coating [6], electro-chemical plating [7], etc. The mechanical stability on tiny optical fibers is still problematic, which could be a challenge for industrial applications.

Fiber optic sensors with thin films as sensing elements can be plotted in Fig. 1. In principle by integration of sensitive thin films with many fiber structures, novel fiber optic sensors can be developed.

The main principle can be listed as follows:

(1) Evanescent wave interaction

Evanescent wave is an oscillating electric and/or magnetic field which does not propagate as an electromagnetic wave but whose energy is spatially concentrated in the vicinity of the source (oscillating charges and currents). Even when there in fact is an electromagnetic wave produced (e.g. by a transmitting antenna) one can still identify as an evanescent field the component of the electric or magnetic field that cannot be attributed to the propagating wave observed at a distance of many wavelengths (such as the far field of a transmitting antenna).

When optical fiber is etched or side-polished to a certain level, and nano-metal layer is deposited on the etched or side-polished area, evanescent wave interaction with surrounding environment is enabled. Any change in the surrounding environment will change the dielectric property of nano-metal film, thus the transmitted or reflected spectrum will be influenced. Signal change in the spectrum can be wavelength-based spectrum drift or intensity-based amplitude change. Therefore the correlation of light signal change with surrounding environment can be correlated for sensing application [8].

(2) Micro-mirror

Fiber-optic sensor with nano-film in micro-mirror style is easy to understand. Nano-film is deposited on the polished fiber-tip, which generates a micro-mirror [9]. The reflected light is principally dependent on the refractive index of micro-mirror; normally the micro-mirror is a kind of metal layer or dielectric layer, which is sensitive to environmental parameter. When the refractive index of this nano-film is varied due to the surrounding environment, such change can be recorded by the variation of the reflected intensity. Therefore by measuring the intensity change, it is possible to sense the environmental parameter. However such technology is a kind of intensity measurement, which is easily suffered from instability of the system, such as fluctuation of power intensity.

(3) Fiber Bragg grating

Fiber Bragg grating (FBG) is a type of distributed Bragg reflector constructed in a short segment of optical fiber that reflects particular wavelengths of light and transmits all others. This is achieved by creating a periodic variation in the refractive index of the fiber core, which generates a wavelength-specific dielectric mirror. A fiber Bragg grating can therefore be used as an inline optical filter to block certain wavelengths, or as a wavelength-specific reflector. Fiber Bragg gratings are created by “inscribing” or “writing” systematic (periodic or aperiodic) variation of refractive index into the core of a special type of optical fiber using an intense ultraviolet (UV) source such as a UV laser. Two main processes are used: interference and masking [10, 11]. The method that is preferable depends on the type of grating to be manufactured. Normally a germanium-doped silica fiber is used in the manufacture of fiber Bragg gratings. The germanium-doped fiber is

photosensitive, which means that the refractive index of the core changes with exposure to UV light. The amount of the change depends on the intensity and duration of the exposure as well as the photosensitivity of the fibre. To write a high reflectivity fiber Bragg grating directly in the fiber the level of doping with germanium needs to be high. However, standard fibers can be used if the photosensitivity is enhanced by pre-soaking the fiber in hydrogen.

Sensitive thin films or coatings can also be integrated with fiber bragg grating technology for sensing application [12]. In this case, sensitive thin films or coatings act as transducers for environmental parameters, while fiber grating itself acts as light signal carrier. The sensitive thin films or coatings can be realized by means of e-beam evaporation, magnetron sputtering and spin-coating. Furthermore, long-period grating and tilted fiber grating are also of great interest for sensing application, these gratings are intrinsic sensitive to the refractive index change of surrounding environment.

(4) Micro-structured fiber

Micro-structured fiber is also called photonic crystal fiber, photonic-crystal fiber (PCF) is a new class of optical fiber based on the properties of photonic crystals [13]. Because of its ability to confine light in hollow cores or with confinement characteristics not possible in conventional optical fiber, PCF is now finding applications in fiber lasers, fiber-optic communications, nonlinear devices, high-power transmission, highly sensitive gas sensors, and other areas. More specific categories of PCF include photonic-bandgap fiber (PCFs that confine light by band gap effects), holey fiber (PCFs using air holes in their cross-sections), hole-assisted fiber (PCFs guiding light by a conventional higher-index core modified by the presence of air holes), and Bragg fiber (photonic-bandgap fiber formed by concentric rings of multilayer film). Photonic crystal fibers may be considered a subgroup of a more general class of microstructured optical fibers, where light is guided by structural modifications, and not only by refractive index differences. These micro-structured fibers can also be employed as sensing platform with nano-film as sensitive element. There are many research work on this topic, such as filling nano-film in the micro-hole of the structure for high sensitive gas or chemical detection.

(5) Micro-machined

Micro-machined fiber means fiber is micro-treated by other techniques, these techniques include chemical etching, side-polishing, laser micromachining. In case of laser machining, CO_2 gas laser and femto-second laser can both by employed as heating sources, whereas femto-second micro-machining shows advantages due to its intrinsic properties such as ultra-short pulse time and ultra-high intensity of laser power, which is very promising especially for precise micro-structure [14]. Chemical etching [15] and side-polishing [16] process are also well-established concerning its feasibility on fiber micro-machining, especially chemical etching can be controlled step-by-step for precise machining. When the fiber is

micro-machined, there exists the coupling and interaction of transmitted light with surrounding environment. When the micro-machined area is coated with sensitive films, such films can be regarded as transducers for specific parameter sensing.

(6) Fabry-Perot

Fabry–Perot interferometer or etalon is typically made of a transparent plate with two reflecting surfaces, or two parallel highly reflecting mirrors. (Precisely, the former is an etalon and the latter is an interferometer, but the terminology is often used inconsistently.) Its transmission spectrum as a function of wavelength exhibits peaks of large transmission corresponding to resonances of the etalon. The varying transmission function of an etalon is caused by interference between the multiple reflections of light between the two reflecting surfaces. Constructive interference occurs if the transmitted beams are in phase, and this corresponds to a high-transmission peak of the etalon. If the transmitted beams are out-of-phase, destructive interference occurs and this corresponds to a transmission minimum.

Fabry–Perot structure can also be used as sensing platform in fiber-optic sensing technology [17]. Such Fabry–Perot structure can be realized nano-film deposition on fiber tip, when such thin film-based Fabry–Perot structure is achieved, there exists interference fringes in the reflected spectrum. The reflected interference fringes are very sensitive to the change of optical path deviation, which is dependant on the thin films. So the sensitive thin films can therefore be regarded as transducers.

Micro- and nano-fiber [18] is kind of fiber with diameter in tens of micro- or nano-scale. Such fibers itself are sensitive to surrounding environment, when nano-film is integrated with these platform, novel sensors can be expected. Also the so-called "hybrid fiber [19]" is kind of photonic crystal fiber with some specific holes filled with other materials, such as liquid crystal, semiconductor, metal or dielectric material. This platform is another area for novel fiber-optic sensor development.

The combination of fiber optics with nano-structure technologies and sensitive thin films offers great potential for the realization of novel sensor concepts. Minitured optical fiber sensors with thin films as sensitive elements could open new fields for optical fiber sensor applications. Thin films work as sensitive elements and transducer to get response and feedback from environments, optical fiber here are employed to work as signal carrier. Figure 2 shows some examples of thin films or coatings as sensitive elements for constructing novel sensor concepts. This chapter reviews some research work on the topic of fiber-optic sensors based on sensitive thin films, which are developed the National Engineering Laboratory for Fiber-Optical Sensing Technology (NEL-FOST) in Wuhan University of Technology (WUT), China in recent years. In Sect. 2, Optical fiber hydrogen sensors based on WO_3-Pt thin film on fiber tip will be reported, and Sect. 3 presents the latest development on optical fiber relative-humidity sensors with dielectric coatings as sensing elements. In Sect. 4 sapphire fiber-based high-temperature sensors

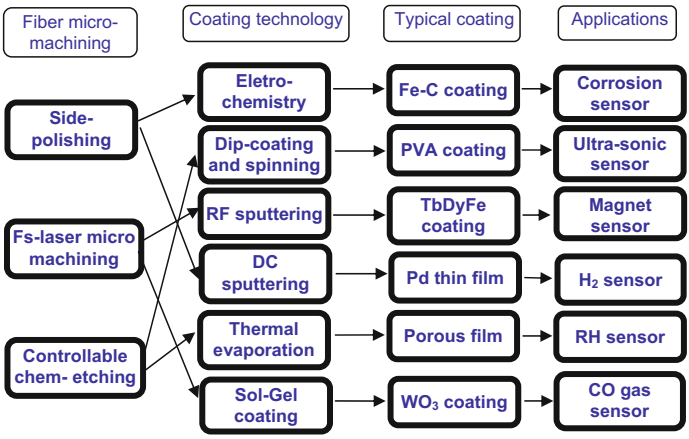

Fig. 2 Novel sensor concepts based on thin films or coatings

with dielectric multilayer F-P structure will be reviewed. Finally this chapter is concluded with discussion and future outlook.

2 Optical Fiber Hydrogen Sensors Based on WO_3-Pd Thin Film on Fiber Tip

Hydrogen is a promising candidate for the next generation energy and is regarded as the backbone of future energy systems based on renewable and sustainable resources. Hydrogen is highly explosive in the presence of oxygen with wide flammability range of 4–75 volume percentages in air, its timely detection and alarming is of great importance as a safety concern. Monitoring of hydrogen concentration is also essential to nuclear reactor and space applications, coal mine operations, medical diagnostics, environment pollutions and many other industrial processes. Therefore the development of reliable, sensitive and inexpensive hydrogen sensors is very important. Conventional hydrogen sensors based on metal-oxide electrochemical reaction are usually bulky and suffer from poor selectivity and cross-sensitivity. The commercially-available electrochemical hydrogen sensors operate mostly at high temperatures of 100–300 °C, due to the possibility of generating electric sparks, these electrochemical hydrogen sensors could be combustion sources in high hydrogen concentration, and therefore is not intrinsic safe. New proposal of solutions for hydrogen concentration sensing and metrology is always welcome, especially for the case of optical measurement, which shows inherently safe nature when compared to other techniques that require electrical contacts.

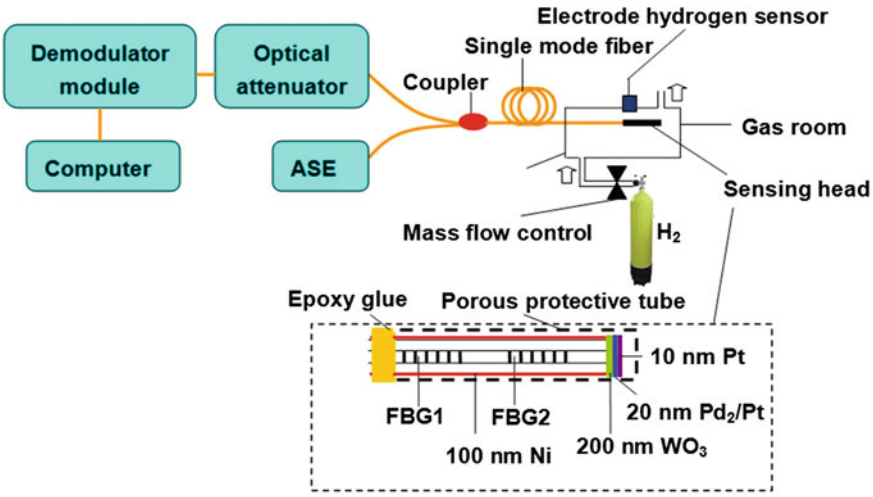

Fig. 3 Concept and configuration of optical fiber hydrogen sensing system

Optical fiber hydrogen sensing has attracted intensive research interests due to its potential as next generation of hydrogen sensor. At present there are several kinds of optical fiber hydrogen sensors, such as evanescent sensor [20], micro-mirror sensor [21, 22], interference sensor [23], surface plasmon resonance sensor [24], and fiber Bragg grating sensor [25, 26]. However, resolution of optical fiber hydrogen sensor is still much lower when compared to conventional electrode hydrogen sensor. Improvements are still required to ensure hydrogen sensitivity down to ppm level.

Fiber Bragg grating (FBG) pair with high-low reflectivity is employed for hydrogen sensing and measurement as shown in Fig. 3. FBG with different reflectivity can be prepared by controlling the exposure time to excimer laser [27]. The peak intensity of high reflective FBG (FBG1), which is hardly influenced by the hydrogen sensitive film, is used as reference. While the peak intensity of low reflective FBG (FBG2), which is sensitive to the reflectivity of hydrogen coating deposited on the tip of optical fiber, is employed as element for hydrogen characterization.

WO_3 film has good gasochromic effect when Pd or Pt film is employed as catalyst layer. Pd film has good selectivity towards hydrogen and Pt has good stability in air. In this work WO_3 thin film and Pd/Pt composite films are selected as sensitive and catalyst layer, respectively. WO_3-Pd/Pt composite films were deposited on the end-face of singe mode fiber as sensing element.

Figure 4 is the SEM image of the sensing head. There are some dusts and defects on the edge of single mode fiber tip, which is due to improper operation during the testing. However, the morphology of film deposited on single mode fiber core looks uniform after hydrogen response, demonstrating the good stability of WO_3-Pd-Pt multilayer.

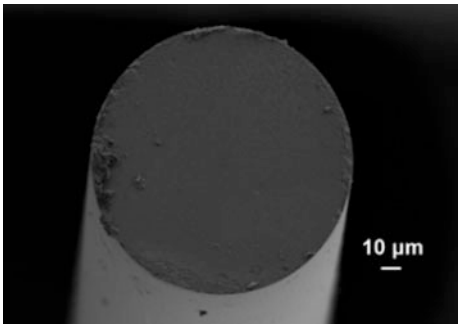

Fig. 4 Proposed coating of WO_3-Pd-Pt multilayer on fiber tip

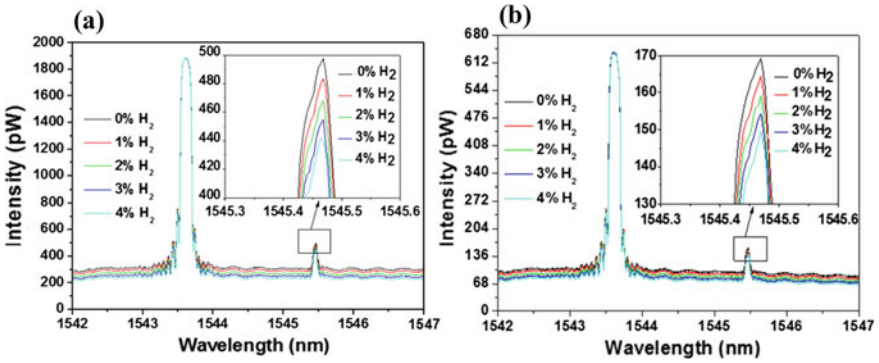

Fig. 5 Reflective spectrums of single mode fiber inscribed with two FBGs under different hydrogen concentrations **a** before and **b** after the bending of the single mode fiber

Figure 5 depicts the hydrogen response of the sensor under different hydrogen concentrations. The peak intensity of FBG2 gradually decreases when hydrogen is flowing into gas room, which is more quickly and obviously with the increase of hydrogen concentrations. The peak intensity of FBG1 hardly changes, which shows a good reference element. When hydrogen concentrations are 1, 2, 3, and 4 %, decrease of I_2/I_1 are 0.0072, 0.0076, 0.0065, 0.0063, respectively. The response time of the hydrogen sensor for 1 % H_2 is about 70 s, which is longer than that of hydrogen sensor in the previous work [28]. The longer response time of hydrogen sensor can be attributed to the thicker catalyst layer and lower ambient temperature. As shown in Fig. 5b, the hydrogen characterization of the sensor is explored when the optic fiber is interrupted. After bending the single mode fiber, the peak intensity of two FBGs is nearly 1/3 of its initial value, and the hydrogen sensor shows 0.0070, 0.0073, 0.0068, and 0.0062 towards 1, 2, 3 and 4 % hydrogen, respectively. Although the optic power in the fiber is greatly reduced, the hydrogen sensor shows good hydrogen responsibility. Therefore, the hydrogen sensor shows good anti-interference capability during the hydrogen response.

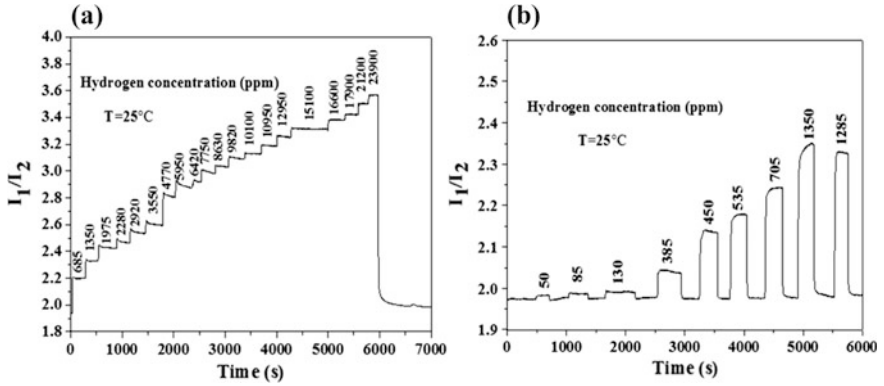

Fig. 6 **a** Response of the hydrogen sensor under continuous increase of hydrogen concentrations in the lower range; **b** several cycles under different hydrogen concentrations down to ppm level

Figure 6a shows the hydrogen response of the hydrogen sensor under continuous increase of hydrogen concentrations. When hydrogen is injected into gas room, the reflectivity of the hydrogen sensitive film decreases quickly, resulting in the lower peak intensity of FBG2. However, the peak intensity of FBG1 hardly changes due to its high reflectivity. Therefore, the value of I_1/I_2 increases quickly with the increase of hydrogen concentration in the gas room. The response time for hydrogen sensor is no more than 20 s at room temperature of 25 °C. The quick response rate of the hydrogen sensor can be attributed to the high optical power focused on the core of single mode fiber. Ou et al. [22] reported that WO_3/Pd film had a quick response rate and better sensitivity when heating at a higher temperature. By utilizing ASE as light source, the hydrogen sensitive film deposited on the fiber core can be maintained at higher temperature. Compared to previous reported optical heating system [28], the power of light source used in this work is much lower, but with a higher heating efficient. Therefore, the hydrogen sensor has good performance during hydrogen characterization. The hydrogen sensor shows better sensitivity towards lower hydrogen concentration, which can be found from Fig. 6b. The hydrogen sensor shows a non-linear hydrogen response, which is similar to the reported work [22]. The reason for this phenomenon is due to the excellent hydrogen responsibility of WO_3-Pd/Pt composite film under higher temperature.

A novel optical fiber hydròogen sensing system which can detect hydrogen as low as 50 ppm at room temperature of 25 °C has been demonstrated. The hydrogen sensor has a quick response during the hydrogen characterization, and the sensor show better sensitivity towards lower hydrogen concentrations. Further improvements, such as optimization of hydrogen sensitive film, utilization of more stable ASE light source and high-low FBGs with smaller wavelength difference, can be conducted to improve the performance of the hydrogen sensor.

3 Optical Fiber Relative-Humidity Sensors with Dielectric Coatings as Sensing Elements

Humidity measurement and control is of great importance in many application fields such as meteorological services, biomedical device, food and electronic processing, chemical gas purification. While fiber-optic sensors have many distinctive characteristics such as small size, flexibility and immunity to electromagnetic interference, there were extensively investigations on optical fiber humidity sensing techniques in the past decades. Optical fiber humidity sensing techniques were extensively investigated utilizing long period gratings [29], tilted fiber Bragg's grating [30], U-bend [31], hetero-core optical fiber [32]. The principle of these humidity sensors rely on the use of the moisture sensitive material to generate secondary effects such as refractive index change or strain on the sensing fiber that result in the shift of output spectra or change in intensity. However, these sensors are expensive, low sensitive and fragile. Therefore, there is a constant need to develop a compact optical fiber humidity sensing system with high reliability, high sensitivity and low cost.

Fabry–Perot interferometer (FPI) is an important technique used for sensing. Different from other fiber interferometric sensors (Match-Zehnder, Michelson and Sagnac), the Fabry–Perot structure is stable and robust since there is no fiber couplers and movable components. In addition, fiber Fabry–Perot interferometric sensors are extremely sensitive to perturbations that affect the optical path difference of sensing region between two reflective mirrors [33].

The refractive index and polarization in an optical humidity sensor are generally explained by the adsorbed water on the metal oxide surface, and also by the capillary water condensation within the pores [34–37], both of these processes are conducive of the existence of a porous structure. Two types of water molecules adsorption take place: in the beginning chemisorption, followed by physisorption.

The water molecules are chemisorbed through a dissociative mechanism [38, 39]. For the case of TiO_2, two surface hydroxyls per water molecule are formed: the hydroxyl group adsorbing on a surface Ti^{4+} ions and the proton forming a second hydroxyl with an adjacent surface O^{2-} ion shown in Fig. 7a, b; for the case of SiO_2, water adsorption is similar to TiO_2.

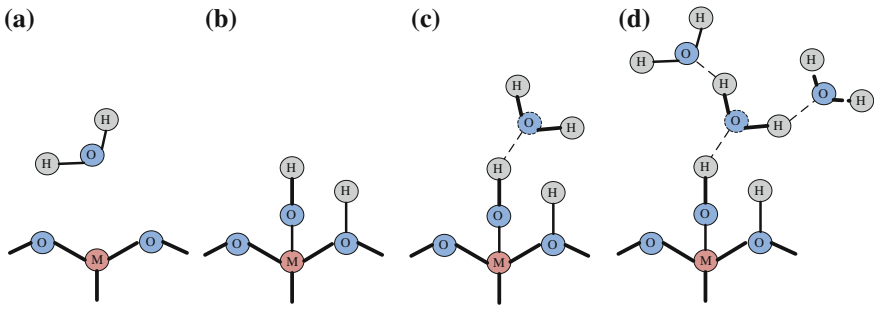

Fig. 7 Water vapor adsorption on metal oxide coating surface

The coordinative unsaturated metal cations, M^+, and oxygen anions, O^{2-}, at the surface facilitate the dissociation of water vapour in the vicinity of the surface (a) into a hydroxyl group, which binds to a metal cation site, and a proton, which binds to an oxygen anion site (b). Once surface hydroxylation is present, water vapour is physisorbed through double hydrogen bonds shared with two surface hydroxyl groups (c). Upon completion of this first physisorbed layer, subsequent layers are adsorbed via single hydrogen bonds (d). The broken lines represent hydrogen bonds.

Thus the initial chemisorbed layer is tightly attached to the surface grains. Once formed, it is no further affected by exposure to humidity. Desorption of the chemisorbed layer only takes place at higher temperatures. As relative humidity (RH) increases, an additional layer of water molecules starts to be formed on the chemisorption one. Many more physisorption layers will be joined as humidity gets higher [40]. With more than one layer of physisorption water molecules, water starts to be condensed into the capillary pores. The pore is filled or unfilled according to its radius and the thickness of the physisorption layer, which depends on the magnitude of the relative humidity. Increasing RH, the thickness of the physisorption layer of water gets bigger which leads to the filling of successively higher diameter pores, according to the prediction of Kelvin equation [41]. Figure 7 illustrates the adsorption mechanism from initial surface hydroxylation through to multi-layer physisorption.

The dielectric films deposited by e-beam evaporation have columnar and porous structures [35, 36]. Thus the effective refractive index (RI) and porosity of porous layer can be calculated in the framework of the Bruggeman effective medium model [42, 43]. The Bruggeman equation for the three-component (water, cylindrical oxide, and air) system as follows:

$$(1-f)\frac{n_{xo}^2-n_{eff}^2}{n_{xo}^2+2n_{eff}^2}+(f-V)\frac{n_{air}^2-n_{eff}^2}{n_{air}^2+2n_{eff}^2}+V\frac{n_{H_2O}^2-n_{eff}^2}{n_{H_2O}^2+2n_{eff}^2}=0 \quad (1)$$

where f is the porosity of the coating. V, which is dependent on RH, means the volume percentage of liquid water in coating as the influence of capillary condensation. n_{xo} is the refractive index of the metal oxide, n_{air} presents the refractive index of the air, n_{H2O} is the refractive index of the liquid water. As the TiO_2 and SiO_2 porous coating absorbs (or releases) water molecules from air, V increases, while the refractive index (n_{eff}) increases (or reduces).

The miniature optical fiber humidity sensing probe is consisted of three-layer optical thin films deposited on a multimode fiber (MMF: 62.5 μm/125 μm) tip as shown in Fig. 8. The first and third layers are TiO_2 coatings, which are employed as mirror layers. A thick SiO_2 coating is used as main sensing layer in the Fabry-Perot structure.

There are four reflection surfaces in the fiber sensor head, and the reflection coefficients and transmission coefficients are r_1, r_2, r_3, r_4, and t_1, t_2, t_3, t_4, respectively. Transmission loss factors in the three films are α_1, α_2, and α_3. Lengths of

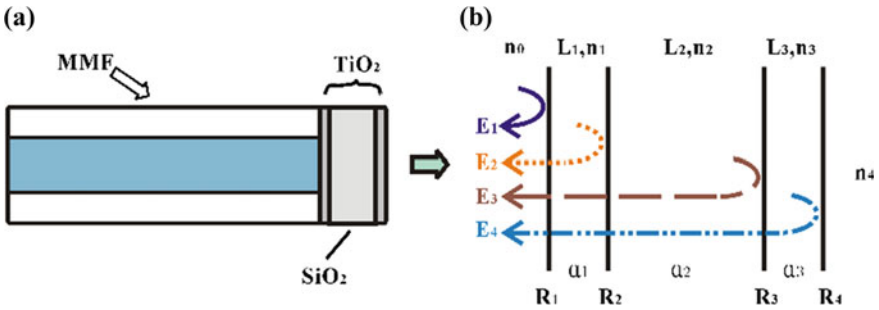

Fig. 8 **a** Structure of the sensor head, and **b** the reflection model

these three physical cavities are L_1, L_2, and L_3. The RIs of fiber, first film, second film, third film, and air are n_0, n_1, n_2, n_3, and n_4, respectively. According to Fresnel formula, $r_x = (n_x - n_{x-1})/(n_x + n_{x-1})$, $t_x = 2n_{x-1}/(n_x + n_{x-1})$, $t_x' = 2n_x/(n_x + n_{x-1})$, while x = 1, 2, 3, 4. Considering the low reflection coefficients, higher-order reflections from these surfaces can be ignored. As a result, the normalized total reflected intensity (I) is given as follows, [44, 45].

$$
\begin{aligned}
&E_1 = r_1 E_0 = A_1 E_0 \\
&E_2 = (1-\alpha_1) r_2 t_1 t_1' \exp\left(-j\frac{4\pi n_1 L_1}{\lambda}\right) E_0 = A_2 \exp\left(-j\frac{4\pi n_1 L_1}{\lambda}\right) E_0 \\
&E_3 = (1-\alpha_1)(1-\alpha_2) r_3 t_1 t_2 t_1' t_2' \exp\left[-j\frac{4\pi(n_1 L_1 + n_2 L_2)}{\lambda}\right] E_0 = A_3 \exp\left[-j\frac{4\pi(n_1 L_1 + n_2 L_2)}{\lambda}\right] E_0 \\
&E_4 = (1-\alpha_1)(1-\alpha_2)(1-\alpha_3) r_4 t_1 t_2 t_3 t_1' t_2' t_3' \exp\left[-j\frac{4\pi(n_1 L_1 + n_2 L_2 + n_3 L_3)}{\lambda}\right] E_0 \\
&\quad = A_4 \exp\left[-j\frac{4\pi(n_1 L_1 + n_2 L_2 + n_3 L_3)}{\lambda}\right] E_0
\end{aligned}
\tag{2}
$$

Thus,

$$
\begin{aligned}
I &= \frac{(E_1 + E_2 + E_3 + E_4)(E_1 + E_2 + E_3 + E_4)^*}{E_0 E_0^*} \\
&= A_1^2 + A_2^2 + A_3^2 + A_4^2 + 2A_1 A_2 \cos\left(\frac{4\pi n_1 L_1}{\lambda}\right) + 2A_1 A_3 \cos\left[\frac{4\pi(n_1 L_1 + n_2 L_2)}{\lambda}\right] \\
&\quad + 2A_1 A_4 \cos\left[\frac{4\pi(n_1 L_1 + n_2 L_2 + n_3 L_3)}{\lambda}\right] + 2A_2 A_3 \cos\left(\frac{4\pi n_2 L_2}{\lambda}\right) \\
&\quad + 2A_2 A_4 \cos\left[\frac{4\pi(n_2 L_2 + n_3 L_3)}{\lambda}\right] + 2A_3 A_4 \cos\left(\frac{4\pi n_3 L_3}{\lambda}\right)
\end{aligned}
\tag{3}
$$

where, E_0 is the original electric field coupled into the sensor. E_1, E_2, E_3, E_4 are the reflected electric fields of the four reflection surfaces, while A_1, A_2, A_3, A_4 stand for the complex amplitude coefficients of reflected electric fields.

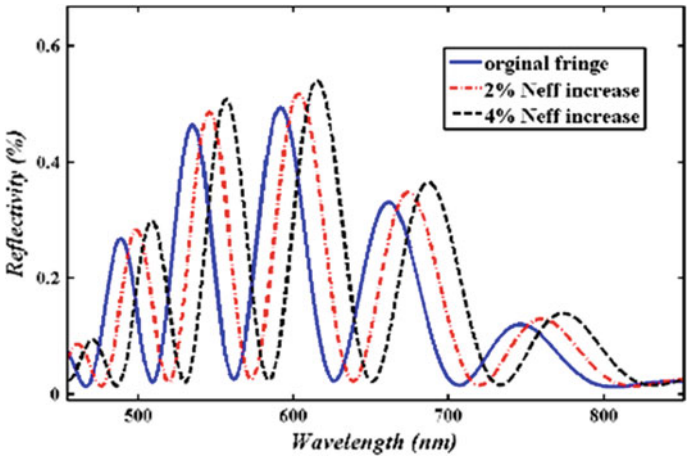

Fig. 9 Theoretical simulation of interference fringe shift

As the parameters L_1, L_2, L_3, n_0, n_4, α_1, α_2, and α_3 can be regarded as constants [44], I is mainly related to n_1, n_2, n_3 in Eq. (3), while n_1, n_2, n_3 are related to RH in Eq. (1). Therefore, the RH can be obtained by measuring the reflection spectrum.

In general, the sensing mechanism is based on the change of reflected interference spectrum when water molecules are absorbed in the porous oxide coating, the absorption of water molecules in coating means the change of effective refractive index, as result this will shift the interference fringe. Figure 9 shows the theoretical simulation of interference fringe shift of the proposed three-layer F-P structure when the effective refractive index have 2 and 4 % increase. The third interference fringe dips are located at 561.5, 573 and 584.5 nm respectively in case of original fringe, 2 and 4 % of effective refractive index increase. It means 11.5 and 23 nm of characteristic wavelength drift exist when effective refractive index increase 2 and 4 % compared to the original fringe.

For the sensitive films preparation, multimode fiber tip was firstly rinsed in alcohol, acetone and deionized water for three times in an ultrasonic cleaner to remove surface contamination, and then was put into vacuum evaporation coating machine. The three-layer FPI structure was manufactured on multimode fiber tip by e-beam evaporation, which showed in Fig. 10. A ZZS1100-8/G Box-type vacuum coating system (RANKUUM MACHINERY LTD) was employed for the coating deposition. The multimode fibers were mounted inside the evaporation chamber with their polished tips pointing down toward the source material. $TiO_2/SiO_2/TiO_2$ films were deposited on the fiber tips. It is possible to control the structural and morphological properties of the deposited thin film by optimization of deposition process parameters [34, 46]. The optimum deposition process is proved as: 0.029 Pa, oxygen (O_2) with a velocity of 160 sccm is supplied as procedure gas, the fiber sample baking temperature is set at 120 °C. The first and third layers are 225 nm TiO_2 film with deposition rate of 0.25 nm/s, while the second layer is

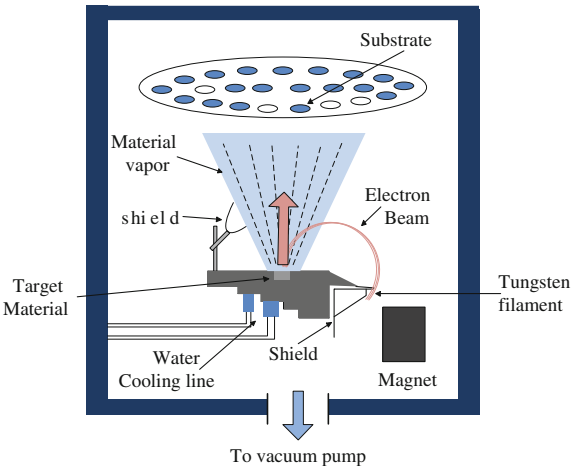

Fig. 10 E-beam evaporation system used for oxide thin film deposition on fiber tip

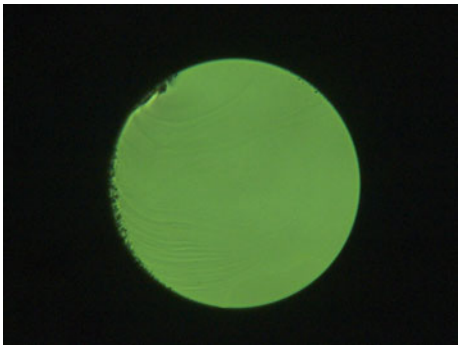

Fig. 11 Proposed coating of $TiO_2/SiO_2/TiO_2$ multilayer on fiber tip

1600 nm SiO_2 film with deposition rate of 0.5 nm/s, and without ion-source assistance.

Fiber tip deposited coating of $TiO_2/SiO_2/TiO_2$ multilayer is showed in Fig. 11. The morphology of film deposited on multimode fiber core looks uniform, demonstrating the good stability of the coating.

Micro-structure of the deposited multilayer samples were investigated by scanned scanning electron microscope (SEM) as shown in Fig. 12. It can be clearly demonstrated that the coating are porous in micro-structure, and the pore size is between 0.01–0.2 μ dependent on the deposition process.

The experimental set-up shown in Fig. 13 consists of a broadband light source (HL-2000 Tungsten Halogen Light Sources from Ocean Optics, wavelength range: 360–2500 nm), miniature fiber spectrometer (S3000-VIS Micro Spectrometer made from Seeman Technology, wavelength range: 320–1050 nm, wavelength resolution: 0.3 nm), multimode optical fiber coupler and the proposed F-P sensor probe working in reflection mode. During sensing characterization experiments, the light

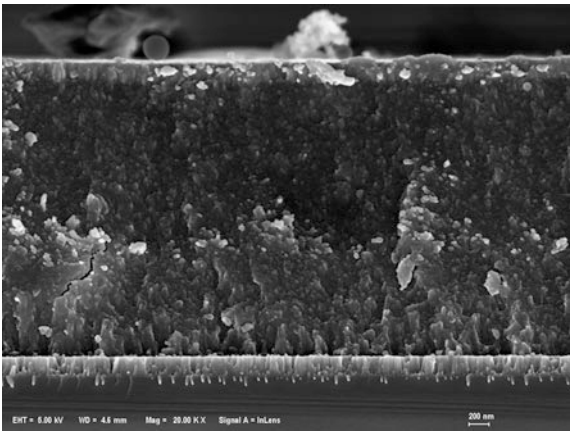

Fig. 12 SEM image of the section of the $TiO_2/SiO_2/TiO_2$ coating

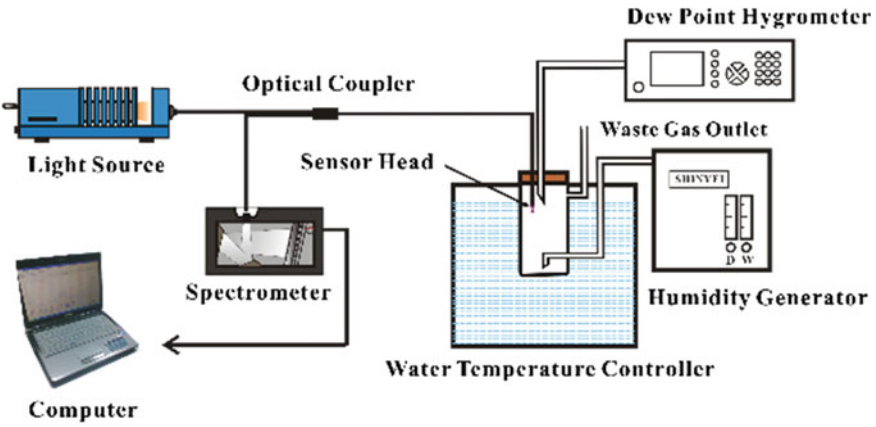

Fig. 13 Experimental set-up of the moisture measuring system

emitted from the Tungsten Halogen broadband light source goes to the optical coupler, one output port is connected to the fiber spectrometer for measuring and recording the reflected optical spectrum, while the second output port is fusion spliced with the fabricated RH sensor.

The fiber-optic humidity sensor was enclosed in an accurate humidity generator (Model SRH-1 made by SHINYEI, Japan) with a high performance dew point hygrometer for calibration. The relative-humidity (RH) can be varied from 1.6 % RH up to 90 % RH with control accuracy at 0.1 % RH. To investigate the cross-sensitivity to temperature, the fiber sample was also tested under different temperatures.

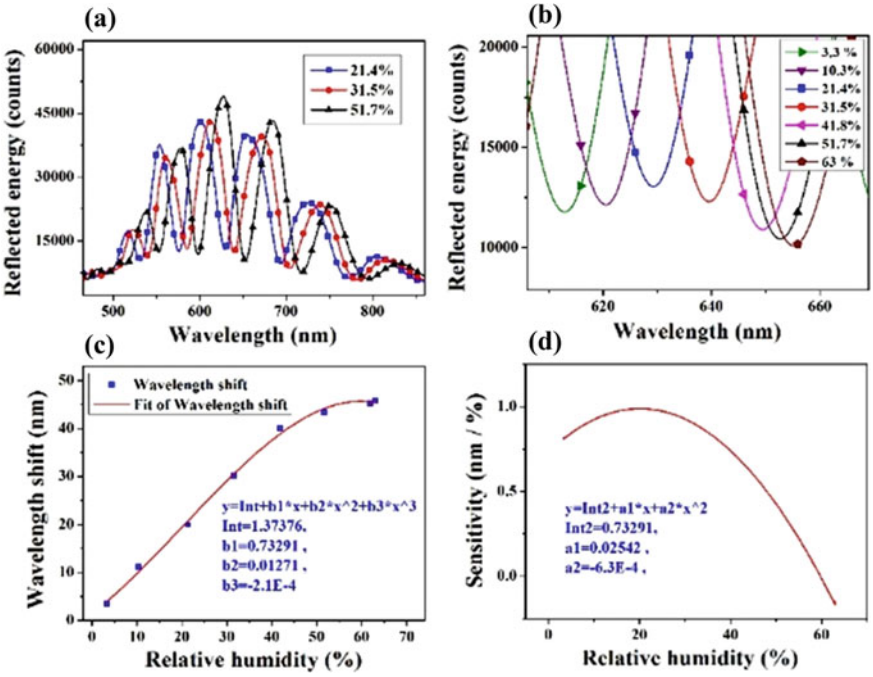

Fig. 14 Humidity sensing properties of the probe with optimum process

Figure 14 shows the spectra data of sample with optimum process, measured by the miniature fiber spectrometer (time of exposure of 510 ms, time sampling interval of 5 ms, spectrum smooth degree of 10) under different RH levels. In Fig. 14a, four spectral dips of minimum reflectivity exist in the spectral region, since the wavelength position of minimum reflectance will be drifted by the effective refractive index change of coating material due to the absorption and desorption of water molecular. Figure 14b shows the detailed view of the dip range of 605–660 nm. It can be observed that the interference fringe shows red-shift when the RH increases, which corresponds to an increase of effective refractive index of the sensing films. The shift of characteristic wavelength to different RH levels are plotted in Fig. 14c, and it can be found that the sensor shifted 42.3 nm when RH increased from 3.3 to 63 % RH. The average humidity sensitivity of proposed sensor is 0.7 nm/%RH approximately. Moreover, it can be concluded that the fiber-optic humidity sensor is more sensitive at lower RH level, whereas its wavelength shift at higher RH level is not apparent. This can be understood with the fact the micro-pore absorbs water molecules due to capillary condensation effect, while at higher RH level, the micro-pore is easy to be saturated.

A key issue to manufacture the fiber-optic humidity sensor is to realize and control the porous structure in the oxide films. A series of contrast experiments were carried out to explore the appropriate process for improving the sensing

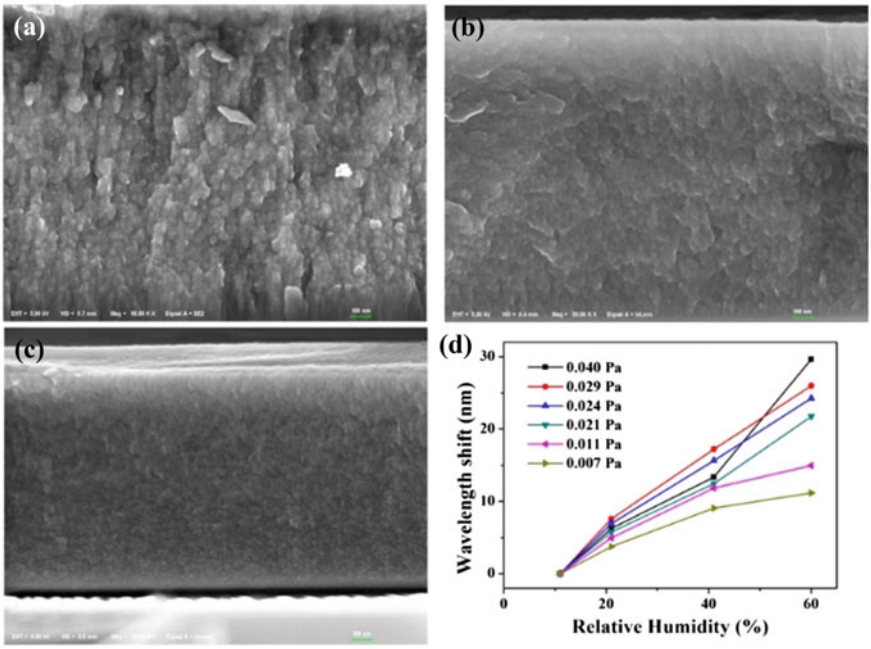

Fig. 15 SEM micrographs of the films deposited in vacuum of **a** 0.029 Pa, **b** 0.011 Pa, and **c** 0.007 Pa, and **d** the wavelength shift of probes

performance. SEM micrographs of the section of the films deposited in vacuum of 0.029, 0.011, and 0.007 Pa are presented in Fig. 15a, b, c respectively. All of them exhibit quasi-reticulated porous structures, with micro-pore dimensions around 10–200 nm. The change in the vacuum degree seems to cause a major change in morphology: the higher air pressure (in a certain range) makes the film more voids and the dimensions of voids bigger. As explained in the previous section, the more porosity causes a higher sensitivity to RH, shown in Fig. 15d. Then, with the large aperture gaps dominated in the film, the film starts to be sensitive to high humidity (40–60 % RH), which is consistent with the exception of the sensor utilizing the film grown at 0.04 Pa.

Similarly, the influence of base temperature on sensor sensitivity is shown in Fig. 16. Sample 1, 2 were deposited in the base temperature of 200 °C, while sample 3, 4 in 150 °C, sample 5, 6 in 120 °C, with the other process as 0.029 Pa, no ion source. In the range from 100 to 200 °C, the sensitivity was reduced for sensors using films deposited at higher based temperature.

Humidity sensitivity of the sensors when manufactured with the different manufacture condition are show in Fig. 17. First of all, the column diagram of a represent that the sensing layer is porous TiO_2 film of 1200 nm, which is processed with 50/0 sccm inflating volumes (0.011 Pa); Next, the (b) is the porous SiO_2 film of 1621 nm with ion-assisted deposition in 0.011 Pa; and the (c) shows the

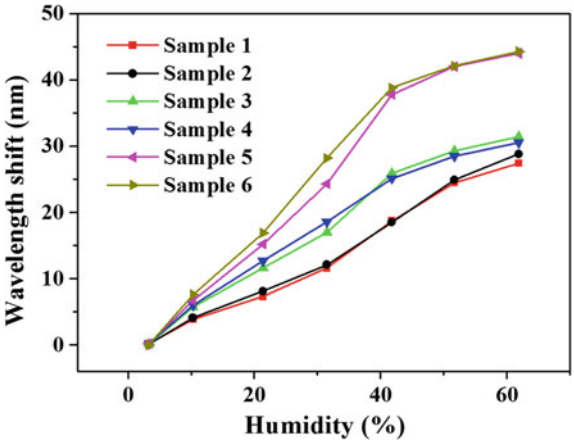

Fig. 16 Wavelength response for probes coated with multilayer films deposited at different base temperature: sample 1, 2, 200 °C; sample 3, 4, 150 °C; sample 5, 6, 120 °C

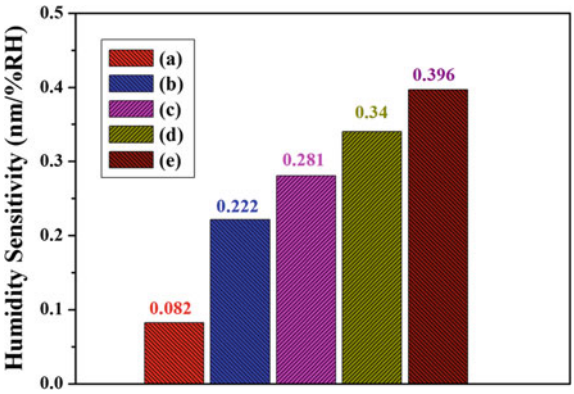

Fig. 17 Humidity sensitivity with different processes: **a**, porous TiO_2 film as the sensing layer, 1200 nm, 0.011 Pa; **b**, porous SiO_2 film, 1621 nm, 0.011 Pa, with ion-assisted deposition; **c**, porous SiO_2, 1200 nm, 0.011 Pa; **d**, porous SiO_2, 2078 nm, 0.011 Pa; **e**, porous SiO_2, 1200 nm, 0.024 Pa

character of porous SiO_2 film of 1200 nm, deposited in 0.011 Pa; The (d) is the same with (c) except of the thickness of the films with 2078 nm; The (e) have no difference with (c) except the vacuum degree of 0.024 Pa. In contrast with (c), the sensitivity of SiO_2 film (a) is higher than TiO_2 with the same process. Furthermore, when comparing (b) with (c), (d), the process of ion-assisted deposition decrease the sensitivity of probe.

Cross-sensitivity to temperature was investigated as for the proposed F-P fiber-optic humidity sensor. Characteristic wavelength shifts of the fiber sample at different RH levels were tested under 15, 25 and 35 °C respectively. Figure 18 shows the temperature effect to the humidity measurement. It can be concluded that the temperature cross-sensitivity is rather low, the characteristic wavelength shift is less than 2 nm within 20 °C of temperature change, while the change is typically more than 20 nm when RH level changes from 20 % RH to 60 % RH.

Experiments on sensing repeatability and consistency were also investigated; the sensing experiments have been repeated over 4 times in order to investigate the

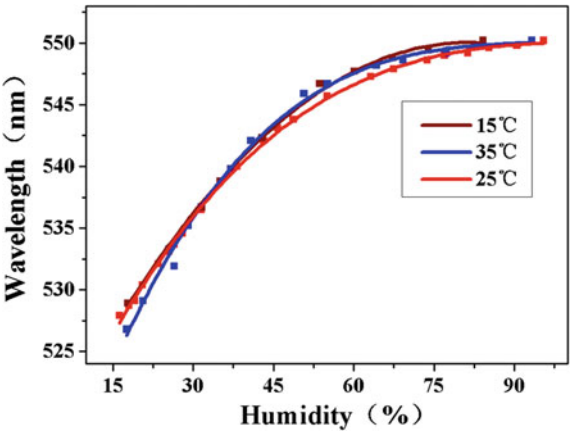

Fig. 18 Temperature effect to the humidity measurement

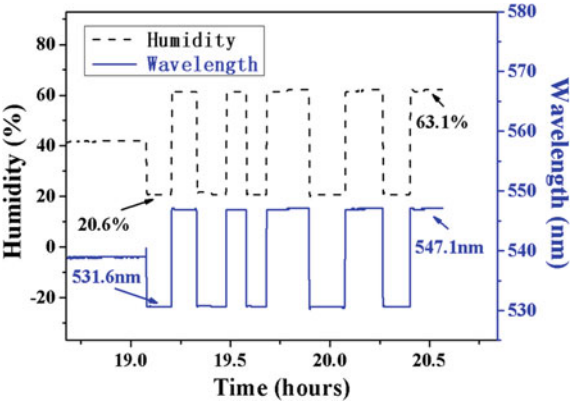

Fig. 19 Repeatability of proposed probes between 20.6 % RH and 63.1 % RH

measurement repeatability and long-term stability. Wavelength shifts of the proposed sensor under different humidity levels in both ascending and descending phases are shown in Fig. 19. The response time is less than 5 s and stability of the proposed sensor was proved to be good.

The F-P fiber optic humidity sensor with porous oxide coatings as sensitive materials is proposed and improved. The sensing elements are multilayer porous films deposited on fiber tip by e-beam evaporation. Experimental investigation on humidity response shows that the wavelength shift can reached 42.3 nm when RH ranges from 3.3 to 63 % RH. The average humidity sensitivity of proposed sensor is 0.7 nm/%RH approximately. However, a series of contrast experiments about vacuum degree, baking temperature etc. were conducted to explore the appropriate process for improving the sensing performance. The cross-sensitivity to temperature change is rather low. The proposed dielectric film based fiber-optic humidity sensor is very promising for application, especially for the low and middle humidity (0–50 % RH).

4 Sapphire Fiber-Based High-Temperature Sensors with Dielectric Multilayer F-P Structure

Optical fiber high-temperature sensing have been reported by means of femtosecond laser technique [47, 48], focused ion beam machining in single-mode fiber taper tips [49, 50] and fiber fusion splicing technique. Fabry-Perot Interferometer structures by fusion splicing single-mode fiber or multimode fiber to photonic crystal fiber [51–54], sandwich a section of hollow-core photonic band-gap fiber or multimode fiber between single-mode fiber [55, 56] were developed. Complicated fabrication process, poor reproducibility, possible mismatch between different parts and difficulty in precise control of the cavity length are disadvantages of these interferometer fabricating techniques. Therefore, compact optical fiber high-temperature sensing system with high reliability, simplicity and low cost is desired.

Among all the schemes proposed in the past decades, Fabry-Perot Interferometer (FPI) sensors are particularly attractive for high temperature sensing owing to their large dynamic range, high resolution, and high accuracy. Optical fiber FPI for high temperature sensing have been reported by means of femtosecond laser technique, focused ion beam machining in single-mode fiber taper tips and fiber fusion splicing technique. These interferometer fabricating techniques have some disadvantages such as complicated fabrication process, poor reproducibility, and mismatch between different parts. Therefore, there is a need to develop a new kind of optical fiber high-temperature sensor with high reliability. Thin films at the end of fiber act as an FPI for high temperature sensing were discussed [57, 58]. The application of evaporative deposition techniques is compatible with batch processing, and the inherent smoothness and parallelism of thin-film FPI sensor makes it ideally suited for interferometric interrogation. FPI based on multilayer coatings by Physical Vapor Deposition (PVD) at the end of commercial MMF for high temperature sensing have been reported [59].

Multilayer coatings of dielectric oxide deposited on sapphire fiber tip acting as an FPI for high temperature sensor have been proposed and experimentally demonstrated in this work. Single-crystal sapphire was used for its high melting point (approximately 2054 °C), superior mechanical properties, excellent chemical resistance in corrosive environments, and high hardness [60]. The proposed sensor has miniature size, simple physical structure, and mechanical stability.

A section of 20 cm sapphire fiber with 75 μm outer diameter was firstly double side polished, then rinsed in alcohol, acetone and deionized water for three times in an ultrasonic cleaner to remove surface contamination before putting into vacuum evaporation coating machine.

A Box-type vacuum coating system showed in Fig. 10 was employed for the coating deposition. The sapphire fibers were mounted inside the evaporation chamber with their polished tips pointing down toward the source material. ZrO_2/Al_2O_3/ZrO_2 (ZAZ) films were deposited on the sapphire fiber tips with ion-assisted PVD process. The basic vacuum was set at 1.0×10^{-2} Pa with filling procedure gas of oxygen (O_2) at a flow velocity of 50 sccm. Under 200 °C baking temperature, the

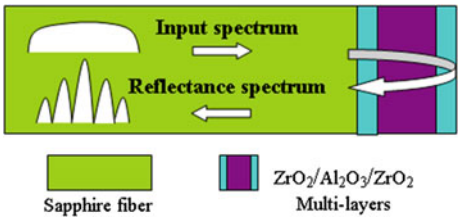

Fig. 20 Schematic of a thin film temperature sensor on sapphire fiber

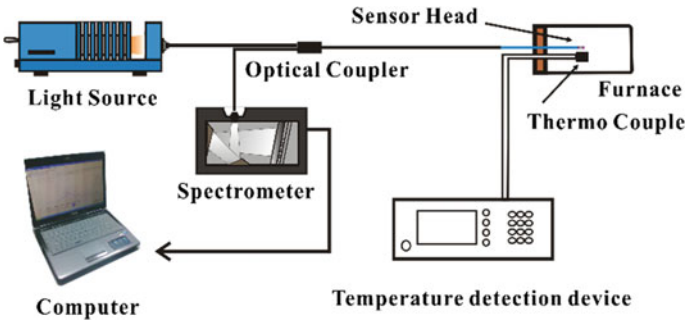

Fig. 21 Measurement and calibration system configuration of the proposed sapphire fiber temperature sensor with multilayer coating on tip

deposition rate for ZrO_2 and Al_2O_3 was 2.5 and 3.5 Å/s respectively. The first layer deposited at the end of the fiber was 204 nm of ZrO_2, followed with 1348 nm of Al_2O_3 and 204 nm of ZrO_2 as the third and the last layer. Figure 20 shows the schematic diagram of the sensing probe.

Alumina (Al_2O_3) and Zirconium dioxide (ZrO_2) were selected as lower and higher refractive index (RI) materials to generate the lower-higher-lower structure. As to a pile of thin dielectric films, the parallel layer structure of the coatings form a multiple beam FPI. Here, instead of single layer, the multilayer coating is employed to optimize the reflected spectrum, i.e. to enhance the contrast of interference spectrum, therefore to improve visibility of interference fringe and to adjust the center wavelength of the reflection in the range of 550–650 nm [61].

The high temperature measurement and characterization system is schematically shown in Fig. 21. A miniature broadband tungsten halogen lamp TLS (HL-2000, Ocean Optics), miniature fiber optic spectrometer (Ocean Optics, USB-2000, wavelength resolution: 0.3 nm), a 3 dB multimode optical fiber coupler are employed to interrogate the thin film temperature sensor. The non-coating end was spliced to a 105/125 μm MMF pigtail and connected to the optical interrogation system.

Light from TLS illuminates the multilayer sensor through the OC, the reflected signals from the interfaces of the ZAZ structure interfere with each other and

generate fringes to be detected by the miniature spectrometer, which is connected to the other arm of the optical coupler. Finally the sensing data were serially transferred to a computer for further data evaluation. The frequency of the interference fringe is governed by the optical path difference (OPD) of the multilayer coating dielectric film.

Variations in temperature will cause both the thickness d and refractive index of the coatings n to change due to thermo-optic and elastic-optic effect. Supposed the surrounding temperature changes from T_0 to T, the OPD of the thin film FPI can be described as Eq. 4.

$$\begin{aligned} \frac{OPD(T)}{OPD(T_0)} &= \frac{2n(T)d(T)}{2n(T_0)d(T_0)} \approx 1 + (\alpha_n + \alpha_d)\Delta T \\ OPD &\equiv 2nd \\ \Delta T &= T - T_0 \end{aligned} \tag{4}$$

Here α_n and α_d are the 1st order thermal coefficients for the refractive index and the physical thickness, respectively. So the OPD change, i.e. ΔOPD of the thin film FPI can be expressed by

$$\Delta OPD / OPD_0 \approx (a_n + a_d)\Delta T \tag{5}$$

As can be concluded from Eq. 5, with the ambient temperature increases, the sensor's ΔOPD becomes larger. The responsibility of the thin film sensor is decided by the material property of the oxide coating and is independent of the initial OPD of thin film sensor.

The changes in OPD result in a shift of the interference spectrum. Wavelength-tracking was used to measure OPD change [62] from the interference spectrum. In this way correlation of temperature change with variations of the OPD is maintained. By monitoring changes of OPD at different temperature levels, environmental temperature under test can be extracted.

A typical reflection spectrum of the post-deposited probes is shown in Fig. 22a. Interference spectra with high fringe visibility can be concluded. Different from the simulation in Fig. 22b, the spectra was raised up. The background is contributed by the reflection from the MMF and sapphire fiber junction. The thermal radiation at high temperature will further level up the spectra. However, the background will be filtered out during the signal processing.

The refractive indexes of the dielectric oxide layer were measured with ellipsometer (VASE J.A. Woollam). As shown in Fig. 23, the actual refractive index of ZrO_2 and Al_2O_3 is about 1.83 and 1.59 respectively which is lower than 2.2 and 1.78 [63, 64]. That could be the reason that the reflection spectrum in Fig. 22a is wider than the simulated curve in Fig. 22b.

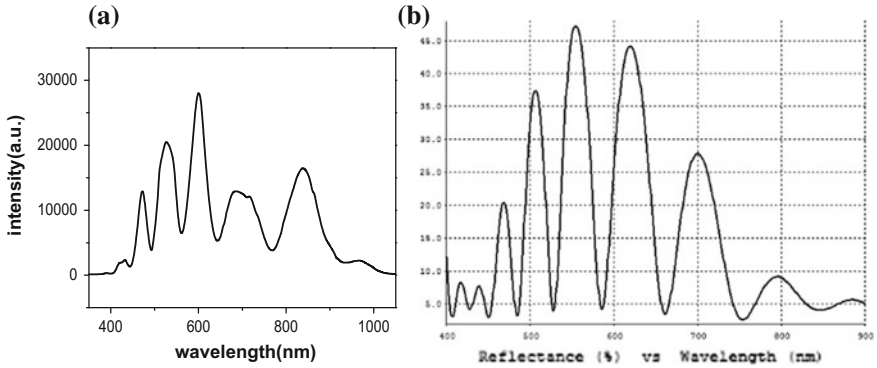

Fig. 22 **a** Measured reflection spectrum of the temperature sensor with deposited ZAZ multilayer; **b** The calculated reflection curve of the designed ZAZ multilayer based on thin film interference theory

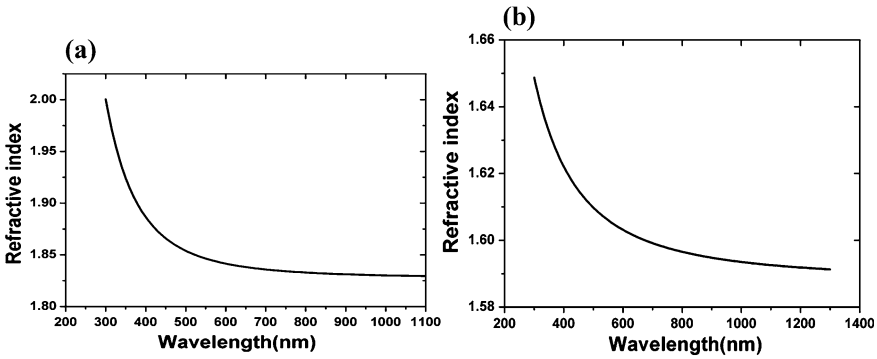

Fig. 23 Measured refractive index of the deposited ZrO_2 layer (**a**) and Al_2O_3 layer (**b**)

Sapphire fiber tip with as-deposited multilayer of ZAZ structure is show in Fig. 24a. It can be concluded that the coating on sapphire fiber is smooth and free of crack. Three thermal cycles from room temperature to 1000 °C with temperature increase speed of 2 °C/min and kept at 1000 °C for 10 h were then carried out to enhance the repeatability of temperature response. For contrast, Fig. 24b shows the image of the annealed samples of sapphire fiber tip with multilayer coating. It can be found that the coating is still stable even after 1000 °C baking for 3 times, also it should be pointed out that the surface changes roughly compared to the as-deposited sample. But this is acceptable since there is still acceptable interference fringe even with such rough surface. Also no clear crack can be detected, only a few contaminations can be found on the surface.

The ZAZ film sensor performance was calibrated by a standard B-type thermocouple, which collocated with multilayer-coated sapphire fiber tip to minimize

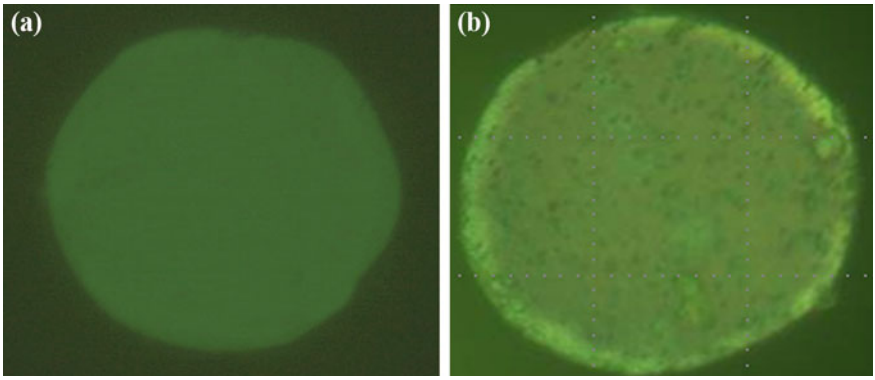

Fig. 24 **a** Sapphire fiber tip with as-deposited multilayer coating, **b** Multilayer coating on sapphire fiber after 1000 °C annealing

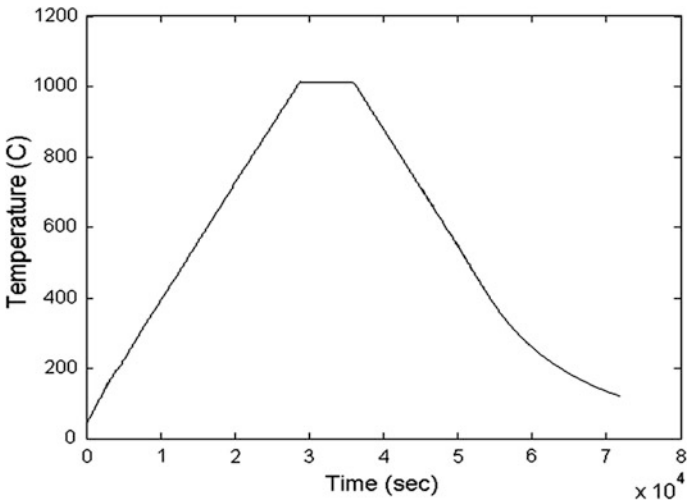

Fig. 25 Experimental curve of temperature increase

the temperature difference between sensor and thermocouple tip, due to the non-uniform thermal distribution in the furnace. The experimental curve of temperature increase was recorded as shown in Fig. 25.

OPD of the thin film interferometer on sapphire fiber tip has correlation with temperature change can be concluded from Fig. 25. The recorded OPD during the temperature increase up to 1000 °C is show in Fig. 26. As shown in Figs. 25 and 26, OPD curve has very similar evolution trend at different status changes including temperature increase, holding and decrease. This has clearly demonstrated that the proposed sensor can be suitable for high temperature measurement up to 1000 °C.

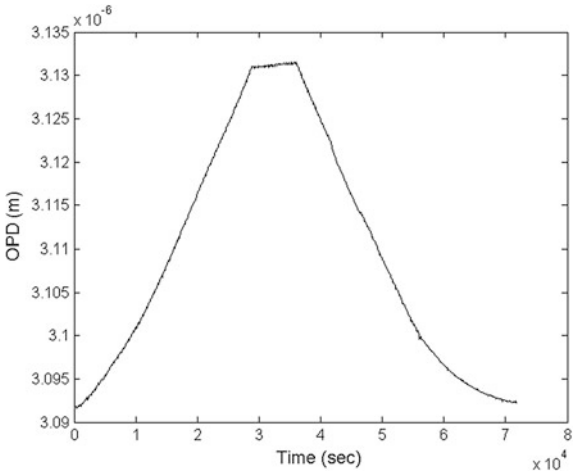

Fig. 26 Recorded experimental OPD curve during temperature increase

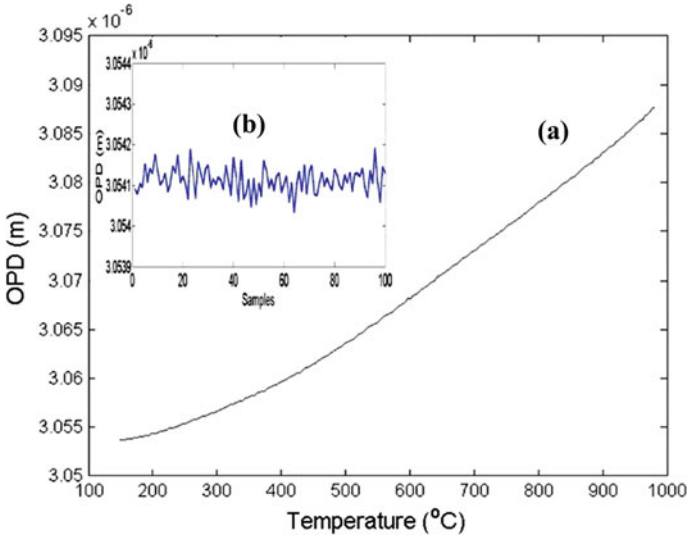

Fig. 27 Correlation of OPD with temperature curve during sensing experiment (**a**) and temporal fluctuation of OPD signal (**b**)

The OPD versus temperature curve is show in Fig. 27. It can be founded that the OPD corresponds well with the temperature up to 1000 °C. The temperature resolution is 40.7 pm/°C. The sub graph in Fig. 27 shows the calculated OPD values for a 100-time continuously spectra acquisition at 43.3 °C. The acquisition was

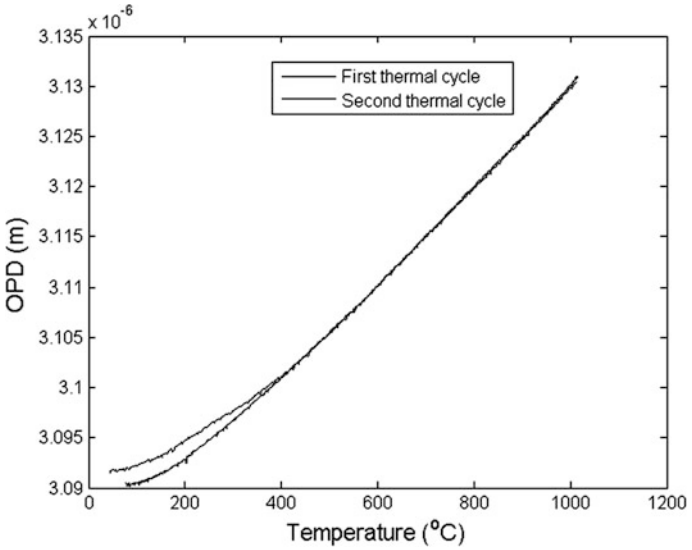

Fig. 28 Repeated measurement of OPD with temperature increase in two thermal cycles

finished within 30 s. Thus the environment was assumed to maintain at a constant temperature. The standard deviation σ of the OPD is 32 pm. Therefore, the temperature precision around room temperature is 4σ (3.2 °C). (The precision usually requires 4σ.)

Repeatability of sensing calibration is show in Fig. 28. It is clear that the two curves match well with each other at temperature above 400 °C.

It should be mentioned that the connected point between MMF with sapphire fiber (20 cm) can't stand up to higher temperature than 1000 °C in the process of experiment. The use of light amplification device makes it possible to increase the length of sapphire fiber, thus the sensor is potential to be used in the higher temperature than 1000 °C. Superior optic spectrometer (such as Ocean Optics, USB-4000) may further improve the performance of the sensor.

Miniaturized high temperature sensor with multilayer coating on sapphire fiber tip as sensitive element has been proposed and experimentally demonstrated. The refractive indexes of the dielectrics by PVD were demonstrated to be lower than their inherent refractive indexes. The proposed sensor has a resolution of 40.7 pm/°C and good linearity when temperature changes from 400 to 1000 °C.

5 Conclusion

Integration of novel functional material with fiber optic components is one of the new trends in the field of novel sensing technologies. The combination of fiber optics with functional materials offers great potential for the realization of novel sensors. This chapter reviews recent works on the topic of fiber-optic sensing technologies with nano thin films and coatings as sensitive elements. As examples, sensors to detect hydrogen concentration, relative humidity and high-temperature based on sensitive thin films have been proposed and experimentally demonstrated. Using physical vapor deposition, thin films were deposited on the end-face or the tip of optical fiber as sensing element. Due to the change of ambient environment, the optical path difference of thin films increased or decreased. So properties of the ambient environment can be measured by optical fiber sensors. The optical fiber hydrogen sensing system can detect hydrogen as low as 50 ppm at room temperature of 25 °C. The hydrogen sensor has a quick response during the hydrogen characterization, and the sensor show better sensitivity towards lower hydrogen concentrations. Experimental investigation of the F-P fiber optic humidity sensor shows that the wavelength shift can reached 42.3 nm when RH ranges from 3.3 to 63 % RH. The average humidity sensitivity of proposed sensor is 0.7 nm/%RH approximately. The proposed high-temperature sensor has a resolution of 40.7 pm/°C and good linearity when temperature changes from 400 to 1000 °C.

References

1. S. Huang, M. LeBlanc, M.M. Ohn, R.M. Measures, Bragg intragrating structural sensing. Appl. Opt. **34**(22), 5003–5009 (1995)
2. H. Naruse, M. Tateda, H. Ohno, A. Shimada, Dependence of the Brillouin gain spectrum on linear strain distribution for optical time-domain reflectometer-type strain sensors. Appl. Opt. **41**(34), 7212–7217 (2002)
3. J. Morita, T. Yoshimura, Analytical characteristics of stimulated Raman scattering in a multimode fiber obtained with an optical time-domain reflectometer. Appl. Opt. **34**(27), 6136–6143 (1995)
4. R. Chow, N. Tsujimoto, Silicon dioxide and hafnium dioxide evaporation characteristics from a high-frequency sweep e-beam system. Appl. Opt. **35**(25), 5095–5101 (1996)
5. O.D. Volpyan, P.P. Yakovlev, B.B. Meshkov, YuA Obod, Optical properties of Ta_2O_5 films obtained by reactive magnetron sputtering. J. Opt. Technol. **70**(9), 669–672 (2003)
6. P.L.G. Jardim, A.F. Michels, F. Horowitz, Optical monitoring for power law fluids during spin coating. Opt. Express **20**(3), 3166–3175 (2012)
7. T.J. Chen, Y.C. Chiou, R.T. Lee, Grinding characteristics of diamond film using composite electro-plating in-process sharpening method. Int. J. Mach. Tools Manuf **49**(6), 470–477 (2009)
8. H. Qiu, S. Gao, P. Chen, Z. Li, X. Liu, C. Z, X. Yuanyuan, S. Jiang, C. Yang, Y. Huo, W. Yue, Evanescent wave absorption sensor based on tapered multimode fiber coated with monolayer graphene film. Opt. Commun. **366**, 275–281 (2016)

9. Q. Rong, X. Qiao, D. Yanying, H. Sun, D. Feng, R. Wang, H. Manli, Z. Feng, In-fiber quasi-Michelson interferometer for liquid level measurement with a core-cladding-modes fiber end-face mirror. Opt. Lasers Eng. **57**, 53–57 (2014)
10. C. Caucheteur, P. Mégret, T. Ernst, D.N. Nikogosyan, Polarization properties of fibre Bragg gratings inscribed by high-intensity femtosecond 264 nm pulses. Opt. Commun. **271**(2), 303–308 (2007)
11. P.E. Dyer, R.J. Farley, R. Giedl, Analysis of grating formation with excimer laser irradiated phase masks. Opt. Commun. **115**(3–4), 327–334 (1995)
12. D.J. Wales, R.M. Parker, J.C. Gates, M.C. Grossel, P.G.R. Smith, An investigation into relative humidity measurement using an aluminosilicate sol–gel thin film as the active layer in an integrated optical Bragg grating refractometer. Sens. Actuators B: Chem. **188**, 857–866 (2013)
13. J. Villatoro, J. Zubia, New perspectives in photonic crystal fibre sensors. Opt. Laser Technol. **78**(Part A) 67–75 (2016)
14. M. Tian, L. Ping, L. Chen, D. Liu, M. Yang, J. Zhang, Femtosecond laser fabricated in-line micro multicavity fiber FP interferometers sensor. Opt. Commun. **316**, 80–851 (2014)
15. H.J. Kbashi, Fabrication of submicron-diameter and taper fibers using chemical etching. J. Mater. Sci. Technol. **28**(4), 308–312 (2012)
16. Y. Han, Z. Chen, D. Cao, Y. Jianhui, H. Li, X. He, J. Zhang, Y. Luo, L. Huihui, J. Tang, H. Huang, Side-polished fiber as a sensor for the determination of nematic liquid crystal orientation. Sens. Actuators B: Chem. **196**, 663–669 (2014)
17. M. Jedrzejewska-Szczerska, P. Wierzba, A. Abou Chaaya, M. Bechelany, P. Miele, R. Viter, A. Mazikowski, K. Karpienko, M. Wróbel, ALD thin ZnO layer as an active medium in a fiber-optic Fabry–Perot interferometer. Sens. Actuators A **221**, 88–94 (2015)
18. J. Zhou, H. Wang, S. Zhao, N. Zhou, L. Li, W. Huang, D. Wang, C. Zhang, In vivo and in vitro studies of borate based glass micro-fibers for dermal repairing. Mater. Sci. Eng., C **60**, 437–445 (2016)
19. S. Chen, W. Ma, H. Xiang, Y. Cheng, S. Yang, W. Weng, M. Zhu, Conductive, tough, hydrophilic poly(vinyl alcohol)/graphene hybrid fibers for wearable supercapacitors. J. Power Sources **319**, 271–280 (2016)
20. M. Tabib-Azar, B. Sutapun, R. Petrick, A. Kazemi, Highly sensitive hydrogen sensors using palladium coated fiber optics with exposed cores and evanescent field interactions. Sens. Actuators, B **56**, 158–163 (1999)
21. M.A. Butler, Micromirror optical-fiber hydrogen sensor. Sens. Actuators, B **22**, 155–163 (1994)
22. J.Z. Ou, M.H. Yaacob, J.L. Campbell, M. Breedon, K. Kalantar-zadeh, W. Wlodarski, H_2 sensing performance of optical fiber coated with nano-platelet WO_3 film. Sens. Actuators, B **166–167**, 1–6 (2012)
23. M. Wang, M.H. Yang, J. Chen, J.X. Dai, M.W. Yang, D.N. Wang, Femtosecond laser fabricated micro Mach-Zehnder interferometer with Pd film as sensing material for hydrogen sensing. Opt. Lett. **37**(11), 1940–1942 (2012)
24. K. Lin, Y. Lu, J. Chen, R. Zheng, P. Wang, H. Ming, Surface plasmon resonance hydrogen sensor based on metallic grating with high sensitivity. Opt. Express **16**(23), 18599–18604 (2008)
25. B. Sutapun, M. Tabib-Azar, A. Kazemi, Pd-coated elastooptic fiber optic Bragg grating sensors for multiplexed hydrogen sensing. Sens. Actuators, B **60**, 27–34 (1999)
26. J.X. Dai, M.H. Yang, Z. Yang, Z. Li, Y. Wang, G.P. Wang, Y. Zhang, Z. Zhuang, Enhanced sensitivity of fiber Bragg grating hydrogen sensor using filexible substrate. Sens. Actuators, B **196**, 604–609 (2014)
27. Y. Chen, J.F. Li, Y. Yang, M. Chen, J. Li, H.Y. Luo, Numerical modeling and design of mid-infrared FBG with high reflectivity. Optik **124**, 2565–2568 (2013)
28. M. Buric, T. Chen, M. Maklad, P.R. Swinehart, K.P. Chen, Multiplexable low-temperature fiber Bragg grating hydrogen sensors. IEEE Photon. Technol. Lett. **21**(21), 1594–1596 (2009)

29. L. Alwis, T. Sun, K.T.V. Grattan, Design and performance evaluation of polyvinyl alcohol/polyimide coated optical fibre grating-based humidity sensors. Rev. Sci. Instrum. **84** (2013)
30. X. Dong, T. Li, Y. Liu, Y. Li, C.L. Zhao, C.C. Chan, Polyvinyl alcohol-coated hybrid fiber grating for relative humidity sensing. J. Biomed. Opt. **16**, 077001–077004 (2011)
31. A. Vijayan, M. Fuke, R. Hawaldar, M. Kulkarni, D. Amalnerkar, R.C. Aiyer, Optical fibre based humidity sensor using Co-polyaniline clad. Sens. Actuators B: Chem. **129**, 106–112 (2008)
32. S. Akita, H. Sasaki, K. Watanabe, A. Seki, A humidity sensor based on a hetero-core optical fiber. Sens. Actuators B: Chem. **147**, 385–391 (2010)
33. F. Arregui, Y. Liu, I.R. Matias, R.O. Claus, Optical fiber humidity sensor using a nano Fabry-Perot cavity formed by the ionic self-assembly method. Sens. Actuators B: Chem. **59**, 54–59 (1999)
34. J.J. Steele, Nanostructured thin films for humidity sensing. PhD thesis of Alberta University, Canada (2008)
35. P.M. Faia, C.S. Furtado, Effect of composition on electrical response to humidity of TiO_2: ZnO sensors investigated by impedance spectroscopy. Sens. Actuators B: Chem. **181**, 720–729 (2013)
36. B.M. Kulwicki, Ceramic sensors and transducers. J. Phys. Chem. Solids **45**, 1015–1031 (1984)
37. B. Fubini, V. Bolis, M. Bailes, F.S. Stone, The reactivity of oxides with water vapor. Solid State Ionics **32–33**, 258–272 (1989)
38. J.H. Anderson, G.A. Parks, The electrical conductivity of silica gel in the presence of adsorbed water. J. Phys. Chem. **72**, 3362–3368 (1968)
39. S.J. Gregg, K.S.W. Sing, *Adsorption, Surface Area and Porosity*, 2nd edn. (Academic Press, London, 1982)
40. W.M. Sears, The effect of oxygen stoichiometry on the humidity sensing characteristics of bismuth iron molybdate. Sens. Actuators B **67**, 161–172 (2000)
41. P.M. Faia, A.R. Ferreira, C.S. Furtado, AC impedance spectroscopy: a new equivalent circuit for titania thick film humidity sensors. Sens. Actuators B **107**, 353–359 (2005)
42. E.V. Astrova a, V.A. Tolmachev, Effective refractive index and composition of oxidized porous silicon films. Mater. Sci. Eng., B **69–70**, 142–148 (2000)
43. C. Pickering, M.I.J. Beale, D.J. Robbins, Optical properties of porous silicon films. Thin Solid Films **125**, 157–163 (1985)
44. Z.L. Ran, Y.J. Rao, W.J. Liu, X. Liao, K.S. Chiang, Laser-micromachined Fabry-Perot optical fiber tip sensor for high-resolution temperature-independent measurement of refractive index. Opt. Express **16**, 2252–2263 (2008)
45. G.L. Zhang, M.H. Yang, Y.T. Dai, Fabry-Perot fiber tip sensor based on an inner air-cavity for refractive index sensing. Chin. Opt. Lett. **S11202**(3), 2014
46. K. Robbie, M.J. Brett, Sculptured thin films and glancing angle deposition: growth mechanics and applications. J. Vac. Sci. Technol. A: Vac. Surf. Films **15**, 1460–1465 (1997)
47. Z.L. Ran, Y.J. Rao, H.Y. Deng, X. Liao, Miniature in-line photonic crystal fiber etalon fabricated by 157 nm laser micromachining. Opt. Lett. **32**, 3071–3073 (2007)
48. T. Wei, Y.K. Han, H.L. Tsai, H. Xiao, Miniaturized fiber inline Fabry-Perot interferometer fabricated with a femtosecond laser. Opt. Lett. **33**, 536–538 (2008)
49. M.H. David, V.P. Minkovich, J. Villatoro, High-temperature sensing with tapers made of microstructured optical fiber. Photonics Technol. Lett. **18**, 511–513 (2006)
50. J.L. Kou, J. Feng, L. Ye, F. Xu, Y.Q. Lu, Miniaturized fiber taper reflective interferometer for high temperature measurement. Opt. Express **18**, 14245–14250 (2010)
51. H.Y. Choi, K.S. Park, S.J. Park, U.C. Paek, B.H. Lee, E.S. Choi, Miniature fiber-optic high temperature sensor based on a hybrid structured Fabry-Perot interferometer. Opt. Lett. **33**(21), 2455–2457 (2008)

52. H.Y. Choi, G. Mudhana, K.S. Park, U.C. Paek, B.H. Lee, Cross-talk free and ultra-compact fiber optic sensor for simultaneous measurement of temperature and refractive index. Opt. Express **18**(1), 141–149 (2010)
53. X. Lai-Cai, M. Deng, D.-W. Duan et al., High-temperature measurement by using a PCF-based Fabry-Perot interferometer. Opt. Lasers Eng. **50**, 1391–1396 (2012)
54. D.W. Duan, Y.J. Rao, W.P. Wen, J. Yao, D. Wu, L.C. Xu, T. Zhu, In-line all-fibre Fabry-Perot interferometer high temperature sensor formed by large lateral offset splicing. Electron. Lett. **47**, 401–402 (2011)
55. Z.Y. Huang, Y.Z. Zhu, X.P. Chen, A.B. Wang, Intrinsic Fabry-Perot sensor for temperature and strain measurements. Photonics Technol Lett. **17**, 2403–2405 (2005)
56. Y.-J. Rao, M. Deng, T. Zhu, H. Li, In-line fabry-perot etalons based on hollow-core photonic bandgap fibers for high-temperature applications. J. Lightw. Technol. **27**(19), 4360–4365 (2009)
57. J. Wang, E.M. Lally, B. Dong, J. Gong, A. Wang, Fabrication of a miniaturized thin-film temperature sensor on a sapphire fiber tip. IEEE Sens. J. **11**(12), 3406–3408 (2011)
58. J. Wang, E.M. Lally, X. Wang, J. Gong, G. Pickrell, A. Wang, ZrO_2 thin-film-based sapphire fiber temperature sensor. Appl. Opt. **51**(12), 2129–2134 (2012)
59. D. Lee, M. Yang, C. Huang, J. Dai, Optical fiber high-temperature sensor based on dielectric films extrinsic Fabry-Perot cavity. IEEE Photonics Technol. Lett. **26**(21), 2107–2110 (2014)
60. G.N. Merberg, J.A. Harrington, Optical and mechanical properties of single-crystal sapphire optical fibers. Appl. Opt. **32**(18), 3201–3209 (1993)
61. D. Lee, Z. Tian, C. Huang, M. Yang, High temperature sensor based on dielectric multilayer Fabry-Perot interferometry on Sapphire fiber tip, in *OFS 2014 23rd International Conference on Optical Fiber Sensors, International Society for Optics and Photonics*, vol. 9157, 9157D6-1 (2014)
62. Y. Zhu, A. Wang, Surface-mount sapphire interferometric temperature sensor. Appl. Opt. **45**, 6071–6076 (2006)
63. P.V. Patil, D.M. Bendale, R.K. Puri et al., Refractive index and adhesion of Al_2O_3 thin films obtained from different processes—a comparative study. Thin Solid Films **288**, 120–124 (1996)
64. C.M. Perkins, B.B. Triplett, P.C. McIntyre, K.C. Saraswat, S. Haukka, M. Tuomminen, Electrical and materials properties of ZrO_2 gate dielectrics grown by atomic layer chemical vapor deposition. Appl. Phys. Lett. **78**, 2357–2359 (2001)

Lossy Mode Resonance Based Fiber Optic Sensors

Nidhi Paliwal and Joseph John

Abstract In the past couple of years, lossy mode resonance (LMR) phenomena has attracted the attention of researchers with its promising benefits in the field of fiber optic sensing. LMR based sensors have become a useful tool in sensing applications ranging from physical sensing to biosensing in a short span of time. In addition to sensing, LMR phenomena can also be utilized as wavelength filters for communication purposes. LMR based sensors are able to work independently of the specific polarization of light for sensing operations. Also, unlike evanescent wave and surface plasmon resonance (SPR) based sensors, the sensitivity of these LMR sensors does not get affected by the geometrical parameters of fiber and primarily depends on the thickness of thin film material. Till date, various geometries of fiber probes such as straight, D-shaped, tapered etc., have been explored. Bending and tapering of multimode fiber based LMR sensors improve the detection accuracy without affecting their sensitivity. However, in single mode fiber based LMR sensors the side polishing and tapering of fibers improve both the detection accuracy and sensitivity. Another method to improve the sensitivity is by using two LMR supporting thin film layers of higher refractive index instead of one. This chapter describes the theory and developments made in the field of LMR based fiber optic sensors for various sensing applications. Finally, future scope of the LMR sensing technology and possible research in this emerging area are suggested.

1 Introduction

Fiber optic sensing technology has been very popular in the past few decades with its promising benefits. Use of low cost optical sources and detectors in place of conventional devices for measuring various physical, chemical, and biological parameters has resulted in great economical benifts. One of the important reasons for the

N. Paliwal (✉) · J. John
Department of Electrical Engineering, Indian Institute of Technology Bombay,
Mumbai 400076, India
e-mail: nidhi83paliwal@gmail.com

© Springer International Publishing Switzerland 2017

I.R. Matias et al. (eds.), *Fiber Optic Sensors*, Smart Sensors,
Measurement and Instrumentation 21, DOI 10.1007/978-3-319-42625-9_2

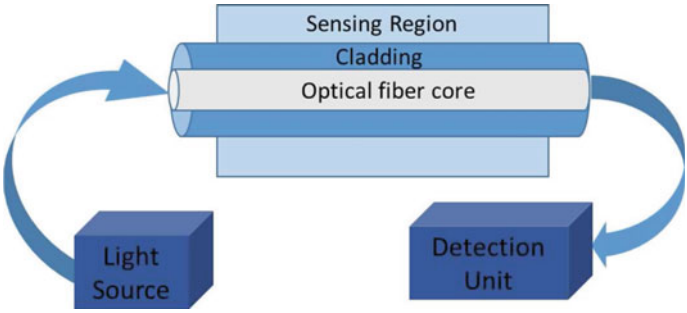

Fig. 1 Schematic representation of fiber optic sensor system

increased demand for fiber optic sensors is its pure dielectric nature due to which they can be effortlessly used in many perilous areas where conventional sensors may not work effectively. Another adavantage, especially for remote sensing and telemetry applications is the fast response of fiber optic sensors which makes it possible to send large amount of sensing information over long distances via optical fibers [1–4]. A typical fiber optic sensing system shown in Fig. 1 consists of a light source, fiber as a sensing element and a detector. Light is transmitted from a light source and passes through an optical fiber sensing probe, which senses change in the desired environmental parameter. The sensor modulates one or more characteristics of light viz, intensity, wavelength, amplitude or phase and then the modulated light is transmitted from the sensor to a signal processor, which in turn converts it into a signal for processing. In order to modulate the properties of light, optical waveguides coated with metal and semiconductors have been very popular [5–8]. It is known that the propagation of light in a medium depends on its properties. In optical fiber sensors, the medium for the propagation of light rays is an optical fiber. If fiber cladding is removed and some other thin film material is deposited over the unclad portion, it introduces losses in the light propagation and the extent of these losses depend upon the properties of thin film material.

2 Theory of LMR

2.1 Selection of Thin Film Material for Generation of LMR

Though LMR is similar to the other well established resonance phenomenon of SPR, there is a basic difference between these two resonance phenomena. Thin film material conditions for generating the surface plasmon modes and the lossy modes which eventually leads to the phenomenon of SPR and LMR respectively, are completely different. The permittivity of any thin film material is given by

$$\epsilon = \epsilon_r + i\epsilon_i \tag{1}$$

Table 1 LMR and SPR generating conditions

Phenomenon	Resonance condition	Suitable thin film materials
LMR	$\epsilon_r = +ive$ and $\lvert\epsilon_r\rvert > \epsilon_i, \epsilon_s$	Polymers, semiconductors, dielectrics, etc.
SPR	$\epsilon_r = -ive$ and $\lvert\epsilon_r\rvert > \epsilon_i, \epsilon_s$	Metals, semiconductors

where ϵ_r is the real part and ϵ_i is its imaginary part. For a given ϵ_s which is the permittivity of any surrounding medium, Table 1 defines the different conditions under which LMR and SPR can be generated. Thin film materials can be classified into two categories depending upon the resonance phenomena as shown in Table 1. LMR is generated when the real part of permittivity is positive and also higher in magnitude than both the permittivity of surrounding medium and its imaginary part. On the other hand, SPR is generated when the real part of thin film's permittivity is negative and also higher in magnitude than both the permittivity of surrounding medium and its imaginary part. There are also some materials whose real part is approximately zero and imaginary part of thin film permittivity is very large. These materials are suitable for generating long range surface exciton polariton. However, these are not in the scope of our studies because the choice of such materials is very limited.

2.2 Surface Plasmons and Surface Plasmon Resonance

Surface plasmons or surface plasma waves are electromagnetic modes associated with a metal-dielectric interface. Any metal thin film coated glass substrate in contact with a dielectric media supports charge density oscillations. These charge density oscillations along the metal-dielectric interface are known as surface plasma oscillations. The quantum of these oscillations is referred to as surface plasmon. A large number of negatively charged free electrons exists inside a conductor (free electron charge density is 10^{23} cm^{-3}) with an equally charged positive ion lattice. Since positive ions have an infinitely large mass compared to these free electrons, these ions can be replaced by a positive constant background. However, the total charge density inside the conductor still remains zero. If the density of free electrons is perturbed by applying an external field on the conductor, movement of free electrons may take place and they begin to get attracted by the positive ion background. This attraction acts as a driving force for free electrons and they start moving towards positive region and accumulate with a density higher than necessary to obtain charge neutrality. This results in the Coulomb repulsion among the moving free electrons which acts as a restoring force and produces motion in the opposite direction. The resultant of these two forces (i.e., attractive driving force and repulsive restoring force) set up the longitudinal oscillations among the free electrons, known as plasma oscillations. Surface plasmons cannot be excited by direct light over a metal-dielectric interface as their wave numbers are greater than the light wave number in the dielectric. Special

geometries are used to excite the surface plasma waves using TM-polarized light. When TM-polarized light is incident on the glass-metal interface within the range of incidence angles, total internal reflection occurs. If the wave vector of the incident light matches the electron oscillation frequency of the metal film surface, the incident light will be coupled to the plasma surface and an electronic resonance is produced. Therefore light energy is absorbed and the intensity of reflected light reduces, so the resonant excitation of surface plasmons can be seen as the dip in reflected light intensity at a certain incident angle, which is known as the resonance angle of SPR. This resonance angle is different for various combinations of the refractive index (RI) of the metal and dielectrics and is very sensitive to the RI changes in the vicinity of a surface. Fiber optic sensors based on SPR phenomenon have been studied extensively in the field of physical, biological and chemical sensing [9–13].

2.3 Lossy Modes and Lossy Mode Resonance

Similar to the SPR phenomenon, a substrate coated with metal oxides, such as indium tin oxide (ITO) [14–16], titanium dioxide (TiO_2) [17], indium oxide (In_2O_3) [18] or polymers [15, 19] in contact with other dielectric media of higher RI, support many number of modes called lossy modes or long range guided modes leading to the phenomenon of LMR. These lossy modes are guided in the thin film and can be generated with both TE and TM polarized light. Based on detailed mode analysis, it was reported that if thin film thickness is increased, lossy modes cross the cut-off condition and start guiding in the thin film leaving the fiber core [5, 20, 21]. In the lossy mode resonance (LMR), coupling between a waveguide mode and a specific lossy mode of thin film takes place at a particular value of film thickness. This coupling requires two conditions to be satisfied, one is the condition of mode fields overlapping and the other one is the phase matching condition. In the phase matching condition, real part of propagation constant of the lossy mode should be equal to the real part of propagation constant of the waveguide mode. In order to completely understand the LMR phenomenon, one can analyze the evolution of modal effective index in the form of evanescent wave which is given as

$$n_{eff} = n_s sin\theta \tag{2}$$

where n_s is the RI of glass substrate and θ is the angle of incidence. Therefore, the effective index of evanescent wave can be modified by changing either the angle of incidence or the wavelength of incident light. At a particular angle or wavelength, the effective index of evanescent wave matches with the effective index of lossy modes and the coupling between evanescent wave and the lossy modes becomes maximum. As a consequence of maximum coupling, LMR is generated at a particular value of thin film thickness resulting in attenuation dips in the transmission spectra.

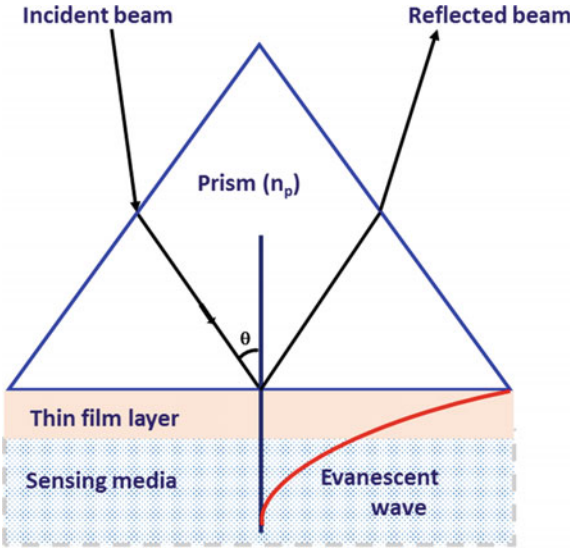

Fig. 2 Kretschmann configuration

2.4 Kretschmann-Reather ATR Method for LMR Generation

Kretschmann configuration which is shown in Fig. 2, is the most popular attenuated total reflection (ATR) method for coupling of the waveguide mode and the modes guided in the thin film coated on a prism base [22]. When a light is incident on a prism at an angle greater than the ATR angle, an evanescent wave is generated at the prism-film layer interface. The coupling between evanescent wave and thin film modes takes place under certain conditions, leading to the phenomenon of LMR. If the phase matching and mode field overlapping conditions are satisfied, the effective coupling between thin film modes and an evanescent wave takes place which results in the transfer of energy from waveguide modes to lossy modes leading to a dip in the reflected light intensity. This dip in the normalized reflected power occurs at a particular incident angle or wavelength of light due to maximum transfer of energy from the waveguide modes to lossy modes. This specific angle and wavelength are called resonance angle (θ_{res}) and resonance wavelength (λ_{res}) respectively.

2.5 LMR Sensing Principle and Performance Parameters

The principle of LMR sensing is based on either angular interrogation or wavelength interrogation. Angular interrogation utilizes various angles of incidence for the measurement of reflectance while keeping the frequency of incident light fixed. In this method, reflectance is minimum at a particular angle of incidence which is called the resonance angle (θ_{res}). This θ_{res} is generally sensitive to the surrounding medium

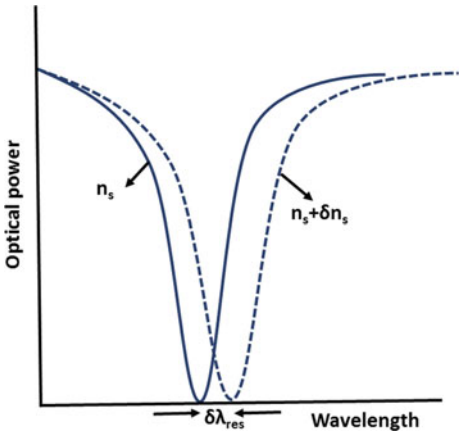

Fig. 3 Reflection spectra obtained with two surrounding medium refractive indices n_s and $n_s + \delta n_s$

refractive index (SRI) variations. Consequently, determination of dielectric constant of surrounding medium is possible if the dielectric constant and thickness of the thin film layer are known. On the other hand, wavelength interrogation utilizes various wavelengths for the reflectance measurement while keeping the angle of incidence fixed. In this method, a broadband light source is generally used for launching the light and minimum reflectance is measured at a particular wavelength. This specific wavelength is called the lossy mode resonance wavelength (λ_{res}). The performance of an LMR based sensor is characterized by its sensitivity and detection accuracy. A perfect LMR sensor has the high sensitivity and high detection accuracy. Sensitivity of an LMR based RI sensor is given by the shift in resonance angle or the wavelength with respect to the SRI variation. It means that, large change in the resonance angle or wavelength shift leads to better sensitivity of the LMR sensor. The reflectance curves for two SRIs viz., n_s and $n_s + \delta n_s$ are shown in Fig. 3. These curves can be used to find out the λ_{res} or λ_{res} and sensitivity can be calculated from the angular or wavelength interrogation method by the following relations

$$S_\lambda = \frac{\delta\lambda_{res}}{\delta n_s} \text{.....(Wavelength interrogation)} \tag{3}$$

$$S_\theta = \frac{\delta\theta_{res}}{\delta n_s} \text{.....(Angular interrogation)} \tag{4}$$

The Second performance parameter viz., detection accuracy is defined by the ability of an LMR sensor to determine the resonance angle/wavelength accurately. Therefore, better detection accuracy provides a precise detection of the resonance angle/wavelength to determine the unknown SRI. Detection accuracy is inversely proportional to the width of LMR curve and therefore narrower LMR curve provides a better detection accuracy besides the detection limitations of the measurement device.

3 Advantages of LMR over SPR

LMR based devices have the following major advantages over the SPR based devices:

1. LMR does not require specific polarization of light and can be generated with both TE and TM polarized light while SPR can be generated only by TM polarized light.
2. Choice of materials is unlimited as most thin film materials have real part of thin film permittivity positive and higher in magnitude than both the imaginary part of the permittivity and the surrounding medium. Therefore unlike SPR, specific plasmonic materials like silver and gold are not required.
3. It is possible to generate multiple LMRs or attenuation dips in the transmittance spectra by increasing the thickness of coating material. The advantage of this feature is that sensitivity to the measurand can be tuned by just changing the thickness of the thin film layer which is not possible in the case of SPR.

4 LMR Based Fiber Optic Sensors

During the last few decades a lot of research work have been reported on SPR, but very few authors have explored the field of LMR. For the first time, Del Villar et al. [14] proposed the LMR phenomenon for fiber optic sensing applications. Thin film material and substrate are the main ingredients in designing a sensing probe. For the substrate, optical fiber is considered to be a good choice due to its small size, light weight, immunity to electromagnetic interference (EMI), capability of multiplexing, wide operating temperature range and capability of remote sensing.

Now coming to the sensor material, ITO was the first material explored by the I. Del villar group since it satisfies the condition of LMR generation as given in Table 1. ITO is a transparent conducting oxide (TCO) and thin films of ITO are chemically stable. Also, various deposition methods such as sputtering, dip coating etc. can be used for the deposition of ITO onto the optical fiber. In addition to this, it can be seen from the dispersion curve of ITO shown in Fig. 4 that it is a suitable material for the generation of both LMR and SPR in two different spectral regions [14, 23]. Fiber optic SPR sensors fabricated with ITO coating have also been utilized in mid-IR spectral region sensing. However, these are very expensive due to the high cost of IR-light sources and detectors. On the contrary, VIS-NIR light sources and detectors are of lower cost and are easily available. Additionally, LMR based humidity sensors [15] and pH sensors [19] show comparable sensitivity to the SPR sensors. In view of the above factors ITO coated LMR fiber optic sensors have been explored for various kinds of sensing applications.

Mostly, wavelength interrogation method is used in LMR fiber optic sensors because multiple reflections take place from the core of an optical fiber due to launching of all the guided modes into the fiber. All those light rays whose incident angle are greater than the critical angle undergo TIR at the fiber-cladding interface. Criti-

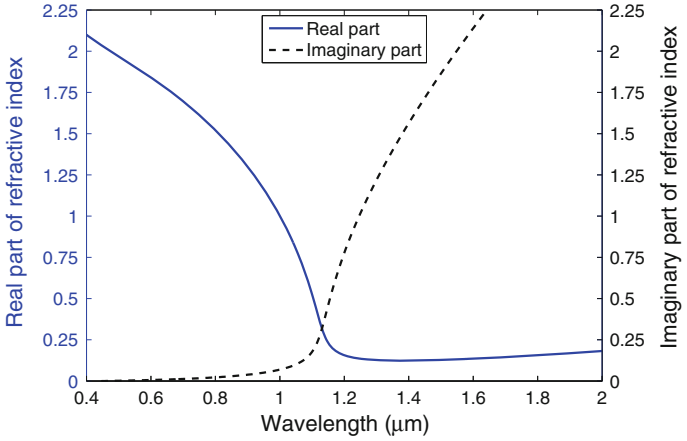

Fig. 4 Dispersion curve of ITO

cal angle is determined by the light acceptance angle or numerical aperture (NA) of the fiber and the wavelength of light. This results in the generation of an evanescent wave, which eventually couple to thin film modes under certain conditions.

Previously in some studies [6], thin film thickness was utilized to satisfy the mode cut-off condition that eventually leads to attenuation maxima of lossy modes, resulting to the LMR. However, LMR generation is also possible by launching broadband spectra into the fiber and observing the mode-cut off at a specific wavelength of spectra keeping the thin film thickness conthstant. Generally, light from a broadband source is incident at one end of the thin film coated fiber optic LMR sensing probe, and detected at the other end. Due to the LMR phenomenon attenuation dip occurs at a specific wavelength, called the resonance wavelength (λ_{res}). This λ_{res} is sensitive to the SRI variations and therefore this LMR phenomena can be utilized in RI sensors by just analyzing the λ_{res} shift in the LMR transmission spectrum. The plot of resonance wavelengths vs refractive indices of the surrounding media, provides the calibration curve for LMR fiber optic RI sensors as shown in Fig. 5.

Further, in order to completely understand the separate contribution of TE, TM and TE+TM modes in generating SPR and LMR phenomena, transmission curves have been plotted using ITO as a thin film material. As seen in Fig. 6a TE polarized light contributes only a single transmission dip appearing in the LMR's spectral region. However, TM polarized light contributes two dips appearing in two different spectral regions as shown in Fig. 6b. Among these two transmission dips, the first dip appears in LMR spectral region and the second dip in SPR region. In addition to this, the combined effect of both TE and TM modes or the unpolarized (TE+TM) light on the transmission spectra is shown in Fig. 6c. From these observations, it can be concluded that contribution of both TE and TM modes leads to the generation of LMR, whereas only TM modes contributes towards the generation of SPR as depicted in Fig. 6b. Another special feature of LMR is its ability to generate multiple LMRs with

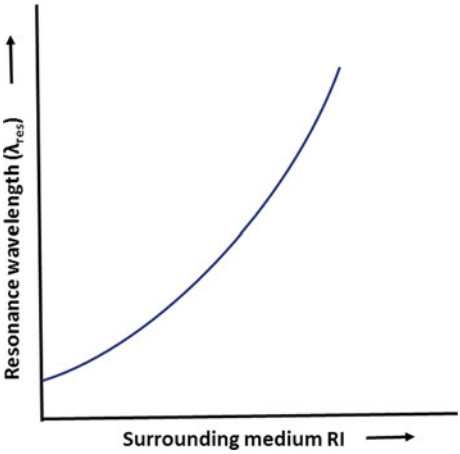

Fig. 5 Calibration curve for LMR fiber optic RI sensor

increasing thicknesses of the thin film as shown in Fig. 7a, b. This is due to the fact that on increasing the thin film thickness, multiple modes are guided in the sensing region [14] leading to the generation of multiple LMR without any modification in the fiber geometry.

5 Theoretical Model for Lossy Mode Resonance Based Fiber-Optic Sensors

This section describes a simulation model for LMR based fiber optic RI sensors with Indium tin oxide (ITO) as an LMR generating layer. Attenuated total reflection (ATR) method in combination with the well known Kretschmann configuration was used for the MATLAB simulations. Fiber parameters considered for the theoretical studies were: core diameter = 200 μm, sensing region length = 30 mm and numerical aperture (NA) = 0.22. The optical power (*dP*) transmitted from the fiber-end is given by [14]

$$dP \propto n_1^2 \sin\theta \cos\theta d\theta \tag{5}$$

We have considered launching of all guided rays into the fiber structure. Due to the cylindrical geometry of fiber, for the exact analysis of modes the effect of skew rays along with the meridional rays has also been taken into account. Hence, the normalized transmitted power P_t, can be written as [14]

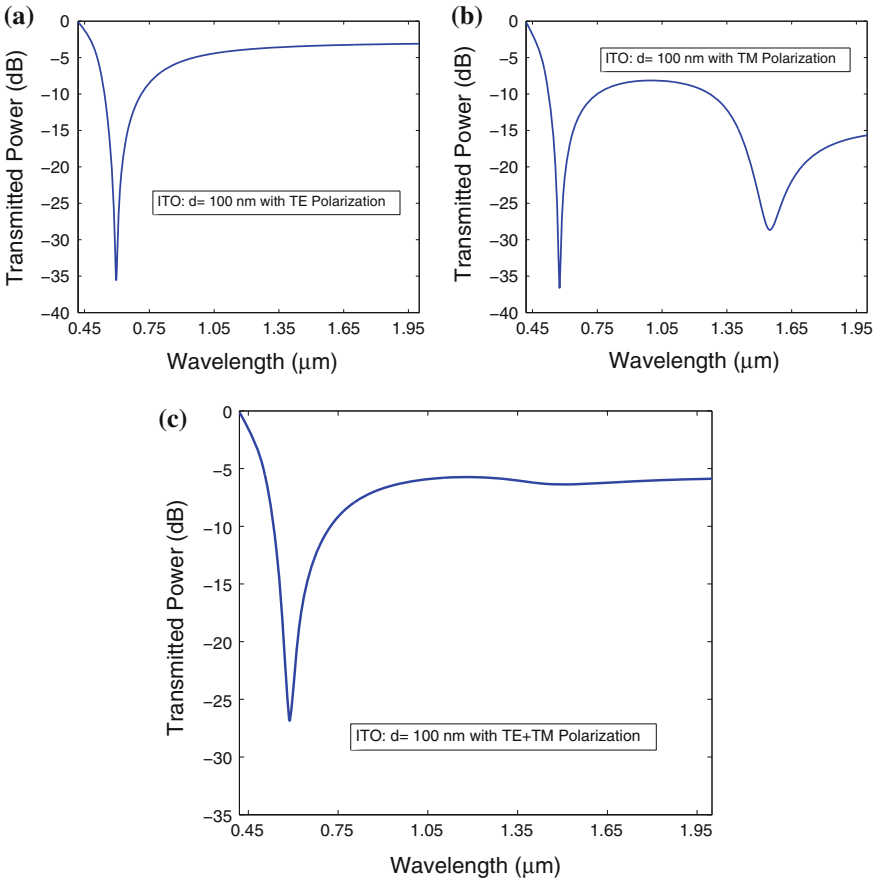

Fig. 6 (Colour Online) Theoretical transmission spectra with light of **a** TE polarization, **b** TM polarization, **c** TE+TM polarization. Other parameters are: sensing region length = 3 cm, core diameter = 200 μm, NA = 0.22, ITO layer thickness d = 100 nm and SRI = 1.33

$$P_t = \frac{\int_0^{\delta_{max}} \int_{\theta_{cr}}^{\pi/2} R^{N_{ref}(\theta,\delta)} k_0^2 n_1^2 \sin\theta \cos\theta d\theta d\delta}{\int_0^{\delta_{max}} \int_{\theta_{cr}}^{\pi/2} k_0^2 n_1^2 \sin\theta \cos\theta d\theta d\delta} \tag{6}$$

where $\theta_{cr} = \sin^{-1}\left(\frac{n_{cl}}{n_1}\right)$ is the critical angle of the fiber with n_{cl} and n_1 as the refractive indices of cladding and core respectively. $R^{N_{ref}(\theta,\delta)}(\theta, \lambda)$ is the reflected power for unpolarized light given by the expression

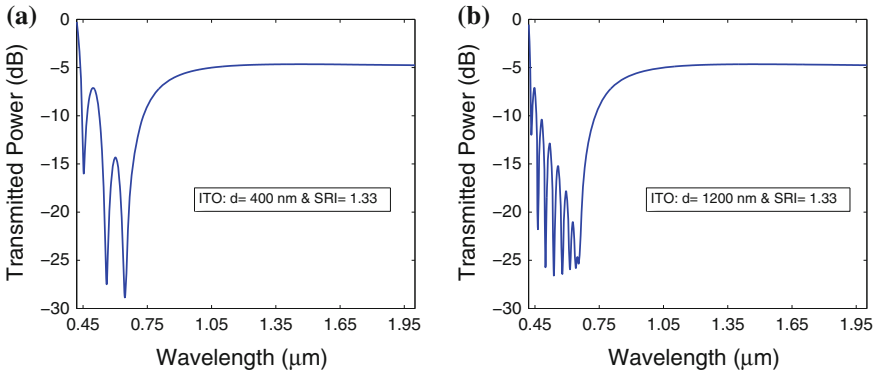

Fig. 7 (Colour Online) Theoretical multiple LMR generation by unpolarized light with ITO layer thickness of **a** d = 400 nm, **b** d = 1200 nm. Other parameters are: sensing region length = 3 cm, core diameter = 200 μm, NA = 0.22 and SRI = 1.33

$$R^{N(\theta,\delta)}(\theta,\lambda) = \frac{R_{TE}^{N(\theta,\delta)}(\theta,\lambda) + R_{TM}^{N(\theta,\delta)}(\theta,\lambda)}{2} \tag{7}$$

and $N_{ref}(\theta,\delta)$ is the number of reflections at the core- thin film interface expressed by the equation given below

$$N_{ref}(\theta,\delta) = \frac{L}{D\tan\theta\cos\delta} \tag{8}$$

Here, D is the core diameter of fiber, L is the length of sensing region, θ is the angle of incident ray with respect to the normal to core-thin film interface and δ is the skewness angle. In order to calculate the reflection intensity coefficient R(θ, λ) for unpolarized light beam, N-layer (transfer matrix) method is used [24].

5.1 Transfer Matrix Method for a Multilayer System

This method assumes that all thin film layers are uniform, isotropic, non-magnetic and stacked along the z-axis as shown in Fig. 8. These layers are characterized by the dielectric constant ϵ_n, permeability μ_n and thickness d_n. The tangential fields at the boundaries $Z = Z_1 = 0$ and $Z = Z_{N-1}$ are related by the relation [24].

$$\begin{bmatrix} E_1 \\ H_1 \end{bmatrix} = M \begin{bmatrix} E_{N-1} \\ H_{N-1} \end{bmatrix} \tag{9}$$

where E_1, H_1 and E_{N-1}, H_{N-1} are the tangential components of electric and magnetic fields at the first layer's boundary and the Nth layer's boundary respectively. Here,

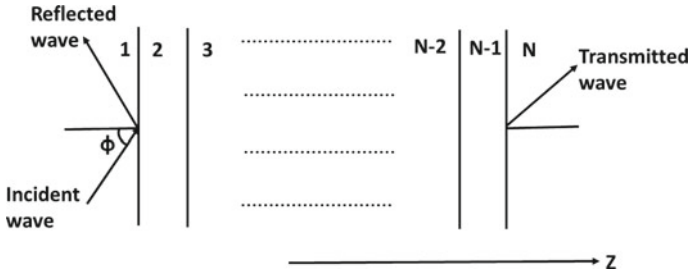

Fig. 8 N-Layers method for the calculation of reflected light intensity

M is the characteristic matrix for the multilayer structure and is given by

$$M = \prod_{n=2}^{N-1} M_n \tag{10}$$

where

$$M_n = \begin{bmatrix} \cos\beta_n & -\frac{i}{q_n}\sin\beta_n \\ -iq_n \sin\beta_n & \cos\beta_n \end{bmatrix} \tag{11}$$

and

$$q_n = \frac{\sqrt{\epsilon_n - n_1^2 \sin\phi^2}}{\epsilon_n} \text{.....(TM modes)} \tag{12}$$

$$q_n = \sqrt{\epsilon_n - n_1^2 \sin\phi^2} \text{.....(TE modes)} \tag{13}$$

$$\beta_n = \frac{2\pi d_n}{\lambda}\sqrt{\epsilon_n - n_1^2 \sin\phi^2} \tag{14}$$

The reflection amplitude for unpolarized incident light is calculated by

$$r = \frac{(M_{11} + M_{12}q_N)q1 - (M_{21} + M_{22}q_N)}{(M_{11} + M_{12}q_N)q1 + (M_{21} + M_{22}q_N)} \tag{15}$$

Therefore, reflection intensity for unpolarized light containing TE and TM modes is given by

$$R = \frac{|\, r_{TE}\,|^2 + |\, r_{TM}\,|^2}{2} \tag{16}$$

In order to calculate the refractive indices of various layers the following dispersion models were used:

5.2 Dispersion Relation of ITO Layer

The following Drude and Lorentz oscillator dispersion model was used to describe the dispersion relation of ITO.

$$\epsilon(\omega) = \epsilon_\infty - \frac{\omega_p^2}{\omega^2 + i\frac{\omega}{\tau}} + \frac{s_0\omega_0^2}{\omega_0^2 - \omega^2 + i\gamma\omega} \tag{17}$$

where $\epsilon_\infty = 3.5$ is the high frequency dielectric constant, $\omega_p = 4.557 \times 10^{15}$ rad/s is the plasma frequency, $s_0 = 1$ is the oscillator strength, $\omega_0 = 8.27 \times 10^{15}$ rad/s is the oscillator resonance frequency, $\gamma = 1.321 \times 10^{14}$ rad/s is the damping constant and $\tau = 1.324 \times 10^{-14}$ s/rad is the electronic scattering time.

5.3 Dispersion Relation of Silica

In our theoretical studies we assume that the core of the fiber is made of fused silica. The expression for the wavelength dependent refractive index of fused silica is given by the Sellmeier relation [25] as

$$n_1(\lambda) = \sqrt{1 + \frac{a_1\lambda^2}{\lambda^2 - b_1^2} + \frac{a_2\lambda^2}{\lambda^2 - b_2^2} + \frac{a_3\lambda^2}{\lambda^2 - b_3^2}} \tag{18}$$

where λ denotes the wavelength (in μm) and the Sellmeier coefficients are $a_1 = 0.6961663$, $a_2 = 0.4079426$, $a_3 = 0.8774794$, $b_1 = 0.0684043$, $b_2 = 0.1162414$ and $b_3 = 9.896161$.

The different SRIs used for the analysis were 1.33, 1.35, 1.37, 1.39, 1.41, 1.43. Wavelength interrogation method was used to obtain the LMR transmission spectra for different SRIs as shown in Fig. 9a. In order to calculate the sensitivity, resonance wavelengths can be found out from these transmission spectra. Additionally, the effect of ITO thickness on the sensitivity of LMR fiber optic RI sensor is shown in Fig. 9b. As observed in Fig. 9b spacing between LMR curves gets reduced with increasing film thickness which results in decreased sensitivity.

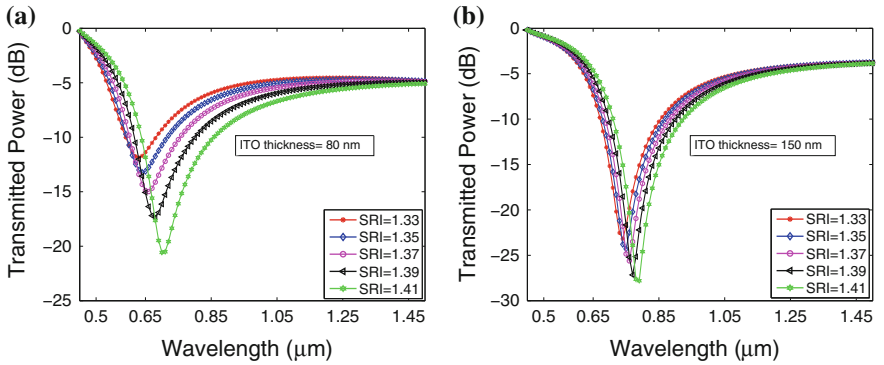

Fig. 9 (Colour Online) LMR transmission spectra obtained with different surrounding medium refractive indices (SRIs) for ITO layer thickness of **a** d = 80 nm, **b** d = 150 nm. Other parameters are: sensing region length = 3 cm, core diameter = 200 μm, NA = 0.22

6 Recent Advancenents in LMR Bsed Fiber Optic Sensors

Till 2010 LMR remained an unexplored phenomenon for fiber optic sensing applications before it was proposed by Del Villar et al. [14] for RI sensing. The sensitivity of this first LMR based RI sensor was evaluated with ITO film thickness of 115 and 220 nm using water-glycerin solutions of different RIs, whose sensitivities were found to be 1617.4 nm/RIU and 2952.6 nm/RIU respectively. A typical experimental-setup which can be used for LMR based fiber optic RI sensing is shown in Fig. 10. Here, an optical fiber is de-cladded from the middle and a thin film overlay is deposited onto the uncladded region. This fiber structure is surrounded by the medium whose RI is under investigation.

Around the same time, optical fiber refractometer based on the same ITO coating was fabricated by Zamarreno et al. [26] in which they found the sensitivity of refractometer to be independent of the sensing region length. They reported an average sensitivity of 3125 nm/RIU which was comparable to the SPR sensors. LMR phenomenon was also utilized for relative humidity sensing [15] and a tunable humidity sensor was fabricated by depositing ITO and poly allylamine hydrochloride (PAH) and poly acrylic acid (PAA) film which is sensitive to relative humidity. The sensitivities of tuned and non-tuned RH sensors were compared. Around 5 fold increase in the sensitivity was reported for the tuned RH sensor.

Due to the limitation of ITO material in generating LMR within the specific spectral range, another metal oxide TiO_2 was explored. It was discovered that TiO_2 is free from the limitations of LMR generation in specific wavelength spectrum as can be seen from the dispersion curve of TiO_2 [17]. Therefore, unlike ITO, the complete wavelength range of 500–1500 nm is available for LMR generation in TiO_2 because the real part of dielectric constant always remains positive and higher than its imaginary part for the entire wavelength spectrum. Keeping this fact in view, the

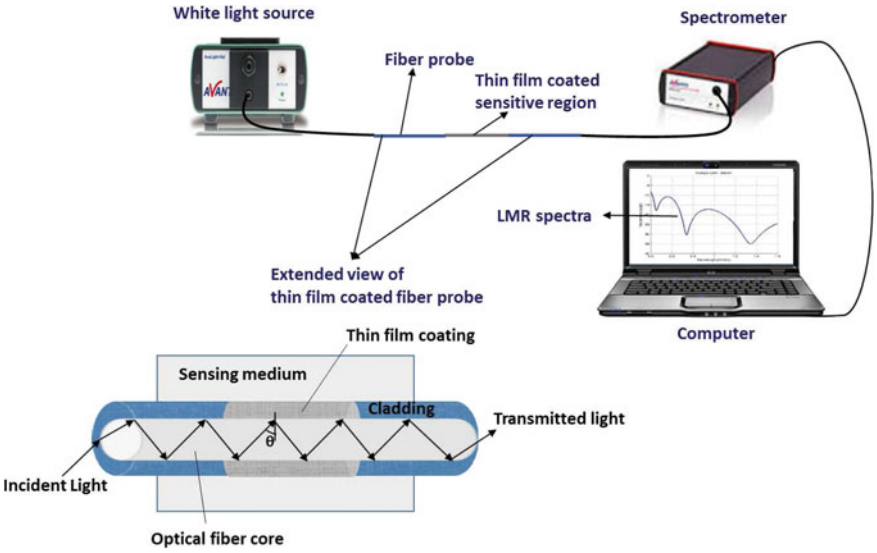

Fig. 10 Experimental setup used for LMR based fiber optic sensing

optical fiber refractometers were fabricated by depositing TiO_2/PSS (poly sodium 4-styrenesulfonate) thin films by using layer-by-layer (LbL) method. All studies on these LMR based refractometers show that thin film thickness plays an important role in determining the sensitivity. Better sensitivity can be achieved if thin film thickness is kept less. Consequently, the major advantage of LMR based fiber optic refractometers is that sensitivity, position and number of transmission dips can be fine tuned by just changing the film thickness. Also, another composite oxide material indium oxide (In_2O_3) was studied for LMR generation and it was reported that with In_2O_3 dual peak LMR can be generated which is useful for performing very precise measurements with better accuracy and two fold sensitivity enhancement [18]. Besides RI and RH measurements, LMR phenomenon had also shown its potential in pH sensing [19]. For the fabrication of LMR based pH sensor, PAH/PAA coatings were chosen because LMR can be generated with these polymers. Also, PAH/PAA thin films are suitable for pH measurement because thickness of these films increase or decrease with the pH variation of the solution which causes the SRI change. A fairly good sensitivity of 0.027 pH units/nm with an accuracy of 0.001 pH units was achieved with this pH sensor for a pH range of 3–6. Though, many materials including metal oxides and polymers were explored for various physical and chemical sensing utilizing LMR phenomena, some other design parameters which affect the sensitivity and resolution of these LMR sensors also need to be addressed. Therefore, to achieve the better performance of LMR sensor some design studies were presented [27]. For the optimization of LMR sensing design parameters, TiO_2/PSS and PAH/PAA were chosen because both these materials are suitable for LMR generation. In these studies it was concluded that only the real part of thin

film RI is responsible for the wavelength shift which eventually provides the sensitivity of the LMR device. However, the imaginary part of thin film RI accounts for the losses occurring in the structure and thus the depth of resonance curve. Hence, there is no role for the imaginary part of the thin film RI in determining the sensitivity of an LMR device. As we know thin film properties drastically vary with the deposition techniques [28–30], ITO coated LMR based optical fiber refractometer was also studied where ITO was deposited by sputtering technique unlike LbL and dip coating techniques reported in literature [14, 15, 17]. After the successful development of pH, RH and RI sensors, fiber optic immunoglobulin G (IgG) biosensor was reported utilizing LMR phenomena [31]. This biosensor was fabricated by depositing PAH/PSS thin films because these films provide a suitable medium for IgG-anti-IgG immunoreactions and also capable of generating LMR. With this IgG biosensor, 50 μg/ml concentration of Immunoglobulins were detected in a response time of 12 min. In an another work, a new LMR based fiber optic RH sensor was reported in which multiple LMR phenomena was utilized as a notch band filter [32]. Further, in order to show the effect of fiber geometry, the use of side-polished, D-shaped single mode fiber (SMF) coated with TiO_2/PSS was reported for fiber based LMR devices [33]. Their experimental results demonstrate the importance of D-shape SMF in determining the individual contribution of TE and TM polarizations in LMR generation.

A different kind of LMR based chemical vapor sensor for the detection of volatile organic compounds (VOCs) was developed by depositing an organometallic compound $[Au_2Ag_2(C_6F_5)_4(C_6H_5C{\equiv}CC_6H_5)_2]_n$ which is sensitive to organic vapors [34]. The performance of this sensor was evaluated with different concentrations of ethanol, methanol and isopropanol vapors taking the effect of humidity and temperature into account. Furthermore, for monitoring human breath an LMR based sensor was designed with silver nanoparticle loaded films onto the fiber [35]. The dynamic range of 27.3 nm and sensitivity of 0.455 nm/RH% was achieved for this human breath sensing device.

All the LMR sensors discussed so far utilized only a single LMR generating thin film layer. In order to enhance the sensitivity of an LMR device, fiber optic RI sensors with bilayer combination of ITO/TiO_2 was theoretically investigated [36] using transfer matrix method described in Sect. 5.1. This work reports the capability of combined ITO and TiO_2 thin films in enhancing the RI sensitivity when combined in a particular ratio. A comparison of sensitivity was carried out utilizing ITO/TiO_2 bilayer and single absorbing layer in LMR based RI sensors. It was concluded from these theoretical studies that with ITO/TiO_2 bilayer combination, a much better sensitivity can be achieved as compared to single absorbing layer. An another LMR based biosensor was reported for thrombin and C-reactive protein detection [37, 38]. Again in another work, two different bilayer combinations viz. AZO/TiO_2 and AZO/Cu_2O were theoretically investigated for the enhancement of RI sensitivity [39] and AZO/TiO_2 was reported to be a much better combination for increasing the RI sensitivity up to five fold.

Another important LMR based biosensor was reported for the diagnosis of celiac disease [40]. This work was carried out first utilizing different geometries of the

fibers and then choosing the appropriate geometry for fabrication of the biosensor. Among all the geometries, best detection accuracy was achieved with tapered single-mode optical fibers (T-SMFs). These T-SMFs were used to fabricate the sensing device to detect anti-gliadin antibodies (AGAs) for the diagnosis of celiac disease. The devices fabricated in this work have the potential for other biological and chemical applications. LMR phenomena was also theoretically exposed for temperature sensing [41]. In this work, TiO_2 coated LMR based fiber optic temperature sensor was reported and the sensitivity was evaluated by considering air and water as the surrounding media. The role of different TiO_2 thicknesses in determining the sensitivity was discussed. As compared to fiber Bragg grating (FBG) and localized surface plasmon resonance (LSPR) based fiber optic temperature sensors [42, 43], the proposed sensor promises higher temperature sensitivity with 100 nm thickness of TiO_2. The major benefit of LMR based temperature sensor is that, it does not require an extra metal layer unlike FBG and LSPR temperature sensors and its sensitivity can be tuned by just changing the TiO_2 thickness. Recently, improvement in the reduction of spectral width by utilizing D-shaped optical fibers for fabrication of LMR based refractometers was reported [44]. This work presented a highly sensitive ITO coated D-shaped optical fiber refractometer with very narrow spectral width and high attenuation of 6.9 nm and 36 dB. In a recent review article a detailed analysis of LMR phenomena along with its major fields of applications was reported [45].

7 Conclusion

This chapter presents details of the LMR phenomena and considered various designs and performance parameters for LMR based fiber-optic sensors. The basic principle of LMR based fiber-optic sensors was explained and various benefits such as sensitivity and detection accuracy enhancement by using double thin film layers, tapered and D-shape geometry for LMR based fiber-optic sensors were addressed. The popularity of LMR sensors is primarily based on two reasons: first, these are free from the requirement of specific polarization of light, and secondly due to the capability of tuning its sensitivity by just adjusting thickness of the thin film. Also, another exclusive property of LMR devices is multiple LMR generation with increasing thickness which can be utilized in wavelength filtering applications. LMR technology has motivated research on the geometry of fiber optic probe for further enhancing the sensitivity and detection accuracy for various sensing applications. LMR cannot be considered just a cost effective solution in the field of sensing as all the LMR generating materials show high sensitivity in the NIR spectral range. This calls for future research of suitable materials with enhanced sensitivity of LMR sensors in the visible spectral region. LMR phenomena can also be explored with other nanoparticle based sensing techniques like LSPR. In view of all these LMR based fiber optic sensing technology would be a very promising research field. The present chapter is a small attempt to provide an insight into the recent advancements in this emerging field. Fiber optic sensor technology promises bright future prospects with signifi-

cant advancements in the coming years. LMR based fiber-optic sensors are expected to be a major contributor to the sensing research community with comparably high sensitivity along with its various advantages over the other fiber optic sensors.

References

1. A. Kersey, A. Dandridge, Applications of fiber-optic sensors. IEEE Trans. Compon. Hybrids Manuf. Technol. **13**(1), 137–143 (1990)
2. B. Culshaw, A. Kersey, Fiber-optic sensing: a historical perspective. J. Lightwave Technol. **26**(9), 1064–1078 (2008)
3. R. Bogue, Fibre optic sensors: a review of today's applications. Sens. Rev. **31**(4), 304–309 (2011)
4. B. Lee, S. Roh, J. Park, Current status of micro- and nano-structured optical fiber sensors. Opt. Fiber Technol. **15**(3), 209–221 (2009)
5. T. Batchman, G. McWright, Mode coupling between dielectric and semiconductor planar waveguides. IEEE Trans. Microwave Theory Tech. **30**(4), 628–634 (1982)
6. M. Marciniak, J. Grzegorzewski, M. Szustakowski, Analysis of lossy mode cut-off conditions in planar waveguides with semiconductor guiding layer. Optoelectr. IEE Proc. J. **140**(4), 247–252 (1993)
7. T. Takano, J. Hamasaki, Propagating modes of a metal-clad-dielectric-slab waveguide for integrated optics. IEEE J. Quantum Electr. **8**(2), 206–212 (1972)
8. F. Yang, J.R. Sambles, Determination of the optical permittivity and thickness of absorbing films using long range modes. J. Modern Opt. **44**(6), 1155–1163 (1997)
9. J. Homola, S.S. Yee, G. Gauglitz, Surface plasmon resonance sensors: review. Sens. Actuators B: Chem. **54**, 3–15 (1999)
10. A.K. Sharma, R. Jha, B.D. Gupta, Fiber-optic sensors based on surface plasmon resonance: a comprehensive review. Sens. J. IEEE **7**(8), 1118–1129 (2007)
11. A. Leung, P.M. Shankar, R. Mutharasan, A review of fiber-optic biosensors. Sens. Actuators B: Chem. **125**(2), 688–703 (2007)
12. X.D. Wang, O.S. Wolfbeis, Fiber-optic chemical sensors and biosensors (2008–2012). Anal. Chem. **85**(2), 487–508 (2013)
13. I. Abdulhalim, M. Zourob, A. Lakhtakia, Surface plasmon resonance for biosensing: a mini-review. Electromagnetics **28**(3), 214–242 (2008)
14. I.D. Villar, C.R. Zamarreno, M. Hernaez, F.J. Arregui, I.R. Matias, Lossy mode resonance generation with indium-tin-oxide-coated optical fibers for sensing applications. J. Lightwave Technol. **28**(1), 111–117 (2010)
15. C.R. Zamarreno, M. Hernaez, I.D. Villar, I.R. Matias, F.J. Arregui, Tunable humidity sensor based on ITO-coated optical fiber. Sens. Actuators B: Chem. **146**(1), 414–417 (2010)
16. D. Kaur, V. Sharma, A. Kapoor, High sensitivity lossy mode resonance sensors. Sens. Actuators B: Chem. **198**, 366–376 (2014)
17. M. Hernaez, I.D. Villar, C.R. Zamarreno, F.J. Arregui, I.R. Matias, Optical fiber refractometers based on lossy mode resonances supported by TiO_2 coatings. Appl. Opt. **49**, 3980–3985 (2010)
18. I.D. Villar, C.R. Zamarreno, P. Sanchez, M. Hernaez, C.F. Valdivielso, F.J. Arregui, I.R. Matias, Generation of lossy mode resonances by deposition of high-refractive-index coatings on uncladded multimode optical fibers. J. Opt. **12**(9), 095503 (2010)
19. C.R. Zamarreno, M. Hernaez, I.D. Villar, I.R. Matias, F.J. Arregui, Optical fiber pH sensor based on lossy-mode resonances by means of thin polymeric coatings. Sens. Actuators B: Chem. **155**(1), 290–297 (2011)
20. R.F. Carson, T.E. Batchman, Multimode phenomena in semiconductor-clad dielectric optical waveguide structures. Appl. Opt. **29**(18), 2769–2780 (1990)

21. I.D. Villar, I.R. Matias, F.J. Arregui, M. Achaerandio, Nanodeposition of materials with complex refractive index in long-period fiber gratings. J. Lightwave Technol. **23**(12), 4192–4199 (2005)
22. E. Kretschmann, H. Reather, Radiative decay of non-radiative surface plasmons excited by light. Zeitschrift fur Naturforschung **23**, 21352136 (1968)
23. I.D. Villar, C.R. Zamarreno, M. Hernaez, P. Sanchez, F.J. Arregui, I.R. Matias, Generation of surface plasmon resonance and lossy mode resonance by thermal treatment of ITO thin-films. Opt. Laser Technol. **69**, 1–7 (2015)
24. J. Chilwell, I. Hodgkinson, Thin-films field-transfer matrix theory of planar multilayer waveguides and reflection from prism-loaded waveguides. J. Opt. Soc. Am. A **1**(7), 742–753 (1984)
25. G.P. Agarwal, *Nonlinear Fiber Optics*, 3rd edn. (Academic, New York, 2001)
26. C.R. Zamarreno, M. Hernaez, I.D. Villar, I.R. Matias, F.J. Arregui, ITO coated optical fiber refractometers based on resonances in the infrared region. Sens. J. IEEE **10**(2), 365–366 (2010)
27. I.D. Villar, M. Hernaez, C.R. Zamarreno, P. Sanchez, C. Fernandez-Valdivielso, F.J. Arregui, I.R. Matias, Design rules for lossy mode resonance based sensors. Appl. Opt. **51**(19), 4298–4307 (2012)
28. S.H. Brewer, S. Franzen, Optical properties of indium tin oxide and fluorine-doped tin oxide surfaces, correlation of reflectivity, skin depth, and plasmon frequency with conductivity. J. Alloys Compd. **338**, 73–79 (2002)
29. I. Hamberg, A. Hjortsberg, C. Granqvist, High quality transparent heat reflectors of reactively evaporated indium tin oxide. Appl. Phys. Lett. **40**(5), 362–364 (1982)
30. S. Laux, N. Kaiser, A. Zoller, R. Gotzelmann, H. Lauth, H. Bernitzki, Room-temperature deposition of indium tin oxide thin films with plasma ion-assisted evaporation. Thin Solid Films **335**, 1–5 (1998)
31. A. Socorro, J. Corres, I.D. Villar, F.J. Arregui, I.R. Matias, Fiber-optic biosensor based on lossy mode resonances. Sens. Actuators B: Chem. **174**, 263–269 (2012)
32. P. Sanchez, C.R. Zamarreno, M. Hernaez, I.D. Villar, I.R. Matias, F.J. Arregui, Considerations for lossy-mode resonance-based optical fiber sensor. Sens. J. IEEE **13**(4), 1167–1171 (2013)
33. C.R. Zamarreno, P. Zubiate, M. Sagues, I.R. Matias, F.J. Arregui, Experimental demonstration of lossy mode resonance generation for transverse-magnetic and transverse-electric polarizations. Opt. Lett. **38**(14), 2481–2483 (2013)
34. C. Elosua, I. Vidondo, F.J. Arregui, C. Bariain, A. Luquin, M. Laguna, I.R. Matias, Lossy mode resonance optical fiber sensor to detect organic vapors. Sens. Actuators B: Chem. **187**, 65–71 (2013)
35. P.J. Rivero, A. Urrutia, J. Goicoechea, I.R. Matias, F.J. Arregui, A lossy mode resonance optical sensor using silver nanoparticles-loaded films for monitoring human breathing. Sens. Actuators B: Chem. **187**, 40–44 (2013)
36. N. Paliwal, J. John, Theoretical modeling of lossy mode resonance based refractive index sensors with ITO/TiO_2 bilayers. Appl. Opt. **53**, 3241–3246 (2014)
37. C.R. Zamarreno, I. Ardaiz, L. Ruete, F. Munoz, I.R. Matias, F.J. Arregui, C-reactive protein aptasensor for early sepsis diagnosis by means of an optical fiber device. Sens. IEEE **2013**, 1–4 (2013)
38. L. Razquin, C.R. Zamarreno, F. Munoz, I.R. Matias, F.J. Arregui, Thrombin detection by means of an aptamer based sensitive coating fabricated onto LMR-based optical fiber refractometer. Sens. IEEE **2012**, 1–4 (2012)
39. N. Paliwal, J. John, Sensitivity enhancement of aluminium doped zinc oxide (AZO) coated lossy mode resonance (LMR) fiber optic sensors using additional layer of oxides. Frontiers in Optics. Optical Society of America, p. JTu3A.40 (2014)
40. A. Socorro, I.D. Villar, J. Corres, F.J. Arregui, I.R. Matias, Spectral width reduction in lossy mode resonance-based sensors by means of tapered optical fibre structures. Sens. Actuators B: Chem. **200**, 53–60 (2014)
41. N. Paliwal, J. John, Theoretical modelling of lossy mode resonance (LMR) based fiber optic temperature sensor utilizing TiO_2 sensing layer. in *12th International Conference on Fiber Optics and Photonics* (Optical Society of America, 2014), p. M4A.22

42. S.K. Srivastava, B.D. Gupta, Simulation of a localized surface-plasmon-resonance-based fiber optic temperature sensor. J. Opt. Soc. Am. A **27**(7), 1743–1749 (2010)
43. N. Liu, Y. Li, Y. Wang, H. Wang, W. Liang, P. Lu, Bending insensitive sensors for strain and temperature measurements with bragg gratings in bragg fibers. Opt. Exp. **19**(15), 13 880–13 891 (2011)
44. P. Zubiate, C.R. Zamarreno, I.D. Villar, I.R. Matias, F.J. Arregui, High sensitive refractometers based on lossy mode resonances (LMRs) supported by ITO coated D-shaped optical fibers. Opt. Exp. **23**(6), 8045–8050 (2015)
45. N. Paliwal, J. John, Lossy mode resonance (LMR) based fiber optic sensors: a review. Sens. J. IEEE **15**(10), 5361–5371 (2015)

Plasmonics-Based Fiber Optic Sensors

Anuj K. Sharma

Abstract Since the unveiling of optical fiber technology in the field of plasmonics-based optical sensors, a lot of advancements have been witnessed. This chapter discusses a detailed mechanism of the technique of surface plasmon resonance (SPR) applied in optical fiber sensors. Some selected research works in the area of plasmonics-based fiber optic sensors reported in last 25–30 years along with future scope of work are also discussed.

1 Evolution of Plasmonics: A Brief History

The origin of plasmonics is more than a century old. In 1907, Zenneck formulated a special surface wave solution to Maxwell's equations and theoretically established that radio frequency surface waves occur at the boundary of lossy (e.g., metal) and loss-free media [1]. In 1909, Sommerfeld found that the field amplitudes of surface waves postulated by Zenneck varied inversely as the square root of the horizontal distance from the source dipole [2]. However, a significant progress in this context was made by Ritchie in 1957 when he theoretically demonstrated the existence of surface plasma excitations at a metal surface [3]. In 1960, Powell and Swan stated the excitation of surface plasmons at metal interfaces using electrons [4]. Soon after, Stern and Ferrell showed that surface electromagnetic (EM) waves at a metallic surface involved EM radiation coupled to surface plasmons [5]. They also derived the dispersion relations for EM surface waves at metal surfaces. Further, in 1968, Otto devised the attenuated total reflection (ATR) prism coupling method to enable the coupling of light wave with surface EM waves [6]. The Otto configuration, due to a finite gap between prism base and metal layer, was more suited to the surfaces, which would not be damaged or touched by the prism and is important for the study of single crystal surfaces. Kretschmann and Raether modified the Otto

A.K. Sharma (✉)
Department of Applied Sciences, National Institute of Technology Delhi, Delhi 110040, India
e-mail: anujsharma@gmail.com

© Springer International Publishing Switzerland 2017

I.R. Matias et al. (eds.), *Fiber Optic Sensors*, Smart Sensors, Measurement and Instrumentation 21, DOI 10.1007/978-3-319-42625-9_3

configuration and proposed a more practical configuration for the optical excitation of plasmons [7]. In Kretschmann-Raether configuration, a thin metal layer with a thickness of the order of 10–100 nm is deposited on the prism base.

2 Plasmons or Plasma Oscillations

There is a dense assembly of negatively charged free electrons inside a conductor (free electron charge density is 10^{23} cm^{-3} and, therefore, the group of free electrons can be compared with a plasma of particles), and also an equally charged positive ion lattice. Since, positive ions have an infinitely large mass compared to these free electrons, therefore, according to jellium model, this ion assembly can be replaced by a positive constant background. However, the total charge density inside the conductor still remains to be zero. If the density of free electrons is locally reduced by applying an external field on the conductor so that the movement of free electrons may take place, the negative free electrons are no longer screened by the background and they begin to get attracted by the positive ion background. This attraction acts as a driving force for free electrons and they move to positive region and accumulate with a density greater than necessary to obtain charge neutrality. Now, at this point, the Coulomb repulsion among the moving free electrons acts as a restoring force and produces motion in opposite direction. The resultant of the two forces (i.e., attractive driving force and repulsive restoring force) set up the longitudinal oscillations among the free electrons. These oscillations are known as plasma oscillations and a plasmon is a quantum of these oscillations. The existence of plasma oscillations has been demonstrated in electron energy-loss experiments [3, 4].

3 Surface Plasmons

The electron density oscillations along the metal-dielectric interface are known as surface plasma oscillations. The quantum of these oscillations is referred to as surface plasmon (also a surface plasmon wave or a surface plasmon mode), and is accompanied by a longitudinal (p-polarized) electric field, which decays exponentially in metal as well as dielectric (Fig. 1). The field has its maximum at metal-dielectric interface itself. By the solution of Maxwell's equation, one can also show that the surface plasmon wave propagation constant (K_{SP}) is continuous through the metal-dielectric interface and is given by

$$K_{SP} = \frac{\omega}{c}\left(\frac{\varepsilon_m \varepsilon_s}{\varepsilon_m + \varepsilon_s}\right)^{1/2} \tag{1}$$

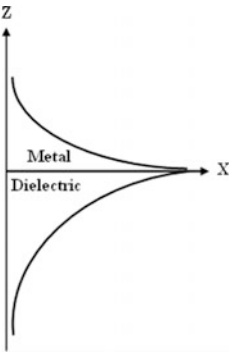

Fig. 1 Exponential decay of field intensity of surface plasmon mode in a metal and dielectric system

where ε_m and ε_s represent the dielectric constants of metal layer and the dielectric medium; ω represents the frequency of incident light and c is the velocity of light. The above equation implies that the properties of surface plasmon wave-vector depend on both media, i.e., metal as well as dielectric.

4 Excitation of Surface Plasmons by Light: Otto and Kretschmann-Raether Configurations

The maximum propagation constant of the light wave at frequency ω propagating through the dielectric medium is given by

$$K_g = \frac{\omega}{c}\sqrt{\varepsilon_s} \tag{2}$$

Since $\varepsilon_m < 0$ (i.e., for metal) and $\varepsilon_s > 0$ (i.e., for dielectric), for a given frequency, the propagation constant of surface plasmon is greater than that of the light wave (of same polarization state as that of the surface plasmon wave, i.e., p-polarized) in dielectric medium (Fig. 2).

Hence, the direct light cannot excite surface plasmons at a metal-dielectric interface and is referred to as non-radiative surface plasmon. Therefore, to excite surface plasmons the momentum and hence the wave vector of the exciting light in dielectric medium should be increased. In other words, an extra momentum (and energy) must be imparted to light wave in order to get the surface plasmons excited at a metal-dielectric interface.

The general idea behind Otto configuration was the coupling of surface plasmon wave with the evanescent wave, which is set up due to total internal reflection (TIR) at the base of a coupling prism when a light beam is incident at an angle greater than the critical angle (θ_{ATR}) at prism-air interface [6] (Fig. 3).

The nature of evanescent wave is known to have the propagation constant along the interface and to decay exponentially in the dielectric medium adjacent to the

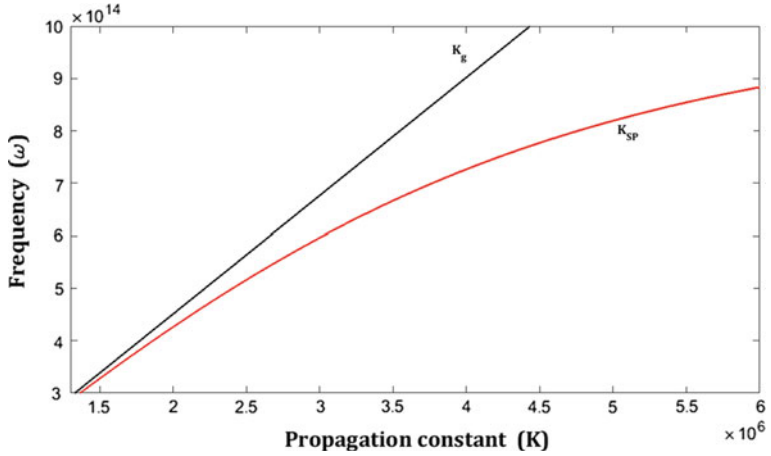

Fig. 2 Dispersion curves for surface plasmon wave (K_{SP}) and the direct light incident through the dielectric medium (K_g)

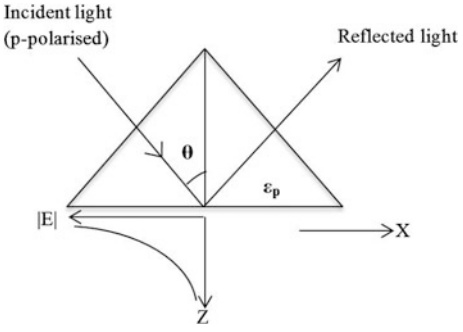

Fig. 3 Illustration of setting-up of an evanescent wave at prism-metal interface at $\theta > \theta_{ATR}$. ε_p is the dielectric constant of prism material

medium where TIR occurs. Both of these characteristics of evanescent wave are similar to those of a surface plasmon wave, therefore, there is a strong possibility of interaction between these waves. The horizontal component of the propagation constant of evanescent wave at prism-air interface is given by

$$K_{ev} = \frac{\omega}{c}\sqrt{\varepsilon_p}\sin\theta \tag{3}$$

As per the method devised by Otto, if a metal surface is brought in contact of this decaying evanescent field in such a way that an air gap remains between the prism base and metal layer, then the evanescent field at prism-air interface can excite the surface plasmons at the air-metal interface (Fig. 4).

However, this configuration is difficult to realize practically as the metal has to be brought within around 200 nm of the prism surface. This approach has been

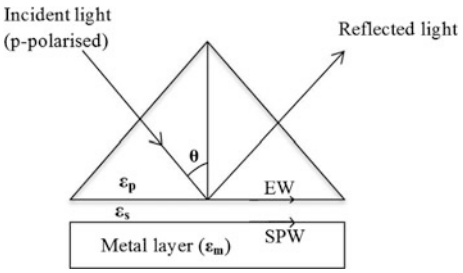

Fig. 4 Otto configuration for the excitation of surface plasmons

found to be very useful in studying the single crystal metal surfaces and adsorption on them.

As a significant improvement to Otto configuration, Kretschmann and Raether realized that the metal layer could be used as the spacing layer, i.e., evanescent wave generated at the prism-metal layer interface can excite surface plasmons at the metal-air interface so long as the metal layer thickness is not too large. They devised a new configuration [7], given in Fig. 5. In this configuration also, surface plasmons are excited by an evanescent wave from a high refractive index glass prism at attenuated total reflection (ATR) condition.

However, unlike Otto configuration, the surface of the glass substrate (e.g., prism) is coated with a thin metal film (typically around 50 nm thick) and is kept in direct contact with the dielectric medium of lower refractive index (such as air or some other dielectric sample). When a p-polarized light beam is incident through

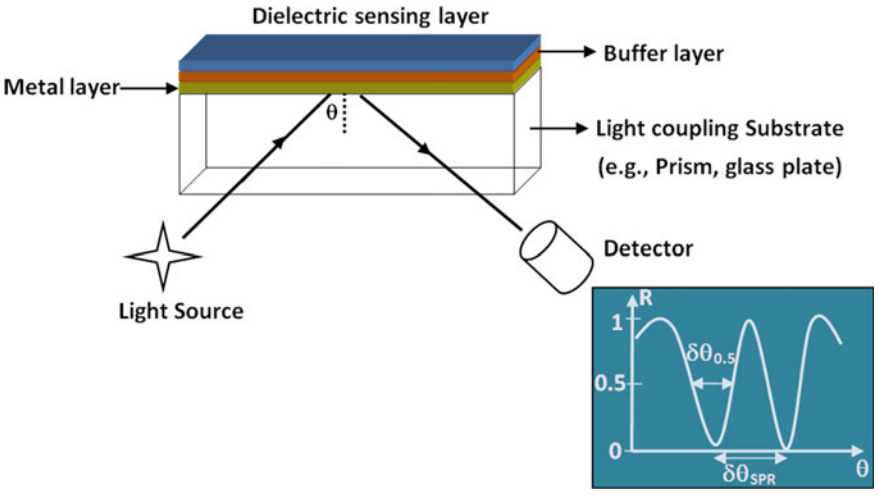

Fig. 5 An alternative schematic representation of the Kretschmann-Raether configuration for the excitation of surface plasmons at metal-dielectric interface. An ultrathin buffer layer may be used to protect the metal layer from oxidation etc

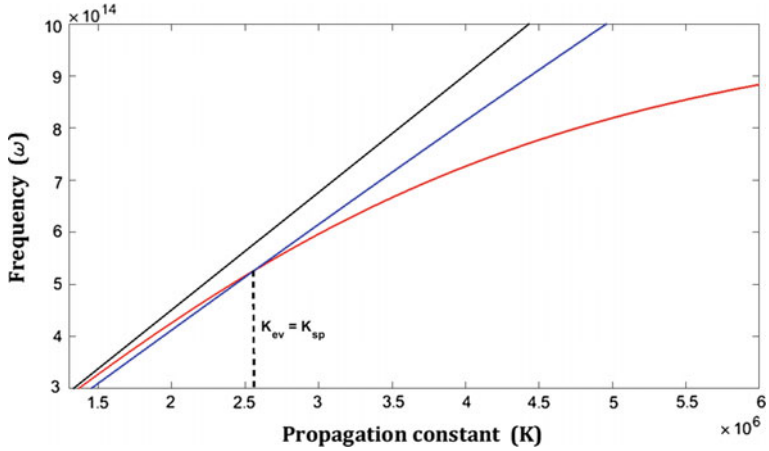

Fig. 6 Dispersion curves for direct light wave in dielectric (K_s, *Black line*), evanescent wave (K_{ev}, *Blue line*), surface plasmon wave K_{SP} (*Red curve*) at metal-dielectric interface

the prism on the prism-metal layer interface at an angle θ equal to or greater than the angle required for ATR (θ_{ATR}), the evanescent wave is generated at the prism-metal layer interface. Figure 6 shows the dispersion curves of the surface plasmon along with those of the direct light and the light incident through a glass prism of higher refractive index. The wave-vector K_{ev} of the evanescent wave, corresponding to incident angle θ, is equal to the lateral component of the wave-vector of the incident light in the prism as given in Eq. (3). The excitation of surface plasmon occurs when the wave vector of the propagation constant of evanescent wave exactly matches with that of the surface plasmon of similar frequency and state of polarization.

This occurs at a particular angle of incidence θ_{SPR} and the corresponding resonance condition for surface plasmons is written as

$$\frac{\omega}{c}\sqrt{\varepsilon_p}\,Sin\,\theta_{SPR} = \frac{\omega}{c}\left(\frac{\varepsilon_m\,\varepsilon_s}{\varepsilon_m+\varepsilon_s}\right)^{1/2} \tag{4}$$

Figure 6 indicates that the propagation constant curves corresponding to surface plasmon wave and evanescent wave may intersect each other at many positions for different sets of angle of incidence and frequency (i.e., θ and ω). This implies that the propagation constant of evanescent wave (K_{ev}) may match with that of the surface plasmon wave (at the metal-dielectric interface) depending on the frequency and angle of incidence of light beam.

5 Minimum of Reflectance at Resonance

The excitation of surface plasmons at metal/dielectric interface results in the transfer of energy from incident light to surface plasmons, which reduces the energy of the reflected light. If the normalized reflected intensity (R) is measured as a function of incident angle θ by keeping other parameters and components (such as frequency, metal layer, and dielectric layer) unchanged, then a sharp dip is observed at resonance angle θ_{SPR} due to transfer of energy to surface plasmons (Fig. 7). The light wave is incident at an angle greater than the corresponding ATR angle. At this point, one has to keep in mind that the energy conservation requires that R + A + T = 1, i.e., the sum of relative reflection, absorption, and transmission is unity. Since T = 0 at ATR, hence we are left with A + R=1 in the present case. The light wave having passed the glass prism (ε_p), is reflected partially at prism-metal interface. A part of the incident light wave energy traverses the metal film (of thickness d_m) as an exponentially decaying evanescent wave. At the metal-dielectric interface it induces the surface plasmon excitation, which radiates light back into the metal film. If the metal layer thickness (d_m) is small, the back-scattered field tends to increase.

Since, this back-scattered wave is out-of-phase with the incoming wave, the two interfere destructively and cause R to reduce. For minimum value of d_m, they compensate each other and R becomes equal to zero. Thus, the absorption A becomes equal to 1, i.e., whole radiation field is captured in the metal film. On the other hand, if the metal layer thickness is large enough, then the back-scattered field disappears and R approaches to 1. It means that no absorption of incident light

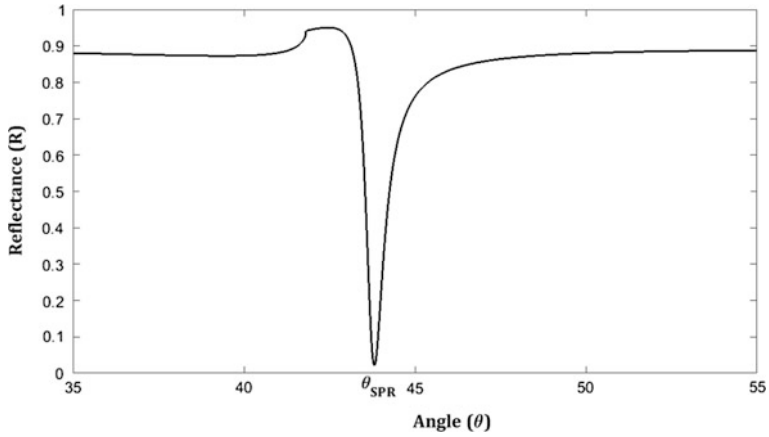

Fig. 7 Reflectance (R) as a function of angle of incidence (θ) at the prism-metal interface (angular interrogation). A sharp drop in reflected signal is observed at angle θ_{SPR}

wave is taking place [8]. As a conclusive statement, one can say that the value of R depends on the combination of incident light frequency, angle of incidence, and the thickness of the metal layer.

6 Optical Sensing Principle of SPR: Performance Parameters

The sensing principle of SPR sensors is based on Eq. (4). For a given frequency of the light source and the dielectric constant of metal film one can determine the dielectric constant (ε_s) of the sensing layer adjacent to metal layer by knowing the value of the resonance angle (θ_{SPR}). The resonance angle is determined by using angular interrogation method as discussed above. The resonance angle is very sensitive to variation in the refractive index (or, dielectric constant) of the sensing layer. Increase in refractive index of the dielectric sensing layer increases the resonance angle. The performance of a SPR sensor is analyzed with the help of two parameters: sensitivity and detection accuracy or signal-to-noise ratio (SNR). For the best performance of the sensor both the parameters should be as high as possible to attain a perfect sensing procedure. Sensitivity of a SPR sensor depends on how much the resonance angle shifts with a given change in refractive index of the sensing layer. If the shift is large, the sensitivity is large. Figure 8 shows a plot of reflectance as a function of angle of the incident light beam for sensing layers with refractive indices n_s and $n_s + \delta n_s$.

The sensitivity of a SPR sensor with angular interrogation is defined as

$$S_n = \frac{\delta\theta_{SPR}}{\delta n_s} \tag{5}$$

The detection accuracy or the signal-to-noise ratio (SNR) of a SPR sensor depends on how accurately and precisely the sensor can detect the resonance angle and hence, the refractive index of the sensing layer. Prior to the evaluation of SNR, a commonly more natural and practical parameter (S_L) related to the SNR in terms of the reflectivity (R) and resonance angle (θ_{SPR}) can be defined as

$$S_L = \frac{\delta R}{\delta\theta_{SPR}} \tag{6a}$$

This simply represents the slope of the reflectivity curve. The above parameter provides primary information regarding the detection sensitivity for SPR sensing system. Apart from the limitations of a real instrument, the accuracy of detection of resonance angle further depends on the width of the SPR curve. Narrower the SPR curve, higher is the detection accuracy. Therefore, if $\delta\theta_{0.5}$ is the angular width of the SPR response curve corresponding to 50 % reflectance, the detection accuracy of the sensor can be assumed to be inversely proportional to $\delta\theta_{0.5}$ (Fig. 8).

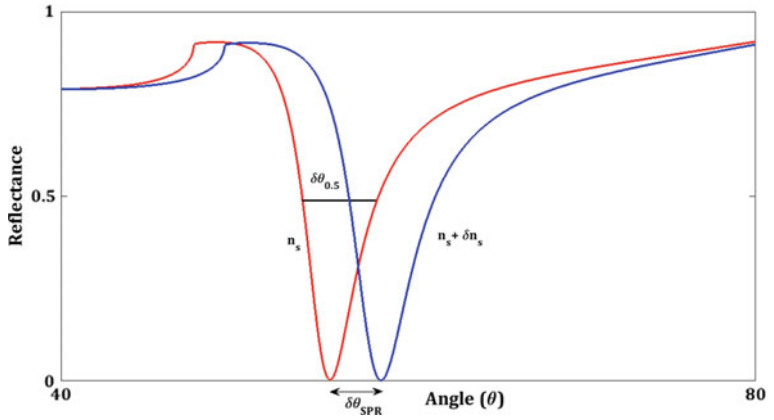

Fig. 8 The shift in resonance angle ($\delta\theta_{SPR}$) with a change in refractive index of the sensing layer (n_s) by δn_s. $\delta\theta_{0.5}$ is the angular width of the curve at half reflectance

The signal-to-noise ratio (SNR) of the SPR sensor with angular interrogation is, thus, defined as [9]

$$SNR = \frac{\delta\theta_{SPR}}{\delta\theta_{0.5}} \tag{6b}$$

Actual SNR of the real SPR sensing system critically depends on how well one measures the signals with real instruments.

7 Fiber Optic SPR Sensor

Introduction of optical fibers in SPR sensing system is based on a very logical reason that guidance of light in optical fibers is also based on TIR. Since, a prism is used in SPR sensing system in order to create TIR at the prism-metal interface; therefore, coupling prism used in the basic SPR theory can be conveniently replaced by the core of an optical fiber to design a fiber optic SPR sensor. Among other important reasons are the advantages of optical fiber over coupling prism such as simple and flexible design, miniaturized sensor system, and capability of remote sensing. In general, the cladding from a certain small portion (middle portion for most of the cases) of the fiber core is removed and is coated with a metal layer, which is further surrounded by a dielectric sensing layer (Fig. 9).

The light from a polychromatic source, if spectral interrogation method is used, is launched into one of the ends of the optical fiber. The TIR takes place for the rays propagating with an angle (θ) in the range varying from the critical angle (depending upon the numerical aperture of the fiber and the light wavelength) to approximately 90°. Consequently, evanescent field is generated, which excites the

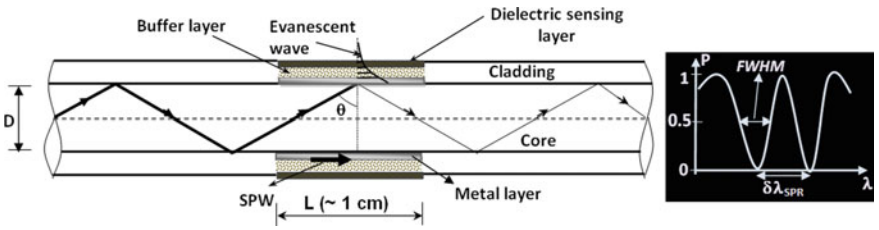

Fig. 9 Illustration of a typical fiber optic SPR sensor. D is fiber core diameter and L is SPR sensing region length

surface plasmons at the fiber core-metal layer interface. This coupling of evanescent field with surface plasmons strongly depends upon light wavelength, fiber parameters, fiber geometry, and metal layer properties. For instance, coupling mechanism will be different for single-moded and multi-moded optical fibers due to having different mode transmission properties depending upon number of modes a fiber will support. Similarly, a straight fiber and a tapered fiber will show different strengths of light coupling because these fibers will show different penetration depths of the evanescent field due to having different geometrical configurations. A tapered fiber shows a substantial variation in evanescent field penetration along the tapered sensing region length whereas an un-tapered fiber exhibits uniform penetration of the evanescent field along the sensing region. Further, penetration of evanescent field and, therefore, strength of light coupling with surface plasmons depends on an important fiber parameter known as numerical aperture, which is related to light acceptance limit of the fiber. Unlike prism based SPR sensor where angular interrogation method is used, the spectral interrogation method is generally used in fiber optic SPR senor because in the fiber optic sensor all the guided modes are launched in the fiber. Furthermore, unlike prism based SPR geometry, number of reflections for most of the angles is more than one for fiber based SPR sensor geometry. Besides its angle, the number of reflections for any ray depends on other fiber parameters, namely, sensing region length and fiber core diameter. The number of reflections directly affects the SPR curve width, therefore, performance parameters (SNR and sensitivity) of the sensor depends upon fiber properties in this way also.

Finally, the spectrum of the light transmitted after passing through the SPR sensing region is detected at the other end. The sensing is accomplished by observing the wavelength corresponding to the dip in the spectrum. This wavelength is called as the resonance wavelength (λ_{SPR}). A plot of resonance wavelength with the refractive index of the sensing layer gives the calibration curve of the fiber optic SPR sensor. The fiber-optic SPR sensor can also be designed as a tip-probe, which may be highly useful in biomedical diagnostic applications such as endoscopy (Fig. 10).

As far as the wave-optics analysis is concerned, the guided mode propagating in the optical fiber core can excite a surface plasmon wave at the interface between the

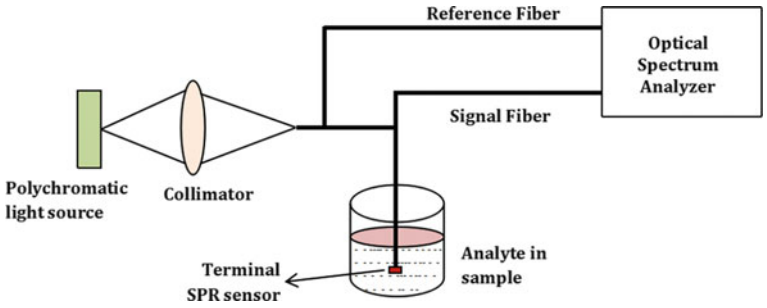

Fig. 10 Fiber optic SPR sensor as tip-probe suitable for biomedical diagnostic applications

metal and a sensing medium, if the two modes are closely phase matched. As the surface plasmon wave is lossy, the coupling results in damping of the fiber mode. Because the coupling strength depends dramatically on the refractive index of the dielectric adjacent to the metal film (sensed medium), even small variations in the refractive index of the sensed medium may produce large changes in the attenuation of the fiber mode. Since surface plasmons are inherently TM-polarized waves, only fiber modes of the corresponding polarization state may be involved in this interaction (TM-polarized mode), while the modes with the orthogonal polarization state (TE-polarized mode) are attenuated only due to ohmic loss in the metal layer. The TE-polarized mode, the attenuation of which is not sensitive to changes in optical properties of the sensed medium, may be used as a reference. Such single-moded fiber based SPR sensors are considered to be more sensitive, more accurate, and containing less noise in comparison to those with multi-moded fibers. However, their fabrication is much more complex and sophisticated compared with those for multi-moded fibers.

8 Selected Significant Works in the Area of Plasmonics-Based Fiber Optic Sensors

The development of fiber optic SPR sensors began in early nineties of last century. Among the first reports on fiber optic SPR sensors was the one proposed by Villuendas and Palayo [10]. They presented the experimental results for sensitivity and dynamic range in the measurement of sucrose concentration in aqueous solution. Soon after, a sensor based on excitation of SPR on the tip of a single-mode fiber was reported, which was based on the analysis of the state of polarization of the reflected beam [11]. At the same time, Jorgenson and Yee reported the theoretical as well as experimental work on a fiber optic chemical sensor based on SPR by fabricating the probe on a highly multimoded optical fiber and using a white light source instead of a monochromatic one [12]. The sensor proposed by them was able to detect the changes in the parameters like bulk refractive index, film

thickness, and film refractive index. As another significant application, fiber optic SPR sensor was first time used to monitor the deposition of a multilayered cadmium arachidate Langmuir-Blodgett film [13]. Experiments showed that there were constant shifts in resonance wavelength as the number of monolayers was increased. This provided the method of calculating the film thickness by measuring the changes in SPR spectra.

In another significant work [14], the sensitivity to refractive index was reported to be of the order of 10^{-5} RIU while the dynamic range was found to be between 1.25 and 1.40 RIU. Soon after, a fiber optic SPR remote sensor for the detection of tetrachloroethene was proposed by using a gas sensitive polymer film on the metal layer [15]. The sensor showed good response time (of 2 s), and reproducibility apart from a long-term stability (of more than 3 months). Homola and Slavik [16] reported a SPR sensor using side polished single mode optical fiber and a thin metal overlayer. The sensor was highly sensitive (sensitivity around −2500 dB/RIU for a refractive index range of 1.41–1.42 RIU) and a very small amount of sample was required for measuring the refractive index.

Study of self-assembled monolayers (SAMs) such as n-alkanethiol for the protection of silver film due to oxidation on fiber core was carried out [17]. Also, the sensor with SAM was shown to have no ageing problem and had high stability. The SAM was later used in a fiber optic SPR sensor for gas detection [18]. A side-polished single mode fiber optic SPR sensor discussed above was further modified [19]. In the modified design, the output end of the fiber was made reflecting. Therefore in the modified sensor, instead of measuring transmitted light, the back reflected light from the mirrored end face of the fiber was detected. In another work, chemical sensing with gold-coated SPR fiber optic sensor was proposed [20]. Theoretical simulations showed that the proposed configuration allowed reaching a 30-fold increase in sensitivity in comparison to the previous SPR based sensors. The effect of polarization of the incident light in a multimode fiber is another critical factor in context of an SPR sensor. An important research was carried out in this direction [21]. A three-dimensional skew ray model was developed to completely explain the experimental phenomenon for an intrinsic SPR multimode fiber sensor. The model was important to explain the variations of the refractive index of the bulk medium and thickness of the thin dielectric layer. As another crucial development, gold island fiber optic SPR sensor was proposed [22]. The fundamental optical absorbance at around 535 nm for gold particles was shown to shift if the fiber was immersed in different media.

The other configuration studied for SPR sensor was metal-coated tapered fiber for refractive index sensing [23]. Quasi-circular polarization insensitive devices and asymmetric polarization sensitive devices were fabricated and their characteristics as refractive index sensors were measured. Another sensor probe based on monochromatic skew ray excitation of SPR was demonstrated to monitor the SAM formation and the immunoassay [24]. A fiber optic SPR sensor based on spectral interrogation in a side polished single mode fiber using depolarized light was reported [25]. The sensor was able to measure refractive index variation as small as 10^{-7} and its suitability for biosensing was demonstrated by detecting IgG through

respective monoclonal antibodies immobilized on the SPR sensor surface. Lin et al. [26] developed a fiber optic sensor based on silver for chemical and biological applications.

A theoretical approach was applied to provide a better understanding of surface plasmon excitation in fiber optic sensors [27]. The model was based on the calculation of the fields in the waveguide structures and that enabled to evaluate the optical power loss from energy conservation considerations. Further, another improvement was made in context of fiber optic SPR biosensor when the fast detection of Staphylococcal enterotoxin B (SEB) was reported [28]. As another important development, an SPR sensor using an optical fiber with an inverted Graded-Index profile was proposed [29]. A fiber optic SPR sensor for the detection of hydrogen was reported [30]. A thin palladium layer deposited on the metal-coated core of a multimode fiber was used as the transducer. The modification of the SPR was due to variation in the complex permittivity of palladium in contact with gaseous hydrogen. This effect was enhanced by using selective injection of high-order modes in the fiber through a collimated beam on the input end of the fiber. Measurements of concentrations as low as 0.8 % of hydrogen in pure nitrogen were reported.

The use of single mode polarization maintaining fiber (PMF) for SPR sensors was another milestone [31]. A fiber optic sensor with nanocomposite multilayered polymer and nanoparticle ultra-thin films was reported for biosensing [32].

A new approach of hetero-core structure for a fiber optic SPR sensor was introduced [33]. The hetero-core structured fiber optic SPR probe consists of two fibers with different core diameter connected by thermal fusion splicing. This was done, deliberately, to leak the transmitted power into the cladding layer of small core diameter fiber so that the leaked light may induce an optical evanescent wave required for SPR excitation. This structure has no need to eliminate the cladding layer of fiber, therefore, it is able to provide the characteristic advantage of optical fibers for remote monitoring. Next, a fiber optic SPR sensor with asymmetric metal coating on a uniform waist single mode tapered fiber was reported [34]. Due to the varying film thickness the sensor transmission spectrum exhibited multiple resonance dips, which increase the dynamic range of the sensor. SPR-based conical microsensor using chemically etched single mode fiber was reported [35]. Among the biosensors, a real time fiber optic SPR sensor to detect biologically-relevant concentrations of myoglobin and cardiac troponin I in less than 10 min was proposed [36]. A comprehensive model of on absorption based fiber optic SPR sensor for the detection of concentration of chemicals was proposed [37].

Fast responding fiber optic SPR biosensor [38], analysis of a fiber optic SPR sensor based on a crossing point of the two SPR spectra obtained from the sample fluid and the de-ionized water [39], the application of single-crystal sapphire-fiber optic SPR sensor in the extreme environment [40], and the use of tapered fiber optic SPR sensor for vapor and liquid phase detection [41] were some of the other advancements in this area. Application of D-type optical fiber sensor based on heterodyne interferometry has also been a very interesting addition to the fiber optic SPR sensor technology [42]. A detailed sensitivity analysis along with performance

optimization for multilayered fiber optic SPR concentration sensor has been reported [43]. The sensitivity and signal-to-noise ratio analysis of a fiber optic SPR refractive index sensor has been carried out for different conditions related to metal layer, optical fiber and light launching conditions along with an extension to remote sensing [44].

Fiber optic SPR sensors with bimentallic alloy nanoparticles was reported [45]. Furthermore, the application of localized surface plasmon resonance (LSPR) in optical fiber sensors [46] and a colloidal gold-modified long period fiber grating (LPFG) for chemical and biochemical sensing [47] was reported. Among the main advantages of the LPFG based SPR sensors is their simple construction and ease of use. Moreover, the sensor has the potential capability for on-site and remote sensing, can be easily multiplexed to enable high-throughout screening of bimolecular interactions, and has the potential use for disposable sensors. The above sensor with long period fiber grating has shown a detection limit for anti DNP (dinitrophenyl compound) of 9.5×10^{-9} M.

Among the other techniques, fiber Bragg gratings (FBG) have also found applications in SPR sensing [48]. A novel technique of FBG assisted surface plasmon polariton (SPP) sensor has been proposed [49]. As another advance in this direction, the theoretical model of a new hollow core fiber sensor based on the specific properties of the SPP excited with a fiber Bragg grating is proposed [50]. The main principle of operation of this new device is based on the efficient energy transfer between the fiber waveguide mode (FWM) and the surface plasmon-polariton (SPP). These new models based on FBG paved the way to design a highly flexible sensor system.

A model of LSPR based planar multireflection sensing system with gold nanospheres was reported [51]. SPR sensor based on photonic crystal fiber [52] has been proposed in the visible to near-infrared spectral regions. As another crucial advancement, the concept of a microstructured optical fiber-based SPR sensor with optimized microfluidics is proposed [53].

Fiber optic SPR sensors have been reported for gas sensing (utilizing resonant SiO_2-TiO_2 multilayered dielectric films) [54] and for blood-group determination [55].

9 Conclusion and Future Scope

The collaboration of plasmonics and optical fiber technology has brought a lot of advancements in sensing of various physical, chemical, and biochemical parameters. This chapter has highlighted in detail the fundamentals of plasmonics along with some selected research works on plasmonics-based fiber optic sensors reported in last 25 years or so.

There is still a lot of scope for work in plasmonics-based fiber optic biosensors with high sensitivity, detection accuracy, and reproducibility for an early detection of different diseases and biological processes.

Plasmonics fiber optic sensors have a lot of potential to work in infrared for various defense and biomedical applications. In order to make it happen, different types of

fibers such as chalcogenide and fluoride fibers are potential candidates. Since the plasmonic properties vary significantly when the wavelength shifts from visible to near or mid-infrared region, therefore, selection of metals and dielectrics in infrared becomes a critical factor. Therefore, highly comprehensive theoretical and experimental analyses of plasmonics-based fiber optic sensors in infrared are required.

Plasmonic sensors based on photonic crystal fibers as well have a significant scope of research. The phenomena related to metamaterials (such as MoS_2 and graphene), magnonics, spin waves, and photo-thermo-refractive (PTR) glasses are also potential candidates to be implemented in developing high-performance plasmonic sensors for biomedical and industrial applications.

Acknowledgments The author acknowledges the motivation and encouragement from the Director (NIT Delhi), colleagues, friends, and family during preparation of this chapter. The authors also thanks his former mentors and colleagues in India, Germany, and the Netherlands for their kind support in respective durations.

References

1. J. Zenneck, Uber die Fortpflanztmg ebener elektro-magnetischer Wellen langs einer ebenen Leiterflache und ihre Beziehung zur drahtlosen Telegraphie. Annals der Physik **23**, 846–866 (1907)
2. A. Sommerfeld, Propagation of waves in wireless telegraphy. Annals der Physik **28**, 665–736 (1909)
3. R.H. Ritchie, Plasma losses by fast electrons in thin films. Phys. Rev. **106**, 874–881 (1957)
4. C.J. Powell, J.B. Swan, Effect of oxidation on the characteristic loss spectra of aluminum and magnesium. Phys. Rev. **118**, 640–643 (1960)
5. E.A. Stern, R.A. Ferrell, Surface plasma oscillations of a degenerate electron gas. Phys. Rev. **120**, 130–136 (1960)
6. A. Otto, Excitation of nonradiative surface plasma waves in silver by the method of frustrated total reflection. Zeitschrift für Physik **216**, 398–410 (1968)
7. E. Kretschmann, H. Raether, Radiative decay of non-radiative surface plasmons excited by light. Z. Naturforsch. **23**, 2135–2136 (1968)
8. H. Raether, *Surface Plasmons on Smooth and Rough Surfaces and on Gratings* (Springer, 1988)
9. S.A. Zynio, A.V. Samoylov, E.R. Surovtseva, V.M. Mirsky, Y.M. Shirsov, Bimetallic layers increase sensitivity of affinity sensors based on surface plasmon resonance. Sensors **2**, 62–70 (2002)
10. F. Villuendas, J. Pelayo, Optical fibre device for chemical sensing based on surface plasmon excitridon. Sens. Actuators A **23**, 1142–1145 (1990)
11. L.D. Maria, M. Martinelli, G. Vegetti, Fiber-optic sensor based on surface plasmon interrogation. Sens. Actuators B **12**, 221–223 (1993)
12. R.C. Jorgenson, S.S. Yee, A fiber-optic chemical sensor based on surface plasmon resonance. Sens. Actuators B **12**, 213–220 (1993)
13. M. Mar, R.C. Jorgenson, S. Letellier, S.S. Yee, In-situ characterization of multilayered Langmuir-Blodgett films using a surface plasmon resonance fiber optic sensor, in *Proceedings of the 15th Annual International Conference of the IEEE* (1993), pp. 1551–1552
14. R.C. Jorgenson, S.S. Yee, Control of the dynamic range and sensitivity of a surface plasmon resonance based fiber optic sensor. Sens. Actuators A **43**, 44–48 (1994)

15. M. Niggemann, A. Katerkamp, M. Pellmann, P. Bolsmann, J. Reinbold, K. Cammann, Remote sensing of tetrachloroethene with a micro-fibre optical gas sensor based on surface plasmon resonance spectroscopy, in *The 8th International Conference on Solid-State Sensors and Actuators, and Eurosensors IX*, Stockholm, Sweden, vol. 2 (1995), pp. 797–800
16. J. Homola, R. Slavik, Fibre-optic sensor based on surface plasmon resonance. Electron. Lett. **32**, 480–482 (1996)
17. A. Abdelghani, J.M. Chovelon, J.M. Krafft, N. Jaffrezic-Renault, A. Trouillet, C. Veillas, C. Ronot-Trioli, H. Gagnaire, Study of self-assembled monolayers of n-alkanethiol on a surface plasmon resonance fibre optic sensor. Thin Solid Films **284–285**, 157–161 (1996)
18. A. Abdelghani, J.M. Chovelon, N. Jaffrezic-Renault, C. Ronot-Trioli, C. Veillas, H. Gagnaire, Surface plasmon resonance fibre-optic sensor for gas detection. Sens. Actuators B **39**, 407–410 (1997)
19. R. Slavík, J. Homola, J. Ctyroký, Miniaturization of fiber optic surface plasmon resonance sensor. Sens. Actuators B **51**, 311–315 (1998)
20. E. Fontana, Chemical sensing with gold coated optical fibers. Microwave Optoelectr. Conf. **2**, 415–419 (1999)
21. W.B. Lin, N. Jaffrezic-Renault, A. Gagnaire, H. Gagnaire, The effects of polarization of the incident light-modeling and analysis of a SPR multimode optical fiber sensor. Sens. Actuators A **84**, 198–204 (2000)
22. F. Meriaudeau, A. Wig, A. Passian, T. Downey, M. Buncick, T.L. Ferrell, Gold island fiber optic sensor for refractive index sensing. Sens. Actuators B **69**, 51–57 (2000)
23. A. Díez, M.V. Andrés, J.L. Cruz, In-line fiber-optic sensors based on the excitation of surface plasma modes in metal-coated tapered fibers. Sens. Actuators B **73**, 95–99 (2001)
24. W.B. Lin, N. Jaffrezic-Renault, J.M. Chovelon, M. Lacroix, Optical fiber as a whole surface probe for chemical and biological applications. Sens. Actuators B **74**, 207–211 (2001)
25. R. Slavík, J. Homola, J. Ctyroký, E. Brynda, Novel spectral fiber optic sensor based on surface plasmon resonance. Sens. Actuators B **74**, 106–111 (2001)
26. W.B. Lin, M. Lacroix, J.M. Chovelon, N. Jaffrezic-Renault, H. Gagnaire, Development of a fiber-optic sensor based on surface plasmon resonance on silver film for monitoring aqueous media. Sens. Actuators B **75**, 203–209 (2001)
27. O. Esteban, R. Alonso, C.C. Navarrete, A. Gonzalez-Cano, Surface plasmon excitation in fiber-optics sensors: a novel theoretical approach. J. Lightwave Technol. **20**, 448–453 (2002)
28. R. Slavík, J. Homola, E. Brynda, A miniature fiber optic surface plasmon resonance sensor for fast detection of staphylococcal enterotoxin B. Biosens. Bioelectron. **17**, 591–595 (2002)
29. F. Bardin, I. Kasik, A. Trouillet, V. Matejec, H. Gagnaire, M. Chomat, Surface plasmon resonance sensor using an optical fiber with an inverted graded-index profile. Appl. Opt. **41**, 2514–2520 (2002)
30. X. Bévenot, A. Trouillet, C. Veillas, H. Gagnaire, M. Clément, Surface plasmon resonance hydrogen sensor using an optical fibre. Meas. Sci. Technol. **13**, 118–124 (2002)
31. M. Piliarik, J. Homola, Z. Maníková, J. Ctyroký, Surface plasmon resonance sensor based on a single-mode polarization-maintaining optical fiber. Sens. Actuators B **90**, 236–242 (2003)
32. P.S. Grant, S. Kaul, S. Chinnayelka, M.J. McShane, Fiber optic biosensors comprising nanocomposite multilayered polymer and nanoparticle ultrathin films, in *Proceedings of the 25th Annual International Conference of the IEEE*, vol. 4 (2003), pp. 2987–2990
33. M. Iga, A. Seki, K. Watanabe, Hetero-core structured fiber optic surface plasmon resonance sensor with silver film. Sens. Actuators B **101**, 368–372 (2004)
34. D. Monzón-Hernández, J. Villatoro, D. Talavera, D. Luna-Moreno, Optical-fiber surface-plasmon resonance sensor with multiple resonance peaks. Appl. Opt. **43**, 1216–1220 (2004)
35. K. Kurihara, H. Ohkawa, Y. Iwasaki, O. Niwa, T. Tobita, K. Suzuki, Fiber-optic conical microsensors for surface plasmon resonance using chemically etched single-mode fiber. Anal. Chim. Acta **523**, 165–170 (2004)
36. J.F. Masson, L.A. Obando, S. Beaudoin, K.S. Booksh, Sensitive and real-time fiber-optic-based surface plasmon resonance sensors for myoglobin and cardiac troponin I. Talanta **62**, 865–870 (2004)

37. A.K. Sharma, B.D. Gupta, Absorption-based fiber optic surface plasmon resonance sensor: a theoretical evaluation. Sens. Actuators B **100**, 423–431 (2004)
38. R. Micheletto, K. Hamamoto, S. Kawai, Y. Kawakami, Modeling and test of fiber-optics fast SPR sensor for biological investigation. Sens. Actuators B **119**, 283–290 (2005)
39. W. Tsai, Y. Tsao, H. Lin, B. Sheu, Cross-point analysis for a multimode fiber sensor based on surface plasmon resonance. Opt. Lett. **30**, 2209–2211 (2005)
40. Y.C. Kim, J.F. Masson, K.S. Booksh, Single-crystal sapphire-fiber optic sensors based on surface plasmon resonance spectroscopy for in situ monitoring. Talanta **67**, 908–917 (2005)
41. Y. Kim, W. Peng, S. Banerji, K.S. Booksh, Tapered fiber optic surface plasmon resonance sensor for analyses of vapor and liquid phases. Opt. Lett. **30**, 2218–2220 (2005)
42. S.F. Wang, M.H. Chiu, R.S. Chang, Numerical simulation of a D-type optical fiber sensor based on the Kretschmann's configuration and heterodyne interferometry. Sens. Actuators B **114**, 120–126 (2006)
43. B.D. Gupta, A.K. Sharma, Sensitivity evaluation of a multi-layered surface plasmon resonance-based fiber optic sensor: a theoretical study. Sens. Actuators B **107**, 40–46 (2005)
44. A.K. Sharma, B.D. Gupta, On the sensitivity and signal-to-noise ratio of a step-index fiber optic surface plasmon resonance sensor with bimetallic layers. Opt. Commun. **45**, 159–169 (2005)
45. A.K. Sharma, B.D. Gupta, Fiber-optic sensor based on surface plasmon resonance with Ag-Au alloy nanoparticle films. Nanotechnology **17**, 124–131 (2006)
46. L.K. Chau, Y.F. Lin, S.F. Cheng, T.J. Lin, Fiber-optic chemical and biochemical probes based on localized surface plasmon resonance. Sens. Actuators B **113**, 100–105 (2006)
47. J.L. Tang, S.F. Cheng, W.T. Hsu, T.Y. Chiang, L.K. Chau, Fiber-optic biochemical sensing with a colloidal gold-modified long period fiber grating. Sens. Actuators B **119**, 105–109 (2006)
48. S. Jette-Charbonneau, P. Berini, Theoretical performance of Bragg gratings based on long-range surface plasmon-polariton waveguides. J. Opt. Soc. Am. A **23**, 1757–1767 (2006)
49. G. Nemova, R. Kashyap, Fiber Bragg grating assisted surface plasmon-polariton sensor. Opt. Lett. **24**, 3789–3796 (2006)
50. G. Nemova, R. Kashyap, Modeling of plasmon-polariton refractive-index hollow core fiber sensors assisted by a fiber Bragg grating. J. Lightwave Tech. **24**, 3789–3796 (2006)
51. K. Hamamoto, R. Micheletto, M. Oyama, A. Ali-Umar, S. Kawai, Y. Kawakami, An original planar multireflection system for sensing using the local surface plasmon resonance of gold nanosphere. J. Opt. A: Pure Appl. Opt. **8**, 268–271 (2006)
52. A. Hassani, M. Skorobogatiy, Photonic crystal fiber-based plasmonic sensors for the detection of biolayer thickness. J. Opt. Soc. Am. B. **26**, 1550–1557 (2009)
53. A. Hassani, M. Skorobogatiy, Design of the microstructured optical fiber-based surface plasmon resonance sensors with enhanced microfluidics. Opt. Express **14**, 11616–11621 (2006)
54. A.K. Sharma, G.J. Mohr, Theoretical understanding of an alternating dielectric multilayer-based fiber optic SPR sensor and its application to optical sensing. New J. Phys. **10** (2008) (Art. 023039)
55. A.K. Sharma, R. Jha, H.S. Pattanaik, G.J. Mohr, Design considerations for surface plasmon resonance based detection of human blood group in near infrared. J. Biomed. Opt. **14** (2009) (Art. 064041)

POF Biosensors Based on Refractive Index and Immunocapture Effect

Marcelo Werneck, Rafaela Lopes, Greice Costa, Domingos Rodrigues, Ariadny Arcas, Fabio Dutra, Vanessa Queiroz and Regina Allil

Abstract The combat against tropical diseases is becoming an increasingly important issue in developing countries and they need to rely on readily available and rapid response diagnostic assays. The diagnostic methods for the detection of common pathogens are still time consuming, require laboratories and specialized personnel. To the effective combat of these diseases, the diagnostic needs to be fast, reliable and accurate, not only to the clinical area, but also to immediate detection of contaminants, particularly for water quality, clinical diagnosis or food security. With the development of new technologies, especially in methods based on immunological assays, one expects increased sensitivity, specificity and speed in the detection of important microorganisms for health, veterinary medicine, agriculture and industry. This advance serves as a basis for various other techniques such as the use of biosensors for the detection of pathogens. Optical biosensors offer several advantages when compared with conventional biosensors and some of these advantages are electrical passiveness, long distance sensing and electromagnetic immunity. The objective of this work is to develop three biosensor platforms based on refractive index measurement by the following techniques: surface plasmon resonance, evanescent wave and gold thin film evanescent wave techniques using a plastic optical fiber. We aimed at the best configuration of the optical setup, sensitivity, response time, a simple fabrication method, and a good specificity for *Escherichia coli* detection.

M. Werneck (✉) · R. Lopes · G. Costa · D. Rodrigues · A. Arcas · F. Dutra · V. Queiroz · R. Allil
Photonics and Instrumentation Laboratory, Universidade Federal do Rio de Janeiro, Rio de Janeiro, Brazil
e-mail: werneck@lif.coppe.ufrj.br

F. Dutra
Petrobras S.A., R&D in Upstream Processing, Rio de Janeiro, Brazil

R. Allil
Brazilian Army Technological Center (CTEx), Biological Defence Laboratory, Institute of Chemical, Biological, Radiological and Nuclear Defence, Rio de Janeiro, Brazil

© Springer International Publishing Switzerland 2017

I.R. Matias et al. (eds.), *Fiber Optic Sensors*, Smart Sensors, Measurement and Instrumentation 21, DOI 10.1007/978-3-319-42625-9_4

1 Introduction

The combat against tropical diseases is becoming an increasingly important issue in developing countries and they need to rely on readily available and rapid response diagnostic assays. The diagnostic methods for the detection of common pathogens are still time consuming and require laboratories and specialized personnel. The main methods of detection of known microorganisms can be divided into two groups: conventional methods, widely employed, and fast methods, the biosensors, a relatively newer technology that focus on a biochemistry essay for obtaining the results. With the development of new technologies, especially in antibody-based methods, as for example, the world widely known enzyme-linked immunosorbent assay (ELISA), it was possible to obtain an increased sensitivity, specificity and rapidity in the detection of microorganisms which are important for health, veterinary medicine, agriculture, industry, in the environment control.

Indeed, we are witnessing in the last decades a significant growing in biosensor technologies substituting all conventional methods. Biosensor technology involves a fully multidisciplinary area; the development of this new technology requires several different areas to be connected. In general, biosensors are compact devices that incorporate a biological recognition element, which can be an enzyme, an antibody, a protein, nucleic acid, a receiver, a cell or a tissue. The principle of detection of a biosensor is based on the specific interaction between the analyte and the element of recognition. As a result of this union, occurs the variation of one or more physical chemical properties (pH, electron transfer, heat, change of potential, in mass variation of optical properties, etc.) detected by the transducer or signal transduction system. Thus, the biosensor relies on a biological recognition element that interacts with the target (bacteria, virus, DNA, etc.) and produces a calibrated output signal that is used as a parameter transducer. The biosensors technologies can be divided into several categories such as physicochemical, amperometric, piezoelectric, electrochemical or optical.

The optical technology has relatively recently emerged on the market, as a powerful, cheap and reliable tool, allowing the development of new techniques for biological detection. Optical biosensors offer several advantages when compared with their conventional electric counterparts such as electric passiveness, long distance sensing, possibility of multiplexing several sensing channels, electromagnetic immunity, etc.

For this reason, the development of new types of optical biosensors and their further use is growing fast, as shown in a review work conducted by Lazcka et al. [1].

Optical biosensors can be further split into several different techniques. Some studies detect the presence of the cells around the fiber by refractive index (RI) variation such as in our previous works found in Ferreira et al. [2], Beres et al. [3] and Wandemur et al. [4], whereas other studies detect the fluorescence emitted by the cells [5, 6], and by enzymatic reaction [7].

Biological detection through RI measurements can be performed in several ways by the use of optical fiber sensors. Surface Plasmon Resonance (SPR) is one of

these methods and is used widely as a detection principle in different fields. SPR is very attractive because it can attain resolutions as high as 10^{-7} RIU (refraction index units) [8]. Other well-known technology is based on the light interference phenomenon and can be implemented either in optical fibers or in planar wave-guides producing accuracies as high as those produced by SPR [9].

Fiber Bragg grating (FBG) is another very accurate technique for measuring RI as demonstrated by Baldini et al. [10]. In order to adapt an FBG to be sensitive to the RI of the surrounding medium it is necessary to expose, by etching or polishing, the evanescent field present close to the interface between the core and the cladding just over the grating location.

Evanescent field or evanescent wave (EW) occurs in the interface between the core and the cladding of the fiber. When a total internal reflection of a light beam in the core-cladding interface occurs, it generates an EW at the other side of the core and around it. The EW occupies about one wavelength in distance from the core-cladding interface. EW-based biosensor is based on the exposition of the core-cladding interface of an optical wave-guide in order to promote an interaction between the EW and the surrounding medium. To reach the EW it is necessary to etch, polish or tapering the fiber by heating and drawing [3, 11, 12].

As it has been shown above, RI measurement techniques demand some previous preparation of the fiber, i.e. polishing, etching, pulling, FBG scribing, thin film deposition, etc. These techniques, are either difficult to accomplish (taper, SPR and interferometry), expensive to fabricate (FBG) or complicated and expensive to interrogate (FBG and fluorescence).

However, for developing a sensor probe with a larger possibility of ending up in a commercial and large-scale production, it is necessary to think of simple and easy-to-fabricate sensor probes.

In this work, we demonstrate and test three innovative biosensor platforms based on RI measurement in plastic optical fiber (POF). They are: Localized surface plasmon resonance (LSPR) sensor, evanescent wave (EW) U-shape sensor and gold thin film evanescent wave sensor. Then, one of these three sensor probes is functionalized to be sensitive to *Escherichia coli* and experimentally tested under different concentrations of this bacterium. Three main objectives were aimed at: determination of the best optical setup configuration (the probe), the simplest method of developing the sensor probe and the performance evaluation of the field-portable biosensor system, functionalized for rapid detection of specific microorganisms.

2 Sensing Principles

2.1 Refractive Index as a Sensing Parameter

A bacterium due to its intracellular components, including water, salts, RNA, proteins, etc., presents a RI about 1.39, slightly higher than that of pure water ($n = 1.334$) [3]. Due to this small difference, it is possible to detect bacteria by

measuring RI with a very high accuracy. However, two steps must be previously taken: Because even in a heavily contaminated water, the bacteria concentration is so small that the water RI does not change enough to be sensed, in order to detect bacteria one has to concentrate them around the fiber. The other limitation is that most bacterium presents the same RI, therefore, in order to construct a sensor for a specific bacterium we must concentrate only those wanted bacteria around the fiber. These two mentioned steps can be simultaneously accomplished by covalently bonding the specific antibody around the sensitive region of the fiber. In this way, all bacteria of that specific species will be captured and fixed around the sensitive part of the sensor producing an increase of the RI that will be detected by the sensor. This technique is known as immunocapture.

2.2 The Principle of Evanescent Wave (EW)

When modes of light propagate through a waveguide, they are bounded inside the core by the phenomenon known as total internal reflection (TIR). All light rays incident at the core-cladding interface with angles greater than the critical angle will suffer TIR. This angle is given by:

$$\theta_c = \sin^{-1}\left(\frac{n_{cl}}{n_{co}}\right) \tag{1}$$

where n_{cl} is the RI of the cladding and n_{co} is that of the core.

Evanescent waves are formed when waves traveling in a medium undergo total internal reflection at its boundary because they strike it at an angle greater than the critical angle.

The phenomenon of TIR by light rays was first observed by Newton when a part of the incident light penetrates into the rarer medium (in our case, the cladding) and travel some distance inside it before re-emerging into the denser medium (the core). The electromagnetic energy outside the core, close to its surface is known as the EW.

At a fiber bend, the propagation conditions alter because light rays propagating close to θ_c will reach the interface core-cladding in a angle smaller than θ_c and will refract to the cladding instead of reflecting by TIR and then part of the power is lost into the cladding. However, the cladding also supports a few propagating modes refilled by those lost modes from the core. At the cladding interface with the solution there will be another critical angle θ_c so that all cladding modes hitting this interface at higher angles will be guided. However, in the curve some modes will reach the interface at angles smaller than the critical angle and will be lost forever into the solution.

These cladding empty modes will be immediately refilled by the core modes and some power will be lost at the end of the fiber. In this way, the solution's RI will dominate the output power of light that is guided by the fiber.

The power attenuation along the propagation axis (z) is described by

$$\mathrm{P(z)} = \mathrm{P(0)exp}(-\gamma\,\mathrm{z}) \tag{2}$$

where P(0) is the power at beginning of the fiber and γ is the attenuation coefficient. By analogy, the power attenuation along de bent fiber can be described as function of the curvature angle ϕ:

$$\mathrm{P}(\phi) = \mathrm{P(0)exp}(-\gamma\phi) \tag{3}$$

An analysis already developed for a fiber curve [13, 14], as shown in Fig. 1, determines the relationship between the input and output power as a function of the angle of the curve, as in Eq. (4). This equation shows that the output power is proportional to the curvature radius.

$$P_s(\phi) = P(0) \int_{R-\rho}^{R+\rho} dr \int_{-\theta_c(r)}^{\theta_c(r)} \exp(-\gamma\phi) d\theta \tag{4}$$

From Eq. (4), with $\phi = 180°$, it is possible to arrive at the following equation [15]:

$$\mathrm{P_s(n_2)} = 4\mathrm{P(n_{2_{min}})}\rho\theta_c(\mathrm{n_2})\,\exp[-\gamma(\mathrm{n_2})\pi] \tag{5}$$

where

$$P(n_{2_{min}}) = \frac{1}{4\rho\theta_c n_{2_{min}} \exp[-\gamma n_{2_{min}}\pi]} \tag{6}$$

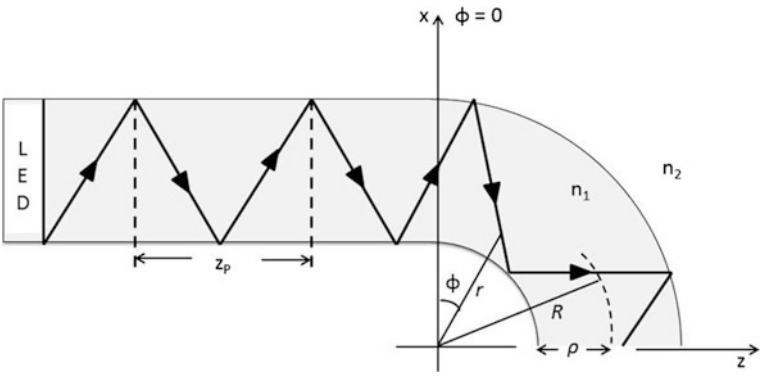

Fig. 1 Fiber bent by variation of the angle (ϕ): ρ—core radius; R—curvature radius, r—distance between the center of the curve and the guided light beam; zp—distance between successive reflections in the straight fiber section [22]

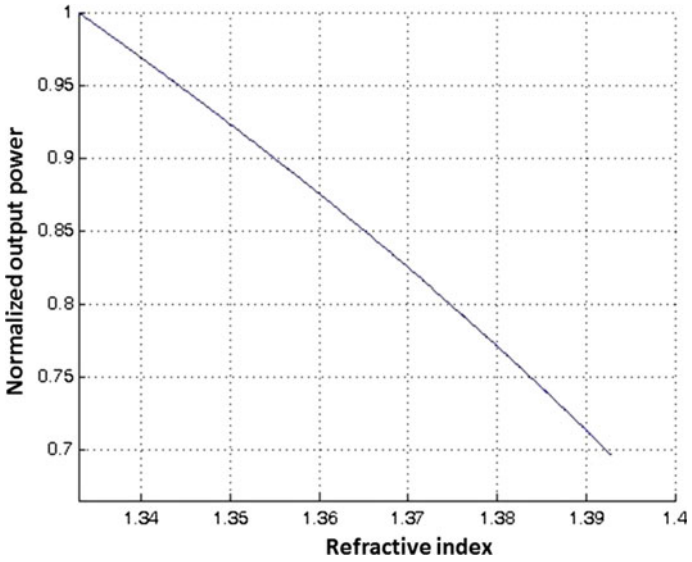

Fig. 2 Normalized output power as a function of the refractive index (optical fiber with a fixed bent angle of 180°)

where n_{2min} is the RI of the outside medium, in our case the water.

A simulation using theoretical values in Eq. (5) was carried out in order to observe the response curve tendency of the system. Figure 2 show the power attenuation with the refractive index normalized using water as a reference ($n_{2min} = 1.33$). It is possible to observe that there is an attenuation of approximately 30 % for RI variation up to 1.39.

2.3 Surface Plasmon Resonance (SPR) and Localized Surface Plasmon Resonance (LSPR)

Over the past years, surface plasmon resonance (SPR) biosensor technology has made great success, and a large number of SPR sensors have been developed. SPR is a very sensitive technique for determining small refractive index changes at the interface between a metallic layer and a dielectric medium (analyte). This technique is widely used as a detection principle for many sensors that operate in the areas of biological and chemical sensing.

SPR in metallic materials occurs through the coherent oscillation of the electrons of the valence band are excited with an electromagnetic field, causing a power absorbance in this region.

The SPR effect depends on the shape of the metallic nanoparticles, as for example in the case of gold nanospheres that have symmetric shape. In this case,

the interaction of the electromagnetic field (white light source) with the electrons of the valence band will result only in one band of absorption, that extends from the green to red region and this band position depends on the size of the nanoparticle.

Gold nanorods are elongated nanoparticles and so, different from nanospheres, display two distinct plasmon bands resulting in oscillation of the electrons in the longitudinal direction and in the transversal direction of the rods. This resonance shows in the absorption spectrum one weak band in the green region (Transversal Surface Plasmon Resonance-TSPR) and one strong absorption band in the red or near infra-red (NIR) region (Longitudinal Surface Plasmon Resonance-LSPR). The position of the LSPR band depends highly of the aspect ratio of the gold nanorods.

3 Fabrication Methods and Optical Setups for EW and LSPR

3.1 Evanescent Wave U-Shape Sensor

3.1.1 Preparation of U-Shaped Sensor Probes

A multi-mode Mitsubishi Rayon Eska GH 4001 plastic optical fiber (POF) was used. The POF has a poly(methyl methacrylate) (PMMA) core of 980 μm in diameter and a fluorinated polymer cladding with 10 μm in thickness. The RI in the visible range of interest is about 1.49 for PMMA and 1.41 for fluorinated polymer.

First, the plastic optical fiber was cut into several 10-cm-long sections and both end surfaces were cleaved and polished with polishing paper for a better light coupling. Following that, the optical fiber was rinsed with deionized water and blow-dried with nitrogen. Then, the POFs were heated at about 70 °C and bent around a mold to produce U-shaped tapers. This task was carried out with the aid of a custom-made device shown in the Fig. 3. About 30 U-Shaped probes with 25 mm length and 9 mm waist diameters in average were produced.

The sensors were tested under different RI in order to study their sensitivity and further functionalized with antibodies. The results of such tests are presented in the next sessions.

3.1.2 Instrumentation and Electronic Set-up

The measurement set-up consists of an LED connected to the end of the bent fiber. The light is received by the photodiode located on the opposite fiber end, according to Fig. 4. In the bent fibers some modes scape depending on the refractive index of the surrounding medium, in this case the sucrose concentration and after the functionalization, the concentration of *Escherichia coli* in water. The photodiode

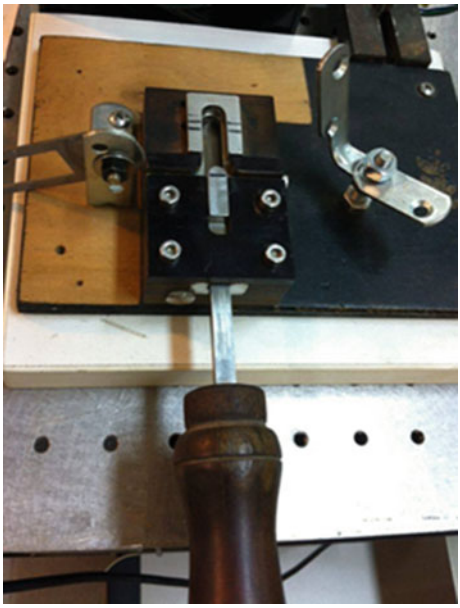

Fig. 3 Custom-made device for molding U-Shaped probes

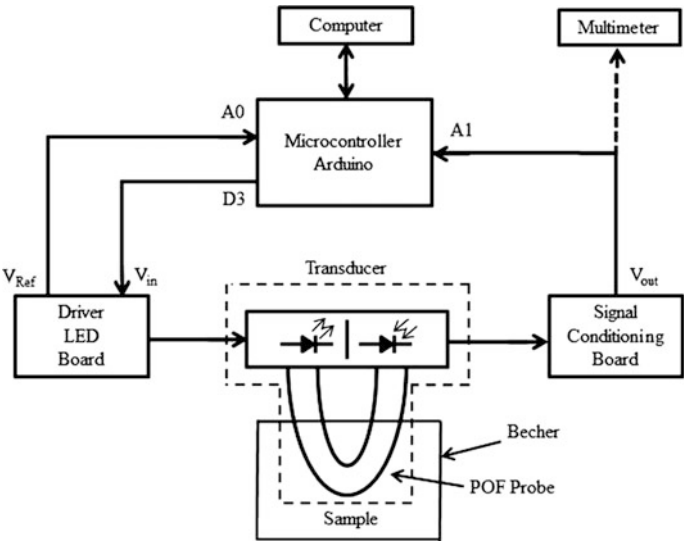

Fig. 4 Schematic diagram of the optoelectronic setup

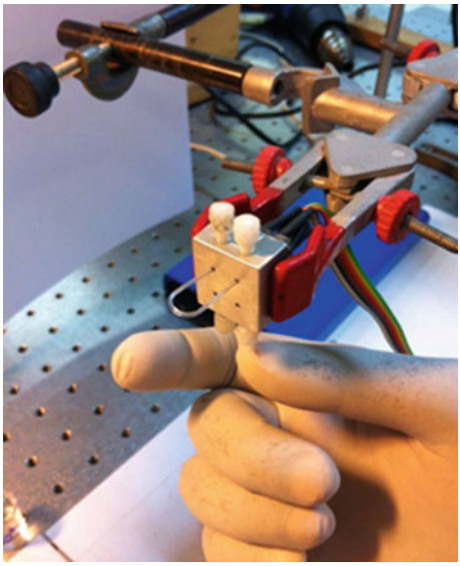

Fig. 5 The sensor connected to the LED-Photodiode housing

voltage signal varies accordingly to alterations on sucrose concentration or the bacteria concentration.

The 880 nm LED is powered by a current source controlled by an Arduino Microcontroller. The electronic setup keeps the current, providing the best LED operation. Thus, the light received by a PIN photodiode decreases accordingly to the different RI or accordingly to the bacteria that is captured by an antibody fixed in the biosensor.

Figure 5 shows a picture of the sensor in its casing.

3.2 Gold Thin Film Evanescent Wave

The POF sensors in this case were made by the same process shown in last section and interrogated by the same optical setup. Generally, the functionalization with antibodies is usually done directly on the surface of the fiber, core or cladding, or on another material deposited over the fiber, depending on the sensing effect, such as: evanescent wave, LSPR, Raman or SERS. Nevertheless, there are few examples of biosensor functionalized directly onto PMMA surface of a POF [16]. On the other hand, there are several examples of gold-coated optical fiber biosensor functionalized being this technique very well established and a lot of protocols were published and widely tested [17].

The conventional protocol to bind antibodies at the surface of an optical fiber is very well known for glass fibers and PMMA fibers. However, a conventional telecom POF such as the one used throughout this work presents a PMMA core and

another material in the cladding, a fluorinated polymer. In this way the conventional functionalizing protocol does not work well and the antibody binding to the fiber surface does not produce a homogeneous layer resulting in a lower sensitivity to the presence of the bacteria.

In order to enhance the functionalization process of a fiber optical biosensor with antibodies, and consequently improve the sensitivity by the evanescence wave technique, coating the U-Shaped probe with gold thin film was proposed. The gold film should be thin enough to be transparent, allowing the EW to pass through. The PMMA surface guarantees a good adhesion of the gold film due to its high roughness. Besides, gold is a metal particularly important due to its chemical stability, high conductivity, high work function, atomic mass, and optical properties. Although gold is golden, opaque and reflective in the macroscale, on the nanoscale, it presents a high light transmission rates [18].

With this idea in mind, we produced several U-Shaped sensors with gold thin film deposits and tested them under different RI in order to study their sensitivity.

3.2.1 Deposition of Gold Thin Film

For the gold thin film coating, a RF magnetron sputtering system was used (Aja International). The gold target size was 25.4 mm (1 in.) in diameter and 0.3 mm in thickness, shown in Fig. 6.

The sputtering process was performed with Argon gas at a flow rate of 12 sccm (standard cubic centimeter per minute) under the pressure of 3 mTorr. A 40 W RF power was applied to ionize the gas for various sputtering times. The generated negative ions hit the gold target to vaporize the gold atoms. As a result, the deposition of a gold film on the probes surface occurs.

The U-shaped probes were attached to a support and placed on the substrate base of the sputtering as shown in Fig. 7. Sensitive areas of probes were placed 50 mm above from the gold target, which is tilted 45° from vertical. The substrate base was rotated during the deposition process in order to expose all probes to the same deposition rate.

Probes packs were exposed to the sputtering process for 1, 2, 3, 5 and 20 min. Under that operation conditions, the deposition rate is about 3.5 nm/min. So, it was produced probes coated with 3, 7, 10, 18 and 70 nm thickness of gold thin film. As shown in Fig. 8, a 70 nm-thick film shows a bright golden color while thinner films show blue color.

The sensors were tested under different RI in order to study their sensitivity. The results of such tests are presented in the next sessions.

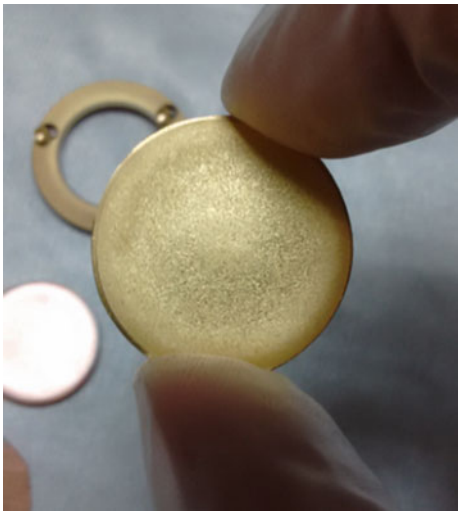

Fig. 6 Gold target used for U-Shaped probe coating by sputtering

Fig. 7 Bare U-Shaped probes installed inside the sputtering chamber

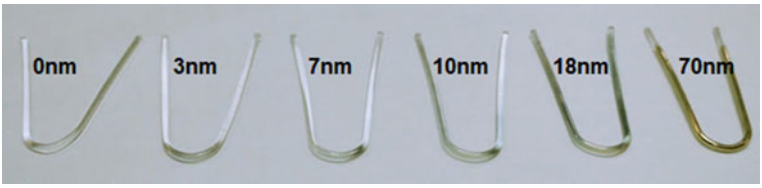

Fig. 8 U-Shaped probes coated with different thickness of gold thin film

3.3 Localized Surface Plasmon Resonance Sensor

3.3.1 Au Nanorods Production

Au nanorods were produced by seed-mediated method as described by Fontana [19]. Gold(III)-chloride-trihydrate reagent was reduced in DI water with Sodium borohydride forming small nanospheres that act as nucleation seeds when added to a growth solution containing gold ions and HCTAB. The seed solution was produced by mixing 5 mL of the HCTAB solution (10 mL, 0.7289 g) with $HAuCl_4$ (5 mL, 0.0019 g) followed by the addition of 600 μL of $NaBH_4$ (3 mL, 0.0011 g) stirring for 2 min. The growth solution was made by adding 100 μL of $AgNO_3$ (2 mL, 0.0013 g) to the 5 mL left of HCTAB followed by the addition of 5 mL $HAuCl_4$ (5 mL, 0.0019 g) and 70 μL of ascorbic acid (1 mL, 0.0138 g). To grow nanorods, 12 μL of the seed solution is added to the prepared growth solution and kept on room temperature for 24 h. After the synthesis, the AuNR suspension was placed into Eppendorf tubes to remove the excess of HCTAB from the suspension and centrifuged for 30 min at 8000 rpm. After the first cycle the Eppendorf tubes are decanted to a volume of less than 0.5 mL per tube. 5 mL of DI water is distributed between the Eppendorf tubes, mixed thoroughly, then poured into another tube, repeating until all the AuNRs are concentrated into one tube. The washing process is repeated for a third time with the final dilution bringing the volume to 10 mL. Transmission Electron Microscopy (TEM) image of Au NRs can be visualized in Fig. 9a with aspect ratio of 1.7 and a LSPR absorbance curve at 648 nm is shown in Fig. 9b.

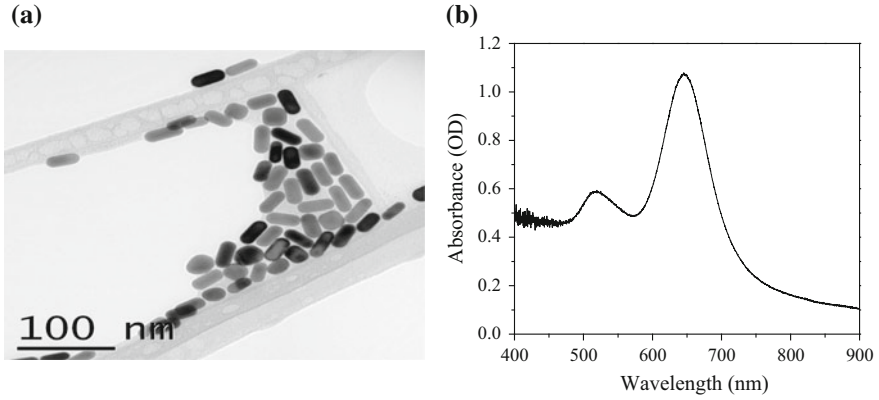

Fig. 9 **a** TEM image of the AuNRs; **b** LSPR absorbance curve with a peak at 648 nm

3.3.2 AuNRs Capped on the Tip of Plastic Optical Fibers

The sensor was built using POF 980/1000 μm and gold nanorods capped to the tapered tip of the POF. The whole process was performed as follows: The POF was cut into 12 cm long segments and about 2 cm long of theirs tips were dipped in acetone for 20 s, following by the remove of the cladding of this region with Kim wipes. After this step the POF tip was rinsed with water and isopropyl alcohol in sequence. The tapering POF tip was performed by dipping the region previously treated for 6 h in cyclopentanone solution. Figure 10a shows a 980/1000 μm POF and in (b) the tapered POF tip at 808.75 μm.

The Gold nanorods were attached on the POF tip by dipping it in a solution of octanethiol and tetrahydrofuran for 30 min and then, a drop of AuNRs was placed onto the tip and allowed to dry at room temperature.

3.3.3 Sensor's Setup

Figure 11 shows the optical setup used for the POF sensors in the measurements of reflectance of the AuNRs on the POF tip with a change of the surrounding RI. The configuration consisted of a white light source (Ocean Optics HL-2000), an spectrometer (Ocean Optics USB 4000) connected by a 3 dB coupler to the sensing element (AuNRs capped POF tip).

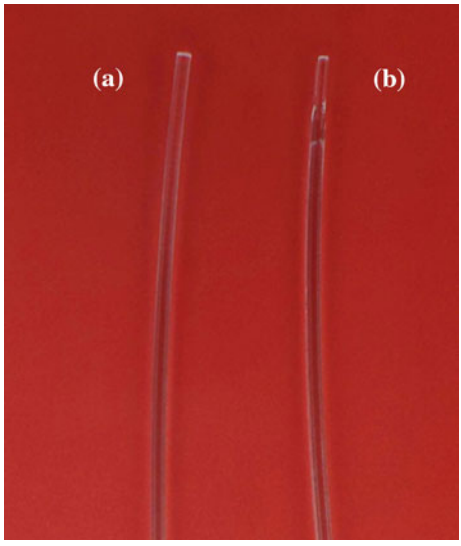

Fig. 10 **a** POF 980/1000 μm and **b** the taper POF tip at 808.75 μm

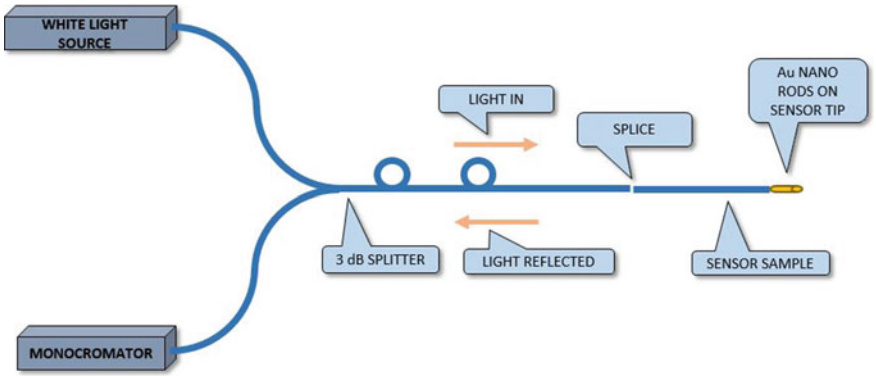

Fig. 11 Setup for refractive index sensing

4 Experiments on Refractive Index (RI) Measurements for EW and LSPR

In this section, we test all sensors produced for its sensitivity under liquids with different RI and so simulating the presence of different bacteria concentration. The RI of the liquids were measured by an Abbe refractometer (Quimis, Brazil, Model Q767BD) under a range of n = 1.33–1.38.

4.1 U-Shaped Sensor

Figure 12 shows a typical response of the U-shaped sensor under liquids of different RI.

Notice that, as expected, the output signal decays with increasing RI, according to theoretical analysis performed in Sect. 2.2 and shown in Fig. 2. The simplest explanation for this phenomenon is that, as the surrounding RI increases and get closer to the cladding RI, the critical angle given by Eq. (1) increases, allowing less guided modes inside the cladding. As these modes escape from the optical fiber, some other modes guided by the core exit it to fill the voids left by the leak modes, decreasing thus the output power that reaches the photodiode.

4.2 Gold Thin Film U-Shaped Sensor

About 30 U-shaped probes coated with different thickness of gold film were tested into solutions of varying refractive indexes, ranging from n = 1.33–1.39. Figure 13

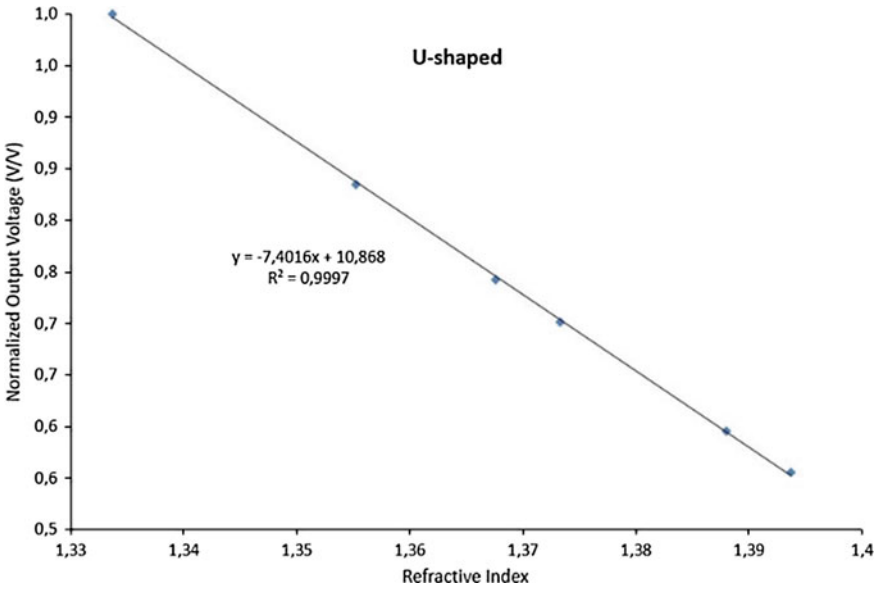

Fig. 12 Response of the U-Shaped sensor under different refractive indexes

shows the plots with the results of one probe for each group of gold film thickness. Figure 14 shows a plot with the average values for each group of probes.

As expected, since they are similar, the bare U-Shaped probe response shown in Fig. 13a presents about the same sensitivity as the one shown in Fig. 12, that is, falls about 50 % within the range 1.33–1.39. Notice however, that the U-shaped probes coated with gold thin films have had their sensitivity reduced as their coat thickness increase from 3 to 70 nm.

It was also expected that the output light power of the POF probes were inversely proportional to the RI of the surrounding medium, except for the thickness of 70 nm, where the output response is directly proportional to the changing in RI. This happened probably because the low refractive index of gold makes it working as a second fiberoptic cladding, guiding back the light to the POF core. Its effect becomes more and more representative as its thickness increases with respect to the wavelength. However, this a unexpected and new result that needs further studies.

The U-Shaped probes coated with gold thin films have had their sensitivity reduced. The inclusion of the gold layer between the fiber cladding and the external environment contributes to an attenuation of the light rays as they cross the interface between the cladding and the surrounding medium and back again into the cladding, producing the EW. Therefore, it was already expected a lower sensitivity of these sensors as compared with the bare U-Shape sensor whose responses are shown in Fig. 12 and in Fig. 13a. In addition, the sensitivity decreases as the thickness increases.

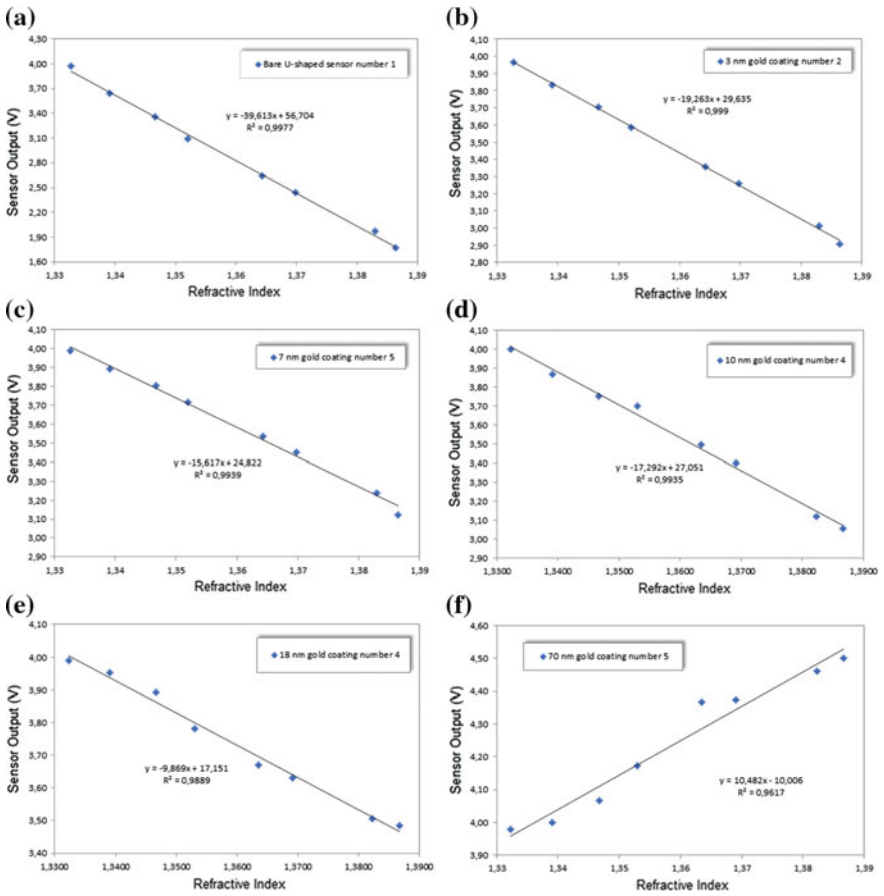

Fig. 13 Plots of the output signal (Volts) vs. the RI for **a** bare U-shaped probe; **b** 3 nm gold coating; **c** 7 nm gold coating; **d** 10 nm gold coating; **e** 18 nm gold coating; **f** 70 nm gold coating

Since we expect a better adhesion of the antibody molecules with the gold layer as compared with the adhesion to pure PMMA, this decrease of sensitivity will be compensated by the increase of capture power of the antibody layer. We are at the moment of writing this chapter functionalizing these coated sensors for bacteria detection.

4.3 Localized Surface Plasmon Resonance Sensor

The RI sensing was tested in a range of n = 1.33–1.38 through the use of different sucrose solutions acting as variable surrounding medium. In Fig. 15a it is observed a blue shift of the LSPR and the sensitivity of the sensor have been calculated

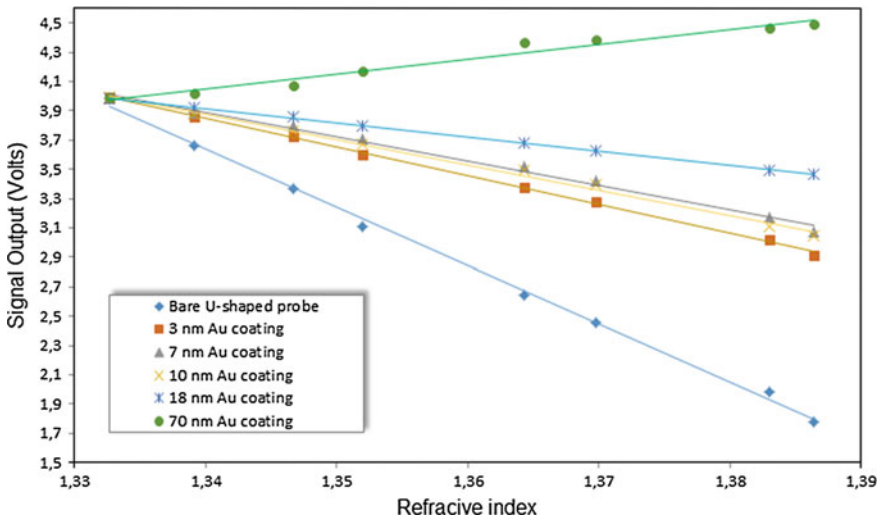

Fig. 14 Average values for each gold coating thickness including the bare U-Shaped probe

through the position of the wavelength dip for each refractive index, as shown in Fig. 15b. In this range the sensitivity obtained was of (-156.32 ± 4.84) nm/RIU in the same interval of the expected RI of the *E. coli* [4], that suggested the possibility to use this sensor for *E. coli* detection after its functionalization.

5 Functionalizing POF Sensors for Bacteria Sensing

The technique used by this biosensor relies on the immunocapture effect, that is, the biological principle is based in the antigen-antibody interaction. This kind of biosensor is characterized by antibodies as biological recognition element, responsible for the specificity of the biosensor. Antibodies are molecules of glycoproteins produced by B-lymphocytes in response to the presence of an antigen in the analyte to be detected, resulting in a molecular connection of high affinity and specificity.

The methodology of an immunosensor construction starts with the correct binding of the antibodies on the surface of the sensors with appropriated uniformity. With the active antibody fixed to the fiber surface, the specific bacteria, if present in the solution, will be captured and covalently fixed to the fiber, modifying thus the RI around the EW present there.

The immobilization technique to be applied to the sensor must provide a stable link between the surface and the reconnaissance element, without interfering in the biological activity of the system. The PMMA allows the formation of amino grouping on its surface, making the technique by chemical reactions through covalent bonds the most suitable technique for the sensor functionalization.

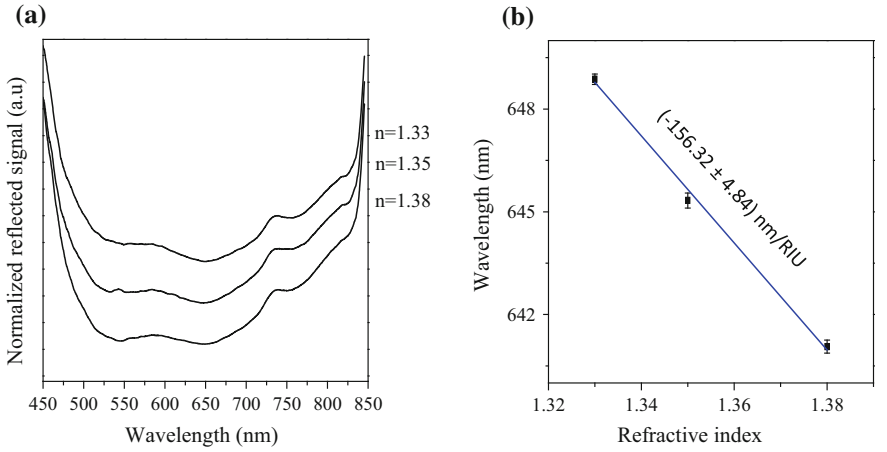

Fig. 15 **a** Blue shift of the LSPR with the change of surrounding RI and **b** sensitivity of the sensor have been calculated through of the position of the wavelength dip for each RI shown in (**a**)

The PMMA of the plastic optical fiber has to be treated to allow the formation of amino grouping on its surface through the use of hexametilenodiamine (HMDA). These groups allow the use of substances such as glutaraldehyde, responsible for the formation of a covalent bond with protein A and antibodies [20].

We have used the following protocol for the functionalization:

1. Sensor cleaning with a solution of isopropyl alcohol for 5 min and subsequent washing with distilled water;
2. Sensor amination in a solution of 10 % borate buffer HMDA by 2 h at 30 °C;
3. Activation of amination surface by adding 2.5 % glutaraldehyde solution in phosphate buffer for 2 h at 30 °C;
4. Covalent bond of protein on the PMMA by incubating into a solution of protein A with 0.05 mg/mL of sodium carbonate buffer by 1 h at 30 °C;
5. Blocking of nonspecific sites with BSA solution at 10 % for 1 h at 30 °C.
6. Binding antibodies to the sensor in a 0.1 % solution followed by a 4-h incubation.

6 Experiments with Bacteria

In this section, we present the results obtained with the U-Shaped sensor functionalized with antibody against *Escherichia coli*, according to the protocol demonstrated by Fixe et al. [20]. In all experiments we used a concentrations of 10^4 CFU/mL of *Escherichia coli*.

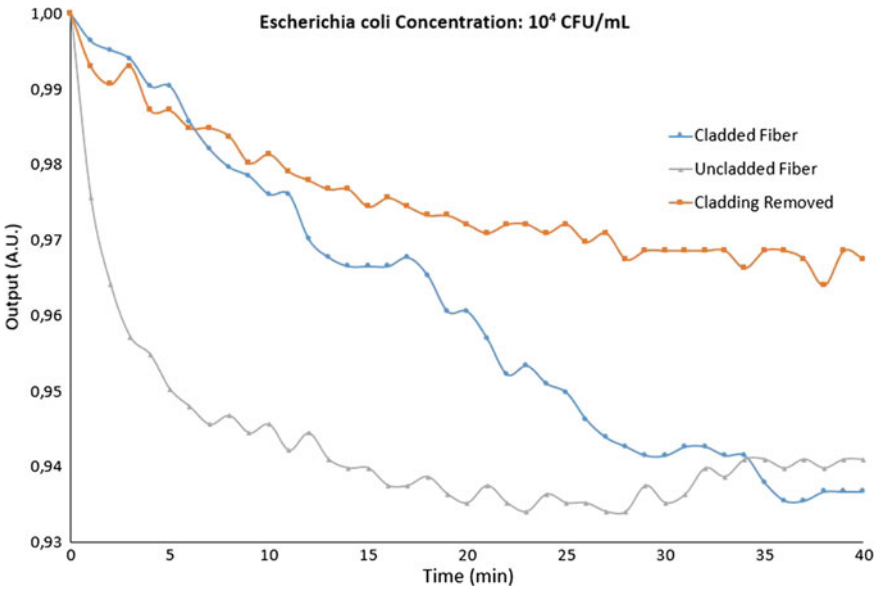

Fig. 16 Results of the U-Shaped sensor under a bacteria concentration of 10^4 CFU/mL

Figure 16 shows the results of three types of U-Shaped sensors: one using conventional ESKA telecom fiber, one using pure PMMA claddless POF and one using ESKA POF with its cladding removed by acetone. All sensors showed a decrease in output with time, suggesting an increase in the surrounding RI, supposedly due to the immunocapture effect as the antibody layer keeps capturing the bacteria presented in the water.

The better sensitivity (smaller time response) was found to be presented by the claddless POF, suggesting that the antibody layer was better adhered and concentrated around this sensor.

The cladding removal process does not leave a uniform fiber surface, rather, some residues can be found when inspecting the sensor under a microscope. These residues may be preventing the capture of the bacteria in a uniformly distributed manner over the fiber surface and therefore decreasing the sensor sensitivity.

When comparing the sensitivity of cladded and uncladded fibers we can conclude that our suspicion that the functionalizing protocol would not work well for the fluorinated polymer was right. This becomes clear when we notice that the claddless sensor sensitivity is much better than the cladded sensor.

7 Conclusions

All three platform tested in this work presented good sensitivity with RI variation. However, of these three techniques the U-Shaped EW sensor showed to be the best configuration for a mass-production fabrication for its low cost and simplicity. Therefore, this platform was chosen to be functionalized for *Escherichia coli* detection.

7.1 LSPR Sensor

A sensor for refractive index was performed using POF and gold nanorods. The results show that this it is very sensitive to the change of surrounding RI in the range of the *E. coli* RI. The sensitivity shown by our sensor (-156.32 ± 4.84) nm/RIU in the range of *E. coli* is nearly 7 times larger than the sensor using gold nanoparticles and long period fiber gratings with sensitivities of −23.45 nm/RIU demonstrated by Tang et al. [21] and nearly 2 times larger than gold nanostars capped along the sides of the POF with sensitivities of 84 nm/RIU demonstrated by Cennamo et al. [8]. Therefore, the sensor here developed is robust and presents high sensitivity in the range of the *E. coli*, suggesting that it can be used for the detection of this bacterium after its functionalization.

7.2 Gold Thin Film U-Shaped Sensor

The results demonstrated that the ideal thickness to coat U-Shaped probes for using as an EW-based sensor should be less than 10 nm avoiding a too large attenuation that would put the sensitivity in jeopardy. This conclusion needs more studies in order to determine whether the gold layer will in fact increase the antibody molecules adhesion, contributing thus for a general sensitivity improvement.

7.3 U-Shaped Sensor

The U-Shaped sensor functionalized with antibody presented several advantages as compared with conventional diagnostic techniques.

The sensor response time to the presence of *E. coli* was less than 10 min, which improved conventional diagnostic time, normally about 72 h.

Additionally, the detection technique presented here does not require a specific laboratory or a qualified technician to operate the system, which facilitates the use of this biosensor in the field.

The other two platforms tested in this work also presented good sensitivity and therefore, will be studied in future works. Therefore, we are intended to perform the functionalization in the three platforms aiming to improve sensitivity, detection time and fabrication costs in order to choose the best one to be developed as a field prototype.

References

1. O. Lazcka, F.J. Del Campo, F.X. Muñoz, Pathogen detection: a perspective of traditional methods and biosensors. Biosens. Bioelectron. **22**, 1205–1217 (2007)
2. A.P. Ferreira, M.M. Werneck, R.M. Ribeiro, Aerobiological pathogen detection by evanescent wave fibre optic sensor. Biotechnol. Tech. **13**(7), 447–452 (1999) (Kluwer Academic Publisher), ISSN: 0951-208X
3. C. Beres, F.V.B. de Nazaré, N.C.C. de Souza, M.A.L. Miguel, M.M. Werneck, Tapered plastic optical fiber-based biosensor—tests and application. Biosens. Bioelectron. **30**, 328–332 (2011). doi:10.1016/j.bios.2011.09.024
4. G. Wandemur, D. Rodrigues, R. Allil, V. Queiroz, R. Peixoto, M. Werneck, M. Miguel, Plastic optical fiber-based biosensor platform for rapid cell detection. Biosens. Bioelectr. **54**, 661–666 (2014). doi:10.1016/j.bios.2013.11.030. ISSN: 0956–5663
5. G. Emiliyanov, P.E. Hoiby, L.H. Pedersen, O. Bang, Selective serial multi-antibody biosensing with TOPAS microstructured polymer optical fibers. Sensors **13**, 3242–3251 (2013)
6. M. Fischer, M. Wahl, G. Friedrichs, Design and field application of a UV-LED based optical fiber biofilm sensor. Biosens. Bioelectron. **33**, 172–178 (2012)
7. C. Chai, G. Liu, B. Yao, A portable optical sensor based on a one-off test strip for fast evaluation of bacterial contamination in raw tofu. Sens. Actuators B **152**, 1–7 (2011)
8. N. Cennamo, G. D'Agostino, A. Donà, G. Dacarro, P. Pallavicini, M. Pesavento, L. Zeni, Localised surface plasmon resonance with five-branched gold nanostars in a plastic optical fiber for bio-chemical sensor implementation. Sensors **13**, 14676–14686 (2013)
9. X. Fan, I.M. White, S.I. Shopova, H. Zhu, J.D. Suter, Y. Sun, Sensitive optical biosensors for unlabeled targets: a review. Anal. Chim. Acta **620**, 8–26 (2008)
10. F. Baldini, M. Brenci, F. Chiavaioli, A. Giannetti, C. Trono, Optical fiber grating as tools for chemical and biochemical sensing. Anal. Bioanal. Chem. **402**, 109–116 (2012)
11. H.A. Rahman, S.W. Harun, M. Yasin, S.W. Phang, S.S.A. Damanhuri, H. Arof, H. Ahmad, Tapered plastic multimode fiber sensor for salinity detection. Sens. Actuators A: Phys. **171**(2), 219–222 (2011)
12. V.V.R. Sai, T. Kundu, S. Mukherji, Novel U-bent fiber optic probe for localized surface plasmon resonance based biosensor. Biosens. Bioelectr. **24**(9), 2804–2809 (2009), http://doi.org/10.1016/j.bios.2009.02.007
13. B.D. Gupta, H. Dodeja, A.K. Tomar, Fibre-optic evanescent field absorption sensor based on a U-shaped probe. Opt. Quantum Electr. **28**, 1629–1639 (1996)
14. W.A. Snyder, J.D. Love, *Optical Waveguide Theory* (Chapman and Hall, New York, 1983)
15. D.M.C. Rodrigues, Development and characterization of plastic optical fiber sensors for refractometry based on amplitude modulation. M.Sc. Dissertation, COPP/UFRJ, Rio de Janeiro (2013)
16. B. Hsieh, Y. Chang, M. Ng, W. Liu, C. Lin, H. Wu, C. Chou, Fiber-optic biosensor with gold nanoparticles. **79**(9), 3487–3493 (2007)
17. M. Roushani, A. Valipour, M. Valipour, Layer-by-layer assembly of gold nanoparticles and cysteamine on gold electrode for immunosensing of human chorionic gonadotropin at

picogram levels. Mater. Sci. Eng.: C **61**, 344–350 (2016), http://doi.org/10.1016/j.msec.2015.12.088
18. A. Kossoy, V. Merk, D. Simakov, K. Leosson, S. Kéna-Cohen, S.A. Maier, Optical and structural properties of ultra-thin gold films. Adv. Opt. Mater. n/a–n/a (2014), http://doi.org/10.1002/adom.201400345
19. J.P. Fontana, Kent State University, Electronic-Liquid Crystal Communications, Kent, OH, EUA, 44240, dissertation (2011)
20. F. Fixe, M. Dufva, P. Telleman, C.B.V. Christensen, Functionalization of poly(methyl methacrylate) (PMMA) as a substrate for DNA microarrays. Nucleic Acids Res. **32**(1), e9 (2004). http://doi.org/10.1093/nar/gng157
21. J.L. Tang, S.F. Cheng, W.T. Hsu, T.Y. Chiang, L.K. Chau, Fiber-optic biochemical sensing with a colloidal gold-modified long period fiber grating. Sens. Actuators B Phys. Rev. B. **119**, 105–109 (2006)
22. D.M. Rodrigues, F.V.B. de Nazaré, M.M. Werneck, Enhanced plastic optical fiber sensor for refractometry based on amplitude modulation. IEEE International Instrumentation and Measurement Technology Conference—I2MTC, Montevideo, Uruguay (2014)

Author Biographies

Marcelo Martins Werneck was born in Petrópolis, Brazil. He received the Degree in electronic engineering from the Pontifícia Universidade Católica of Rio de Janeiro, Rio de Janeiro, Brazil, in 1975 and his M.Sc. degree from the Biomedical Engineering Program, Federal University of Rio de Janeiro (UFRJ), Rio de Janeiro, in 1977. His Ph.D. degree was obtained from the University of Sussex, Brighton, U.K., in 1985. He has been with UFRJ since 1978, where he is currently a Lecturer and Researcher. He is also the Coordinator of the Instrumentation and Photonics Laboratory at the Electrical Engineering Program, UFRJ. His research interests include fiber optics sensors, nanobiosensors, transducers and instrumentation.

Professional Address
Universidade Federal do Rio de Janeiro (UFRJ)
POBox 68.564, Centro de Tecnologia, Cidade Universitária
Rio de Janeiro, RJ, Brazil, 21945-972
Phone: +55 21 39388200
E-mail: werneck@lif.coppe.ufrj.br
Home page: http://www.lif.coppe.ufrj.br

Rafaela Nascimento Lopes was born in Barbacena, state of Minas Gerais, Brazil, on June, 15th, 1985. She graduated in Biomedicine from the University of Uberaba in 2007. She is currently pursuing the M.Sc. degree with Biotechnology Program at the Federal University of Rio de Janeiro (UFRJ). She is a specialist in Microbiology and Parasitology, working mainly in inmunobiological assays, antigen-antibody interaction and identification techniques of pathogens. She is a member of the research team in the Instrumentation and Photonics Laboratory (LIF) COPPE/UFRJ, where she develops, with the optoelectronic sector, biosensors based on inmunocapture techniques for the detection of microorganisms. E-mail: rafaela@lif.coppe.ufrj.br

Greice Kelly Bezerra da Costa was born in Rio de Janeiro, Brazil. She received her physicist degree in 2005, the bachelor degree in Physics in 2007, M.Sc. degree in Physics in 2009 and D.Sc. degree in Science in 2013 from the Universidade do Estado do Rio de Janeiro, Rio de Janeiro, Brazil. She made her first Post-doctoral in 2014 on the Laboratório de Optoeletrônica, Physics Department at the Pontifícia Universidade Católica do Rio de Janeiro—PUC-RIO. She is currently in her second Post-doctoral research at the Instrumentation and Photonics Laboratory at the Electrical Engineering Program, Universidade Federal do Rio de Janeiro. Her research interests include fiber optics sensors, nanobiosensors, optical spectroscopy of ceramic materials doped with transitions metals and application of gold nanoparticles in sensors. E-mail: greice@lif.coppe.ufrj.br

Domingos Marcelus Carias Rodrigues was born in São Gonçalo, State of Rio de Janeiro, Brazil. He graduated in Physics from Fluminense Federal University (UFF), in Niterói, State of Rio de Janeiro, Brazil (2010). He has a M.Sc. degree in Electrical Engineering at the Electrical Engineering Program in the Federal University of Rio de Janeiro (COPPE/UFRJ) in 2013. Currently, he is a physics lectures at the State Secretary of Education (SEEDUC) in Rio de Janeiro and a D.Sc. student in Electrical Engineering Program in the Instrumentation and Photonics Laboratory (LIF) from COPPE/UFRJ, with completion expected in 2017. His research interests include fiber optics sensors, nanobiosensors and instrumentation. E-mail:domingos@lif.coppe.ufrj.br

Ariadny da Silva Arcas was born in Goiânia, state of Goiás, Brazil. She received a degree in Food Engineering from the Instituto Federal de Mato Grosso, Brazil in 2015. She is currently pursuing the M.Sc. degree with the Nanotechnology Engineering Program, Photonics and Instrumentation Laboratory (LIF), Federal University of Rio de Janeiro. Her current research interests include fiber optics nanobiosensors applied to bacteria detection. E-mail: ariadny@lif.coppe.ufrj.br

Fábio da Silva Dutra was born in Rio de Janeiro, Brazil, in 1975. He received the B.Sc. degree from the Department of Electronic Engineering from Rio de Janeiro Federal University (UFRJ), in 1998 and M.Sc. degree in Microelectronic from the Electrical Engineering Program from COPPE/UFRJ, in 2001. His M.Sc. dissertation dealt with an acquisition system integrated on a chip for petroleum pipeline inspection inside a pig. In 2004, he joined Petróleo Brasileiro S.A. (Petrobras) as an equipment engineer. Since then, he has worked in the basic design of oil and gas platforms where he has become an expert in the technical and Brazilian law requirements regard flow metering. Since 2014, he has been in charge of fluid measurement, metrology and nanotechnology applied for oil and gas sensing researches. He received the CENPES Award for excellence in Results of the Petrobras in 2010 for his dedication in the basic design of the 8-firsts Petrobras Pre-Salt FPSOs. He is currently working toward the D.Sc. degree at the Nanotechnology Engineering Program from COPPE/UFRJ where he is focusing his research on MOF@AuNPs-coated optical fibers for gases sensing.

Vanessa de Moura Queiroz was born in Rio de Janeiro, Brazil. She received the Degree in Biological Sciences from the Augusto Motta University (UNISUAM) of Rio de Janeiro, Rio de Janeiro, Brazil, in 2008. She has seven years of experience in microbiology and biochemistry in the areas of research, reference, quality control, supervision and biosecurity in pharmaceutical and food industry. She is currently part of the team in the Researchers in Instrumentation Laboratory and Photonics (LIF) at UFRJ, in the project of development of biosensors in plastic optical fibers to detect bacteria in water. E-mail: vanessa@lif.coppe.ufrj.br

Regina Célia da Silva Barros Allil was born in Rio de Janeiro, Brazil. She received her BSc Degree in electronic engineering from the Faculdade Nuno Lisboa, Rio de Janeiro, in 1988, and the M.Sc. degree from the Biomedical Engineering Program, Federal University of Rio de Janeiro (UFRJ), Brazil, in 2004. Her D.Sc. degree was obtained from the Electrical Engineering Program, Instrumentation and Photonics Laboratory, UFRJ, in 2010. Her Post-Doctoral performed research and development in biosensors based on optical fiber for identification of biological agents. She is currently a researcher with the Biological Defence Laboratory, Institute of Chemical, Biological, Radiological and Nuclear Defence, Brazilian Army Technological Center (CTEx), Rio de Janeiro and a researcher at Instrumentation and Photonics Laboratory, UFRJ. Her research interest lies in fiber optical sensors, optoelectronic instrumentation and biosensors.

Professional Address
Brazilian Army Technological Center
Institute of Chemical, Biological, Radiological and Nuclear Defence,
Biological Defense Laboratory
Rio de Janeiro, RJ, Brazil, 23.020-470
Phone: +55 21 24106335
E-mail: regina@lif.coppe.ufrj.br

Plasma-Based Deposition and Processing Techniques for Optical Fiber Sensing

M. Dominik, M. Koba, R. Bogdanowicz, W.J. Bock and M. Śmietana

Abstract Plasma-based techniques are widely applied for well-controlled deposition, etching or surface functionalization of a number of materials. It is difficult to imagine fabrication of novel microelectronic and optoelectronic devices without using plasma-enhanced deposition of thin films, their selective etching or functionalization of their surfaces for subsequent selective binding of chemical or biological molecules. Depending on the process parameters, i.e., generator frequency and power, composition of gases, pressure, temperature, and applied substrates, different effects of the process can be obtained. The chapter discusses current trends in application of plasma-based techniques for fabrication of novel optical sensing devices. Fabrication of materials with different structure (from amorphous to crystalline, porous, and multilayers), optical properties (absorption, refractive index), and surface activity, as well as their processing are reviewed. Application of the plasma methods enhancing sensing properties of various optical fiber sensing structures, namely long-period gratings, intermodal interferometers based on photonic crystal fiber, sensing structures based on lossy mode resonance or stacks of nano-films are given as examples and are discussed.

M. Dominik · M. Koba · M. Śmietana (✉)
Institute of Microelectronics and Optoelectronics, Warsaw University of Technology, Warsaw, Poland
e-mail: M.Smietana@elka.pw.edu.pl

M. Koba
National Institute of Telecommunications, Warsaw, Poland

R. Bogdanowicz
Faculty of Electronics, Telecommunications and Informatics, Gdańsk University of Technology, Gdańsk, Poland

W.J. Bock
Centre de Recherche en Photonique, Université du Québec en Outaouais, Gatineau, QC, Canada

© Springer International Publishing Switzerland 2017

I.R. Matias et al. (eds.), *Fiber Optic Sensors*, Smart Sensors, Measurement and Instrumentation 21, DOI 10.1007/978-3-319-42625-9_5

1 Introduction

More than 99 % of visible matter in the universe is originated from plasma. It consists of positive and negative ions, electrons and neutral species. Plasma is regarded officially as the fourth state of matter. Consequently, a significant amount of energy has to be applied to gas to achieve exited or ionized state of species creating plasma matter. Due to the presence of excited atoms, molecules and electrons it interacts freely and actively with other states of matter modifying them or fabricating new products. Plasma processing is a significant area of science in broad range of applications. The plasma environment offers a number of advantages, such as ability for low-temperature processes of deposition or modification of thin films, low process cost, its control, as well as high efficiency and process repeatability. In fabrication of optical fiber sensing devices, as well as in microelectronics, plasma can be applied mainly for enhancing deposition of thin films, e.g., plasma enhanced chemical vapor deposition or reactive magnetron sputtering, as well as for reactive ion etching, implantation, surface cleaning and modification, which include e.g., hydrogenation, fluorination, and other surface functionalization processes of thin films in these devices.

Main advantages of optical fiber sensors include their low weight and small size (from several to hundreds of microns in diameter), as well as low attenuation and low signal to noise ratio. When optical fiber is applied, the sensor can work in distant locations, what is more it can be exposed to high electromagnetic radiations. Moreover, this type of sensing devices exhibits good thermal stability, high degree of flexibility, and also their principle of operation is already well known and controlled. These devices can be applied in wide range of applications from sensors for measuring a vast range of properties starting from mechanical forces and material deformation, pressure, variations in material composition or density, electric and magnetic field, electric current or temperature [1, 2] to biomedical devices for protein analysis [3], pesticide detection [4] or determination of deoxyribonucleic acid (DNA) oligomers [5].

There have been shown many techniques for improving or even initiating sensitivity of optical fibers to some selected physical or chemical influences. They include deposition of thin films and coatings (one or multilayers), surface modification or well-controlled etching. Principles of operation and influence of modification and coating deposition on various optical sensing devices has already been presented and explained. In this chapter both the basic processes using plasma as well as current plasma application trends for fabrication of novel optical sensing devices are discussed.

2 Plasma-Based Processes

Many interesting optical fiber sensing devices can be fabricated using plasma-based deposition and surface processing of thin films. Following section reviews the range of plasma-based processes and their suitability for specific optical fiber sensors.

2.1 Deposition

In general, the thin films can be obtained either by deposition of a layer onto a substrate or by causing a chemical or physical change of a substrate material, e.g., by means of ion exchange or implantation. In case of optical fibers, deposition on glass substrate is mainly taken into consideration. And thus, here we present a review of plasma-based process, namely various physical (PVD) and chemical vapor depositions (CVD), both suitable for glass substrates. In these two types of deposition methods species (atom and molecules) exist in vapor state, while condensation on the substrate needs a chemical reactions (CVD) or conversion to form a solid material (PVD) [6]. In case of PVD, plasma can be employed for sputtering of a target material, while in CVD methods it is used for inducing chemical reactions between the gas molecules. Growth of films from the plasma-based vapor phase produces films with lower levels of contamination, comparing to wet techniques, such as dip-coating or sol-gel deposition [7]. Mechanisms responsible for thin film deposition in case of PVD and CVD processes are schematically shown in Fig. 1.

The thin films applied in fiber based devices must have defined thickness, optical constants (refractive index, extinction coefficient) and be of high optical quality, i.e., low level of impurities and low surface roughness. The boundaries between the films in multi-layer structure should also be as smooth as possible. In Fig. 2 applied

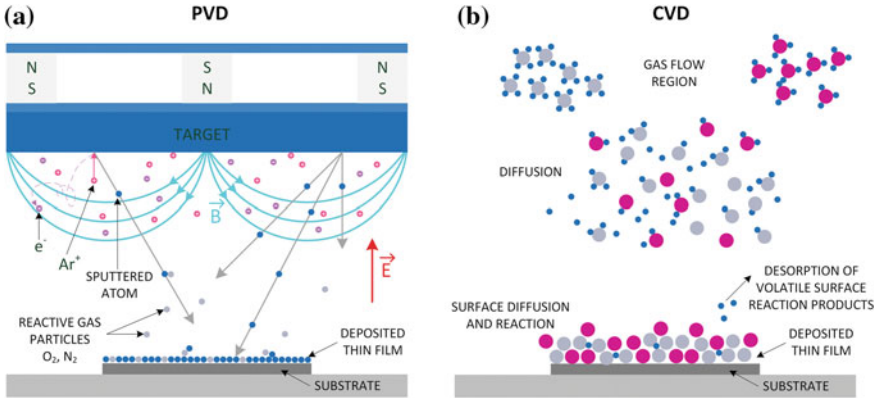

Fig. 1 Diagram showing basic phenomena taking place during **a** physical and **b** chemical vapor deposition process

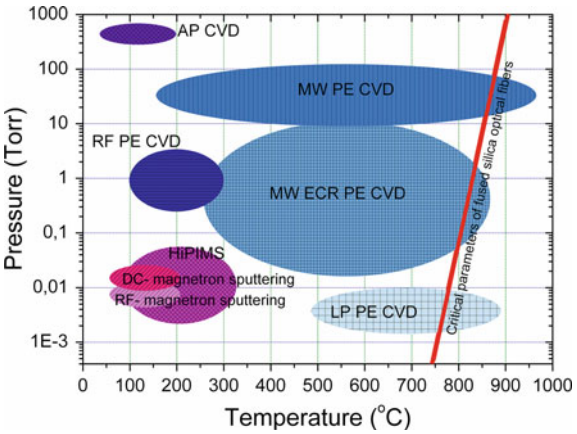

Fig. 2 Pressures and temperature ranges used in specific PVD and CVD techniques. Diagram also shows limits in application of the techniques for fused silica optical fiber sensing devices

pressures and temperature ranges for specific PVD and CVD techniques are compared, showing their limitations when applied for fiber sensing devices.

2.1.1 Physical Vapor Deposition (PVD)

Magnetron sputtering (MS) belongs to group of PVD techniques and is one of the most popular method widely used for deposition of thin metal and metal oxide or nitride films. In the method, atoms or molecules are sputtered from the surface of a target material by bombarding it with high-energy ions in a vacuum. Additionally, the magnetic field confines electrons near the target to sustain plasma (Fig. 1a). In the method argon is mainly used as an inert gas responsible for target sputtering. The gas ionization can be generated either in direct current (DC) or radio frequency (RF, 13.56 MHz) modes [8] and the films are typically deposited at relatively low substrate temperatures (up to 300 °C) [9]. The metal oxides or nitrides can be deposited due to the chemical reactions of the atoms released from the target with oxygen or nitrogen molecules. The reactions are mainly controlled by a suitable gas ratio and pressure in the chamber. When such reactions take place the process is called as reactive magnetron sputtering (RMS). Users of the RMS method typically face phenomenon of poisoning of the target elements by the reactive gas. Thin oxide on nitride film formed at the surface of the target creates a barrier for sputtering which strongly decreases erosion rate. To overcome this problem novel pulsed techniques like high-power impulse magnetron sputtering (HiPIMS) were developed. By applying higher voltage pulses to the electrodes the higher current density has been obtained in comparison to conventional MS [10, 11]. Such design also makes possible meaningful film densification [12], what in turn increases thin film refractive index and decreases its growth rate [13].

Sputtering is mainly used in the field of optical fiber sensing for deposition of thin metal films used as reflectors or for achieving surface plasmon resonance effect. Films such as aluminum [14] or gold [15] are applied for fabrication of mirrors on

the end-face of fiber. The MS technique allows for relatively fast and uniform deposition of metal films, with good adhesion to fiber surface, therefore it is the most commonly used method for fabrication of reflectors. Ultra-thin film of sputtered TiO_2 was also applied as an adhesion-enhancing interlayer on the surface of optical fiber sensors [16] or photocatalytically active devices [17]. Moreover, a variety of optical sensors for gas sensing applications have been developed based on MS coatings. Hamagami et al. [18] reported that sputtered MoO_3 film coated with Pd changed its transmittance when exposed to H_2. Sumida et al. [19] deposited Pt/WO_3 films on the optical fiber tip to detect hydrogen in mixture of H_2:N_2 (99:1 %) by the use of optical time domain reflectometry (OTDR). However, in most of the works the devices are based on sputtered amorphous films [20, 21]. Generally, the thickness and refractive index of the sputtered thin film can be easily controlled by the duration and energy of the ion bombardment [22]. The MS deposited films are very uniform even over large surface areas (scalable process) and contain low amount of contaminants.

2.1.2 Chemical Vapor Deposition (CVD)

Plasma Enhanced Chemical Vapor Deposition (PE CVD) is a process where solid films are synthesized from chemically reactive gas mixture (Fig. 1b). The energy needed to provide the chemical reactions is supplied by high electric fields and is known as cold plasma or electric discharge. Electrical discharge is the most flexible measure of creating and sustaining low temperature plasma. The DC as well as AC power sources have been widely applied for induction of plasma. Among other, radio (RF PE CVD @13.56 MHz) and microwave (MW PE CVD @ 2.45 GHz) frequencies [23] are the most efficient and widespread configurations used for ionizing plasma. From the technical point of view two most common methods for coupling electrical energy into a gas discharge are via capacitive coupling (CCP) or via induction as is done with inductively coupled plasma (ICP).

Wide range of process pressure and temperature is applied to obtain deposition of various thin films, which include dielectrics and semiconductors. The suitable precursors are dosed or vaporized and delivered to a vacuum reactor. A synthesis process includes enhanced by plasma chemical precursor reactions in the vapor phase near or at a substrate resulting in growth of a solid film. Most of the CVD processes are capable for uniform deposition on three dimensional objects. Nevertheless, CVD synthesis is relatively complex and to get high reproducibility of the processes, a set of parameters needs to be controlled [24]. The CCP is considered as resulting in relatively low plasma density, but in turn allows for high energy ion bombardment of a substrate. On the other hand remote plasma processes such as ICP [25] or Electron Cyclotron Resonance (ECR) [26, 27] make possible achieving higher plasma density and the precursors are introduced downstream of the plasma source. Such sources are useful in applications where high level of ion bombardment of a substrate is not desired. In optical fiber devices, it is in particularly expected to reduce the process temperature during thin films deposition in order to

retain the nanostructure of the deposited material ensuring high sensitivity and rapid response of the sensor, as well as to avoid high temperature solid-state reactions at the film/silica-fiber interface ($T_{substrate} < 800$ °C) during the deposition [28]. For temperature sensitive substrates this heat load may be partly relieved by cooling a stage where substrate is placed. However, the substrate surface staying in contact with the plasma still experiences elevated temperature due to continues ion bombardment [29].

Mechanically and chemically stable thin films in wide range of thicknesses can be deposited on optical fiber components with PE CVD methods [16, 23]. The average deposition rate ranged from nm up to μm per minute and the optical quality of the obtained films is usually very good resulting in low optical losses. The deposition rate depends mostly on used gas precursors and their flow rate, as well as applied discharge power. The CVD processes make also possible to add dopants to the deposited material which on top of changing sensing properties of the films have also influence on their optical properties [30] and/or some other properties such as UV photosensitivity [31] or melting temperature [32]. As a good example of CVD process application in field of optical fiber sensing can be used work of Cheng et al. [33] where has been shown thin-film Fabry-Perot interferometers based on polycrystalline SiC grown by CVD and used for temperature measurements in harsh environment. The SiC-based temperature sensors were compact in size, robust, and stable at high temperatures (22–540 °C ± 3.5 °C). The detailed description of more CVD application in optical fiber devices is given in Sect. 4.

Another useful method for deposition functional layers in optical fiber sensing is Atomic Layer Deposition (ALD). ALD can be considered as a special mode of CVD process, but in contrast to it ALD procedures feature alternating exposures of chemical precursors to react at the surface of a desired material [34]. The ALD process is based on sequential alternating pulses of gaseous chemical precursors that react with the substrate material. Due to ALD significant advantages, such as high conformity and a great control over materials thickness and composition, it is recently often applied to obtain deposition of various thin films on optical fiber sensors [35].

2.2 *Etching*

Dry etching uses plasma generated free radicals to remove a material. It plays critical role in creating geometries of extremely small size for highly integrated devices or tuning spectral response and sensitivity of optical fiber sensors. There are four basic types of plasma etching processes [36]: pure chemical etching, physical etching, ion enhanced energy-driven etching, and ion-enhanced inhibitor etching. Pure chemical etching involves isotropic and selective removal of surface atoms by plasma-induced gaseous etchant atoms or molecules (free radicals). They

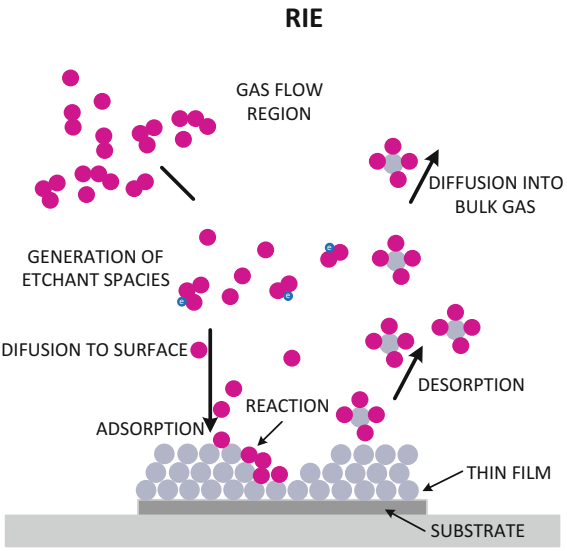

Fig. 3 A simplified diagram showing the main phenomena taking place during RIE process

chemically react with the surface layer forming gaseous volatile etching products. Physical plasma etching in turn is an anisotropic process which employs ion bombarding and leads to ejection of atoms form the surface. Ion enhanced, energy-driven etching is a process where both etchants atoms and energetic ions are involved in etching. Last type of the etching process, namely ion-enhanced inhibitor etching involves an additional inhibitor spaces that adsorb or deposit on the substrate to form a protective layer or polymer film. Protective layer usually slows down the etching process of selected parts and leads to obtain highly anisotropic effects of the process.

One of the most diverse and widely used plasma etching method is reactive ion etching (RIE). The RIE uses both physical and chemical etching mechanism. The combination of both types of interactions leads to increase in etching rates as well as enhancement in etching anisotropy. In the RIE process, ions are produced from reactive gases which are accelerated with high energy to the substrate and chemically react with the etched thin film material (Fig. 3). The typically used in RIE gases are CF_4 (for etching of SiO_2, Si_3N_4, InP, Si), CHF_3 (etching of SiO_2, Si_3N_4), SF_6 (Si etching), O_2 (etching of photoresists, polymers, and C) and $BCl_2 + Cl_2$ (etching of Si, GaAs, Al) [36].

The RIE process in optical sensing can be used for efficient and well controlled etching of sensor surface resulting in effective tuning of spectral response to certain external influence [37, 38] or modification of its surface structure [39]. The RIE process allows for changing properties of materials which are very difficult to be modified using wet chemical etching. A hard carbon films, such as diamond [37] may serve as a good example.

2.3 Surface Modification and Functionalization

Plasma-based surface modification is a well-known method for improving device multifunctionality, their tribological, chemical, electrical and mechanical properties, as well as biocompatibility. The unique advantage of plasma modification is that the surface properties can be enhanced selectively while the bulk attributes of the materials remain unchanged [39]. Modification of surface properties devices such as wettability, hardness, refractive index, chemical inertness, lubricity, roughness or adhesion can be performed in several ways, but in case of optical fiber sensing devices two main categories can be distinguished, namely deposition of thin films and surface activation.

Plasma surface activation involves gases, such as hydrogen, oxygen, nitrogen, ammonia (NH_2) or carbon tetrafluoride, that dissociates and reacts with the surface which leads to creating various chemical functional groups on the surface as a result of the plasma process. The process leads to modification in chemical activity of the surface by these functional groups. In the case of materials such as polycrystalline aluminum nitride (AlN) with CVD diamond coating applied as neuroprosthetics or (bio-sensing) diamond-based acoustic device, fluorination process is used for enhanced diamond nucleation on the AlN film [40]. Plasma treatment with carbon tetrafluoride also caused forming hydrophobic coating of fluorine-containing groups (CF, CF_2, CF_3) which leads to decreasing surface wettability [41]. In the case of biomaterials surface functionalization and modification, wettability plays a crucial role [39]. Bioactive films such as plasma deposited polymers are often used as interface layer for the covalent immobilization of biologically active molecules, e.g., at cell culture plates or at bone-implants [42, 43], where they have to be modified by amination (loading of amine groups). The plasma polymerization of amine-based monomers is an efficient way to prepare bioactive amino-functionalized polymer surface [42]. Such aminated surfaces are well suited for the interaction with hyaluronan and thus play a key role in the initial adhesion of osteoblasts to implants [42, 44].

The PE CVD process was also usefully applied for fabrication of polymerized thin films such as allylamine (PPAAm), which can be used to prepare direct modification or activation of various optical surfaces [45]. Films are highly transparent and FT-IR shows that the molecular structure of the plasma deposited polymer film reproduces the monomer structure $H_2C{=}CH{-}CH_2{-}NH_2$.

Furthermore, the aminated surface is useful for the most of biofunctionalization methods [46], because such interface may further act as a receptor, i.e., active layer of a sensor used for molecular recognition [35]. Diamond-like Carbon (DLC) thin films, widely applied as a coating for optical sensor sensitivity tuning [1, 16, 37, 47–49], can also be modified with plasma treatment by NH_2 implantation in order to improve their biocompatibility [50]. Plasma treatment is also often used for surface modification of polymers [51] aiming to activate they surface or study aging. The polymers, such as polymethyl methacrylate (PMMA) or polydimethylsiloxane (PDMS), are often used for fabrication of fibre-based biosensors [52] or micro-fibers [53].

3 Plasma Processing for Optical Fibers

3.1 Introduction

Novel materials and deposition techniques on the nano-scale level brought a breakthrough in the field of optical fiber sensors. Deposition of different nano-coatings make it possible to use electromagnetic effects such as lossy mode resonance or Bragg reflection in various fiber sensing applications.

The electromagnetic wave traveling through the medium is subject to its optical properties. Material's properties are expressed by refractive index (n), which is defined as the ratio of the velocity of light in free space c to the velocity of light in the medium v:

$$n = \frac{c^2}{v^2} = \frac{\varepsilon_r \mu_r}{\varepsilon_0 \mu_0} - i\frac{\mu_0 \sigma}{\omega \varepsilon_0} = n_r - ik \tag{1}$$

where ε_0 and μ_0 are the permittivity and permeability of free space, respectively; ε_r and μ_r are the relative permittivity and permeability, respectively; σ is the electric conductivity, and ω is the angular frequency of the wave. The n is often referred to as the complex refractive index, where n_r is known as the real part of the n (in an ideal dielectric material only real part exists), and k is known as imaginary part represented by the extinction coefficient (and is related to the absorption coefficient α by: $\alpha = 4\pi k/\lambda$). Optical properties of different deposited layers vary in value, and in general n_r as well as k can be functions of frequency.

Thin film layers can be exploited in several different scenarios for coating of fiber structures. Every single scenario may act the way that would alternate structure properties. Thus, each composition of thin film requires a specific theoretical approach and appropriately applied investigation technique. There are many less and more complex analytical and numerical methods. Among others there are coupled mode theory [54, 55], beam propagation method [56, 57], transfer matrix method [58, 59], finite element method [60, 61] and whole family of finite difference methods [62].

3.2 Multilayers

Figure 4 shows a schematic of a multilayer structure deposited on a tip of the single mode fiber. This system employs one-dimensional stack of alternating dielectric layers as a specific filter. In fact, this structure resembles a well-known Bragg mirror. Such system, despite its sensing capabilities, is a good example of exploiting relatively simple yet very convenient, powerful, fast, and reliable technique, namely the transfer matrix method (TMM).

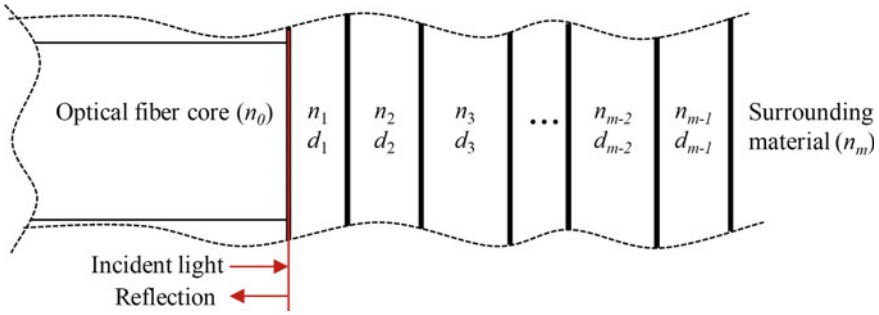

Fig. 4 A schematic model for calculations of multilayer deposited on the end-face of single mode fiber. The figure is not drawn to scale

The TMM in general aggregates properties of each consecutive layer in so called characteristic matrix:

$$M = \prod_{i=1}^{m-1} M_i = \begin{bmatrix} M_{11} & M_{12} \\ M_{21} & M_{22} \end{bmatrix}. \tag{2}$$

In Eq. (2) matrices M_i describe optical properties of corresponding layers and by multiplication they create the final matrix M. The characteristic matrix represents whole system substituting the layered medium by a bulk one. The transmission, reflection and absorption of the system is then a function of the matrix M.

In case of standard Bragg structures the number of periods state the quality of system and thus strength of a spectral response. While in contrast, for the sensing applications the number of periods should be significantly smaller to allow for strong interaction of the light traveling through the multilayer with the last layer, i.e., analyte. In order to improve sensing capabilities an optimal number of periods versus possibility to interact with tested liquid should be established. Such optimal structure would provide strong spectral response induced by the tested material. In this sense, work presented in [63], where PECVD method was used to deposit stack of high and low n silicon nitride (SiN_x) films, is a good example of achieving same balance. It also shows that even with using some simplifications (such as assumption of plane wave in the medium, calculation of overall reflection at the fiber-multilayer interface, the fiber core diameter is much smaller than the diameter of multilayer structure) the agreement of numerical and experimental results is high. Whereas [64] presents a comparative study on sensing capabilities of stacks of nano-films consisted of SiN_x and TiO_2/Al_2O_3 materials deposited with PECVD (SiN_x) and RMS (TiO_2, Al_2O_3), respectively. Studies have shown that PECVD based sensor is both refractive index and temperature sensitive, whereas RMS is sensitive only for refractive index variations. On the other hand Yang et al. [65] suggested optical fiber sensor based on the Fabry-Perot structure with end-face multilayer consisting of a stack of TiO_2 and MgF_2 films deposited with composition

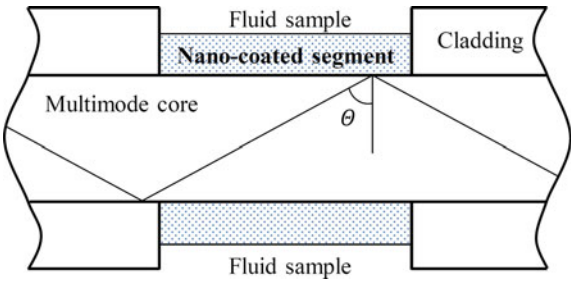

Fig. 5 A schematic cross-section of multimode fiber with deposited nanolayer. The figure is not drawn to scale

of e-beam evaporation and RMS method, which provided high quality thin films with carefully controlled thickness.

3.3 Multimode Fiber Coated Sensors

Another very interesting sensing structure is shown in Fig. 5, where the thin film layer is deposited on a multimode fiber core. In this particular situation modes supported by the thin film are classified as different types according to the permittivities of the constituting layers [66]. Three cases are possible. First, if the thin film has a negative real part of permittivity ϵ_r, and it is larger in magnitude than its imaginary part ϵ_i and surrounding dielectric ϵ_{out}, then the transverse magnetic mode (TM) is called surface plasmon resonance (SPR) [66–68]. Second, if the thin film's permittivity $\epsilon_r > 0$ and $\epsilon_r > |\epsilon_i| \; \Lambda \; \epsilon_r > \epsilon_{out}$, then the film supports a lossy mode resonance (LMR), which exists both for transverse electric (TE) and magnetic (TM) polarizations [66]. Finally, if $\epsilon_r \sim 0$ and $|\epsilon_i| >> 0$, then the supported mode is called surface exciton-polariton [69, 70].

For sensing application most commonly used structures display SPR and LMR phenomena. Although both effects are interesting, the main drawback of utilization of SPR based devices is its limitation to TM polarized light. In consequence the setup requires polarization controlled setup. In contrast the LMR is generated for both TM and TE polarization and thus overcomes the problem of polarization. Moreover the sensitivity of the LMR based device may be controlled by the change in the coating thickness in monotonic manner (it decreases with increasing thickness).

Simple model allowing to calculate effective transmitted power through LMR based device (schematically shown in Fig. 5) uses a commonly applied formulation (e.g., [71, 72]):

$$P_{transmitted} = \frac{\int_0^{\alpha_{\max}} \int_{\Theta_c}^{\pi/2} R^{N(\Theta,\alpha)} P_{in} d\Theta d\alpha}{\int_0^{\alpha_{\max}} \int_{\Theta_c}^{\pi/2} P_{in} d\Theta d\alpha} \tag{3}$$

Equation (3) expresses transmitted power as a function of various structure parameters, namely power at the fiber input P_{in}, number of reflection in the fiber N (Θ,α), the skewness angle α, the angle between the ray and the normal to the core-metal interface Θ, and optical properties through reflectivity $R^{N(\Theta,\alpha)}$. In Eq. (3) the reflectivity can be calculated by specific utilization of TMM, i.e., the method is used for three layered medium consisting of core, nano-coated region, and analyte. It is important to mention that this method is valid for core radius greater than 200 μm [72]. Plasma based methods, especially PECVD are effective in LMR based sensors due to possibility of easy modification of deposited coatings optical properties by changing flow rates of precursor gases.

By using RF PECVD thin film layers of DLC [47] and SiN_x [73] were deposited. Studies conducted upon these structures with respect to layer quality and thickness showed usability of this CVD-based method for optical sensor coatings.

3.4 Long Period Gratings

Another, and well know sensing structures exploited for over a decade are long-period gratings (LPG) (or long-period fiber gratings—LPFG). The schematic drawing of a long-period fiber structure is shown in Fig. 6.

The LPGs are periodic modulation of the refractive index of cladding and/or core along an optical fiber [74]. The grating couples the fundamental core mode (LP_{01}) to m discrete cladding modes (LP_{0m}) by satisfying specific phase-matching conditions. While propagating the cladding modes are attenuated due to absorption and scattering. Additionally the coupling depends on wavelength and thus a spectrally selective loss for each of the cladding modes is obtained. This selective mode attenuation makes the LPGs a remarkable sensing structure characterized by high sensitivity to changes in external refractive index. This sensitivity is typically defined as a shift of the resonance wavelength λ_{res}^{m} induced by a measurand [75]. Equation (4) relates the resonance wavelength λ_{res}^{m} with effective refractive index of the propagating core mode $n_{eff}^{0_1}$, effective refractive index of the mth cladding mode $n_{eff}^{0_m}$, and the LPG period Λ.

$$\lambda_{res}^{m} = (n_{eff}^{0_1} - n_{eff}^{0_m})\Lambda \tag{4}$$

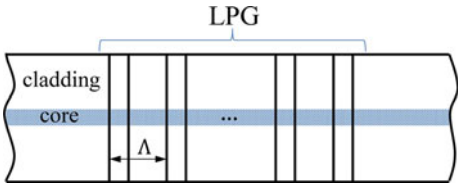

Fig. 6 A schematic cross-section view of long-period grating, Λ is a grating period. The figure is not drawn to scale

Physically, Eq. (4) describes coupling from the guided core mode (LP_{01}) to the mth cladding mode (LP_{0m}). It implies that there are many possible ways to influence the resonant wavelength. For example in sensing applications, the resonance wavelength shift can be induced by external refractive index variation. An analytical expression describing this change can be written in the following form (after [75]):

$$\frac{d\lambda_{res}^{m}}{dn_{ext}} = -\frac{\lambda_{res}^{m}\frac{d\lambda_{res}^{m}}{d\Lambda}}{n_{eff}^{0_1} - n_{eff}^{0_m}} \frac{u_m^2 \lambda_{res}^{m\ 3} n_{ext}}{8\pi r_{cl}^3 n_{cl}(n_{eff}^{0_1} - n_{eff}^{0_m})(n_{cl}^2 - n_{ext}^2)^{3/2}} \tag{5}$$

where u_m is the mth root of the zeroth-order Bessel function of the first kind, and r_{cl} and n_{cl} are the radius and refractive index of the fiber cladding, respectively.

A very important feature considerably boosting the sensitivity of the LPGs is the existence of a resonance turning point, i.e., it is possible to couple energy into the same cladding mode for two different wavelengths. This occurs when Λ is short enough, and displays in the spectrum as dual resonant peaks [76].

Numerical simulations and investigation of LPG require different approaches, depending on the required physical insight. The simplest techniques dealing with basic LPGs system involve semi-analytical approaches, e.g., coupled mode theory and transfer matrix method, while with the increasing complexity of the system more sophisticated methods are being used, such as finite difference time domain or finite element methods.

Optical fiber sensors based on LPG are one of the widely studied structures. They have been used as chemical sensor [76] or for monitoring of loads on a wind turbine blade [77] and for sensing of refractive index [81, 88, 91], strain [75] or temperature [75]. Nowadays these structures enjoy a great interest in biosensing, including detection of DNA [78], biotin-avidin complex [79], antibody-antigen interaction [80] or specific bacteria detection using bacteriophages [35]. These advanced applications were possible to develop due to very high sensitivity of LPG sensors structure. Among the main methods of increasing the LPG sensitivity one's should mention: determining dispersion turning point (DTP) and deposition nm-thick coating. DTP is a working point, where LPG exhibits very high sensitivity for a particular wavelength. DTP corresponds to two resonant wavelength and results in coupling to a single cladding mode characterized by dual resonant peaks in its transmission spectrum [75]. The conditions required to achieve DTP include both external (e.g., surrounding RI, temperature, strain) and internal (the period of the grating, the dimension of the fiber and doping) [81]. The most common method of achieving DTP is precise reduction of fiber cladding, which can be done by wet etching in hydrofluoric acid (HF) [35, 81, 88, 91] or by RIE method [37, 38]. DTP was also obtaining by other external influences, e.g., by temperature [82] or bending [83].

Another method of LPG sensitive improvement is deposition of thin film coatings. In general the higher the order of the cladding mode is the higher the sensitivity. In case of higher n of the overlay, as the thickness of the overlay increases it can guide cladding mode of the lowest order. This causes shift in the

cladding modes' effective index to higher values and thus higher order cladding mode at the same wavelength (in comparison to the structure without the overlay). Therefore, covering sensor with the overlay having higher n than the fiber cladding can enhance sensor's sensitivity [84]. Modification of sensor sensitivity by overcoating is therefore possible by applying thick coating with respectively low n (but still higher than those for fused silica—1.46) or thin film with much higher n.

The most popular methods for deposition nano-coatings on LPGs are based on immersing the LPGs in a liquid precursor, e.g. Langmuir-Blodgett [85] or sol-gel [86]. However, these methods do not provide efficient control of properties of the overlays, such as uniformity or symmetrical deposition around the fiber. To overcome some of the mentioned disadvantages the vapor deposition methods such as ALD or PECVD are used. It was reported in a number of papers application of PECVD thin films as LPG coating such as SiN_x [81, 87, 88] or DLC [37, 48, 49]. In this method properties of LPG's coatings can be easily changed by variation of process parameters, but the control of symmetrical deposition around the fiber is a challenging task. In the case of ALD methods this problem does not exists—ALD coatings have a great uniformity and gives precise control of overlay properties all over a fiber. In this subject ALD coatings with high n such as TiO_2 [35] or HfO_2 [89] are used. There were also applied coatings with relatively low n such as Al_2O_3 [90, 91].

3.5 *Photonic Crystal Fiber Based Sensing Structure*

Another very interesting sensing structure incorporating endlessly single-mode photonic crystal fiber (ESM PCF) is presented schematically in Fig. 7.

This simple all-fiber structure is based on intermodal interference between the core and cladding modes of a section of ESM PCF spliced between two pieces of SMF-28 fiber [92–96]. In the process of fabricating such a structure the holes at the SMF/PCF interfaces collapse and form a tapper allowing for independent excitation of core and higher-order modes in the PCF section. These modes propagate with different phase velocities and thus at the second splice interfere with one another. The optical transmitted power as a function of wavelength for such device can be expressed as follows [97]:

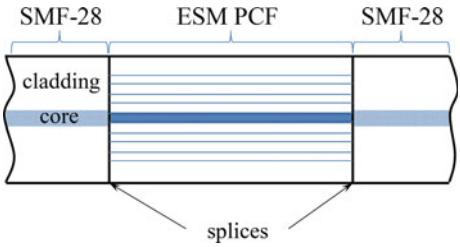

Fig. 7 A schematic cross-section view of fiber sensor structure based on endlessly single-mode photonic crystal fiber spliced between two single-mode (SMF-28) fibers. The figure is not drawn to scale

$$T(\lambda) = I_{co}(\lambda) + I_{cl}(\lambda) + 2\sqrt{I_{co}(\lambda) I_{cl}(\lambda)} \cos \frac{2\pi \Delta n_{eff} L}{\lambda} \quad (6)$$

where I_{co} and I_{cl} are the intensities of the core and cladding modes, respectively, Δn_{eff} is the difference between the effective refractive indexes of the core and cladding modes, and L is a length of the ESM PCF segment.

Equation (6) reveals periodical variations of transmitted power in spectral analysis, and indicates relation between core and cladding modes. Since cladding modes are sensitive to changes in external medium they play the crucial sensing function.

Those structures are compact, stable and display low sensitivity to temperature variations (less than 10 pm/^{o}C [93–95])—feature which is a drawback of many other sensors. Further, this PCF based structures are sensitive to pressure, strain, bending and external refractive index changes. Plasma techniques in this sensor type is mainly used for deposition an overlay to modify the distribution of cladding modes and thus tune the refractive index sensitivity of interferometer. Work presented in [97] describes application of PECVD deposited SiN_x film as a coating of a 45-mm segment of ESM fiber. Deposition of SiN_x resulted in increase of refractive index sensitivity eightfold. PECVD method allows for deposition of high hardness SiN_x with excellent adhesion to sensor surface films which leads to fabrication sensors with improvement sensitivity and high robustness.

4 Conclusions

The chapter contains a brief overview of plasma based techniques for optical fiber sensing. Plasma treatment, including precise deposition, etching and modification, is a versatile technique for fabrication sensors based on optical fibers. The main advantage of these methods is the ability to perform plasma processes at low temperatures, which in the case of optics fibers with polymer, protective coatings is extremely significant. Moreover, based on plasma technology it is possible to increase the sensitivity of the sensor and extension of their functionality by surface modification. As a result, biosensors-based on fiber optic sensors were developed, which are now very rapidly growing field of research.

References

1. M. Śmietana, W.J. Bock, J. Szmidt, G.R. Pickrell, *Nanocoating Enhanced Optical Fiber Sensors. Advances in Materials Science for Environmental and Nuclear Technology*, vol. 22 (Wiley, Hoboken, NJ, USA, 2010)
2. R.Y. Shah, Y.K. Agrawal, Introduction to fiber optics: sensors for biomedical applications. Indian J. Pharm. Sci. **73**, 17 (2011)

3. W. Mantele, Reaction induced infra-red spectroscopy for the study of protein function and reaction mechanisms. TIBS **18**, 197 (1988)
4. R. Rajan, S. Chand, B.D. Gupta, Surface plasmon resonance based fiber optic sensor for the detection of pesticide. Sens. Actuators B **123**, 661 (2007)
5. K.R. Bier, A.F. Frieder, Scheller Fibre-optic genosensor for specific determination of femtomolar DNA oligomers. Anal. Chim. Acta **350**, 51 (1997)
6. K. Seshan, *Handbook of thin film deposition techniques, processes, and technologies* (Elsevier, Amsterdam, 2012)
7. P.M. Martin, *Handbook of Deposition Technologies for Films and Coatings Science, Applications and Technology* (William Andrew, Elsevier Science, Norwich, N.Y., Oxford, 2009)
8. K. Wasa, S. Hayakawa, *Handbook of Sputter Deposition Technology: Principles, Technology, and Applications* (Noyes Publications, Park Ridge, N.J., U.S.A, 1992)
9. M.-J. Lee, S.I. Kim, C.B. Lee, H. Yin, S.-E. Ahn, B.S. Kang, K.H. Kim, J.C. Park, C.J. Kim, I. Song, S.W. Kim, G. Stefanovich, J.H. Lee, S.J. Chung, Y.H. Kim, Y. Park, Low-temperature-grown transition metal oxide based storage materials and oxide transistors for high-density non-volatile memory. Adv. Funct. Mater. **19**, 1587 (2009)
10. K. Macák, V. Kouznetsov, J. Schneider, U. Helmersson, I. Petrov, Ionized sputter deposition using an extremely high plasma density pulsed magnetron discharge. J. Vac. Sci. Technol. A **18**, 1533 (2000)
11. J.T. Gudmundsson, J. Alami, U. Helmersson, Evolution of the electron energy distribution and plasma parameters in a pulsed magnetron discharge. Appl. Phys. Lett. **78**, 3427 (2001)
12. V. Stranak, M. Quaas, R. Bogdanowicz, H. Steffen, H. Wulff, Z. Hubicka, M. Tichy, R. Hippler, Effect of nitrogen doping on TiOxNy thin film formation at reactive high-power pulsed magnetron sputtering. J. Phys. D Appl. Phys. **43**, 285203 (2010)
13. V. Straňák, M. Čada, M. Quaas, S. Block, R. Bogdanowicz, Š. Kment, H. Wulff, Z. Hubička, C.A. Helm, M. Tichý, R. Hippler, Physical properties of homogeneous TiO2 films prepared by high power impulse magnetron sputtering as a function of crystallographic phase and nanostructure. J. Phys. D Appl. Phys. **42**, 105204 (2009)
14. M. Jiang, A.P. Zhang, Y.-C. Wang, H.-Y. Tam, S. He, Fabrication of a compact reflective long-period grating sensor with a cladding-mode-selective fiber end-face mirror. Opt. Express **17**, 17976 (2009)
15. P. Hlubina, M. Kadulova, D. Ciprian, J. Sobota, Reflection-based fibre-optic refractive index sensor using surface plasmon resonance. J. Eur. Opt. Soc. Rap. Public. **9**, 14033 (2014)
16. R. Bogdanowicz, M. Śmietana, M. Gnyba, M. Ficek, V. Straňák, Ł. Goluński, M. Sobaszek, J. Ryl, Nucleation and growth of CVD diamond on fused silica optical fibres with titanium dioxide interlayer. Phys. Status Solidi A **210**, 1991–1997 (2013)
17. W. Choi, J.Y. Ko, H. Park, J.S. Chung, Investigation on TiO2-coated optical fibers for gas-phase photocatalytic oxidation of acetone. Appl. Catal. B **31**, 209 (2001)
18. J. Hamagami, Y. Oh, Y. Watanabe, M. Takata, Preparation and characterization of an optically detectable H2 gas sensor consisting of Pd/MoO3 thin films. Sens. Actuators B Chem. **13**, 281–283 (1993)
19. S. Sumida, S. Okazaki, S. Asakura, H. Nakagawa, H. Murayama, T. Hasegawa, Distributed hydrogen determination with fiber-optic sensor. Sens. Actuators B: Chem. **108**, 508 (2005)
20. J. Villatoro, D. Luna-Moreno, D. Monzón-Hernández, Optical fiber hydrogen sensor for concentrations below the lower explosive limit. Sens. Actuators B: Chem. **110**, 23–27 (2015)
21. E. Maciak, Z. Opilski, Transition metal oxides covered Pd film for optical H2 gas detection. Thin Solid Films **515**, 8351 (2007)
22. V. Stranak, A.-P. Herrendorf, S. Drache, M. Cada, Z. Hubicka, R. Bogdanowicz, M. Tichy, R. Hippler, Plasma diagnostics of low pressure high power impulse magnetron sputtering assisted by electron cyclotron wave resonance plasma. J. Appl. Phys. **112**, 093305 (2012)
23. J.R. Roth, Industrial plasma engineering, vol. 2. (u.a.: Institute of Physics Publications, Bristol, 2001)

24. R. Bogdanowicz, L. Golunski, M. Sobaszek, Spatial characterization of H2:CH4 dissociation level in microwave ECR plasma source by fibre-optic OES. Eur. Phys. J. Spec. Topics **222**, 2223 (2013)
25. J.L. Zhang, S.J. Yu, T.C. Ma, Optical emission kinetics of argon inductively coupled plasma and argon dielectric barrier discharge. Vacuum **65**(3–4), 327–333 (2002)
26. P. Bulkin, N. Bertrand, B. Drevillon, Deposition of SiO2 in integrated distributed electron cyclotron resonance microwave reactor. Thin Solid Films **296**(1–2), 66–68 (1997)
27. R. Bogdanowicz, M. Gnyba, P. Wroczyński, Optoelectronic monitoring of plasma discharge optimized for thin diamond film synthesis. Journal de Physique IV (Proceedings) **137**, 57–60 (2006)
28. Z. Fang, *Fundamentals of Optical Fiber Sensors* (Wiley, Hoboken, 2012)
29. H. Sunami, Y. Itoh, K. Sato, Stress and thermal-expansion coefficient of chemical-vapor deposited glass films. J. Appl. Phys. **41**(13), 5115–5117 (2003)
30. A. Martín, J.P. Espinós, A. Justo, J.P. Holgado, F. Yubero, A.R. González-Elipe, Preparation of transparent and conductive Al-doped ZnO thin films by ECR plasma enhanced CVD. Surf. Coat. Technol. **289**, 151–152 (2002)
31. Q.Y. Zhang, K. Pita, S.C. Tjin, C.H. Kam, L.P. Zuo, S. Takahashi, Laser-induced ultraviolet absorption and refractive index changes in Ge–B–SiO2 planar waveguides by inductively coupled plasma-enhanced chemical vapor deposition. Chem. Phys. Lett. **379**, 534 (2003)
32. F. Iacopi, P.M. Vereecken, M. Schaekers, M. Caymax, N. Moelans, B. Blanpain, O. Richard, C. Detavernier, H. Griffiths, Plasma-enhanced chemical vapour deposition growth of Si nanowires with low melting point metal catalysts: an effective alternative to Au-mediated growth. Nanotechnology **18**, 505307 (2007)
33. L. Cheng, A.J. Steckl, J. Scofield, SiC thin-film Fabry-Perot interferometer for fiber-optic temperature sensor. IEEE Trans. Electron Devices **50**, 2159 (2003)
34. R.W. Johnson, A. Hultqvist, S.F. Bent, A brief review of atomic layer deposition. Mater. Today **17**, 236 (2014)
35. M. Smietana, M. Koba, E. Brzozowska, K. Krogulski, J. Nakonieczny, L. Wachnicki, P. Mikulic, M. Godlewski, W.J. Bock, Label-free sensitivity of long-period gratings enhanced by atomic layer deposited TiO2 nano-overlays. Opt. Express **23**, 8441 (2015)
36. M.A. Lieberman, A.J. Lichtenberg, *Principles of Plasma Discharges and Materials Processing*, 2nd edn. (Wiley-Interscience, 1994)
37. M. Śmietana, M. Koba, P. Mikulic, W.J. Bock, Tuning properties of long-period gratings by plasma post-processing of their diamond-like carbon nano-overlays. Meas. Sci. Technol. **25**, 114001 (2014)
38. M. Śmietana, M. Koba, P. Mikulic, W.J. Bock, Measurements of reactive ion etching process effect using long-period fiber gratings. Opt. Express **22**, 5986–5994 (2014)
39. P.K. Chu, J.Y. Chen, L.P. Wang, N. Huang, Plasma-surface modification of biomaterials. Mater. Sci. Eng. R **36**, 143 (2002)
40. P. Pobedinskas, G. Degutis, W. Dexters, W. Janssen, S.D. Janssens, B. Conings, B. Ruttens, J. D'Haen, H.-G. Boyen, A. Hardy, M.K. Van Bael, K. Haenen, Surface plasma pretreatment for enhanced diamond nucleation on AlN. Appl. Phys. Lett. **102**, 201609 (2013)
41. T.E.F.M. Standaert, C. Hedlund, E.A. Joseph, G.S. Oehrlein, T.J. Dalton, Role of fluorocarbon film formation in the etching of silicon, silicon dioxide, silicon nitride and amorphous hydrogenated silicon carbide. J. Vac. Sci. Technol. A **22**(1), 53 (2004)
42. B. Finke, F. Hempel, H. Testrich, A. Artemenko, H. Rebl, O. Kylián, J. Meichsner, H. Biederman, B. Nebe, K.-D. Weltmann, K. Schröder, Plasma processes for cell-adhesive titanium surfaces based on nitrogen-containing coatings. Surf. Coat. Technol. **205**, S520 (2011)
43. S. Grassini, E. Angelini, M. Parvis, F. Faraldi, Surface modification plasma treatments of PMMA optical fibres for sensing applications. Surf. Interf. Anal. **2012**, 44 (1068)
44. B. Finke, F. Lüthen, K. Schröder, P.D. Müller, C. Bergemann, M. Frant, A. Ohl, B.J. Nebe, The effect of positively charged plasma porymerization on initial osteoblastic focal adhesion on titanium surface. Biomaterials **28**, 4521 (2007)

45. R. Bogdanowicz, M. Sawczak, P. Niedzialkowski, P. Zieba, B. Finke, J. Ryl, J. Karczewski, T. Ossowski, Novel functionalization of boron-doped diamond by microwave pulsed-plasma polymerized allylamine film. J. Phys. Chem. C **118**, 8014 (2014)
46. S. Avvakumova, M. Colombo, P. Tortora, D. Prosperi, Biotechnological approaches toward nanoparticle biofunctionalization. Trends Biotechnol. **32**, 11 (2014)
47. M. Śmietana, M. Dudek, M. Koba, B. Michalak, Influence of diamond-like carbon overlay properties on refractive index sensitivity of nano-coated optical fibers. Phys. Status Solidi A **210**, 2100–2105 (2013)
48. M. Smietana, J. Szmidt, M.L. Korwin-Pawlowski, W.J. Bock, J. Grabarczyk, Application of diamond-like carbon films in optical fibre sensors based on long-period gratings. Diam. Relat. Mater. **16**, 1374 (2007)
49. W.J. Bock, T. Eftimov, M. Smietana, P. Mikulic, Efficient distributed moisture-ingress sensing using diamond-like carbon-nanocoated long-period gratings. Optics Commun. **284**, 4470 (2011)
50. M. Wang, Y. Zhao, R.Z. Xu, M. Zhang, R.K.Y. Fu, P.K. Chu, Plasma modification of DLC films and the resulting surface biocompatibility. Mater. Sci. Forum **783–786**, 1396 (2014)
51. A. Vesel, M. Mozetic, Surface modification and ageing of PMMA polymer by oxygen plasma treatment. Vacuum **86**, 634 (2012)
52. Y. Jin, K.H. Wong, A.M. Granville, Developing localized surface plasmon resonance biosensor chips and fiber optics via direct surface modification of PMMA optical waveguides. Colloids Surf. A **492**, 100 (2016)
53. L. Le, Y. Xinghua, Y. Libo, Z. Enming, T. Fengjun, L. Shenzi, L. Yanxin, Electrospinning of Poly(Methyl Methacrylate) (PMMA) for optical waveguide. Sens. Lett. **10**, 1544 (2012)
54. A. Snyder, Coupled-mode theory for optical fibers. J. Opt. Soc. Am. **62**, 1267 (1972)
55. L. Jin, W. Jin, J. Ju, Y. Wang, Coupled local-mode theory for strongly modulated long period gratings. J. Lightwave Technol. **28**, 1745 (2010)
56. M.D. Feit, J.A. Fleck, Light propagation in graded-index optical fibers. Appl. Opt. **17**, 3990 (1978)
57. R. Scarmozzino, R.M. Osgood, Comparison of finite-difference and fourier-transform solutions of the parabolic wave equation with emphasis on integrated-optics applications. J. Opt. Soc. Am. A **8**, 724 (1991)
58. B.E.A. Saleh, M.C. Teich, *Fundamentals of Photonics*, 2nd edn. (Wiley, 2007), chap. 7
59. H.A. Macleod, *Thin-Film Optical Filters* (Institute of Physics Publishing, Bristol and Philadelphia, 2001)
60. Y.-J. He, Long-period fiber grating using the finite element method and eigenmode expansion method. Sens. Actuators B: Chem. **183**, 319 (2013)
61. G. Demésy, F. Zolla, A. Nicolet, M. Commandré, C. Fossati, The finite element method as applied to the diffraction by an anisotropic grating. Opt. Express **15**, 18089 (2007)
62. P. Yeh, *OpticalWaves in Layered Media* (Wiley, New York (NY), 1988)
63. M. Śmietana, M. Koba, R. Różycki-Bakon, Stack of PECVD silicon nitride nano-films on optical fiber end-face for refractive index sensing, in *23rd International Conference on Optical Fibre Sensors* (2014), pp. 9157, 91575F
64. M. Koba, R. Rózycki-Bakon, P. Firek, M. Śmietana, Sensing properties of periodic stack of nano-films deposited with various vapor-based techniques on optical fiber end-face. Proc. SPIE Int. Soc. Opt. Eng. **9655**, 96550R (2015)
65. M. Yang, Y. Sun, X. Li, D. Jiang, Optical fiber sensors based on Fabry-Perot multilayer coatings. Chin. Opt. Lett. **8**, 189 (2010)
66. F. Yang, J.R. Sambles, Determination of the optical permittivity and thickness of absorbing films using long range modes. J. Mod. Opt. **44**, 1153 (1997)
67. D. Sarid, Long-range surface-plasma waves on very thin metal films. Phys. Rev. Lett. **1981**, 47 (1927)
68. J.C. Quail, H.J. Simon, Second-harmonic generation with phase-matched long-range and short-range surface plasmons **56**, 2589 (1984)

69. J. Lagois, B. Fischer, Experimental observation of surface exciton polaritons. Phys. Rev. Lett. **36**, 680 (1976)
70. J. Lagois, B. Fischer, Introduction to surface exciton polaritons. Adv. Solid State Phys. **18**, 197 (1978)
71. I. Del Villar, M. Hernaez, C.R. Zamarreño, P. Sánchez, C. Fernández-Valdivielso, F. J. Arregui, I.R. Matias, Design rules for lossy mode resonance based sensors. Appl. Opt. **51**, 4298 (2012)
72. I. Del Villar, C.R. Zamarreno, M. Hernaez, F.J. Arregui, I.R. Matias, Lossy mode resonance generation with indium-tin-oxide-coated optical fibers for sensing applications. J. Lightwave Technol. **28**, 111 (2012)
73. B. Michalak, M. Koba, M. Śmietana, Silicon nitride overlays deposited on optical fibers with RF PECVD method for sensing applications: overlay uniformity aspects. Acta Phys. Pol. A **127**, 1587 (2015)
74. A.M. Vengsarkar, P.J. Lemaire, J.B. Judkins, V. Bhatia, T. Erdogan, J.E. Sipe, Long-period fiber gratings as band-rejection filters. J. Lightwave Technol. **14**, 58 (1996)
75. X. Shu, L. Zhang, I. Bennion, Sensitivity characteristics of long-period fiber gratings. J. Lightwave Technol. **20**, 255 (2002)
76. X. Shu, D. Huang, Highly sensitive chemical sensor based on the measurement of the separation of dual resonant peaks in a 100-mm-period fiber grating. Opt. Commun. **171**, 65 (1999)
77. L. Glavind, S. Buggy, J. Canning, S. Gao, K. Cook, Y. Luo, G.D. Peng, B.F. Skipper, M. Kristensen, Long-period gratings for selective monitoring of loads on a wind turbine blade. Appl. Opt. **53**, 3993 (2014)
78. X. Chen, L. Zhang, K. Zhou, E. Davies, K. Sugden, I. Bennion, M. Hughes, A. Hine, Real-time detection of DNA interactions with long period fiber-grating-based biosensor. Opt. Lett. **17**, 2541 (2007)
79. P. Pilla, P.F. Manzillo, V. Malachovska, A. Buosciolo, S. Campopiano, A. Cutolo, L. Ambrosio, M. Giordano, A. Cusano, Long period grating working in transition mode as promising technological platform for label free biosensing. Opt. Express **17**, 20039 (2009)
80. L. Marques, F.U. Hernandez, S.W. James, S.P. Morgan, M. Clark, R.P. Tatam, S. Korposh, Highly sensitive optical fibre long period grating biosensor anchored with silica core gold shell nanoparticles. Biosens. Bioelectron. **75**, 222 (2016)
81. A.K. Dębowska, M. Śmietana, P. Mikulic, W.J. Bock, High temperature nano-coated electric-arc-induced long-period gratings working at the dispersion turning point for refractive index sensing. Jpn. J. Appl. Phys. **53**, 08ME01 (2014)
82. M. Śmietana, W.J. Bock, P. Mikulic, C. Jiahua, Tuned pressure sensitivity of dual resonant long-period gratings written in boron codoped optical fiber. J. Lightwave Technol. **2012**, 30 (1080)
83. M. Szymańska, K. Krogulski, P. Mikulic, W.J. Bock, M. Śmietana, Sensitivity of long-period gratings modified by their bending. Procedia Eng. **87**, 1180 (2014)
84. Z. Wang, Z. Heflin, R. Stolen, S. Ramachandran, Analysis of optical response of long period fiber gratings to nm-thick thin-film coating. Opt. Express **13**, 2808 (2005)
85. I.M. Ishaq, A. Quintela, S.W. James, G.J. Ashwell, J.M. Lopez-Higuera, R.P. Tatam, Modification of the refractive index response of long period grating using thin film overlays. Sens. Actuators B Chem. **107**, 738 (2005)
86. Z. Gu, Y. Xu, Design optimization of a long-period fiber grating with sol–gel coating for a gas sensor. Meas. Sci. Technol. **18**, 3530 (2007)
87. M. Smietana, W.J. Bock, P. Mikulic, J. Chen, Pressure sensing in high-refractive-index liquids using long-period gratings nanocoated with silicon nitride. Sensors **10**, 11301 (2010)
88. J. Grochowski, M. Myśliwiec, P. Mikulic, W.J. Bock, M. Śmietana, Temperature cross-sensitivity for highly refractive index sensitive nanocoated long-period gratings. Acta Phys. Pol. A **124**, 421 (2013)

89. L. Melo, G. Burton, P. Kubik, P. Wild, Long period gratings coated with hafnium oxide by plasma-enhanced atomic layer deposition for refractive index measurements. Opt. Express **24**, 7654 (2016)
90. F. Zou, Y. Liu, C. Deng, Y. Dong, S. Zhu, T. Wang, Refractive index sensitivity of nano-film coated long period fiber gratings. Opt. Express **23**, 1114 (2015)
91. M. Śmietana, M. Myśliwiec, P. Mikulic, B.S. Witkowski, W.J. Bock, Capability for fine tuning of the refractive index sensing properties of long-period gratings by atomic layer deposited Al2O3 overlays. Sensors **13**, 16372 (2013)
92. H.Y. Choi, M.J. Kim, B.H. Lee, All-fiber Mach-Zehnder type interferometers formed in photonic crystal fiber. Opt. Experss **15**, 5711 (2007)
93. W.J. Bock, T.A. Eftimov, P. Mikulic, J. Chen, An inline core-cladding intermodal interferometer using a photonic crystal fiber. J. Lightwave Technol. **27**, 3933 (2009)
94. R. Jha, J. Villatoro, G. Badenes, V. Pruneri, Refractometry based on a photonic crystal fiber interferometer. Opt. Lett. **34**, 617 (2009)
95. J. Villatoro, V. Finazzi, G. Badenes, V. Pruneri, Highly sensitive sensors based on photonic crystal fiber modal interferometers. J. Sens. **2009**, 747803 (2009)
96. Y. Geng, X. Li, X. Tan, Y. Deng, Y. Yu, A cascaded photonic crystal fiber Mach Zehnder interferometer formed by extra electric arc discharges. Appl. Phys. B **102**, 595 (2010)
97. M. Smietana, D. Brabant, W.J. Bock, P. Mikulic, T. Eftimov, Refractive index sensing with inline core-cladding intermodal interferometer based on silicon nitride nano-coated photonic crystal fiber. J. Lightwave Technol. **30**, 1185 (2012)

Trends in Fibre-Optic Uses for Personal Healthcare and Clinical Diagnostics

A.B. Socorro and S. Díaz

Abstract Along this chapter, a different point of view on the sensing uses of optical fibre is shown, focusing on its applicability to medical diagnostics. A wide majority of the fibre-optic-based structures described in this book can be used in medicine. But there are some challenges for fibre-optics to be fulfilled in the future when talking about healthcare. First, current society strongly demands day-by-day applications. This means, technologies that permit their use 'on the go' such as wearables or their integration in our smartphones. Second, due to the reduced dimensions of the optical fibre, there is an increasing interest in introducing it into the body, as it occurs when using catheters or fibrescopes. Moreover, the need for analysing biological substances makes it crucial to use reduced size devices that permit their interaction with the biomolecules, once the samples have been extracted from the patient. And of course, all the addressed applications must be achieved in order to search for cheap devices that work under exigent conditions. The main goal of this chapter is to search for those applications that will lead us to use fibre-optics for self-healthcare and diagnose patients in the next times.

1 Introduction

1.1 Motivation

Biomedical engineering has become a crucial profession in our current society. There is an increasing need for ensuring a good healthcare system because one of the main issues nowadays is the appearance of many bad health conditions that

A.B. Socorro (✉) · S. Díaz
UPNA Sensors Group, Department of Electrical and Electronic Engineering, Public University of Navarre, 31006 Pamplona, Navarre, Spain
e-mail: ab.socorro@unavarra.es

A.B. Socorro · S. Díaz
Institute of Smart Cities, Jeronimo de Ayanz, Public University of Navarre, 31006 Pamplona, Navarre, Spain

© Springer International Publishing Switzerland 2017

I.R. Matias et al. (eds.), *Fiber Optic Sensors*, Smart Sensors, Measurement and Instrumentation 21, DOI 10.1007/978-3-319-42625-9_6

were not present just a few decades ago. The development of the society requires being updated on the new illnesses and try to solve every of them (or at least, most of them), at the same time that the technology improves to extract more information of every single case. This information is again introduced in the technological development to keep improving the devices. This kind of feedback is the motor of every biomedical engineering application.

In this sense, those applications based on developing technology for medicine cover from the molecular treatment of the illnesses to hospital management, patient tracking and data security. In the middle, medical instrumentation, patient diagnosis and therapy are challenging objectives to pursue. Hence, there is a need for people interested in enforcing the current and future technology possibilities, in order to inform both physicians and patients about their needs. In the end, they are the clients for these applications.

When talking about healthcare, a very important word should be repeated in everyone's mind: prevention. And in order to afford the high cost that developed countries (mainly) are going to support in the future because of the population ageing, it is important to invest in early diagnostics as soon as possible. Thus, the need for devices that help improve the early-diagnostics of patients that may involve a higher cost in every national health system is urgent. This chapter tries to give an idea of what can be done in these terms from the field of fibre-optics.

1.2 Applicability of Fibre-Optics for Medicine

Regarding the main topic of this book, optical fibre-based sensors, technology has developed a wide variety of applications, in patient diagnostics mainly, that help physicians cure patients just by using the light adequately both inside and outside the organism. But from a biomedical engineering point of view, there are many reasons why optical fibre deserves to be used in medicine. Some of them are listed and briefly explained below:

A. Biocompatibility
An optical fibre is essentially silicon dioxide, silica. A material that is worldwide extended and that it seems not to present side effects when subjected to biological substances [1, 2].

B. Reduced Size
Even when the diameter of the fibre core is 1 mm, it can be introduced in the body, in order to illuminate its inner cavities [3]. In the rest of cases, the size of the optical fibre is adequate or it can be modified to interact with biological molecules, so it can be used as a good platform to detect illnesses, for instance [2, 4].

C. Low Cost
It is well known that optical fibre is a cheap material that can be purchased almost worldwide. Nevertheless, as long as the designed devices are low-sized, it is possible to even reduce the cost of the final application.

D. Flexibility and Low Weight
This has been one of the most valuable achievements when designing optical fibres. But this characteristic is especially critical when using it in biomedicine. Otherwise, it would have not been possible to reach those places in the human body where it is impossible to actuate unless an open surgery is practised. For instance, nowadays it is possible to cauterize varicose veins by launching a laser light through an optical fibre [5]. Also, the most known technology when introducing the optical fibre in the body is the fibrescope. This chapter will provide some details on the recent advances on it.

E. Capability to Work in Hazardous Media
Optical fibre has demonstrated to work in good conditions under complex media such as in nuclear environments [6] or in the salty ocean shore [7]. Moreover, there are many applications that address the use of optical fibres in complex matrices such as blood serum, where the presence of erythrocytes, lymphocytes, platelets or the serum itself normally do not permit optimal detection conditions [4, 8].

F. Diversity of Light Propagation Configurations
The optical fibre, as a cable, guides the light, but it is possible to interact with it by actuating on the fibre structure. Along this book, many ways to approach this interaction are shown, including reflection and transmission configuration set-ups, tapering, etching, thin-film deposition, access to the higher order modes propagating inside the structure… A good set of simple configurations and phenomena referring to fibre-optic-based sensors for biomedical applications are collected in [9].

G. Optical Fibre Itself Is a Sensing Platform
Structures such as Bragg gratings (both FBGs and LPFGs), interferometers (Fabry-Perots or multimode interference devices), tapered/etched structures, etc., somehow modulate the light propagating inside them. Plenty of applications are detailed along this book. Therefore, it is possible to use and optimize these phenomena to work for improving their response when addressing any kind of sensing application and specifically biomedical applications.

However, as commented in the abstract, this chapter will not revise the current sensing applications of optical fibres as usual in biomedicine. Instead, the goal will be try to set the trends for future applications that this technology will have to cover in the future, based on the most recent advances.

To this purpose, the reminder of this chapter will be the following: Sect. 2 will talk about a global point of view of what it is going to be described later, regarding the use of fibre-optics as a current and future technology to help physicians cure

patients. Then, Sects. 3–5 will try to summarize the recent advances in what it is going to be called 'fibre on the body', 'fibre in the body' and 'fibre at the lab' (see Fig. 1). Finally, the chapter will finish with some conclusions and a prospective of what it is expected to work with in the future regarding fibre-optics for medicine.

2 An Updated Concept of Biosensor

Trying to be technically strict, a biosensor could be defined as a device capable of detecting biological or biochemical substances, called analytes, with high sensitivity and using a rapid, direct and specific biomolecular recognition.

However, this concept exceeds accuracy nowadays. It is true that since the majority of the current diseases involves to recognize the key biomolecule involved in the symptoms, the scientific community is focusing on developing biosensors based on attaching bioreceptors to the different substrates, depending on the transducing phenomenon. For instance, a novel technique tries to detect as lower concentration as possible of beta-amyloid or tau proteins for Alzheimer's disease [10].

The biomolecular recognition of specific diseases should be continuously addressed in the future, but there is a need for something else if a complete definition of a biosensor is to be achieved. Recent technologies permit patients to take care of themselves, developing mobile applications that monitor the cardiac activity or the calories burnt during a work-out. Clothing permits to have a comfortable experience when doing sports because of the materials they are made, but it is currently starting to incorporate measurements that can guide people to be healthier [11]. These are also biosensing applications, since they are monitoring biological variables to be taken into account to improve our personal health statistics. What is more, the use of complex devices such as fibrescopes or the lab-on-chip technology involves extracting information from the biological variables of the patient, process it and even offer a diagnosis of the patient's health. Therefore, the concept of biosensor should be updated to something more generic like "*device capable of monitoring a specific biomedical variable (including biochemical or physical) and provide information that can give a rapid and accurate diagnosis of a patient's health condition*".

This definition can be also applied to the field of fibre-optics, and the following sections will try to address this issue. But before that, a simple scheme of what is going to be described may clarify the proposed concepts. It is depicted in Fig. 1. First, a revision on the day-by-day uses of fibre-optics will give an idea of the trending topics regarding personal healthcare and mobile applications. Thus, 'wearables' or even the technology that can be attached to current smartphones will be addressed in the following section. Then, the chapter will focus on those uses of optical fibres that require penetrating into the human body to obtain information about its health condition. In this sense, some novelties on fibrescopes, catheters and endomicroscopy will be presented. Finally, outside the organism, this means 'at

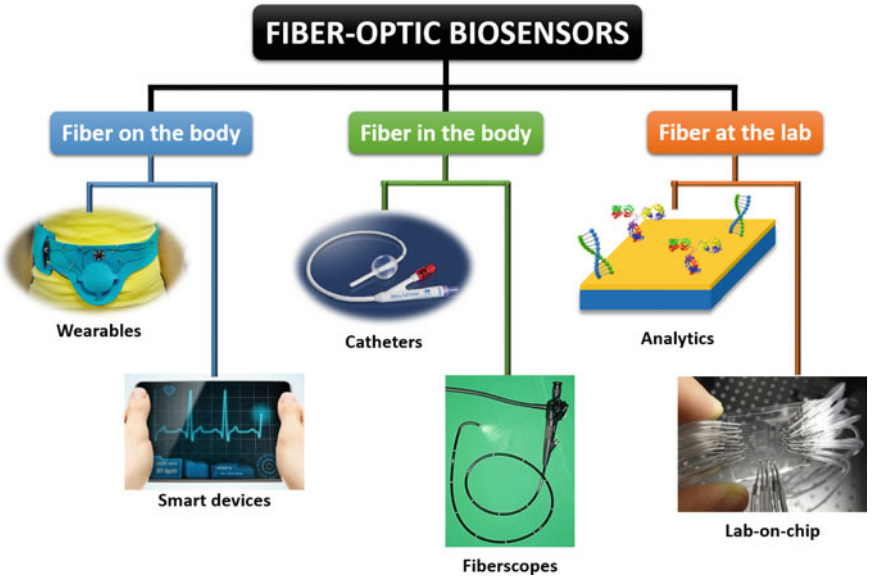

Fig. 1 Scheme of the addressed issues in this chapter, based on the new biosensor concept defined.The classical biomolecule recognition definition is also included. *Source* Combination of own images and Creative Commons licensed images

the lab', is where optical fibre is widely used as a classical biosensor. In this sense, a brief reminder of how to attach biomolecules to the optical fibre will be presented but at the same time trying to show the advances in the lab-on-fibre technology, trying to pursue a future combination between these two technologies.

3 Fibre on the Body

Since the apparition of 'wearables' and smartphones, the interest of the population in being healthy have encouraged to wear clothes that monitor basic biomedical variables such as respiratory or cardiac rhythm. This is especially curious when practising sports, since clothing can be manufactured from a combination of natural or synthetic fibres that embed optical fibres inside [11, 12]. Regarding smartphones, the current technology is capable of designing novel integrated black-boxes with optical fibre sensors inside that are attached to the device. This black-box communicates with the smartphone via software and the corresponding application is in charge of managing the obtained information of what is happening in the sensing fibre. Both technologies are good examples of 'fibre on the body'. Therefore, the global diffusion of such devices explains that there is an increasing interest in the population to take care of themselves at the same time they are capable of informing physicians about their health condition in real time. Consequently, the research and

development on these topics should be a 'must do' in the future. That is why the recent trends on the use of fibre-optics for these topics are described in the next lines.

3.1 Wearables

Terms such as 'wearable technology', 'wearable devices' or 'wearables' refer to electronic technologies or computers that are incorporated into items of clothing and accessories which can comfortably be worn on the body. As mobile phones and laptop computers, these wearable devices can perform the same computing tasks. However, in some cases, wearable technology can be better than these hand-held devices entirely. Wearable technology tends to be more sophisticated than hand-held technology on the market today, because it can provide different features, such as sensory and scanning properties, not typically seen in mobile and laptop devices. One example of this is the capability of wearable devices to give biofeedback and tracking of physiological function [13].

There are many examples of wearable technology. The most important characteristic of these devices is that they have some form of communications capability and they can allow the access to information in real time. Data-input capabilities are also a feature of such devices, such as local storage. Among the different examples of wearable devices, we can include watches, glasses, contact lenses, e-textiles and smart fabrics, headbands, jewellery such as rings, bracelets, and hearing aid-like devices that are designed to look like earrings (see Fig. 2a).

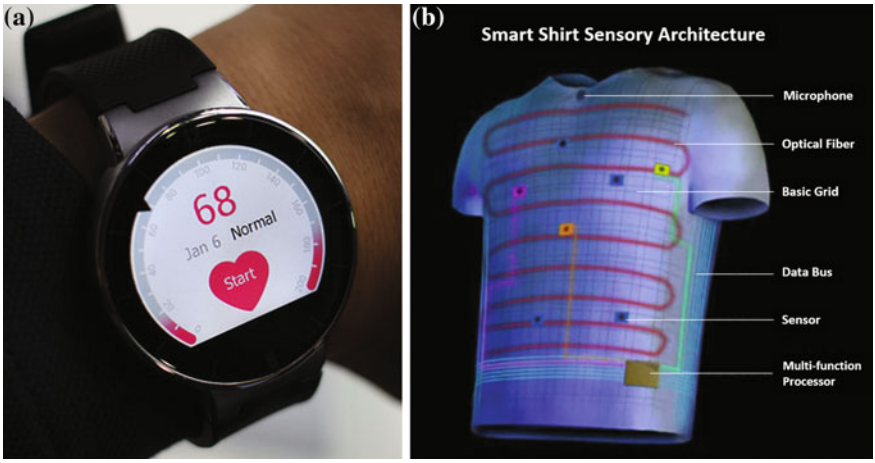

Fig. 2 **a** Smart watch from Apple Inc. **b** Wearable smart shirt. *Source* **a** Creative Commons licensed image and **b** reproduced image from http://www.sensatex.com

While wearable technology tends to refer to items which can be put on and taken off easily, there are more invasive versions of the concept, as it occurs in the case of implanted devices such as micro-chips or even smart tattoos. In the future, whether a device is worn on or incorporated into the body, the purpose of wearable technology will be to create constant, convenient, portable, and mostly hands-free access to electronics and computers.

The implications and uses of wearable technology are far reaching and can influence the fields of health and medicine, fitness, ageing, disabilities, education, transportation, enterprise, finance, gaming and music. The goal of wearable technologies in each of these fields will be to smoothly incorporate functional, portable electronics and computers into the daily life of the individuals. As it usually happens, wearable devices were primarily used in the field of military technology and had the biggest implications for healthcare and medicine. In fact, just 10 years ago, medical engineers were talking about wearable devices which could monitor the health and well-being of patients in the form of a "Wearable Motherboard" or the "Smart Shirt," aimed at monitoring vital signs and sending that biofeedback information to a hub station in real time [14], as shown in Fig. 2b.

The "Smart Shirt" shown in Fig. 2b, can monitor the vital statistics of the wearer. It can be worn under the wearers clothing as an undershirt and is, in fact, washable. The actual name of this piece of engineering is GTWM, which stands for Georgia Tech Wearable Motherboard. The shirt includes a microphone, multiple sensors, and a multi-function processor. The processor collects and sends data from the wearer to a hospital for processing using Bluetooth and WLAN technology [15].

Even though wearable technology could potentially have the most impact in the fields of health and fitness, it also promises great influence on gaming and entertainment. Augmented reality and wearable technology can be combined to create a much more realistic and immersive environment in real time. The concept is not necessarily new, since augmented reality through the use of wearable devices has been discussed since the late 1990s [16]. However, the prototypes are moving away from large goggles and backpacks, to smaller, lightweight and more mobile systems. The even more fashion designs of mobile phones and digital cameras currently on the market are an indication for the future of wearable devices. This consideration for both technology and esthetics is already evident in devices such as Google Glass, which has a very elegant and lightweight design.

As the potential uses in various fields keeps on growing, the sociological and cultural impact that wearable technology will have in the future should not be minimized. The current hand-held devices available to consumers, such as Smart Phones, iPods® or tablets, have changed the technological and social landscapes on a global scale to a point that walking out in public and seeing an individual engaging with a hand-held device is commonplace. Such an image was nonexistent only 20 years ago. With that in mind, developers and analysts predict that wearable technology will very quickly change the technological and cultural landscapes once again, and may even change the nature of mobile phones and other hand-held devices entirely.

Considering the trends in fibre-optics based wearables, it is obvious that optical fibres have some inherent good properties, such as light weight, small size and no threat of electrical hazard. They resemble textile fibres, and therefore they could be used in the clothing to add new features [13, 17]. Fibre-optic sensors have been studied since 1960s, and nowadays they can challenge the most traditional sensors in many applications [18]. The most effort in the past was made to integrate non-optical sensors into textiles. Optical fibres integrated in textiles were mostly explored for illumination or luminescent purposes.

Smart technical textiles containing fibre-optic sensors are still an exception. When integration of sensors into textiles is considered, optical fibres have an interesting advantage when compared to other kind of sensors due to their fibrous nature. The optical fibre is similar to textile fibres and can be ideally processed like standard textiles. In particular, the integration of polymer optical fibres (POF), with their good material properties, into technical textiles offer additional benefits to users. They are lightweight, robust, cheap and easy to handle. Because of their high elasticity and high breakdown strain, POF are ideally suited for integration into technical textiles [19].

Geotextiles with incorporated fibre-optic sensors based on fibre Bragg gratings (FBG) were demonstrated in the past by Voet et al. [20]. The feasibility of using fibre-optic sensors for respiratory monitoring was demonstrated, by using fibre sensors woven into bandages or attached onto garments mainly using FBGs and LPGs (long-period gratings) based on silica fibres [21]. However, the poor compatibility of these sensors with industrial textile processes limits their flexibility and use for medical monitoring purposes. When monitoring the health condition of the patients, smart underwear containing fibre-optic sensors is being developed. Special attention is paid to the development of a heart rate sensor to be used as a textile-integrated sensor in underwear. A first sensor prototype is based on macrobending effects in POF [22]. The POF macrobending sensor is joint to an elastic fabric, and measures the small elongations of the textile which is caused by the heart movement.

Hence, smart technical textiles with embedded optical fibres are a potential new market niche for fibre-optic sensors. Particularly, sensors based on POF take advantage of the high robustness, high elasticity and high break-down strain of POF allowing distributed sensing of strong mechanical deformations of soil and walls. Multifunctional, smart technical textiles incorporating fibre-optic sensors are a cost-effective solution to increase the structural safety of such structures (see Fig. 3). The breakthroughs include the use of these textiles for reinforcement and at the same time for monitoring of earthworks and walls. In this way, online information on the state and the performance of the structures could be received and so avoid possible collapses. Such on-line and long-term monitoring systems will improve the capability to react rapidly and to control damages.

Novel monitoring systems based on medical textiles with embedded fibre-optic sensors will be used at medium-term in the healthcare monitoring and for personal protection of rescues in high-risk environments where standard, non-optical monitoring systems show significant limits.

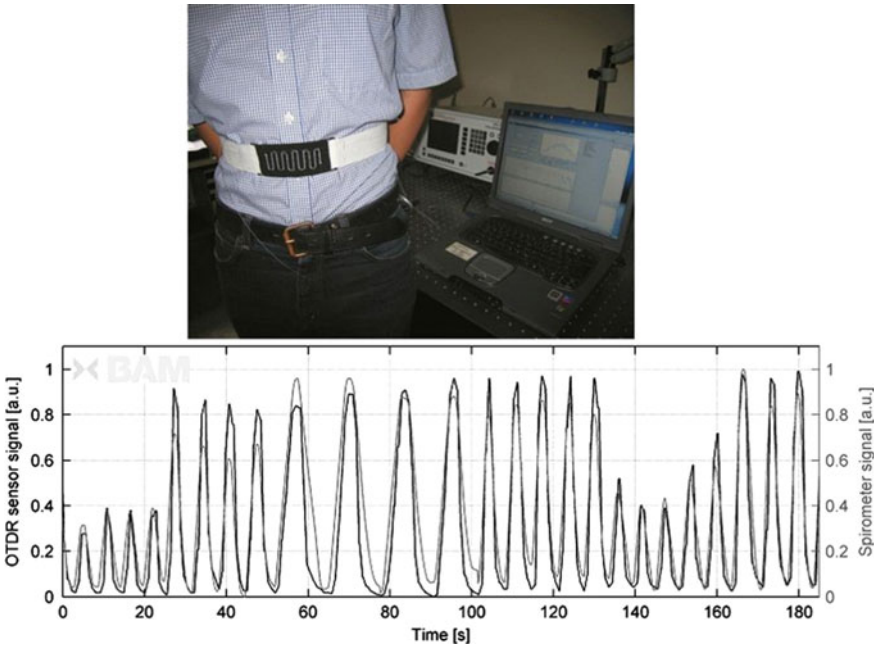

Fig. 3 Monitoring of the respiratory abdominal movement of a human adult by a POF optical time-domain reflectometer (OTDR) sensor embedded in medical textiles (the OTDR sensor signal was compared with the signal measured by a spirometer). *Source* © 2013 Krebber K. Published in [17] under CC BY 3.0 license. Available from: http://dx.doi.org/10.5772/54244

3.2 Smartphones

It is obvious that the demand on the use of smartphones is increasing even more because of the need for being communicated and updated on what is happening around the world [23]. But it is even more common to search for mobile applications that permit the monitoring and further diagnostics of symptoms that may indicate chronic or acute diseases [24]. Therefore, the own smartphone can be used either as a sensor or a transducer of biomedical variables and, at the same time, guide the user to achieve an improvement of his/her health condition. Moreover, this goal is reached by using friendly interfaces that interact with the users, so people find it helpful for their lives.

Regarding the biomedical variables that can be sensed using smartphones, it is important to remember that they already own sensors, e.g. their own CCD camera. For instance, a smartphone can be used as an inclination measurement device and thereby calculate angles. This means that by just taking a photo it can act as a goniometer and so be used to evaluate the adequate functioning of a joint [25, 26]. However, the key point of a smartphone is its capability of being used as a portable spectrometer (see Fig. 4a). This can be taken into account to design devices that

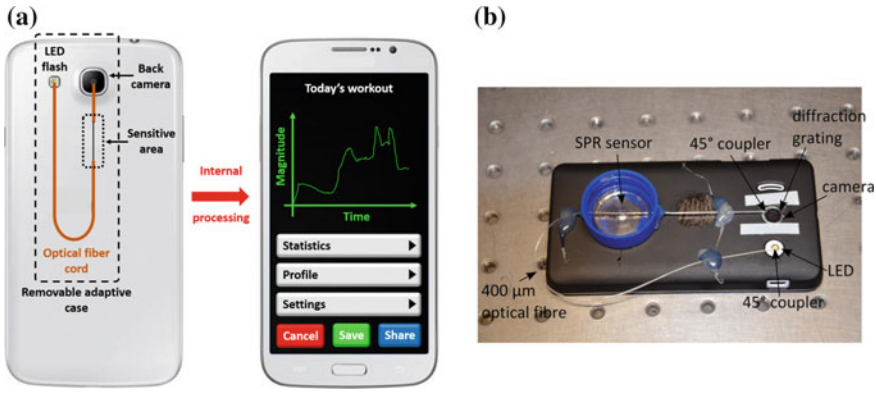

Fig. 4 **a** A schematic of a future removable adaptive case for smartphones, capable of obtaining data of self-health condition. **b** A recent suggestion by Bremer and Roth [29] depositing a gold nanocoating onto the optical fibre to obtain an SPR-based refractometer on a smartphone. *Source* **b** Reprinted with permission of [29]

incorporate some fibre-optic-based tool in order to obtain information or images from the launched/received light. Some examples are given below.

Berg et al. [27], have designed an attachable and detachable 3D-printed case that is coupled to a smartphone with the objective of performing an Enzyme Linked ImmunoSorbent Assay (ELISA) for drastically reducing the time taken to make this kind of experiments. A typical 96 well-plate to perform ELISAs is put on a platform while irradiated with blue LEDs. Below the plate, an optical fibre bundle transports the collected light point by point to the smartphone's camera where the optical response in the whole plaque can be observed in less than a minute. The further development of this work would permit to diagnose genetic or immune diseases clearly faster than nowadays. Moreover, taking into account that smartphones are kind of affordable, the possibility of readout automation and the replacement of bulky and expensive materials with a hand-held design, may enable the standardization and the worldwide expansion of the technology.

Another application where the optical fibre is used as image transporter is described in [28]. In this case, the peculiarity is that the light is introduced in and detected from a microfluidic device called 'lab-on-chip' which will be described later in Sect. 5. A first smartphone is used to launch light into the micro-optofluidic channel, whereas a second smartphone is in charge of receiving the optical signal through its 5 megapixel-camera. The application is to detect antigen-antibody complexes normally occurring in presence of Plasmodium falciparum (malaria). Very low concentrations from 10 pg/ml to 1 ng/ml are detected in less than 10 min by just detecting the light intensity change in channel blue of the obtained image.

However, probably the most interesting application using fibre-optics to design an universal case that permits clinical diagnostics is that presented at Leibniz University Hannover [29] (see Fig. 4b). The contribution shows a novel refractometer based on coupling light to a 400 micron-diameter fibre through the flash

LED of the mobile phone and then detect and track the variations of light in the back camera. To this purpose, light is introduced in and extracted from the ending fibres using a 45º coupler. In the middle of the device, a silver coating is deposited, generating a surface plasmon resonance and so increasing the sensitivity of the system to surrounding medium refractive index (SRI). The data collection is spectral, based on tracking the wavelength shift of the generated SPR and using an FBG as a little spectrometer by separation of the different color components. A very interesting conclusion is extracted from this work regarding the resolution of the measurements. In order to enhance this magnitude, there is a need from lower fibre diameters and higher camera resolution. A lower diameter will lead to lower losses once the light beam is coupled from the fibre to the grating, whereas a higher resolution will allow to better locate the SPR position. In fact, by doing so, the sensitivity improvement obtained in this contribution is triplicated up to 5.96×10^{-4} RIU/pixel.

Almost the same idea is pursued slightly later by Liu et al. [30]. Figure 5 gives an idea of the process followed to achieve the application. Here, a 50 nm-thick gold coating is deposited to generate a SPR that will be used afterwards to address an IgG-anti-IgG biodetection by monitoring the resonance absorption. The sensitive

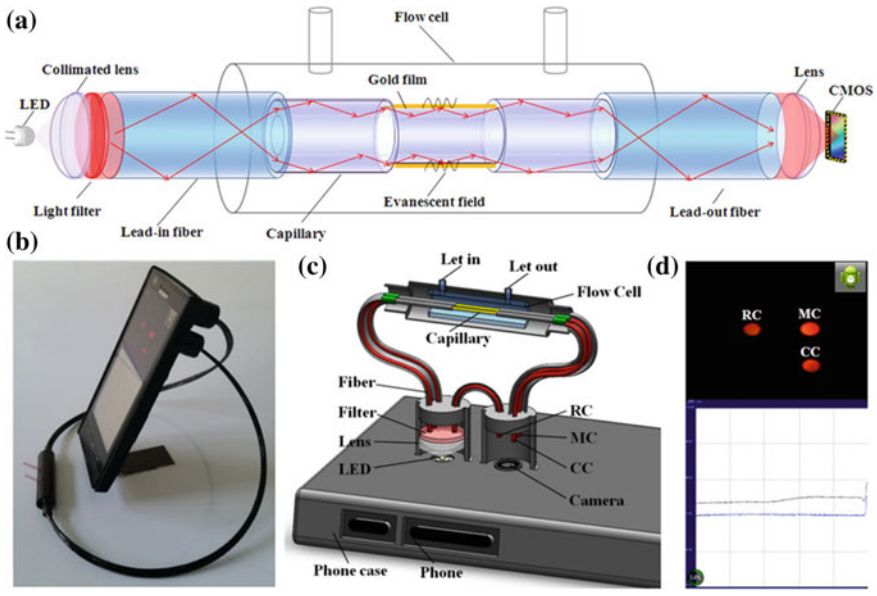

Fig. 5 **a** Schematic of the smart phone-based SPR sensor. **b** Photograph of the SPR sensor installed on an Android-based smartphone. **c** 3D schematic illustration of the internal structure of the opto-mechanical attachment. **d** The camera of the smart phone captures the images of the measurement channel, control channel and reference channel; then, the images are rapidly processed to obtain the relative intensity. The data points are plotted and displayed on the screen. *Source* Reproduced with permission of [30] under a Creative Commons Attribution 4.0 International License (http://creativecommons.org/licenses/by/4.0/)

area is encapsulated in a flow cell where the biological molecules are sequentially introduced. Prior to this, a sensitivity analysis is done, obtaining a sensitivity of 1136 %/RIU and a resolution greater than 7.4×10^{-5} RIU. Then a remarkable comparison of features is done with respect to a commercial device based on the same technology. The contribution concludes that using a smartphone with an adapted fibre-optic sensor based technology is more affordable and less volumetric that a standard SPR-based equipment.

4 Fibre in the Body

As explained in the introduction, the fact of being flexible and low-sized permits the optical fibre to be introduced in the organism, either through its veins and arteries or introducing it into the digestive tube. That is why this section will focus on the use of optical fibres when practising catheters and also when exploring vital organs for our surveillance such as the stomach or the intestine.

A transmission configuration is not affordable in this case, since it is not possible to launch the light on one side and collect it in the other. Therefore, all the configurations shown in this section will be reflective. Moreover, in most of the cases, the optical fibre inside the body is used for imaging, since it is more reliable to observe inside the cavities in real-time. However, there are also occasions in which simple sensors can be introduce to monitor physiological variables. A brief review of interesting applications using fibre-optics is done below.

4.1 Catheters

Designing and manufacturing a catheter is not an easy task. It requires choosing the correct position and introduce a relatively thick tube that remains in that location while the medical treatment takes place, trying to avoid sudden movements that break any blood vessel and make the patient bleed. But once it is done, is one of the most effective methods to introduce thin sensors, releasing drugs, repair blood vessels or reach determined organs to proceed with some therapy. The objective, as occurs in laparoscopy, is to obtain information or actuate inside the organism without the need for practising an open surgery, what would mean a tough post-operative process for the patient. In this sense, fibre-optics has much to do, since its dimensions make it be a very interesting tool to diagnose patients based on this method.

It is typical to associate catheters with introducing a thin tube into the blood vessels or musculature. Here, the optical fibre structure normally used is the fibre Bragg Grating (FBG), since it is quite sensitive to pressure/strain and the gratings can be induced wherever it is desired. A first example can be found in a research work by Shi et al. [31]. The goal is to obtain a solid reconstruction of an aorta

phantom shape based on a catheter where three optical fibres indicate the actual position in every moment. The optical shape sensor consists of 3 optical fibres with a length of 1000 mm and an assembly diameter of 0.6 mm. Each fibre has 8 FBG sensors distributed along it with a pitch of 125 mm. The three optical fibres are assembled together in triangle configuration. This shape sensor is connected with an FBG interrogator and the obtained results are transferred to the control system in real time along the virtual intervention. As a result, a well-defined rendering is obtained by combining the data from the FBG-based position sensor with the intravascular ultrasound imaging (IVUS) data.

A less bulky sensor is that proposed by Nilson et al. [32], where a fibre-optic sensor is introduced into a leg muscle to evaluate its performance as intramuscular pressure sensor (IMP). This time, the sensing equipment is provided by Samba Sensors Inc., company that develops Fabry-Perot interferometers for diverse sensing applications. The patient is supine and adequately positioned so that the leg is aligned with the heart. Then, under anaesthesia, a needle is introduced in the leg with the optical sensor inside and the blood pressure is monitored. The IMP was elevated by venous obstruction using a thigh tourniquet. Then, a saline solution is introduced in order to monitor the pressure increment in the area. Due to the rapid response of the FP-based interferometer, the manuscript concludes that this fibre-optic technique is quite useful for monitoring the IMP and also abnormal IMP increments due to muscular excess of hydration (see Fig. 6).

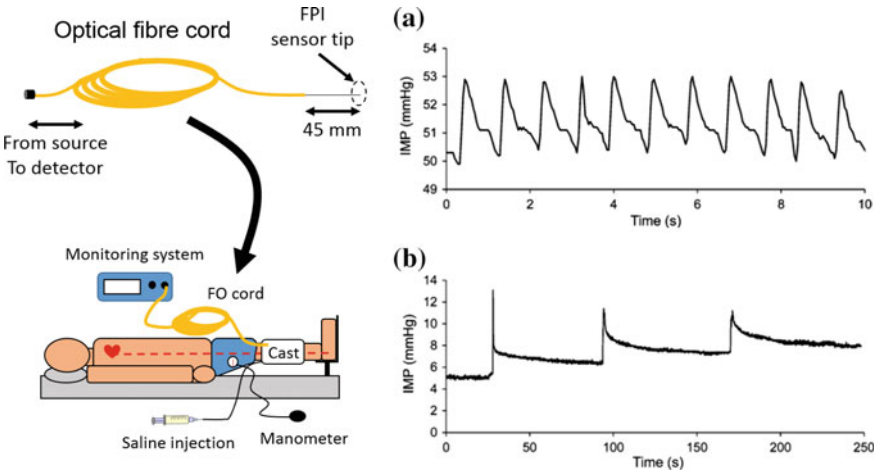

Fig. 6 Schematic of the optical fibre set-up included in the experiment. **a** Pulse-synchronous pressure oscillations recorded with the FPI cavity. **b** IMP response to three injections of 0.1 ml of saline. The IMP remains elevated in each step. Rapid events like an injection transient can be recorded. *Source* **a** and **b** Reproduced with permission of [32]

FPs are also the main characters in a contribution by Poeggel et al. [33], where a monitoring of dual bladder and abdominal pressure measurement throughout the full course of a urodynamic analysis is carried out. The fabrication of EFPI probes is based on two steps: fabrication of the Fabry-Perot cavity, and functionalization to pressure sensing. To this purpose, a single-mode fibre was spliced to a quartz capillary, having an inner/outer diameter of 130/200 μm. Then, a multimode fibre segment (62.5/200 μm core/cladding) was spliced to the capillary leaving a 25 micron length-air camera, in order to generate the FP cavity. The final step is to polish and etch the multimode segment by immersing it in hydrofluoric acid until it thickness is 2.3 μm. An all silica biocompatible probe is thus constructed.

Then, the probes are introduced through catheters in the bladder and in the abdominal cavity while an external switch obtains both data sending them to a spectrometer to be processed. When compared to a medical equipment normally used to these purposes, the rapid response of the EFPI sensor makes the signal be more distinguishable when several events take place, such as in coughing or during the urination.

Finally, one interesting application of fibre-optics on this issue is the Swan-Ganz catheter [34]. This device permits to monitor the introduction of a probe that passes through the heart reaching the pulmonary artery and monitoring the blood pressure in every moment. By doing so, it is possible to early diagnose the risk of suffering from cardiac diseases or further actuations in the area. Among the different channels that this catheter owns, probably the most interesting from a fibre-optics point of view is the Continuous Mixed Venous Oxygen Saturation Monitoring (SvO_2). It consists of an optical module with a LED and a photodetector that plays the role of a remote pulse oximeter (see Fig. 7). This means, monitor how saturated of oxygen is the blood and therefore check that the whole process is well done.

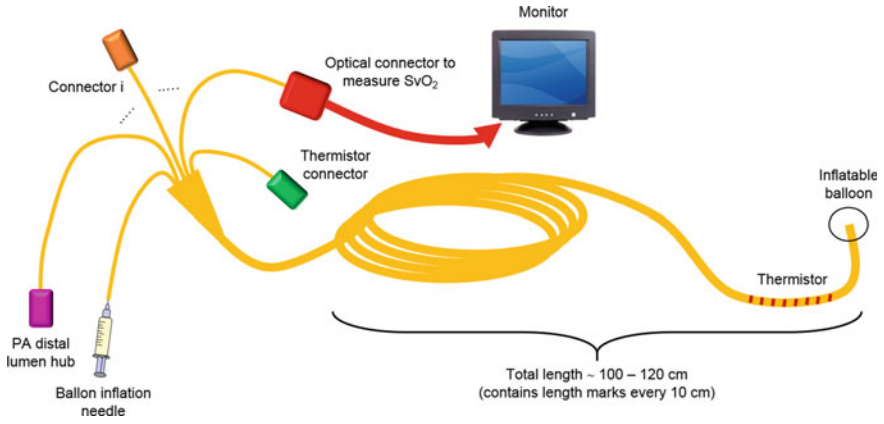

Fig. 7 Schematic of a Swan-Ganz catheter showing the different channels and also the optical module connector, to measure the oxygen saturation in the blood during the process

4.2 Fibrescopes

Fibre-optic-based devices such as fibrescopes and endoscopes allow physicians to view internal organs and tissues of patients by inserting tiny fibre-optic tubes into the body. These devices are increasingly used in medicine for both diagnosis and treatment of various illnesses.

A fibrescope consists of two separate and different fibre-optic bundles running through a protective insertion tube that has viewing optics on the distal end and an eyepiece on the other. The fibrescope is used to examine and inspect small, difficult-to-reach places such as inside machines, locks or the human body [35]. As shown in Fig. 8, a fibre bundle is designed to carry light from a light source to the viewing tip, called the illumination bundle or light guide. The other is designed to carry an image from the viewing tip to the eyepiece and is called the imaging bundle or image guide. One end of each bundle terminates in the distal tip with the purpose of illuminating and capturing an image, while the opposite ends terminate separately, the imaging bundle in the eyepiece and the illumination bundle in the light guide connector. Imaging performance is primarily dependent on the quality of these fibres and lens sets.

Fibrescopes are based on the science of fibre-optic bundles, which consists of using numerous fibre-optic cables. The fibrescope is composed of three systems: the imaging system, the illumination system and the articulation system. The imaging system includes the eyepiece optics, the fibre-optic imaging bundle, and the distal lens set. The illumination system includes a fibre-optic light guide that carries light from a light source to the target area and any distal lenses that may focus or spread the light as it is projected. The articulation system gives the operator the ability to "steer" the fibrescope tip. Fibrescopes are either 4-way articulated with a set of knob controls, 2-way articulated with a lever control, or non-articulated.

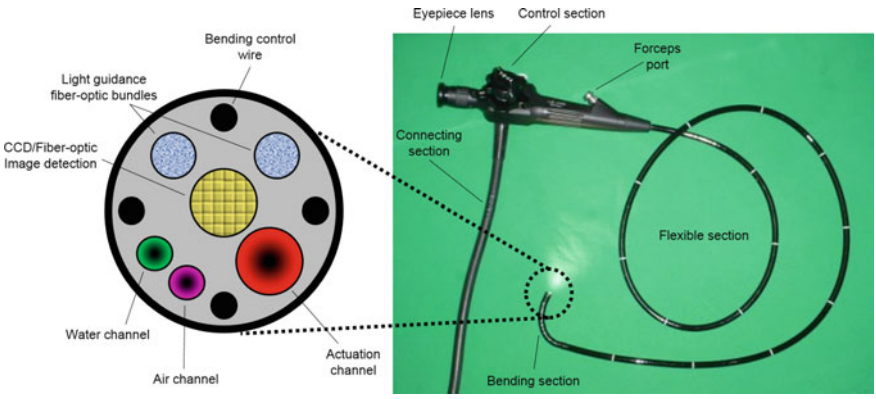

Fig. 8 A fibrescope with its components. Inset: distal end and all the components inside. The image detection channel can be made of fibre-optic bundle or HD CCD camera. *Source* Combination of own images and Creative Commons Licensed images

With the discovery of fibre-optics, in 1854, the physicist John Tyndall proved that light could be conducted through a curved stream of water, demonstrating that light could be guided and bent. Then in 1930, Heinrich Lamm, a German medical student, became the first person to put together a bundle of optical fibres to obtain an image. These discoveries led to the invention of endoscopes and fibrescopes [36]. The incorporation of fibre-optics into flexible endoscopes started with the development of the flexible gastroscope in 1950 by a University of Michigan team lead by Basil Hirschowitz [37].

In the 1960s the endoscope was upgraded with glass fibre, a flexible material that allowed light to transmit, even when bent. While this provided users with the capability of real-time observation, it did not provide them with the ability to take photographs. In 1964 the fibrescope, the first gastro camera, was invented. It was the first time that an endoscope had a camera that could take pictures. This innovation led to more careful observations, and more accurate diagnoses [38].

A new material called glassfibre, developed in the United States in the 1960's, attracted a great deal of attention in various industrial sectors. The developers of endoscopes were among the first ones to turn to glassfibre. Basil Hirschowitz and his associates, for instance, used glassfibre in their endoscopes to take advantage of the glassfibre's characteristic of transmitting light from one end to the other even when it is bent [39]. Their endoscopes allowed direct observation of the interior of a stomach. After all these years, physicians were capable of performing real-time observation of the stomach interior for the first time. The device, however, was not equipped to take a photograph. This feature did not become available until 1964 when the first gastrocamera with a fibrescope was invented.

The gastrocamera with a fibrescope eliminated the weaknesses associated with "eyeless" gastrocameras at once [40]. It was very well received, as an innovative product, since it allowed direct obervations of the stomach tissues for dynamic analyses. The era of gastrocameras came to an end around 1975, when they were replaced by fibrescopes.

Fibrescopes are used in the medical field as a tool to help doctors and surgeons examine problems inside the body of a patient without having to make large incisions. This procedure is called 'endoscopy'. Doctors use this method when they suspect that a determined organ is infected, damaged, or cancerous. Although any medical technique has its potential risks, using a fibrescope for endoscopy has a very low risk of causing infection and blood loss [41].

Regarding propagation inside a fibrescope, it is well-known that light is guided by means of total internal reflection along the optical fibre bundles, what permits a proper confinement into the core of the fibres. However, a small percentage can be lost in the cladding. In the case of the fibrescope, fibres are designed to transmit signals with transmission losses as low as possible, so they can reach the receiver with acceptable quality. In this sense, the type of fibres used in medical applications tend to be multimode fibres with diameters between 50–60 microns. The length of the fibre is usually 1.5 m or 2 m, so the attenuation is a negligible factor [42]. Actually, there is a need for developing fibrescopes with outer diameter lower than 2 mm. Such fibrescopes are used for endoscopy in cardiology, pulmonary

medicine, neurosurgery, otolaryngology and dentistry. There is a distinction between thin fibrescopes, with outer diameters of 1–2 mm and ultrathin fibrescopes, with outer diameters below 1 mm. The thinner fibrescopes could consist of up to 10000 individual fibres of typical diameter 5 μm, whereas the ultrathin devices may consist of 3000–5000 individual fibres of typical diameter 3–4 μm [43].

Nowadays, progress is being made from fibre-optics to video systems, enhancing opportunities for visualization, teaching, and improving the ease of doing endoscopy. It has also been taken advantage of the properties of light to enhance visualization. White light sources have has now been expanded to multiple modalities that can better characterize lesions and, in fact, now potentially provide endoscopic histology [41, 44, 45]. These emerging technologies include narrow-band imaging which enhance the mucosal vascular pattern that is abnormal in neoplastic tissue [46]. White light sources can now be magnified for high-resolution again better characterizing lesions.

5 Fibre at the Lab

This last section will address a brief review on the classical use of fibre-optics to design biosensors. This means, the functionalization of the optical fibre surface in order to obtain an adequate attachment of molecular bioreceptors capable of detecting the biomolecules they are specifically designed for.

Two are the main applications on this issue: analytics and lab-on-fibre. The first one involves actuating on either the surface or the structure of the optical fibre to achieve the application. The second uses the optical cable as a transmitter and receptor of the signals involved in the detection process, normally carried out in microfluidic channels. Both subsections will address these issues, searching for the challenging applications of the future.

5.1 Analytics

Generally, classical biosensors are made of substances that are always specific and selective by nature, such as antibodies, enzymes, DNA chains, proteins or aptamers. Moreover, the substrate can be gently reduced in size, since the biological reaction is going to occur anyway with independence on the substrate size. This leads to a higher detection resolution, less cost of resources and, therefore, less cost for the final device [47]. Besides, if adequately treated, they can be used for in situ and continuous monitoring and sometimes with reversibility in the measurements, something that will give the possibility of being reutilized.

Every biosensor is composed of three well-differentiated parts, as shown in Fig. 9. First of all, the substrate. Regarding optical fibre-based sensors, the substrate will be the material that the fibre is made of, generally silica or plastic. On top of the

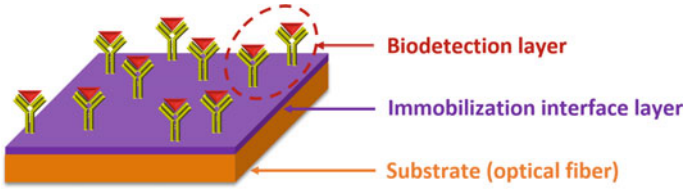

Fig. 9 Schematic showing the different layers of a generic fibre-optic biosensor. Antibody–antigen complexes are depicted, although it is also possible to detect single-stranded DNA chains, enzymatic reaction products, proteins or aptamer—protein entrapments

sensor, the biodetection layer is in charge of detecting the analytes based on the corresponding bioreactions. According to what type of biomolecule is necessary to detect, biosensors can be classified as enzyme/protein-based sensors, immunosensors, cell/tissue sensors, aptasensors or sensors based on DNA chains or even on microorganisms. Finally, to make the biological layer attach the substrate, there is another important layer known as the immobilization interface. This is probably the most important step to address when fabricating a biosensor [48]. The attachment of the bioreceptors to the substrate must be done in such way that the environmental conditions are similar to their natural state or at least in not an aggressive atmosphere. The objective is to maintain the bioreceptors in good conditions so that they can work efficiently and without degrading their structures. Otherwise, this may induce mistakes in the measurements. In this sense, a wide variety of immobilization techniques has been developed during the last times [49, 50]. For instance, those based on direct adsorption, cross-linking with other substances, membrane embedding, entrapment in a polymeric structure, or covalent attachment to the substrate. The goal of these methods is to deposit bioreceptors in an oriented way, so that a homogeneous and more sensitive effective surface is obtained.

As it has been mentioned, in the field of fibre-optic biosensors a wide variety of optical configurations can be set-up, depending on the substrates used and the immobilization methods. For instance, the biodetection can be carried out by using techniques such as absorbance [51], fluorescence [52] or modulating the evanescent field of the optical structure [53], but also other techniques based on interferometers [54] or in the generation of electromagnetic resonances such as surface plasmons [55]. The working principle of the last two techniques is based on tracking the wavelength shift of the resonant bands generated due to a biomolecular attachment. This sort of measurements is more reliable and provides higher robustness.

Moreover, when addressing a biosensing application using wavelength shift tracking, it is important to take into account that biological magnitudes vary in a very small range and this should be distinguishable by appropriately separating the resonances between changes. This is the main issue of the biosensing field, without taking into account that the size of the detector should be as small as possible, in order to detect the anomalies in a reduced quantity. In view of this, this subsection will only analyse those trending solutions based on wavelength shift tracking that have achieved maximum resolution and sensitivity measurements.

One of the trending topics in the field of biosensors is the development of electromagnetic resonances (EMRs). An EMR can be defined as a physical phenomenon obtained by the coupling of light modes from a silica waveguide where they are initially propagating to a thin-film deposited on it. Those modes that have been coupled to the deposited thin-film are modulated by the intrinsic characteristics of the thin-film, intimately related to its frequency dependent permittivity (ε) and, therefore, to its refractive index and absorption. Moreover, this coupling of modes is produced in a restricted wavelength range and it is no longer returned to the original waveguide. So when observing the obtained spectrum in the output signal, a dip is obtained for that wavelength range. At the same time, both the substrate and the thin-film set the adequate conditions to modulate the coupling to the thin-film, which may lead to a wide variety of phenomena and applications [56]. Examples of EMRs are surface plasmon resonances (SPRs), lossy mode resonances (LMRs) and long-range surface exciton-polaritons (LRSEPs), although this subsection will only focus on SPRs and LMRs since their technology is being currently developed. Moreover, the benefits of working with SPRs or LMRs will not be described here, since they have been commented in previous chapters. Instead, a sample of the different achievements made by both technologies will be shown when developing biosensors.

Regarding SPRs, it was the first technology to obtain classical biosensors, since gold biofunctionalization is quite easy to carry out and, therefore, it is possible to attach biomolecules to the substrate [49, 57]. The process normally starts with the deposition of a gold thin-film around the optical fibre surface. This thin-film can be deposited by using sputtering [58] or bifunctional crosslinkers that attach to the fibre on one side and to the gold nanoparticles on the other [59]. The next step is to attach the bioreceptors to the fibre, and this can be done by using different methods, as previously mentioned [49, 50]. Then, the biodetection is addressed, normally using the tracking of the SPR shift in wavelength as a function of the increasing analyte concentration.

In this sense, one of the most cited contributions in recent years is the written by Cao et al. [60], where two types of gold nanoparticles (nanospheres and nanorods) are deposited using silanes onto two optical fibre tips in reflective configuration. When monitoring the spectra, the gold nanosphere (GNS)-based fibre presents the typical SPR centered at 520 nm, whereas the gold nanorod (GNR)-based fibre presents two SPRs, one belonging to the GNR length (~800 nm) and the other to the GNR width (~510 nm). By subjecting both sensors to SRI changes, all SPRs red-shift to higher wavelengths but the results are better as the device is longer. In fact, a maximum sensitivity to SRI of is obtained by using a 2 cm-length fibre-optic segment. The rise in sensitivity may be attributed to a greater level of nanoparticle–incident light interaction at the longer sensing lengths. The GNS-based sensor shows a refractive index sensitivity of ~914 nm/RIU, whereas the length peak of the GNR-based sensor shows a refractive index sensitivity of ~601 nm/RIU. Then, both sensors are activated to attach human IgGs and detect human anti-IgGs, being capable of detecting increasing concentrations of anti-IgGs from 1.6 to 80 nM with time responses of 20 min (see Fig. 10).

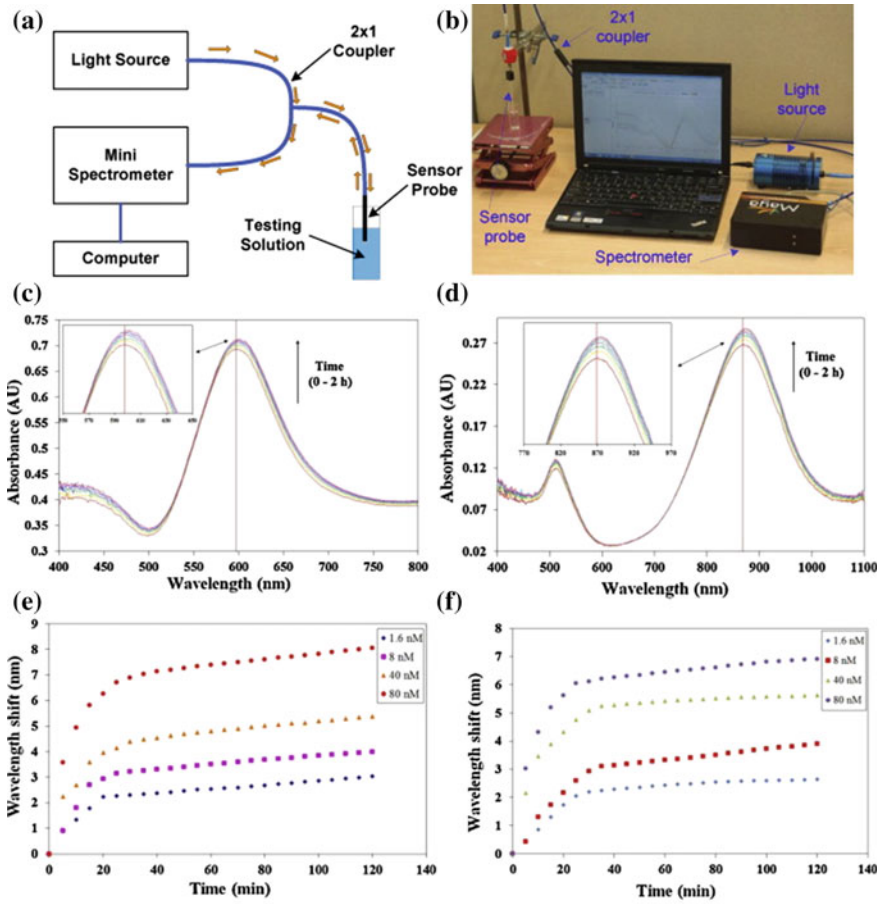

Fig. 10 **a** and **b** Simple reflective set-up to obtain the data along the process. Obtained spectra with the GNSs **c** and GNRs **d** when subjected to increasing concentrations of human anti-IgGs. Stabilization curves for the SPRs obtained with GNSs **e** and GNRs **f** at increasing concentrations of anti-human IgGs, varying from 1.6 to 80 nM. *Source* Reproduced with permission of [60]

SPRs technology has evolved extensively since their first apparition in the 1980s. An interesting review on the recent advances on this SPR-based fibre-optic biosensors has been written by Caucheteur et al. [61], exploring the limits of sensitivity. Several strategies are analysed, such as the geometry-modified fibres, gratting assisted-fibres, the use of special fibres and the deposition of several types of gold nanoparticles combined with the mentioned techniques. Focusing on a SRI ranging from 1.32–1.39, where biological reactions normally take place, one of the maximum sensitivities obtained is 5000 nm/RIU (SPR between 500 and 800 nm) and it is done by depositing a 50 nm-thick silver thin-film on a hetero-core structure [62]. By using unclad/etched fibres in the same SRI medium and depositing around

50 nm-thick gold layers, the sensitivities of the biosensors can reach up to 4000 nm/RIU [63–65].

Now focusing on LMRs, they are an emerging EMR-based technology that can complement the biosensing demands of the society. Unlike SPRs, they show interesting characteristics suitable for addressing the manufacturing of biosensors as shown in [66]. They are briefly summarized below.

The first one is the kind of materials that can be deposited to generate them. As long as the real part of the thin-film permittivity is positive and the absorption coefficient (k) is low (just the opposite to SPRs), many materials except pure metals can induce LMRs. For instance, several contributions using metal oxides [67, 68] or polymer coatings [69] have successfully proved to produce LMRs so far. They are cheaper materials than gold-based colloids or targets and can be deposited by different methods, such as Langmuir-Blodgett, layer-by-layer assembly, sputtering or dip-coating. Moreover, they can be easily functionalized in order to attach biomolecules that lead to further biodetection.

The second aspect is that in the LMRs case, these resonances can be excited by simply launching a white light spectrum, no matter the light polarization. This fact has some important implications. In SPRs, not maintaining the polarization means that the resonance increases its bandwidth and this is not good in terms of measurements resolution. LMRs are propagated in both polarizations, so in spite of being broader initially, it is always possible to polarize and take measurements with both polarizations, obtaining resolutions competitive to SPRs [70, 71]. This is crucial when designing biosensors based on wavelength detection of resonances, since both the sensitivity and the resolution of the measurements leads to an accurate detection that will be translated in a further efficient diagnosis and medical actuation.

The third aspect is that unlike SPRs, LMRs have the capability of generating several resonances in the transmission spectrum as a function of the increasing thin-film thickness. Thus, as the material keeps on depositing, it is possible to tune the LMRs and locate them wherever desired in the optical spectrum by just controlling the amount of deposited material [67]. This facilitates the robustness of the measurements, since by locating several LMRs in the same detection window a more accurate characterization of the sensor can be carried out.

This three important aspects are being taken into account when designing LMR-based biosensors. A first contribution used a polymeric coating as the LMR supporting coating [72]. Then, anti-IgGs were fixed onto the polymeric coating to complete this label-free biosensor. A 5 μg/ml concentration of IgGs is detected. The same authors also developed a biosensor to detect anti-gliadin antibodies (AGAs) using a tapered single-mode optical fibre with 40 μm of waist diameter and 11 mm of waist length and 3 mm of transition region. As it can be observed in Fig. 11, the detection limit of this sensor is 5 μg/ml [73].

Some of the most recent advances in LMR-based biosensors consisted of the utilization of DNA aptamers for thrombin [74] and C-reactive protein (CRP) [75] detection. In these cases, a layer-by-layer assembly polymeric structure with the corresponding aptamers embedded was deposited onto 200 μm core indium tin

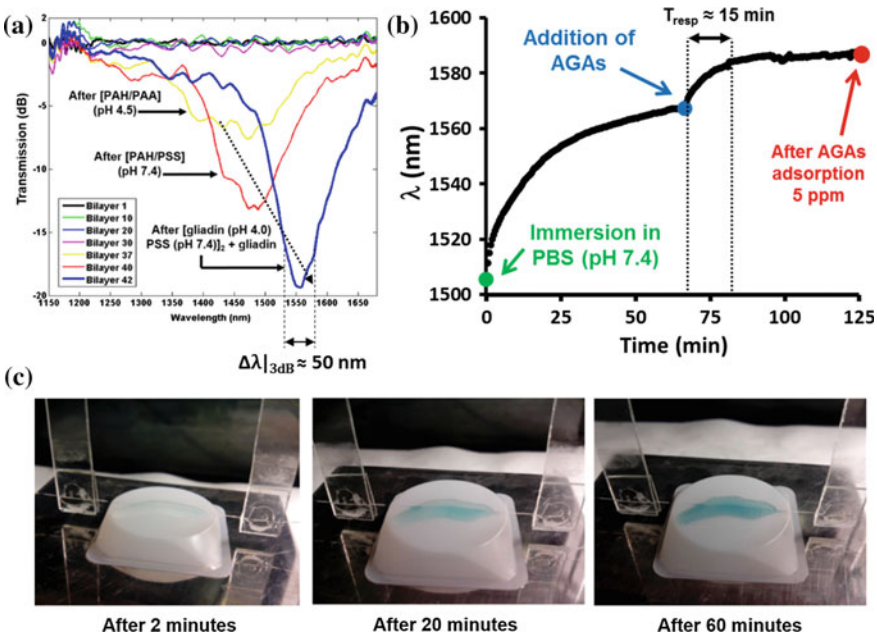

Fig. 11 **a** Generation of the polymeric LMR onto a T-SMF. **b** Detection of AGAs. **c** Verification of the gliadin-AGAs complex formation by means of HRP-TMB colorimetric reaction. *Source* Combination of own images and own contribution [79]

oxide-coated plastic cladding multimode fibres. The obtained results revealed detection ranges down to 2 mg/l for CRP. A last biosensing contribution permits to repeatedly detect 20 mg/l of CRP concentration by depositing aptamers onto a tin oxide-coated 200 core micron-diameter cladding-removed optical fibre [76], where the sensitivities of the tin oxide deposited layer have reached 5200 nm/RIU in a biological SRI range [77]. Recently, the group has been working on obtaining the maximum sensitivity provided by LMRs. It has been reached by depositing an indium tin oxide (ITO) coating onto a D-shaped optical fibre. Around 304,000 nm/RIU can be reached near the silica refractive index with ITO, whereas in the biological SRI range it is possible to rise up to 14,500 nm/RIU [78] thanks to SnO_2.

Finally, a brief review on the development of turn around/dispersion point long-period fibre gratings (TAP/TDP-LPFGs) is done, since it is one of the recent trends in biochemical sensors. The discovery of the TDP in LPFGs has reborn the interest in the development on this kind of structures, since it involves a clear enhancement in their sensitivity. For specific combinations of both the grating period and the working wavelengths, it is possible to increase the sensitivity of certain coupling modes of interest. Moreover, if a higher refractive index thin-film is deposited onto the LPFG, then a higher sensitivity can be obtained [80]. Together

with the adequate resolution of the produced resonances, these characteristics make LPFGs be one of the most studied structures to address fibre-optic biosensors.

The group of Chiavaioli et al. have contributed intensively in the recent times to increase the interest in developing this kind of structures and bring them to biosensing techniques. Among others, they have signed several manuscripts where they first etch the TDP-LPFG in order to obtain an increased sensitivity and then deposit Eudragit® L100 copolymer onto them to finally biofunctionalize this substrate and attach biomolecules covalently. An IgG–anti-IgG detection is presented in [81] (see Fig. 12). Here, authors make a comparison between a non-TDP-LPFG and a TDP-LPFG, in terms of sensitivity. The explanation of the sensitivity enhancement in the case of a TDP-LPFG, according to the authors, is a noticeable increment in the evanescent wave coupling to the cladding modes of the LPFG, which is of much importance when designing biosensors. Moreover, in [82] the lower detection limit achieved is 460 pM.

Other groups to take into account when designing this kind of biosensors are Korposh, James et al. who are focusing in developing TDP-LPFGs near the visible - near infrared (VIS-NIR) region of the spectrum. One of their most recent contributions deposits gold nanoparticles onto silica spheres that are then covalently attached to a TDP-LPFG [83]. The purpose of this procedure is to increase the

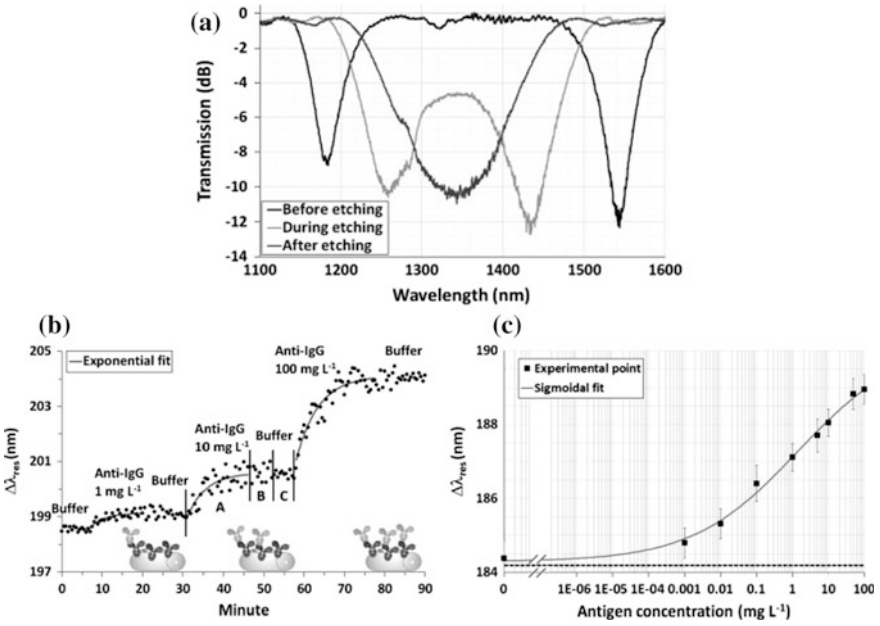

Fig. 12 **a** Etching process of a TDP-LPFG. **b** Sensorgram during three antigen (anti-IgG) injections (1, 10 and 100 mg L^{-1}). Calibration curve of the bioassay performed with TDP LPFG. Each experimental point (squares) is the average of 15 subsequent peak acquisitions. *Source* Reproduced with permission of [82]

functional surface in order to attach more biotin as molecular bioreceptor. Then streptavidin is detected from 19 nM to 2.7 μM concentration. Long period gratings operating at TDP and coated with thin films of high refractive index materials have been reported in [84, 85] for chemical/biochemical sensing applications. Also, the group of Cusano et al. suggest a set of contributions working with LPFGs in a reflective configuration, which make sense in the biosensing field since it reduces the complexity of the set-ups and, therefore, the cost of the devices is reduced [86, 87].

5.2 From 'Lab on Chip' to 'Lab on Fibre'

'Lab on chip' or 'lab on a chip' (LOC), is a multidisciplinary area that feeds from microfluidics, chemistry, physics and biology, but also from surface engineering and materials science. The main goal of this technology is to translate the normal research that can be carried out in a laboratory to a miniaturized device capable of developing different functions, involving the efficient detection of bio-analytes. To this purpose, really small sample volumes are used, reducing costs not only in the materials to fabricate these devices, but also in the reactants used, obtaining a quick response that can be characterized.

In LOC technology two main trending technologies converge: micro-electromechanical systems (MEMS) and micro-optics. The first uses integrated micron-sized components capable of carrying out specific mechanical tasks to achieve a more complex function. The latter also uses microcomponents to process the light inside the chip and obtain the desired signals. The combination of MEMS and micro-optics has led to micro-opto-electromechanical systems or MOEMS, which is the technology currently used to develop LOC-based technologies [88]. Therefore, it seems logical to think that optical fibre or at least some structures based on it have to do with this technology. Actually, most of the LOC contributions that use fibre-optics only take advantage of its propagation properties, since the light is coupled inside/ouside the microchip via the optical cable, either using specific optical fibres or tapering them [89, 90] (see Fig. 13a and b).

However, in view that the LOC technology is expanding so quickly, it may be interesting to explore what can be done in these terms with fibre-optics. This means that if it is possible to deal with optical waveguides in such low sizes, the goal would be try to imitate some techniques to develop paths or geometric structures that can be applied to the optical fibre surface and so create biosensors based on what happens in this new situation. Without being strict with the definition this is the idea behind the 'lab on fibre' (LOF) technology.

One of the basic principles to create a LOF is to have a surface that somehow makes a pattern and induce some changes on this structure and, therefore, on the light propagating throughout it. In this sense, it is obvious that microstructured FBGs [91] (MOFs) or nanocoated LPFGs are direct examples of this technology. But also combinations of several modifications, such as the generation of LPGs within D-shaped optical fibres [92] or the use of nanostructured functional materials

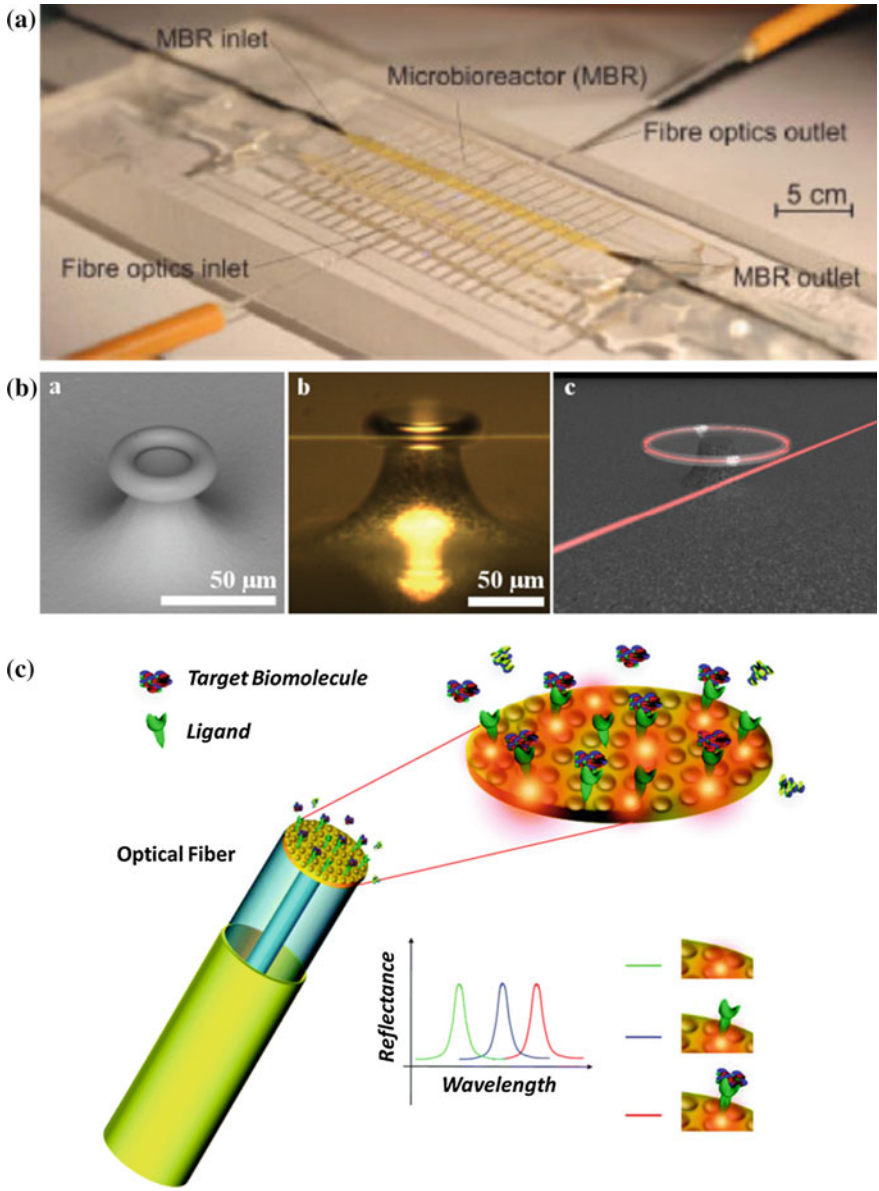

Fig. 13 **a** LOC with two tapered single-mode fibres to launch and collect the light from both sides of the chip. [89] **b** SEM images and rendering 3D images of a microtoroidal ring resonator into which light is coupled by means of a tapered optical fibre [90]. **c** Schematic of a lab-on-fiber-based biosensor by [96]. *Source* **a** Reproduced with permission of [89]. **b** Reproduced with permission of [90] under a Creative Commons Attribution 3.0 International License http://creativecommons.org/licenses/by/3.0. **c** Reproduced with permission of [96]

such as SnO_2 particles [93]. What is more, the use of nanostructured materials onto optical fibres, for instance, SPR (planar or nanoparticle-based thin-films) or LMR-based sensors can also generate patterns that may lead to sensing applications, as shown in the previous subsections.

The recent trends in this LOF technology go further, searching for novel deposition strategies or phenomena to be analysed. Besides fabricating new optical fibres that embed materials that make them be sensitive to the desired phenomena, the idea is to develop micro/nano-technologies directly operating on optical fibre substrates. Several approaches have shown up in the last times, although it is interesting the technique used by Ricciardi et al. [94]. The typical process is to first deposit a thin-film of a dielectric on the tip of the optical fibre, then subject the fibre tip to a focused ion beam (FIB) process where the dielectric surface is patterned and then a final deposition of a metal or a higher refractive index thin-film. The light interaction with the deposited pattern once it faces the fibre-optic tip can be characterized in order to optimize the spectral/intensity response of the sensor. For instance, in [94, 95] several simulations varying the different distances and thicknesses of the proposed structure is shown, combined with a variation in the materials. The goal is to make a study on the behavior of the novel structure presented. Sensitivity values of 125 nm/RIU are obtained when subjected to SRI changes, although there is plenty of room for improving the sensing performance.

6 Conclusions

This chapter has shown a wide variety of technical aspects involving fibre-optics to diagnose diseases. The classical biosensor definition involving biomolecules that detect (bio)chemical substances has been substituted by a more general definition of biosensor, based on the recent advances that biomedical engineering has done and the new needs that patients demand in our current society, influenced by the Information and Communication Technologies.

The term ‘fibre on the body’ stands for those sets of devices that can work outside our body. These lines have reviewed the recent trends in wearables as an example of how the optical fibre can be taken in advantage to detect simple health condition measurements. Also, in developed countries but especially for developing countries, the possibility of owning a device that can measure biomedical variables, process this information and send it to the nearest hospital is crucial. That is why current smartphones are being complemented with innovative solutions that combine the already existing interactivity and communication capabilities with novel technologies that are expected to permit the standardization for an improved healthcare experience. In spite of the current developments, fibre-optics is expected to be present in every step, helping achieve the future advances on portable biosensors based on light processing.

Talking about ‘fibre in the body’ involves introducing the optical fibre in the organism. The fact of being biocompatible or having such low dimensions to be

introduced inside cavities such as the digestive tube or the veins and arteries makes optical fibre be a great ally to detect and even facilitate an actuation inside the human body, both regarding digestive imaging and when practising catheters.

Finally, a subsection called 'fibre at the lab' has made a brief review on the classical definition of biosensors. This means, those which are normally used in clinical analytics once that a blood sample has been extracted from the patient. In spite of the existing different types of biosensors, fibre-optic-based ones are still developing. A special attention has been paid to those trending technologies nowadays: surface plasmon resonances (SPRs), lossy mode resonances (LMRs) and turn dispersion point-long period fibre gratings (TDP-LPFGs). Since biological substances vary in a very narrow concentration range, there is a need for detection phenomena that ensure high sensitivity and a high resolution (low bandwidth) in a reduced refractive index range around that of water (n=1.33). SPRs have been developing for decades and, combined with other technologies, can still improve and keep on being the most utilized technique when developing wavelength detection-based biosensors. However, both LMRs and TDP-LPFGs can compite against SPRs in these topics. LMRs own more versatility and currently can equal or even overcome SPRs in terms of maximum sensitivity and resolution. Also, TDP-LPFGs present much more enhanced capabilities than former LPFGs in these two crucial parameters. It is possible that the future of these three technologies will be promising when obtaining a single device to be used as early diagnostics at the hospital's lab.

Moreover, novel ways to perform biodetection are on the way to be developed. Lab on chip technology only uses optical fibre to launch and collect light, but it will be interesting to check whether this two technologies can be combined in the future. At the moment, a similar technology currently emerging, lab on fibre, is trying to create optical patterns that help obtain biosensing applications in reduced devices such as the tip of an optical fibre, among other possibilities.

All things considered, it is clear that the expansion of optical fibre technologies in the biomedical world is in constant evolution. There is still a long way to go, but it is possible that a novel scenario with fibre-optic-based micro and nanodevices for biosensing and early diagnostics will emerge, due to the need for multidisciplinary skills in order to achieve a better healthcare for the mankind.

Acknowledgments This work has been supported by the Spanish Economy and Competitiveness Ministry through a project with reference FEDER TEC2013-43679-R.

References

1. M.R.N. Monton, E.M. Forsberg, J.D. Brennan, Tailoring sol-gel-derived silica materials for optical biosensing. Chem. Mater. **24**, 796–811 (2012). doi:10.1021/cm202798e
2. X.D. Wang, O.S. Wolfbeis, Fiber-optic chemical sensors and biosensors (2013–2015). Anal. Chem. **88**, 203–227 (2016). doi:10.1021/acs.analchem.5b04298

3. A. Rosenthal, S. Kellnberger, D. Bozhko, A. Chekkoury, M. Omar, D. Razansky et al., Sensitive interferometric detection of ultrasound for minimally invasive clinical imaging applications. Laser Photon. Rev. **8**, 450–457 (2014). doi:10.1002/lpor.201300204
4. X.-D. Wang, O.S. Wolfbeis, Fiber-optic chemical sensors and biosensors (2008–2012). Anal. Chem. **85**, 487–508 (2013). doi:10.1021/ac303159b
5. R. Sroka, K. Weick, M. Sadeghi-Azandaryani, B. Steckmeier, C.-G. Schmedt, Endovenous laser therapy–application studies and latest investigations. J. Biophoton. **3**, 269–276 (2010). doi:10.1002/jbio.200900097
6. G. Cheymol, B. Brichard, J.F. Villard, Fiber optics for metrology in nuclear research reactors —applications to dimensional measurements. IEEE Trans. Nucl. Sci. **58**, 1895–1902 (2011). doi:10.1109/TNS.2011.2160356
7. W. Hou, G. Liu, M. Han, A novel, high-resolution, high-speed fiber-optic temperature sensor for oceanographic applications, in *IEEE 2015 IEEE/OES Eleveth Current, Waves and Turbulence Measurement (CWTM)*, 2015, pp. 1–4. doi:10.1109/CWTM.2015.7098149
8. M. Pospíšilová, G Kuncová, J Trögl, Fiber-optic chemical sensors and fiber-optic bio-sensors. Sensors (Switzerland) **15,** 25208–25259 (2015). doi:10.3390/s151025208
9. C.R. Zamarreño, A.B. Socorro, P. Sanchez, I.R. Matias, F.J. Arregui, *Fiber-Optic Biosensors. Book chapter in Encyclopedia of Optical and Photonic Engineering, Second Edition (Print)–Five Volume Set* (Taylor & Francis, CRC Press, 2015) p. 3858
10. O. Harbater, I. Gannot, Fluorescent probes concentration estimation in vitro and ex vivo as a model for early detection of Alzheimer's disease. J. Biomed. Opt. **19**, 127007 (2014). doi:10.1117/1.JBO.19.12.127007
11. C. Massaroni, P. Saccomandi, E. Schena, Medical smart textiles based on fiber optic technology: an overview. J. Funct. Biomater. **6**, 204–221 (2015). doi:10.3390/jfb6020204
12. J. Rantala, J. Hännikäinen, J. Vanhala, Fiber optic sensors for wearable applications. Pers. Ubiquit. Comput. **15**, 85–96 (2011). doi:10.1007/s00779-010-0303-y
13. L. Piwek, D.A. Ellis, S. Andrews, A. Joinson, *The Rise of Consumer Health Wearables : Promises and Barriers. Do wearables effect behaviour ?* (2016) pp. 1–10. doi:10.1371/journal.pmed.1001953
14. C. Gopalsamy, S. Park, R. Rajamanickam, S. Jayaraman, The wearable motherboard^{TM}: the first generation of adaptive and responsive textile structures (ARTS) for medical applications. Virtual Reality. **4,** 152–168 (1999), http://www.scopus.com/inward/record.url?eid=2-s2.0-42949160345&partnerID=tZOtx3y1
15. S. Martin, Smart Clothing, (n.d.), http://ldt.stanford.edu/~jeepark/jeepark+portfolio/cs147hw8jeepark.html
16. T. Starner, S. Mann, B. Rhodes, J. Levine, J. Healey, D. Kirsch, et al., Augmented reality through wearable computing. Presence: Teleoperators Virtual Environ. **6,** 386–398 (1997), http://www.scopus.com/inward/record.url?eid=2-s2.0-0039329626&partnerID=tZOtx3y1
17. K. Krebber, S. Liehr, J. Witt, Smart technical textiles based on fibre optic sensors. in *OFS 2012 22 International Conference on Optical Fiber Sensors*, Invited Paper. 8421 (2012) 84212A–10. doi:10.1117/12.981342
18. Novel Sensors and Sensing (Series in Sensors): Roger G. Jackson, ISBN 9780750309899 (Taylor & Francis Group, 2004), p. 512
19. K. Krebber, P. Lenke, S. Liehr, J. Witt, M. Schukar, Smart technical textiles with integrated POF sensors, in *The 15 International Symposium on: Smart Structures and Materials and Nondestructive Evaluation and Health Monitoring*, *International Society for Optics and Photonics*, ed. by W. Ecke, K.J. Peters, N.G. Meyendorf (2008), pp. 69330V–69330V–15. doi:10.1117/12.776758
20. M.R. Voet, A. Nancey, J. Vlekken, Geodetect: a new step for the use of fibre Bragg grating technology in soil engineering, in *International Society for Optics and Photonics*, ed. by M. Voet, R. Willsch, W. Ecke, J. Jones, B. Culshaw (Bruges, Belgium—Deadline Past, 2005), pp. 214–217. doi:10.1117/12.623799
21. T. Allsop, R. Revees, D.J. Webb, I. Bennion, T. Earthrowl, B. Jones, et al., Respiratory monitoring using fibre long period grating sensors, in *Progress in Biomedical Optics and*

Imaging—Proceedings of SPIE (2005), pp. 1–6, http://www.scopus.com/inward/record.url?eid=2-s2.0-28844497766&partnerID=tZOtx3y1
22. J. Witt, K. Krebber, Fiber optic heart rate sensor for integration into personal protective equipment. IEEE Sens. J. **6**, 6–8 (2011). doi:10.1109/IWBP.2011.5954836
23. Manhattan Research, Physicians in 2012: The Outlook for On Demand, Mobile, and Social Digital Media: A Physician Module Report (Manhattan Research, New York, 2009)
24. A.S.M. Mosa, I. Yoo, L. Sheets, A systematic review of healthcare applications for smartphones. BMC Med. Inform. Decis. Mak. **12**, 67 (2012). doi:10.1186/1472-6947-12-67
25. G. Ferriero, S. Vercelli, F. Sartorio, S. Muñoz Lasa, E. Ilieva, E. Brigatti, et al., Reliability of a smartphone-based goniometer for knee joint goniometry. Int. J. Rehabil. Res. Internationale Zeitschrift Für Rehabilitationsforschung. Revue Internationale de Recherches de Réadaptation. **36**, 146–51 (2013). doi:10.1097/MRR.0b013e32835b8269
26. G. Ferriero, S. Di Carlo, F. Sartorio, S. Vercelli, The increasing importance of photographic-based apps for goniometry. Telemed. E-Health. **21**, 1042–1043 (2015). doi:10.1089/tmj.2015.0030
27. B. Berg, B. Cortazar, D. Tseng, H. Ozkan, S. Feng, Q. Wei et al., Cellphone-based hand-held microplate reader for point-of-care testing of enzyme-linked immunosorbent assays. ACS Nano **9**, 7857–7866 (2015). doi:10.1021/acsnano.5b03203
28. C.C. Stemple, S.V. Angus, T.S. Park, J.-Y. Yoon, Smartphone-based optofluidic lab-on-a-chip for detecting pathogens from blood. J. Lab. Autom. **19**, 35–41 (2014). doi:10.1177/2211068213498241
29. K. Bremer, B. Roth, Fibre optic surface plasmon resonance sensor system designed for smartphones. Opt. Express **23**, 17179–17184 (2015). doi:10.1364/OE.23.017179
30. Y. Liu, Q. Liu, S. Chen, F. Cheng, H. Wang, W. Peng, surface plasmon resonance biosensor based on smart phone platforms. Sci. Rep. **5,** 12864 (2015). doi:10.1038/srep12864
31. C. Shi, S. Giannarou, S. Lee, G. Yang, Simultaneous catheter and environment modeling for trans-catheter aortic valve implantation, in *IEEE/RSJ International Conference on Intelligent Robots and Systems* (2014), pp. 2024–2029. doi:10.1109/IROS.2014.6942832
32. A. Nilsson, Q. Zhang, J. Styf, Evaluation of a fiber-optic technique for recording intramuscular pressure in the human leg. J. Clin. Monit. Comput. (2015). doi:10.1007/s10877-015-9750-3
33. S. Poeggel, D. Tosi, F. Fusco, J. Ippolito, L. Lupoli, V. Mirone et al., Fiber-optic EFPI pressure sensors for In Vivo urodynamic analysis. IEEE Sens. J. **14**, 2335–2340 (2014). doi:10.1109/JSEN.2014.2310392
34. E. LifeSciences, *Advanced Hemodynamic Monitoring with the Edwards Swan-Ganz Catheter*, vol. 2 (Edwards LifeSciences, 2009)
35. J. Kovaleva, F.T.M. Peters, H.C. van der Mei, J.E. Degener, Transmission of infection by flexible gastrointestinal endoscopy and bronchoscopy. Clin. Microbiol. Rev. **26**, 231–254 (2013). doi:10.1128/CMR.00085-12
36. W.K. Johnston, The birth of fiberoptics from "light guiding". J. Endourology / Endourological Soc. **18**, 425–426 (2004). doi:10.1089/0892779041271445
37. J.M. Edmonson, History of the instruments for gastrointestinal endoscopy. Gastrointest. Endosc. **37** (1991), http://www.scopus.com/inward/record.url?eid=2-s2.0-0025899993&partnerID=tZOtx3y1
38. Olympus, vol. 3 Birth of Fiberscopes (n.d.), http://www.olympus-global.com/en/corc/history/story/endo/fiber/
39. P. Urquhart, R. Dacosta, N. Marcon, Endoscopic mucosal imaging of gastrointestinal neoplasia in 2013 topical collection on GI oncology. Curr. Gastroenterol. Rep. **15** (2013). doi:10.1007/s11894-013-0330-8
40. H. Niwa, Invention of gastrocamera and it's improvements. Gastroenterol. Endosc. **49,** 1615–1638 (2007), http://www.scopus.com/inward/record.url?eid=2-s2.0-34548011061&partnerID=tZOtx3y1
41. B. Krans, Endoscopy. Healthline **6** (2015), http://www.healthline.com/health/endoscopy#Overview1

42. M. Abad, J.L. Arce, Study of colonoscopic laser surgery applied to tumoral tissue resection, Santander, 2014
43. A. Katzir, *Lasers and Optical Fibers in Medicine* ISBN: 9780124019409 (1993), p. 317
44. J. Sauk, E. Coron, L. Kava, M. Suter, M. Gora, K. Gallagher et al., Interobserver agreement for the detection of barrett's esophagus with optical frequency domain imaging. Dig. Dis. Sci. **58**, 2261–2265 (2013). doi:10.1007/s10620-013-2625-x
45. D.F. Boerwinkel, A.F. Swager, W.L. Curvers, J.J.G.H.M. Bergman, The Clinical Consequences of Advanced Imaging Techniques in Barrett's Esophagus. Gastroenterology. **146**(3), 622–629.e4 (2014). ISSN 0016-5085, http://dx.doi.org/10.1053/j.gastro.2014.01.007
46. R. Singh, S.Y. Lee, N. Vijay, P. Sharma, N. Uedo, Update on narrow band imaging in disorders of the upper gastrointestinal tract. Dig Endosc. **26**, 144–153 (2014). doi:10.1111/den.12207
47. G.L. Cote, R.M. Lec, M.V. Pishko, Emerging biomedical sensing technologies and their applications. IEEE Sens. J. **3**(3), 251–266 (2003). doi:10.1109/JSEN.2003.814656
48. R. Taylor, J.S. Schultz, *Handbook of Chemical and Biological Sensors*, ISBN: 0750303239, IOP Publishing Ltd 1996. Reprinted in 2003, p. 607
49. E. Mauriz, M.C. García-Fernández, L.M. Lechuga, Towards the design of universal immunosurfaces for SPR-based assays: a review. TrAC Trends Anal. Chem. (2016). doi:10.1016/j.trac.2016.02.006
50. M. Soler, M.C. Estevez, M. Alvarez, M.A. Otte, B. Sepulveda, L.M. Lechuga, Direct detection of protein biomarkers in human fluids using site-specific antibody immobilization strategies. Sensors (Basel, Switzerland). **14,** 2239–2258 (2014). doi:10.3390/s140202239
51. J.M. Corres, I.R. Matias, J. Bravo, F.J. Arregui, Tapered optical fiber biosensor for the detection of anti-gliadin antibodies. Sens. Actuators B: Chem. **135**, 166–171 (2008). doi:10.1016/j.snb.2008.08.008
52. D. Futra, L. Heng, A. Ahmad, S. Surif, T. Ling, An optical biosensor from green fluorescent escherichia coli for the evaluation of single and combined heavy metal toxicities. Sensors **15**, 12668–12681 (2015). doi:10.3390/s150612668
53. X. Lv, J. Mo, L. Xu, Z. Jia, Biochemical sensing application based on optical fiber evanescent wave sensor, Proc. SPIE 9620, 2015 International Conference on Optical Instruments and Technology: Optical Sensors and Applications, 96200T (10 August 2015); doi:10.1117/12.2191430
54. Y. Huang, Z. Tian, L.-P. Sun, D. Sun, J. Li, Y. Ran et al., High-sensitivity DNA biosensor based on optical fiber taper interferometer coated with conjugated polymer tentacle. Opt. Express **23**, 26962–26968 (2015). doi:10.1364/OE.23.026962
55. N. Cennamo, M. Pesavento, L. Lunelli, L. Vanzetti, C. Pederzolli, L. Zeni et al., An easy way to realize SPR aptasensor: a multimode plastic optical fiber platform for cancer biomarkers detection. Talanta **140**, 88–95 (2015). doi:10.1016/j.talanta.2015.03.025
56. K.V. Sreekanth, S. Zeng, J. Shang, K.-T. Yong, T. Yu, Excitation of surface electromagnetic waves in a graphene-based Bragg grating. Sci. Rep. **2**, 737 (2012). doi:10.1038/srep00737
57. M.C. Estevez, M.A. Otte, B. Sepulveda, L.M. Lechuga, Trends and challenges of refractometric nanoplasmonic biosensors: a review. Anal. Chim. Acta **806**, 55–73 (2014). doi:10.1016/j.aca.2013.10.048
58. H.-Y. Lin, W.-H. Tsai, Y.-C. Tsao, B.-C. Sheu, Side-polished multimode fiber biosensor based on surface plasmon resonance with halogen light. Appl. Opt. **46**, 800–806 (2007). doi:10.1364/AO.46.000800
59. Y. Jin, K.H. Wong, A.M. Granville, Developing localized surface plasmon resonance biosensor chips and fiber optics via direct surface modification of PMMA optical waveguides. Colloids Surf. A **492**, 100–109 (2016). doi:10.1016/j.colsurfa.2015.11.025
60. J. Cao, M.H. Tu, T. Sun, K.T.V. Grattan, Wavelength-based localized surface plasmon resonance optical fiber biosensor. Sens. Actuators, B: Chem. **181**, 611–619 (2013). doi:10.1016/j.snb.2013.02.052

61. C. Caucheteur, T. Guo, J. Albert, Review of plasmonic fiber optic biochemical sensors: improving the limit of detection. Anal. Bioanal. Chem. 3883–3897 (2015). doi:10.1007/s00216-014-8411-6
62. M. Iga, A. Seki, K. Watanabe, Hetero-core structured fiber optic surface plasmon resonance sensor with silver film. Sens. Actuators B: Chem. **101**(3), 368–372 (2004). http://dx.doi.org/10.1016/j.snb.2004.04.007
63. M. Kanso, S. Cuenot, G. Louarn, sensitivity of optical fiber sensor based on surface plasmon resonance: modeling and experiments. Plasmonics **3**, 49–57 (2008). doi:10.1007/s11468-008-9055-1
64. Y.S. Dwivedi, A.K. Sharma, B.D. Gupta, influence of design parameters on the performance of a surface plasmon sensor based fiber optic sensor. Plasmonics **3**, 79–86 (2008). doi:10.1007/s11468-008-9057-z
65. J. Pollet, F. Delport, M. Wevers, J. Lammertyn, Aptamer-based surface plasmon resonance probe, in *2008 IEEE Sensors*,(IEEE, 2008), pp. 1187–1190. doi:10.1109/ICSENS.2008.4716654
66. A.B. Socorro, *Study and Design of Thin-Film Coated Optical Biosensong Devices Based on Wavelength Detection of Resonances* (Ph.D. dissertation at Public University of Navarre, 2015), http://academica-e.unavarra.es/handle/2454/16736
67. I. Del Villar, M. Hernaez, C.R. Zamarreño, P. Sánchez, C. Fernández-Valdivielso, F. J. Arregui et al., Design rules for lossy mode resonance based sensors. Appl. Opt. **51**, 4298 (2012). doi:10.1364/AO.51.004298
68. I. Del Villar, C.R. Zamarreño, P. Sanchez, M. Hernaez, C.F. Valdivielso, F.J. Arregui et al., Generation of lossy mode resonances by deposition of high-refractive-index coatings on uncladded multimode optical fibers. J. Opt. **12**, 095503 (2010). doi:10.1088/2040-8978/12/9/095503
69. C.R. Zamarreño, M. Hernáez, I. Del Villar, I.R. Matías, F.J. Arregui, Optical fiber pH sensor based on lossy-mode resonances by means of thin polymeric coatings. Sens. Actuators, B: Chem. **155**, 290–297 (2011). doi:10.1016/j.snb.2010.12.037
70. C. Ruiz Zamarreño, P. Zubiate, M. Sagües, I.R. Matias, F.J. Arregui, Experimental demonstration of lossy mode resonance generation for transverse-magnetic and transverse-electric polarizations. Opt. Lett. **38**, 2481–2483 (2013). doi:10.1364/OL.38.002481
71. I. Del Villar, C.R. Zamarreno, M. Hernaez, F.J. Arregui, I.R. Matias, Lossy mode resonance generation with indium-tin-oxide-coated optical fibers for sensing applications. J. Lightwave Technol. **28**, 111–117 (2010). doi:10.1109/JLT.2009.2036580
72. A.B. Socorro, J.M. Corres, I. Del Villar, F.J. Arregui, I.R. Matias, Fiber-optic biosensor based on lossy mode resonances. Sens. Actuators B: Chem. **174**, 263–269 (2012). doi:10.1016/j.snb.2012.07.039
73. A.B. Socorro, I. Del Villar, J.M. Corres, F.J. Arregui, I.R. Matias, Spectral width reduction in lossy mode resonance-based sensors by means of tapered optical fibre structures. Sens. Actuators B: Chem. **200**, 53–60 (2014). doi:10.1016/j.snb.2014.04.017
74. L. Razquin, C.R. Zamarreno, F.J. Munoz, I.R. Matias, F.J. Arregui, Thrombin detection by means of an aptamer based sensitive coating fabricated onto LMR-based optical fiber refractometer, in *2012 IEEE Sensors* (IEEE, 2012), pp. 1–4. doi:10.1109/ICSENS.2012.6411186
75. C.R. Zamarreno, I. Ardaiz, L. Ruete, F.J. Munoz, I.R. Matias, F.J. Arregui, C-reactive protein aptasensor for early sepsis diagnosis by means of an optical fiber device, in *2013 IEEE Sensors* (IEEE, 2013), pp. 1–4. doi:10.1109/ICSENS.2013.6688222
76. P. Sanchez, P. Zubiate, F.J. Munoz, F.J. Arregui, I.R. Matias, C.R. Zamarreño, Lossy mode resonance-based aptasensor for CRP detection, 26th Anniversary World Congress on Biosensors. (Gothenburg, Sweden, 2016)
77. P. Sanchez, C.R. Zamarreño, M. Hernaez, I.R. Matias, F.J. Arregui, Optical fiber refractometers based on lossy mode resonances by means of SnO_2 sputtered coatings. Sens. Actuators B: Chem. **202**, 154–159 (2014). doi:10.1016/j.snb.2014.05.065

78. F.J. Arregui, I. Del Villar, C.R. Zamarreño, P. Zubiate, I.R. Matias, Giant sensitivity of optical fiber sensors by means of lossy mode resonance. Sens. Actuators B: Chem. (2016). doi:10.1016/j.snb.2016.04.015
79. A.B. Socorro, J.M. Corres, I. Del Villar, F.J. Arregui, I.R. Matias, Immunoglobulin G biosensor based on lossy mode resonances generated on coated tapered optical fiber, Proc. Trends in Nanotechnology (TNT) 2012 Conference, (Phantoms Foundation, Madrid (Spain), 2012)
80. I. Del Villar, Ultrahigh-sensitivity sensors based on thin-film coated long period gratings with reduced diameter, in transition mode and near the dispersion turning point. Opt. Express **23**, 8389 (2015). doi:10.1364/OE.23.008389
81. F. Chiavaioli, P. Biswas, C. Trono, A. Giannetti, S. Tombelli, S. Bandyopadhyay, et al., IgG/anti-IgG immunoassay based on a turn-around point long period grating, in *SPIE BiOS, International Society for Optics and Photonics*, ed. by T. Vo-Dinh, A. Mahadevan-Jansen, W. S. Grundfest (2014), p. 89350 V. doi:10.1117/12.2039782
82. F. Chiavaioli, P. Biswas, C. Trono, S. Bandyopadhyay, A. Giannetti, S. Tombelli et al., Towards sensitive label-free immunosensing by means of turn-around point long period fiber gratings. Biosens. Bioelectron. **60**, 305–310 (2014). doi:10.1016/j.bios.2014.04.042
83. L. Marques, F.U. Hernandez, S.W. James, S.P. Morgan, M. Clark, R.P. Tatam et al., Highly sensitive optical fibre long period grating biosensor anchored with silica core gold shell nanoparticles. Biosens. Bioelectron. **75**, 222–231 (2016). doi:10.1016/j.bios.2015.08.046
84. S.W. James, S. Korposh, S.W. Lee, R.P. Tatam. A long period grating-based chemical sensor insensitive to the influence of interfering parameters. Opt. Express **22**(7), 8012–23 (2014). doi:10.1364/OE.22.008012. PubMed PMID: 24718176
85. S. Korposh, R. Selyanchyn, W. Yasukochi, S.-W. Lee, S.W. James, R.P. Tatam, Optical fibre long period grating with a nanoporous coating formed from silica nanoparticles for ammonia sensing in water. Mater. Chem. Phys. **133**, 784–792 (2012). doi:10.1016/j.matchemphys.2012.01.094
86. G. Quero, S. Zuppolini, M. Consales, L. Diodato, P. Vaiano, A. Venturelli et al., Long period fiber grating working in reflection mode as valuable biosensing platform for the detection of drug resistant bacteria. Sens. Actuators B: Chem. **230**, 510–520 (2016). doi:10.1016/j.snb.2016.02.086
87. G. Quero, M. Consales, R. Severino, P. Vaiano, A. Boniello, A. Sandomenico et al., Long period fiber grating nano-optrode for cancer biomarker detection. Biosens. Bioelectron. **80**, 590–600 (2016). doi:10.1016/j.bios.2016.02.021
88. E. Timurdogan, B.E. Alaca, I.H. Kavakli, H. Urey, MEMS biosensor for detection of Hepatitis A and C viruses in serum. Biosens. Bioelectron. **28**, 189–194 (2011). doi:10.1016/j.bios.2011.07.014
89. S. Demming, J. Vila-Planas, S. Aliasghar Zadeh, A. Edlich, E. Franco-Lara, R. Radespiel, et al., Poly(dimethylsiloxane) photonic microbioreactors based on segmented waveguides for local absorbance measurement. Electrophoresis. **32,** 431–439 (2011). doi:10.1002/elps.201000482
90. H.K. Hunt, C. Soteropulos, A.M. Armani, Bioconjugation strategies for microtoroidal optical resonators. Sensors (Switzerland). **10**, 9317–9336 (2010). doi:10.3390/s101009317
91. A. Cusano, D. Paladino, A. Iadicicco, Microstructured fiber bragg gratings. J. Lightwave Technol. **27**, 1663–1697 (2009). doi:10.1109/JLT.2009.2021535
92. G. Quero, A. Crescitelli, D. Paladino, M. Consales, A. Buosciolo, M. Giordano et al., Evanescent wave long-period fiber grating within D-shaped optical fibers for high sensitivity refractive index detection. Sens. Actuators B: Chem. **152**, 196–205 (2011). doi:10.1016/j.snb.2010.12.007
93. A. Buosciolo, M. Consales, M. Pisco, A. Cusano, M. Giordano, Fiber-optic near-field chemical sensors based on wavelength scale tin dioxide particle layers. J. Lightwave Technol. **26**, 3468–3475 (2008). doi:10.1109/JLT.2008.927792

94. A. Ricciardi, M. Consales, G. Quero, A. Crescitelli, E. Esposito, A. Cusano, Lab-on-fiber devices as an all around platform for sensing. Opt. Fiber Technol. **19**, 772–784 (2013). doi:10.1016/j.yofte.2013.07.010
95. A. Ricciardi, M. Consales, G. Quero, A. Crescitelli, E. Esposito, A. Cusano, Versatile optical fiber nanoprobes: from plasmonic biosensors to polarization-sensitive devices. ACS Photon. **1**, 69–78 (2014). doi:10.1021/ph400075r
96. M. Consales, A. Ricciardi, A. Crescitelli, E. Esposito, A. Cutolo, A. Cusano, Lab-on-fiber technology: toward multifunctional optical nanoprobes. ACS Nano **6**, 3163–3170 (2012). doi:10.1021/nn204953e

Optical Fibres for Radiation Dosimetry

S. O'Keeffe

Abstract The use of ionising radiation in a wide range of areas, from industrial processes to medical applications, has become increasingly significant in recent years. Radiation dosimetry, the measurement of absorbed dose delivered by ionising radiation, is fundamental to these radiation processes, ensuring tight control on radiation processes and the safety of personnel. As such it is the focus of much recent research to develop novel dosimeters and to improve dosimetry systems, be it increasing the sensitivity, providing real-time measurements or significantly reducing the costs. The inherent properties of optical fibres lend themselves to be used with great success in monitoring ionizing radiation. Optical fibres provide the means whereby real-time in situ monitoring of radiation doses can be realised, and offer numerous advantages over conventional methods, such as electrochemical and semiconductor sensors. Of significant advantage is the optical fiber's immunity to electromagnetic and chemical interferences and their ability to monitor remotely, whereby the sensor can be placed several hundred metres from the control electronics. This means that they can be employed in harsh environments, such as in high-radiation-level areas in the vicinity of a nuclear reactor or gamma sterilisation facility. The small dimensions and light weight of optical fibres also provide for many opportunities for such sensors in personal dosimetry and medical applications. This chapter will discuss some of the key optical fibre based sensing techniques used in radiation dosimetry and outline their implementation in the different application areas of ionising radiation.

1 Introduction

The most significant feature of an optical fibre dosimeter is that the dose information is transmitted using optical signals as opposed to electrical signals. Consequently, optical fibres are immune to electrical and electromagnetic interferences,

S. O'Keeffe (✉)
University of Limerick, Limerick, Ireland
e-mail: sinead.okeeffe@ul.ie

© Springer International Publishing Switzerland 2017

I.R. Matias et al. (eds.), *Fiber Optic Sensors*, Smart Sensors,
Measurement and Instrumentation 21, DOI 10.1007/978-3-319-42625-9_7

which can be a problem for many electronic dosimeters. Electric dosimetry systems often require a high voltage power supply and must have good electrical insulation. This insulation is known to degrade over time due to a number of radiation related phenomena, such as radiation induced electrical conductivity. This degradation can seriously affect the stability of the system. Another phenomenon, radiation induced electromotive force, generates electric noise that can interfere with the signal transmitting the dose information [1]. The ability to remotely monitor radiation is also an advantage of optical fibres. The sensor can be placed several hundred metres from the control electronics, which means that they can be employed in harsh environments, such as in high-radiation-level areas in the vicinity of a nuclear reactor. Optical fibre sensors can also be multiplexed so that a single controller can monitor a number of sensors. The recent development of radiation resistant fibres has also meant that fibre optics can be used within systems whereby they are used solely to transmit the signal [2].

2 General Properties of Optical Fibre Dosimeters

While selecting an optical fibre for monitoring radiation, a number of key parameters should be considered [2]:

Material sensitivity: The ability for radiation to interact with the material is the primary characteristic for any radiation dosimeter. This interaction varies greatly among the different types of radiation dosimeters. The materials utilised in dosimetry must have a high sensitivity to ionising radiation within the dose ranges required for the specific application.

Post-irradiation fading: The material used as a radiation dosimeter must also show minimum post-irradiation fading. This post-irradiation fading is due to the repair of the physical damage caused to the material during irradiation. Information regarding the irradiation dose is lost if the dosimeter material begins to recover immediately after irradiation. Post-irradiation stability can be achieved through a range of treatments after irradiation, e.g. heat [3]. Alternatively, dopants are sometimes added to the material to reduce the post-irradiated fading. In optical dosimetry systems, the interrogated wavelength is chosen such to minimise the effect of fading on the obtained results. Additionally, it has been shown that in some cases recovery is consistent after every irradiation, thus calibration curves can be used to compensate for any post-irradiation fading [4]. If real-time measurements are available, fading is less of an issue and can in fact contribute towards an extension to the lifetime of the sensor. However, in all cases, it is essential that the post-irradiation effects on the sensor is appropriately considered.

Time dependence: Many materials also exhibit a time dependence of specific absorbance. This means that it is often required to wait up to 3 h before obtaining an accurate reading [5]. For industrial applications it is usually important that the dosimeter is fast to measure. The need for real-time measurements is becoming more important within space and nuclear environments, which is leading towards

the increasing development of in situ dosimeters. These online dosimeters, by providing real-time information, also provide a greater knowledge of the effects of the gamma radiation over time.

Stability and repeatability: Stability and repeatability of the Dosimeter, as with any sensor, are also important. In order to ensure that this can be achieved the dosimeter must be immune to a number of environmental conditions. The effect of humidity and temperature on the dosimeter must be investigated and accounted for. The influence of dose rate on the dosimeter material should also be considered. Immunity to other disturbances, such as those found in electromagnetically harsh environments, is also advantageous for gamma dosimeters as they are often employed in such conditions [1].

Ease of use: For industrial applications it is important that the dosimeters are easy to use. For this to be achieved, the system must be easily installed in the area of application without the risk of affecting the measurements. Maintenance should also be minimum. The readout from the dosimeter should be clear and easy to understand. It is also important that the system is low in cost.

3 Optical Fibre Dosimeter Types

3.1 Sensor Classification

As with other optical fibre based sensors, optical fibre dosimeters can be characterised under two main types; intrinsic sensors, where the interaction occurs within the optical fibre itself and extrinsic sensors, where the optical fibres are used to guide the light to and from the region where the light interacts with the measurand.

It is possible to further classify optical fibre sensors according to the type of modulation to be used [6]:

- Amplitude or intensity sensors detect the amount of light that is a function of the influencing environment. Their ability to use either incoherent or coherent light sources together with simple optical components makes for a low-cost system.
- Phase or interferometric sensors detect a modulation in phase caused by the measurand. This type of source requires coherent light sources making them a relatively costly system. However, they can provide a very high level of sensitivity.
- Polarimetric sensors detect a modulation in the polarisation of the light due to the variable to be measured.
- Spectroscopic sensors detect a modulation in the optical spectrum due to the influencing variable.

Figure 1 outlines how this standard classification system can be applied to optical fibre sensors for radiation monitoring, and some of the techniques most commonly employed are then discussed in more detail.

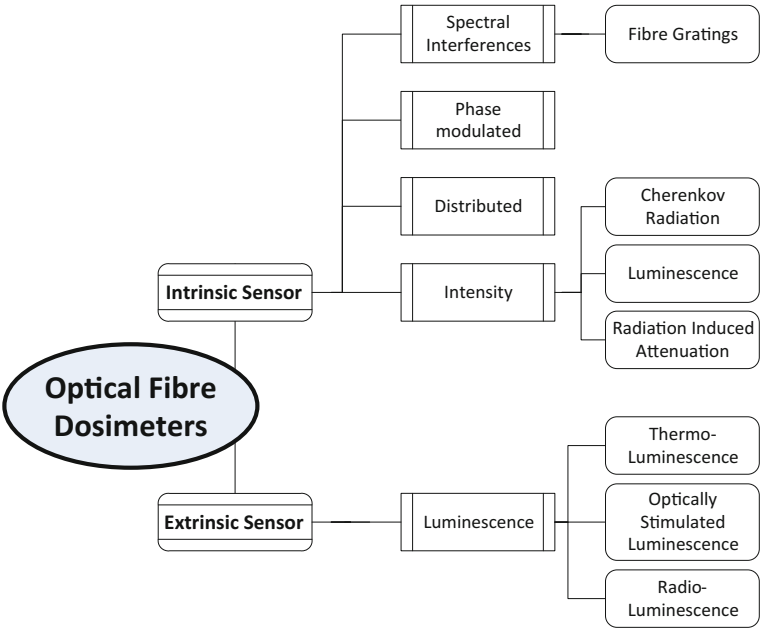

Fig. 1 Classification of optical fibre dosimeters

3.2 Luminescence-Based Sensors

3.2.1 Radio-luminescence (RL)

One of the oldest techniques used in detecting ionising radiation is by scintillation light produced in certain materials, and it remains one of the most popular methods in gamma radiation detection [7]. Scintillation detectors are based on the phenomenon that the material used is capable of converting ionising radiation into detectable light. A photodiode or photomultiplier tube subsequently converts it into an electric signal.

Scintillators can be sub-divided into two broad groups, namely inorganic and organic scintillators. Inorganic scintillators are generally in crystal form and made of Alkali Halides (e.g. Cesium Iodide (CsI), Sodium Iodide (NaI)) or Oxides (e.g. Bismuth Germanate (BGO)). Scintillation is due to the crystalline structures that create the energy bands between which transitions of electrons take place. While some crystals scintillate intrinsically, others need activators to allow for scintillation in the visible region. Thallium (Ti) is an example of an activator and is used in one of the most common inorganic scintillator, NaI(Ti). Organic scintillators are composed of aromatic hydrocarbons and can be divided further into plastic scintillators and liquid scintillators. Organic scintillators scintillate on a molecular level, which means that each scintillator molecule can act as a scintillator centre [8].

3.2.2 Thermo-luminescence (TL)

Thermoluminescence (TL) is the emission of light from a solid due to heating, after it has previously been excited by radiation. When exposed to radiation, the TL material absorbs energy, which it then stores until it is heated. The intensity of the light emitted, as a function of temperature, is the thermoluminescence glow curve [9]. Early work in the area of optical fibre thermoluminescence dosimeter (TLDs) looked at the use of thermo-luminescent phosphors at the tip of an optical fibre and laser heating technique. A number of different phosphors, $CaSO_4$:Mn, CaF_2:Tm, CaF_2:Dy and $CaSO_4$:Dy, have been mounted to the end of silica fibres and have demonstrated a range of sensitivities between 10 mGy and 10 Gy. This system has the advantage of providing accumulated dose information over time that can then be optically interrogated without having to remove the system.

More recent work has focused on the exploitation of the thermoluminescent properties of Ge-doped silica optical fibres. Rahman et al. [10] investigated the ability of a high spatial resolution (~120 μm) Ge-doped SiO_2 TLDs to measure radiation. They also demonstrate negligible post-irradiation fading and good reusability (0.5 %) following thermal annealing [11]. Begum et al. [12] (Fig. 2) has shown purposefully drawn Ge-doped silica fibres to be 4 times more sensitive than commercial Ge-doped silica fibres for communication applications, although still only 26 % of the sensitivity of TLD-100 (LiF:Mg,Ti) chips, the commercial TLD most commonly employed in industry.

Although TLDs typically demonstrate excellent sensitivity, a significant drawback to this technique is that due to the requirement to stimulate the material to produce a signal sometime after irradiation, it cannot deliver real time dosimetry.

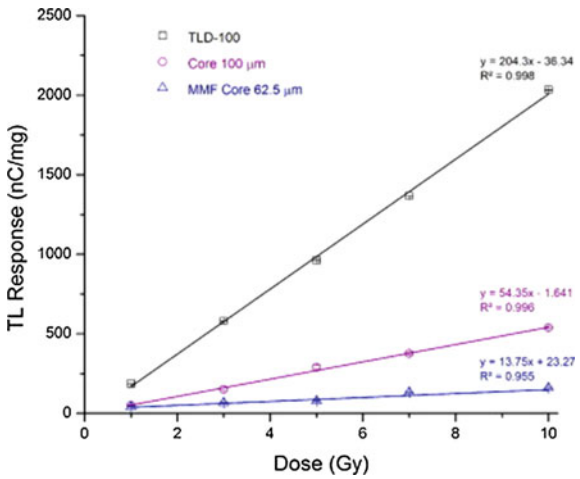

Fig. 2 Comparison of TL response of purposefully drawn Ge-doped silica fibre (core 100 μm), commercial silica fibre (MMF Core 62.5 μm) and commercial TLD (TLD-100) [12]

3.2.3 Optically Stimulated Luminescence (OSL)

Similar to thermoluminescent techniques, photoluminescence, or optically stimulated luminescence (OSL), emits the energy stored, due to irradiation, upon exposure to light. Carbon-doped aluminium oxide (Al_2O_3:C) is the most widely used OSL crystals, particularly for low dose monitoring within the medical and personal dosimetry fields, where it demonstrates a linear response to doses up to 50 Gy. It is stable at room temperature, with negligible fading over a period of 85 days, and demonstrates an excellent response when varying beam parameters such as dose rate, field size and irradiation direction. [13]. However, it does exhibit a change in sensitivity with irradiation history introducing some uncertainty for repeated dosimetry applications. Optical fibre based OSL dosimeters can also be used in conjunction with radioluminensce to provide a second dose measurement and to overcome errors caused by undesirable external luminescence, e.g. Cherenkov radiation. Marckmann et al. [14] couple an Al_2O_3:C crystal to the end of a 500 μm PMMA plastic optical fibre to provide simultaneous RL/OSL measurements giving real-time dose and dose rate information using RL and further verification of dose post-irradiation using OSL.

Optical fibres pose a clear advantage in the development of OSL dosimeters as they can be used to transmit both the stimulating optical source, typically a laser source, to the OSL material and the luminenscence signal back to the detector, allowing for remote analysis of the OSL response. In a similar way to TLDS, recent research has also focussed on the exploitation of the inherent OSL properties of commercial and purposefully drawn optical fibres. Commercial SiO2 optical fibres have demonstrated OSL propertied, with a linear response between 7.34 and 147 Gy beta-doses [15]. Ge-doped SiO2 fibres also exhibit OSL properties, whereby, following exposure to beta-particles for a dose of 20 Gy, a wavelength shift of transmitted light is observed from 827 to 917 nm. Further work has demonstrated the combined RL/OSL response, providing both real-time monitoring of the dose-rate and the delayed read-out of the total absorbed dose. Figure 3 shows the OSL curve for Ge-doped silica fibres following exposure to radiation to a dose of 10 Gy [15].

Optically stimulated luminescence has also been demonstrated in fluoride phosphate glass fibres [16]. The optical fibre demonstrated a linear response between 0.16 and 2 Gy following optical stimulation from a 532 nm laser, after it was irradiated with a 90Sr/90Yr source. Further work has demonstrated that due to its short lifetime at ambient temperatures, this material is not suitable for applications where there is a significant delay between radiation exposure and the interrogation of the dosimeter [17].

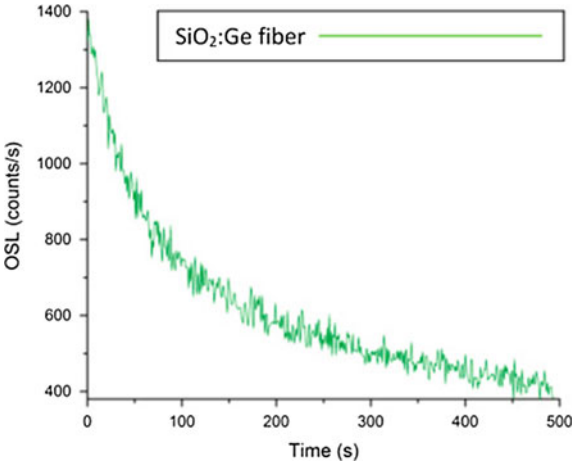

Fig. 3 OSL response of Germanium doped Silica optical fibre. [15]

3.3 *Optical Absorption Dosimetry/Radiation Induced Attenuation*

While radiation can affect the properties of Optical fibres in many ways, the most common effect is the increased attenuation in the optical signal with radiation dose, known as Radiation Induced Attenuation (RIA). Using the Beer-Lambert Law it is possible to determine the radiation-induced attenuation in optical fibres. The radiation-induced attenuation is given by Eq. 1 and can be further explained through the diagram in Fig. 4. The equation is based on using two fibres with different lengths exposed to gamma radiation. As the optical attenuation is directly related to the length of the fibre, by monitoring the optical power in both fibres it is possible to determine the attenuation due to the gamma radiation.

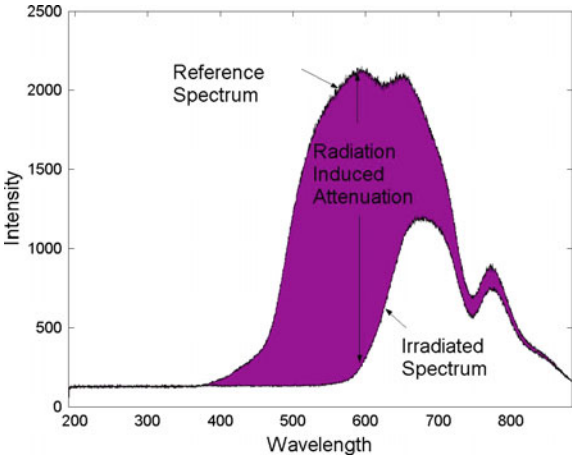

Fig. 4 Diagram showing how radiation-induced attenuation measurements are obtained from the transmission spectra

$$RIA(dB) = -\frac{10}{L - L_0}\log\left\{\frac{P_T(\lambda, t)}{P_T^0(\lambda)}\right\} \quad (1)$$

where L is the irradiated length of fibre, L_0 is the length of the reference fibre, PT(λ, t) is the measured optical power in the irradiated fibre and PT0(λ) is the optical power of the reference fibre [18].

Pure silica-core fibres are reported to have the least sensitivity to radiation [19], although they have been shown as effective sensors for neutron monitoring [20], and as a result such fibres are usually doped to increase their radiation sensitivity making them suitable for radiation dosimetry. One example of such is the phosphorous-doped silica core fibres [21–23]. Sensing is based on radiation-induced attenuation in the infrared region. Sensitivity was found to increase with dose rate at these longer wavelengths and thus these fibres are most suitable for applications with dose rates between 1 and 100 Gy/h [23]. Phosphorous-doped fibres show almost no annealing effects, remaining very stable post irradiation, which is an advantageous feature of these dosimeters.

3.4 Fibre Gratings

Fibre Bragg grating (FBG) based sensors work by monitoring the wavelength shift of the returned Bragg-signal, which changes as a function of the measurand. The Bragg wavelength is related to the refractive index of the material and the grating pitch. The light incident on the grating reflects a narrow spectral component at the Bragg wavelength, and hence in the transmission spectrum this component is missing. Much work has been done in the last number of years investigating the effects of radiation on Fibre Bragg Grating (FBG). This work has primarily concentrated on developing radiation resistant FBGs for use in temperature and strain measurement applications in nuclear environments [24–30]. Krebber et al. [31] demonstrated the use of FBGs for high dose applications (over 2 kGy), where FBGs were written in Hydrogen doped Ge-doped fibres. It was noted that the sensor required a highly stable set-up and a constant temperature, which limits its application in many industrial environments. However, Bragg grating cavity reflectors have recently been shown to be effective in monitoring low radiation doses (2 Gy), due to their sensitivity to radiation induced effects in the silica material of the fibre [32, 33].

3.5 Stem Effect

A term known as the stem effect is used to describe Cerenkov radiation and other radiation induced light that can be produced in an optical fibre [34]. Cerenkov radiation is generated when a charged particle passes through a dielectric medium with a velocity greater than that of light in that medium. Cerenkov emissions only occurs when the refractive index of the material is greater than one, and are only produced above a certain energy threshold. For plastics most commonly used in optical fibre scintillation dosimetry, the refractive index is 1.48–1.6, which means that Cherenkov is seen at energies above 145–180 keV [35]. As the radiation parameters (e.g. energy, dose rate) vary considerably in radiotherapy it is important that Cherenkov radiation is compensated for. A number of techniques are proposed for removing the stem effect in optical fibre-based dosimeters, such as using a dual reference fibre [36–39], optical filtering [40] and a temporal approach, where the measurement reading is timed such that the stem effect has decayed-out [41]. One of the most favoured methods of stem removal is the spectral, or chromatic, method [35, 42, 43] developed by Fontbonne et al. [44]. The technique exploits the difference in optical spectra of the luminescence signal and Cherenkov radiation. It has been shown that by monitoring the light under two different wavelength filters it is possible to isolate the luminescence signal from the Cherenkov signal [42–45]. As a consequence of the large amount of research into this area, it is now widely accepted that the issue of the stem effect has been addressed and no longer poses a limitation in the sensors' potential for radiation dosimetry [46].

4 Applications of Optical Fibre Dosimeters

The different optical fibre dosimetry techniques described above offer a wide monitoring dose range and as such provide a sensing solution for a number of different applications. A summary of some of the different application of radiation is shown in Fig. 5, along with the absorbed doses for the specific process.

4.1 Industrial Processing Applications

One of the main industrial application areas of gamma radiation is in sterilisation, in particular, the sterilisation of medical products using gamma radiation. The ability of radiation to kill pathogenic micro-organisms is the basis on which the sterilisation of medical products depends. It is used in a wide variety of products such as hypodermic needles, surgical sutures, blood handling equipment, implant substances and tissues, surgical gloves and utensils, catheters, dental supplies, etc. Commercial gamma ray irradiation facilities are generally loaded with ^{60}Co, with

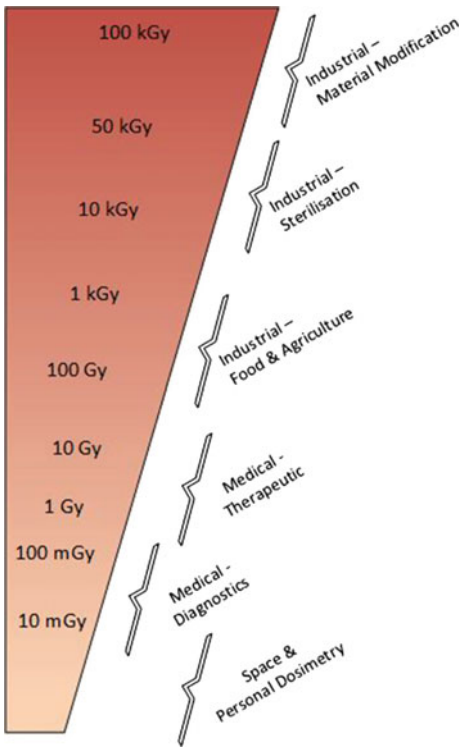

Fig. 5 Dose ranges for various applications of ionizing radiation [48]

activity varying from tens of kCi to several MCi, while commercial e-beam facilities are equipped with one or two electron accelerators generating high power (10–100 kW) beams of 8–10 MeV electrons. [47, 48]

The exact dose of gamma radiation used in the sterilisation of medical products varies for different countries but is usually between 25 and 35 kGy [49]. Gamma radiation can be used for a number of different applications within the food industry. Food can be treated to prevent sprouting in onions, garlic and potatoes, to extend the shelf-life of mushrooms, cherries and strawberries, to eradicate insects in grain and fruit, to kill pathogenic microorganisms in fish and meat, to pasteurize dried herbs and spices, and to delay ripening of fruit and vegetables. A radiation treatment of between 1–7 kGy, depending on the product, can significantly reduce the number of viable pathogenic micro-organisms, e.g. *Salmonella*, *Escherichia coli* and *Lysteria*, which can contaminate food causing serious food poisoning [49]. A number of other applications for radiation are also being investigated, such as in the treatment of sludge, to reduce the amount of bacteria and infectious micro-organisms, before it may be used as a fertiliser. It is also used in the preservation of ancient objects having historic or artistic value by killing the micro-organisms that can destroy the organic material that the objects are made of or have components of. [47, 49, 50]

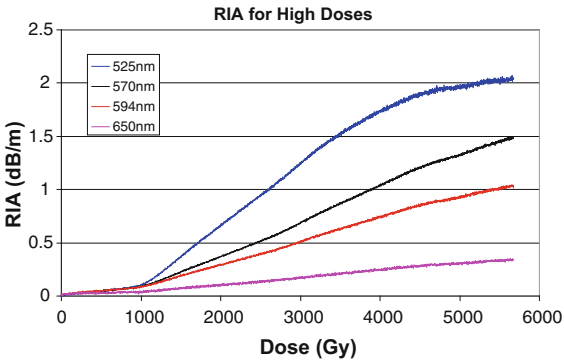

Fig. 6 Radiation-induced attenuation of PMMA optical fibre for peak wavelengths [50]

Table 1 Summary of wavelength dependant sensitivity and dose range [50]

Wavelength (nm)	Sensitivity (dBm^{-1}/kGy)	Dosimetry range (kGy)
525	0. 6	0.03–4
570	0. 3	0.03–10
594	0. 2	0.5–12
650	0.06	1–45

Based on the same principle of radiation-induced attenuation used by commercial PMMA slabs, an in situ system based on PMMA polymer optical fibres was developed by O'Keeffe et al. [54] giving real-time information of the radiation dose received. A 7 m length of PMMA based optical fibre was placed in the irradiation chamber, where it was irradiated by the ^{60}Co source, at a dose rate of 25 kGy/hr. The sensitivity of the PMMA fibre to ionizing radiation is directly related to the wavelength and thus by selecting the correct wavelength the fibre can be used to monitor over a wide dose range, selecting 525 nm for low doses with high sensitivity and selecting 650 nm for high doses with lower sensitivity (Fig. 6).

Table 1 gives a summary of the sensitivity and dose range of the PMMA fibre for individual wavelengths. It shows that the sensitivity decreases with increasing wavelengths, with the dose range also dependant on the wavelength [50].

4.2 Nuclear Industry

While much of the research in optical fibre sensing for the nuclear industry focusses on developing radiation resistant fibres for structural health monitoring of large nuclear infrastructures, e.g. reactor containment buildings and nuclear waste repositories [51, 52], there is also an important role for optical fibres in directly monitoring the radiation doses. Radiation monitoring in the vicinity of nuclear reactors and high energy accelerators is essential to predict the radiation-induced aging of critical components, ensuring timely maintenance [53]. Due to the high

dose ranges associated with these applications, the primary technique employed is Radiation-induced attenuation [18, 53, 54]. Radiation-induced attenuation, also allows for distributed radiation monitoring using optical frequency domain reflectometry (OFDR) [55] and optical time domain reflectometry (OTDR) [56] techniques.

4.3 Medical Applications

Radiation plays an important role in medicine; in diagnostics, monitoring and treatment of a wide range of diseases and medical conditions. The inherent properties of optical fibres; small dimensions, light weight, electrically passive, and water equivalence, make optical fibres attractive for use in diagnostic and therapeutic radiology. As such there has been significant focus in recent times in developing optical fibre sensors for monitoring radiation in clinical environments, with considerable emphasis on luminescent based dosimeters.

Radiotherapy is the use of ionising radiation in the treatment of cancer. It is delivered in two main types: external beam radiation, using a clinical linear accelerator (linac) and internal radiation, known as brachytherapy, whereby radioactive sources are placed internal to the patient. In all cases there is a need to provide real-time, in vivo monitoring of the radiation dose to the patient. An in-depth review of optical fibre sensors for radiotherapy applications is made by O'Keeffe et al. [46]. Yukihara and McKeever provide a detailed overview of the fundamental theory and practical aspects of OSL systems for medical applications [57]. While Bradley et al. reviews doped silica optical fibres for their TL response for radiotherapy applications [58].

The exploitation of radioluminescence from Inorganic scintillators embedded with the core of a plastic optical fibre has been proposed by Woulfe et al. [59] for

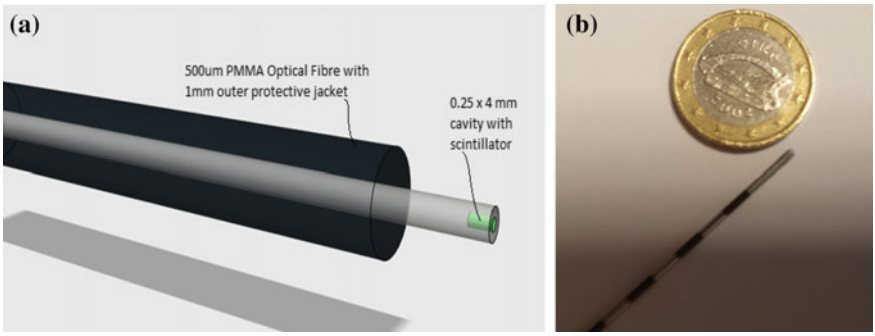

Fig. 7 **a** Optical fibre based radiation probe for in vivo brachytherapy, and **b** image of sensor within brachytherapy needle for direct tumour dose monitoring [59]

in vivo monitoring of the radiation dose from Iodine-125 radio-active seeds used in low dose rate (LDR) brachytherapy. The optical fibre sensor, shown in Fig. 7, is constructed by micromachining a cavity in the 500 μm core of a PMMA (polymethyl methacrylate) plastic optical fibre. The cavity, 250 μm in diameter and 4 mm deep, is filled with the scintillating material, terbium doped gadolinium oxysulphide (Gd_2O_2S:Tb, GOS) and sealed with epoxy. The sensor was demonstrated as suitable for use in monitoring patient dose during seed implantation, with a clear increase in photon counts with increasing radio-activity.

4.4 Space Applications

Monitoring the ionising radiation environment in space remains one of the greatest challenges in radiation dosimetry, due to the complex nature of the radiation fields, with a wide variety of radiation particles and range of energies, encountered in low-Earth orbit and beyond. [60]. Monitoring crew exposure to ionising radiation during spaceflight remains the priority in radiation dosimetry for space applications but dosimeters also have a role in monitoring the radiation exposure of structural components in space, to ensure the structural integrity of equipment over time.

One of the first optical fibre systems for monitoring radiation doses was used in 1977 on the Navigation Technology Satellite 2. It relied on the radiation induced darkening of the core of the optical fibre. A glass fibre doped with oxides of barium, zinc and boron was used to give a linear response with low losses at the expected radiation levels and a low fade rate. The darkening effect observed is influenced by the composition of the glass used and is also wavelength dependant, being attenuated significantly at shorter wavelengths and decreasing considerably above 800 nm [61]

Much of the current research into optical fibre sensors for space applications is focussed on developing radiation hardened optical fibres for sensors to be used in structural health monitoring [62]. However there is a role for optical fibre based dosimeters in space applications, where their small size and immunity to electromagnetic interferences are particularly advantageous. NASA Glenn Research Centre has investigated the use of optical fibres in limited volume areas, whereby an optical fibre ribbon coupled with a thin film scintillator detector is inserted between layers within the space suit assembly [63].

5 Conclusion

This chapter presents an overview of the different optical fibre sensing techniques employed in radiation dosimetry and some of the recent advancements in the development of such sensors for specific applications. The large number of optical fibre dosimeters reported in recent years demonstrates the considerable interest in

this area and the potential for optical fibres within this field. Optical fibres are becoming more important for radiation dosimetry, due to a number of advantages they possess over conventional sensors, primarily their immunity to electrochemical interference and their ability to measure remotely and in real-time. The different techniques provide for an overall wide dose range and so the type of sensor can be selected depending on the dose range of the specific application. For example, luminescent based techniques generally have a high sensitivity over a low dose range (mGy to Gy), making them ideal for medical applications, while radiation induced attenuation has a lower sensitivity but is capable of monitoring at very high doses (up to several hundred kGy) allowing for monitoring in industrial applications.

References

1. T. Shikama, K. Toh, S. Nagata, B. Tsuchiya, Optical dosimetry for ionizing radiation fields by infrared radioluminescence, in *17th International Conference on Optical Fibre Sensors* (Bruges, Belgium, SPIE, 2005)
2. S. O'Keeffe, C. Fitzpatrick, E. Lewis, A.I. Al-Shamma'a, A review of optical fibre radiation dosimeters. Sens. Rev. **28**, 136–142 (2008)
3. A. Kovacs, M. Baranyai, P.G. Fuochi, M. Lavalle, U. Corda, S. Miller, M. Murphy, J. O'Doherty, The application of Sunna dosimeter film for process control at industrial gamma- and electron beam irradiation facilities. Radiat. Phys. Chem. **71**, 327–331 (2004)
4. A. de A Rodrigues, L.V.E. Caldas, Commercial plate window glass tested as routine dosimeter at a gamma irradiation facility. Radiat. Phys. Chem. **63**, 765–767 (2002)
5. M.F. Watts, R. Bett, A new dosimetry system using a portable reader. Radiat. Phys. Chem. **63**, 799–801 (2002)
6. J.M. Lopez-Higuera, *Optical Sensors* (Universidad de Cantabria, 1998)
7. G.F. Knoll, *Radiation Detection and Measurement* (Wiley, 1989)
8. Product Comparisons: Inorganic and Organic Crystals. Saint Gobain Crystals, http://www.detectors.saint-gobain.com (2003)
9. M. Ranogajee-Komor, Thermoluminescence dosimetry—application in environmental monitoring. Radiat. Saf. Manag. **2**, 2–16 (2002)
10. A.T. Abdul Rahman, R.P. Hugtenburg, S.F. Abdul Sani, A.I.M. Alalawi, F. Issa, R. Thomas et al., An investigation of the thermoluminescence of Ge-doped SiO2 optical fibres for application in interface radiation dosimetry. Appl. Radiat. Isot. **70**, 1436–1441 (2012)
11. A.T.A. Rahman, A. Nisbet, D.A. Bradley, Dose-rate and the reciprocity law: TL response of Ge-doped SiO2 optical fibers at therapeutic radiation doses. Nucl. Instrum. Meth. Phys. Res. Sect. A **652**, 891–895 (2011)
12. M. Begum, A.K.M.M. Rahman, H.A. Abdul-Rashid, Z. Yusoff, M. Begum, K.A. Mat-Sharif, Y.M. Amin, D.A. Bradley, Thermoluminescence characteristics of Ge-doped optical fibers with different dimensions for radiation dosimetry. Appl. Radiat. Isot. **100**, 79–83 (2015), ISSN 0969-8043
13. P.A. Jursinic, Characterization of optically stimulated luminescent dosimeters, OSLDs, for clinical dosimetric measurements. Med. Phys. **34**, 4594–4604 (2007)
14. C.J. Marckmann, C.E. Andersen, M.C. Aznar, L. BÃ¸tter-Jensen, Optical fibre dosemeter systems for clinical applications based on radioluminescence and optically stimulated luminescence from Al2O3:C. Radiat. Prot. Dosimetry **120**, 28–32 (2006)
15. A.K.M.M. Rahman, H.T. Zubair, M. Begum, H.A. Abdul-Rashid, Z. Yusoff, N.M. Ung, K.A. Mat-Sharif, W.S. Wan Abdullah, G.A. Mahdiraji, Y.M. Amin, M.J. Maah, D.A. Bradley,

Germanium-doped optical fiber for real-time radiation dosimetry. Radiat. Phys. Chem. **116**, 170–175 (2015), ISSN 0969-806X, http://dx.doi.org/10.1016/j.radphyschem.2015.04.018
16. C.A.G. Kalnins, H. Ebendorff-Heidepriem, N.A. Spooner, T.M. Monro, Radiation dosimetry using optically stimulated luminescence in fluoride phosphate optical fibres, Opt. Mater. Express **2**, 62–70 (2012)
17. C.A.G. Kalnins, N.A. Spooner, H. Ebendorff-Heidepriem, T.M. Monro, Luminescent properties of fluoride phosphate glass for radiation dosimetry. Opt. Mater. Express **3**, 960–967 (2013)
18. S. O'Keeffe, A.F. Fernandez, C. Fitzpatrick, B. Brichard, E. Lewis, Real-time gamma dosimetry using PMMA optical fibres for applications in the sterilization industry. Meas. Sci. Technol. **18**, 3171 (2007)
19. A.L. Huston, B.L. Justus, P.L. Falkenstein, R.W. Miller, H. Ning, R. Altemus, Remote optical fibre dosimetry. Nucl. Instrum. Meth. Phys. Res., Sect. B **184**, 55–67 (2001)
20. B. Brichard, P. Borgermans, A.F. Fernandez, K. Lammens, M. Decreton, Radiation effect in silica optical fiber exposed to intense mixed neutron-gamma radiation field. IEEE Trans. Nucl. Sci. **48**, 2069–2073 (2001)
21. P. Borgermans, B. Brichard, F. Berghmans, F. Vos, M. Decreton, K. Golant, A. Tomashuk, L. Nikolin, On-line gamma dosimetry with phosphorous and germanium co-doped optical fibres. *RADECS 1999* (IEEE, 1999)
22. B. Brichard, P. Borgermans, F. Berghmans, M. Decreton, A.L. Tomashuk, I.V. Nikolin, R.R. Khrapko, K.M. Golant, Dedicated optical fibres for dosimetry based on radiation-induced attenuation: experimental results, in *Photonics for Space and Radiation Environments* (Italy, SPIE, 1999)
23. B. Brichard, A.F. Fernandez, H. Ooms, P. Borgermans, F. Berghmans, True dose-rate enhancement effect in phosphorous doped fibre optic radiation sensors, in *Second European Workshop on Optical Fibre Sensors* (Santander, Spain, SPIE, 2004)
24. A.F. Fernandez, B Brichard, F. Berghmans, M. Decreton Dose rate dependencies in gamma-irradiated fiber Bragg grating filters. IEEE Trans. Nucl. Sci. **49**, 2874–2878 (2002)
25. A.F. Fernandez, G. Rego, A. Gusarov, B. Brichard, J.L. Santos, F. Berghmans, Evaluation of long-period fiber grating temperature sensors in nuclear environments, in *Proceedings of SPIE 5502, Second European Workshop on Optical Fibre Sensors*, (9 June 2004). doi:10.1117/12.566600
26. A. Gusarov, F. Berghmans, O. Deparis, A. Fernandez Fernandez, Y. Defosse, P. Megret et al., High total dose radiation effects on temperature sensing fiber Bragg gratings. IEEE Photon. Technol. Lett. **11**, 1159–1161 (1999)
27. A. Gusarov, A. Fernandez Fernandez, S. Vasiliev, O. Medvedkov, M. Blondel, F. Berghmans, Effect of gamma-neutron nuclear reactor radiation on the properties of Bragg gratings written in photosensitive Ge-doped optical fiber. Nucl. Instrum. Meth. Phys. Res., Sect. B **187**, 79 (2002)
28. M. Perry, P. Niewczas, M. Johnston, Effects of neutron-gamma radiation on fiber Bragg grating sensors: a review. IEEE Sens. J. **12**(11), 3248–3257 (2012)
29. T. Kakuta, H. Yamagishi, T. Iwamura, M. Urakami, Development of new nuclear instrumentation based on optical sensing—irradiation effects on fiber Bragg grating sensors. Proc SPIE **4185**, 816–819 (2000)
30. R.R. Maier, W.N. MacPherson, J.S. Barton, J. Jones, M. Scott, A.F. Fernandez et al., Fibre Bragg gratings of type I in SMF-28 and B/Ge fibre and type IIA B/Ge fibre under gamma radiation up to 0.54 MGy, in *Proceedings of SPIE—the International Society for Optical Engineering* 2005; 5855 PART I: 124, pp. 511–514
31. K. Krebber, H. Henschel, U. Weinand, Fibre Bragg gratings as high dose radiation sensors? Meas. Sci. Technol. **17**(5), 1095 (2006)
32. S. Avino, V. D'Avino, A. Giorgini, R. Pacelli, R. Liuzzi, L. Cella et al., Radiation dosimetry with fiber Bragg gratings, in *OFS2014 23rd International Conference on Optical Fiber Sensors* (International Society for Optics and Photonics), pp. 91574L–91574L

33. S. Avino, V. D'Avino, A. Giorgini, R. Pacelli, R. Liuzzi, L. Cella, P. De Natale, G. Gagliardi, Detecting ionizing radiation with optical fibers down to biomedical doses. Appl. Phys. Lett. **103**(18), 184102 (2013)
34. K. Tanderup, S. Beddar, C.E. Andersen, G. Kertzscher, J.E. Cygler, In vivo dosimetry in brachytherapy. Med. Phys. **40**, 070902 (2013)
35. L. Beaulieu, M. Goulet, L. Archambault, S. Beddar, Current status of scintillation dosimetry for megavoltage beams, in *Journal of Physics: Conference Series*, vol. 444, no. 1 (IOP Publishing, 2013), p. 012013
36. A.S. Beddar, T.R. Mackie, F.H. Attix, Water-equivalent plastic scintillation detectors for high-energy beam dosimetry: I. Physical characteristics and theoretical considerations. Phys. Med. Biol. **37**, 1883 (1992)
37. A.S. Beddar, T.R. Mackie, F.H. Attix, Cerenkov light generated in optical fibres and other light pipes irradiated by electron beams. Phys. Med. Biol. **37**, 925 (1992)
38. J. Lambert, Y. Yin, D.R. McKenzie, S.H. Law, A. Ralston, N. Suchowerska, A prototype scintillation dosimeter customized for small and dynamic megavoltage radiation fields. Phys. Med. Biol. **55**, 1115 (2010)
39. M. Ishikawa, G. Bengua, K.L. Sutherland, J. Hiratsuka, N. Katoh, S. Shimizu et al., A feasibility study of novel plastic scintillation dosimetry with pulse-counting mode. Phys. Med. Biol. **54**, 2079 (2009)
40. T. Teichmann, M. Sommer, J.R. Henniger, Dose rate measurements with a ruby-based fiber optic radioluminescent probe. Radiat. Meas. **56**, 347–350 (2013)
41. M.A. Clift, P.N. Johnston, D.V. Webb, A temporal method of avoiding the Cerenkov radiation generated in organic scintillator dosimeters by pulsed mega-voltage electron and photon beams. Phys. Med. Biol. **47**, 1421 (2002)
42. L. Archambault, A.S. Beddar, L. Gingras, R. Roy, L. Beaulieu, Measurement accuracy and Cerenkov removal for high performance, high spatial resolution scintillation dosimetry. Med. Phys. **33**, 128–135 (2006)
43. L. Archambault, A.S. Beddar, L. Gingras, R. Roy, L. Beaulieu, Measurement accuracy and Cerenkov removal for high performance, high spatial resolution scintillation dosimetry. Med. Phys. **33**, 128–135 (2006)
44. J.M. Fontbonne, G. Iltis, G. Ban, A. Battala, J.C. Vernhes, J. Tillier et al., Scintillating fiber dosimeter for radiation therapy accelerator. Nucl. Sci. IEEE Trans. **49**, 2223–2227 (2002)
45. F. Therriault-Proulx, L. Beaulieu, L. Archambault, S. Beddar, On the nature of the light produced within PMMA optical light guides in scintillation fiber-optic dosimetry. Phys. Med. Biol. **58**, 2073 (2013)
46. S. O'Keeffe, D. McCarthy, P. Woulfe, M.W.D. Grattan, A.R. Hounsell, D. Sporea, L. Mihai, I. Vata, G. Leen, E. Lewis, A review of recent advances in optical fibre sensors for in vivo dosimetry during radiotherapy. Brit. J. Radiol. **88**(1050), 20140702 (2015)
47. K.A. da Silva Aquino, Sterilization by Gamma Irradiation, in *Gamma Radiation*, ed. by Prof. F. Adrovic (2012). ISBN: 978-953-51-0316-5, InTech
48. International Atomic Energy Agency, Industrial Applications and Chemistry Section, Vienna (Austria), in *Gamma Irradiators for Radiation Processing* (INIS-XA–862) (International Atomic Energy Agency (IAEA), 2006)
49. W.L. McLaughlin et al., in *Dosimetry for Radiation Processes* (Taylor & Francis, 1989), p. 251
50. S. O'Keeffe, E. Lewis, Polymer optical fibre for in situ monitoring of gamma radiation processes, in *International Journal on Smart Sensing and Intelligent Systems*, vol. 2 (Christchurch, New Zealand, 2009), pp. 490–502
51. X. Phéron, S. Girard, A. Boukenter, B. Brichard, S. Delepine-Lesoille, J. Bertrand, Y. Ouerdane, High γ-ray dose radiation effects on the performances of Brillouin scattering based optical fiber sensors. Optics Express **20**(24), 26978–26985 (2012)
52. C. Cangialosi, S. Girard, M. Cannas, A. Boukenter, E. Marin, S. Delepine-Lesoille, C. Marcandella, P. Paillet, Y. Ourdane, Raman Based Distributed Fiber Optic Temperature Sensors for Structural Health Monitoring in Radiation Environment, in *2015 15th European*

Conference on, IEEE *Radiation and Its Effects on Components and Systems (RADECS)* (2015), pp. 1–3
53. A.F. Fernandez, B. Brichard, S. O'Keeffe, C. Fitzpatrick, E. Lewis, J.R. Vaille, L. Dusseau, D.A. Jackson, F. Ravotti, M. Glaser, Real-time fibre optic radiation dosimeters for nuclear environment monitoring around thermonuclear reactors. Fusion Eng. Des. **83**, 50–59 (2008)
54. A.V. Faustov et al., Comparison of gamma-radiation induced attenuation in Al-doped, P-doped and Ge-doped fibres for dosimetry. IEEE Trans. Nucl. Sci. **60**(4), 2511–2517 (2013). doi:10.1109/TNS.2013.2273273
55. A.V. Faustov, A. Gusarov, M. Wuilpart, A. Fotiadi, L.B. Liokumivich et al., Remote distributed optical fibre dose measuring of high gamma-irradiation with highly sensitive Al- and P-doped fibres, in *Proceedings of SPIE 8774, Optical Sensors* 2013, 877404 (May 3, 2013). doi:10.1117/12.2017331
56. I. Toccafondo et al., Distributed Optical Fiber Radiation Sensing at CERN High Energy AcceleRator Mixed Field Facility (CHARM), in *2015 15th European Conference on Radiation and Its Effects on Components and Systems (RADECS)* (Moscow, 2015), pp. 1–4. doi:10.1109/RADECS.2015.7365601
57. E.G. Yukihara, S.W.S. McKeever, Optically stimulated luminescence (OSL) dosimetry in medicine. Phys. Med. Biol. **53**, R351 (2008)
58. D.A. Bradley, R.P. Hugtenburg, A. Nisbet, A.T. Abdul Rahman, Fatma Issa, Noramaliza Mohd Noor, A. Alalawi, Review of doped silica glass optical fibre: their TL properties and potential applications in radiation therapy dosimetry. Appl. Radiat. Isot. **71**(Supplement), 2–11 (2012)
59. P. Woulfe, F.J. Sullivan, S. O'Keeffe, *Optical Fibre Luminescence Sensor for Real-time LDR Brachytherapy Dosimetry* (SPIE, European Workshop on Optical Fibre Sensors, 2016)
60. E.R. Benton, E.V. Benton, Space radiation dosimetry in low-earth orbit and beyond. Nucl. Instrum. Methods Phys. Res., Sect. B **184**(1–2), 255–294 (2001)
61. B.D. Evans, G.H. Sigel, J.B. Langworthy, B.J. Faraday, The fiber optic dosimeter on the navigational technology satellite 2. IEEE Trans. Nucl. Sci. **25**(6), 1619–1624 (1978)
62. H.M. Chan, A.R. Parker, A. Piazza, W.L. Richards, Fiber-optic sensing system: Overview, development and deployment in flight at NASA, in *2015 IEEE, Avionics and Vehicle Fiber-Optics and Photonics Conference (AVFOP)* (Santa Barbara, CA, 2015), pp. 71–73
63. J.D. Wrbanek, S.Y. Wrbanek, G.C. Fralick, L.Y. Chen, Micro-Fabricated Solid-State Radiation Detectors for Active Personal Dosimetry NASA/TM, vol. 214674 (2007)

Photonic Bandgap Fibre Based Gas Sensing: Current Status and Future Possibilities

J. Pawlat, X. Li, T. Sugiyama, J. Liang, Y. Zimin, L. Zimin, S. Ikezawa and T. Ueda

Abstract A development of gas concentration sensing systems based on a photonic bandgap fiber (PBGF) is described. Several types of PBG fibers of various parameters and core diameters ranging from 10.9 to 26.25 microns have been designed and tested. The capillary gas flow rate within the fiber has been simulated and measured. A new method for cutting the fiber using focused ion beam in a vacuumed chamber for fine milling was tested to obtain the required angle of the fiber's end, to avoid the destruction of the cladding structure and to create a novel low-loss splice for use between PBGF and the conventional solid-core fiber. The measurement results obtained using proposed systems for selected types of gases are presented. The experimental results clearly indicated a high overlap between the propagating light and filled gas inside the PBGF. Therefore, these studies can contribute to highly sensitive gas sensing, higher accuracy of wavelength references, and other applications.

J. Pawlat (✉)
Lublin University of Technology, Lublin, Poland
e-mail: askmik@hotmail.com

J. Pawlat · X. Li · J. Liang · Y. Zimin · L. Zimin · S. Ikezawa · T. Ueda
Waseda University, IPS, Tokyo, Japan

X. Li
Tongji University, Shanghai, China

T. Sugiyama
Yokogawa Electric Corporation, Tokyo, Japan

J. Liang
Southeast University, Nanjing, China

© Springer International Publishing Switzerland 2017

I.R. Matias et al. (eds.), *Fiber Optic Sensors*, Smart Sensors, Measurement and Instrumentation 21, DOI 10.1007/978-3-319-42625-9_8

1 Introduction and Motivation

Microstructured optical fibers (MOFs) were proposed in the 1990s and based on the pioneering research of Yablonovitch and John [1, 2] on photonic crystals. MOFs have many interesting properties such as high-birefringence, nonlinearity, and the most important: single mode propagation over a wide range of wavelengths [3–7]. There are several types of MOFs, which differ in structure and wave-guiding mechanism. The most general classification includes Photonic crystal fibers (PCFs) with a solid core surrounded by an air-hole cladding structure. PCFs can operate on the same principle as conventional optical fibers, i.e., total internal reflection, which is achieved because of an increased refractive index of the fiber's core. Other type is Bragg fiber, which confine the light through a photonic bandgap in a relatively large diameter hollow core formed by the concentric rings of multilayer films of different materials [8]. To obtain a full bandgap, in dependence on the used materials, usually 6–12 layers of high index contrast are required. Photonic bandgap fibers (PBGFs) of a honeycomb structure with a hollow core surrounded by a highly regular microstructured cladding are main item used as a gas cell in described research. In PBGFs, light can propagate in the core because of photonic band gap phenomena. Such fibers with low bending losses are commercially produced [8–13].

Pure or doped silica have been, for a long time, Basic material for optical fibers, however, the use of other components such as polymers has also been reported. [10, 14–16] The present need for a fast, proper, and accurate measurement of various compounds in ppb levels encouraged our research group to engage in the development of a new sensing system. Huge possibilities of new in situ measurement methods were revealed During preliminary research using a tunable laser and glass or metal tanks [17–19] and PBGFs [20, 21] as the gas cells.

Data obtained by other research groups concerned biosensing and detection of acetylene, [22] hydrogen, [23] and methane [24] employing PCFs. PBGFs were used for acetylene detection by Ritari et al. [25] and Petrovich et al. [26]. Most of the above measurements have been done under uncontrolled flow conditions. This paper reports work performed by group from Waseda University [27–45] that covers the investigation of the micro-capillary gas flow phenomenon inside fibers, examination of properties of PBGFs, the design of proper fibers for our device, and a study into a low concentration gas measurement system for the semiconductor manufacturing industry. The results of gas concentration measurements are shown. Shaping of the end of the fiber is necessary to assure the correct input of light into the PBG waveguide. Traditional cutting methods used in the case of communication optical fibers destroy the fragile cladding structure. However, PBGFs typically have honeycomb structure cladding holes; the widths of the thin silica struts are only 10–100 nm. Machining processes of PBGF require high precision and can lead to a large fraction of damage on the microstructured cladding [38, 46]. Moreover, 193-nm laser and femtosecond (fs) laser mainly have been used [47–49]; however, these methods are generally limited to bigger machining size, and thermal

contributions lead to microstructure collapse. On the other hand, focused ion beam (FIB) milling is recognized as one of the most indispensable microfabricating technologies [50–52]. It is based on the energy transfer of accelerated ions to chemically bonded atoms. Collisions transfer sufficient energy to overcome the atom–atom binding energy and the material work. There is a number of micro-machining applications of the PBGF based on FIB milling processing, focusing on a proper cutting method for the PBGF, achieving a cutting angle on the end face of PBGF to avoid interference from Fresnel reflection, achieving a micrometer-sized channel on the end face of PBGF for allowing gas flow with maintaining good coupling efficiency between two fibers, and opening same punch-channel on the lateral face of PBGF to achieved a high-speed gas flow on a long PBGF gas cell. Finally, a full measurement system based on the PBGF gas cell was developed and implemented for spectroscopy and gas concentration estimation for instance in semiconductor production factories (sensing of ammonia) and natural gas processing facilities (sensing of alkanes).

Especially sensing of ammonia (NH_3), colorless, toxic gas with a pungent odor is of high importance. Its molecule has a pyramidal shape forming oscillating umbrella structure. This wide spread alkaline component causes many problems during semiconductor manufacturing process because even in ppb ranges it can ruin production batches [53]. Ammonia has a significant influence on the photolithography performances. Wafers exposure to ammonia introduces structural defaults, such as “T-topping”, footing, and incorrect line widths or profiles, arising from its interaction with the exposed resist and leading to components failures [54]. The main sources of ammonia in the clean rooms are [55]:

- production processes (chemical reactions between priming agents, wet benches, CVD—Chemical Vapor Deposition, cleaners, coater tracks (formed from HMDS—Hexamethyldisilizane, photoresist adhesion promoter), CMP—Chemical Mechanical Polishing slurries/wafer polishing, Si3N4 and TiN deposition wafers),
- staff members,
- external pollution sources.

2 Experimental Set up

Research was aimed to design a set-up to measure low concentrations of ammonia after further dilution of selected gas usually with high purity nitrogen to required level.

The PBGFs had a unique structure, and light was mostly guided in a hollow, circular core surrounded by a microstructured cladding formed by a periodic arrangement of air holes in undoped silica. Up to 65 % of the fiber cross-section was composed of solid silica but less than 5 % of light propagated in the glass. More than 90 % of the optical power was located in the hollow core or in the holes

Table 1 Fibers used in the experiment

Core diameter, μm/Nominal cladding diameter, μm		Measured clading diameter, μm	Centre operating wavelength, nm	Material
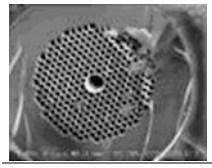	10.9/120	123	1550	Silica
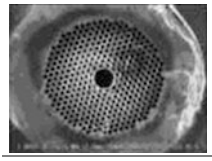	15.2/140	144	~1900	
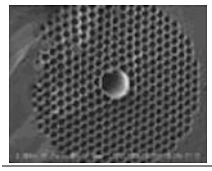	16.2/147	154	~1900	
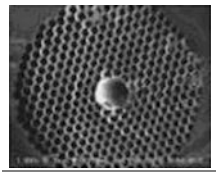	19.4/150	160	~1900	
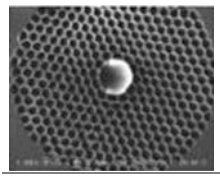	19.9/160	165	~1900	
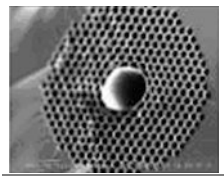	26.25/171	175	~1900	
	700/850 (coating)	–	1500	Composite materials

of the cladding. Holes of the core and cladding were filled with the tested gas. The fiber was coated with a single acrylate layer. The centre operating wavelength of the fiber matched the emission wavelength of the light source and the absorption band of analyzed pollutants. To enhance and expanding possibility of proper wavelength facilitation in the guided spectrum and expanding of the size of the core, the bigger

core size and different light guiding center PBGFs were designed and made by stack-and-draw technique [56, 57].

The core diameters of new fibers used in the experiment were: 15.2, 16.2, 19.4, 19.9 and 26.25 μm. Additionally, 10.9 and 20 μm core fiber, produced by Blaze Photonics and available on the market was tested. Table 1 contains characteristics and SEM photos of some of used fibers.

In initial set-up gas was dosed into a gas cell of special design and it passed throughout the optical fiber for proper measurement of light absorption. The initial gas-providing system is presented in Fig. 1[27–35, 37, 39].

Both ends of the fiber were connected to the rotary pump and a slight pressure difference was maintained to assure the gas flow. 1550 nm emission wavelength tunable laser was chosen for the optical measurement system using commonly produced PBG fiber. The coupling of the light depends on the light source and fiber's bandwidth. Light passed objective lens, the zero-order waveplate and was split using cube beam splitter. The output light was guided inside the optical fiber from and to the gas cells, and passed objective lens with the zero-order waveplate. Finally, both: measurement light wave front and reference light wavefront (adjusted using mirror) were received by two photodetectors. The optical system with laser is

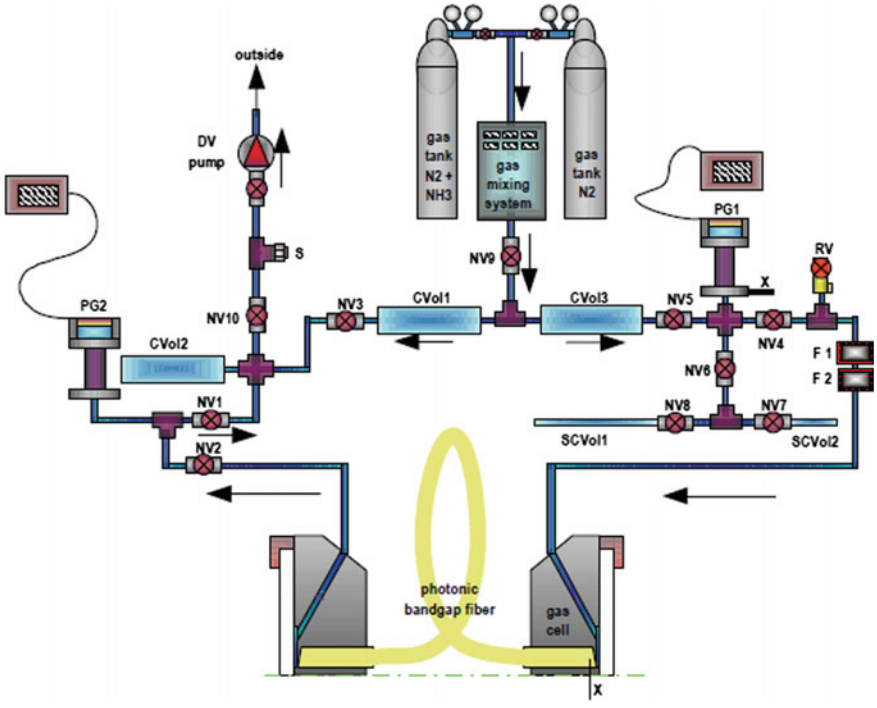

Fig. 1 Gas-providing sub-system of initial PBGF sensing system set-up. (PG1, PG2—pressure control, NV1-NV10—control valves, RF- relief valve, F1, F2—filters, CVol1-CVol3—control volumes, SmallCVol1, SmallCVol2—small control volumes, S1—spare connection [37]

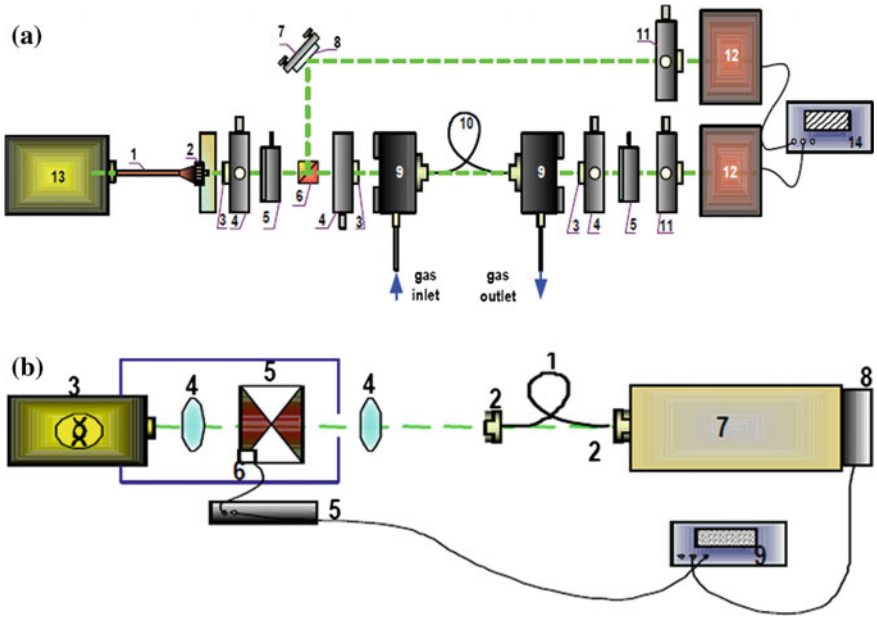

Fig. 2 Optical subsystem of initial PBGF sensing system set-up. **a** With tunable laser: *1*—optical fiber, *2*—optical fiber connector FC, *3*—objective lens with adapter, *4*, *11*—stage, *5*—rotary stage with zero-order waveplate, *6*—beam splitter, *7*—New Focus 9882, *8*—mirror, *9*—gas cell, *10*—photonic crystal fiber, *12*—auto receiver—photodetector, *13*—tunable laser or lamp, *14*—differential amperometer. **b** With lamp: *1*—photonic crystal fiber, *2*—fiber adapter, *3*—lamp, *4*–quartz glass objective lenses with adapters, *5*–chopper with power supply, *6*—opto-couple, *7*—Oriel IR monochrometer (MS 260), *8*—photodetector (IR, EG&G MSD1), *9*—NF lock-In amplifier (LI 570 A) [34]

depicted in Fig. 2a. For measurement of newly designed fibers' properties at 1.5 and 1.9 < m, the set-ups with LED lamps and Oriel Fiber Illuminator with xenon lamp were used (Fig. 2b).

On further stage of research, set-up, presented in Fig. 3 with novel mechanical splicing was proposed [36, 38, 41–45]. The experimental setup consisted of a gas subsystem and an optical subsystem, as shown in Fig. 3. A series of stainless steel tubes and valves were assembled to connect two subsystems to a block that contained the splice and optical fibers. The gas cell included a PBGF and two solid-core fibers. The fibers were connected by two mechanical splices. Mechanical splice was a cylinder made of stainless steel with advanced self-fabriacted connections of PBGF. Also, the input fiber of the PBGF gas cell comprised the single-mode fiber (SMF) with part number SMF-28e, which had an 8.2-μm solid core. The output fiber was a multimode fiber (MMF) with part number Infinicor 300, which had a 62.5-μm solid core. In this set up, mostly the PBGF HC-1550-02 from Crystal Fiber A/S was used. The gas absorptions were measured by coupling light from a tunable laser (Agilent 81600B #201) into the SMF spliced to the PBGF, and the transmission was recorded by a power sensor (Agilent 81634B) at

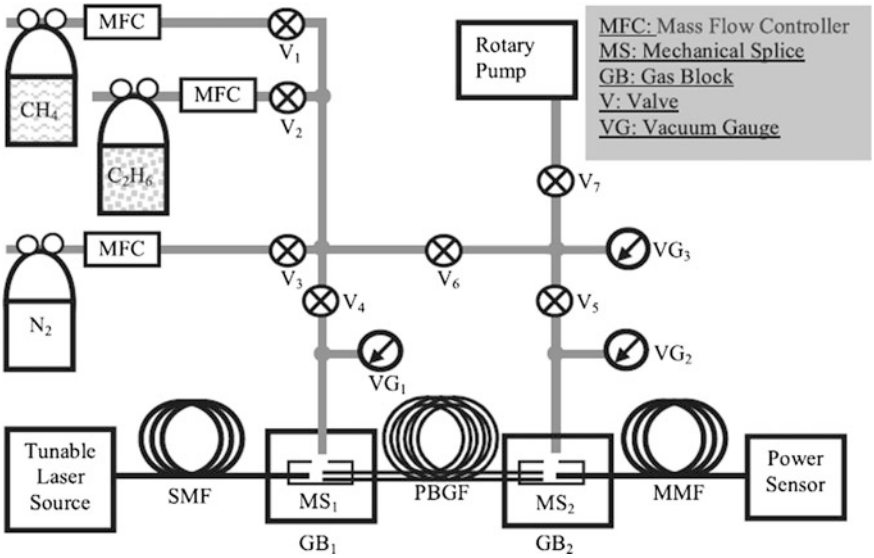

Fig. 3 Experimental setup for filling PBGF with various gases and absorption spectroscopy [43–45]

the output of the MMF as a function of wavelength. The spectrum was scanned with a resolution of 1 pm, with 1640.889-nm maximum wavelength limited by the tunable laser source. To avoid contamination, the gas subsystem and the PBGF gas cell was purged and cleaned using nitrogen (N_2) gas, and evacuated with a rotary pump for 12 h before starting one of the experiments. The experiments were performed in a temperature stabilized environment at 25 ± 0.5 °C.

FIB milling techniques were adopted to obtain clean fiber sections, the PBGFs were milled by Ga ions using the FIB 500 system from FEI Company. Example of milling procedure for micro fabrication of is show in Figs. 4 and 5.

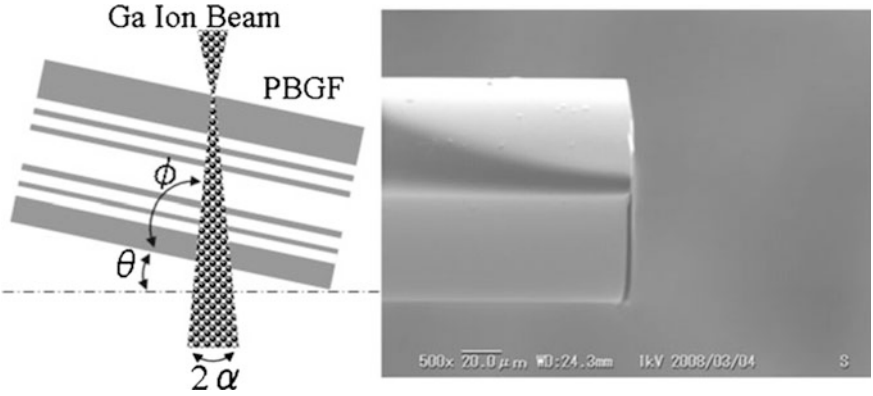

Fig. 4 Scheme of the FIB milling system and SEM image of PBGF [43–45]

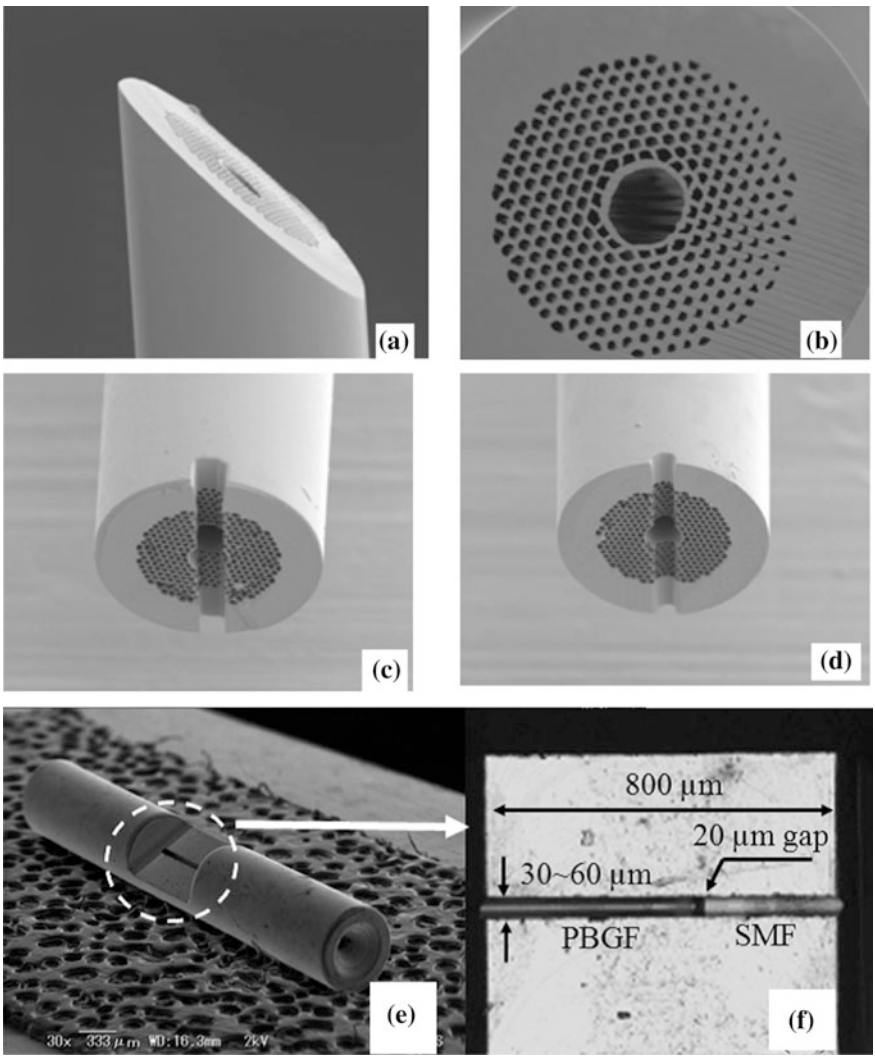

Fig. 5 Images of FIB microfabrication results [36, 38, 41–45]. **a** *Side* view of cut at an angle of 45 of PBGF. **b** *Top* view of PBGF. **c**, **d** Fabricated micrometer-sized channel on the end face of PBGF, **e** micrograph of splice for connection of the PBGF and the solid-core fiber-top view, **f** optical micrograph of the coupled fibers

3 Gas Flow Simulation Within PBGF

Microcapillary gas flow simulations were performed employing the standard mathematical software. Velocity of the gas was calculated using quasi-Panhandle Eq. (1) for modeling of the compressible fluid flow:

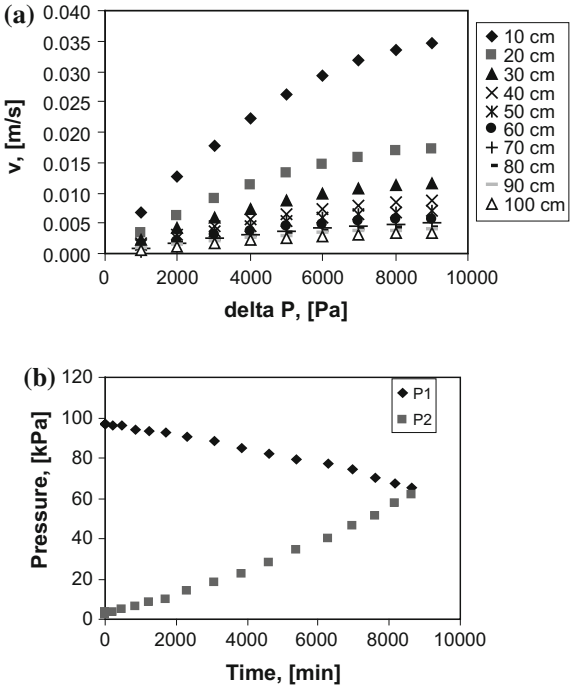

Fig. 6 Simulations of gas velocity for 19.9 micron fiber (**a**) and experimental results of pressure balancing for 0.2 length of 19.9 micron fiber (**b**)

$$p_1^2 - p_2^2 = G^2 RT/F^2 (\lambda(1/d) + 2\log_e(v_2/v_1)) \quad (1)$$

p_1 and p_2 are inlet and outlet pressures, G—mass flow, R—individual gas constant, T—temperature, F—core cross-section area, v_1 and v_2—inlet and outlet velocities, λ—coefficient, which depends on Reynolds number.

Detailed calculation procedure for the microcapillary gas flow within the PBGF was discussed elsewhere [28–31]. Calculated and measured results for nitrogen are depicted below in Figs. 6, 7, and 8.

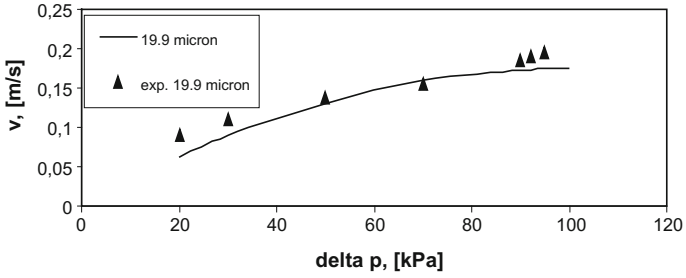

Fig. 7 Simulations of gas velocity and experimental results for 0.2 m and 19.9 micron core fiber

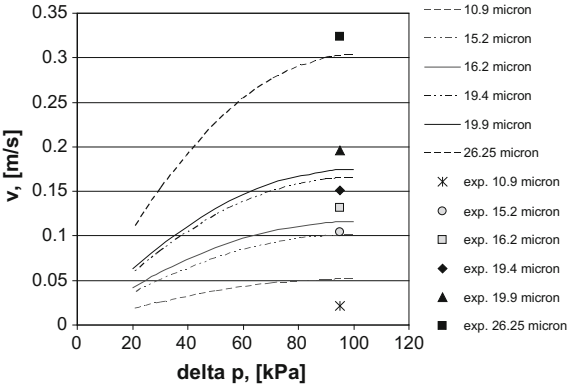

Fig. 8 Simulations of gas velocity and experimental results at 95 kPa (10.9–26.25 micron core—0.2 m length)

As presented in Fig. 6 predicted gas flows were confirmed by the experimental results. It was possible to indirectly measure the flow rate of nitrogen gas inside the PBGF with various pressure differences on the opposite ends. In the case of 1 m fiber the measurement including filling time would take about 10–15 min. According to the simulation result for 0.2 m length of 19.9 μm core fiber, the velocity ranged 0.16 m/s. Velocity confirmed experimentally was higher and ranged 0.19 m/s. The volume of gas present in the system outside the fiber was calculated as precisely as possible, however, the difference between gas volume present in piping, valves and pressure gauges, and the gas volume inside the core of the fiber was huge. That might explain slight differences between simulation and experimental values. Flow rate simulations and experimental results for 19.9 9 μm core fiber and for other fibers are summarized in Figs. 7 and 8, respectively. Δp is the difference between pressures p_1 and p_2.

4 Gas Sensing Using PBGF

Several gases in different concentations were measured using PBGF as a gas cell. Special attention was paid to ammonia. According to HITRAN [58] simulations (Figs. 9 and 10) to measure the ppb level of ammonia, several meters of fiber are required, to ppm levels less than one meter would be enough. Lowering the pressure enables sharpening of the absorption peaks. Thus, peaks caused by the molecules of a chosen pollutant can be distinguished from the other eventual contaminants.

The results of ammonia concentration measurement using initial set up (presented in Figs. 1 and 2a) with 1 m length PBGF of 10.9 μm core and tunable laser and in set up with advanced splicing system (presented in Fig. 3) are depicted in

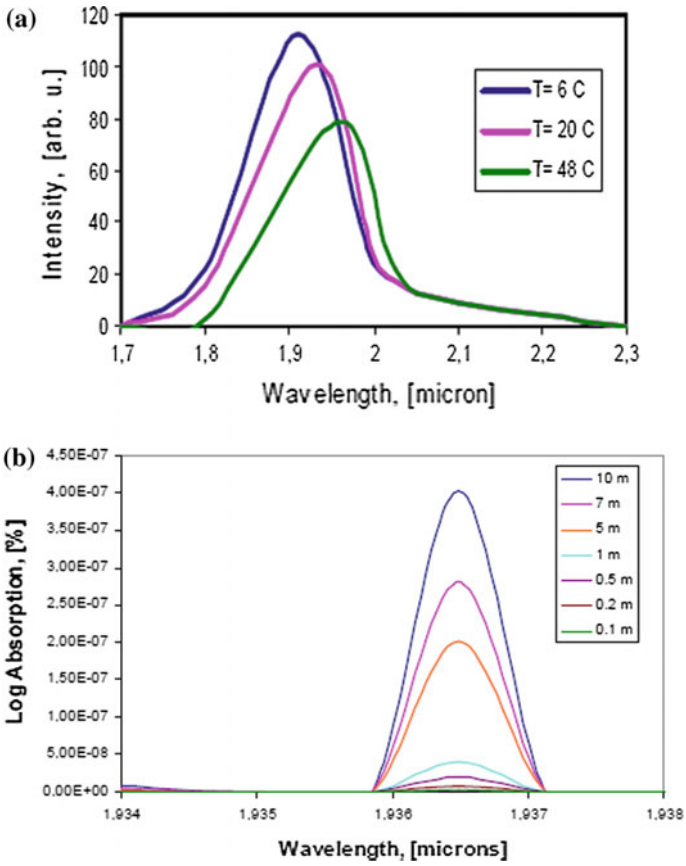

Fig. 9 LED-19: spectral irradiances (**a**), HITRAN simulation of light absorption in dependence on the length of optic fiber (sub-ppb ammonia, 0.1 atm) (**b**)

Figs. 11 and 12, respectively. The ammonia measurement was performed at 0.1 atm average pressure. The PBGFs core volume ranged 8×10^{-5}cc and ammonia concentration in the nitrogen gas was 10 ppm.

The basic peak well matched the results obtained with HITRAN simulation, however during the measurement of ammonia concentration strong side wings next to the absorption peak (not present in the simulation output graph) were observed. The phenomenon might result from the light reflection caused by the straight cut of the ends of the fiber, which was used during the experiment, from noise or less

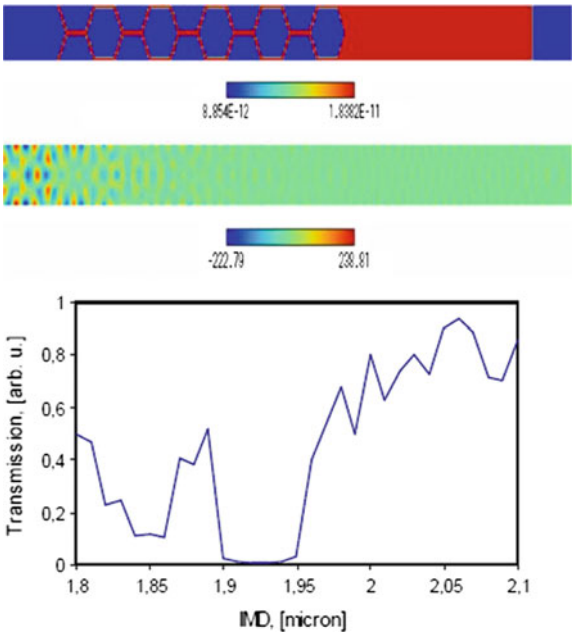

Fig. 10 The bandgap characteristics of 26.25 micron core fiber (λ = 1.936, n = 1.439, transmission = $6.639e^{-03}$ (0.6 %)

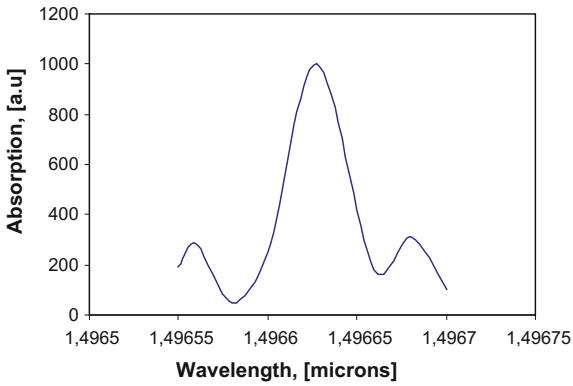

Fig. 11 10 ppm ammonian peak measured in initial set-up

probably from the presence of some impurities. Maximum sensitivity was 0.18 ppb/m.

The result of CO_2 concentration measurement using 1 m length PBG fiber of 10.9 µm core and intial set-up is shown in Fig. 11.

Sensing potential for alkanes was tested using set-up with advanced mechanical splicing system with PBGF gas cell at 100-kPa pressure (Fig. 13).

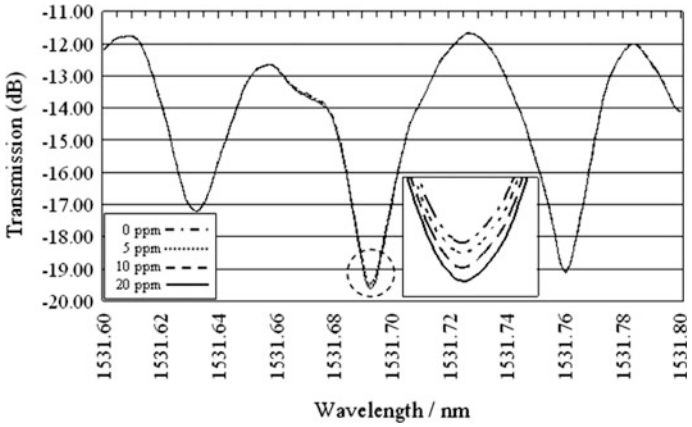

Fig. 12 Comparison of transmission between 0, 5, 10, and 20 ppm NH_3 in PBGF cell at 0.1 atm, set-up with advanced mechanical splicing, 1 m long PBGF spliced to two 1 m long SMFs

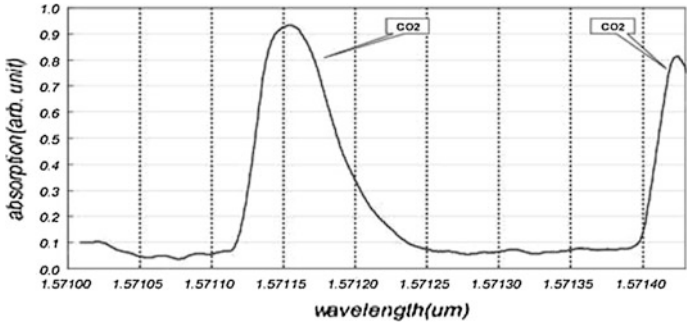

Fig. 13 Absorption spectra of CO_2 measured using photonic fiber cell (length 1 m, gas volume 8×10^{-5}cc, gas concentration about 0.1 %)

Figure 14 shows the normalized transmissions of 0.5–4 % CH_4 gas at 100-kPa pressure, compared with a maximum strength absorption line of 1640.383 nm. It can be noted in the figure that the gas absorptions are visible from 4.5 to 36 dB. The time constants for the filling of CH_4 gas, obtained from the first, are approximately 6 min. Furthermore, the normalized transmission of 10 % C_2H_6 gas at 100-kPa pressure is observed at 1601.3 nm. As shown in Fig. 15, although the absorption of gas is very weak (approximately 0.1 dB), this study has great potential for sensing highly sensitive gas.

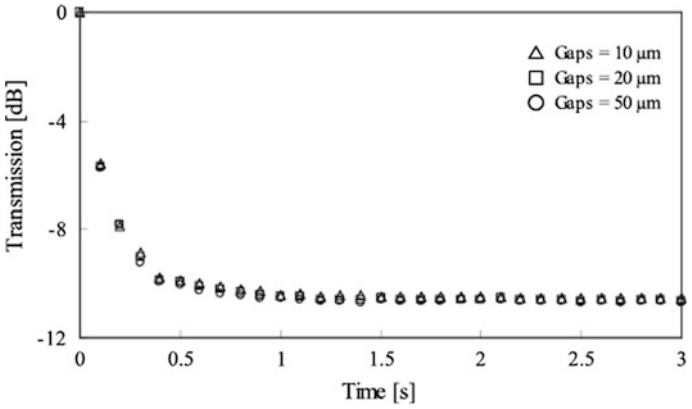

Fig. 14 Normalized transmissions of pure *CH*4 absorption using Tyree 16.5-cm-long HC-150-02 at 1637.68 nm as functions of recording time AT 100-kPa pressure

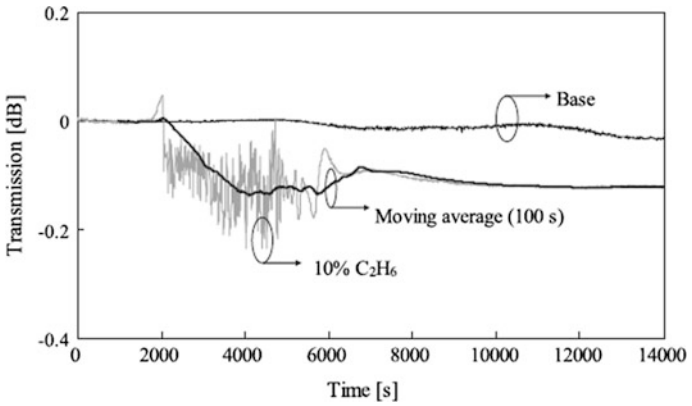

Fig. 15 Normalized transmissions of 10 % *C2H6* gas at 100-kPa pressure and 1601.3 nm

5 Conclusion

The set-up for measuring low concentration of gas concentration of ammonia was designed.

New types PBG fibres were also designed and produced. Simulations of mass flow rate of gas and of gas velocity in dependence on applied pressure and diameter of the optical fiber's core were performed. Gas flow rate in the experimental condition was corresponding to the simulated one. Novel FIB microfabricated splice has been also developed.

It was sufficient for ppm-order measurement using short optic fibres as a gas cells. Experiments for NH_3, CO_2, CH_4 and C_2H_6 measurement were performed.

References

1. E. Yablonovitch, Phys. Rev. Lett. **58**, 2059 (1987)
2. S. John, Phys. Rev. Lett. **58**, 2486 (1987)
3. T. Birks, P. Roberts, P. Russell, D. Atkin, T. Shepherd, Electron. Lett. **1995**, 31 (1941)
4. J. Knight, T. Birks, P. Russel, Opt. Lett. **21**, 1547 (1996)
5. J. Harrington, *Infrared Fibers and Their Applications* (SPIE Press, Washington, USA, 2004)
6. Y. Fink, D. Ripin, S. Fan, C. Chen, J. Joannopoulos, E. Thomas, J. Lightwave Technol. **17**, 2039 (1999)
7. A. Bjarklev, J. Broeng, A. Bjarklev, *Photonic Crystal Fibers* (Kluwer Academic, Dordrecht, The Netherlands, 2003)
8. P. Yeh, A. Yariv, E. Marom, J. Opt. Soc. Am. **68**, 1196 (1978)
9. G. Pickrell, E. Smirnova, in *Proceedings of IEEE Sensors Conference* (Irvine, California, 2005), doi:10.1109/ICSENS.2005.1597801
10. C. Cordeiro, M. Franco, G. Chesini, E. Barretto, R. Lwin, C. Brito-Cruz, M. Large, Opt. Express **14**, 13056 (2006)
11. M. Yan, arXiv:physics/0508139v2 [physics.opticals]
12. J. Laesgaard, A. Bjarklev, J. Am. Ceram. Soc. **89**, 2 (2006)
13. http://www.blazephotonics.com
14. E. Pone, C. Dubois, N. Guo, Y. Gao, A. Dupuis, F. Boismenu, S. Lacroix, M. Skorobogatiy, Opt. Express **14**, 5838 (2006)
15. T. Monro, K. Kiang, J. Lee, K. Frampton, Z. Yusoff, R. Monroe, J. Tucknott, D. Hewak, H. Rutt, D. Richardson, in *Optical Fiber Communication Conference* (OSA Technical Digest Series, Optical Society of Washington, Washington, 2002), p. 70, PD FA1-1
16. M. van Eijkelenborg, A. Argyros, G. Barton, I. Bassett, M. Fellew, G. Henry, N. Issa, M. Large, S. Manos, W. Padden, L. Poladian, J. Zagari, Opt. Fiber Technol. **9**, 199 (2003)
17. T. Ueda, Y. Okamoto, in *Proceedings of 1st Symposium Advanced Photon Processing and Measurement Technology* (1998), pp. 25–28
18. T. Sugiyama, M. Wada, S. Nakajima, T. Ueda, in *Proceedings of 4th Workshop on Advanced Photon Processing and Measurement Technology* (2001), pp. 63–66
19. T. Sugiyama, T. Ueda, in *Proceedings of Technology Meeting on Sensors and Micromachines* (2003), CHS-03-56, pp. 1–4
20. J. Pawl_at, T. Matsuo, T. Sugiyama, T. Ueda, J. Adv. Oxid. Technol. **9**, 150 (2006)
21. J. Pawl_at, T. Sugiyama, T. Ueda, in *Proceedings of 22th Symposium Sensors, Micromachines and Application System* (Tokyo, Japan, 2005), pp. 279–284
22. G. Pickeral, W. Peng, A. Wang, Opt. Lett. **29**, 1476 (2004)
23. V.P. Minkovich, D. Monzo´n-Herna´ndez, J. Villatoro, G. Badenes, Opt. Express **14**, 8413 (2006)
24. S. Li, S. Liu, Z. Song, Y. Han, T. Cheng, G. Zhou, L. Hou, Appl. Opt. **46**, 5183 (2007)
25. T. Ritari, J. Tuominen, H. Ludvigsen, J. Petersen, T. Sørensen, T. Hansen, H. Simonsen, Opt. Express **12**, 4080 (2004)
26. M. Petrovich, A. VanBrakel, F. Poletti, K. Mukasa, E. Austin, V. Finazzi, P. Petropoulos, M. Watson, T. DelMonte, T. Monro, J. Dakin, D. Richardson, in Proceedings of SPIE Opticals East, Boston, USA (2005), pp. 15–29
27. J. Pawłat, T. Matsuo, T. Sugiyama, T. Ueda, Measurement of low gas concentration using photonic bandgap fiber. J.AOTs **9**(2), 150–155 (2006)
28. J. Pawłat, T. Sugiyama, T. Matsuo, T. Ueda, Photonic bandgap fiber for a sensing device. IEEJ Trans. Sens. Micromachines [E] **127**(3), 160–164 (2007)
29. J. Pawłat, T. Matsuo, T. Sugiyama, T. Ueda, Possibility of gas concentration measurement using photonic crystal fiber. Przegląd Elektrotechniczny (Poland) **5**, 31–35 (2007)
30. J. Pawłat, T. Matsuo, T. Sugiyama, T. Ueda, PBG fiber for gas concentration measurement. Plasma Process. Polym. **4**(7–8), 743–752 (2007)

31. J. Pawłat, T. Sugiyama, X. Li, T. Matsuo, S. Ikezawa, T. Ueda, Low concentration gas measurement using photonic bandgap fiber cell sensor. IEEJ Trans. Sens. Micromachines [E] **128**(5), 198–202 (2008)
32. J. Pawłat, T. Sugiyama, X. Li, T. Matsuo, T. Ueda, low concentration gas sensor based on photonic bandgap fiber cell. SPIE newsroom (2007). doi:10.1117/2.1200801.0979
33. J. Pawłat, X. Li, T. Matsuo, T. Sugiyama, T. Ueda, PBG fiber low concentration gas sensor. Solid State Phenom. **144**, 163–168 (2009)
34. J. Pawłat, X. Li, Takahiro Matsuo, T. Sugiyama, Y. Zimin, T. Ueda, High-precision gas sensor based on photonic bandgap fiber cell. Solid State Phenom. **147–149**, 131–136 (2009)
35. T. Sugiyama, T. Ueda, J. Pawłat, Laser spectroscopy of minute amounts of gas using photonic bandgap fiber. IEEJ Trans. Sens. Micromachines **129**(6), 189–193 (2009)
36. X. Li, J. Pawłat, J. Liang, G. Xu, T. Ueda, Fabrication of photonic bandgap fiber gas cell using focused ion beam cutting. JJAP **48**, 06FK05-1–06FK05-5 (2009)
37. J. Pawłat, X. Li, Y. Zimin, T. Sugiyama, T. Matsuo, T. Ueda, Gas sensor based on microstructured optic fiber. Przegląd Elektrotechniczny **5**, 115–117 (2009)
38. X. Li, J. Pawłat, J. Liang, T. Ueda, Measurement of low gas concentrations using photonic bandgap fiber cell. IEEE Sens. J. **10**(6), 1156–1161 (2010)
39. J. Pawłat, X. Li, T. Sugiyama, T. Matsuo, Y. Zimin, Toshitsugu Ueda Sensing of Carbon Dioxide and Hydrocarbons Using Photonic Bandgap Fiber. Solid State Phenom. **165**, 316–320 (2010)
40. S. Ikezawa, M. Wakamatsu, Y.L. Zimin, J. Pawlat, T. Ueda, Multi-spectral analytical systems using LIBS and LII techniques, in *New Developments and Applications in Sensing Technology*, ed. by S.C. Mukhopadhyay, A. Lay-Ekuakille, A. Fuchs. Lecture Notes in Electrical Engineering, vol. 83 (Springer, 2011), pp. 207–232
41. X. Li, J. Liang, T. Ueda, Applied technique of focused ion beam milling based on microstructure of photonic bandgap fiber. Int. J. Adv. Manuf. Technol. **68**, 465–471 (2013)
42. J. Lightwave Technol. **29**(19) (Oct. 1 2011) *U-Band Wavelength References Based on Photonic Bandgap Fiber Technology*, pp. 2934–2939
43. X. Li, J. Liang, T. Ueda, Applied technique of focused ion beam milling based on microstructure of photonic bandgap. Int. J. Adv. Manuf. Technol. **68**, 465–471 (2013)
44. X. Li, J. Pawlat, J. Liang, T. Ueda, measurement of low gas concentrations using photonic bandgap fiber cell. IEEE Sens. J. **10**(6), 1156–1160 (June 2010)
45. IEEE Sens. J. **12**(7) (July 2012) NIR Spectrum Analysis of Natural Gas Based on Hollow-Core Photonic Bandgap Fiber Xuefeng Li, Member, IEEE, Jinxing Liang, Shuo Lin, Yury Zimin, Student Member, IEEE, Yupeng Zhang, Member, IEEE, and Toshitsugu Ueda
46. J.T. Kristensen, A. Houmann, X. Liu, D. Turchinovich, Low-loss polarization-maintaining fusion splicing of single-mode fibers and hollow-core photonic crystal fibers, relevant for monolithic fiber laser pulse compression. Opt. Express **16**, 9986–9995 (2008)
47. H. Lehmann, S. Brueckner, J. Kobelke, G. Schwotzer, K. Schuster, R. Willsch, Toward photonic crystal fiber based distributed chemosensors. Proc SPIE **5855**, 419–422 (2005)
48. Y.J. Rao, M. Deng, D.W. Duan, X.C. Yang, T. Zhu, G.H. Cheng, Micro Fabry-Perot interferometers in silica fibers machined by femtosecond laser. Opt. Express **15**, 14123–14128 (2007)
49. C. Martelli, P. Olivero, J. Canning, N. Groothoff, B. Gibson, S. Huntington, Micromachining structured optical fibers using focused ion beam milling. Opt. Lett. **32**, 1575–1577 (2007)
50. M.Y. Ali, A.S. Ong, Fabricating micromilling tool using wire electrodischarge grinding and focused ion beam sputtering. Int. J. Adv. Manuf. Technol. **31**, 501–508 (2006)
51. Y.Q. Fu, N.K.A. Bryan, O.N. Shing, N.P. Hung, Influence of the redeposition effect for focused ion beam 3D micromachining in silicon. Int. J. Adv. Manuf. Technol. **16**, 877–880 (2000)
52. Y.Q. Fu, N.K.A. Bryan, O.A. San, L.B. Hong, Data format transferring for FIB microfabrication. Int. J. Adv. Manuf. Technol. **16**, 600–602 (2000)
53. K. Dean, R. Carpio, Contamination of positive deep-UV photoresists, in *Proceedings of Interface '94 OCG Microlithography Seminar* (1994), pp. 199–212

54. S. MacDonald, N. Clecak, H. Wendt, C. Willson, C. Snyder, C. Knors, N. Deyoe, J. Maltabes, J. Morrow, A. McGuire, S. Holmes. Airborne chemical contamination of a chemically amplified resist, in *Advances in Resist Technology and Processing VIII*, vol.1466 (Proceedings of SPIE, 1991), pp. 2–12
55. Semiconductor Industry Association International Technology Roadmap for Semiconductors, http://public.itrs.net
56. M. Petrovich, A. VanBrakel, F. Poletti, K. Mukasa, E. Austin, V. Finazzi, P. Petropoulos, M. Watson, T. DelMonte, T. Monro, J. Dakin, D. Richardson, *Microstructured fibres for sensing applications* (Proceedings of SPIE Opticals, EastBoston, USA, 2005), pp. 15–29
57. D. Richardson, F. Poletti, J. Leong, X. Feng, H. Ebendorff-Heidepreim, V. Finazzi, K. Frampton, S. Asimakis, R. Moore, J. Baggett, J. Hayes, M. Petrovich, M. Tse, R. Amezcua, J. Price, N. Broderick, P. Petropoulos, T. Monro, Advances in microstructured fiber technology, in *Proceedings of IEEE/LEOS Workshop on Fibres and Optical Passive Components*, USA, Institute of Electrical and Electronics Engineers (2005), p.1–9
58. L. Rothman, D. Jacquemart, A. Barbe, D. Benner, M. Birk, L. Brown, M. Carleer, C. Chackerian, K. Chance, L. Coudert, V. Dana, V. Devi, J. Flaud, R. Gamache, A. Goldman, J. Hartmann, K. Jucks, A. Maki, J. Mandin, S. Massie, J. Orphal, A. Perrin, C. Rinsland, M. Smith, J. Tennyson, R. Tolchenov, R. Toth, J. Vander Auwera, P. Varanasi, G. Wagner, J. Quant. Spectrosc. Radiat. Transf. **96**, 139 (2005)

Structural Health Monitoring Fiber Optic Sensors

K. Loupos and A. Amditis

Abstract Following the modern technological needs requiring highly increased safety and standards in structures (especially civil) located in densely populated areas with increased seismic activity or other safety critical perturbations, various technologies have been developed, aiming towards improved monitoring requirements, needs for structural performance evaluation and increased safety in general. Fibre-optic technologies provide a lot in the field of structural monitoring as a basis for condition assessment before, during or after a random (e.g. earthquake), human-imposed (e.g. blast) or other operational (e.g. increased load) event. This chapter provides an overview of the structural health monitoring concept and particular requirements per application area, the monitoring systems currently available on the market and a thorough analysis of the fibre optic technologies available today. The chapter starts with the definition of structural health monitoring in terms of the specific industrial needs for monitoring and sensing. It then presents a detailed analysis of the fibre-based monitoring solutions available, their concept of operation and operational (measuring) characteristics and capabilities and closes with a presentation of typical fibre optic installation examples where fibre optics are installed for structural health monitoring.

1 Introduction

1.1 Structural Health Monitoring

By structural health monitoring (SHM) we usually refer to any process or activity relating to damage detection and classification in any engineering structure (civil, energy, aerospace, mechanical etc.). SHM is widely used nowadays as it proves of primal importance for engineers to improve safety and maintainability of critical structures. SHM involves various sensing and/or monitoring technologies and

K. Loupos (✉) · A. Amditis
Institute of Communication and Computer Systems, Athens, Greece
e-mail: kloupos@iccs.gr

© Springer International Publishing Switzerland 2017

I.R. Matias et al. (eds.), *Fiber Optic Sensors*, Smart Sensors,
Measurement and Instrumentation 21, DOI 10.1007/978-3-319-42625-9_9

usually embedded systems able to capture, store and analyse measuring data straight from the structure being monitored. This way the health, operational capability and performance of structures can be assessed through damage classification. Structural health monitoring is usually very associated with damage classification of the structure of interest. This is usually a process following the monitoring task and refers to the determination of damage in the structure that will be used to characterise the whole building regarding its overall operational performance. This also includes safety classification which is in turn used to drive maintenance or safety teams' decision such as the initiation of maintenance activities, the shutdown of the particular section/building etc. recently SHM activities are also closely linked to life-safety and economic benefits that can be enhanced in this aspect [1].

In this framework, the term "damage" is perceived as changes to the physical (geometric) properties of the structures and/or it constituting materials that if modified might affect the overall system stability and thus safety and structural integrity.

Considering civil structure health monitoring, currently we are lacking of quantifiable methods to determine the status of structures after major earthquake or other event that could cause damages to the structure itself. SHM methodologies can be used to determine the status of the structure and thus minimize uncertainties regarding post-event damage assessment. Further to this, SHM methodologies and technologies have a lot to offer in structures undergoing ageing effects. Therefore the ability of monitoring and investigating a structure's health at any time has become extremely important and this is expected to increase more and more over time [1].

SHM activities are implemented on a vast variety of applications, usually critical structures with high safety and reliability requirements.

1.2 Structural Health Monitoring Requirements

Structural health monitoring includes various modules or structural system parts with different monitoring requirements that may depend on operational or other characteristics of the structures themselves. The inspection and maintenance technique that will be used (and is allowed to be used) over such structures depends on the type, performance, safety criticality and ownership while may sometimes be imposed even by law. The largest challenge over real-time monitoring systems is that all these infrastructures are in general unique so per case solutions often need to be investigated [2].

Some of the reasons often leading to the need for structural health monitoring are the following:

- Physical or other alterations to current structure or its parts;
- Structures affected by external or surrounding works or demolitions;

- Critical structures monitoring to ensure flawless operation and performance;
- Monitoring of structural material degradation;
- Structural system assessment after hazardous events;
- Assessment of structure fatigue and system performance;
- Other effects that may question the integrity of the structure.

Some typical applications of SHM are presented in the following table divided per application field (Fig. 1, Table 1).

The selection of the most appropriate sensing technology requires a close investigation of the following parameters required by each industrial application:

- **Measuring scale**: this would require defining the minimum and maximum stress or strain that needs to be measured and would significantly direct towards the available sensing devices, elements and systems.
- **Measuring accuracy**: that defines the accuracy that the monitoring system should have. This is usually expressed in μStrain.
- **Measuring speed**: that defines the time lapse of the monitoring samples that the sensing system will acquire from the structure.
- **Spatial Resolution**: that defines the density of the sensing points on the actual structure. Some monitoring requirements may pose for dense or more spatial separated sensing positions.
- **Hazard-ness of monitoring structure**: a possible hazardous environment would reject some types of monitoring that are not qualified for use in such environments (most of the times due to EMC reasons).

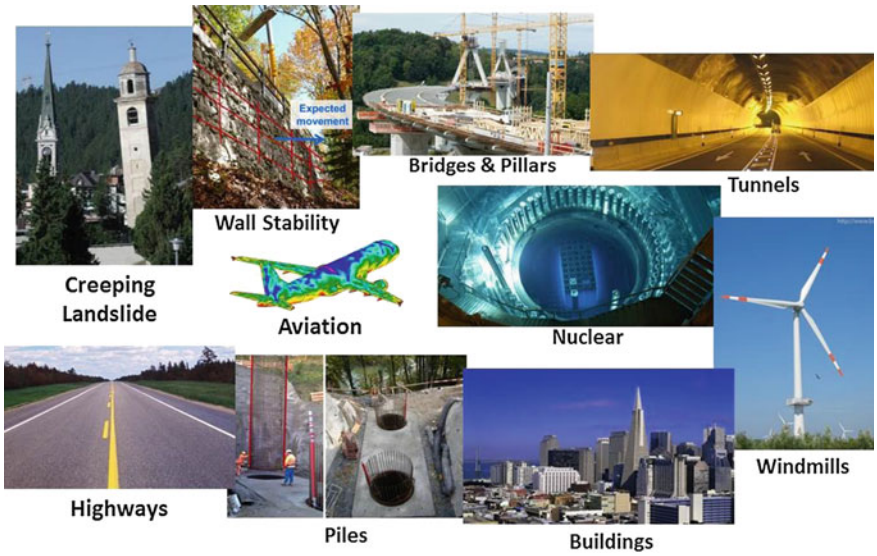

Fig. 1 Applications of structural health monitoring

Table 1 Indicative SHM applications

Application domain	Structure types
Civil infrastructure	• Critical civil buildings • Stadiums • Dams • Ports • Hospitals • Historical structures
Road transport	• Bridges • Tunnels • Highway fragments
Aerospace	• Airports • Aircraft structures (wings etc.)
Energy	• Wind turbines • Oil/gas platforms • Power plants
Mining	• Mining Shovels
Life line	• Water plants • Pipelines
Earth	• Land monitoring • Shores • Other terrestial
Marine	• Port/shores • Ships/yachts • Cargo vessels
Other industry	• Large Machinery • Other equipment

- **Power consumption**: this might also restrict monitoring options defined by the presence of electricity (and types) at the monitoring site.
- **Portability of sensing system**: this would again define the portability (e.g. hand held etc.) of the monitoring system.
- **Installation restrictions**: that would be defined from the ability and restrictions that we may have for the installation of the monitoring system on-site (e.g. space available, connectivity etc.).
- **Cost**: cost considerations for the purchase of the monitoring system, sensors, accompanied software and maintenance should be considered here.

2 Structural Health Monitoring Systems

2.1 Structure-Installed Monitoring Systems

By the term "site-specific" we consider the monitoring systems that are embodied on the structure of interest. Usually they are supported by some interrogation

instruments installed locally or remotely but the difference of these sensors is that they are physically located at the positions of interest on the actual monitored structure. A summary of the existing systems has been included below.

2.1.1 Strain Gauges and Accelerometers

Strain gauges (or strain gages) are devices used very widely in SHM applications. Their most common configuration consists of a metallic foil pattern fixed on some insulating flexible backing. The gauge is usually glued on the position of interest and follows its deformation. As the gauge is deformed, its resistivity changes and thus we are able to correlate this change of resistivity to actual spatial deformation. The resistance is usually measured using a Wheatstone bridge. Strain gauges are used very widely as the sensing elements for structural health monitoring due to their low cost, ease of installation but also high sensitivity in detecting structural deformations of civil or other structures. Strain gauges are most of the times connected with wired or wireless systems increasing their total cost and sometimes restricting their operational (measuring) performance [1]. The combination of strain gauges with acceleration sensors has proved beneficial for SHM applications where the overall structure assessment is of interest.

2.1.2 Fibre Optics Systems

The principle of operation of Fibre Optic (FO) systems used for SHM applications relies in the measurement of deformation of simple (and cheap) telecommunication fibre optic cables. FO systems are currently widely used due to their ease of installation, low price (for installation and maintenance) as well as being often associated to long-time monitoring capabilities. FO sensors are also more durable, stable to sensitivity and insensitive to outside perturbations (EMC etc.). FO systems can be divided into point and distributed sensing, the latter making the system more attractive for spatial monitoring of structures (i.e. measurements along their whole cable length) that has opened a new dimension into structural monitoring. The technology is based on Raman and Brillouin light scattering that make use of the non-linear relation between the light that is passed through the FO cable and the surrounding silica material. By passing light of known wavelength through a FO cable and measuring the scattered light (wavelength difference from initial pulse) we are able to acquire the physical properties of the fibre itself and thus correlate this to structural deformation [3].

2.1.3 Micro-Electro-Mechanical Systems (MEMS) Sensors

Micro-electro-mechanical systems (MEMS) are assimilated devices or systems that integrate electrical and mechanical components for sensing as well as controlling,

movement, actuating etc. MEMS can be forming various sensing components such as accelerometers, gyroscopes, strain gages, pressure or flow sensors and many more. Their concept of operation relies in the piezo-resistive effects of silicon and germanium [4]. MEMS sensors are usually quite smaller in size while can be found in low price and are generally low power and easily integrated.

2.1.4 RIFD Tags

Radio-frequency identification (RFID) tags are quite often used for structural health monitoring applications. To solve power requirement issues usually passive RFIDs are being used. However due to the fact that RFIDs can only drive imperceptible power devices (temp sensors etc.) they are not being directly used to sense deformation but are used to accurately localise particular positions of the structure and thus provide feedback on the relative positions of particular structure sections or positions of interest. There are recent works that have combined RFID tags with measuring sensors (similar to gauge) but these types are considered of low technology readiness and are rarely used in application specific case.

2.2 Site-Installed Monitoring Systems

With on-site monitoring systems we consider the monitoring systems that are used at the structure during the inspection time and require measuring apparatus to be present. This includes laser, radar, acoustic sensing and infrared spectroscopic techniques. A summary of each system has been included below.

2.2.1 Laser Systems

Non-contact laser systems are being also very extensively used in SHM applications whenever Non-Destructive-Testing (NDT) is required. Such laser systems operate via an excitation using pulse and continuous laser and their sensing capabilities are based on laser interferometry and/or Laser Doppler Vibrometers (LDV). Such systems are usually used for applications where no actual surface contact is possible (or not allowed) but are usually more expensive systems and their operation is most of the times prohibited for applications with high safety standards (e.g. nuclear reactors, gas/oil tanks etc.). These systems are often supported with some user interface that represents to the user the measurement results in simple form or can be parts of assessment interfaces that also create 3D representations of the structure.

2.2.2 Microwave Radar and Ground-Penetrating Radar (GPR)

Ground Penetrating Radar systems are also often used in SHM applications. GPR techniques involve the emission of electromagnetic emission (EM) towards the structure surface and analysis of the reflected signal (timing, strength, phase etc.) that can define the structure characteristics and properties. This usually involves a variety of waver forms (e.g. pulses, sine-waves etc.) and frequencies (1–10 GHz) depending on the structure material and depth of interest, known also as Ultra-Wide-band (UWB) technologies. The primal advantage of this technique is that they can provide information inside the structure (endoscopic SHM). A major disadvantage of such technologies is that due to electromagnetic emission they usage is prohibited in hazardous environments (nuclear plants, oil/gas tanks etc.).

2.2.3 Acoustic Emissions

Acoustic emission systems are used quite widely in SHM applications. Their operation relies on the discovery of discontinuities in structure release energy as a result of exercise of load (or stress). This energy is transmitted into high-frequency waves (vibrations) that are captured by transducers for processing. This is based on the usage of piezoelectric sensors of the range 20 kHz–1 MHz to measure responses in all directions. This methodology can offer information on the origin of these discontinuities as well as the development of flaws when continuous loads/testing are applied. This methodology can also be applied to inspection of larger areas in order to detect cracks and defects, however it is not appropriate for locating multiple damage positions. It is also affected by surrounding noise that can interfere with the measurements. Therefore these technologies are often combined with other SHM technologies to localise and measure the defective areas (and damage).

2.2.4 Imaging Type (X-Ray, Gamma Ray, Nuclear Magnetic Resonance (NMR), Ultrasonic etc.)

Imaging methods such as X-ray radiographic, Gamma Ray and Nuclear Magnetic Resonance (NMR) are also being used in cases that require damage identification in depth. Such technologies use high-frequency rays as the above and identify the damage based on their absorption and reflection. These systems can be used to quickly check larger surfaces but are very costly are much less sensitive and accurate and are usually prohibited in high safety areas.

2.3 Distant-Sensing Systems

2.3.1 Photogrammetric

Photogrammetric or optical imagery methodologies use camera images to create accurate 3D measurements of complex structures or objects. This methodology can prove very flexible especially when quick and inexpensive solution is seeked while can also deal with long-term monitoring tasks and can be fully automated. In such applications the accuracy and precision of the detected and reconstructed 3D images highly depends on the visual capabilities of the camera systems being used. It has been proved that for high accuracy higher quality lenses and more detailed (in terms of megapixels) images are needed [5].

2.3.2 Infrared Thermography

Infrared thermography is a technology that detects infrared energy transmitted from objects capturing the temperature distribution along the whole excitation surface. Such techniques for SHM are performed in distance to the structure surface and can be used to detect thermal phenomena associated to the structural deformation of structures. They are also widely used to detect leakages or other defects related to SHM. Infrared thermographic techniques allow for comparison of the surface distribution of temperature over wide areas and are considered as generally easy methodologies. However they are not directly linked to structural health monitoring rather than the thermal/temp effects of the structure deformations. This is why such technologies are often used in comparison with other SHM methodologies.

2.4 Fibre Optics Compared to Conventional Monitoring Techniques

Fibre optics technologies can be regarded as the ideal sensing elements for structural health monitoring especially of civil infrastructures. Fibre optics offer immunity to electromagnetic interference, can measure spatial deformations of structures while can also measure point deformations, can combine temp and strain/stress at any point in length of the installed cable and can provide their monitoring services with cables up to 30 km. In comparison to gauge type sensors that can provide only point measurements and can be subject to electromagnetic interference issues they have proved to be a robust and precise solution. Overall it can be said that fibre optics sensing can provide significant value due to improved quality of measurements, increased reliability and can most of the times replace

Table 2 Pros and cons of sensing technologies

Sensing technology	Advantages	Limitations
Gauge type	• Point measurement • High precision • Low price • Low power	• Not immune to electromagnetic interference • Only point measurements
Fiber optics	• Immune to electromagnetic interference • Can measure spatial deformations • Combine temp and strain/stress at any point in length of cable • Cables up to 30 km can be used • Low signal transmission losses • Corrosion free	• Lower precision of measurement • No point measurement • Can break in larger deformations (>10 %) • Communication is lost after breaking point • Decoding of signal/data required
MEMS	• Smaller size • Low power • Highly integrated • Low price • Very small size • Non-contact communication	• Sometimes not immune to electromagnetic interference
RFID tags	• Can be very low power • Passive operation • High location accuracy	• Do not usually measure stress or strain directly
Imaging	• Can see structure in depth	• High cost • No onboard use
Laser	• No sensor placement • No baseline data required • Less vulnerable to false alarms • Non-intrusive • Easily deployable • Less maintenance needed	• Limited sensitivity • Expensive • Considered hazardous for safety critical cases • Limited operation in harsh surfaces • Larger spatial resolution (can be improved)
Ground penetrating radar	• Investigation in depth • Material type detection • Quick for larger areas	• Prohibited in hazardous environments • Lower precision and accuracy
Acoustic emission	• Can identify severity of damage • Measurement accuracy	• Not suitable for large area detections • Usually combined with other SHM for damage localization • Not immune to noise • Difficult repeatability of measurements
Imagery	• Fast defects detection • Can be very accurate • No contact with structure needed	• High accuracy requires longer inspection • Might require training

Table 3 Comparison of sensing/monitoring technologies

	Gauge	MEMS	FBG	Brillouin	Laser	Photo-Grametry
E/M interference	Very sensitive	Very sensitive	Not sensitive	Not sensitive	Not sensitive	Not sensitive
Spatial resolution	Point	Point, non-linear	Point	1 m (usually reduced)	0.2 mm (could be reduced)	1 mm
Max strain	~6000 με	~10–15000 με	~10–15000με	~10–15000 με	Converted from distance	Converted from distance
Cost/sensor	Cheap	Cheap	Cheap	Cheap	60–150 k€	10 k€
Interrogation/acquisition cost	2–5 k€	2–5 k€	10–20 k€	**200** k€ (slower acq.)	–	–
Acquisition time	Instant	Instant	Instant	Near-instant (in high length)	Slow, post-processing needed	Fast, post-processing needed
Data size	Very small	Very small	Small	Large	Huge	Huge
Installation	In contact, rust prone, difficult post-inst.	In contact, rust prone, Difficult post-inst.	In contact, difficult post-inst.	In contact, difficult post-inst.	Visual (surface measurement)	Visual (surface measurement)
Special needs	Need amplification/buffer	Need amplification/buffer	Sensitive, difficult to glue	Sensitive, difficult to glue	Quite slow (20 min per cm slice)	Needs proper lighting

other types of sensors (gauge etc.) [6]. When FO sensors are supported by high-power tunable laser systems, they can provide measurements over very large distances with very little signal loss. On top of this, each interrogator channel can measure dozens of FBG sensors (through multiplexing) reducing the size and complexity of the measuring system.

What follows is a comparison of the available sensing technologies that can be used for structural health monitoring (Table 2).

Optical sensing can be an ideal sensing solution especially for cases when other sensing devices (gauges, piezoelectric etc.) prove not appropriate or ineffective. Good examples are limitations due to environmental conditions, long distance measurements, electromagnetic interference etc. What follows is a summary table comparison of the currently available sensing technologies, their technical specifications and operational characteristics (Table 3).

3 Fibre Optic Monitoring Systems

Cost reduction in the telecommunication wires has significantly paved the way for stronger and wider usage of fibre optic monitoring systems. This is enhanced by the higher demands of current structures for precise and real-time technologies and inspection/monitoring methodologies and configurations. This technology can be ideal for the constructions sector directly improving current structural monitoring systems or being applied as a stand-alone, real-time monitoring technology.

The concept of operation of Fibre Optics, as monitoring technologies, relies on the light intensity inside the fibre that decreases in cases when the fibre is stretched or compressed. This, following signal processing and decoding, is translated into deformation that informs for elongation or shortening of the attached structural piece. This has to follow a temperature calibration so that the deformation (and light change) can be compared to the one found in an uncompressed fibre (at the same temperature).

To make the monitoring (measuring) possible, special instruments such as the Optical Time-Domain-Reflectometer (OTDR) are being used to characterise the optical fibres. These metering instruments induce a pulse series into the measuring fibre and compute the back scattered (Rayleigh backscatter) light that is reflected from the fibre.

What follows is an OTDR measurement indicating the power loss across the fiber length. OTDR reveals that the fiber length has been optimized with respect to the reflections occurring at connectors, thus minimizing the power losses [7] (Fig. 2).

The correctness and dependability of OTDR equipment replies on the instrument accuracy, range that it can measure, resolving and measuring capability of closely spaced occurrences, speed of measurement and their ability to operate under harsh

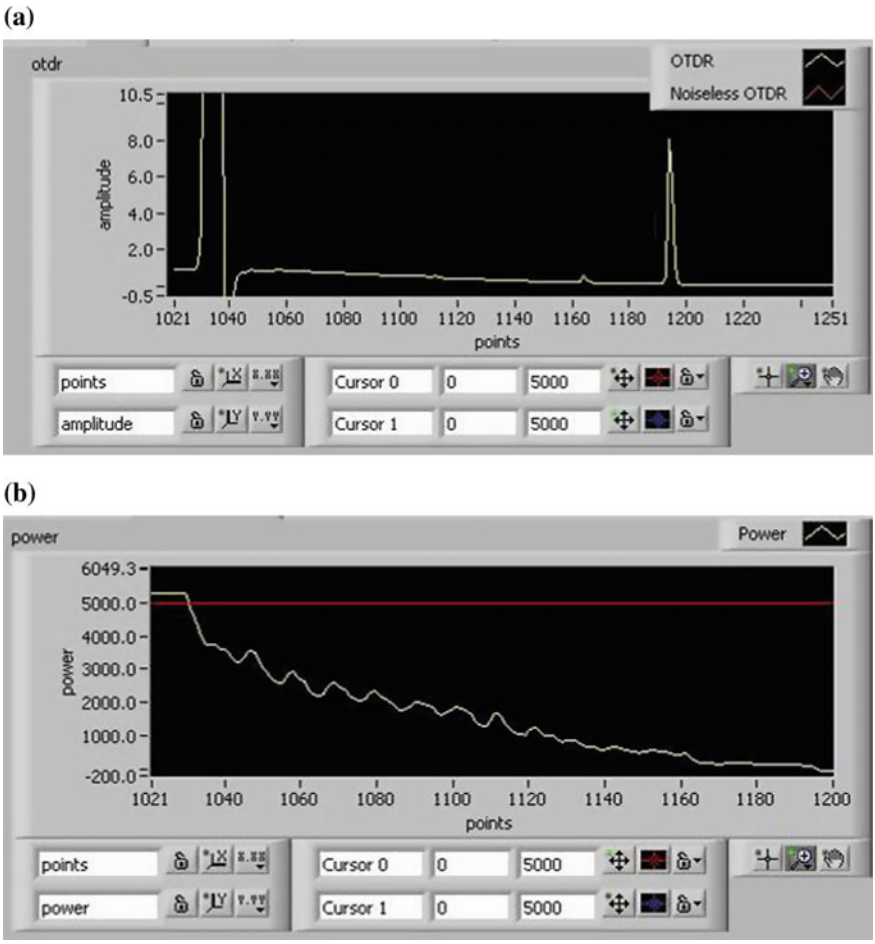

Fig. 2 **a** OTRD measurement **b** optical power versus fiber length [MONICO (FP7) EC co-funded research project] [7]

conditions. In terms of accuracy we define the difference between the real (actual) value and the measured value. By measuring range we define the maximum attenuation of the transmitted signal between the measuring point and the (pulsing) instrument (this should be inside acceptable accuracy limits so the measurement is valid). By instrument resolution we define the minimum distance that two measurements could have and still being considered and analysed as two distinct measurements.

Fibre optic systems can be distinguished between FBG (Fibre Brag Grating) and BRILLOUIN as the two relevant but still different technologies and concept of operation as presented in the paragraphs that follow.

3.1 Brag Grating Fibre Sensors

Fibre Brag Grating are produced by exposing the core of the fibre cable to extreme ultra-violet light that causes the material to increase its refractive index and thus create a fixed index modulation that is called grating. The grating (used as a refractive index) has been created in such a way so that only particular wavelengths are reflected while the rest of the light wavelengths are passing through the grating without attenuation (brag condition). This enables only particular wavelengths to be fully reflected backwards and measured by the OTDR instrument (Fig. 3).

FBG sensing technologies are used in a large variety of sensing applications that include monitoring of civil structures (highways, bridges, buildings, dams, etc.), smart manufacturing and non-destructive testing (composites, laminates, etc.), remote sensing (oil wells, power cables, pipelines, etc.), smart structures (airplane wings, ship hulls, buildings, sports equipment, etc.), as well as traditional strain, pressure and temperature sensing. The advantage of FBGs is that these devices perform a direct transformation of the sensed parameter to optical wavelength, independent of light levels, connector or fiber losses, or other FBGs at different wavelengths [8].

Typical applications of FBG sensors range in a very large spanning in structural assets monitoring starting from civil engineering, marine, airspace up to health applications. The strain range of typical FBG sensors range in ±15000 με (μStrain) with an approximate resolution of 1 με. FBG sensors can also be used a temperature monitoring sensors with a maximum temperature range of −50–120 °C and a resolution of 0.1 °C.

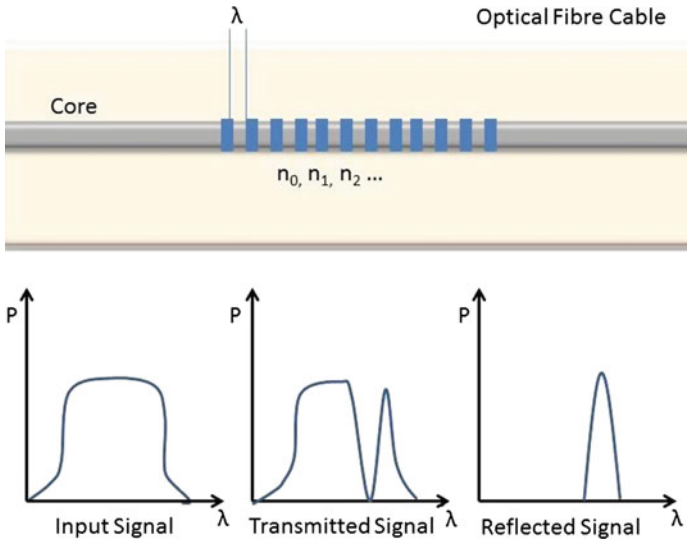

Fig. 3 Fiber brag grating and refraction signals

Table 4 Indicative FBG vendors

Vendor	Equipment	Country
Micron optics	FBG sensors, packagings, glueing, mounting, software	USA
FBGS	High-stength FBG sensors, packagings, glueing, mounting, software	Belgium
AOS-Fiber	FBG sensors, interrogation systems, software	Germany
Proximion	FBG sensors, monitoring systems, analysis software	Sweden

There are noumerous manufactures and vendors of FBG fibre optics sensors and sensing systems (interrogators, analysis software etc.). Some indicative vendors have been included below. This has been added for reference and completeness purposes only (Table 4).

Some typical characteristics of FBG sensors are included (Table 5).

The installation of FBG sensors is usually done on the structure surface while it can also be done on the structure rebars (for civil structures) as shown in the figure below. The positions of the FBG sensors can be recognised by the white coating. What is importance in this installation is to ensure that there is no slippage of the sensor and the sensor coating (if present) follows the structure deformation (Fig. 4).

Table 5 FBG sensor specifications

Max strain	±15000 με (μStrain)
Accuracy	1με (μStrain)
Operational temperature	−50–120 °C
Temperature resolution	0.1 °C
Other	Point sensing

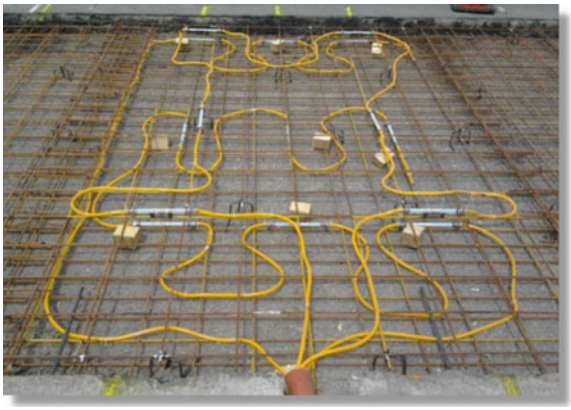

Fig. 4 FBG sensors mounted on civil structure rebars

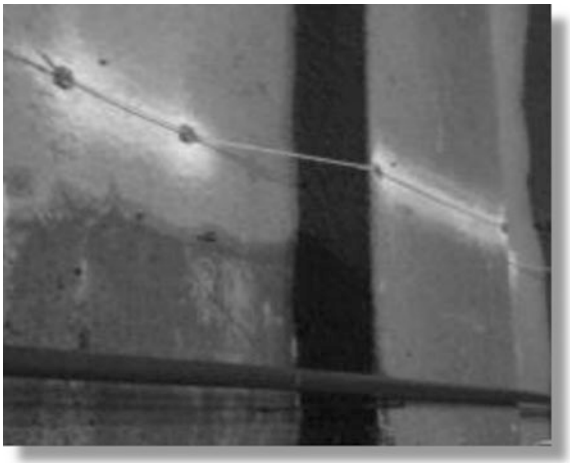

Fig. 5 Distributed sensing cable installed on tunnel wall [SMARTEC, Switzerland]

3.2 Distributed Fibre Sensors

In difference to point sensing technologies (Gauge, FBG, etc.), distributed sensing offers unique characteristics in being able to measure physical parameters along their whole length with a single transducer [3]. The two most complete technologies related to this methodology are the Raman and the Brillouin scattering. The concept of operation of both systems relies on the back scattering of light through the fibre optic medium and its change in wavelength and power in comparison to the original signal transmitted. This enables the interrogation system to provide information on the local properties of the fibre like exercised strain and temperature.

The figure that follows shows the distributed fibre sensing cable as installed on a tunnel wall in Spain (Fig. 5).

3.2.1 Brillouin-Type Distributed Sensors

By the Brillouin optical time domain reflectometry (BOTDR) we consider the most frequently used distributed sensing technique for strain and temperature along arbitrary regions of the optical fibre. With Brillouin scattering we consider a fundamental process of inelastic light scattering occurring due to interaction of light with acoustic waves inside the optical medium. The back-scattering property of light during the Brillouin process is shifted from the frequency of the incident light in proportion to the strain and temperature at the particular point. The Brillouin system requires a suitable interrogation unit to excite the fibre and collect back-scattered light. This is a sophisticated detection device able to measure these frequencies arising from the detuning of the incident and backscattered light.

Table 6 Brillouin sensor specifications

Max strain	±15000 με (μStrain)
Accuracy	1με (μStrain)
Range	Up to 50 km
Sampling rate	~1 Hz
Spatial resolution	1 m
Operational temperature	−50–120 °C
Temperature resolution	0.1 °C
Other	Distributed sensing

Through this frequency shift the system extracts the magnitude of strain and temperature. The location of the strain is calculated from the round-trip time of light (Table 6).

The graph below includes a typical measurement of a Brillouin system. This graph indicates a varying stress on the fibre length (represented in seconds—x axis) at seven points. As can be seen different strains are measured at multiple positions of the fibre. Different strains in the range of −2000–5000 μStrain can be seen (y-axis) (Fig. 6).

As mentioned above, the spatial resolution of the Brillouin system is of 1 m. There are several methodologies to reduce this resolution for cases that lower resolution is needed. One of the most common workarounds has to do with rolling of the optical fibre into parts to reduce the part of the fibre over a particular (smaller) section and thus be able to shrink the mean measurement in smaller parts of the structure. What can be seen below is this solution applied to a test tunnel perimeter

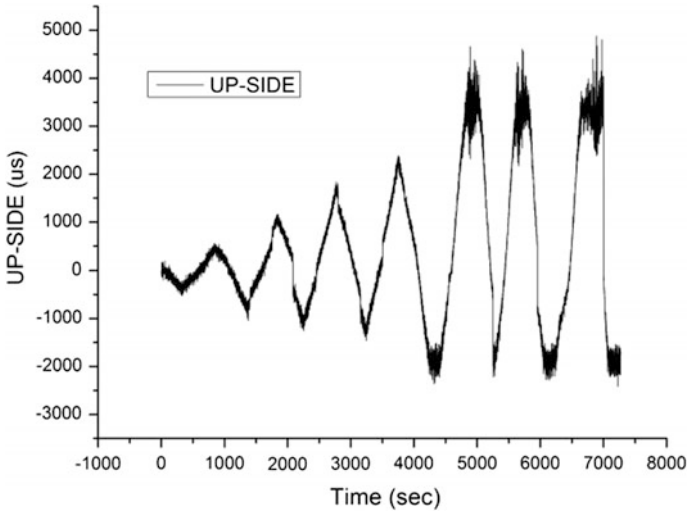

Fig. 6 Measurements of 7 Brilloun sensors as installed at experimental tunnel perimeter in the framework of the MONICO (FP7) EC co-funded research project [7]

Fig. 7 Brillouin Sensors installed at test tunnel perimeter. MONICO (FP7) EC co-funded research project [7]

Table 7 Raman sensor specifications

Range	Up to 8 km
Spatial resolution	1 m
Operational temperature	−50–120 °C
Temperature resolution	0.1 °C
Other	Distributed sensing

that was constructed, sensorised, deformed and measured at the MONICO (FP7) EC co-funded research project (Fig. 7).

3.2.2 Raman-Type Distributed Sensors

Raman sensing systems are slightly different technology systems for distributed temperature sensing. This technology is based on the Raman scattering as a non-linear interaction between the light in the fibre and the fibre surrounding coating [3]. In such systems, the intensity of the light is calculated and defines the local temperature of the fibre. Systems based on Raman scattering are currently commercialized by SMARTEC (Switzerland), Sensornet and Sensa (UK) [3] (Table 7).

4 Application Examples of Structural Health Monitoring Sensors

In this chapter we present some examples of gauge, FBG and Brillouin sensors installed at various structures in research and industrial levels. Details on the peculiarities of each system are also discussed per case.

4.1 Installation of Gauge-Type Sensors on Building Piers

In the figures below, we can see the installation of gauge-type sensors as installed on the piers of a civil building. This work has involved the development and evaluation of strain sensors in an actual newly constructed building in the framework of the MEMSCON [212004-FP7-NMP], 2009–2012, research project that was coordinated by the Institute of Communication and Computer Systems (Greece). In this particular installation, strain sensing of the rebars of the building was required. The installation included surface cleaning of the rebars and gluing of the gauge sensor on each rebar (lower parts). The sensors were connected to a monitoring embedded system that was able to collect the data from each sensor and transmit all measurements to a consolidation Decision Support System for post-processing (Fig. 8).

4.2 Installation of FBG and BRILLOUIN Sensors on Tunnel Test Ring

In the research work presented below, two evaluated and combined fibre optics technologies (i) Bragg grating, (ii) BOTDR principle for continuous tunnel monitoring were installed, tested and evaluated. The MONICO project was an EC FP7 co-funded "Specific Targeted Research Project" (STREP) under the capacity "Research for the benefit of SMEs". The project was active from October 2008 until March 2011 and was coordinated by the Institute of Communication and Computer Systems (Greece). In MONICO, a large scale specimen was developed with an outer diameter of 483 cm; inner diameter of 443 cm and thickness of 20 cm to simulate the section of a tunnel. In order to simulate representing seismic forces on

Fig. 8 Gauge-type sensors installed on civil structure pier. Work executed in the framework of the EC co-funded project "MEMSCON" [FP7-NMP]

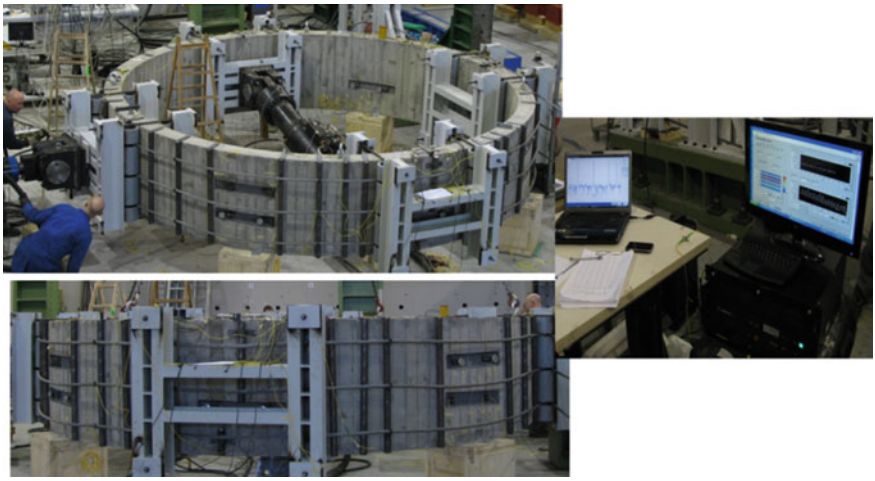

Fig. 9 FBG and BRILLOUIN sensors installed on test tunnel ring [9]

the tunnel, two actuators placed vertical to each other, were used. ECCS procedures of 1986 were used for the cyclic tests and the loading protocol was proportional to a conventional displacement δy which represents the elastic-plastic transition of the cross section. The two technologies were evaluated, validated and tuned on the tunnel circumference in 8 points. This sums to a total of 48 fibre sensors installed (32 FBG, 16 BRILLOUIN) in the outer and inner tunnel surface. In Fig. 3 we can see the tunnel ring before and after the casting. In the figures below the test tunnel ring is presented with both systems installed and simultaneously monitoring the ring deformations [9] (Fig. 9).

In the diagram below we can see the 6 cycles of the dynamic loading in the section-8 of the tunnel ring. At time 7500 s we can observe the concrete failure. As we can see above, there is a very good correlation of both technologies results, monitoring the tunnel ring behaviour. The Brillouin technology can directly be compared to the FBG but provided high noise levels at high strains (Fig. 10).

4.3 Installation of Fibre Optic Sensors for Large Structures' Real-Time Monitoring

The application of fibre optic monitoring systems can prove ideal for cases when monitoring of large infrastructures is required. In the particular case below, the Donghai Bridge—Shanghai/Yangshan, China is monitored. The bridge has a total length of 32 km, a navigation height of 40 m and navigation capacity of 5kt. In this particular case, due to the scale of the structure, the limited spatial resolution (1 m) of the Brillouin system used was not of great importance (Fig. 11).

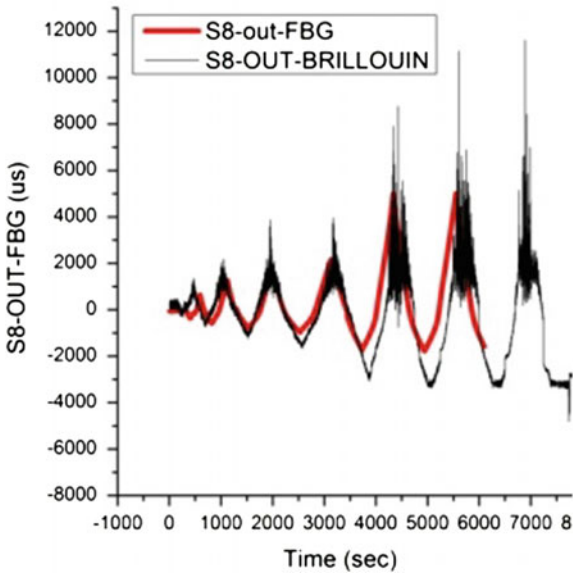

Fig. 10 FBG and BRILLOUIN Measurements for the whole experiment [9]

Fig. 11 Donghai Bridge—Shanghai/Yangshan, China

In this example the monitoring needs included monitoring of the bridge due too: temperature changes, high winds, erosion of the Chloride ion, waves, deformations due to loads, stresses (expected and not), structure dynamics (due to operational loads), lengthy cable tensions as well as displacements of dampers.

5 Conclusions

There is a high need for advanced monitoring of critical structures with increasing safety requirements. This has paved the way for the development and application of technologies that can perform seamless monitoring of these structures and either reporting periodically to an integrated decision support system or being used per case.

The usage of fibre optics as sensing elements for SHM has proved to be a very reliable methodology for a wide range of applications and physical scales. The nature of installation of these sensors proves their application even in difficult to access sections by conventional measurement tools. A good summary indicating the attractiveness of the fibre optics for SHM is their functionality serving as telecom means as well as strain and temperature measurement elements, their reliability (not being affected by weather and electromagnetic turbulences) and their passive nature (need only interrogation at one side (end) of the cable) not forgetting the capability of fibre optics to also operate as point sensors.

Currently the most appropriate sensing/monitoring solution is being selected from a large pool of available technologies depending on the particular peculiarities of the structural application. These can be point, spatial or distributed sensing solutions but they in any case depend on the nature of the structure under monitoring needs and the magnitude of monitoring desired/required.

References

1. K. Loupos et al., fibre optic technologies for tunnel structural monitoring—the MONICO EC Project, in *4th International Conference on Sensing Technology (ICST 2010)* (Lecce, Italy, 2010)
2. K.Loupos, G.Kanellos, O.Bursi, S.Frondistou, J.Meisner, D.Bairaktaris, A.Orfanoudakis, Application of fibre-optic technologies for real-time structural monitoring—The MONICO EC project, in *9th international conference on damage assessment of structures (DAMAS)* (Oxford, 2011)
3. D. Inaudi, B. Glisic, Application of distributed Fiber Optic Sensory for SHM, in *2nd International Conference On Structural Health Monitoring of Intelligent Infrastructure (SHMII-2)* (Shenzen, China, 2005)
4. J. Meyer, R. Bischoff, G. Feltrin, Microelectromechanical Systems (MEMS), *Encyclopedia of Srtuctural Health Monitoring* (2009)
5. E. Protopapadakis, C. Stentoumis, N. Doulamis, A. Doulamis, K. Makantasis, K. Loupos, G. Kopsiautis, A. Amditis, Autonomous robotic inspection in tunnels, in *XXIII International Society for Photogrammetry and Remote Sensing (ISPRS)* (Prague, 2016)
6. D. Inaudi, Overview of fibre optic sensing to structural health monitoring applications, in *International Symposium on Innovation and Sustainability of Structures in Civil Engineering* (Nanjing, China, 2005)
7. MONICO EC Project, D1.3—Embedded Deformation Sensors Evaluated at the Structural Lab and Refined (MONICO, 2011)

8. K. Loupos, G. Kanellos, O. Bursi, S. Frondistou, J. Meisner, D. Bairaktaris, B. Griffoni, A. Orfanoudakis, Real-time structure monitoring using fibre-optic technologies - MONICO EC Project, in *Engineerign Structural Integrity Assessment from plant and structure design, maintenance to disposal (ESIA11)* (Manchester, UK, 2011)
9. K. Loupos, G. Kanellos, M. Bimpas, A. Amditis, O. Bursi, S. Frondistou, J. Meisner, D. Bairaktaris, V. Kallidromitis, B. Groffoni, A. Orfanoudakis, Fiber sensors based system for tunnel linings' structural health monitoring, in *SMAR 2013* (Istanbul (Turkey), 2013)

Brillouin Distributed Temperature Sensor Using Optical Time Domain Reflectometry Techniques

Himansu Shekhar Pradhan, P.K. Sahu, D. Ghosh and S. Mahapatra

Abstract This paper presents the performance improvement of Brillouin distributed temperature sensor (BDTS) using deconvolution algorithm. We have analysed three different OTDR techniques in terms of spatial resolution improvement using Fourier regularized deconvolution (FourRD) algorithm. The effects of coherent Rayleigh noise (CRN) on temperature and spatial resolution of the above system are being investigated. In this paper, using a light source of power 10 mW and 400 ns pulse widths; a spatial resolution of 25 and 20 m is observed for a pseudorandom coded BOTDR in the presence and absence of CRN respectively. Similarly, in case of conventional BOTDR and coherent BOTDR system in the presence of CRN, the spatial resolutions observed are 40 and 35 m respectively. Numerical simulation results indicate that the pseudorandom coded BOTDR is a better candidate for design of BDTS in terms of spatial resolution as compared to the other two schemes as discussed above.

1 Introduction

In recent years fibre sensors are become increasingly important and in demand for monitoring civil, medical, industrial and military applications as well as in oil and gas industries [1, 2]. Fibre optic sensors systems not only provides information about several environmental parameters such as position, strain, temperature, pressure, humidity but also about other ecological parameters. Particularly in oil and gas well applications, fibre sensor is commonly used for monitoring temperature variations in order to improve the extraction of oil and gas. The reliability of conventional electrical sensors decreases under harsh environmental condition and

H.S. Pradhan · P.K. Sahu (✉) · D. Ghosh
School of Electrical Sciences, IIT, Bhubaneswar, Odisha, India
e-mail: pks@iitbbs.ac.in

S. Mahapatra
Department of E&ECE, IIT, Kharagpur, WB, India

© Springer International Publishing Switzerland 2017

I.R. Matias et al. (eds.), *Fiber Optic Sensors*, Smart Sensors,
Measurement and Instrumentation 21, DOI 10.1007/978-3-319-42625-9_10

creates the possibility of an explosion inside the oil or gas wells. However, fibre sensors could offer high reliability due to their passive in nature for in-well applications. Nowadays, most of the commercialized fibre sensors are intrinsic in nature. Distributed fibre sensors are more attractive toward sensing applications in recent years due to a number of advantages such as; intrinsic sensing ability, distributed sensing ability, stable and high repeatable performance. Distributed sensing system is regarded as a cost-effective as well as flexible solution because of the reason that the sensing element is the optical fibre itself, which is cheap, light weight, free from ground loop, free from electromagnetic interference (EMI) [3, 4]. Due to the above advantages, a considerable attention has been paid by researchers and industries to develop distributed fibre sensor for various applications. In 1985, Dakin et al. demonstrated a Raman temperature measurement system [5]. Raman scattering based temperature sensor are widely in use because of ease of Raman signal separation. However, because of weak Raman anti-Stokes Raman backscattered (30 dB weaker than the Rayleigh backscattered signal) a sophisticated detection system. Because of the above limitation researchers started working in the area of Brillouin scattering based distributed sensor. In 1989, T. Horiguchi et al. reported a strain measurement system [6] and D. Culverhouse et al. reported a temperature measurement system based on based on frequency shift of Stokes Brillouin backscattered signal [7]. After their reported work, researchers and the industries developed Brillouin scattering based distributed fibre sensors due to the following reasons: Brillouin based distributed sensors are sensitive to both strain and temperature. Strain is a very important parameter in connection with the reliability of the sensing fibre itself and in addition to its use for monitoring the integrity of large structures such as dams, bridges, important civil and military structures etc. The Brillouin technique offers the potential for long-distance measurement as compared to Raman technique as the Brillouin frequency shift is about 10 GHz and hence the minimum loss wavelength region of the 1550 nm band can be used. However, for Raman scattering, the frequency shift is very large about 100 THz, thus the minimum loss wavelength region cannot be used. In contrast to all these advantages, the Brillouin stokes power is nearly 10 dB higher than the Raman stokes power. In this paper, we have proposed a Brillouin distributed temperature sensor based on OTDR technique. The OTDR technique is a well-established technique for fault or imperfection localisation and diagnostics applications in fibre communications applications [8, 9]. In Brillouin optical time domain reflectometry (BOTDR) sensing system is a single ended access system, where only one end of the fibre is accessible and the other end of the fibre is cleaved. The temperature or strain profiles are extracted from the Brillouin power change due to temperature and strain variation [10]. In the proposed BDTS system, a short pulse of light is launched into the sensing fibre and a spontaneous Brillouin backscattered signal is detected at the launch end of the fibre. The received Brillouin backscattered signal intensity can be expressed as a convolution of the input pulse profile and the temperature distribution along the fibre when the band width of the receiving system is high enough [11]. The minimum spatial resolution of the BDTS system depends on the width of the input laser pulse [11–13]. Therefore, the improvement

of the spatial resolution can only be achieved by reducing the pulse width of the laser source. Koyamada et al. [14] used double pulse technique instead of single pulse for the improvement of spatial resolution of a BDTS system to 20 cm. But the downside is that they have used input pulse power nearly 2 W for achieving sub-meter scale resolution over 1–2 km of sensing range. However, using pseudorandom coded BOTDR technique for the proposed BDTS system we have achieved an improvement in spatial resolution without using narrow width laser pulse over a 50 km long measurement range.

In this paper, we have made a comparative study using three different OTDR techniques such as: conventional BOTDR [15], coherent BOTDR [16] and pseudorandom coded BOTDR [17] for the proposed BDTS system for sensing range of 50 km. The temperature profile from the proposed sensing system is extracted using LPR and FourRD algorithm. We have calculated the temperature resolution and spatial resolution of the proposed system in the presence and absence of CRN. In particular, the numerical simulation results show a significant improvement in spatial resolution using pseudorandom BOTDR technique for temperature sensing up to 50 km distance.

2 Theoretical Model

In this paper, we have investigated a conventional BOTDR, coherent BOTDR and pseudorandom coded BOTDR techniques to calculate the backscattered powers of the proposed BDTS system for 50 km sensing range. In addition, we have calculated the temperature resolution and spatial resolution of the proposed sensor using deconvolution algorithm and above mentioned BOTDR techniques.

The principle of the conventional OTDR technique is that an optical short pulse is launched into fibre and the Rayleigh backscattered signal is detected at the input end of the fibre. The schematic of the OTDR instrument is shown in Fig. 1.

The location information ‘z’ can be found out using the time of flight concept. Here ‘t’ is the time it takes for individual reflection to return (time of flight). The distance ‘z’ and the light velocity v_g in the fibre are related as $= \frac{tv_g}{2}$. The intensity of light inside the fibre in the function of the distance z can be calculated using the following Equation.

$$P_t(z) = P_i \exp(-\alpha z) \tag{1}$$

In the above expression, $\alpha = \alpha_s + \alpha_a$ the sum of the scattering and absorption losses in dB/km. The total scattered power P_{ts} at distance z can be expressed as

$$P_{ts} = \alpha_s \Delta z P_t(z) \tag{2}$$

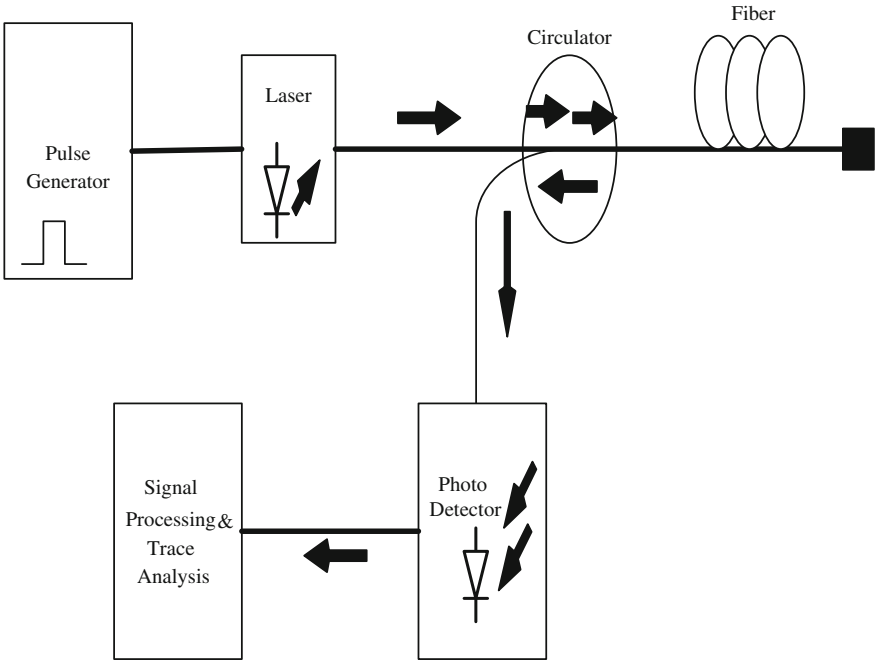

Fig. 1 Schematic of OTDR

where Δz is the spatial length and α_s is the scattering loss in the fibre. The spatial length of the fibre can be expressed using group velocity and the width of the pulse

$$\Delta z = v_g w = \frac{c}{n} w \tag{3}$$

here c is the speed of light in vacuum and n is the refractive index of the fibre. The total backscattered power at the launch end of the fiber can be expressed as

$$P_{bs} = \alpha_s \Delta z S P_i \exp(-2\alpha z) \tag{4}$$

S is the fraction of scattered light propagated backward in the fibre and $z = tv_g/2$ where t is the two way propagation time of the input pulse. The backward capture fraction S for single mode fibre can be expressed as:

$$S = \frac{(NA)^2}{4n^2} \tag{5}$$

The numerical aperture NA can be calculated using the following Equation

$$NA = \sqrt{n_1^2 - n_2^2} \tag{6}$$

where the core and cladding refractive indices are n_1 and n_2 respectively.

In coherent BOTDR technique [16], high power laser source light is divided into two parts by a directional coupler using 90:10 coupling ratio. One part of the total power (90 %) is injected into the sensing fibre and other part (10 %) is used as a local oscillator signal. The backscattered signal, combined with the local oscillator signal is detected at the input fibre end. However, in pseudorandom BOTDR technique [17], instead of a single pulse, a sequence of unipolar non return to zero pluses modulated by an continuous wave laser light using an electro optic modulator are injected into the sensing fibre. The backscattered signal power is measured at the input fibre end. We have utilized the above principles and measured the Rayleigh as well as Brillouin backscattered powers for the proposed sensor in order to extract the temperature information. The temperature information is extracted from the proposed BDTS system using Landau Placzek ratio (LPR) [18], which is defined as the ratio of the Rayleigh backscattered power to Brillouin backscattered power. The expression of LPR dependent on measurand temperature is given by the following equation [18],

$$\frac{P_R}{P_B} = \frac{T_f}{T}(\beta_T \rho_0 V_A^2 - 1) \tag{7}$$

In the above expression, β_T is the isothermal compressibility, ρ_0 is the material density, V_A is the acoustic velocity, T_f is the fictive temperature, P_R and P_B are the backscattered powers of Rayleigh and Brillouin scattering respectively. However, temperature profile along the sensing fibre is obtained using the LPR. T is the unknown temperature T and T_R is the reference temperature. The temperature profile can be expressed as [19]

$$T_{tf} = \frac{1}{K_T}\left(1 - \frac{LPR(T)}{LPR(T_R)}\right) + T_R \tag{8}$$

Here, the extracted temperature profile is T_{tf} and K_T is the temperature sensitivity of the proposed sensor. In order to calculate Brillouin backscattered power of the proposed sensing system, we have considered the backscatter impulse response $f(t)$, which is defined as the backscattered signal power in response to an injected unit delta function signal. Assuming constant propagation loss along the fibre under consideration, $f(t)$ is expressed as,

$$f(t) = \frac{1}{2}\alpha_B v_g S P_{in} \exp(-2\alpha z) \tag{9}$$

Here, v_g is the group velocity within the fibre defined as $\frac{c}{n}$, S is the backward capture coefficient, P_{in} is the optical power injected to the sensing fibre, c is the light velocity in vacuum, n is the refractive index of silica fibre and α_B is the Brillouin scattering coefficient of the fibre defined as [20]

$$\alpha_B = \frac{8\pi^3 n^8 p^2 k T_a}{3\lambda_0^4 \rho V_A^2} \tag{10}$$

In the above expression, n is the refractive index, the photo-elastic coefficient is p, the Boltzmann constant is k, the ambient temperature or room temperature of the fibre is T_a, ρ, is the density of the silica, V_A is the acoustic velocity in the sensing fibre and the wavelength of the continuous wave incident light is λ_0.

In the proposed system, at the input of the fibre, the convolution of the injected pulsed power $p(t)$ and the backscatter impulse response $f(t)$ represent the received Brillouin backscattered power and is expressed by the following expression;

$$P(t) = p(t) \otimes f(t) \tag{11}$$

In the simulation process, we have considered $p(t)$ as the pulse power injected to the sensing fibre for conventional BOTDR technique. However, the modulated pulse power $p_m(t)$ instead of $p(t)$ is injected to the sensing fibre for pseudorandom OTDR technique. We have used an ideal electro-optic amplitude modulator for the modulation process. The average modulated output power of the modulator can be defined as [21]

$$p_m(t) = P_{in}(t) \times \sqrt{(1 + MI) + MI \times R(t)} \tag{12}$$

where $P_{in}(t)$ input optical power to modulator, MI is the modulation index used for simulation and $R(t)$ is the electrical input signal to modulator.

We have verified the validity of Eq. 11 by considering a pulse as well as a sequence of pulses of width w_0, and power P_i are launched into the 50 km long fibre. The Brillouin backscattered power at the input fibre end is received with the addition of white Gaussian noise of power $10^{-7}w$ using FourRD algorithm and three different OTDR techniques. Similarly, for calculation of LPR we have calculated the Rayleigh backscattered power of the proposed sensing system. Theoretically, an input pulse of duration w_0 will generate the Rayleigh backscattered power P_{Ra}, at the input end of the fibre as a function of time in accordance with the following equation [22]

$$P_{Ra}(t) = \frac{1}{2} P_i \gamma_R w_0 S v_g \exp(-\gamma_R v_g t) \tag{13}$$

The above Rayleigh backscattered power P_{Ra} can be modified as a function of fibre length, z and is expressed as below.

$$P_{Ra}(z) = \frac{1}{2} P_i \gamma_R w_0 S v_g \exp(-2\gamma_R z) \tag{14}$$

In the above modified expression, γ_R is the Rayleigh scattering coefficient, S is backward capture coefficient, v_g is the group velocity within the fibre. In order to analyse the effect of CRN, in the numerical simulation process, we have calculated the backscattered Rayleigh power with and without CRN. The temporal amplitude fluctuations on the backscattered Rayleigh signal due to the disruption among a large number of light waves backscattered at different positions along the fibre generate CRN. It is inherent to Rayleigh backscattered power. In other words, the interference between the light backscattered at different positions along the fibre results the CRN [23]. The measurement accuracy as well as precision is degraded by fluctuations in the backscattered Rayleigh signals that are triggered by CRN. The root-mean-square (r.m.s) value of CRN as fraction of the Rayleigh signal, f_{CRN} can be stated as [23]

$$f_{CRN} = \sqrt{\frac{v_g}{4\Delta z \Delta v}} \tag{15}$$

where v_g is the group velocity of light in fibre, Δz is the spatial resolution, and Δv is the linewidth of the optical laser source.

3 Simulations and Results

The schematic diagram of the proposed 50 km long Brillouin scattering based temperature sensing system is shown in Fig. 2.

Rayleigh backscattered power as well as the Brillouin backscattered power over a sensing range of 50 km is calculated in the presence of additive white Gaussian noise of non-zero variance, using the numerical simulation. In the simulation process, we have used a continuous wave optical laser source with peak input power of 10 mW and having center wavelength at 1550 nm and of 10 MHz linewidth. As CRN plays major role in measurement and precision of the sensing system, we have calculated Rayleigh backscattered power with and without CRN. A rectangular pulse of 400 ns duration used for simulation. However, in pseudo-random coded BOTDR, a pseudo-noise sequence of order 7, having a sequence length of 128 bits (unipolar NRZ pulses) with peak power of 10 mW are used for simulation. The modulation index used in simulation is 0.5 for pseudorandom coded BOTDR. The other parameters based on silica fibre used for simulation are tabulated in Table 1.

We have used Fourier regularised deconvolution (FourRD) algorithm to minimise the noise of extracted temperature profile of the proposed sensing system. We have calculated the temperature resolution and spatial resolution of the proposed

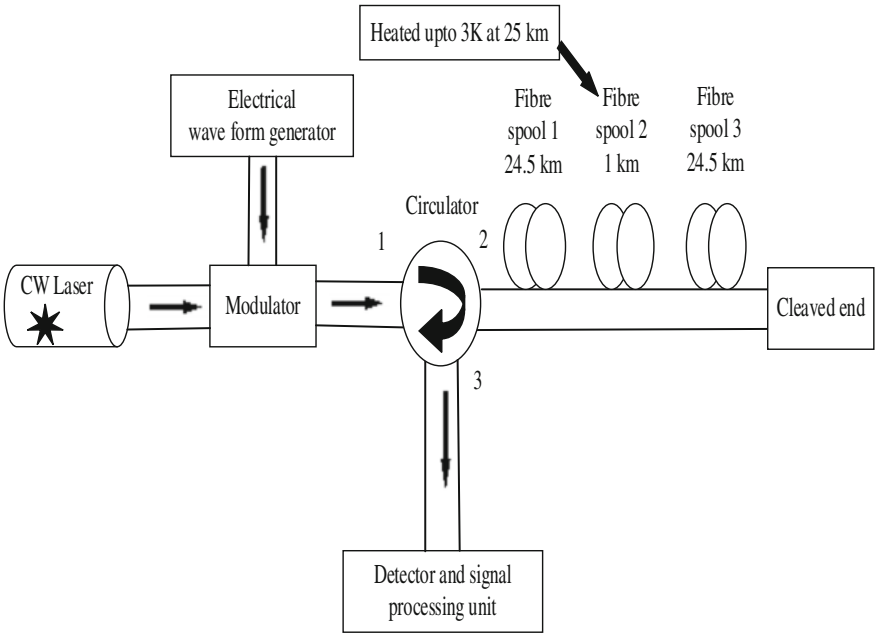

Fig. 2 Proposed distributed temperature measurement system

Table 1 Simulation parameters of the proposed system

Simulation parameters	Values
Fibre attenuation coefficient (α)	0.2 dB/km
Boltzmann's constant (k)	1.38×10^{-23} J/K
Numerical aperture (NA)	0.12
Fibre refractive index (n)	1.5
Rayleigh scattering coefficient (γ_R)	4.6×10^{-5} 1/m
Photo-elastic coefficient (p)	0.286
Density of silica (ρ)	2330 kg/m^3

50 km distributed temperature sensing system employing FourRD deconvolution and three different BOTDR techniques with and without CRN

In the simulation process, FourRD algorithm is used, the steps involved are:

a. Obtain Brillouin backscattered signal performing Fourier deconvolution.
b. The noisy signal as obtained from step (a) is shrinkaged with the parameter α of Tikhonov filter and then calculate the inverse Fourier transform.

The Brillouin backscattered power of the proposed sensor for 50 km sensing range is simulated using Eq. 11. In our simulation process, we modeled a leakage source with an artificial rectangular pulse variation of temperature distribution around the point $z = 25$ km from the end point of the optical fibre, whereas the rest

of the sensing fibre remains at reference temperature. We have considered the reference temperature as 300 K and increased the temperature by a step of 3 K at z = 25 km in the simulation process. The temperature of the proposed sensing system was obtained using the using FourRD algorithm. In simulation, the temperature profile is extracted using Eq. 8. Here we have considered a temperature sensitivity K_T of 0.33 %/K [24] for simulation.

We have shown the extracted temperature profiles without and with CRN using FourRD algorithm and conventional OTDR technique in Fig. 3. Similarly, for coherent OTDR technique, the extracted temperature profiles without and with CRN using FourRD algorithm are shown in Fig. 4. Figure 5 shows the extracted temperature profiles without and with CRN using FourRD algorithm and pseudo-random coded BOTDR technique.

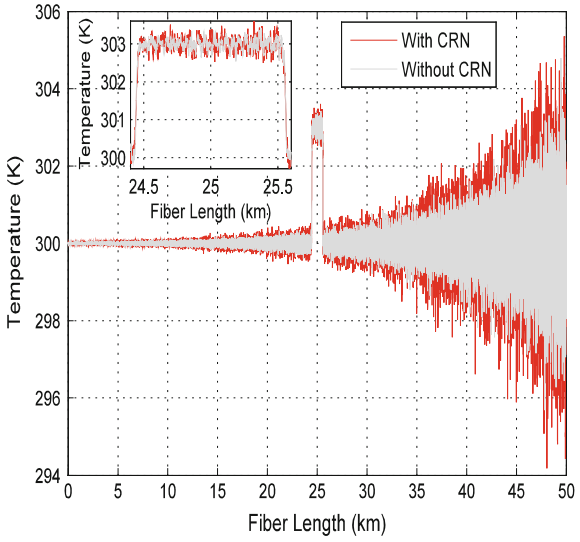

Fig. 3 Simulated temperature profiles using conventional OTDR technique

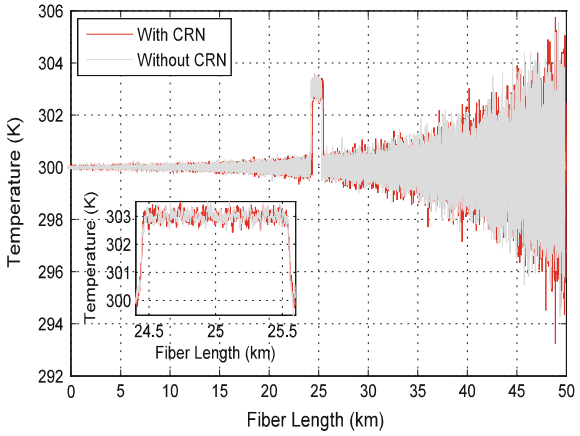

Fig. 4 Simulated temperature profiles using coherent OTDR technique

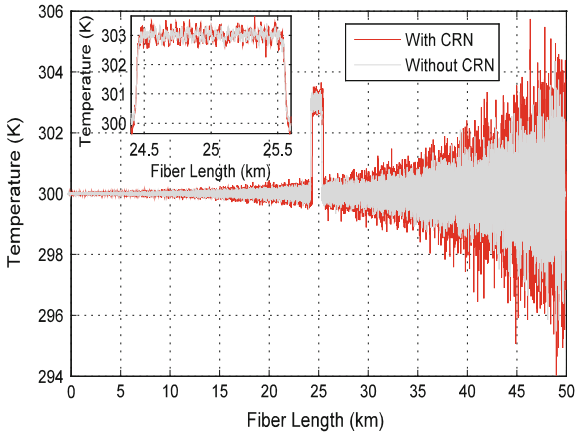

Fig. 5 Simulated temperature profiles using pseudorandom coded OTDR technique

In order to show the capability of the FourRD technique towards the deconvolution and denoising of the Brillouin backscattered signal, the Tikhonov shrinkage parameter α is applied to the output signal. The normalized mean square error values verses shrinkage parameter α are calculated. The normalization has been done with respect to the energy of the received backscattered signal. The value of $\alpha = 0.00035$ [25] is chosen for the numerical simulation process.

The temperature resolutions without and with CRN employing conventional BOTDR technique and FourRD deconvolution algorithm are shown in Fig. 6. Similarly, the temperature resolutions without and with CRN employing coherent BOTDR technique and FourRD deconvolution algorithm are shown in Fig. 7.

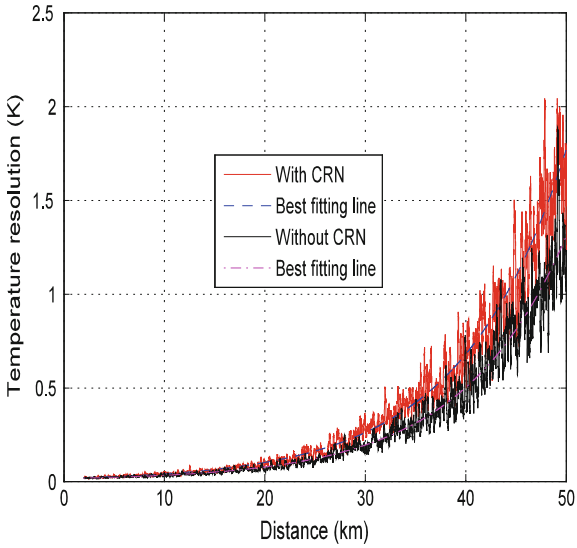

Fig. 6 Temperature resolutions using conventional OTDR technique

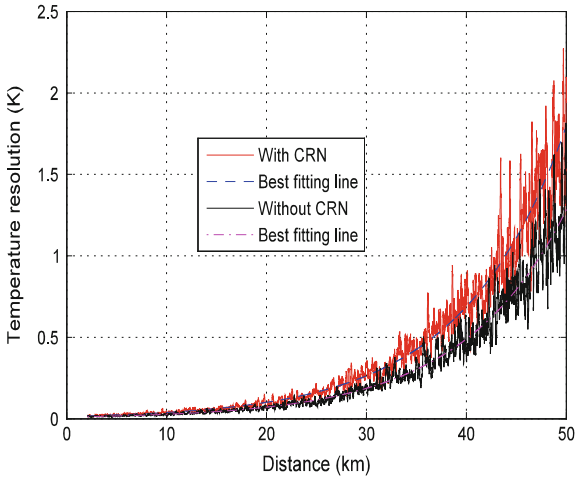

Fig. 7 Temperature resolutions using coherent OTDR technique

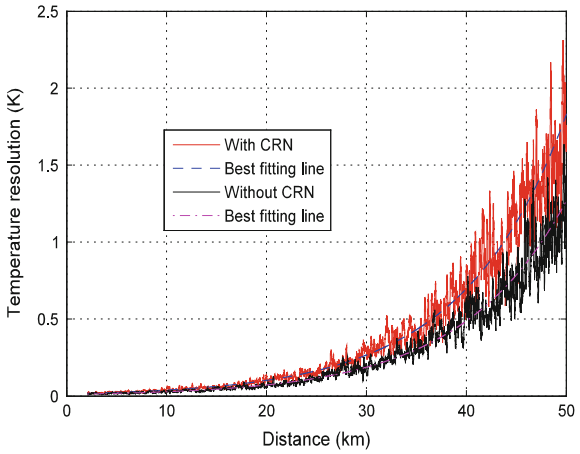

Fig. 8 Temperature resolutions using pseudorandom coded OTDR technique

Figure 8 shows the temperature resolutions without and with CRN employing pseudorandom coded BOTDR technique and FourRD deconvolution algorithm.

The temperature resolution has been estimated as an exponential fit of the standard deviation of the measured temperature distribution vs distance of the proposed sensing system for 50 km sensing distance. In contrast to temperature resolution, the spatial resolution of the proposed system obtained by calculating the 10–90 % response of the rising temperature or 90–10 % response of the falling temperature with respect to the sensing distance. The spatial resolution of the proposed sensing system is calculated by the spline fit of the 10–90 % response of rising temperature. The spatial resolutions of the proposed sensing system without and with CRN using conventional BOTDR technique are shown in Fig. 9. Similarly, the spatial resolutions of the proposed sensing system without and with CRN

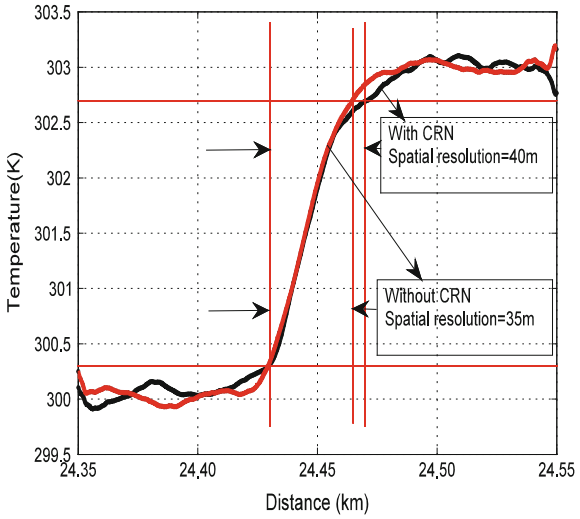

Fig. 9 Spatial resolutions using conventional OTDR technique

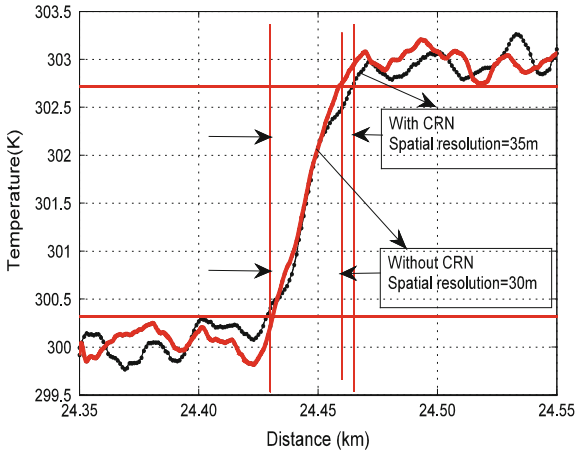

Fig. 10 Spatial resolutions using coherent OTDR technique

using coherent BOTDR technique are shown in Fig. 10. Figure 11 shows the spatial resolution without and with CRN pseudorandom coded BOTDR technique.

Tables 2 and 3 reports the temperature and spatial resolution of the proposed system. A spatial resolution improvement of 15 m in presence of CRN was observed using the pseudorandom coded BOTDR technique over the conventional BOTDR technique.

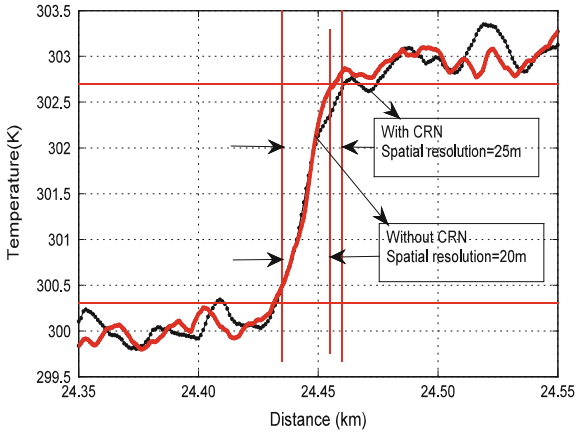

Fig. 11 Spatial resolution using pseudorandom coded OTDR technique

Table 2 Temperature resolutions observed in proposed sensing system

OTDR techniques	Without CRN (K)	With CRN (K)
Conventional	1.30	1.76
Coherent	1.26	1.79
Pseudorandom coded	1.27	1.84

Table 3 Spatial resolutions observed in proposed sensing system

OTDR techniques	Without CRN (m)	With CRN (m)
Conventional	35	40
Coherent	30	35
Pseudorandom coded	20	25

4 Conclusion

In this paper, we have studied different BOTDR techniques based Brillouin distributed temperature sensor. The comparative study indicate that the proposed BDTS system with pseudorandom coded BOTDR technique and FourRD algorithm is capable of achieving extremely low temperature uncertainties of the order of 1.84 K in the presence of CRN, for a sensing range up to 50 km using 10 mW of peak input power only. For the above measurement, the spatial resolution reported is 25 m. Numerical simulation results indicate that the FourRD algorithm and pseudorandom coded BOTDR technique can be successfully applied in BDTS to improve the performance features of the sensing system, e.g., spatial resolution as well as the temperature resolution at a very low input power level. It can be concluded that the proposed pseudorandom coded BDTS, allows for accurate temperature sensing, providing a high-performance, simple and cost-effective solution for long range temperature sensing applications.

References

1. M. Nikles, F. Ravet, Distributed fibre sensors: depth and sensitivity. Nat. Photonics **4**, 431–432 (2010)
2. S.Z. Yan, L.S. Chyan, Performance enhancement of BOTDR fibre optic sensor for oil and gas pipeline monitoring. Opt. Fibre Technol. **16**, 100–109 (2010)
3. J.M. Lopez-Higuera, *Handbook of Optical Fibre Sensing Technology* (Wiley, New York, USA, 2002)
4. B. Lee, Review of the present status of optical fibre sensors. Opt. Fibre Technol. **9**, 57–79 (2003)
5. J.P. Dakin, D.J. Pratt, G.W. Bibby, J.N. Ross, Distributed optical fibre Raman temperature sensor using a semiconductor light source and detector. Electron. Lett. **21**, 569–570 (1985)
6. T. Horiguchi, T. Kurashima, M. Tateda, Tensile strain dependence of Brillouin frequency shift in silica optical fibres. IEEE Photonics Technol. Lett. **1**, 107–108 (1989)
7. D. Culverhouse, F. Farahi, C.N. Pannell, D.A. Jackson, Potential of stimulated Brillouin scattering as sensing mechanism for distributed temperature sensors. Electron. Lett. **25**, 913–915 (1989)
8. Y. Koyamada, M. Imahama, K. Kubota, K. Hogari, Fibre-optic distributed strain and temperature sensing with very high measurand resolution over long range using coherent OTDR. J. Lightw. Technol. **27**, 1142–1146 (2009)
9. R. Feced, M. Farhadiroushan, V.A. Handerek, A.J. Rogers, Advances in high resolution distributed temperature sensing using the time-correlated single photon counting technique. IEE Proc. Optoelectronics **144**, 183–189 (1997)
10. M.A. Davis, A.D. Kersey, Simultaneous measurement of temperature and strain using fibre Bragg gratings and Brillouin scattering. IEE Proc. Optoelectron. **144**, 151–155 (1997)
11. H. Liu, S. Zhuang, Z. Zhang, C. Feng, The optimisation of the spatial resolution of a 30-km distributed optical fibre temperature sensor. in *Proceedings of the Advanced Sensor Systems and Applications II*, Beijing, China, SPIE 5634, November 2004, pp. 225–231
12. M.A. Soto, P.K. Sahu, G. Bolognini, F.D. Pasquale, Brillouin based distributed temperature sensor employing pulse coding. IEEE Sens. J. **8**, 225–226 (2008)
13. G. Bolognini, J. Park, M.A. Soto, N. Park, F. Di Pasquale, Analysis of distributed temperature sensing based on Raman scattering using OTDR coding and discrete Raman amplification. Meas. Sci. Technol. **18**, 3211–3218 (2007)
14. Y. Koyamada, Y. Sakairi, N. Takeuchi, S. Adachi, Novel technique to improve spatial resolution in Brillouin optical time-domain reflectometry. IEEE Photonics Technol. Lett. **19**, 1910–1912 (2007)
15. M.C. Farries, M.E. Fermann, R.I. Laming, S.B. Poole, D.N. Payne, Distributed temperature sensor using Nd3 + doped fibre. Electron. Lett. **22**, 418–419 (1986)
16. J.P. King, D.F. Smith, K. Richards, P. Timson, R.E. Epworth, S. Wright, Development of a coherent OTDR instrument. J. Lightw. Technol. **LT-5**, 616–624 (1987)
17. A.S. Sudbo, An optical time-domain reflectometer with low-power InGaAsP diode lasers. J. Lightw. Technol. **LT-1**, 616–618 (1983)
18. P.C. Wait, T.P. Newson, Landau Placzek ratio applied to distributed fibre sensing. Optics Commun. **122**, 141–146 (1996)
19. K. De Souza, T.P. Newson, Improvement of signal-to-noise capabilities of a distributed temperature sensor using optical pre-amplification. Meas. Sci. Technol. **12**, 952–957 (2001)
20. M.N. Alahbabi, Distributed optical fibre sensors based on the coherent detection of spontaneous Brillouin scattering. PhD Thesis, University of Southampton, Southampton, U.K. (2005)
21. J. Ahamed, A. Khan, M. Ahmed, Investigation of Modulators in OTDM system. Int. J. Comput. Appl. **90**, 16–19 (2014)
22. M. Nakazawa, Rayleigh backscattering theory for single-mode optical fibers. J. Opt. Soc. America **73**, 1175–1180 (1983)

23. K. De Souza, Significance of coherent Rayleigh noise in fibre-optic distributed temperature sensing based on spontaneous Brillouin scattering'. Meas. Sci. Technol. **17**, 1065–1069 (2006)
24. T. Chang, D.Y. Li, T.E. Koscica, H.-L. Cui, Q. Sui, L. Jia, Fibre optic distributed temperature and strain sensing system based on Brillouin light scattering. Appl. Opt. **47**, 6202–6206 (2008)
25. H.S. Pradhan, P.K. Sahu, High-performance Brillouin distributed temperature sensor using Fourier wavelet regularised deconvolution algorithm. IET Optoelectron. **7**, 1–7 (2014)

Optical Sensing Based on Photonic Crystal Structures

J. Sevilla and A. Andueza

Abstract Photonic crystals (PhC) are materials which present periodic variations of the dielectric constant over distances of the same order of the light wavelength. Their optical properties are highly dependent on construction details such as dielectric constants and sizes of their different constituents. It is possible to turn PhC structures into optical sensors by making some of their structural characteristics responsive to the desired mesurand. These sensors are small, compact, compatible with electronic integration in some cases, and may present some other advantages like high sensitivity and selectivity. In recent years the development of PhC sensors has experienced a substantial increase due to their performance and to the increasing demand of sensing applications such as instrumentation, healthcare, environment security, food quality and industrial control. In this paper we present an overview of PhC sensors focused on their physical working principles. It covers a description of PhC structures, their interaction with radiation, the general strategies to make them responsive and, finally, a selection of sensor proposal of a variety of mesurands.

1 Introduction

Automation is a desired feature of most products and services in our life; qualified as smart when successfully attained: smart appliances, smart buildings, smart cities, etc. One of the key elements in the process of developing a smarter world are sensors. They are the entrance gate of information from the real world in the automation system. Among the many possible approaches to develop sensors, in this paper we will focus in optical sensors, those encoding the measured information in an optical signal. And more precisely, in the optical sensors that implement some kind of PhC structure.

J. Sevilla (✉) · A. Andueza
Universidad Pública de Navarra, Pamplona, Spain
e-mail: joaquin.sevilla@unavarra.es

© Springer International Publishing Switzerland 2017

I.R. Matias et al. (eds.), *Fiber Optic Sensors*, Smart Sensors,
Measurement and Instrumentation 21, DOI 10.1007/978-3-319-42625-9_11

Wave propagation though materials periodically structured have been studied for many years. In the second half of 20th century semiconductor materials allowed the development of electronic, revolutionizing many aspects of our lives. The extraordinary characteristics of these materials are due to the interaction of its electrons with the periodic array of atoms of the lattice. The translation of the idea to the flow or photons instead of electrons was straightforward [1, 2]. It was attained introducing a periodic variation of the refractive index in the photons path. The resulting materials presented energy bands for the photons, including forbidden bands, analogous to the typical electronic ones. These materials, called photonic band gaps or PhCs, have been subject of extensive research since the 80s [3–5].

PhCs are materials which present variations of the dielectric constant over distances of the same order of the light wavelength. This variations are mostly regular, although quasi crystalline [6, 7] or hiperunifomly disordered PhCs [8, 9] have also been studied. Dielectric constant variation can take place in a single dimension, two or in the three directions of space. These materials are relevant because of their optical response, highly dependent of the geometrical distribution of its dielectric constant. Therefore, if these characteristics are changed by an external stimuli, the PhC becomes an optical sensor.

In this paper we discuss the use of PhC structures to make sensors. The main focus is in the working principle of the different structures used for sensing, and not in the fabrication techniques. In Sect. 2 we present a general description of PhC structures. Next the interaction of PhC with radiation (Sect. 3). Section 4 covers the general strategies to make these structures responsive to physical inputs. Finally, in Sect. 5, we present a brief review of PhC sensors of different mesurands.

2 Photonic Crystal Structures

From a structural point of view PhCs may be regarded as arrangements, mainly regular, of dielectric materials with different dielectric constant and sizes of the same order of magnitude of light. In the interaction of light with these materials, some wavelengths will be transmitted while others are completely forbidden. Therefore, the flow of light can be tailored through the adequate design of these materials. The first studies ok PhCs were made by Ohtaka et al. [4, 5], Yablanovitch [1] and John [2] in 1982 and 1987, respectively. Three types of PhCs can be distinguished depending on how the spatial variation of the dielectric constant is distributed over the three orthogonal axis: one-dimensional (1D), two-dimensional (2D) and three-dimensional (3D) PhCs (Fig. 1).

In 1D PhCs the variation in the dielectric constant is obtained by piling layers of alternate materials [10]. They can be fabricated by techniques such as layer-by-layer deposition, multiple spin coating, photolithography, etc. They respond optically as Bragg reflectors.

2D PhCs are structured in two dimensions while the third remains constant, what can be achieved by stacking dielectric rods [11] or, alternatively, drilling holes in a

slab of high refractive index [12]. The fabrication of these structures can be done by photolithography and etching techniques.

When the dielectric constant variation takes place in the three spatial dimensions we have 3D PhCs such as opals and inverse opals. Opals are sackings of spheres of dielectric materials in air, and take the name from the semi-precious mineral that are composed of microspheres of silica. The most common fabrication method is based in self-assembly of nanoscopic spheres, creating a crystal lattice [13–15]. This structures can be used as template, infiltrated with a different material and then etching the original spheres. The resulting structure is an inverse opal [16–18].

Apart from this typical classification of PhCs by dimensionality, it is interesting to point out the case of PhC optic fibers. In ordinary optical fibers, light is confined in its core by total internal reflection at the interface of the core and the cladding of the fiber. Instead of creating the cladding by a difference in refractive index with the core, it can be made by introducing a PhC structure. The lack of states in the photonic band gap impedes light transmission across it, forcing then its confinement in the core. The way of producing a PhC cladding in a fiber is by introducing holes in it [19, 20]. It is then a case of 2D PhC.

3 Wave Propagation in Photonic Crystals

How light propagates in a medium is described by the Maxwell equations. For homogeneous materials with simple interfaces the solutions are also simple, allowing much intuitive explanations. For example in the interface of two homogeneous media we talk of reflection and refraction phenomena, and describe them with the Snell's law, much simpler than the whole set of Maxwell equations. In PhCs, however, different materials are intermingled in sizes below the light wavelength. This make necessary a complete analysis, without simplifications. This analysis can be approached in two ways, an analytical one taking advantage of the crystal symmetries, reproducing for photons the results developed by solid state physics for electrons: Green and Block theorems, etc. [21]. The second approach benefits form the advances in computer power and is based on numerical solutions of the Maxwell equations (that can be done by a number of different methods). By either mean, the final solution of how light behaves inside a PhC is summarized in the photonic band structure (PBS), or also called, the dispersion relation of the crystal (Fig. 2).

Even though the complete problem of solving light propagation in PhCs is quite complex, there are some simpler concepts that allow an intuitive approach and that can be considered valid in many cases. The calculated PBS (solid black line) and measured (dotted red line) of a 3D PhC made of spheres is presented in Fig. 2 together with the transmission spectrum of several layers of spheres of the same structure. These experimental data were obtained with a "macroscopic" PhC built up with 6 mm of diameter spheres exposed to microwave radiation [22]. The scalability of the Maxwell equations assure the same behavior as long as the relation of sizes of

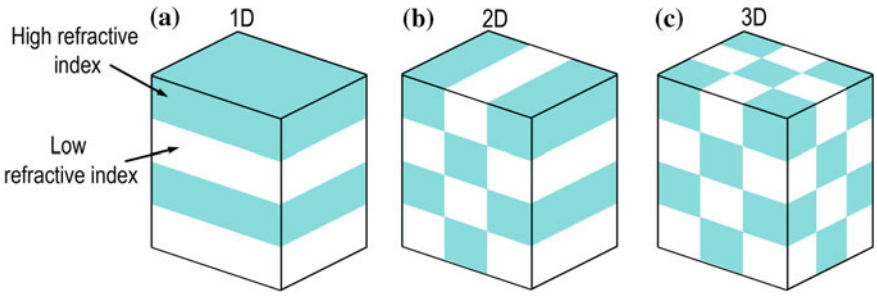

Fig. 1 Schematic illustration of PhCs **a** 1D, **b** 2D, **c** 3D

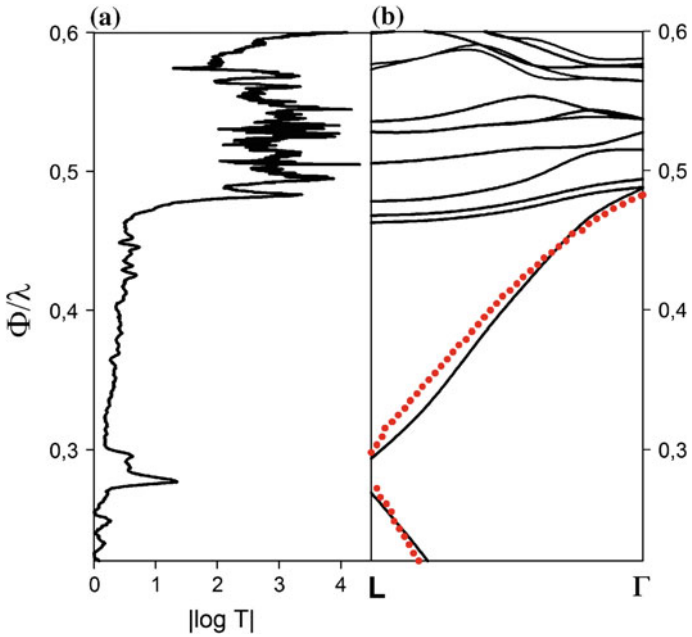

Fig. 2 **a** Transmission spectra of an opal-like crystal made of 6 mm sphere arrangement in hcp configuration. **b** Photonic band structure in the first Brillouin zone Γ-L direction of hcp array of spheres with a background index of $n_m = 1$ and sphere refractive index of $n_p = 2.65$. The y axis has been normalized to sphere diameter, and x axis at the transmission spectra is given by the module of the transmittance. *Red dotted line* corresponds to experimental photonic bands of low frequency

the structure and radiation wavelength are kept constant. The dielectric constant of the materials considered has to be the same in the corresponding frequency ranges. In the case presented in Fig. 2, glass spheres of refractive index of $n_p = 2.65$ in the measurement range (10–30 GHz) were used. Similar values for optic radiation can be found in materials like titania (TiO_2) for example.

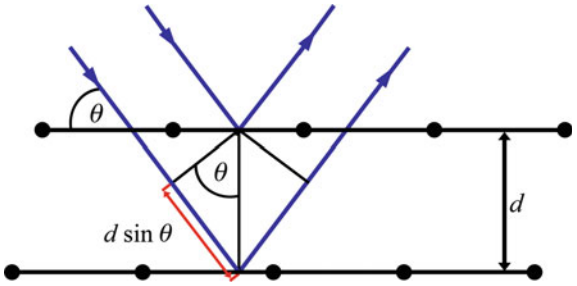

Fig. 3 Schematic representation of Bragg diffraction

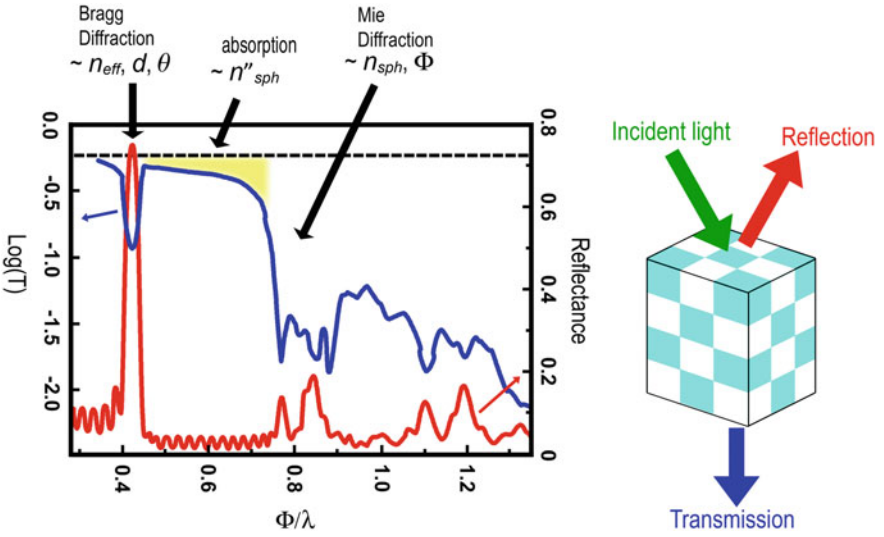

Fig. 4 General light response of a 3D PhC made of discrete spherical scatterers. Reflectance response (*red solid line*) and transmission response (*blue solid line*) from a close-packed 3D PhC of dielectric spheres of latex [103]. Yellow shaded area represents absorption effects of the PhC. Φ corresponds to the diameter of the spheres, d to the distance between consecutive planes of spheres, θ to the incidence angle, n_{eff} the effective refractive index of 3D PhC, n_{sph} the refractive index of the spheres and n''_{sph} the absorption coefficient of refractive index of the spheres

As can be seen in Fig. 2, the PhC is quite transparent except for two regions: (i) a small peak at lower frequencies (value normalized to the sphere diameter around $\Phi/\lambda = 0.29$) and (ii) a deeper band at higher frequencies (starting around $\Phi/\lambda = 0.48$). The fist region coincides with a pseudogap (a gap open in certain incidence directions but not in others) opening in the center of the Brillouin zone of the PBS while the second matches the position of a complex set of relatively flat bands. These two features can be explained, respectively, by Bragg diffraction and Mie scattering.

Bragg law of diffraction consider the reflection in successive equidistant planes, assessing the conditions where the reflection from all planes suffer constructive interference. Calling d the distance inter planes and θ the incidence angle, the Eq. (1) gives the values of wavelength (λ) meeting the Bragg condition for all orders of diffraction (m = 1, 2 3, …) [23]. The same idea is readily applied to x-ray diffraction from atoms, as we can consider their nuclei structured in well-defined planes placed in a vacuum (Fig. 3).

$$2d\ \cos\theta = \mathrm{m}\lambda \tag{1}$$

In the case of the PhC we have spheres (of n_p refractive index) touching each other in a close packed arrangement submerged in a dielectric (of $\mathrm{n_m}$ refractive index) such as air or water. Then we can consider an effective refractive index averaging those of the particles and the surrounding media with their respective occupied volumes ($\mathrm{V_p}$ and $\mathrm{V_m}$) as shown in Eq. (2). Applying the Snell´s to the incident radiation, the Bragg condition can be restated as in Eq. (3). Finally, we can express the distance between planes d in terms of the distance between centers of the particles as D ($D = 2/3\Phi$ for a close-packed face cubic center configuration) by simple geometrical calculations [24], leading to Eq. (4), that is a good description of how Bragg diffraction takes place in opal-like PhCs.

$$n_{\mathrm{eff}}^2 = n_{\mathrm{p}}^2 V_{\mathrm{p}} + n_{\mathrm{m}}^2 V_{\mathrm{m}} \tag{2}$$

$$2d(n_{\mathrm{eff}}^2 - \sin^2\theta)^{1/2} = \mathrm{m}\lambda \tag{3}$$

$$\sqrt{\frac{8}{3}}D(n_{\mathrm{eff}}^2 - \sin^2\theta)^{1/2} = \mathrm{m}\lambda \tag{4}$$

Maxwell equations can be analytically solved for a homogenous dielectric sphere. This was first done by Mie and Debye at the beginning of the 20th century [25]. One of the most interesting features found in Mie scattering is the existence of certain frequencies of the incident light that produce no forward transmission. The incident radiation at this frequencies resonates in the sphere being mostly slightly backscattered and absorbed. Therefore spheres may be regarded as well-defined electromagnetic resonators. The Mie resonant frequencies in spheres play for photons an analogous role than for electrons the electronic levels of atoms [26]. The Mie resonant frequencies can be calculated, and are solely dependent on the sphere radius and its refractive index. The opaque band at higher frequencies in Fig. 2 is due to the existence of Mie resonances at these frequencies. Thus, the energy of the incident radiation resonated from sphere to sphere and cannot traverse the material.

In summary, the general optical response of a 3D PhC made of spheres can be considered as the composition of three physical phenomena (Fig. 4): (i) Bragg diffraction, (ii) Mie scattering and (iii) absorption. The details of these phenomena depend on the structure characteristics, namely: sphere diameter (Φ), sphere refraction index (n_p), crystalline structure, refractive index of the medium

surrounding the spheres (n_m) and light incidence angle (θ). Therefore, the design of sensors will be based in making some of these parameters responsive to the desired input variable. The most versatile, and actually used in many practical sensors, is the Bragg diffraction. It has a well-defined frequency value, can be observed in transmission as well as in reflection, and has a simple dependence on the structure variables (as described by Eq. (4) above).

Above we have described the physical phenomena of light interaction with a particular 3D PhC; the same type of behavior also takes place in other PhC configurations. The general response of 1D PhC is limited to the Bragg reflection of the layer stacking. The Bragg diffraction in the 3D case appears in the PBS as a pseudogap, however in the2D case it is easy to find wide complete gaps. In these structures, the main strategy to have responsive systems is the introduction of states in the gap (by local defects) with characteristics dependent on the external variable to be measured.

4 (General) Strategies for (Making) Sensible Photonic Crystals

In order to have optical sensors based in PhC we need responsive structures, materials that change their structural parameters under the influence of the external variables to be sensed. First of all we can differentiate two possibilities: (i) the use of the structural parameters of the PhCs, those listed in the previous section and (ii) the introduction of defects in the "intrinsic" PhCs. The design of sensors based on 3D PhCs is mainly based in the first approach while in the case of 2D the introduction of defects is the most common case. In 1D structures both alternatives are used.

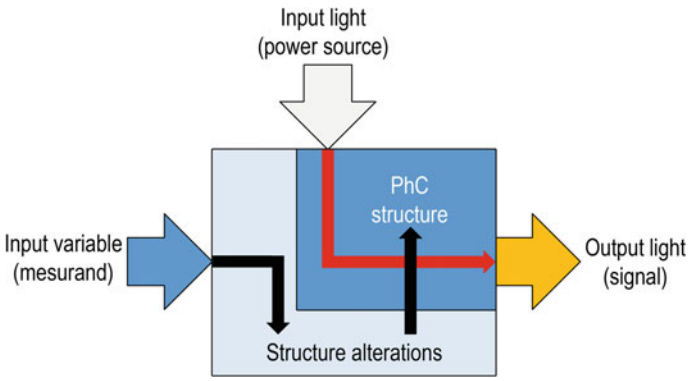

Fig. 5 General sensor system block diagram

The conceptual structure of an optical sensor based on PhCs is shown in Fig. 5. The input variable (i.e. the external stimulus to be measured) produces some alteration in the structural characteristics of the PhC and therefore, the response of the material to an input light beam changes correspondingly. The input light is the power source of the system, and the output signal is the optical response of the PhC to this light. As an example we can consider a 3D PhC made of spheres embedded in a hydrogel matrix that expands with temperature increases, then the Bragg reflection will be shifted to longer wavelengths. So the reflected color under white illumination will encode the temperature of the material, we have a temperature sensor [27].

The rest of this section is devoted to describe the items of Fig. 5: (i) output signal, (ii) physical phenomena that transform the input light in the output signal and (iii) the structural parameters that can be varied to make a sensing device. A list of some input variables and the more successful ways of measuring them will be presented in the following section.

The output of the sensor is an optical signal that incorporates the information of the input variable. In the vast majority of the existing sensors, the output light encodes the measurand information in its wavelength. However, in some cases, light intensity at a particular wavelength is used as information carrier. The output light is obtained upon illumination with ultraviolet (UV)/white light either by reflection or by transmission trough the PhC. Particularly interesting is the case of reflection of ordinary illumination because the measurement can be visually appreciated as color changes of the sensor.

Bragg diffraction is the physical phenomenon underlying sensor operation in most of the existing sensors, however, there are some other alternatives such as the Mie scattering (also mentioned in the previous section), Fano resonances or the existence of a photonic band gap.

Fano resonance is used to describe asymmetric-shaped resonances generated by constructive and destructive interference of discrete states with broadband continuum states [28]. This situation takes place in many physical situations, particularly when a quasi 2D structure (like a single-layer of spheres or a hole array in a slab) is illuminated perpendicularly to the surface. The structure holds discrete states while the free space above and below present a continuum of states for the photons. Examples of sensors based on these resonances can be found the reference [29] and in the extensive review of Zhou et al. [30].

Mie scattering in 3D PhCs is not useful for sensing purposes because, as seen in Fig. 4, extinguish input light, providing extremely low signal both in reflection and in transmission. However, in quasi 2D systems as single layers of spheres, it is the main process of light interaction and present interesting properties. We refer to ‘quasi 2D systems’ to those that are infinite in two directions and not in the third, the one used to launch the input radiation. Applying the definition of Fig. 1, these system clearly are not 2D PhCs. Therefore, in order to avoid confusion, in this text we use the term quasi 2D systems. With the same criterion, crystal fiber PhCs can be regarded as quasi 1D systems.

An extensive summary of the use of quasi 2D systems for chemical and biomolecular sensors can be found in [31] (although they refer to this systems as "2D PhCs", using a different definition as the one we are following here). In our group we have studied in detail how a single layer of dielectric spheres varies its optical output in response to several structural variations, making this system suitable for sensing purposes. In summary the single-layer holds some photonic states that are made by composition of the Mie modes of the sphere and some structural contributions. The frequency value where these states tales place depend on the dielectric constant of the spheres [32] and on the compactness of the structure [33]. Surprisingly the dependence of the crystalline structure (square or triangular) is not so important, in fact is irrelevant in a wide range of compactness values [34]. Structural disorder was also studied [34] finding that even for highly disordered layers, some structure modes were still useful for sensing purposes.

Other uses of PhCs for sensing, not using Bragg, Mie or Fano, benefit from the photonic band gap itself. Thus light can be better confined in certain regions where other sensing principles may be used. This is the case when defects are introduced in the PhC. Particularly relevant is the case of sensors based on cavities introduced in regular 2D PhCs. The typical structure of a PhC cavity (PCC) is formed by introducing point defects in the orderly arranged 2D lattices. Light in the defect presents a strong spatial and temporal light confinement [35]. Therefore, the interaction strength between optical field and the material of defected region is greatly enhanced. The resonant mode of the cavity is strongly affected by this interaction, making its frequency very sensitive to the characteristics of the material in the cavity, a very interesting platform for sensing applications [36]. Besides, this structures can be built with sizes and technologies that allow their integration with electronic components, making these structures very promising for integrated smart sensors. An extensive review on this type of sensors can be found in Ref. [37].

After describing all the physical phenomena that give rise to variations in the output signal (see Fig. 5), let's consider the variables governing these phenomena. In the end, the ability to make these variables respond to input parameters such as temperature or gas pressure is what give the actual possibility of measuring them with photonic PhCs. These variables are presented schematically in Fig. 6, depicted for the case of 3D PhCs, although are also valid for the other geometries. Can be described as follows:

- The relative spaces filled by the two dielectric materials. This can be the spheres sizes and their spacing in a matrix (in the case of 3D opal like structures), air holes diameter and spacing in a dielectric slab or thickness of a foil stacking.
- Refractive index of the two dielectric materials.
- Structure tilting angle with respect to the input light direction.
- Crystalline structure and disorder (in 2D and 3D structures)
- Defect geometry and disposition (in the case of non-intrinsic PhCs)

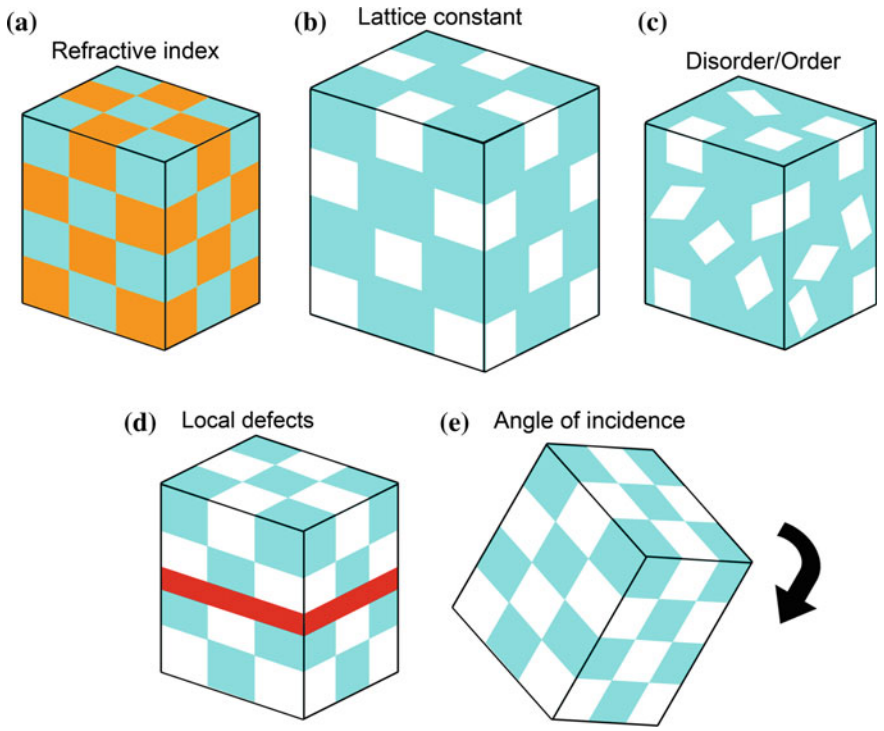

Fig. 6 Graphical representation of more significant PhC parameters controlled to sensing application. **a** Refractive index of the PhC and background, **b** lattice constant of the structure, **c** Order and disorder of the PhC, **d** local defects and **e** the angle of incidence of the radiation with respect to the PhC

5 Some Examples of Photonic Crystal Sensors

In the context of measurement systems and sensors, it is possible to classify the PhC sensors following different criteria such as the measured parameter, the physical principle of operation or the fabrication technique employed. Next section is intended to present a classification based on the responsive parameter of the PhC sensors. In the following we describe the most important sensors based on PhCs technology for each type of mesurand: chemical, mechanical, thermal, electrical, magnetic and optical sensibility.

5.1 Chemical Photonic Crystal Sensors

The need for sensitive and selective detection of chemicals agents and biological species has increased due to industrial and environmental demand. Many

technological areas of industry (i.e. healthcare, environment security or food quality) require to identify and measure chemicals and biological agents before their concentrations reach dangerous levels. In this context, sensing technology from 3D PhCs can be used. There are many proposals based on PhC hydrogel, where a 3D PhC interacts with the chemical agents altering the particle distance (lattice parameter), shifting their diffractionwavelength. Many 3D PhC sensors have been proposed and fabricated for sensing chemical agents, some examples could be glucose [31, 38–41], metal cations [38, 42–45], creatinine [46], protein kinase activity [47], pH [48, 49], ethanol [49], humidity [50, 51], ionic strength [48, 52] and ammonia [53].

5.2 Mechanical Photonic Crystal Sensors

In the same way that strain gages modify their resistance when a mechanical stress (stretching or compression) is applied, a mechanically responsive PhC sensor changes its reflected Bragg diffraction wavelength. [54–56]. This effect can be obtained when the lattice constant is altered as result of the mechanical stress applied. Examples of this technique has been reported using composite films of polystyrene colloids embedded in an N-vinylpyrrolidone/acrylamide copolymer for uniaxial stretching [42], poly(methyl acrylate) and poly(ethylene glycol methacrylate) (PEGMA) to measure pressure until a 1 kPa with a response totally reversible [57, 58] and PEGMA gel with 2-methoxyethyl acrylate [59] which improves substantially the performance of the abovementioned references.

5.3 Electrical Photonic Crystal Sensors

Nowadays it is possible to find two fundamental sensing principles commonly employed in photonic electrical sensing: (i) sensors stimulated by electrical external signals based on PhCs with liquid crystals (LCs) [60–62] and (ii) those that respond to an electrochemical change in their surroundings. The first one produce a change in the refractive index of the sensor when an electric field generate a change in the orientation of a LC, which results in a shift of the diffraction wavelength of the crystal. The PhCs sensor sensitive to electrochemical stimulus are the most relevant of this type and are based on redox-active compound (like polyferrocenylsilane) to modify the optical responsivity. In fact, any variation of oxidation or reduction potential in the sensor generates a shift of the reflected light to a longer or shorter wavelength. This kind of sensor has been fabricated and analyzed for different 3D PhCs configurations of opal [63, 64], inverse opal [65] and polyelectrolyte hydrogels [66].

5.4 Magnetic Photonic Crystal Sensors

Sensors based on PhCs are fabricated with dielectric materials, so they does not present any magnetic response. For that reason, if we want to fabricate a PhC sensitive to magnetic stimuli, the PhC must be combined with a magnetic materials in order become magnetic sensitive [67, 68]. When magnetic particles are incorporated into the PhC, the wavelength of the bandgap undergoes changes under the influence of magnetic fields. Some examples can be found for magnetic species of magnetite (Fe_3O_4) [68–70], iron [71, 72] and ferromagnetic cobalt ferrites ($CoFe_2O$) [73].

5.5 Thermal Photonic Crystal Sensors

PhCs can be also used to design temperature sensors [74]. The principle of operation of the PhC temperature sensors is based on the shift observed in the Bragg peak or the photonic stop band as the temperature of the material that forms the PhC changes. It is possible to distinguish between two categories of thermally responsive PhCs, those based on polymer swelling, and those based on phase transitions when incorporated into inorganic host materials. Such materials can be used in place of conventional optical probes or other temperature sensors.

PhCs polymers are traditionally fabricated by combination of colloidal system with a thermosensitive hydrogel such as poly(N-isopropylacrylamide) (PNIPAM) [75–79]. The polymer shrinks by the action of the PNIPAM when the temperature changes and generate a wavelength shift in the reflected light. The process of measurement is reversible and tunable to the visible range, presenting good stability and response time. As well, a poly(p-methylstyrene) hydrogel was used to fabricate 1D PhC sensitive to temperature, as reported by Chiappelli et al. [80]. Last years, other new sophisticated strategies have been implemented to improve the sensor based on PNIPAM. So, an inverse opal combined with LCs, a shell of microsphere fabricated from microfluidic techniques [81] and close-packed silica array of particles combined with PNIPAM [82] have been fabricated and satisfactory tested.

In spite of the good results, previously shown, for the thermally responsive PhCs based on polymer swelling, sensors designed from phase transitions in inorganic material hosts present better performance; the measurements are faster and more stable. The operation principle of these sensor arise from changing the distance between particles of the core-shell during the phase transition when the temperature varies. In the literature, different materials have been used to design the core-shell, particles of selenium and Ag_2Se, [83], $BaTiO_3$ and silica [84] and VO_2 [85]. Furthermore, this thermoresponsive PhC technology has been applied to color readout in organic light emitting diodes (OLEDs) [86].

5.6 Optical Photonic Crystal Sensors

The optical response of a PhC can be disturbed using an external UV or visible light since the characteristic distance of the lattice can be changed. So, this physical mechanism can be employed to design intensity sensors. For example, if a surface of silica nanospheres coated with Malachite Green carbinol is illuminated by UV light, the order/disorder of the PhC is altered, what produces changes in the optical response of the sensor [87]. Other possibility uses LCs, that undergo light-sensitive variations, incorporated if an inverse silica opal to build the sensor [88, 89]. Finally, other strategy turns to volume changes in the matrix of the PhC to shifts in the reflected wavelength as result of the photoisomerization of the molecules of azobenzene and spirobenzopyran chromophore [90, 91]. It is interesting to note that the process is totally reversible.

Optical sensors of refractive index represent the most widespread class of Optically PhC sensors. There are two fundamental sensing procedures commonly employed in photonic refractive index sensing: (i) sensors responsive to external radiation and (ii) sensors based on resonant cavities. PhCs can be used for sensing because they are very responsive to any modification of refractive index surrounding them, their shape and the refractive index of the resonant cavity. Nowadays, there are many designs to sense and measure refractive index based on photonic molecules (PM) and defect cavities. For instance, different PhC's cavities have been proposed as sensing refractive index using dielectric 2D microdisks [92] or 1D double resonant cavities [93]. Other sensor, such as microcavities in 2D arrays of PC [94], sandwich air holes [95], waveguides defect cavities [96], double hole defects [97], ring defects coupled resonators [98] and clusters of microparticles [99] are also successfully used to design and fabricate optical refractive index sensors. A different strategy proposed in the literature to measure refractive index is based on Fano resonances [29, 30]. Summarizing, it is possible to design sensors based on in-plane guided modes and photonic bandgaps in photonic crystal slabs (PCS's) with in-plane light coupling into high index dielectric slabs [100, 101], or based on a Fano resonance in PCS with light coupled from out-of- the-plane directions [102].

6 Conclusion

We have presented a general overview of PhC sensors, their working principles and the main available designs. This global vision allow to extract some conclusions. In the last 15 years the number of papers reporting PhC sensors has grown exponentially. There are sensors with good performance of a great number of variables, particularly of chemical and biochemical ones. PhC sensors require complex fabrication process; this is the main limitation to their commercial expansion. However, this field benefits from all advances in fabrication techniques and new

materials development, what guarantees a continuous improvement of sensor performance in the foreseeable future. The vast majority of the reviewed sensors are based on detecting reflected frequency (and intensity) modifications of the Bragg diffraction signal (for 3D PhCs) or resonant cavities (for 2D PhCs). Only recently conceptual variations like Fano or Mie resonances are beginning to gain presence in the published literature. We believe that optic sensors based in PhC structures continue gaining presence in research and in the market in future years.

References

1. E. Yablonovitch, Inhibited spontaneous emission in solid-state physics and electronics. Phys. Rev. Lett. **58**, 2059–2062 (1987). doi:10.1103/PhysRevLett.58.2059
2. S. John, Strong localization of photons in certain disordered dielectric superlattices. Phys. Rev. Lett. **58**, 2486–2489 (1987). doi:10.1103/PhysRevLett.58.2486
3. K. Ohtaka, Energy band of photons and low-energy photon diffraction. Phys. Rev. B **19**, 5057–5067 (1979). doi:10.1103/PhysRevB.19.5057
4. K. Ohtaka, M. Inoue, Light scattering from macroscopic spherical bodies I. Integrated density of states of transverse electromagnetic fields. Phys. Rev. B **25** (1982)
5. M. Inoue, K. Ohtaka, S. Yanagawa, Light scattering from macroscopic spherical bodies. II. Reflectivity of light and electromagnetic localized state in a periodic monolayer of dielectric spheres. Phys. Rev. B **25**, 689–699 (1982). doi:10.1103/PhysRevB.25.689
6. Villa A. Della, S. Enoch, G. Tayeb et al., Localized modes in photonic quasicrystals with Penrose-type lattice. Opt. Express **14**, 10021 (2006). doi:10.1364/OE.14.010021
7. K. Wang, Light wave states in two-dimensional quasiperiodic media. Phys. Rev. B—Condens. Matter Mater. Phys. **73**, 1–5 (2006). doi:10.1103/PhysRevB.73.235122
8. S. Torquato, F.H. Stillinger, Local density fluctuations, hyperuniformity, and order metrics. Phys. Rev. E: Stat., Nonlin, Soft Matter. Phys. **68**, 041113 (2003). doi:10.1103/PhysRevE.68.041113
9. W. Man, M. Florescu, K. Matsuyama et al., Photonic band gap in isotropic hyperuniform disordered solids with low dielectric contrast. Opt. Express **21**, 19972–19981 (2013). doi:10.1364/OE.21.019972
10. E. Hecht, A. Zajac, *Optics*, 2003rd edn. (Addson-Wesley, Reading, Mass, 1974)
11. J.N. Winn, R.D. Meade, J.D. Joannopoulos, Two-dimensional Photonic Band-gap Materials. J. Mod. Opt. **41**, 257–273 (1994). doi:10.1080/09500349414550311
12. R.D. Meade, K.D. Brommer, A.M. Rappe, J.D. Joannopoulos, Existence of a photonic band gap in two dimensions. Appl. Phys. Lett. **61**, 495 (1992)
13. S. Wong, V. Kitaev, G.A. Ozin, Colloidal crystal films: advances in universality and perfection. J. Am. Chem. Soc. **125**, 15589–15598 (2003). doi:10.1021/ja0379969
14. H. Míguez, V. Kitaev, G.A. Ozin, Band spectroscopy of colloidal photonic crystal films. Appl. Phys. Lett. **84**, 1239 (2004). doi:10.1063/1.1644913
15. A.-P. Hynninen, J.H.J. Thijssen, E.C.M. Vermolen et al., Self-assembly route for photonic crystals with a bandgap in the visible region. Nat. Mater. **6**, 202–205 (2007). doi:10.1038/nmat1841
16. C.I. Aguirre, E. Reguera, A. Stein, Tunable colors in opals and inverse opal photonic crystals. Adv. Funct. Mater. **20**, 2565–2578 (2010)
17. J.S. King, D.P. Gaillot, E. Graugnard, C.J. Summers, Conformally back-filled, non-close-packed inverse-opal photonic crystals. Adv. Mater. **18**, 1063–1067 (2006)
18. F. Meseguer, Colloidal crystals as photonic crystals. Colloids Surf. A Physicochem. Eng. Asp. **270–271**, 1–7 (2005)

19. A.M.R. Pinto, M. Lopez-Amo, Photonic crystal fibers for sensing applications. J. Sens. (2012). doi:10.1155/2012/598178
20. Y. Zhao, X.C. Li, Refractive index sensing based on photonic crystal fiber interferometer structure with up-tapered joints. Sens. Actuators B Chem. **221**, 406–410 (2015)
21. N.W. Ashcroft, N. Mermin, Solid State Physics: Amazon.es: Libros en idiomas extranjeros. https://www.amazon.es/Solid-State-Physics-Neil-Ashcroft/dp/0030839939. Accessed 6 May 2016
22. A. Andueza, M. Sáenz, R. Echeverria et al., Photonic band effects in three dimensional lattices of macroscopic-sized dielectric spheres derived from microwave transmission spectroscopy. Opt Quantum Electron **40**, 1043–1051 (2009). doi:10.1007/s11082-009-9300-7
23. W.H. Bragg, W.L. Bragg, The reflection of X-rays by crystals. Proc. R Soc. A Math. Phys. Eng. Sci. **88**, 428–438 (1913)
24. A. Andueza, R. Echeverría, P. Morales, J. Sevilla, Transmission spectra changes produced by decreasing compactness of opal-like structures. J. Appl. Phys. **105**, 024910 (2009). doi:10.1063/1.3068475
25. G. Mie, Beiträge zur Optik trüber Medien, speziell kolloidaler Metallösungen. Ann. Phys. **330**, 377–445 (1908)
26. M. Bayer, T. Gutbrod, J.P. Reithmaier et al., Optical modes in photonic molecules. Phys. Rev. Lett. **81**, 2582–2585 (1998)
27. X. Wang, O.S. Wolfbeis, R.J. Meier, Luminescent probes and sensors for temperature. Chem. Soc. Rev. **42**, 7834–7869 (2013). doi:10.1039/c3cs60102a
28. U. Fano, Effects of Configuration Interaction on Intensities and Phase Shifts. Phys. Rev. **124**, 1866–1878 (1961)
29. S. Amoudache, R.P. Moiseyenko, Y. Pennec et al., Optical and acoustic sensing using Fano-like resonances in dual phononic and photonic crystal plate. J. Appl. Phys. **119**, 114502 (2016). doi:10.1063/1.4944600
30. W. Zhou, D. Zhao, Y.C. Shuai et al., Progress in 2D photonic crystal Fano resonance photonics. Prog. Quantum Electron. **38**, 1–74 (2014). doi:10.1016/j.pquantelec.2014.01.001
31. Z. Cai, N.L. Smith, J.T. Zhang, S.A. Asher, Two-dimensional photonic crystal chemical and biomolecular sensors. Anal. Chem. **87**, 5013–5025 (2015). doi:10.1021/ac504679n
32. P. Morales, A. Andueza, J. Sevilla, Effect of dielectric permittivity variation in the transmission spectra of non-compact 2D-arrays of dielectric spheres. J. Appl. Phys. **113**, 084906 (2013). doi:10.1063/1.4790880
33. A. Andueza, R. Echeverría, J. Sevilla, Evolution of the electromagnetic modes of a single layer of dielectric spheres with compactness. J. Appl. Phys. **104**, 043103 (2008). doi:10.1063/1.2969659
34. A. Andueza, R. Echeverría, P. Morales, J. Sevilla, Erratum: "Transmission spectra changes produced by decreasing compactness of opal like structures" [J. Appl. Phys. 105, 024910 (2009)]. J Appl Phys 109:019902 (2011). doi:10.1063/1.3524566
35. P. Lalanne, C. Sauvan, J.P. Hugonin, Photon confinement in photonic crystal nanocavities. Laser Photonics Rev. **2**, 514–526 (2008). doi:10.1002/lpor.200810018
36. S. Chakravarty, A. Hosseini, X. Xu et al., Analysis of ultra-high sensitivity configuration in chip-integrated photonic crystal microcavity bio-sensors. Appl. Phys. Lett. **104**, 191109 (2014). doi:10.1063/1.4875903
37. Y.-N. Zhang, Y. Zhao, R.-Q. Lv, A review for optical sensors based on photonic crystal cavities. Sens. Actuators A Phys. **233**, 374–389 (2015). doi:10.1016/j.sna.2015.07.025
38. S.A. Asher, V.L. Alexeev, A.V. Goponenko et al., Photonic crystal carbohydrate sensors: low ionic strength sugar sensing. J. Am. Chem. Soc. **125**, 3322–3329 (2003)
39. M.M.W. Muscatello, L.E. Stunja, S.A. Asher, Polymerized crystalline colloidal array sensing of high glucose concentrations. Anal. Chem. **81**, 4978–4986 (2009)
40. D. Yang, P.T. Zhang, Ultrahigh-Q and low-mode-volume parabolic radius-modulated single photonic crystal slot nanobeam cavity for high-sensitivity refractive index sensing. IEEE Photonics J. **7** (2015)

41. C. Zhang, G.G. Cano, P.V. Braun, Linear and fast hydrogel glucose sensor materials enabled by volume resetting agents. Adv. Mater. **26**, 5678–5683 (2014)
42. S.A. Asher, J. Holtz, L. Liu, Z. Wu, Self-assembly motif for creating submicron periodic materials. Polymerized crystalline colloidal arrays. J. Am. Chem. Soc. **116**, 4997–4998 (1994)
43. A.V. Goponenko, S.A. Asher, Modeling of stimulated hydrogel volume changes in photonic crystal Pb2+ sensing materials. J. Am. Chem. Soc. **127**, 10753–10759 (2005)
44. F. Yan, S. Asher, Cation identity dependence of crown ether photonic crystal Pb2+ sensing. Anal. Bioanal. Chem. **387**, 2121–2130 (2007)
45. D. Arunbabu, A. Sannigrahi, T. Jana, Photonic crystal hydrogel material for the sensing of toxic mercury ions (Hg2+) in water. Soft Matter **7**, 2592 (2011)
46. A.C. Sharma, T. Jana, R. Kesavamoorthy et al., A general photonic crystal sensing motif: creatinine in bodily fluids. J. Am. Chem. Soc. **126**, 2971–2977 (2004)
47. K.I. MacConaghy, C.I. Geary, J.L. Kaar, M.P. Stoykovich, Photonic crystal kinase biosensor. J. Am. Chem. Soc. **136**, 6896–6899 (2014)
48. K. Lee, S.A. Asher, Photonic Crystal Chemical Sensors: pH and Ionic Strength. J. Am. Chem. Soc. **122**, 9534–9537 (2000)
49. X. Xu, A.V. Goponenko, S.A. Asher, Polymerized PolyHEMA photonic crystals: pH and ethanol sensor materials. J. Am. Chem. Soc. **130**, 3113–3119 (2008)
50. R.A. Barry, P. Wiltzius, Humidity-sensing inverse opal hydrogels. Langmuir **22**, 1369–1374 (2006)
51. H. Hu, Q.-W. Chen, K. Cheng, J. Tang, Visually readable and highly stable self-display photonic humidity sensor. J. Mater. Chem. **22**, 1021–1027 (2012)
52. C. Fenzl, S. Wilhelm, T. Hirsch, O.S. Wolfbeis, Optical sensing of the ionic strength using photonic crystals in a hydrogel matrix. ACS Appl. Mater. Interfaces **5**, 173–178 (2013)
53. K.W. Kimble, J.P. Walker, D.N. Finegold, S.A. Asher, Progress toward the development of a point-of-care photonic crystal ammonia sensor. Anal. Bioanal. Chem. **385**, 678–685 (2006)
54. A.C. Arsenault, T.J. Clark, G. von Freymann et al., From colour fingerprinting to the control of photoluminescence in elastic photonic crystals. Nat. Mater. **5**, 179–184 (2006). doi:10.1038/nmat1588
55. J. Li, Y. Wu, J. Fu et al., Reversibly strain-tunable elastomeric photonic crystals. Chem. Phys. Lett. **390**, 285–289 (2004)
56. I.B. Burgess, M. Lončar, J. Aizenberg, Structural colour in colourimetric sensors and indicators. J. Mater. Chem. C **1**, 6075 (2013)
57. J.M. Jethmalani, W.T. Ford, Diffraction of visible light by ordered monodisperse silica − Poly(methyl acrylate) composite films. Chem. Mater. **8**, 2138–2146 (1996)
58. S.H. Foulger, P. Jiang, A.C. Lattam et al., Mechanochromic response of Poly(ethylene glycol) methacrylate hydrogel encapsulated crystalline colloidal arrays. Langmuir **17**, 6023–6026 (2001)
59. S.H. Foulger, P. Jiang, A. Lattam et al., Photonic crystal composites with reversible high-frequency stop band shifts. Adv. Mater. **15**, 685–689 (2003)
60. K. Hwang, D. Kwak, C. Kang et al., Electrically tunable hysteretic photonic gels for nonvolatile display pixels. Angew. Chemie. **123**, 6435–6438 (2011)
61. M. Ozaki, Y. Shimoda, M. Kasano, K. Yoshino, Electric field tuning of the stop band in a liquid-crystal-infiltrated polymer inverse opal. Adv. Mater. **14**, 514–518 (2002)
62. Y. Shimoda, M. Ozaki, K. Yoshino, Electric field tuning of a stop band in a reflection spectrum of synthetic opal infiltrated with nematic liquid crystal. Appl. Phys. Lett. **79**, 3627 (2001)
63. A.C. Arsenault, H. Míguez, V. Kitaev et al., A polychromic, fast response metallopolymer gel photonic crystal with solvent and redox tunability: a step towards photonic ink (P-Ink). Adv. Mater. **15**, 503–507 (2003)
64. A.C. Arsenault, D.P. Puzzo, I. Manners, G.A. Ozin, Photonic-crystal full-colour displays. Nat. Photonics **1**, 468–472 (2007)

65. D.P. Puzzo, A.C. Arsenault, I. Manners, G.A. Ozin, Electroactive inverse opal: a single material for all colors. Angew. Chemie. **121**, 961–965 (2009)
66. K. Ueno, J. Sakamoto, Y. Takeoka, M. Watanabe, Electrochromism based on structural colour changes in a polyelectrolyte gel. J. Mater. Chem. **19**, 4778 (2009)
67. Y. Saado, M. Golosovsky, D. Davidov, A. Frenkel, Tunable photonic band gap in self-assembled clusters of floating magnetic particles. Phys. Rev. B **66**, 195108 (2002)
68. S. Sacanna, A.P. Philipse, Preparation and properties of monodisperse latex spheres with controlled magnetic moment for field-induced colloidal crystallization and (dipolar) chain formation. Langmuir **22**, 10209–10216 (2006)
69. J. Ge, Y. Hu, M. Biasini et al., Superparamagnetic magnetite colloidal nanocrystal clusters. Angew. Chemie. **119**, 4420–4423 (2007)
70. J. Ge, Y. Yin, Magnetically responsive colloidal photonic crystals. J. Mater. Chem. **18**, 5041 (2008)
71. C. Zhu, L. Chen, H. Xu, Z. Gu, A magnetically tunable colloidal crystal film for reflective display. Macromol. Rapid Commun. **30**, 1945–1949 (2009)
72. X. Xu, G. Friedman, K.D. Humfeld et al., Synthesis and utilization of monodisperse superparamagnetic colloidal particles for magnetically controllable photonic crystals. Chem. Mater. **14**, 1249–1256 (2002)
73. X. Xu, S.A. Majetich, S.A. Asher, Mesoscopic Monodisperse Ferromagnetic Colloids Enable Magnetically Controlled Photonic Crystals. J. Am. Chem. Soc. **124**, 13864–13868 (2002)
74. J. Ballato, A. James, A ceramic photonic crystal temperature sensor. J. Am. Ceram. Soc. **82**, 2273–2275 (2004)
75. X. Wang, O.S. Wolfbeis, R.J. Meier, Luminescent probes and sensors for temperature. Chem. Soc. Rev. **42**, 7834–7869 (2013)
76. J.M. Weissman, H.B. Sunkara, A.S. Tse, SA. Asher thermally switchable periodicities and diffraction from mesoscopically ordered materials. Science (80-) **274**, 959–963 (1996)
77. J.D. Debord, L.A. Lyon, Thermoresponsive photonic crystals. J. Phys. Chem. B **104**, 6327–6331 (2000)
78. Z. Hu, X. Lu, J. Gao, Hydrogel opals. Adv. Mater. **13**, 1708–1712 (2001)
79. C.E. Reese, A.V. Mikhonin, M. Kamenjicki et al., Nanogel nanosecond photonic crystal optical switching. J. Am. Chem. Soc. **126**, 1493–1496 (2004)
80. M.C. Chiappelli, R.C. Hayward, Photonic multilayer sensors from photo-crosslinkable polymer films. Adv. Mater. **24**, 6100–6104 (2012)
81. Y. Hu, J. Wang, H. Wang et al., Microfluidic fabrication and thermoreversible response of core/shell photonic crystalline microspheres based on deformable nanogels. Langmuir **28**, 17186–17192 (2012)
82. T. Dey, Colloidal crystalline array of hydrogel-coated silica nanoparticles: effect of temperature and core size on photonic properties. J. Sol-Gel. Sci. Technol. **57**, 132–141 (2010)
83. U. Jeong, Y. Xia, Photonic crystals with thermally switchable stop bands fabricated from Se@Ag2Se spherical colloids. Angew. Chem. Int. Ed. Engl. **44**, 3099–3103 (2005)
84. J. Zhou, C.Q. Sun, K. Pita et al., Thermally tuning of the photonic band gap of SiO[sub 2] colloid-crystal infilled with ferroelectric BaTiO[sub 3]. Appl. Phys. Lett. **78**, 661 (2001)
85. A.B. Pevtsov, D.A. Kurdyukov, V.G. Golubev et al., Ultrafast stop band kinetics in a three-dimensional opal- V O 2 photonic crystal controlled by a photoinduced semiconductor-metal phase transition. Phys. Rev. B **75**, 153101 (2007)
86. A.T. Exner, I. Pavlichenko, B.V. Lotsch et al., Low-cost thermo-optic imaging sensors: a detection principle based on tunable one-dimensional photonic crystals. ACS Appl. Mater. Interfaces **5**, 1575–1582 (2013)
87. Z.-Z. Gu, A. Fujishima, O. Sato, Photochemically tunable colloidal crystals. J. Am. Chem. Soc. **122**, 12387–12388 (2000)

88. S. Kubo, Z.-Z. Gu, K. Takahashi et al., Control of the optical band structure of liquid crystal infiltrated inverse opal by a photoinduced nematic – isotropic phase transition. J. Am. Chem. Soc. **124**, 10950–10951 (2002). doi:10.1021/ja026482r
89. S. Kubo, Z.-Z. Gu, K. Takahashi et al., Tunable photonic band gap crystals based on a liquid crystal-infiltrated inverse opal structure. J. Am. Chem. Soc. **126**, 8314–8319 (2004). doi:10.1021/ja0495056
90. M. Kamenjicki, I.K. Lednev, A. Mikhonin et al., Photochemically controlled photonic crystals. Adv. Funct. Mater. **13**, 774–780 (2003)
91. M. Kamenjicki Maurer, I.K. Lednev, S.A. Asher, Photoswitchable Spirobenzopyran- Based Photochemically Controlled Photonic Crystals. Adv. Funct. Mater. **15**, 1401–1406 (2005)
92. S.V. Boriskina, Spectrally engineered photonic molecules as optical sensors with enhanced sensitivity: a proposal and numerical analysis. J. Opt. Soc. Am. B **23**, 1565 (2006). doi:10.1364/JOSAB.23.001565
93. H. Lin, Z. Yi, J. Hu, Double resonance 1-D photonic crystal cavities for single-molecule mid-infrared photothermal spectroscopy: theory and design. Opt. Lett. **37**, 1304–1306 (2012)
94. E. Chow, A. Grot, L.W. Mirkarimi et al., Ultracompact biochemical sensor built with two-dimensional photonic crystal microcavity. Opt. Lett. **29**, 1093 (2004). doi:10.1364/OL.29.001093
95. X. Wang, Z. Xu, N. Lu et al., Ultracompact refractive index sensor based on microcavity in the sandwiched photonic crystal waveguide structure. Opt. Commun. **281**, 1725–1731 (2008). doi:10.1016/j.optcom.2007.11.040
96. D.F. Dorfner, T. Hürlimann, T. Zabel et al., Silicon photonic crystal nanostructures for refractive index sensing. Appl. Phys. Lett. **93**, 181103 (2008). doi:10.1063/1.3009203
97. L.A. Shiramin, R. Kheradmand, A. Abbasi, High-sensitive double-hole defect refractive index sensor based on 2-D photonic crystal. IEEE Sens. J. **13**, 1483–1486 (2013). doi:10.1109/JSEN.2012.2237093
98. L. Huang, H. Tian, D. Yang et al., Optimization of figure of merit in label-free biochemical sensors by designing a ring defect coupled resonator. Opt. Commun. **332**, 42–49 (2014). doi:10.1016/j.optcom.2014.06.033
99. A. Francois, M. Himmelhaus, Optical biosensor based on whispering gallery mode excitations in clusters of microparticles. Appl. Phys. Lett. **92**, 141107 (2008). doi:10.1063/1.2907491
100. H. Kurt, M.N. Erim, N. Erim, Various photonic crystal bio-sensor configurations based on optical surface modes. Sens. Actuators B Chem. **165**, 68–75 (2012). doi:10.1016/j.snb.2012.02.015
101. W.-C. Lai, S. Chakravarty, Y. Zou et al., Slow light enhanced sensitivity of resonance modes in photonic crystal biosensors. Appl. Phys. Lett. **102**, 41111 (2013). doi:10.1063/1.4789857
102. O. Levi, M.M. Lee, J. Zhang et al., Sensitivity analysis of a photonic crystal structure for index-of-refraction sensing, ed. by A.N. Cartwright, D.V. Nicolau, Biomed. Opt. 2007 (International Society for Optics and Photonics, 2007), p 64470P–64470P–9
103. H. Míguez, V. Kitaev, G.A. Ozin, Band spectroscopy of colloidal photonic crystal films. Appl. Phys. Lett. **84**, 1239 (2004)

Long Period Grating Based Fibre Optic Chemical Sensors

Sergiy Korposh, Seung-Woo Lee and Stephen James

Abstract The principle of operation of optical fibre long period grating (LPG) sensors is described. In particular, the chapter explores the use of LPGs as a chemical sensing platform, discussing the fabrication of LPGs and the various approaches that have been employed to modify the cladding of the LPG and thus sensitise the LPG. Examples of the practical application of LPG chemical sensors are provided.

1 Introduction

The development of optical fibre long period grating (LPG) based sensors is an area of considerable research activity, with the interest driven by their sensitivity to a number of parameters, principally temperature, strain, bending and the surrounding refractive index, by the potential for multi-parameter sensing using as single optical element, and by the ability to tune the sensitivity of the devices by appropriate choice of period. Over the past decade there has been a particular interest in the deposition onto the cladding of optical fibres containing LPGs of chemically sensitive coatings that change their refractive index in response to specific chemical stimuli. This chapter will focus on the use of LPGs as a chemical and bio-sensing platform, outlining approaches used to fabricate LPGs, the techniques used to deposit materials onto the optical fibres, means for optimising sensitivity, and examples of their use. The chapter will draw upon work that has been conducted as collaboration between teams at the Universities of Kitakyushu, Cranfield and Nottingham.

S. Korposh (✉)
Advanced Optics Group, The University of Nottingham, Nottingham, UK
e-mail: S.Korposh@nottingham.ac.uk

S.-W. Lee
The University of Kitakyushu, Kitakyushu, Japan

S. James
Engineering Photonics, Cranfield University, Cranfield, UK

© Springer International Publishing Switzerland 2017

I.R. Matias et al. (eds.), *Fiber Optic Sensors*, Smart Sensors,
Measurement and Instrumentation 21, DOI 10.1007/978-3-319-42625-9_12

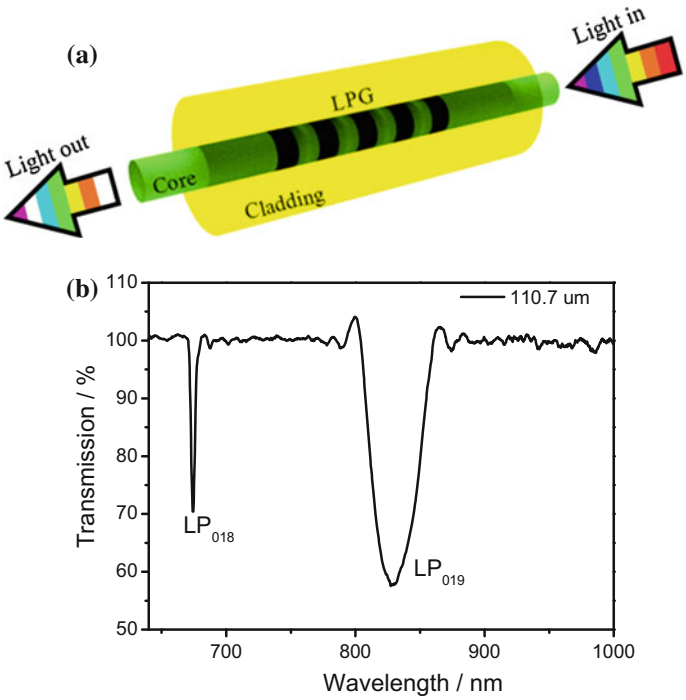

Fig. 1 **a**, schematic illustration of the LPG optical fibre, shown the attenuation bands introduced to the broad input spectrum; **b**, transmission spectrum, measured in air, of an LPG period of 110.7 μm and length 30 mm fabricated in an optical fibre of cut off wavelength 670 nm, coupling to the LP_{018} and LP_{019} cladding modes. Adopted from [49]

An LPG, shown schematically in Fig. 1a, is a periodic modulation of the properties of an optical fibre, which facilitates the coupling of light from the propagating core modes to a set of co-propagating cladding modes. The high attenuation of the cladding modes results in a series of resonance bands in the transmission spectrum of the optical fibre, as shown in Fig. 1b. The resonance bands centred at wavelengths satisfying the phase matching condition:

$$\lambda_x = \left(n_{core} - n_{clad(x)}\right)\Lambda \tag{1}$$

where λ_x represents the is coupled to the LP_{0x} cladding mode, n_{core} is the effective refractive index of the mode propagating in the core of the fibre, $n_{clad(x)}$ is the effective index of the LP_{0x} cladding mode and Λ is the period of the LPG.

The modulation of the fibre properties may take the form of a change in the refractive index of the core of the fibre, induced for example by exposure of the fibre to the output from a UV laser, a femtosecond pulsed laser or a CO2 laser, or by a perturbation to the diameter of the fibre. The efficiency of coupling, and thus depth of the resonance bands, is determined by the "strength" of the grating (e.g. the

amplitude of the refractive index modulation), the overlap of the mode profiles of the modes of the core and cladding, and the length of the grating. Environmental parameters that can influence the period of the gratings and/or the difference between the effective refractive indices of the core and cladding modes can be sensed by monitoring the concomitant changes in the central wavelength of the resonance bands.

2 LPGs as a Chemical Sensing Platform

Among the wide variety of optical fibre based sensor designs and measurement schemes that have been reported and demonstrated for chemical sensing, refractometers and chemical sensors based on optical fibre gratings have attracted considerable interest, in part because they offer wavelength-encoded information, which overcomes the referencing issues associated with intensity based approaches. Such devices have been investigated extensively [1–3].

The sensitivity of LPGs to the refractive index of their surrounding medium arises from the dependence of the phase matching condition (Eq. 1) upon the effective refractive index of the cladding mode. This sensitivity may be used to measure the refractive index of a solution, providing information on its concentration, but this is not chemically selective. To provide the sensor with selective response to specific analytes, the cladding of the region of the optical fibre containing the LPG can be coated with a material that exhibits a change in its optical thickness in response to a target analyte. Similarly to surface plasmon resonance and planar waveguide devices, LPG have been shown to provide highly precise analytical information about adsorption and desorption processes associated with the RI and thickness of the sensing layer.

The phase matching condition in Eq. 1 can be used to generate a family of curves that allow the prediction of the resonance wavelengths by calculating the dispersion of the core and cladding modes. The phase matching curves can be used to explain the way in which LPGs can be used as a chemical sensing platform.

For higher order cladding modes the curves contain a turning point, the so-called phase matching turning point, PMTP, or turn around point, TAP. Due to the gradient of the curves, the resonances bands of LPGs fabricated to access the phase matching turning point exhibit their maximum sensitivity to external perturbations [4]. The evolution of the transmission spectrum of an LPG at the PMPT in response to, for example, changes in the optical thickness of a coating despotised on the optical fibre can be understood with reference to Fig. 2. The LPG is fabricated with a period such that, without a coating, it is not possible to couple to the LP_{019} mode. The corresponding spectrum contains a resonance band for coupling to the LP_{018} band (Fig. 2a, b). As the optical thickness (product of the geometrical thickness and refractive index) of the coating increases, the effective index of the cladding mode is changed, causing the phase matching curves move in the direction of the arrow shown in Fig. 2a. When the horizontal line corresponding to the LPG period is

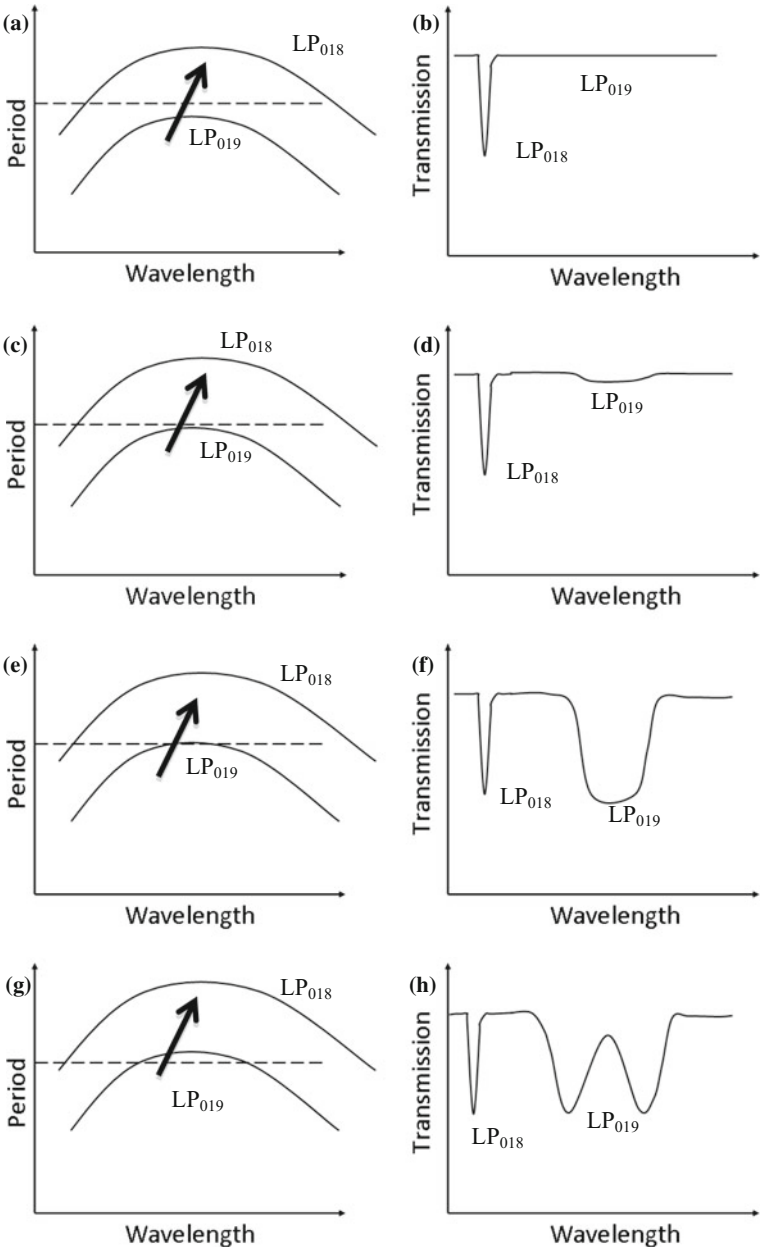

Fig. 2 Illustration of the properties of an LPG near the phase matching turning point (PMTP); arrow shows direction of the shift of the phase matching curve at the increase of the effective refractive index of the cladding mode caused by increasing optical thickness. Adapted from [6]

tangential to the phase matching curve at the PMTP, a broad resonance band corresponding to coupling to LP_{019} begins to form, and there is a small blue shift in the central wavelength of the LP_{018} resonance band. Further increases in the optical thickness of the coating result in conditions at which the coupling to the same cladding mode occurs at 2 different wavelengths as the further development of the LP_{019} resonance band causes it to split into two bands, the so called dual resonance [4]. LPGs of appropriate period, coated with functional materials and operating at the PMTP, have been used to demonstrate sensors for chemical analytes in gaseous [5] or liquid media [6].

The deposition of a thin coating onto an LPG causes a further phenomenon that has a significant influence on the sensitivity of the resonance bands to changes in the properties of the coating. The evolution of the transmission spectrum of an LPG of period 400 μm (not at the PMTP) to the deposition of such a coating is shown in Fig. 3 [7]. Here, the responses of the resonance bands to an increase of the coating thickness are characterised by blue wavelength shifts, which accelerate as the coating thickness increases (region T_1). The region of high sensitivity to coating thickness is termed the "mode transition region". As the thickness is increased further, movement of the bands slows, with the band taking on the characteristics of the adjacent lower order resonance band. Further mode transition regions are observed with increasing coating thickness.

The physical processes underlying this behavior were clarified by a number of theoretical treatments [8–13]. Using an LP mode approximation, it has been shown that, as the optical thickness of the coating is increased, the coating becomes phase matched with one of the cladding modes. This is accompanied by a rapid change in the effective index of the mode, as shown in Fig. 4 [11]. The loss of the cladding mode results in a reorganization of the remaining cladding modes, such that the effective index, and the electric field profile, of each changes to become that of the adjacent lower order mode [13].

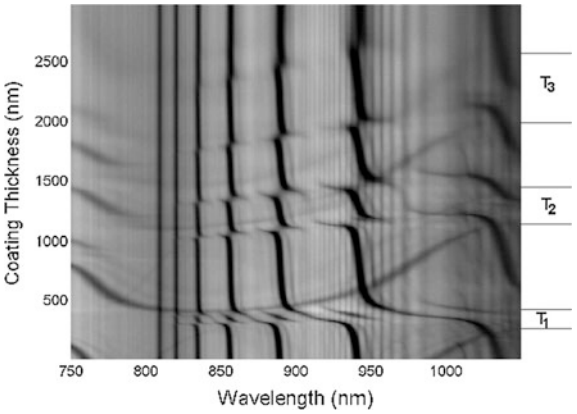

Fig. 3 Evolution of the spectrum of an LPG of period 400 μ fabricated in boron-germanium co-doped fibre in response to the deposition of a coating of ω-tricosanoic acid (refractive index 1.57). *Black* represents 0 % transmission, and *white* 100 % transmission. The labels T_1, T_2 and T_3 refer to mode transition regions. All spectra recorded with the LPG in air. Adapted from [7]

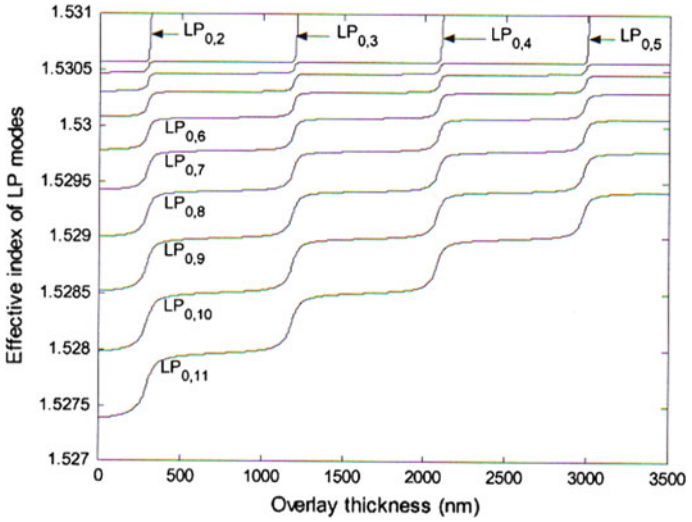

Fig. 4 Effective refractive indices of the cladding modes, calculated using the LP approximation, as a function of overlay thickness, illustrating the reorganisation of the cladding modes during the transition to guidance by the overlay. Adapted from [11]

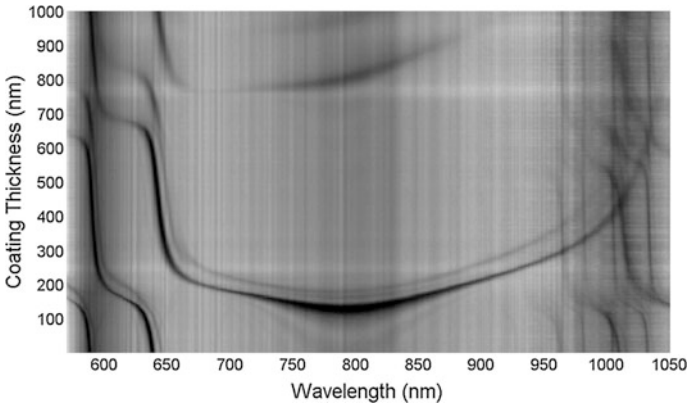

Fig. 5 Evolution of the transmission spectrum of an LPG of period 100 μm, fabricated in a single mode optical fibre of cut-off wavelength 700 nm, in response to the deposition of a coating of ω-tricosanoic acid using the Langmuir Blodgett Technique. Spectra recorded with the LPG below the water sub-phase. Adapted from [4]

By careful selection of the period of the LPG it is possible to ensure that, for a particular coating material, the PMTP and the mode transition region can coincide, offering optimized sensitivity to changes in the optical thickness of the coating, as illustrated in Fig. 5 [4].

3 Fabrication of LPGs

The modulation of the optical properties of the fibre required to fabricate an LPG may be achieved by modifying periodically the refractive index of the core by photoinduction or by physically deforming the optical fibre. The refractive index of the core may be modified by exposing locally the fibre to the output from a high-powered UV laser [14, 15], a CO_2 laser [16, 17], an infrared femtosecond laser [18], or by ion implantation [19]. Deformation of the fibre can be caused mechanically (e.g., inducing physical periodic corrugations on the fibre) [20] or by periodically tapering the fibre using a CO_2 laser [21] or an electrical arc discharge [22] as the heat source. In recent years there have been considerable advances in the fabrication of LPGs using electric arc [23] and CO_2 lasers [24], as they offer the ability to fabricate gratings in fibres that are not photosensitive—for example photonic crystal fibres and fibres with pure silica cores. The also allow the fabrication of short LPGs, of length as low as 2 periods. In the work described in this chapter, the LPGs have been fabricated via UV laser based inscription, as is allows gratings with shorter periods to be fabricated, allowing coupling to higher order cladding modes and thus access to the PMTP.

The inscription of an LPG via UV irradiation can be carried out via a point-by-point method [25] or by using an amplitude mask [25], as illustrated in Fig. 6. An amplitude mask introduces a spatial modulation to the intensity of the laser beam incident on the optical fibre, Fig. 6a. In the point-by-point technique (Fig. 6b), the LPG is formed by exposing a section of length equal to half the period of the LPG to the UV beam for a set time and then translating either the fibre or the laser beam by a distance equal to the period, repeating the process until the desired length is attained. Although the fabrication of LPGs using the point-by-point approach can be more time consuming than using an amplitude mask, the flexibility of the technique allows the user to create LPGs with arbitrary period, with non-uniform period, and with arbitrary refractive index modulation profile by varying the dwell time at each point.

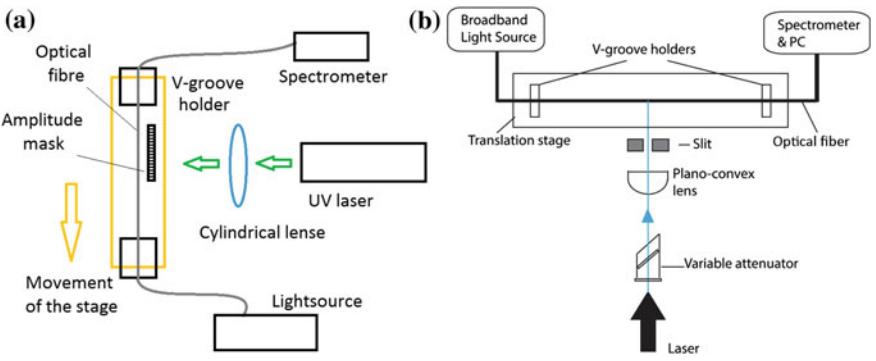

Fig. 6 Schematic illustration of the LPG fabrication using UV laser beam via **a** amplitude mask; and **b** point-by-point technique. Adapted from [26]

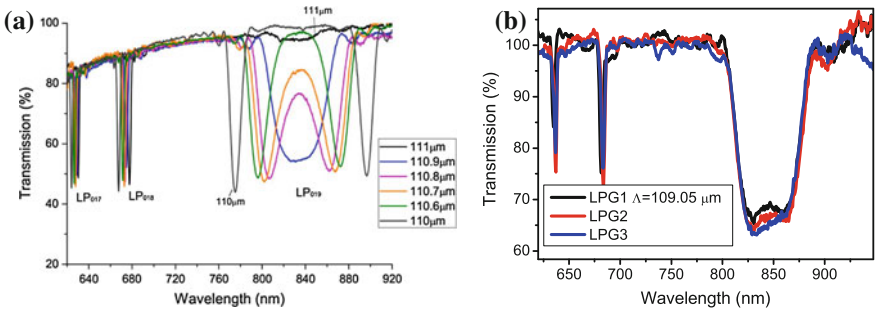

Fig. 7 Transmission spectra of LPGs at and around the PMTP with different grating periods written using **a** point-by-point technique [26]; **b** Transmission spectra of LPGs at the PMTP with the same grating period written using amplitude mask

It is known that optical fibre LPGs exhibit their highest sensitivity to environmental perturbation when the period is such that the phase matching condition is satisfied at its turning point. The reproducible fabrication of LPGs with parameters satisfying this condition requires high resolution control over the properties of the grating. The performance of an LPG fabrication system based on the point-by-point UV exposure approach was analysed by Wong et al. [26]. It was demonstrated that the control of factors influencing reproducibility, such as period, duty cycle, and the environment in which the device is fabricated, is extremely important. In particular, the changes in grating period as small as 0.1 μm have a significant influence on the final transmission spectrum of the LPG sensor as shown in Fig. 7a.

The repeatability of the fabrication procedure is one of the important requirements for mass production of LPG based sensors and it is highly challenging to achieve this especially when LPG operates close to or at the PMTP. The repeatability of the point-by-point LPG fabrication system was investigated by fabricating four LPGs of nominally identical period in [26]. Once the period of the LPG at which the optimum sensitivity for the particular application has been identified, amplitude masks can be used for reliable and reproducible mass production. It should be noted that optimum sensitivity of the LPG for the particular application depends on the bulk RI range at which sensor needs to operate, on the coating used to sensitize the LPG and the range of the analyte that needs to be measured. Figure 7b shows the repeatability achieved using an amplitude mask. The main advantage of the amplitude mask over point-by-point approach is the reduced fabrication time. For same parameters of the writing laser, length and the strength of the LPG, the average fabrication time can be reduced from hours to minutes when compare amplitude mask with point-by-point approach [27].

4 Surface Modification

The combination of optical fibres and nanomaterials provides the prospect for the fabrication of chemical sensors with high sensitivity and that offer specific response to targeted chemical species [28, 29]. Achieving the coating thickness that provides optimized sensitivity requires control on the nm scale, which is why many reports have exploited the Langmuir Blodgett (LB) and layer-by-layer (LbL) electrostatic self-assembly (ESA) coating deposition techniques, where a multilayer coating is deposited with each layer having a thickness of order 1 nm. Based on this principle, sensors for organic vapors, metal ions, humidity, organic solvents and biological materials have been reported [30–32].

4.1 Layer by-Layer Electrostatic Self-assembly of Mesoporous Thin Films

The LbL technique, which is based on the alternate adsorption of polycations and polyanions onto the surface of a substrate, is a powerful surface modification method, Fig. 8. This alternate adsorption technique is still expanding its potential because of its versatility and convenience for the fabrication of nano-assembled thin films employing various organic and inorganic materials.

We have demonstrated an approach to LPG based chemical sensing that consists of a 2 stage process. The first stage involves the deposition of a mesoporous coating onto an LPG operating near the phase matching turning point. In the second stage, a functional material, chosen to be sensitive to the analyte of interest, is infused into the base mesoporous coating. The mesoporous thin film be used for sensing utilising functional groups of the polycation [33] or a functional compound can be infused into the film, increasing the range of possible applications [6]. The initially low RI of the mesoporous coating, 1.2@633 nm, can be increased significantly by the chemical infusion, resulting in a large change in the LPG's transmission spectrum.

In a typical procedure, SiO_2 NPs are deposited onto the surface of the fibre using the LbL process, as illustrated in Fig. 9 [6]. Briefly, the section of the optical fibre containing the LPG, with its surface treated such that it is terminated with OH

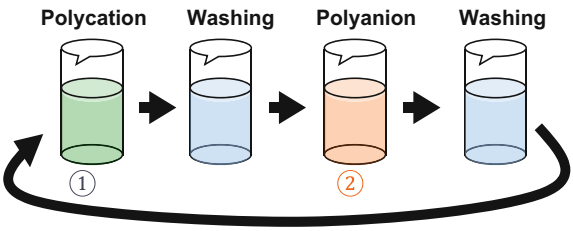

Fig. 8 Schematic illustration of the layer-by-layer electrostatic self-assembly method

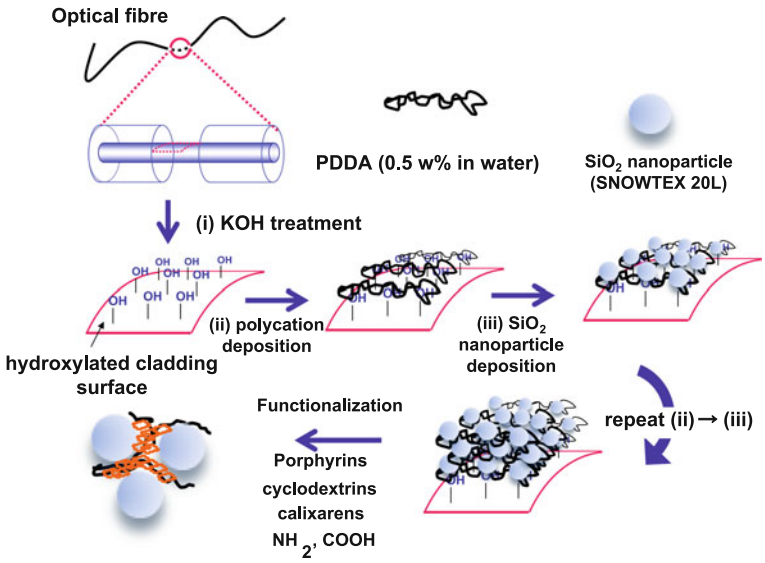

Fig. 9 Schematic illustration of the deposition of a mesoporous coating onto the LPG fibre. Adapted from [6]

groups, is alternately immersed into a 0.5 wt% solution containing a positively charged polymer, Poly(diallyldimethylammonium chloride), PDDA, and, after washing, into a 1 wt% solution containing the negatively charged SiO_2 NPs solution, each for 20 min. This process is repeated until the required coating thickness is achieved. The coated fibre is immersed in a solution of, for example, Tetrakis (4-sulfophenyl)porphine, TSPP, or polyacrylic acid, PAA, as functional compound for 2 h, which infuses into the porous coating and provides the sensor with its specificity. Due to the electronegative sulfonic groups present in the TSPP and carboxylic in PAA, an electrostatic interaction occurs between the infused compound and the positively charged PDDA in the $(PDDA/SiO_2)_x$ film (where x subscript denotes number of bilayers) [6]. PAA is considered as a promising sensor element for ammonia sensing, owing to the presence of free carboxylic function groups that lead to high affinity towards amine compounds [34]. On the other hand it has been shown that protonation and deprotonation of TSPP leads to the changes in its optical properties [6]. After immersion into the TSPP or PAA solutions, the fibre is rinsed in distilled water, in order to remove physically adsorbed compounds, and is dried by flushing with N_2 gas. The compounds remaining in the porous silica structure are bound to the surface of the polymer layer that coats each nanosphere. This effectively increases the available surface area for the compounds to bond to. The presence of functional chemical compounds increases the RI of the porous coating and results in a significant change in the LPG's transmission spectrum [33], consistent with previous observations for increasing the coating thickness [4].

4.2 Molecular Imprinting

Molecular imprinting is one of the most promising approaches for achieving specific molecular recognition. The technique is versatile, as any compound with functional groups can, in principle, be imprinted in different porogens (either water or organic solvents). The sensing and transduction principles combined with the imprinting approach are used to make the imprinting process quantifiable, thus providing detailed information about the recognition phenomenon occurring on the imprinting interface. The basic concept of molecular imprinting is based on the creation of imprints of a template compound (i.e. a chemical molecule or biological species that needs to be detected—the analyte) in a polymeric matrix, achieved by its incorporation during the polymerization step. Molecular imprinting is achieved in three steps, the first being the complex formation of the template with selected functional monomers, followed by a polymerization step for creation of a matrix that fixes the monomers in the right position to interact with the analyte and with the final step being the removal of the template to leave behind cavities specific for the template, as illustrated in Fig. 10 [35].

A large body of work discussing the use of molecular imprinting can be found in the literature. Generally, the imprinting approach can be divided into two wide branches, based on the matrix material used for template incorporation. These approaches are discriminated by the use of organic and inorganic matrices.

4.2.1 Organic MIPs

To date, most examples of high fidelity molecular imprinting have used highly cross-linked organic polymers as the imprinting matrix [36]. Due to the variety of materials and the flexibility of the approach, molecular imprinting in organic

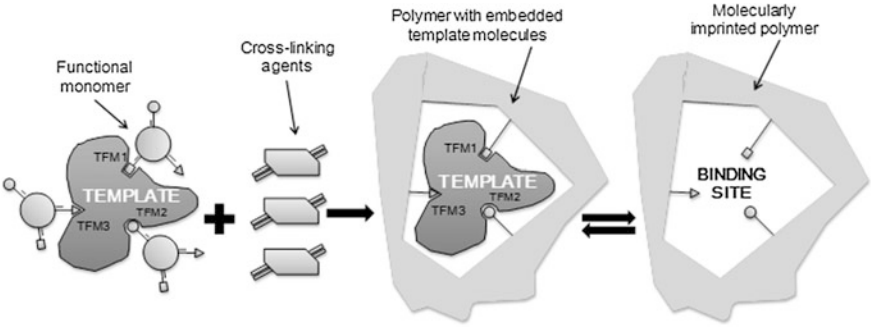

Fig. 10 Schematic illustration of the molecular imprinting procedure. Adapted from [35]

matrices is more effective than it is in inorganic matrices [37]. Several approaches for the creation of MIP materials have been developed and are classified as covalent and non-covalent, depending on the nature of the binding between template and polymer matrix.

4.2.2 Inorganic MIPs

Molecular imprinting technique employing inorganic materials is generally based on the same principle as that of organic materials, consisting of covalent and/or non-covalent interaction between template and functional monomer, polymerization and template removal. Instead of organic monomer inorganic precursors, metal alkoxides, are usually used to form inorganic matrices via sol-gel process that incorporates template molecules, as shown in Fig. 11 [37].

The ability to deposit such materials in the form of a thin film is of significance for sensor applications. In comparison with bulk materials, ultrathin films provide faster binding, better accessibility of the imprinted sites, higher binding efficiency and improved adsorption rate [37].

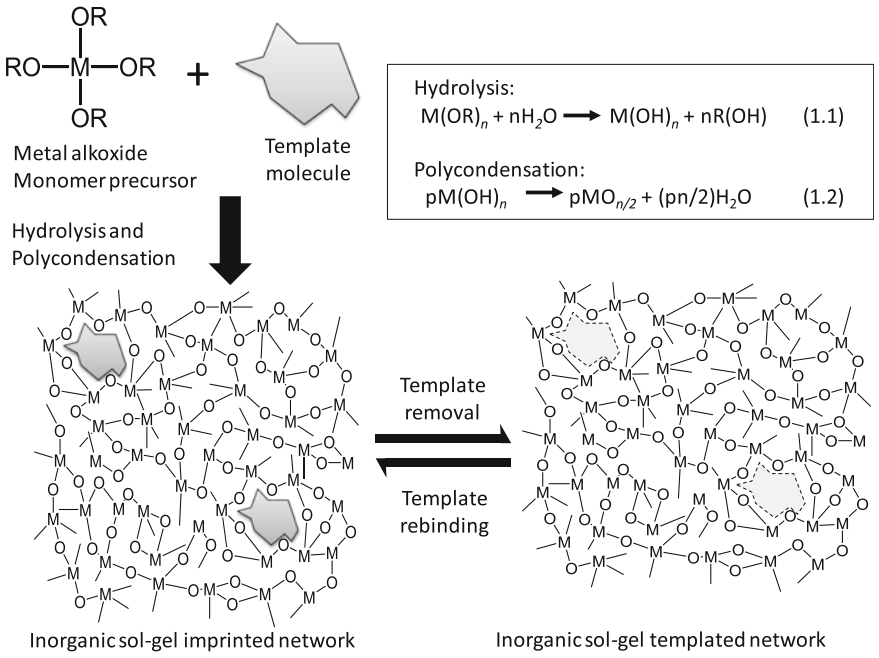

Fig. 11 Schematic illustration of the molecular imprinting using sol-gel process; R-alkyl radical; M represents a network-forming element such as Si, Ti, Zr, Al etc. Adapted from [37]

5 Experimental Results

5.1 Ammonia Sensors

An LPG of period 100 μm, with a mesoporous coating of PDDA/SiO_2 nanoparticles (NPs) (SNOWTEX 20L (40–50 nm), Nissan Chemical) deposited using the LbL process and infused with TSPP as the functional compound, was used for the detection of ammonia in the gas phase and in solution [6].

For the detection of ammonia in solution, the LPG the deposition process used is illustrated in Fig. 12. The sensitivity to ammonia in water of an LPG coated with a TSPP infused $(PDDA/SiO_2)_{10}$ film was characterized by sequential immersion of the coated LPG into ammonia solutions with concentrations 0.1, 1, 5 and 10 ppm. The lower ammonia concentrations were prepared by dilution of the stock solution of 28 wt%. In order to assess the stability of the base line, the coated LPG was immersed several times into 150 μL of pure water. The decrease of attenuation of the second resonance band, LP_{021}, at 800 nm, suggests the partial removal of the adsorbed TSPP molecules [6]. The equilibrium state was achieved after several exposures into water. For the ammonia detection, the LPG fibre was exposed into a 150 μL ammonia solution of 0.1 ppm, followed by drying and immersion into ammonia solutions of 1, 5 and 10 ppm [6].

The response of the transmission spectrum to varying concentration of ammonia is shown in Fig. 12a. The dynamic response of the sensor was assessed by monitoring the transmission at the centre of the LP_{021} resonance band at 800 nm. The response is shown in Fig. 12b, where the "air", "H_2O" and "NH_3" regions correspond to the transmission recorded at 800 nm after drying the LPG and immersing the device into water and ammonium solutions, respectively. After repeating the

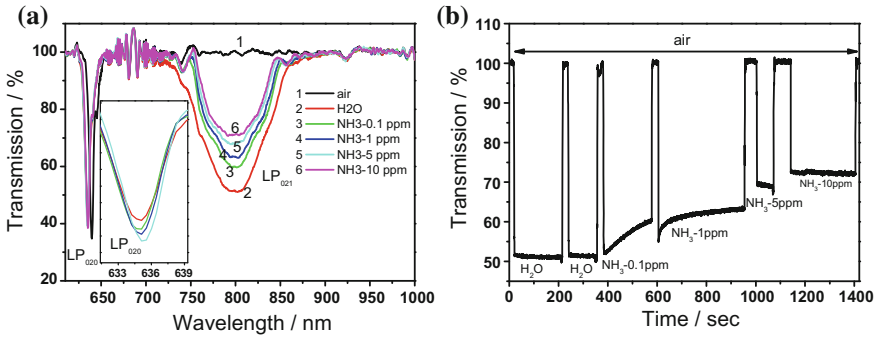

Fig. 12 **a** Transmission spectra of the LPG coated with a TSPP -nfused $(PDDA/SiO_2)_{10}$ film due to immersion into water and into ammonia solutions of different concentrations: "H_2O", LPG exposed into water; "air", LPG in air after drying with N_2 gas; "NH_3 x ppm", LPG exposed into a x ppm ammonia solution, where x = 0.1, 1, 5 and 10. **b** Dynamic response to water and ammonia solutions (0.1, 1, 5 and 10 ppm) recorded at 800 nm; LP_{020} and LP_{021} are labelling the linear polarized 020 and 021 modes, respectively. Adapted from [6]

process of immersion in water and drying 4 times, the recorded spectrum was stable, demonstrating the robustness and stability of the employed molecules in aqueous environments (H_2O regions indicated in Fig. 12b). On immersion in 1 ppm and 5 ppm ammonia solutions, the transmission measured at 800 nm increased. The transmission when the coated LPG was immersed in a 10 ppm ammonia solution exhibited a further increase, reaching a steady state within 100 s, as shown in Fig. 12b [6]. The resonance feature corresponding to coupling to the LP_{020} cladding mode exhibited additional small red shifts of 0.5 and 1.5 nm when subsequently immersed in solutions of 1 and 10 ppm ammonia concentration, respectively, along with decreased amplitude, as shown in Fig. 9a. The limits of detection (LOD) for the 100 μm period LPG coated with a $(PDDA/SiO_2)_{10}$ film that was infused with TSPP were 0.14 and 2.5 ppm when transmission and wavelength shift were measured respectively. The LOD was derived from the calibration curve and the following equation [6, 38].

$$\mathrm{LOD} = 3 \cdot \sigma / m \tag{4}$$

where σ is the standard uncertainty obtained as a symmetric rectangular probability [39]; m is the slope of the calibration curve.

For ammonia detection in gas phase, the LPG was coated, using the LbL approach with, an thin film composed of alternate layers of PAA, (M_w:4000000) and PDDA, as shown in Fig. 13. PAA is a promising candidate for the creation of ammonia sensors, of which free carboxylic acid groups lead to the high sensitivity and selectivity toward amine compounds [40]. A quartz crystal microbalance (QCM) gas sensor based on the alternate deposition of TiO_2 and PAA for the sensitive detection of amine odors has been reported, [34]. However, QCM sensors still have a weakness that the sensor response can be affected easily by humidity. The operation of the coated LPG sensor here is based on the acid-base interaction of amine odors to the COOH moiety of PAA under humid conditions, which showed no sensitivity to humidity.

On exposure of the coated LPG to increasing ammonia concentration, a linear wavelength shift of the resonance band was observed (Fig. 14a). The selectivity of the sensor was investigated using several amine and non-amine compounds

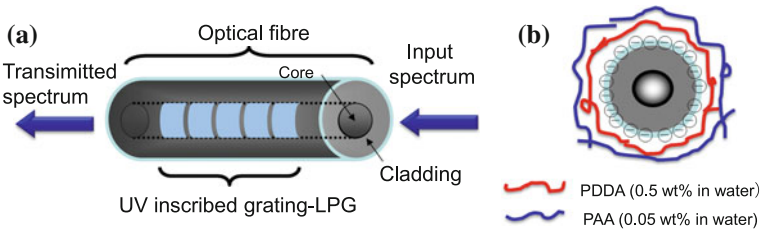

Fig. 13 **a** Schematic illustration of an LPG and its surface modification using coating of PDDA and PAA deposited using the LbL approach. Adapted from [40]

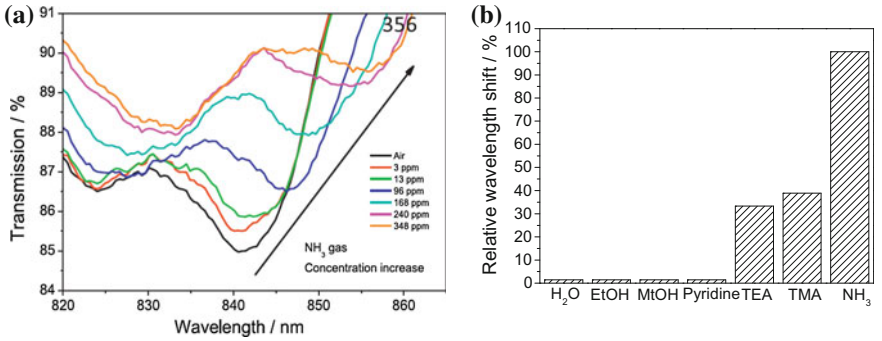

Fig. 14 **a** Changes of the transmiossion spectrum of the LPG modified with a 7-cycle PAH/PAA film at the exposure to different concentrations of ammonia gas and **b** Relative wavelength shifts of the resonance bands in the TS of the LPG modified with a 7-cycle PAH/PAA film at the exposure to ammonia (100 ppm) and other analytes (saturated gas). Adapted from [5]

(Fig. 14b). When the coated LPG was exposed to saturated non-amine compounds, no measurable changes were observed. The sensor demonstrated superior sensitivity towards ammonia as compared to other amine compounds (as saturated gases) such as triethylamine (TEA) and trimethylamine (TMA), which show relative wavelength shifts less than 40 % of that measured in response to exposure to the ammonia gas at 100 ppm [40]. The limit of section of the LPG sensor coated with the 7 layer thick film was 10.7 ppm [5].

The detection of ammonia was also investigated using an LPG of period 100 μm that was coated with a multilayer film consisting of 15 layers of PDDA and TSPP (Fig. 15) [41]. This device exhibited a limit of detection of 0.67 ppm for ammonia gas. TSPP molecules in the film acted as ammonia receptors because the TSPP

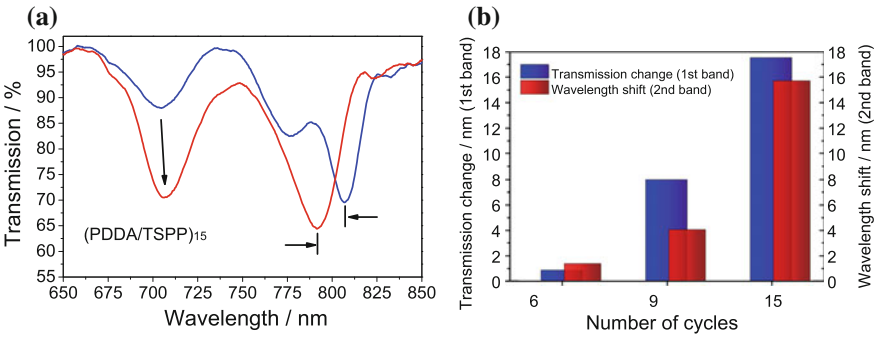

Fig. 15 **a** Transmission spectra of LPG sensor of period 100 μm and 4 cm length modified with PDDA/TSPP films produced using fifteen deposition cycles before (*blue lines*) and after (*red lines*) the sensors were exposed to 100 ppm ammonia. **b** Comparison of the wavelength shifts and the transmission changes obtained using the sensors with films produced using six, nine, and fifteen deposition cycles. Adapted from [41] (Color figure online)

morphologically changed from *J*- or *H*-aggregates to free base monomers when it was deprotonated by being exposed to ammonia. It was found that HCl vapour could be used to increase the relative amount of *J*-aggregation in the TSPP and to restore the sensor response. The reversibility of the morphological change in the TSPP allowed reversible changes to occur in the properties of the coating, including the refractive index, film thickness and density, and electrostatic interactions; these influenced the transmission spectrum of the LPG [41].

5.2 *Detection of Aromatic Carboxylic Acids*

The infusion of a functional compound into a mesoporous thin film coating an LPG can be used to tailor the selectivity of the LPG sensor. This section will provide several examples on how various functional compounds can be used to detect aromatic carboxylic acids [33], volatile organic compounds [42] and polyamines, which are cancer biomarkers. Aromatic carboxylic acids (ACAs) play an important role in the metabolizing process and their concentration in living organisms is strongly linked with some diseases [43]. For instance, a glycine conjugate of benzoic acid (BA) has been used in occupational medicine to monitor exposure to toluene [44]. The detection of ACAs using a coated LPG was reported in [33]. Mesoporous thin films were fabricated using a layer-by-layer self-assembly of poly (allylamine hydrochloride) (PAH) and SiO_2 with a diameter in the range of 40–50 nm as described in Sect. 5.1. The amino (NH_2) functional group of PAH was used as binding site for the detection of ACAs. High sensitivity, with binding constants of $1.36 \pm 0.01 \times 10^6$ and $5.6 \pm 0.01 \times 10^8$ M^{-1} for benzoic acid and mellitic acid, respectively, was achieved. The lowest measured concentration of 1 nM of mellitic acid was achieved selectively over structurally (phenol) and functionally (acetic acid) related compounds.

The transmission spectrum of the $(PAH/SiO_2)_{10}$ film coated LPG was changed drastically by the adsorption of BA, as shown in Fig. 16a. In particular, the resonance band at 663 nm corresponding to coupling to the LP_{020} cladding mode, shifted in wavelength by 0.5, 1, 1.5 and 6 nm when exposed to BA with concentrations of 1, 10, 100 and 1000 μM, respectively. In addition, a second resonance band corresponding to the coupling to the LP_{021} cladding mode developed at ca. 825 nm, at the PMPT. As the concentration of BA increased, the change in the TS became more pronounced, indicating the increase of the amount of BA adsorbed inside the $(PAH/SiO_2)10$ film. The sensor response was fast and saturated within 300 s for lower BA concentrations (<1000 μM), as shown in Fig. 16b. For the higher concentration (1000 μM), however, the time to reach equilibrium was more than 1500 s, indicating that interaction process was not completed for these values of concentration.

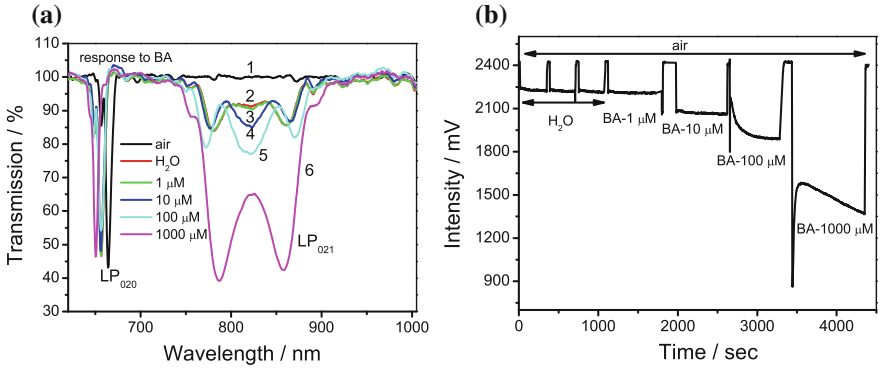

Fig. 16 **a** Evolution of the transmission spectra of the optical fibre LPG coated with a $(PAH/SiO_2)_{10}$ film at different concentrations of BA and **b** time-dependence of the intensity measured at 825 nm. Adapted from [33]

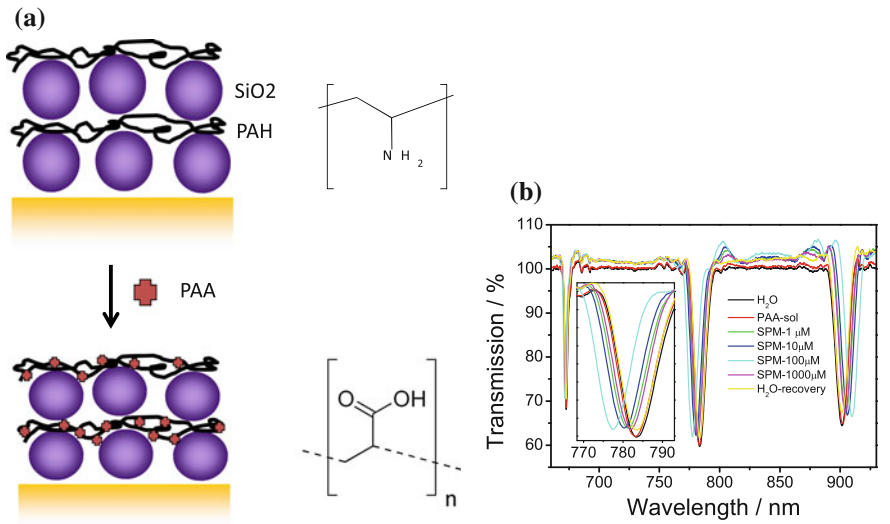

Fig. 17 **a** Schematic illustration of the infusion of the PAA into PAH/SiO_2 thin film; and **b** evolution of the TS at the exposure to different concentrations of the SPM

5.3 *Detection of Polyamines*

The infusion of PAA into a mesoporous thin film consisting of SiO_2 NPs and an organic moiety of a PAH polycation, was employed for the sensitive detection of a cancer biomarker, spermine (SPM), Fig. 17a. The sensing mechanism is based on the measurement of the RI change induced by the binding of the SPM to the PAA. The lowest detected concentration of SPM was 1 μM with a relatively fast, within

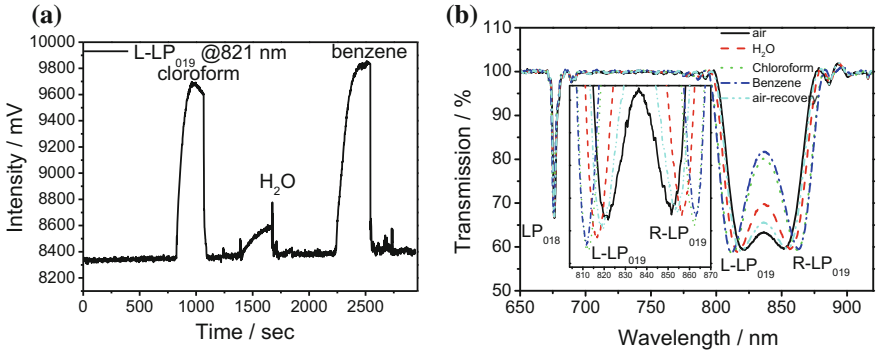

Fig. 18 **a** Dynamic sensor response at the exposure to chloroform, water and benzene of the LPG with grating period of 111.5 μm modified with the mesoporous $(PAH/SiO_2)_5$ C [3] A film measured 821 nm. **b** TS spectra measured in atmospheres of: air, chloroform, water vapour and benzene. Adapted from [42]

few minutes, sensor response time achieved using an LPG modified with 5 cycles $(SiO_2$ NPs/PAH$)_5$PAA film, Fig. 17b.

5.4 *Detection of VOCs*

An LPG modified with a mesoporous film of SiO_2 NPs, infused with a calixarene as a functional compound, was employed for the detection of a volatile organic compounds (VOCs) mixture [42]. The sensing mechanism is based on the measurement of the RI change of the coating induced by the complexion of the VOCs with the calixarene. The LPG, modified with 5 cycles of SiO_2 NPs/PAH that was infused with a calixarene [3], was exposed to chloroform, benzene, toluene and acetone vapours, Fig. 18. Calixarene molecules contain of a number of phenol or resorcinol aromatic rings connected together to a larger ring and the molecule is shaped like a bowl [45]. The analyte of the interest reacts with calixarene and becomes temporarily entrapped via gas state complexion. As only weak interactions occur (no covalent bond is created) the analyte is liberated easily from the cavity, with the result that the sensor is reversible. The sensitivity of the reaction depends on the morphology and charge of the molecule of interest and for this reason semi-specific reactions to different VOCs has been reported [46, 47].

5.5 *Development of Biosensors*

The fast, reliable and highly sensitive detection of proteins and antigen-antibody reaction kinetics are desired in biology and medicine because it can facilitate

prompt disease diagnosis. The presence of various proteins, or changes in their concentration, can be linked with alterations in physiology and act as an indicator of problems in the organism [48].

An LPG, modified with a coating of silica core gold shell (SiO_2:Au) nanoparticles (NPs) (Fig. 19a) deposited using the layer-by-layer method, was employed for the development of a biosensor [49]. The SiO_2:Au NPs were electrostatically assembled onto the LPG with the aid of a PAH polycation layer. The LPG sensor was designed to operate at the phase matching turning point, to provide the highest sensitivity. The SiO_2:Au NPs were modified with biotin, which was used as a ligand for streptavidin (SV) detection. The sensing mechanism is based on the measurement of the refractive index change induced by the binding of the SV to the biotin. The effect on sensitivity of increasing the surface area by virtue of the SiO_2:Au nanoparticles' diameter and film thickness was studied. The lowest measured concentration of SV was 2.5 nM, achieved using an LPG modified with a 3 layer (PAH/SiO_2:Au) thin film composed of SiO_2 NPs of 300 nm diameter with a binding constant of k = 1.7 (pM^{-1}), sensitivity of 6.9 nm/(ng/mm^2) and limit of detection of 19 pg/mm^2, Fig. 19b.

5.5.1 Vancomycin Detection

An LPG modified with molecularly imprinted polymer nanoparticles (nanoMIPs) for the specific detection of antibiotics was reported in [35]. The operation of the sensor was based on the measurement of changes in refractive index induced by the

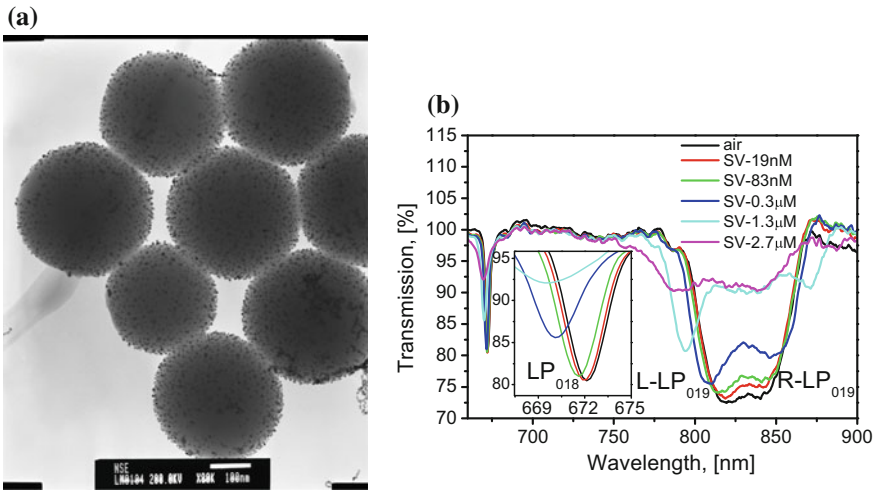

Fig. 19 **a** TEM images of 300 nm (scale bars: *left hand* 100 nm and *right hand*, 20 nm); **b** Transmission spectrum of the $(PAH/SiO_{2(300\ nm)}:Au)_3$ coated LPG modified on exposure to SV of different concentrations in: **a** air. Adapted from [49]

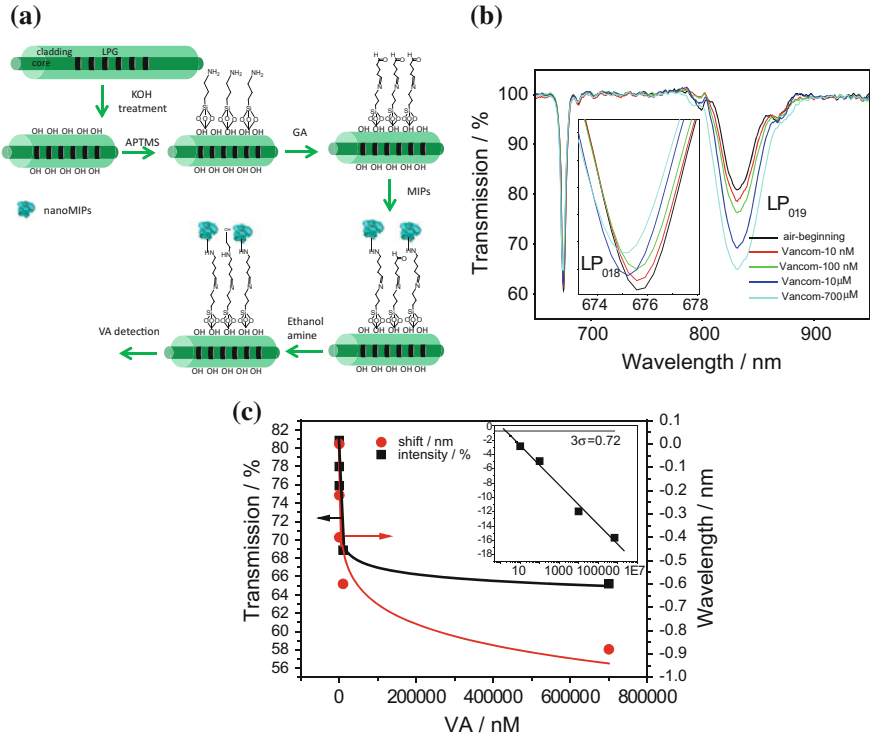

Fig. 20 Schematic illustration of the protocol used to immobilize nanoMIPs. **a** Transmission spectrum of the nano-MIP coated LPG measured in air after exposure to VA concentrations ranging from 10 nM to 700 μM; **b** Dependence of the transmission at the centre of the resonance band corresponding to coupling to the LP019 mode (*square*) and wavelength shift of the resonance band corresponding to coupling to the LP018 mode (*circle*) on the concentration of VA. The *red* and *black lines* are fits using the Langmuir adsorption isotherm. The *inset* shows the logarithmic dependence of transmission at the centre of the resonance band corresponding to coupling to the LP019 mode on VA concentration. Adapted from [35] (Color figure online)

interaction of nanoMIPs deposited onto the cladding of the LPG with free vancomycin (VA). The binding of nanoMIPs to vancomycin was characterised by a binding constant of $4.3 \pm 0.1 \times 10^{-8}$ M. The lowest concentration of analyte measured by the fibre sensor was 10 nM. In addition, the sensor exhibited selectivity, as much smaller responses were obtained for high concentrations (~700 μM) of other commonly prescribed antibiotics such as amoxicillin, bleomycin and gentamicin. In addition, the response of the sensor was characterised in a complex matrix, porcine plasma, spiked with 10 μM of VA, Fig. 20.

5.6 Applications

Examples of the practical application of the LPG sensors reported in literature are rather limited. This is related to the complexity in fabricating of the reliable and reproducible devices that can operate at optimal sensitivity regime, i.e., at the phase matching turning point. Perhaps one of the first examples of practical application of the LPG sensor was reported by Falate et al. [50] to measure the soybean oil concentration in samples obtained from the mixture of pure biodiesel and commercial soybean oil. The operation of the device was based purely on the sensitivity of the LPGs to the surrounding medium refractive index, which led to measurable modifications in the transmission spectrum. The sensor did not possess any specificity and was measuring only the RI change. The proposed analysis method results in errors in the oil concentration of 0.4 and 2.6 % for pure biodiesel and commercial soybean oil, respectively. Techniques including total glycerol, dynamic viscosity, density, and hydrogen nuclear magnetic resonance spectroscopy were also employed to validate the method [50]. This section will describe the application of LPGs modified with sensitive thin films for measurement of indoor air quality (IAQ) and for assessment of the quality of beverages.

5.6.1 Indoor Air Quality Assessment Using LPG Sensors

One of the key advantages of fibre optic sensors is the ability to multiplex an array of sensors, sensitive to the same or to different parameters. This can be of significant benefit in real environments, where the influence of interfering factors such as temperature or relative humidity should be reduced. Simultaneous detection of several parameters at the same location using a single optical fibre offers additional information that allows correction for changes of the interfering parameters [2].

Urrutia et al. [51] demonstrated simultaneous measurements of the humidity and temperature using novel dual-wavelength based sensing method. The LPG was partially coated with the humidity sensitive thin film in such a way that the main attenuation band was split into two different contributions allowing observing humidity and temperature change. The method however was based purely on the refractive index change.

Alternatively, a more tradition WDM approach can be adopted by fabricating an array of LPGs, each with different grating period, in a single optical fibre The LPGs can be functionalised to measure simultaneously several parameters, such as temperature, relative humidity and concentration of VOCs. The experimental arrangement is illustrated in Fig. 21.

The LPGs have periods selected such that they all operate near the phase matching turning point and that differ by up to 1 μm to facilitate wavelength division multiplexing, Fig. 22. A mesoporous coating of silica nanospsheres was deposited onto LPG1, such that it was sensitive to RH. The surface of LPG2 was left unmodified and was used to measure temperature. A functional material,

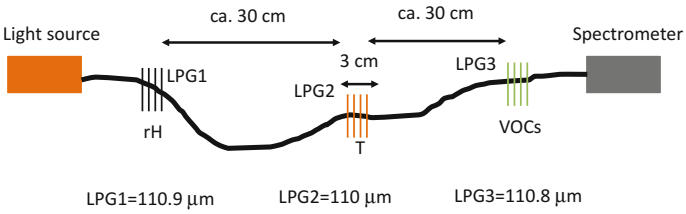

Fig. 21 Schematic illustration of the LPG sensor array. The individual LPGs were used to measure: LPG1 relative humidity (RH); LPG2 temperature; LPG3 volatile organic compounds (VOCs)

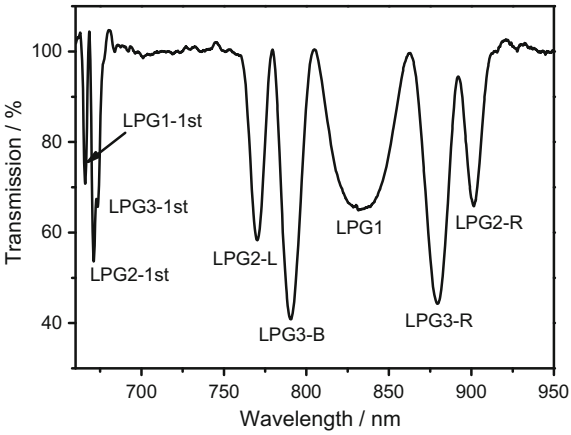

Fig. 22 Transmission spectrum of the optical fibre LPG sensor array containing 3 LPGs of period 110.9 (LPG1), 110.0 (LPG2) and 110.8 µm (LPG3) (L and R labels indicate short and long wavelength, respectively, positions of the resonance bands corresponding to the coupling of the same cladding mode, 1st indicates the positions of first resonance bands)

calixarene [3], was infused into a mesoporous silica nanospshere coating deposited onto LPG3 to sensitise the LPG to VOCs [46, 47].

The sensors were calibrated in the laboratory and the simultaneous measurement of the key indoor air quality parameters such as temperature, relative humidity and VOC was undertaken in laboratory and office environments. It was demonstrated successfully that the data produced by the LPG sensor array under real conditions was in a good agreement with that produced by commercially available sensors. The average differences between values obtained by the optical fibre sensor and standard temperature and RH sensors were better than 0.5 °C and 5 % respectively, Fig. 23. Further, the potential application of fibre optic sensors for VOCs detection at high levels has been demonstrated.

5.6.2 Beverage Quality Assessment

An LPG functionalized with a mesoporous thin film was employed for the identification and quality assessment of beverages [52]. The principle of the discrimination of beverages using an LPG sensor is based on the measurement of the

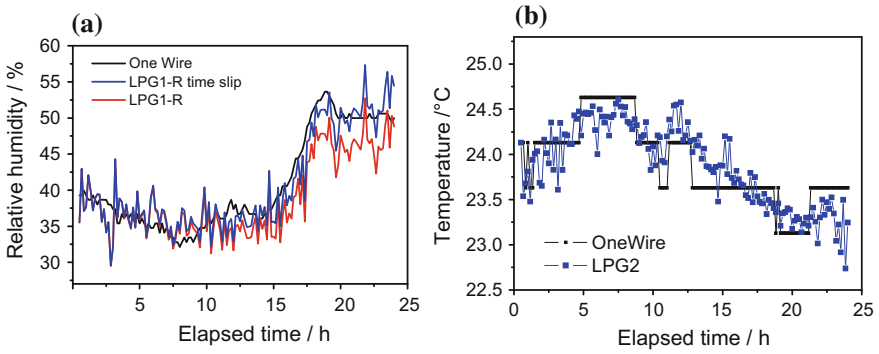

Fig. 23 **a** Change of the RH measured using LPG sensor array; RH values were calculated from wavelength shift using calibration curves (use LPG1-R, Fig. 7): *black line* RH measured using humidity and temperature data logger; *blue line* with and *red line*, without use of time slip correction; and **b** *blue line* change of the temperature measured using LPG sensor array; temperature values were calculated from wavelength shift using calibration curves (use LPG2-R); *black line* temperature measured using temperature data logger (Color figure online)

change in refractive index of a sensitive film, induced by the binding of the chemical compounds present in the beverage. The sensitive film deposited onto the LPG consisted of PAH and SiO_2 NPs with diameters ranging from 40 to 50 nm. PAH imparts selectivity, while the SiO_2 NPs endow the film with high porosity and enhanced sensitivity. In this study, five different types of beverages, red and white wines, brandy, nihonshyu (sake, a Japanese rice wine), and shochu (a Japanese distilled beverage), prepared via distillation and fermentation, were used to assess the capability of the sensor to identify the origin of the beverages. In addition, a selection of red wines was used to evaluate the use of the sensor in the assessment

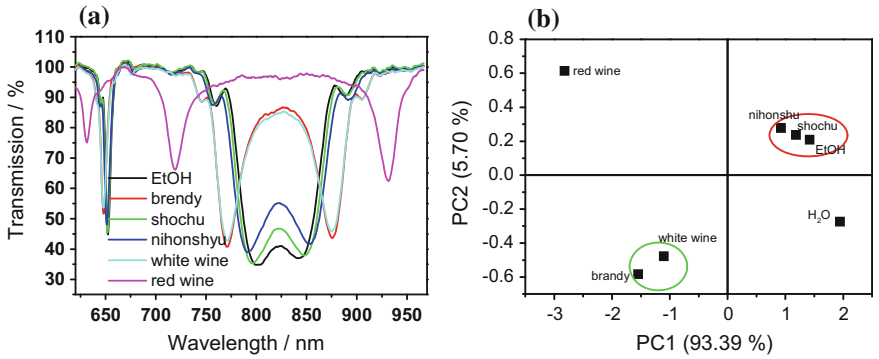

Fig. 24 **a** Evolution of the transmission spectra of an the LPG coated with a $(PAH/SiO_2)_{10}$ film immersed in different beverages with the alcohol concentration adjusted to 10 %; *black line*, EtOH; *red line* brandy; *green line* shochu; *blue line* nihonshu; *cyan line* white wine; and *magenta line* red wine. PCA performed using the data obtained with the LPG sensor. Adapted from [52] (Color figure online)

of the quality of beverages. The results obtained were benchmarked against those obtained using gas chromatography–mass spectrometry for the determination of volatile compounds contributing to the flavours of a set of red wines, Fig. 24a. Principal component analysis (PCA) was employed for data analysis, Fig. 24b. This approach enabled both quality assessment of beverages and identification of the methods and materials used for their preparation.

6 Conclusion

In summary, in this chapter we have presented a comprehensive review of the development and fabrication of LPG chemical for application in sensing. The deposition of a sensitive coating onto the surface of an LPG creates a prospect for the development of highly sensitive sensor with the wide range of applications. LPG operating at the phase matching turning point has highest sensitivity to the range of measurands such as temperature, bending, strain and refractive index. Specificity, however, becomes an issue that limits practical application of the optical fibre LPG sensors operating at the PMTP. The possible solution for this is multiparameter measurement system that is based on the multiplexing of the array of sensors in the wavelength domain. This technique has been extensively employed in the interrogation of the fibre Bragg gratings. Its application with LPG hasn't been explored the same extent. The main reason for this is an ability to fabricate reliably and reproducibly LPGs at the PMTP. Fabrication methods based on the point-by-point and amplitude masks allow reliability and reproducibility of the LPGs, opening up opportunities for real world application of the LPG sensors. In this chapter we have provided examples of the practical application of LPG chemical sensors.

References

1. S.W. James, R.P. Tatam, Optical fibre long-period grating sensors: characteristics and application. Meas. Sci. Technol. **14**, R49–R61 (2003)
2. S. James, R. Tatam, Fibre optic sensors with nano-structured coatings. J. Opt. A: Pure Appl. Opt. **8**, S430–S444 (2006)
3. S.C. Cheung, S.M. Topliss, S.W. James, R.P. Tatam, Response of fiber-optic long-period gratings operating near the phase-matching turning point to the deposition of nanostructured coatings. J. Opt. Soc. America B. **25**(6), 897–902 (2008)
4. S.W. James, C.S. Cheung, R.P. Tatam, Experimental observations on the response of 1st and 2nd order fibre optic long period grating coupling bands to the deposition of nanostructured coatings. Opt. Express **15**, 13096–13107 (2007)
5. I. Del Villar, M. Achaerandio, I.R. Matias, F.J. Arregui, Deposition of overlays by electrostatic self-assembly in long-period fiber gratings. Opt. Lett. **30**, 720–722 (2005)
6. T. Wang, S. Korposh, S. James, R. Tatam, S.-W. Lee, Optical fibre long period grating sensor with a polyelectrolyte alternate thin film for gas sensing of amine odors. Sens. Actuators B: Chem. **185**, 117–124 (2013)

7. I. Del Villar, I.R. Matias, F.J. Arregui, M. Achaerandio, Nanodeposition of materials with complex refractive index in long-period fiber gratings. J. Lightw. Technol. **23**, 4192–4199 (2005)
8. A. Cusano, A. Ladicicco, P. Pilla, L. Contessa, S. Campopiano, A. Cutolo, M. Giordano, Cladding mode reorganization in high-refractive-index-coated long-period gratings: effects on the refractive-index sensitivity. Opt. Lett. **30**, 2536–2538 (2005)
9. I. Del Villar, Theoretical analysis and fabrication of nanostrctures with electrpstatic slef-assembly monolayer porcess. PhD Thesis, Universida Publica de Navarra (2006)
10. Z.Y. Wang, J.R. Helfin, R.H. Stoeln, S. Ramachandran, Analysis of the optical response of long period fibre gratings to nm-thick thin-film coatings. Opt. Express **13**, 2808–2813 (2005)
11. I. Del Villar, I.R. Matias, F.J. Arregui, Influence on cladding mode distribution of overlay deposition on long-period fiber gratings. J. Opt. Soc. Am. A: **23**, 651–658 (2006)
12. V. Bhatia, A.M. Vengsarkar, Optical fiber long-period grating sensors. Opt. Lett. **21**, 692–694 (1996)
13. J. Blows, D.Y. Tang, Gratings written with tripled output of Q-switched Nd:YAG laser. Electron. Lett. **36**, 1837–1839 (2000)
14. D.D. Davis, T.K. Gaylord, E.N. Glytsis, S.G. Kosinski, S.C. Mettler, A.M. Vengsarkar, Long-period fiber grating fabrication with focused CO_2 laser beams. Electron. Lett. **34**, 302–303 (1998)
15. X. Lan, Q. Han, T. Wei, J. Huang, H. Xiao, Turn-aroundpoint long-period fiber gratings fabricated by CO_2 laser pointby- point irradiations. IEEE Photon. Technol. Lett. **23**, 1664–1666 (2011)
16. Y. Kondo, K. Nouchi, T. Mitsuyu, M. Watanabe, P. Kazansky, K. Hirao, Fabrication of long-period fiber gratings by focused irradiation of infra-red femtosecond laser pulses. Opt. Lett. **24**, 646–648 (1999)
17. M. Fujumaki, Y. Ohki, J.L. Brebner, S. Roorda, Fabrication of long-period optical fiber gratings by use of ion implantation. Opt. Lett. **25**, 88–90 (2000)
18. S. Savin, M.J.F. Digonnet, G.S. Kino, H.J. Shaw, Tunable mechanically induced long-period fiber gratings. Opt. Lett. **25**, 710–712 (2000)
19. G. Kakarantzas, T.E. Dimmick, T.A. Birks, R. Le Roux, P.S.J. Russell, Miniature all-fiber devices based on CO_2 laser microstructuring of tapered fibers. Opt. Lett. **26**, 1137–1139 (2001)
20. G. Rego, O. Okhotnikov, E. Dianov, V. Sulimov, High temperature stability of long-period fiber gratings using an electric arc. J. Lightw. Technol. **29**, 1137–1139 (2001)
21. G.M. Rego, P.V.S. Marques, J.L. Santos, H.M. Salgado, Arc-Induced long-period gratings. Fiber Integrat. Opt. **24**, 245–259 (2005)
22. Y. Wang, Review of long period gratings written by CO_2 laser. J. Appl. Phys. **108**, 081101 (2010)
23. L. Zhang, W. Zhang, I. Bennion, In-fiber grating optic sensors, in *Fiber Optic Sensors*, ed. by S. Yin, P.B. Ruffin, F.T.S. Yu, 2nd ed. (CRC Press, 2008), pp. 109–162
24. R.Y.N. Wong, E. Chehura, S.E. Staines, S.W. James, R.P. Tatam, Fabrication of fiber optic long period gratings operating at the phase matching turning point using an ultraviolet laser. Appl. Opt. **53**(21), 4669–4674 (2014)
25. J. Hromadka, R. Correia, S. Korposh, Fabrication of fiber optic long period gratings operating at the phase matching turning point using an ultraviolet laser via phase mask, in *Proceedings of the SPIE* (2016), in press
26. I. Del Villar, M. Achaerandio, I.R. Matias, F.J. Arregui, Deposition of overlays by electrostatic self assembly in long-period fibre gratings. Opt. Lett. **30**, 720–722 (2005)
27. I. Del Villar, I.R. Matias, F.J. Arregui, Influence on cladding mode distribution of overlay deposition on long period fiber gratings. J. Opt. Soc. Am. A: **23**, 651–658 (2006)
28. S.C. Cheung, S.M. Topliss, S.W. James, R.P. Tatam, Response of fibre optic long period gratings operating near the phase matching turning point to the deposition of nanostructured coatings. J. Opt. Soc. Am. B. **25**, 897–902 (2008)

29. J.M. Corres, I.R. Matias, I. del Villar, F.J. Arregui, Design of pH sensors in long-period fiber gratings using polymeric nanocoatings. IEEE Sens. J. **7**, 455–463 (2007)
30. J. Keith, L.C. Hess, W.U. Spendel, J.A. Cox, G.E. Pacey, The investigation of the behavior of a long period grating sensor with a copper sensitive coating fabricated by layer-by-layer electrostatic adsorption. Tatanta **70**, 818–822 (2006)
31. S. Korposh, T. Wang, S. James, R. Tatam, S.-W. Lee, Pronounced aromatic carboxylic acid detection using a layer-by-layer mesoporous coating on optical fibre long period grating. Sens. Actuators B: Chem. **173**, 300–309 (2012)
32. S.-W. Lee, N. Takahara, S. Korposh, D.-H. Yang, K. Toko, T. Kunitake, Nanoassembled thin film gas sensors. III. Sensitive detection of amine odors using TiO_2/poly(acrylic acid) ultrathin film quartz crystal microbalance sensors. Anal. Chem. **82**, 2228–2236 (2010)
33. B. Sellergren, A.J. Hall, Molecularly Imprinted Polymers. Man-made Mimics of Antibodies and Their Applications in Analytical Chemistry, ed. by B. Sellegren, in *Chapter 2 "Fundamental Aspects on the Synthesis and Characterization of Imprinted Network Polymers* (Elsevier Science B.V., Amsterdam, 2003), pp. 21–57
34. S.-W. Lee, S. Korposh, R. Selyanchyn, T. Kunitake, Fundamentals and perspectives of molecular imprinting in sensor applications", in: *Handbook of Molecular Imprinting: Advanced Sensor Applications*, ed. by S.-W. Lee, T. Kunitake. (Pan Stanford Publishing Pte Ltd), ISBN: 9789814316651, 2012
35. A. Urrutia, J. Goicoechea, A.L. Ricchiuti, D. Barrera, S. Sales, F.J. Arregui, Simultaneous measurement of humidity and temperature based on a partially coated optical fiber long period grating. Sens. Act. B. **227**, 135–141 (2016)
36. M.E. Swartz, I.S. Krull, *Analytical Method Development and Validation* (Marcel Dekker Inc, NY USA, 1997)
37. G. Rafael, C. Possetti, R.C., Kamikawachi, M. Muller, J.L. Fabris, Metrological evaluation of optical fiber grating-based sensors: an approach towards the standardization. J. Lightw. Technol. (OFS-21). **2167500** (2011). doi:10.1109/JLT.2011.2167500
38. T. Wang, S. Korposh, R. Wong, S. James, R. Tatam, S.-W. Lee, A novel ammonia gas sensing using a nanoassembled polyelectrolyte thin film on fiber optic long period gratings. Chem. Lett. **41**(10), 1297–1299 (2012)
39. T. Wang, W. Yasukochi, S. Korposh, S.W. James, R.P. Tatam, S.-W. Lee, A long period grating optical fiber sensor with nano-assembled porphyrin layers for detecting ammonia gas. Sens. Actuators B: Chem. (2016), in press
40. C.L. Sprague, A.A. Eelfarra, Detection of carboxylic acids and inhibition of hippuric acid formation in rats treated with 3-butene-1,2-diol, a major metabolite of 1,3-butadiene. Drug Metab. Dispos. **31**, 986–992 (2003)
41. N. Penner, R. Ramanathan, J. Zgoda-Pols, S. Chowdhury, Quantitative determination of hippuric and benzoic acids in urine by LC–MS/MS using surrogate standards. J. Pharmaceut. Biomed. Anal. **52**, 534–543 (2010)
42. J.D. Wulfkuhle, L.A. Liotta, E.F. Petricoin, Proteomic applications for the early detection of cancer. Nat. Rev. Cancer **3**, 267–275 (2003)
43. S. Korposh, F. Davis, S.W. James, T. Wang, S.-W. Lee, S. Higson, R.P. Tatam, Detection of volatile organic compounds using an optical fibre long period grating with a calixarene anchored mesoporous thin film. Proc. SPIE **8794**, 87941I(4) (2013)
44. A.K. Hassan, A.V. Nabok, A.K. Ray, A. Lucke, K. Smith, C.J.M. Stirling, F. Davis, Thin films of calix-4-resorcinarene deposited by spin coating and Langmuir-Blodgett techniques: determination of film parameters by surface plasmon resonance. Mater. Sci. Eng., C **8–9**, 251–255 (1999)
45. S. Korposh, I. Chianella, A. Guerreiro, S. Caygill, S.A. Piletsky, S.W. James, R.P. Tatam, Selective vancomycin detection using optical fibre long period gratings functionalised with molecularly imprinted polymer nanoparticles. Analyst **139**, 2229–2236 (2014)
46. S. Korposh, R. Selyanchyn, S.W. James, R.P. Tatam, S.-W. Lee, Identification and quality assessment of beverages using a long period grating fibre-optic sensor modified with a mesoporous thin film. Sens. Bio-Sens. Res. **1**, 26–33 (2014)

47. L. Marques, F.U. Hernandez, S.W. James, S.P. Morgan, M. Clark, R.P. Tatam, S. Korposh, Highly sensitive optical fibre long period grating biosensor anchored with silica core gold shell nanoparticles. Biosens. Bioelectron. **75**, 222–231 (2015)
48. R. Falate, K. Nike, P. Ramos da Costa Neto, E. Cação Jr., M. Muller, H.J. Kalinowski, J.L., Fabris, Alternative technique for biodiesel quality control using an optical fiber long-period grating sensor. Química Nova **30**(7), 1677–1680 (2007)
49. K. Grattan, B. Meggitt, *Chemical and Environmental Sensing* (Kluwer Acad Publisher, Boston, 1999)
50. S.M. Topliss, S.W. James, F. Davis, S.P.J. Higson, R.P. Tatam, Optical fibre long period grating based selective vapour sensing of volatile organic compounds. Sens. Actuators, B **143** (2), 629–634 (2010)
51. S. Korposh, F. Davis, S.W. James, T. Wang, S.-W. Lee, S. Higson, R.P. Tatam, Detection of volatile organic compounds using an optical fibre long period grating with a calixarene anchored mesoporous thin film. Proc. SPIE **8794**, 87941I
52. S. Korposh, R. Selyanchyn, W. Yasukochi, S.-W. Lee, S. James, R. Tatam, Optical fibre long period grating with a nanoporous coating formed from silica nanoparticles for ammonia sensing in water. Mater. Chem. Phys. **133**, 784–792 (2012)

Magnetic Field Sensors Based on Optical Fiber

J. Ascorbe and J.M. Corres

Abstract This chapter is focused in the different optical structures and materials that have been used for the development of optical fiber magnetic field sensors and optical fiber current transducers. First of all, this chapter starts with a short introduction of the main fields of application of these sensors and where they are used, and how materials can be classified with regard to their magnetic behavior. Then, a brief review of different ways of measuring magnetic fields will be made. It will be also introduced the main magneto-optical effects. A brief summary of the different options that have been developed by now will be made, showing the evolution of this research field. Then, a deeper look at the most used structures, the most common materials and the devices having greater sensitivity and resolution will be made.

1 Introduction

1.1 Application Fields

Electric current measurement is a basic and important technique for the control and supervision in most facilities sustaining industry and community, such as the power facility [1] or metallurgy industry [2]. The production of metals such as aluminum, copper, zinc, etc. requires dc currents as high as 500 kA. Electric current must be measured for process control and equipment protection. Conventional transducers for the measurement of high dc currents are based on the Hall Effect [2]. However, the followings are recognized as problems of these devices [1]:

- Current transformers are heavy and bulky.
- It is difficult to install them to thick and/or high voltage conductors and also is difficult to install them in the existing apparatus.

J. Ascorbe (✉) · J.M. Corres
Universidad Pública de Navarra, Pamplona, Navarra, Spain
e-mail: jokin.ascorbe@gmail.com

© Springer International Publishing Switzerland 2017

I.R. Matias et al. (eds.), *Fiber Optic Sensors*, Smart Sensors,
Measurement and Instrumentation 21, DOI 10.1007/978-3-319-42625-9_13

- The measurement signals are influenced by the electromagnetic induction noise.
- It is difficult to measure the large current, especially the low frequency component, which flows in a power system under the accident condition.

Furthermore, an analysis of the magnetic field distribution is necessary to minimize errors due to asymmetries in the field or other sources of error. Erroneous output can result for example from inhomogeneous heat dissipation in the measurement head and amplifier saturation at local field maxima or from a local reversal in the field direction caused by neighbor currents [2].

In the 1960s, as a hopeful solution for the problems, the optical current sensing method applying the Faraday-effect was proposed [3]. Since then, the research and development of the current sensing technique using the proposed principle has been carried out in many institutes worldwide.

Fiber optical current sensor (FOCS) is a technique considered to be also compatible with the ITER nuclear environment. The measurement of the plasma current and eddy currents in thermonuclear fusion reactor is considered as a fundamental parameter for plasma diagnostic. Until now, the measurement of the plasma current in existing tokamaks is carried out by inductive coils of various forms (Rogowski coils, pick-up coils) placed all around the vacuum vessel. FOCS presents several advantages such as high frequency bandwidth, high linearity over a wide current range, sufficient radiation resistance, low installation volume and a measurement of the plasma current independent on the plasma pulse duration [4].

1.2 Materials

Materials can exhibit diamagnetic, paramagnetic, ferromagnetic, ferrimagnetic, or antiferromagnetic behavior. Every material presents at least one of those kind of magnetism and the final behavior depends on the response of the atomic and electronic magnetic dipoles when an external magnetic field is applied [5].

Diamagnetism is a non-permanent weak form of magnetism and it appears in all materials. It is the tendency of a material to oppose an applied magnetic field, and therefore, to be repelled by a magnetic field. Diamagnetic behavior is observed only in a purely diamagnetic material and it can be explained by the Lorentz force that experience electrons while circling the nucleus. This results in a small bulk magnetic moment, with an opposite direction to the applied field [6]. Some materials that exhibit diamagnetism are bismuth, hydrogen, water, noble gases, sodium chloride, copper, carbon, gold, silica, mercury and antimony. Diamagnetic materials have a relative magnetic permeability that is less than or equal to 1, and therefore a magnetic susceptibility less than or equal to 0, and they have not unpaired electrons.

Paramagnetic can be considered as the opposite behavior of diamagnetism. Paramagnetic materials are weakly attracted by a magnetic field or by a magnet. Paramagnetic properties are due to the presence of some unpaired electrons, and from the realignment of the electron paths caused by the external magnetic field.

When an external magnetic field is applied paramagnetic materials form internal, induced magnetic fields in the direction of the applied magnetic field that are not permanent because thermal motion randomizes the spin orientations. Paramagnetic materials include magnesium, molybdenum, lithium, and tantalum [5, 7]. Paramagnetic materials have a small, positive susceptibility to magnetic fields and a relative magnetic permeability greater than or equal to 1. Most chemical elements and some compounds presents paramagnetism.

Ferrimagnetic and antiferromagnetic behavior are considered subclasses of ferromagnetism because all of them have permanent magnetic domains [5]. The spin of the electrons in atoms is the main source of ferromagnetism and it generates magnetic dipoles. When these magnetic dipoles in a piece of matter are aligned, their individually tiny magnetic fields add together to create a much larger macroscopic field. Ferromagnetic materials have a large, positive susceptibility to an external magnetic field. They exhibit a strong attraction to magnetic fields and are able to retain their magnetic properties after the external field has been removed. Ferromagnetic materials have some unpaired electrons so their atoms have a net magnetic moment. They get their strong magnetic properties due to the presence of magnetic domains. When a magnetizing force is applied, the domains become aligned to produce a strong magnetic field within the part. Iron, nickel, and cobalt are examples of ferromagnetic materials [8]. The susceptibility of ferromagnetic materials is positive, much greater than 1. Examples of these materials are iron, cobalt and nickel and several rare earth metals and their alloys [9].

1.3 Conventional Magnetometers

A magnetometer is a device used for measuring the magnetic field or the magnetization of a material. From an induction coil to the superconducting quantum interference devices (SQUIDs), there are a lot of ways to measure magnetic field [10], each one with its own application field. Here, we are going to classified them and make a brief explanation of the most relevant (Fig. 1).

Magnetic field sensors are called gaussmeters when they measure magnetic fields greater than 1 mT and magnetometers for magnetic fields lower than 1 mT. Gaussmeters include those based on Hall Effect, those based on magnetoresistance, magnetodiodes and magnetotransistors. The Hall Effect is the production of a voltage difference across an electrical conductor, transverse to an electric current in the conductor and a magnetic field perpendicular to the current [11, 12]. It is especially useful for measuring extremely high fields. The magnetoresistive sensors cover the middle ground between the low- and high-field sensors [10]. They are based on changes on the resistance caused by an external magnetic field, which may influence the material resistivity in several ways, i.e. altering the current path length by Lorentz force [13]. Magnetoresistance magnetometers are very attractive for low cost applications [14]. Magnetodiodes are semiconductor diodes with current-voltage characteristic changing in the magnetic field. The magnetodiode is different

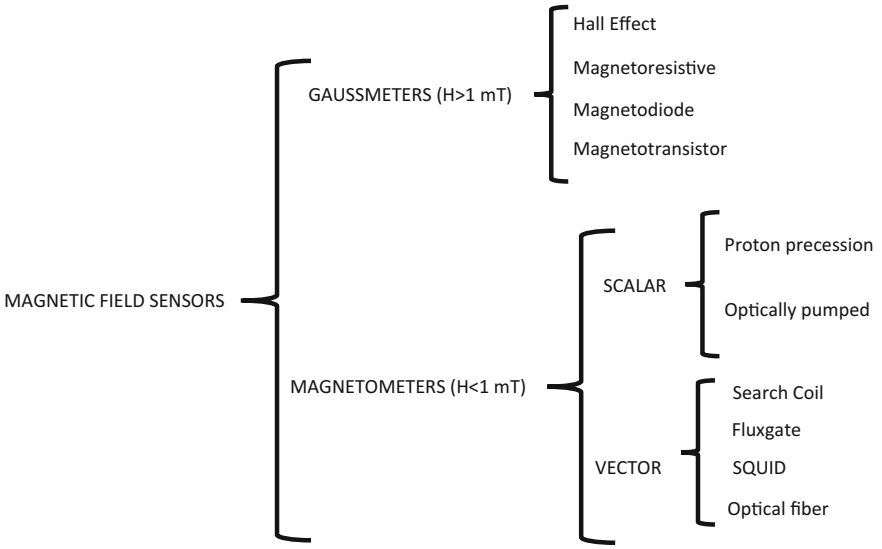

Fig. 1 Classification of magnetic field sensors

from a simple p-i-n diode because one of its faces has been treated to form a surface at which electrons and holes readily recombine. When a bias voltage is applied, electrons are injected from the n+ electrode into the intrinsic region, as are holes from the p+ region. In the presence of a magnetic field as shown, the Lorentz force acting on both types of carrier pushes them in the same direction. If the two types of carrier are deflected by the magnetic field towards the face with high recombination rate, they recombine there and the current flow is impeded. If they are deflected toward the other face, much less recombination takes place and more current flows [15].

Inside magnetometers it can be differentiated those named scalar and those named vectorial, which allow to determine the components of the magnetic field. Nuclear or proton precession and the optically pumped magnetometer are included inside scalar magnetometers. The nuclear precession magnetometer works on the principle that a spinning nucleus, which has both angular momentum L and a magnetic moment, will precess about a magnetic field like a gyroscope. The precession frequency is proportional to the applied field. When the magnetic field H is applied to the nucleus, it will produce a torque on the nucleus. Because the nucleus has angular momentum, this torque will cause the nucleus to precess about the direction of the field. The optically pumped magnetometer is based on the Zeeman Effect. This effect is most pronounced in alkaline vapors (rubidium, lithium, cesium, sodium, and potassium). The Zeeman Effect is the effect of splitting a spectral line into several components in the presence of a static magnetic field [10]. Inside vectorial magnetometers are the search or induction coil, which is based on Faraday's Law of induction, the fluxgate magnetometer, superconducting quantum

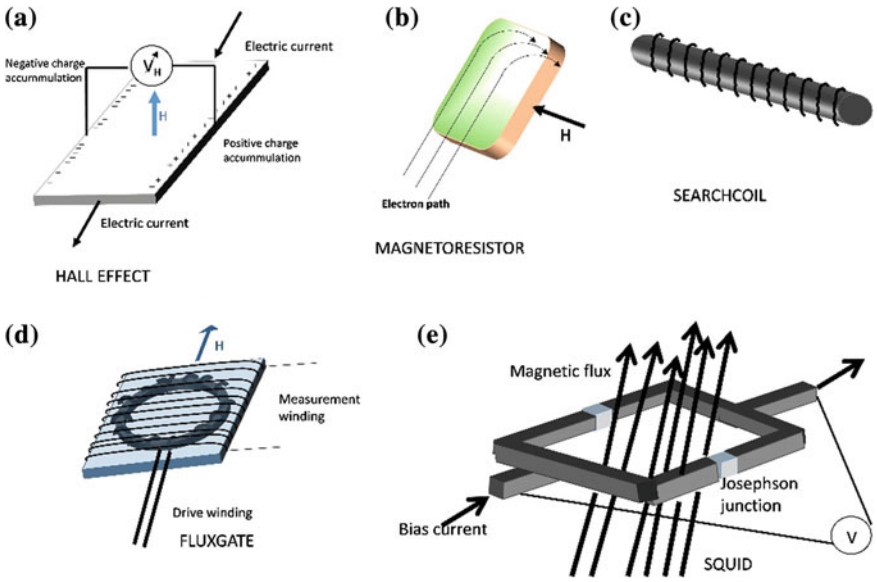

Fig. 2 Schematic representation of **a** Hall Effect, **b** magnetoresistive effect, **c** search coil and **d** fluxgate magnetometer and **e** SQUID

interference device (SQUID), some magnetoresistive magnetometers and those based on optical fiber. There are more magnetometers that might be included on this category, as Lorentz force MEMS [15] or those based on electron tunneling [16]. Fluxgate magnetometers are based on changes on the permeability of an easily saturable ferromagnetic material when it is saturated. They are rugged, reliable, physically small, and requires very little power to operate [10]. SQUIDs magnetometers are based on the Josephson Effect which says that a superconducting current can flow between two superconductors that are separated by a thin insulation layer. The magnitude of that current through this "Josephson junction" is affected by the presence of a magnetic field and forms the basis for the SQUID magnetometer. SQUIDs magnetometers are currently the most sensitive instruments available for measuring magnetic field strength [10]. Finally, there are some magnetometers based on optical fiber which will be explained in detail in following sections (Fig. 2).

1.4 Magneto-Optical Effects

There are two well-known magneto-optical effects which are the magneto-optic Kerr Effect (MOKE) and the Faraday rotation. MOKE is named like that to distinguish it from the electro-optic Kerr Effect, which refers to changes on the

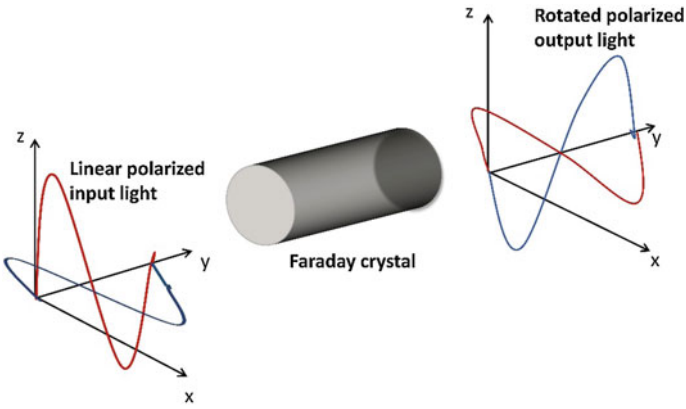

Fig. 3 Faraday effect

refractive index of a material when it is subjected to an external electric field. The magneto-optical Kerr effect (MOKE) describes the change of polarization state of light reflected from magnetized media while the Faraday rotation refers to changes on the polarization plane when the light goes through a magnetic field. Main difference between these effects is that MOKE needs a magnetized surface where light can reflect, while for Faraday rotation light must go through the medium, which does not need to be ferromagnetic, where the magnetic field is applied. Faraday rotation depends on the Verdet constant of the medium, which is strongly dependent of the wavelength, on the path length and on the magnetic flux density on the direction of light propagation [17] (Fig. 3).

However, there are other effects that are becoming extensively studied for this purpose, as it can be magnetostriction and the magneto refractive effect that occurs, for example, in magnetic fluids. Magnetostrictive materials change their size when an external magnetic field is applied. It has its electrical comparison with the piezoelectric effect. Magnetic fluids are dispersions of magnetic nanoparticles and their refractive index changes when a magnetic field is applied.

2 Optical Fiber Magnetic Field Sensors

In this section we are going to make a tour around the different configurations that have been used for developing optical fiber magnetic field sensors (OFMFS). This section is divided in several parts classified by the kind of optical fiber or the optical phenomena used. First of all, we will start with a brief review of the first optical fiber magnetic field sensors developed. Then, some sensors developed by Faraday Effect and MOKE will be shown. Other optical phenomena that will be explained are interferometers, including Fabry-Pèrot, Mach-Zehnder and modal interferometers. Next part will include Long Period Fiber Gratings (LPFGs) and Bragg

gratings. In the third part adiabatic tapered single mode optical fiber will be commented.

2.1 First Optical Fiber Magnetic Field Sensors

First OFMFS reported date from 1980 [18–23]. Some of them use magnetostrictive jackets in conjunction with Mach-Zehnder interferometry [18], others take advantage of changes on the state of polarization of the light when the optical fiber is deformed by the action of a magnetostrictive cylinder at which it is attached [19, 20]. Faraday Effect [21] and MOKE [22] has been also investigated in these first papers. Finally, it must be commented that magnetic fluids or ferrofluids were also studied on this period for their application in OFMFS [23, 24]. All these different configurations will be explained in more detail in next sections for newer research.

2.2 Optical Fiber Current Transducers: Faraday Effect

Faraday Effect has been used to develop optic fiber current transducers (FOCTs). As it has been mentioned before, Faraday Effect consists on a rotation of the polarization plane when the light is subjected to a magnetic field. According to the method of Faraday rotation detection, there are two major approaches, namely polarimetric [25, 26] and interferometric [27, 28] configurations. The polarimetric configuration is a direct way to measure these changes in polarization, while in the interferometric configuration this rotation of the polarization plane is converted into changes of amplitude. In order to measure the rotation of the azimuth φ of the output light from an optical Faraday current sensor, a considerable number of different detection schemes have been proposed and reported [29]. One commonly used detection schemes is the so-called dual-quadrature polarimetric configuration. This set-up consists on a light source, a polarizer, the optic fiber coil enclosing the current conductor, a polarization beam splitter and two photodetectors. The arrangement of the basic detection scheme is illustrated in Fig. 4. In the basic scheme [30] of polarimetric readout, a linearly polarized wave is launched in the fiber and the output is analyzed by a polarization beam-splitter (e.g. a Glan or a Wollaston prism) with the principal axes oriented at 45° with respect to the input, and hence the intensity of the light which is detected after propagating through the system is given by,

$$I = (I_0/2)(1 + \sin(2\varphi)) \tag{1}$$

where I, is the input intensity of the light. In order to eliminate the above dependence on the light intensity, the final output can be obtained by dividing the ac component of Eq. (1) by the dc component, and S, the ratio, can be given by,

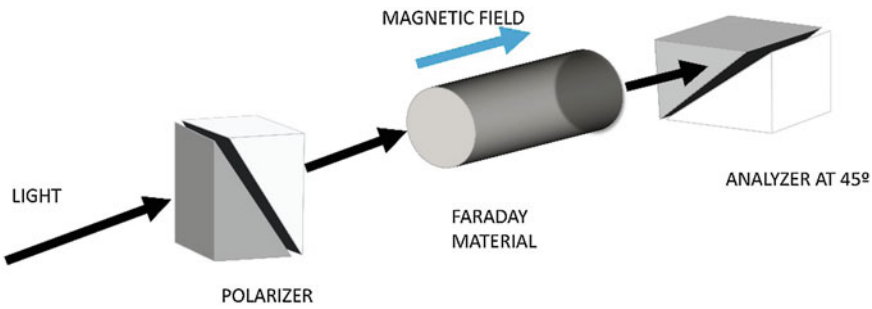

Fig. 4 Basic polarimetric detection scheme

$$S = (1 + \sin(2\varphi)), \tag{2}$$

The nonreciprocal Faraday phase shift 2Φ between orthogonal circularly polarized waves propagating in the same direction or, equivalently, between parallel polarized waves propagating in opposite directions, can be read by a variety of interferometric configurations. However, to cancel the reciprocal birefringence that is residual in the fiber, the Sagnac interferometer is the mandatory choice. The measurement configuration based on this interferometer is well established and readily adapted to current sensing, as shown in Fig. 5. In the interferometric readout two right (or left) handed circularly polarized waves are launched in opposite directions in the sensing coil by inserting quarter-wave retarders oriented at 45° with respect to the linear polarizer P. After propagation, the two waves exhibit a relative phase shift 2φ and, because of the folding in the winding, reappear at the quarter wave retarders as left (or right) handed circular polarization. Thus, they are retransformed back to linear polarized waves, parallel to the launched one, and recombine on the photodetector yielding a beating signal $I0(1 + \cos 2\varphi)$. Other components in Fig. 5, as the gyroscope, serve to ensure the reciprocity in

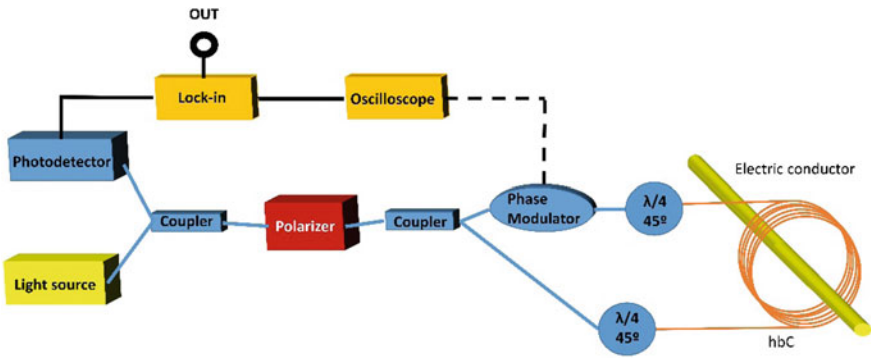

Fig. 5 Interferometric readout

splitting/recombining scheme (the two coupler), to discriminate against spurious mode errors (the polarizer P), and to impress a phase modulation PM [31] which overcomes the difficulty of measuring φ and its sign from the signal cos 2φ [30].

The Faraday rotation is not the only effect that will modify the state of polarization (SOP) of the light travelling in the fiber. Intrinsic and induced linear birefringence inherent to single-mode optical fibers will indeed generate an unwanted birefringence that will affect the SOP. The random nature of linear birefringence, inherently present as a result of intrinsic manufacturing imperfections (core ellipticity, drawing-induced anisotropic stresses), or induced by mechanical and temperature perturbations, cancels the possibility of a predetermination and results in an important distortion of the sensor output [4] when using a typical transmission set-up. Besides, Faraday Effect is quite small, so several turns of optical fiber must be enclosing the current conductor, increasing the induced birefringence. The most used technique for minimization the induced birefringence is the employment of specific optical fibers such as high birefringence and spun fibers [32–34]. Compensation techniques also rely on the non-reciprocity properties of the Faraday Effect, and that is the reason why the most used set-up is based on reflective Sagnac interferometer [2] or two-pass optical scheme with a Faraday mirror used as a reflector [4].

Recent research based on Faraday Effect is focused on its use as current transducer. For example, the device developed in [35] consists of a magnetic ring core which can open and enclose the electric conductor. This sensor head acts as a flux concentrator. The magnetic field induced by the conductor in this magnetic circuit is concentrated in the gap containing the receptive crystal. This crystal is made of a material with a high Verdet constant. Faraday crystal (Gadolinium Gallium Garnet doped with Terbium) is placed in the air gap between the polarizer and analyzer and optical fibers transmit the light to and from sensing element. The device is completed with the optoelectronic components which consist of the light source, the polarizer, the analyzer and all the electronics needed to signal conditioning and processing.

Another device is the one developed by the people of ABB [2]. Measurements up to 500 kA can be accomplished with this device. Here, the basis is also the Faraday Effect, but they do not use a Faraday crystal, just optical fiber. As the standard SMF has a very low Verdet constant, this device has to form a coil consisting of several turns around the electric conductor. Due to the length of the optical fiber, low birefringence must to be used for avoiding undesired rotations of the polarization plane. Other scheme of a polarization-rotated reflection interferometer and fiber gyroscope is used here to measure the magneto-optic phase shift. It has some advantages as the sensor can be installed without opening the current-carrying bus bars and that subsequent re-calibration is not necessary (Fig. 6).

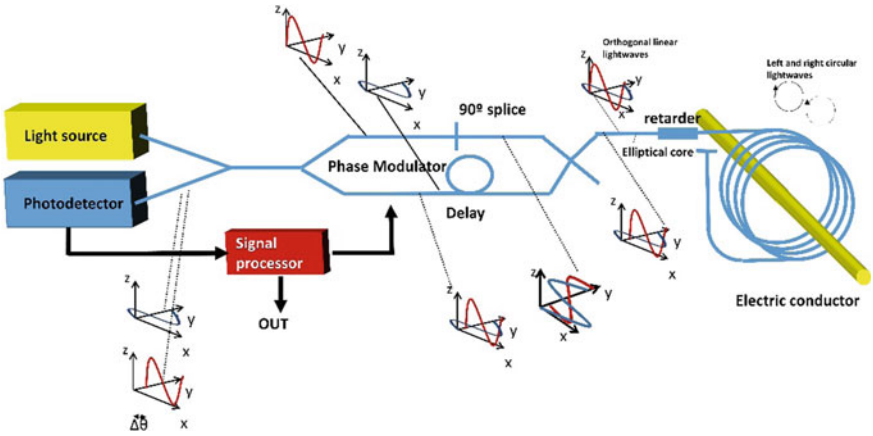

Fig. 6 Scheme of a polarization-rotated reflection interferometer and fiber gyroscope used in [2]

2.3 Fabry-Pèrot Interferometers

Fabry-Pèrot interferometers are based on the multiple reflections suffered by light when it crosses two reflective surfaces. When a light beam goes through a surface that separates one medium from another, it is well-known that part of this beam is reflected while other part is refracted. The refracted beam crosses the second medium and when it reaches the second surface, that separates the second medium from the third one, it is reflected and refracted again. This reflected beam cross the medium and the first surface, being refracted, and it interferes with the reflected beams of the first surface, creating a pattern of interference.

Interference pattern of Fabry-Pèrot interferometers is given by the difference of refractive index between the different mediums, by the path length of the interferometer and by the wavelength of the light. Then, there are different ways to change the pattern of interference of a Fabry-Pèrot interferometer: changing the path length of the interferometer or changing the refractive index of the medium.

The first option has been used by Zhang et al. [36] for the development of an extrinsic fiber optic Fabry-Pèrot interferometer (EFFPI). The EFFPI was simply formed by placing two well-cleaved single-mode fibers with carefully designed spacing and it was bonded to the surface of a Terfenol-D slab by epoxy resin. Terfenol-D is an alloy compound of terbium, iron and dysprosium, and it presents the highest magnetostriction of any alloy. The maximal sensitivity of magnetic field measurement we obtained is 854.73 pm/Oe (Fig. 7).

The same phenomena has been used by Oh et al. [37], but in this case the second surface has been chosen to be the magnetostrictive material, amorphous metallic wire Unitika A F-10 (Fe77.5B15Si7.5). In that paper, the measurement have been done for just one wavelength, 1310 nm, and they have obtained a resolution of 50 nT over a range of 50–40,000 nT (Fig. 8).

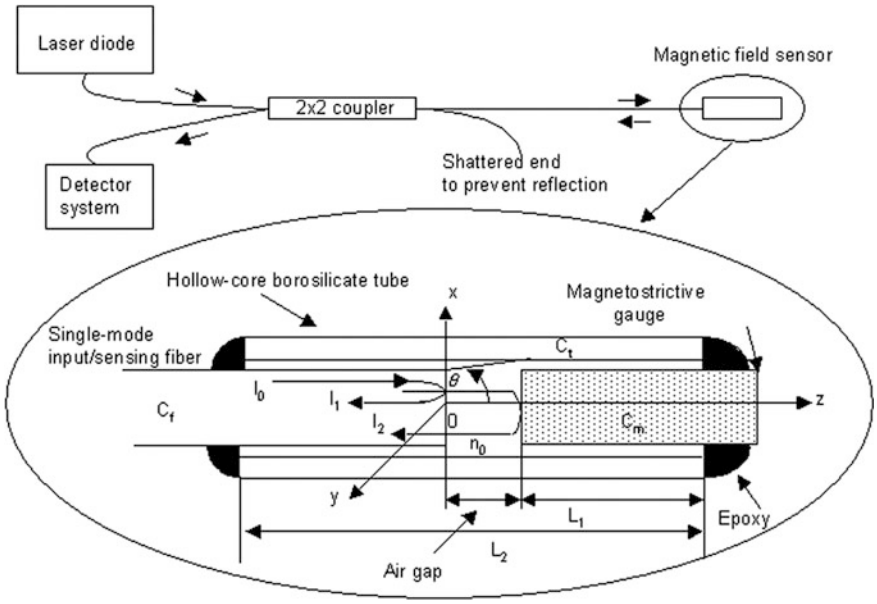

Fig. 7 Schematic of an extrinsic Fabry–Perot interferometry-based dc magnetic field sensor. Reprinted from Ki D. Oh, Anbo Wang, Richard O. Claus, "Fiber-optic extrinsic Fabry–Perot dc magnetic field sensor," Opt. Lett. 29, 2115–2117 (2004); https://www.osapublishing.org/ol/abstract.cfm?uri=ol-29-18-2115, with permission of OSA Publishing

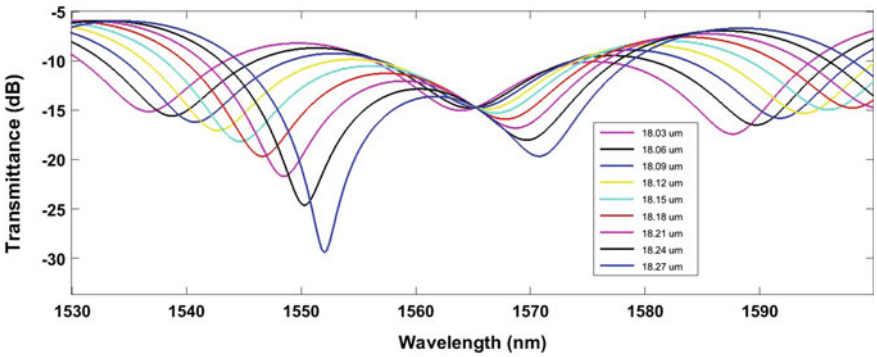

Fig. 8 Simulated results of a Fabry-Pèrot interferometer for different length of the air cavity

2.4 Mach-Zehnder Interferometers

Although there are some modal interferometers which can be considered as MZI, those ones will be explained in the section named Modal Interferometers and here we are going to focus on classical concept of MZI.

Mach-Zehnder interferometers (MZI) are based on the phase difference in a light beam that has been split into two different paths of different lengths. Both beams are equals at the beginning of the experiment. Then, both beams arrive photodetector 1 in phase, so this photodetector will see constructive interference. On the other hand at detector 2, in the absence of a sample, the sample beam and reference beam will arrive with a phase difference of half a wavelength, yielding complete destructive interference. When introducing a sample in the sample beam, the intensities of the beams entering the two detectors will change, allowing the calculation of the phase shift caused by the sample. All-fiber MZI sensor is built on a similar way, having two equal arms. Then, only one of the arms is subjected to the physical parameter which needs to be measured. Examples of both kind of MZI will be shown.

By utilizing the magnetically tunable refractive index of magnetic fluid films as one arm, a Mach–Zehnder interferometer is designed and its feasibility is demonstrated. The modulation of the interfered intensity was observed when an external magnetic field was applied to the magnetic fluid film. It was further observed that the modulation behavior can be adjusted by using magnetic fluids of various concentrations [38] (Fig. 9).

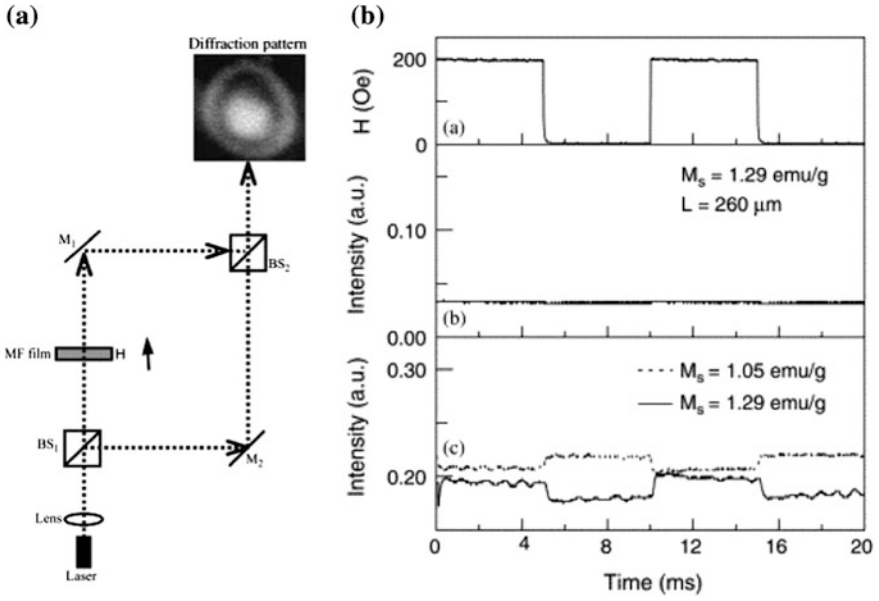

Fig. 9 **a** Scheme of Mach–Zehnder interferometer with a magnetic fluid film located in one of the arms of the MZI and **b** Temporal variations of (**a**) applied magnetic field, and the corresponding (**b**) transmitted intensity through the magnetic fluid film and **c** interfered intensity of the Mach–Zehnder interferometer. Reprinted from Journal of Magnetism and Magnetic Materials, vol. 297 C.-Y. Hong, S.Y. Yang, K.L. Fang, H.E. Horng, and H.C. Yang, pp. 71–75, (2006) with permission from Elsevier

An optical fiber MZI for magnetic field sensing consists of two single mode optical fiber coated with a magnetostrictive jacket [39]. Spinel oxide thin film materials included magnetite or Fe_3O_4, sodium modified λ–Fe_2O_3, nickel ferrite or $NiFe_2O_4$ and cobalt doped nickel ferrite or $Ni0.97Co0.03Fe_2O_3$. A typical coated fiber length ranged from 20 to 30 cm. One of the optical fiber was housed in two solenoid coils which were used to generate the AC and DC components of the applied external field. A function generator was used to generate the AC signal field intensity up to 3.2 kA/m. This signal was superimposed to the DC bias field up to 13.4 kA/m. A minimum detected field of 2.5×10^{-3} A/m for an optical fiber jacketed with 2-mm-thick and 1-m-long cobalt doped nickel ferrite was achieved. The dimensions of this MZI make it useless as a commercial device, but it was a first approach of all-fiber MZIs. MZIs have been also used to characterize the magnetostrictive properties of some materials [40, 41] (Fig. 10).

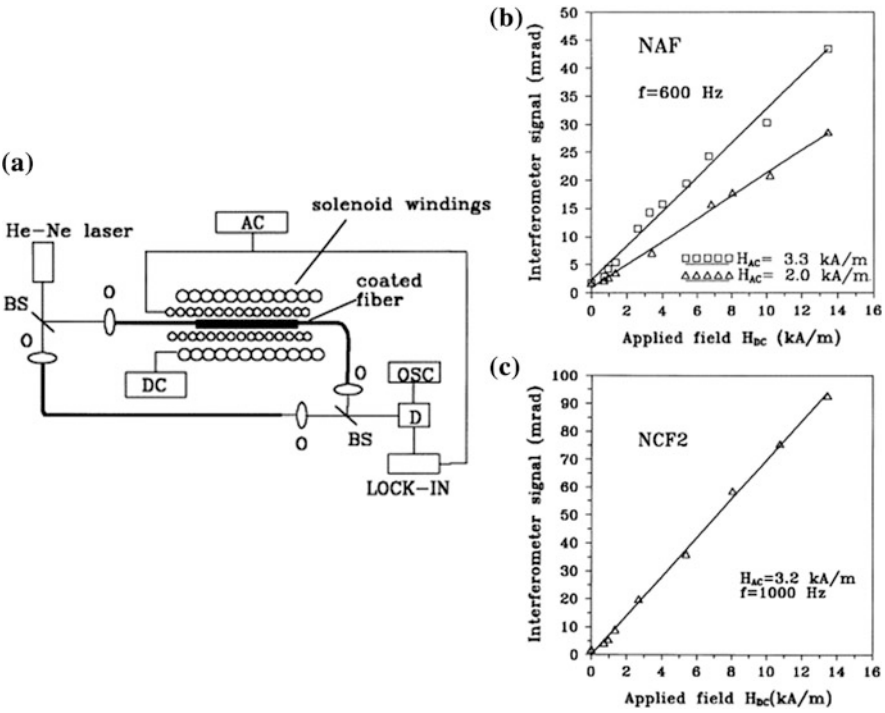

Fig. 10 **a** Figure 1. General experimental setup of the Mach–Zehnder magnetometer; the inner solenoid provides the high frequency signal, the outer solenoid is used to bias the ceramic-coated optical fibre to reach higher sensitivity. BS: beam-splitter, O: objective, OSC: oscilloscope and DC magnetic field response of the NAF jacketed fibre (**b**) and of the NCF2 jacketed fibre (**c**), higher output is achieved with greater AC amplitude. Reprinted from Sens. and Actuators A, 84(3), 297–302, Sedlar, M., Matejec, V., and Paulicka, I. (2000), Optical fibre magnetic field sensors using ceramic magnetostrictive jackets, with permission from Elsevier

2.5 *Modal Interferometers*

There are different ways to obtain a modal interferometer. Modal interferometers are devices where different modes interact between them, generating an interference pattern, that can be or not periodic.

2.5.1 Non-adiabatic Tapered Optical Fiber

One way to obtain a modal interferometer is making a non-adiabatic tapered optical fiber. A tapered optical fiber is considered adiabatic when the transition region has a determined slope. In general, the tapered segment of a single-mode fiber functions like a multimode fiber that supports LP0m modes. In the analysis of a uniform-waist SMTF, however, only the fundamental LP01 modes taken into account. Note that excitation of the modes in the taper uniform-waist region is produced from an adiabatic transition between this and a single-mode fiber. In this kind of transition the excitation of the LP01 mode from the fundamental fiber mode can be carried out with an efficiency as high as 99.5 %. Thus, the contribution of higher-order modes is insignificant and is not used to be taken into consideration [42]. A non-adiabatic tapered optical fiber (NATOF) operates like a Mach-Zehnder interferometer due to the difference of the optical path between the fundamental core mode and the higher order cladding modes. At the NATOF, the fundamental core mode in SMF is partly coupled to the LP0m cladding modes. Passing through the interferometer arm, part of the light traveling inside the cladding is coupled back into the core at the end part of taper. Due to the difference between the propagation constants of core and cladding modes, the device can be considered as a modal interferometer [39]. NATOF used by Layeghi et al. [43] were in the range of 1.0–1.5 cm of length and 7–11 μm of diameter. Then, this NATOF surrounded by a water-based magnetic fluid was placed in the middle of the poles of the electromagnet, which generates a uniform magnetic field in the waist region of the NATOF and perpendicular to the fiber axis. Here, wavelength shifts of 2.8 nm for applied magnetic fields of 45 mT have been obtained, which implies a sensitivity of 7.17×10^{-2} nm/mT.

2.5.2 Single Mode-Multimode-Single Mode Structure

Other way to obtain a modal interferometer is by splicing a multimode optical fiber between two single mode optical fibers. Single mode-multimode-single mode (SMS) fiber structure is a well-known optical configuration, which is obtained by splicing a multimode fiber segment (coreless MMF) between two single-mode fiber (SMF) segments. The basic physical principle of the device is that light transmitted through the fundamental mode of the SMF segment is coupled to several modes into the MMF section and recoupled to the fundamental mode of the SMF at the end

of the MMF segment [44]. Due to the phenomenon of multimodal interferometry [45], both transmission and attenuation bands are obtained in the optical spectrum [44, 46]. SMS structure relies on the self-imaging [44]. The principle can be stated as follows: Self-imaging is a property of multimode waveguides by which an input field profile is reproduced in single or multiple images at periodic intervals along the propagation direction of the guide [45]. Particularly, the transmission bands obtained by the self-image effect exhibit minimum losses [45], and its central wavelength can be controlled as a function of the MMF segment dimensions, mainly the MMF segment length and diameter [44].

Multimode interferometry in SMS devices can be used for the development of interesting applications [44, 47–60]. Optimization of this structure has been also studied [61]. In the research domain of sensors, devices have been developed that permit to detect, among others, displacement, strain, pressure, temperature, relative humidity or refractive index [46–53, 61, 62]. More recently it has been designed to be used as a magnetic field sensor [54–58] using magnetic fluids (MF). Most of them consists on a SMS structure and MF sealed in a capillary tube as the magnetic sensitive media. Some variations can be found between this devices, as the type of multimode fiber used, that can be cylindrical or square fiber, or the optical set-up which can be a transmission or a reflective set-up. Here, we have select the most typical magnetic field sensor based on SMS structure to show how it works.

There is also another way to develop magnetic field sensors based on SMS structure and it consists on coating it by a thin film of a magnetic alloy [60]. Two reasons justify the application of an additional coating. The first one is the ability to improve the performance of the same devices without coating [60]. As an example it has been possible to obtain a 10 fold increase in long-period fiber grating refractometers [46]. The second reason is the possibility to use thin-films that are sensitive to chemical compounds or physical magnitudes [63]. Thus, the presence of a thin-film can improve the sensitivity of the measurements done with optical devices [59].

Then, for developing an OFMFS based on SMS structure, the optical fiber was coated with a thin film of a magnetic alloy by means of sputtering. The dimensions, length and diameter, of the MMF segment are the critical parameters for the design of the device. The first step to fabricate this device is to cut a 58 mm length piece of multimode coreless optical fiber (POFC, Inc.) at 90° in both sides. Its length was of 58 mm, because it permits to obtain a higher transmission than for smaller segments [48, 62]. Then, this segment was spliced to two standard SMF from Telnet, Inc. The diameter of all fibers is 125 μm. The SMS structure was glued with epoxy to a U-holder for next steps.

In [48] it has been studied the sensitivity of a SMS structure coated with a complex refractive index material as a function of the thickness of the coating. Materials with a complex refractive index means that they have an extinction coefficient different from zero. When the nanocoating thickness increases the transmission and attenuation bands present a wavelength shift, whose rate is maximum in the proximity of a fading region. This fading region is caused by coupling to a lossy guided mode in the nanocoating [64]. After the fading region the

bands reappear and experiment a wavelength shift rate that is reduced as the coating increases.

The SMS optical fiber was introduced to the vacuum chamber of a Pulsed DC Sputtering System. The SMS was coated with a magnetic alloy of cobalt and nickel. The materials that conform the alloy present magneto-optic properties and the alloy is also magnetostrictive. The sputtering process was done with argon as the noble gas. The pressure was maintained at 3×10^{-1} mbar and the current for the sputtering process was 40 mA. The process was monitored to stop at the exact moment when the greatest sensitivity is achieved, which happens just before the fade region [44]. Optical spectra acquired during the sputtering process are shown in next figure, Fig. 11. As it can be seen, at the end of the sputtering process there is a change on the rate of the wavelength shift, which implies that the device has its maximum sensitivity.

Then, by placing the optical fiber inside the air gap of an electrical transformer, a magnetic field is applied to the device. Two different experimental set-ups have been used as a function of the measurement phenomena we are interested in. For measuring changes in the spectrum, a DC power supply (Agilent E3614A), controlled by a function generator (Hameg HM 8130), was used to apply DC current to a transformer and the spectra were then collected by an optical spectrum analyzer (HP 86142A). The light source was a broadband light source which consists of four LEDs at 1200, 1310, 1430 and 1550 nm (Agilent 83437A). The current which flows through the winding was collected by a data acquisition unit (HP 34970A). This experimental set-up is shown in Fig. 12.

DC magnetic fields were applied to the SMS based OFMFS, and changes on the transmitted spectrum are shown in Fig. 13. The transmission bands shift to greater

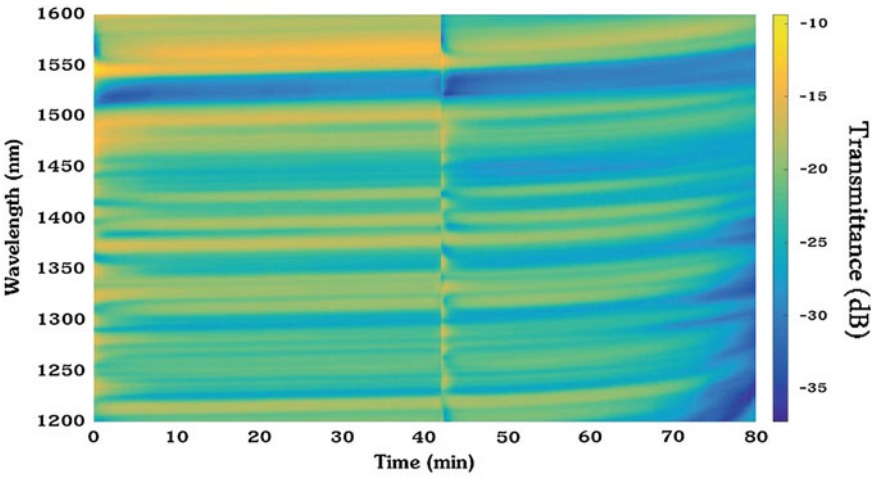

Fig. 11 Evolution of the transmitted optical spectrum as the thin film thickness increases collected during the sputtering process

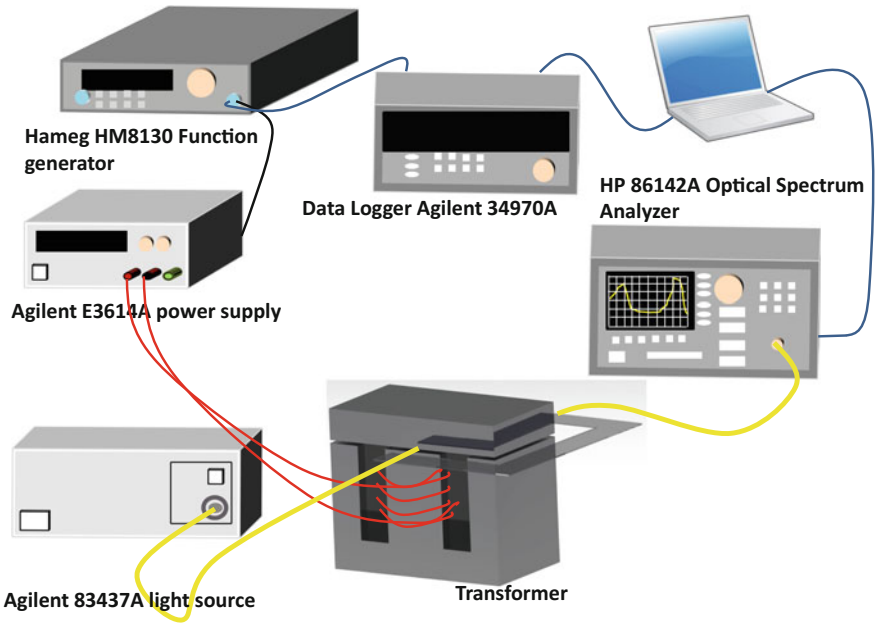

Fig. 12 Experimental set-up for the characterization of the thin-film coated SMS

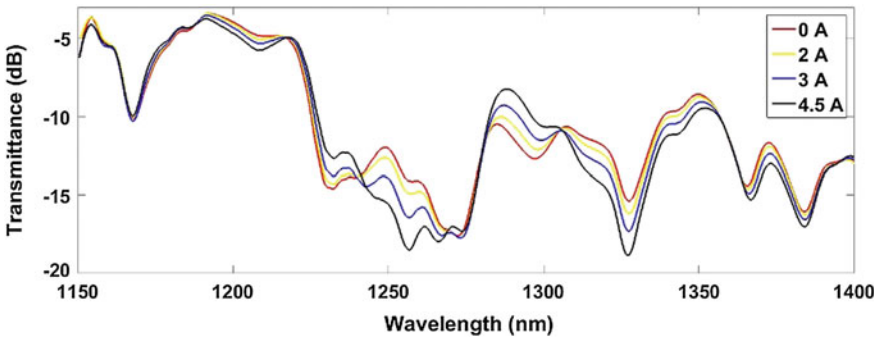

Fig. 13 Optical spectrum of a SMS structure coated with a magnetic thin film and subjected to different magnetic fields

wavelengths when an external magnetic field is applied. This is due to changes on the refractive index of the coating. Wavelength shifts of 0.67 nm/A have been obtained for a SMS structure coated by an alloy of cobalt and iron.

As it can be seen there is a wavelength displacement of the transmission bands as well as changes in the optical power transmitted. Transmission bands increases their optical power transmitted while attenuation bands decreases it. Wavelength shifts of

3 nm and changes in the optical power transmitted of 3 dB have been achieved. In Fig. 14 it is shown changes on the transmitted optical power (measured with a similar set-up, but changing the OSA by an optical power meter and the broadband light source by a laser transmitter) when several current pulses were applied to the transformer winding.

Other configuration consists of a SMS structure sealed inside a capillary tube filled with magnetic fluid [55]. A scheme of this configuration can be seen in the next figure, Fig. 15.

This optical structure was connected from one side to a broadband light source and the other side to an optical spectrum analyzer. Then, an external magnetic field has been applied to the device by means of a permanent magnet. Sensitivities of 905 pm/mT have been obtained. The wavelength of the left dip shifts monotonically from 1534.5 to 1542.5 nm when H changes from 0 and 120 Oe. Over 120 Oe,

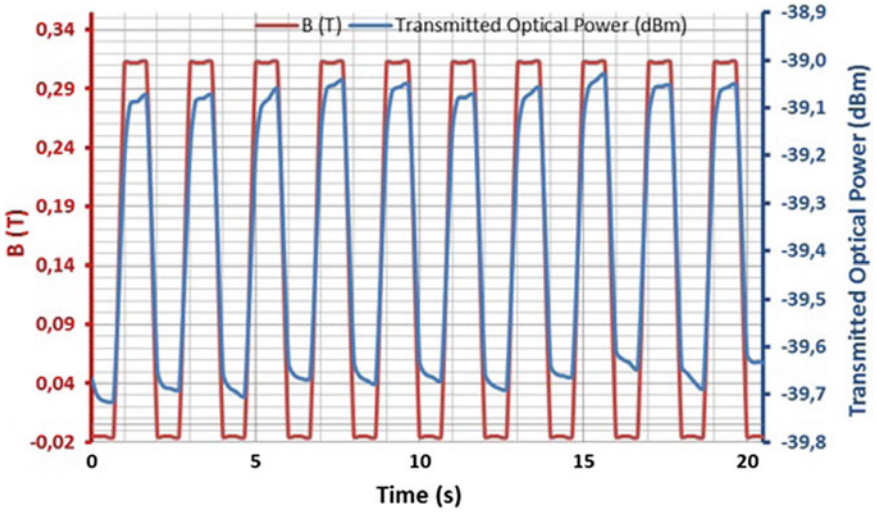

Fig. 14 Changes on the transmitted optical power of a SMS coated with Co-Ni alloy for several pulses of magnetic field

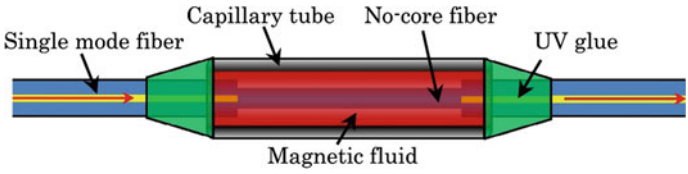

Fig. 15 Schematic of the magnetic field sensor. Reprinted from Optics Letter, Vol. 38 (20), Yaofei Chen, Qun Han, Tiegen Liu, Xinwei Lan, and Hai Xiao, Optical fiber magnetic field sensor based on single-mode–multimode–single-mode structure and magnetic fluid, (2013), pp. 3999–4001, with permission of OSA Publishing

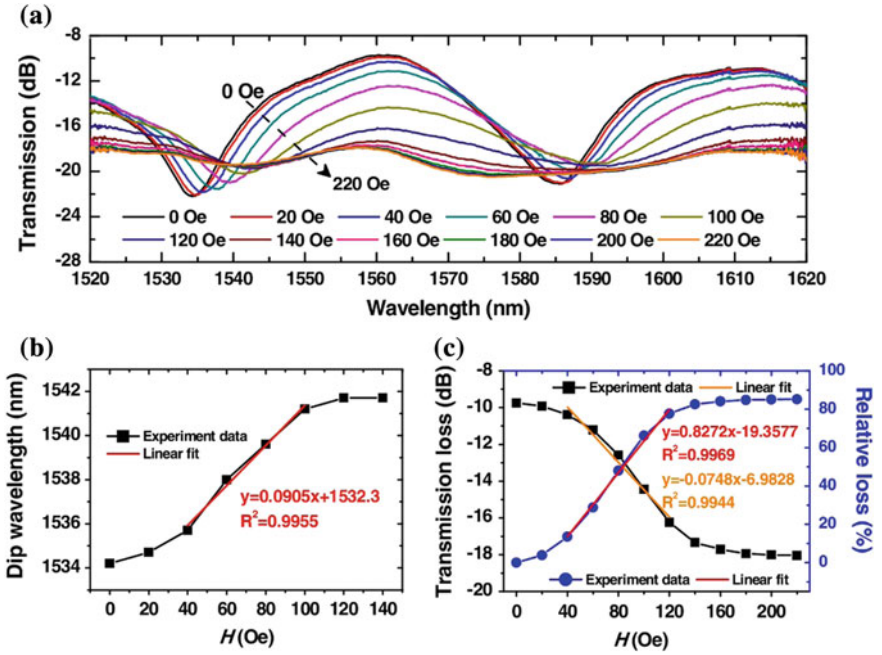

Fig. 16 **a** Response of the transmission spectra of the sensor to magnetic field strength, **b** dip wavelength, and **c** transmission loss change as a function of magnetic field strength. Reprinted from Optics Letter, Vol. 38 (20), Yaofei Chen, Qun Han, Tiegen Liu, Xinwei Lan, and Hai Xiao, Optical fiber magnetic field sensor based on single-mode–multimode–single-mode structure and magnetic fluid, (2013), pp. 3999–4001, with permission of OSA Publishing

the dip almost disappears. The response of the wavelength shift to H is generally nonlinear, but between 40 and 100 Oe the response has fairly good linearity. Spectrum collected for different values of magnetic field are shown in Fig. 16.

2.6 Fiber Gratings

2.6.1 Long Period Fiber Gratings

Long period fiber gratings (LPGs) has some desirable characteristics for their use as optical fiber sensors. LPGs structure consists on a periodic modification of the refractive index of the optical fiber. Several approaches have been followed to develop LPGs. Modification of the refractive index of the optical fiber can be obtained by exposing to UV radiation hydrogen-loaded germanosilicate fibers [65, 66], or by methods based on the physical deformation of the fiber [67], diffusion of the core dopants in special nitrogen-doped Ge free fibers [68, 69], or refractive

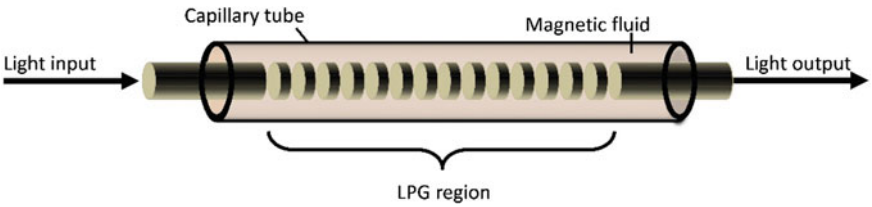

Fig. 17 Diagram of the magneto-optical tunable filter used in [86]

index variation produced by CO_2 lasers [70], CO laser [68], infrared femtosecond laser pulses [71], ion implantation [72], or electrical discharges [68, 73–75] (Fig. 17).

In LPGs there is a coupling of light between the guided core mode and various co-propagating cladding modes. This coupling produces a series of attenuation bands in the optical fiber transmission spectrum, each one centered at a different resonant wavelength (see Fig. 10). These resonant wavelengths depend mainly on the effective index of the coupled modes and the grating pitch [76, 77]. Although LPGs were initially developed as rejection-band filters [78], they also present interesting characteristics for sensing. The central wavelength of each LPG resonance depends critically on the refractive index difference between the core and the cladding, and hence any variation caused by strain, temperature, or even changes in the external refractive index may cause large wavelength shifts in the resonances [76, 79, 80].

Maybe the most advantageous characteristic is their small full width at half maximum (FWHM). FWHM provides a relative measurement of the quality of the attenuation band. LPGs have been studied for its application as humidity sensors [80], as gas sensors [81], as biosensors [82], for strain measurements [83] and they have been also used for magnetic field measurements [84–87].

Work developed in [84] involves the fabrication of a LPG onto a microstructured optical fiber (MOF). MOFs with air holes running along the fiber axis provide the possibility of filling them with functional materials. LPGs were successfully inscribed in MOF filled with ferrofluid using a scanning CO_2 laser, and a highly sensitive magnetic field sensor was proposed based on MOF-based LPG filled with ferrofluid. When the magnetic field strength is less than 300 Oe, is when this device is more sensitive and there is a linear relationship between wavelength shift and magnetic field, with a sensitivity of 1.946 nm/Oe. When the magnetic field is greater than 300 Oe, the shift of the resonant wavelength changes slowly, as the refractive index of magnetic fluid gets saturated.

Other set-up is that one used in [86, 87] and [88], where the LPG is sealed inside a capillary tube and immersed into a magnetic fluid. Wavelength shifts of 7.4 nm have been obtained in [86] for applied magnetic fields of 1700 Oe, with a maximum sensitivity of 0.02 nm/Oe in the 0–300 Oe range. In [85, 87] it has been also studied the wavelength position dependence of the resonance wavelength as a function of

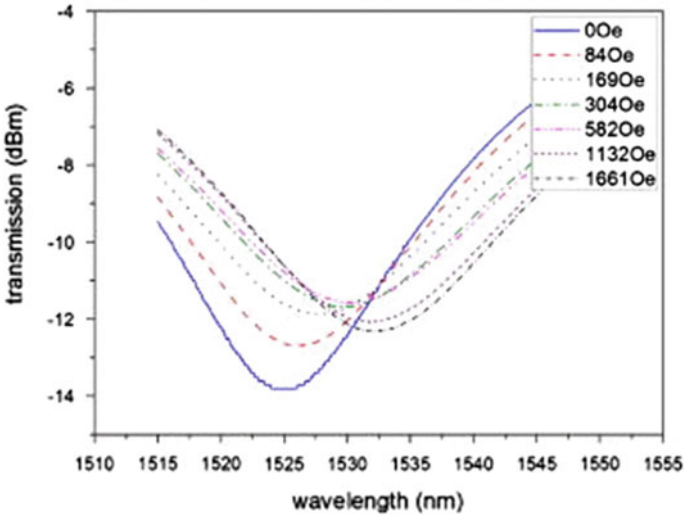

Fig. 18 Transmission spectra of the magneto-optical tunable filter based on long-period fiber gratings and magnetic fluids. Reprinted from Applied Physics Letters, 91(12), 121116, Liu, T., Chen, X., Di, Z., Zhang, J., Li, X., and Chen, J. (2007). Tunable magneto-optical wavelength filter of long-period fiber grating with magnetic fluids, with permission of AIP Scitation

the length of the LPG that is covered by the magnetic fluid, which make it usable as a tunable wavelength filter (Fig. 18).

2.6.2 Fiber Bragg Grating

Fiber Bragg grating (FBGs) are formed on the core of a single mode fiber by changing its refractive index. When a broadband light goes through an FBG, the light at a certain wavelength will be reflected while all the other light will go through [88]. Main difference between LPGs and FBGs is the grating period which leads to changes on the physical phenomena suffered by the light. In FBGs the light is successively reflected while in LPGs light is coupled from a guided mode into forward propagating cladding modes.

By using a magnetostrictive material to change the strain of an FBG according to the magnetic field, many FBG magnetic field sensors have been developed [89–98]. Some of these devices have been developed by mounting the FBG on a magnetostrictive base [90, 91]. For example, in [91] the sensor head consists of an FBG mounted on a base made of two metal alloys, Terfenol-D and MONEL 400, which are bonded together. These materials have similar thermal expansion coefficients while only Terfenol-D has magnetostriction. This situation allows to measure magnetic field with temperature compensation.

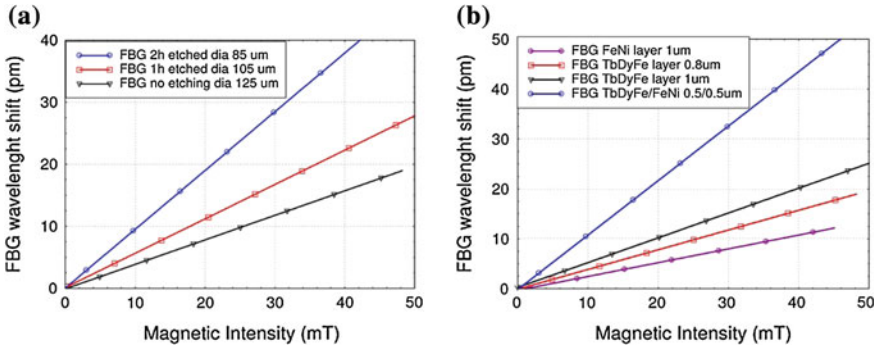

Fig. 19 **a** Central wavelength shift of three FBGs deposited with the same 0.8 μm TbDyFe coating, but with different chemically-etched cladding thickness and **b** Central wavelength shift of four standard single-mode FBGs (unetched) deposited with 1 μm FeNi, 0.8 μm TbDyFe, 1 μm TbDyFe, and 0.5 μmTbDyFe/0.5 μmFeNi respectively. Reprinted from Optics express, 17(23), Yang, M., Dai, J., Zhou, C., and Jiang, D. (2009). Optical fiber magnetic field sensors with TbDyFe magnetostrictive thin films as sensing materials. 20777-20782, with permission of OSA Publishing

But the magnetostrictive material can be also coated onto the FBG allowing to reduce the size of the device, as in [93]. FBG has been etched with hydrofluoric acid to reduce the cladding diameter. Then, thin films of giant magnetostrictive material TbDyFe were coated on the etched FBG by means of sputtering. Sensitivity increases for thinner FBGs achieving a maximum sensitivity of 1.08 pm/mT (Fig. 19).

2.7 Microresonators (Whispering Galleries Modes)

There are other kind of optical structures that allows to achieve great Q factors and that have been studied as a magnetic field sensor. Q factor is a measure of the quality of the device as a filter and it is the ratio of the wavelength to the full width at half-maximum [88]. Resonators are devices which consists of two optical structures. One of them acts as the waveguide and the other acts as a coupler. Then, light at certain wavelength guided by the first optical structure is evanescently coupled to the second structure in the so called whispering galleries modes (WGMs). Another point of view of the same phenomena is that the sensor is just the coupler, and the waveguide is the way to interrogate the sensor.

WGMs are electromagnetic surface oscillations supported by dielectric microresonators with circular structures such as spheres, cylinders, disks, or toroids. WGMs arise as a result of the trapping of light within the microresonator by almost total internal reflections from the resonator's curved surface. Such reflections force the light to take on a polygonal path within the curved structure, effectively

confining its energy to very small volumes and thus, leading to high power densities and high-quality (Q) factors [99]. The spectral positions of the transmission dips are strongly dependent on the geometry of the resonator, the optical properties of the resonator material, and its effective refractive index (RI).

Two different approaches are going to be explained here. Both of them achieve their sensitivity to the magnetic field using magnetic fluids and are based on resonances, but there are some differences. The first device [99] consists on a photonic crystal fiber (PCF) infiltrated with magnetic fluid as the sensor head. The PCF is formed by a section of silica-fiber cylinder (LMA-10 PCF from NKT Photonics), which has a solid core with a radius of 5 μm and a cladding with an outer radius of 62.5 μm. The cladding has an outer region formed by solid silica and an inner holey region formed by a periodic seven-ring lattice of hollow capillaries surrounding the core and running through the entire length of the fiber cylinder, parallel to its axis. The hollow capillaries have a diameter (d) of 3.04 μm and are arranged in a triangular pattern so that $d/\Lambda = 0.5$. Such a configuration can be approximately treated as a ring resonator formed by a cylindrical silica wall with an outer radius of 62.5 μm and an inner radius of ~45 μm (Fig. 20).

For sensor interrogation, a fiber taper with a waist diameter of 1 μm was fabricated from a short length of a single-mode fiber (SMF-28). Then, one end of the tapered fiber was connected to a superluminescent diode (SLED) and the other to an

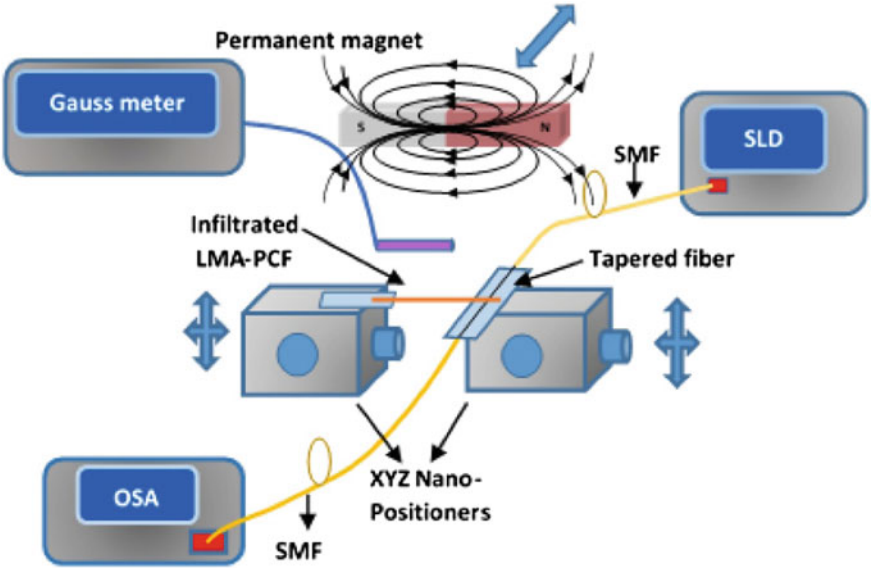

Fig. 20 Schematic diagram of the experimental setup for the magnetic-field sensor characterization. Reprinted from Optics letters, 40(21), 4983-4986, Mahmood, A., Kavungal, V., Ahmed, S. S., Farrell, G., and Semenova, Y. (2015), Magnetic-field sensor based on whispering-gallery modes in a photonic crystal fiber infiltrated with magnetic fluid, with permission of OSA Publishing

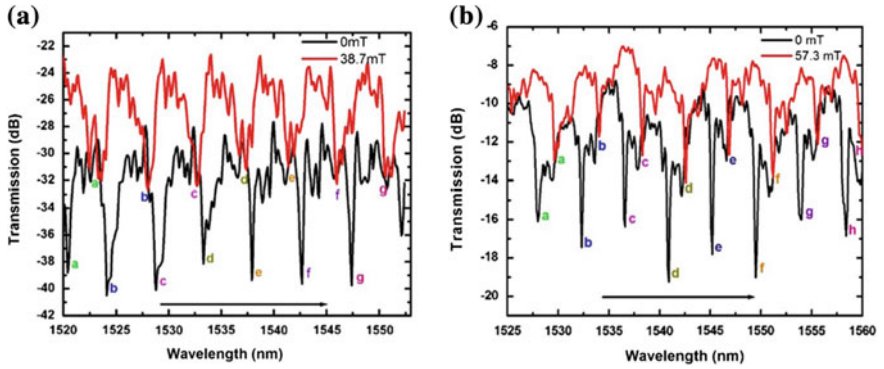

Fig. 21 **a** WGM spectra generated by the LMA-10 PCF infiltrated with the MF containing 5 nm diameter nanoparticles in the absence of a magnetic field (0 mT) and at 38.7 mT; **b** WGM spectra generated by the LMA-10 PCF infiltrated with the MF containing 10 nm diameter nanoparticles in the absence of a magnetic field (0 mT) and at 57.3 mT. Reprinted from Optics letters, 40(21), 4983–4986, Mahmood, A., Kavungal, V., Ahmed, S.S., Farrell, G., and Semenova, Y. (2015), Magnetic-field sensor based on whispering-gallery modes in a photonic crystal fiber infiltrated with magnetic fluid, with permission of OSA Publishing

optical spectrum analyzer. PFC and tapered fiber are in direct contact to achieve high coupling efficiency.

Then, the device was subjected to varying magnetic fields by changing the distance between a permanent magnet and the PFC. That varying magnetic field causes changes on the refractive index of the MF and thus, on the characteristics of the resonator. Then, the resonator with its new characteristics produces the resonance at a different wavelength. The maximum spectral shift values observed for each of the samples are 4.15 nm for applied magnetic fields of 40 mT. The MF saturates at this value of magnetic field due to the complete alignment of the nanoparticles. This lead to a sensitivity of 110 pm/mT in the range 0–40 mT.

Other approach to develop an optical fiber resonator is the followed in [100]. There, a microfiber knot resonator (MKR) has been developed. For this purpose, a coupler fabrication device has been used to taper the fiber to diameters up to 2.92 μm. Then, a knot was made into the fiber and it was stretched until it reaches a diameter of 500 μm. It was coated with Teflon® to protect the MKR without sacrificing its evanescent wave interaction. It was placed into a MgF_2 crystal and then inserted into a small glass cell filled with ferro-fluid. In next figure, Fig. 21, it can be seen a scheme of the proposed device as well as a real photo of the final packaged device (Fig. 22).

The magnetic field was applied by placing the structure between to coils. The *Q*-factor of the resonance wave of the sensor is 12400 and the resonance wavelength in sensor transmission spectra redshifted approximately 90 pm when the magnetic field was varied in the range from 0 to 300 Oe. The change of resonance wavelength tends to be saturated gradually when the magnetic-field strength exceeds 300 Oe (Fig. 23).

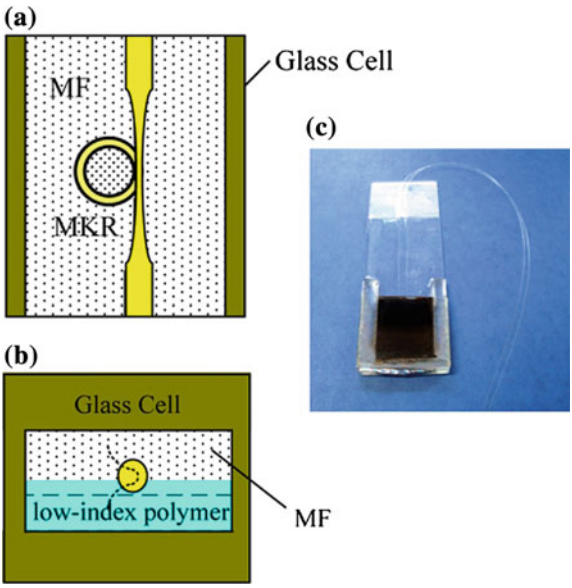

Fig. 22 Transmission spectra of the sensor under different magnetic-field strength. Reprinted from Optics letters, 37(24), 5187–5189, Li, X., and Ding, H. (2012), All-fiber magnetic-field sensor based on microfiber knot resonator and magnetic fluid, with permission of OSA Publishing

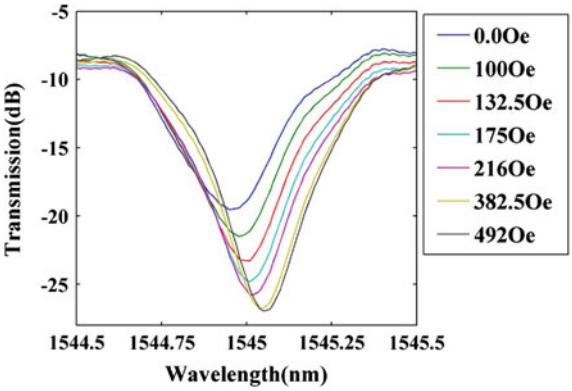

Fig. 23 Transmission spectra of the sensor under different magnetic-field strength. Reprinted from Optics letters, 37(24), 5187–5189, Li, X., and Ding, H. (2012), All-fiber magnetic-field sensor based on microfiber knot resonator and magnetic fluid, with permission of OSA Publishing

3 Conclusions

Development of optical fiber magnetic field sensors attract great interest, especially for using them as current transducers in industries such as the power facility or metallurgy industry. Several researching groups are actually working in the development of this kind of sensors, with more than 160 groups having published some research related to optical fiber magnetic field sensors, including universities, researching groups and companies.

Recent research has been done taking advantage of the high changes on the Refractive index of magnetic fluids. These materials are relatively easy to develop

Table 1 Different structures, materials and characteristics of the devices

Optical structure	Material	Effect	Sensitivity (pm/mT)	FWHM	Range (mT)	References
Fabry-Pèrot	Terfenol-D	Magnetostriction	8547	~3 nm	0–90	[36]
NATOF	Magnetic fluid	Magnetorefractive	71.7	>20 nm	45	[43]
SMS	Magnetic fluid	Magnetorefractive	905	~10 nm	12	[55]
LPG	Magnetic fluid	Magnetorefractive	160	~10 nm	160	[86]
FBG	TbDyFe	Magnetostriction	1.08	–	50	[93]
Resonator PCF	Magnetic fluid	Magnetorefractive	110	~2 nm	40	[99]
μK not resonator	Magnetic fluid	Magnetorefractive	3.3	~250 pm	50	[100]

and they have been proved successfully for their use as the cladding of several optical fiber structures and the development of magnetic field sensors. However, they have some disadvantages as the need of introducing the optical fiber inside a capillary tube and sealing it. This set-up gets worse one of the advantages of the use of optical fibers as sensors: their small size. Nevertheless, their weak point is their long-time behavior and their response to hard environmental conditions.

On the other hand, there are some optical fiber magnetic field sensors that have been developed by thin film coatings over an optical fiber structure. Probably, these kind of sensors have a longer useful life and better behavior for hard environmental conditions, but they show lower sensitivity to external magnetic fields than magnetic fluids.

Regarding sensitivities of the different structures commented here a table is shown, trying to resume the most important parameters (Table 1).

Although Faraday Effect was discovered in 1845, there still are some research involving this phenomenon. Main research about this kind of devices is related to improvements about the accuracy of the measurements as well as more precise and simpler ways to measure the rotation of the plane of polarization.

Finally, it should be commented that the magneto optic Kerr effect has not been mentioned here because there are relatively few devices developed exclusively on optical fiber. For measuring MOKE other configurations, as the Kretschmann configuration [101], are usually used. However, it can be used for measuring electric current measurement [102] although it is not the most habitual approach.

References

1. K. Kurosawa, Development of fiber-optic current sensing technique and its applications in electric power systems. Photonic Sens. **4**(1), 12–20 (2014)
2. K. Bohnert, P. Gabus, H. Brändle, P. Guggenbach, Fiber-optic dc current sensor for the electro-winning industry, in *Bruges, Belgium-Deadline Past. International Society for Optics and Photonics* (2005) pp. 210–213
3. S. Saito, J. Hamasaki, Y. Fujii, K. Yokoyama, Y. Ohno, Development of the laser current transformer for extra-high-voltage power transmission lines. IEEE J. Quantum Electron. **3** (11), 589–597 (1967)
4. M. Aerssens, A. Gusarov, B. Brichard, V. Massaut, P. Mégret, M. Wuilpart, Faraday Effect based optical fiber current sensor for tokamaks, in *2011 2nd International Conference on Advancements in Nuclear Instrumentation Measurement Methods and their Applications (ANIMMA)*, IEEE (2011), pp. 1–6
5. W.D. Callister, Introducción a la ciencia e ingeniería de los materiales. Reverté, vol. 1 (2002)
6. C. Westbrook, C.K. Roth, *MRI in Practice* (Wiley, 2011)
7. G.L. Miessler, P.J. Fischer, D.A. Tarr, Inorganic Chemistry: Pearson New International Edition. Pearson Higher Ed (2013)
8. https://www.nde-ed.org/EducationResources/CommunityCollege/MagParticle/Physics/MagneticMatls.htm
9. D. Jiles, *Introduction to Magnetism and Magnetic Materials* (CRC press, 2015)
10. S.A. Macintyre *Magnetic Field Measurement*. vol. 200 (CRC Press, 1999), p. 18
11. E.H. Hall, On a new action of the magnet on electric currents. Am. J. Math. **2**(3), 287–292 (1879)
12. R.S. Popovic, *Hall Effect Devices* (Institute of Physics, Bristol, U.K., 2004)
13. S. Tumanski, *Thin Film Magnetoresistive Sensors* (CRC Press, 2001)
14. J. Lenz, A.S. Edelstein, Magnetic sensors and their applications. Sens. J. IEEE **6**(3), 631–649 (2006)
15. J. Heremans, Solid state magnetic field sensors and applications. J. Phys. D Appl. Phys. **26** (8), 1149 (1993)
16. L.M. Miller, J.A. Podosek, E. Kruglick, T.W. Kenny, J.A. Kovacich, W.J. Kaiser, A μ-magnetometer based on electron tunneling, *in Proceedings of the Ninth Annual International Workshop on Micro Electro Mechanical Systems, 1996, MEMS'96*, An Investigation of Micro Structures, Sensors, Actuators, Machines and Systems. IEEE (1996), pp. 467–472
17. H.S. Bennett, E.A. Stern, Faraday effect in solids. Physical. Review **137**(2A), A448 (1965)
18. A. Dandridge, A.B. Tveten, G.H. Sigel, E.J. West, T.G. Giallorenzi, Optical fibre magnetic field sensors. Electron. Lett. **16**(11), 408–409 (1980)
19. S.C. Rashleigh, Magnetic-field sensing with a single-mode fiber. Opt. Lett. **6**(1), 19–21 (1981)
20. K.P. Koo, G.H. Sigel, Characteristics of fiber-optic magnetic-field sensors employing metallic glasses. Opt. Lett. **7**(7), 334–336 (1982)
21. T. Yoshino, Y. Ohno, Highly sensitive all-optical method for measuring magnetic fields. Fiber Integr. Opt. **3**(4), 391–399 (1981)
22. K. Sato, Measurement of magneto-optical Kerr effect using piezo-birefringent modulator. Jpn. J. Appl. Phys. **20**(12), 2403 (1981)
23. H.W. Davies, J.P. Llewellyn, Magnetic birefringence of ferrofluids. I. Estimation of particle size. J. Phys. D Appl. Phys. **12**(2), 311 (1979)
24. D.Y. Chung, T.R. Hickman, R.P. De Paula, J.H. Cole, Magneto-optics of ferrofluids, using fiber optics. J. Magn. Magn. Mater. **39**(1), 71–74 (1983)
25. H. Katsukawa, H. Ishikawa, H. Okajima, T.W. Cease, Development of an optical current transducer with a bulk type Faraday sensor for metering. IEEE Trans. Power Delivery **11**, 702–707 (1996)

26. A. Cruden, Z.J. Richardson, J.R. McDonald, I. Andonovic, Optical crystal based devices for current and voltage measurement. IEEE Trans. Power Delivery **10**, 1217–1223 (1995)
27. G. Frosio, R. Dandliker, Reciprocal reflection interferometer for a fiber-optic Faraday current sensor. Appl. Opt. **33**(25), 6111–6122 (1994)
28. F. Maystre, A. Bertholds, Magneto-optic current sensor using a helical-fiber Fabry-Perot resonator. Opt. Lett. **14**(11), 587–589 (1989)
29. Y.N. Ning, Z.P. Wang, A.W. Palmer, K.T. Grattan, D.A. Jackson, Recent progress in optical current sensing techniques. Rev. Sci. Instrum. **66**(5), 3097–3111 (1995)
30. S. Donati, V. Annovazzi-Lodi, T. Tambosso, Magneto-optical fibre sensors for electrical industry: analysis of performances. IEE Proc. J. (Optoelectronics) **135**(5), 372–382 (1988)
31. T.G. Giallorenzi, J.A. Bucaro, A. Dandridge, G.H. Sigel Jr., J.H. Cole, S.C. Rashleigh, R.G. Priest, Optical fiber sensor technology. IEEE Trans. Microw. Theory Tech. **30**(4), 472–511 (1982)
32. A.H. Rose, S.M. Etzel, C.M. Wang, Verdet constant dispersion in annealed optical fiber current sensors. J. Appl. Res. Technol. **15**, 803–807 (1997)
33. A.H. Rose, Z.B. Ren, G.W. Day, Twisting and annealing optical fiber for current sensors. J. Appl. Res. Technol. **14**(11), 2492–2498 (1996)
34. R.I. Laming, D.N. Payne, Electric current sensors employing spun highly birefringent optical fibers. J. Appl. Res. Technol. **7**, 2084–2094 (1989)
35. P. Mihailovic, S. Petricevic, Z. Stojkovic, J.B. Radunovic, Development of a portable fiber-optic current sensor for power systems monitoring. IEEE Trans. Instrum. Meas. **53**(1), 24–30 (2004)
36. P. Zhang, M. Tang, F. Gao, B. Zhu, S. Fu, J. Ouyang, Z. Zhao, H. Wei, J. Li, P.P. Shum, D. Liu, An Ultra-sensitive magnetic field sensor based on extrinsic fiber-optic Fabry-Perot interferometer and Terfenol-D. J. Lightwave Technol. **33**(15), 3332–3337 (2015)
37. K.D. Oh, A. Wang, R.O. Claus, Fiber-optic extrinsic Fabry-Perot dc magnetic field sensor. Opt. Lett. **29**(18), 2115–2117 (2004)
38. C.Y. Hong, S.Y. Yang, K.L. Fang, H.E. Horng, H.C. Yang, Mach-Zehnder interferometer by utilizing phase modulation of transmitted light through magnetic fluid films possessing tunable refractive index. J. Magn. Magn. Mater. **297**(2), 71–75 (2006)
39. M. Sedlar, V. Matejec, I. Paulicka, Optical fibre magnetic field sensors using ceramic magnetostrictive jackets. Sens. Actuators, A **84**(3), 297–302 (2000)
40. M.H. Kim, K.S. Lee, S.H. Lim, Magnetostriction measurements of metallic glass ribbon by fiber-optic Mach-Zehnder interferometry. J. Magn. Magn. Mater. **191**(1), 107–112 (1999)
41. J.E. Lenz, C.D. Anderson, L.K. Strandjord, Magnetic materials characterization using a fiber optic magnetometer. J. Appl. Phys. **57**(8), 3820–3822 (1985)
42. J. Villatoro, D. Monzón-Hernández, E. Mejía, Fabrication and modeling of uniform-waist single-mode tapered optical fiber sensors. Appl. Opt. **42**(13), 2278–2283 (2003)
43. A. Layeghi, H. Latifi, O. Frazao, Magnetic field sensor based on nonadiabatic tapered optical fiber with magnetic fluid. Photonics Technol. Lett. IEEE **26**(19), 1904–1907 (2014)
44. S. Silva, E.G. Pachon, M.A. Franco, J.G. Hayashi, F.X. Malcata, O. Frazão, P. Jorge, C.M. Cordeiro, Ultrahigh-sensitivity temperature fiber sensor based on multimode interference. Appl. Opt. **51**(16), 3236–3242 (2012)
45. L.B. Soldano, E. Pennings, Optical multi-mode interference devices based on self-imaging: principles and applications. J. Lightw. Technol. **13**(4), 615–627 (1995)
46. L.L. Xue, L. Yang, Sensitivity enhancement of RI sensor based on SMS fiber structure with high refractive index overlay. J. Lightw. Technol. **30**, 1463–1469 (2012)
47. W.S. Mohammed, P.W.E. Smith, All-fiber multimode interference bandpass filter. Opt. Lett. **31**, 2547–2549 (2006)
48. A.B. Socorro, M. Hernaez, I. Del Villar, J.M. Corres, F.J. Arregui, I.R. Matias, Single-mode—multimode—single-mode and lossy mode resonance-based devices: a comparative study for sensing applications. Microsyst. Technol. 1–6 (2015)
49. A. Mehta, W. Mohammed, E.G. Johnson, Multimode interference-based fiber-optic displacement sensor. IEEE Photon. Technol. Lett. **15**(8), 1129–1131 (2003)

50. Q. Wu, Y. Semenova, P. Wang, A.M. Hatta, G. Farrell, Experimental demonstration of a simple displacement sensor based on a bent single-mode–multimode–single-mode fiber structure. Meas. Sci. Technol. **22**, 025203 (2011). (5 pp.)
51. Q. Wu, Y. Semenova, A.M. Hatta, P. Wang, G. Farrell, Single-mode–multimode–single-mode fiber structures for simultaneous measurement of strain and temperature. Microw. Opt. Technol. Lett. **53**(9), 2181–2185 (2011)
52. V.I. Ruiz-Pérez, M.A. Basurto-Pensado, P. LiKamWa, J.J. Sánchez-Mondragón, D.A. May-Arrioja, Fiber optic pressure sensor using multimode interference, in *Journal of Physics: Conference Series*, vol. 274, No. 1, (IOP Publishing, 2011) p. 012025
53. Q. Wu, Y. Semenova, P. Wang, G. Farrell, High sensitivity SMS fiber structure based refractometer–analysis and experiment. Opt. Express **19**(9), 7937–7944 (2011)
54. L. Li, Q. Han, Y. Chen, T. Liu, R. Zhang, An all-fiber optic current sensor based on ferrofluids and multimode interference. Sens. J. IEEE **14**(6), 1749–1753 (2014)
55. Y. Chen, Q. Han, T. Liu, X. Lan, H. Xiao, Optical fiber magnetic field sensor based on single-mode–multimode–single-mode structure and magnetic fluid. Opt. Lett. **38**(20), 3999–4001 (2013)
56. W. Lin, Y. Miao, H. Zhang, B. Liu, Y. Liu, B. Song, Fiber-optic in-line magnetic field sensor based on the magnetic fluid and multimode interference effects. Appl. Phys. Lett. **103** (15), 151101 (2013)
57. T. Liu, Y. Chen, Q. Han, X. Lu, Magnetic field sensor based on U-bent single-mode fiber and magnetic fluid. Photonics J. IEEE **6**(6), 1–7 (2014)
58. L. Li, Q. Han, T. Liu, Y. Chen, R. Zhang, Reflective all-fiber current sensor based on magnetic fluids. Rev. Sci. Instrum. **85**(8), 083107 (2014)
59. A.B. Socorro, I. Del Villar, J.M. Corres, F.J. Arregui, I.R. Matias, Mode transition in complex refractive index coated single-mode–multimode–single-mode structure. Opt. Express **21**(10), 12668–12682 (2013)
60. J. Ascorbe, J.M. Corres, F.J. Arregui, I.R. Matias, Magnetic field sensor based on a single mode-multimode-single mode optical fiber structure, in *SENSORS, 2015 IEEE* (2015), pp. 1–4
61. I. Del Villar, A.B. Socorro, J. Corres, F. Arregui, I. Matias, Optimization of sensors based on multimode interference in single-mode–multimode–single-mode structure. J. Lightw. Technol. **31**(22), 3460–3468 (2013)
62. J.E. Antonio-Lopez, A. Castillo-Guzman, D.A. May-Arrioja, R. Selvas-Aguilar, P. LiKamWa, Tunable multimode-interference band pass fiber filter. Opt. Lett. **35**, 324–326 (2010)
63. A. Cusano, A. Iadicicco, P. Pilla, L. Contessa, S. Campopiano, A. Cutolo, M. Giordano, Mode transition in high refractive index coated long period gratings. Opt. Express **14**(1), 19–34 (2006)
64. I. Del Villar, I.R. Matías, F.J. Arregui, P. Lalanne, Optimization of sensitivity in long period fiber gratings with overlay deposition. Opt. Express **13**(1), 56–69 (2005)
65. J. Lemaire, R.M. Atkins, V. Mizrahi, K.L. Walker, K.S. Kranz, W.A. Reed, High pressure H2 loading as a technique for achieving ultrahigh UV photosensitivity and thermal sensitivity in GeO2 doped optical fibers. Electron. Lett. **29**, 1191–1193 (1993)
66. T. Erdogan, Cladding-mode resonances in short-and long-period fiber grating filters. JOSA A **14**(8), 1760–1773 (1997)
67. C. Narayanan, H.M. Presby, A.M. Vengsarkar, Band-rejection fibre filter using periodic core deformation. Electron. Lett. **33**(4), 280–281 (1997)
68. V.I. Karpov, M.V. Grekov, E.M. Dianov, K.M. Golant, S.A. Vasiliev, O.I. Medvedkov, R. R. Khrapko, Mode-field converters and long-period gratings fabricated by thermo-diffusion in nitrogen-doped silica-core fibers, in *Optical Fiber Communication Conference and Exhibit, 1998. OFC'98,* Technical Digest. IEEE (1998) pp. 279–280
69. E.M. Dianov, V.I. Karpov, M.V. Grekov, K.M. Golant, R.R. Khrapko, Ultra-thermostable long-period gratings induced in nitrogen-doped silica fiber, in *ECOC'97 Technical Digest*, paper 2–56

70. D.D. Davis, T.K. Gaylord, E.N. Glytsis, S.G. Kosinski, S.C. Mettler, A.M. Vengsarkar, Long-period fibre grating fabrication with focused CO2 laser pulses. Electron. Lett. **34**(3), 302–303 (1998)
71. Y. Kondo, K. Nouchi, T. Mitsuyu, M. Watanabe, P.G. Kazansky, K. Hirao, Fabrication of long-period fiber gratings by focused irradiation of infrared femtosecond laser pulses. Opt. Lett. **24**(10), 646–648 (1999)
72. M. Fujimaki, Y. Ohki, J.L. Brebner, S. Roorda, Fabrication of long-period optical fiber gratings by use of ion implantation. Opt. Lett. **25**, 88–89 (2000)
73. S.G. Kosinski, A.M. Vengsarkar, Splice-based long-period fiber gratings, in *OFC'98 Technical Digest*, paper ThG3, pp. 278–279
74. N. Godbout, X. Daxhelet, A. Maurier, S. Lacroix, Long-period fiber grating by electrical discharge, in *Proceedings of the ECOC'98*, pp. 397–398
75. G. Rego, O. Okhotnikov, E. Dianov, V. Sulimov, High-temperature stability of long-period fiber gratings produced using an electric arc. J. Lightw. Technol. **19**(10), 1574–1579 (2001)
76. A.D. Kersey, M.A. Davis, H.J. Patrick, M. LeBlanc, K.P. Koo, C.G. Askins, M.A. Putnam, E.J. Friebele, Fiber grating sensors. J. Lightw. Technol. **15**(8), 1442–1463 (1997)
77. S.W. James, R.P. Tatam, Optical fibre long-period grating sensors: characteristics and application. Meas. Sci. Technol. **14**(5), R49 (2003)
78. A.M. Vengsarkar, P.J. Lemaire, J.B. Judkins, V. Bhatia, T. Erdogan, J.E. Sipe, Long-period fiber gratings as band-rejection filters. J. Lightw. Technol. **14**(1), 58–65 (1996)
79. V. Bhatia, A.M. Vengsarkar, Optical fiber long-period grating sensors. Opt. Lett. **21**(9), 692–694 (1996)
80. A. Urrutia, J. Goicoechea, A.L. Ricchiuti, D. Barrera, S. Sales, F.J. Arregui, Simultaneous measurement of humidity and temperature based on a partially coated optical fiber long period grating. Sens. Actuators B: Chem. **227**, 135–141 (2016)
81. T. Wang, W. Yasukochi, S. Korposh, S.W. James, R.P. Tatam, S.W. Lee, A long period grating optical fiber sensor with nano-assembled porphyrin layers for detecting ammonia gas. Sens. Actuators B: Chem (2016)
82. G. Quero, M. Consales, R. Severino, P. Vaiano, A. Boniello, A. Sandomenico, M. Ruvo, A. Borriello, L. Diodato, S. Zuppolini, M. Giordano, Long period fiber grating nano-optrode for cancer biomarker detection. Biosens. Bioelectron. **80**, 590–600 (2016)
83. R. Guyard, D. Leduc, C. Lupi, Y. Lecieux, Global overview of the sensitivity of long period gratings to strain. Opt. Laser Technol. **79**, 62–73 (2016)
84. Y. Miao, K. Zhang, B. Liu, W. Lin, H. Zhang, Y. Lu, J. Yao, Ferrofluid-infiltrated microstructured optical fiber long-period grating. Photonics Technol. Lett. IEEE **25**(3), 306–309 (2013)
85. W. Liao, X. Chen, Y. Chen, S. Pu, Y. Xia, Q. Li, Tunable optical fiber filters with magnetic fluids. Appl. Phys. Lett. **87**(15), 151122 (2005)
86. T. Liu, X. Chen, Z. Di, J. Zhang, X. Li, J. Chen, Tunable magneto-optical wavelength filter of long-period fiber grating with magnetic fluids. Appl. Phys. Lett. **91**(12), 121116 (2007)
87. M. Konstantaki, A. Candiani, S. Pissadakis, Magnetic tuning of optical fibre long period gratings utilizing ferrofluids, in *11th International Conference on Transparent Optical Networks, 2009. ICTON'09*. IEEE, pp. 1–4
88. K. Li, Review of the strain modulation methods used in fiber bragg grating sensors. J. Sens. **2016** Article ID 1284520, 8 pp (2016). doi:10.1155/2016/1284520
89. Y. Dai, M. Yang, G. Xu, Y. Yuan, Magnetic field sensor based on fiber Bragg grating with a spiral microgroove ablated by femtosecond laser. Opt. Express **21**(14), 17386–17391 (2013)
90. J. Mora, A. Díez, J.L. Cruz, M.V. Andrés, A magnetostrictive sensor interrogated by fiber gratings for DC-current and temperature discrimination. IEEE Photonics Technol. Lett. **12** (12), 1680–1682 (2000)
91. K.S. Chiang, R. Kancheti, V. Rastogi, Temperature-compensated fiber-Bragg-grating-based magnetostrictive sensor for dc and ac currents. Opt. Eng. **42**(7), 1906–1909 (2003)
92. C. Ambrosino, S. Campopiano, A. Cutolo, A. Cusano, Sensitivity tuning in terfenol-D based fiber Bragg grating magnetic sensors. IEEE Sens. J. **8**(9), 1519–1520 (2008)

93. M.H. Yang, J.X. Dai, C.M. Zhou, D.S. Jiang, Optical fiber magnetic field sensors with TbDyFe magnetostrictive thin films as sensing materials. Opt. Express **17**(23), 20777–20782 (2009)
94. J.X. Dai, M.H. Yang, X.B. Li, H.L. Liu, X.L. Tong, Magnetic field sensor based on magnetic fluid clad etched fiber Bragg grating. Optical Fiber Technology **17**(3), 210–213 (2011)
95. G.N. Smith, T. Allsop, K. Kalli et al., Characterisation and performance of a Terfenol-D coated femtosecond laser inscribed optical fibre Bragg sensor with a laser ablated microslot for the detection of static magnetic fields. Opt. Express **19**(1), 363–370 (2011)
96. H. Liu, S.W. Or, H.Y. Tam, Magnetostrictive composite-fiber Bragg grating (MC-FBG) magnetic field sensor. Sens. Actuators, A **173**(1), 122–126 (2012)
97. X.-Z. Lin, Y. Zhang, H.-L. An, H.-D. Liu, Electrically tunable singlemode fibre Bragg reflective filter. Electron. Lett. **30**(11), 887–888 (1994)
98. P.M. Cavaleiro, F.M. Araújo, A.B.L. Ribeiro, Metal-coated fibre Bragg grating sensor for electric current metering. Electron. Lett. **34**(11), 1133–1135 (1998)
99. A. Mahmood, V. Kavungal, S.S. Ahmed, G. Farrell, Y. Semenova, Magnetic-field sensor based on whispering-gallery modes in a photonic crystal fiber infiltrated with magnetic fluid. Opt. Lett. **40**(21), 4983–4986 (2015)
100. X. Li, H. Ding, All-fiber magnetic-field sensor based on microfiber knot resonator and magnetic fluid. Opt. Lett. **37**(24), 5187–5189 (2012)
101. C. Yan, L. Han, J. Yang, W. Gu, Y. Liao, Magnetic field sensing using evanescent waves in the Kretschmann configuration. Sens. Actuators, A **220**, 85–91 (2014)
102. D. Karasawa, M. Sonehara, S. Kitazawa, T. Sato, Development of optical probe current sensor with Kerr effect for power electronics. in *Sensors, 2014 IEEE*. IEEE (2014), pp. 1928–1931

Sensing at Terahertz Frequencies

P. Rodríguez-Ulibarri and M. Beruete

Abstract In this chapter a review of sensing applications working at terahertz (THz) frequencies is performed. Firstly, an introductory section putting in context the THz regime and highlighting particularities and potential applications at this frequency band is outlined. Then, a comprehensive examination of sensing solutions following different technologies investigated during the last two decades is presented. Special attention is given to the fibre optics solutions and free-space approaches based on metasurfaces. Finally, plasmonic sensing platforms and waveguide solutions are discussed as well.

1 Introduction

The terahertz (THz) band is usually defined as the spectral region that lies between microwaves and far-infrared. It is generally accepted that it extends from 0.1 to 10 THz [1], but there is not a total consensus about its exact limits yet. For example, some scientists extend the upper limit up to 30 THz, in contradiction with the classical infrared band limits used in optics that puts the far-infrared boundary at 1 THz. Likewise, the lower limit of 0.1 THz does not agree with the classical band classification of microwave engineering, wherein millimetre-waves cover the frequency span from 30 to 300 GHz. This disagreement comes from the intrinsic multidisciplinary character of THz, with scientists and technologists of multiple and varied disciplines sharing knowledge and working together to devise new devices and concepts in this relatively new band. That being said, and being aware that it is still under debate, in this chapter we will consider that the THz band goes from 0.1 to 10 THz, which is the most accepted definition so far. Figure 1 shows the electromagnetic spectrum wherein the different frequency ranges are delimited. Since depending on the background of the reader, he or she might be used to work in terms of wavelength, wavenumber, or frequency, the correspondence units are also outlined.

P. Rodríguez-Ulibarri · M. Beruete (✉)
Public University of Navarra, Pamplona, Spain
e-mail: miguel.beruete@unavarra.es

© Springer International Publishing Switzerland 2017

I.R. Matias et al. (eds.), *Fiber Optic Sensors*, Smart Sensors,
Measurement and Instrumentation 21, DOI 10.1007/978-3-319-42625-9_14

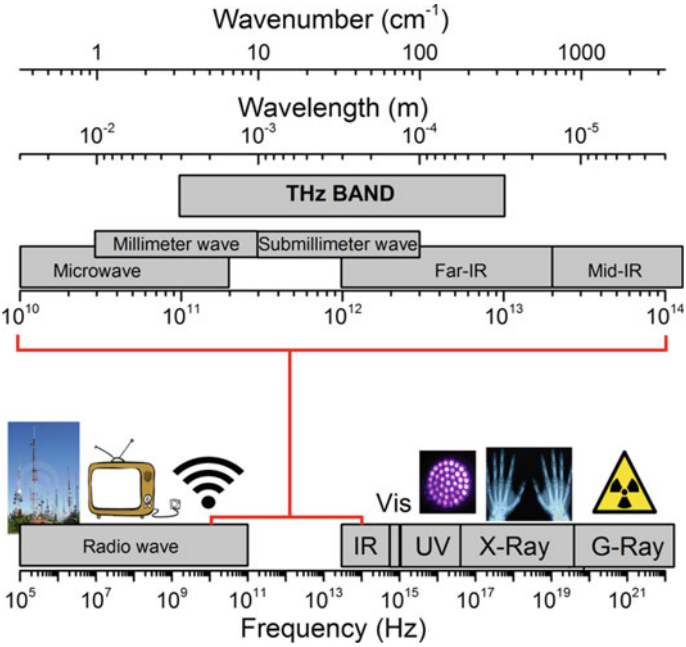

Fig. 1 Electromagnetic spectrum and its associated applications

Until recently, the THz range was known as the "THz gap" due to the lack of efficient and cost-effective generators and detectors. In fact, for a long time there were only two main niches for THz applications, astronomy and spectroscopy. The classical THz sources were based on tubes (carcinotrons, klynstrons and backward wave oscillators) and free electron lasers (FEL). Those solutions were bulky, expensive and had low efficiency. Similarly, classical THz detectors usually relied on bolometers which need to be cooled at cryogenic temperatures. The situation changed completely with the emergence of new THz generation techniques based on optical rectification and photomixing plus new genuine THz sources like quantum cascade lasers (QCLs) as well as the improvement of classical microwave up-converters based on solid state multipliers, on the one hand, and new, cheaper, and user-friendly detectors as those based on photomixing or microwave heterodyne detection, on the other hand. These discoveries paved the way towards affordable complete THz systems leading soon to Time Domain Spectroscopy devices working at THz (TDS-THz) that contributed decisively to the popularization of THz research. In practice, one should find the most appropriate generation/detection approach depending on the application. The evaluation of these methods is beyond of the scope of this chapter, so the reader is encouraged to consult excellent review articles and books treating the subject [1–3].

Bridging the THz gap has opened many potential applications. This has generated a feedback process where applications push technology leading to a constant

improvement. For example the revolutionary space applications envisioned with THz have led to significant advances in sources, detectors and other THz components [4] producing a cross-fertilization that has been also transferred to ground applications. An example of massive modern technology that can get a direct benefit of the advances in THz research is the field of communications. Nowadays there is an increasing demand of high data rates for multimedia applications in portable electronic devices like tablets and smartphones. This requires high-capacity, as derived from Shannon's theorem. The THz band offers a wide bandwidth with the capability to achieve terabyte data rates communications, improving by a factor of more than 10^3 the fastest communication systems currently available. However, there are some hurdles that limit the performance of THz waves for data transmission. First, the atmospheric absorption is very high at these frequencies (mainly due to the presence of water vapour absorption bands). Secondly, even in absence of absorption loss, the short wavelength of THz radiation entails short wireless propagation distances, as deduced from the direct application of the Friis transmission formula. For these reasons, THz communications are still in a research stage and have not been exploited yet but the perspectives are very promising, especially at certain scenarios such as indoor communications, short-distance devices or point to point communications, short range secure communications, and so on [5, 6].

Another field that has experienced a rapid development is THz spectroscopy. At THz waves some large-size molecules of biological and biomedical interest such as amino-acids have special fingerprints which allow their identification in this band. In particular, THz waves have a wavelength comparable to vibrational motion modes of bending, stretching or torsion of macromolecules. This opens up new possibilities for detection and sensing applications in a variety of sectors such as security [7], pharmaceutical [8], biomedicine [9], etc.

Although an exhaustive compilation is impossible due to space restrictions, it should be clear from the previous paragraphs that the THz range holds promise in numerous and diverse applications. Here, in conformity with the subject of the book, we will concentrate on sensing applications. In this context, THz complements other frequency bands, offering new opportunities for detection of substances and materials. As mentioned above, with THz waves one can collect and extract valuable information (molecular bonds, concentration …) from transmittance/reflectance and absorbance measurements thanks to their microscale wavelength. This information can be obtained from direct characterization on the target sample followed by a data analysis post-processing. With this approach it might be necessary to prepare sample pellets as an intermediate step, which is a timely task and subject to experimental errors, increasing the degree of uncertainty in the experiment. This type of sensing will be covered in the first part of the chapter.

Alternatively, a more "engineer-oriented" approach can be taken, in which engineered platforms (devices, reactive substances…) are employed to enhance the response of the measured material. Furthermore, adequate sample channels can be designed and optimized depending on the sample form (solid, fluid, liquid or gaseous) to minimize the amount of the required analyte for a successful detection.

This approximation definitely expands the possibilities of THz sensor design, enabling different perspectives and technologies, so we will dedicate a significant part of this chapter to cover it in detail.

This chapter is organized as follows: Sect. 2 presents a review of some biological, chemical and security sensing applications with direct detection. In Sect. 3, sensors based on THz fibre optics solutions are outlined. Section 4 deals with metasurfaces, i.e. resonant thin-film devices with a metallic pattern that provide a strong field concentration allowing for an enhancement of detection of the material under test. This is a very active field with very promising perspectives. Therefore, we will perform a detailed review of the latest achievements. Section 5 is devoted to the discussion of sensing solutions based on guiding structures such as metallic and dielectric guides or surface waves platforms relying of surface plasmons polaritons (SPP). Finally, Sect. 6 covers other THz sensor alternatives based on microwave classical components such as waveguides and transmission lines.

2 THz Sensing: Biosensing, Imaging

As mentioned in the introduction, THz waves are promising in biosensing applications given that their wavelength is comparable with intramolecular vibrational modes. For this reason, an exhaustive research activity has been carried out in chemical, biological and biomolecular sensing. Another discipline where THz science has had a great impact is in security applications. For example, THz waves have been used to detect hazardous materials, such as explosive compounds. This topic has strong bonds with THz imaging techniques [10] of major importance in multiple applications such as dental caries detection, observation of water content in leaves or see-through-cloth cameras, able to detect concealed weapons that are nowadays operating at some airports. In this section a literature review of works related with these topics is presented. Due to the vast amount of bibliography, this list cannot and does not pretend to be exhaustive. In turn, some selected examples have been extracted which in the authors' opinion, are representative of the great deal of effort made by worldwide scientists in the development of the THz technology and applications. Of course, this appreciation is completely subjective and hence we apologize in advance in case we have overlooked relevant works that should have been included here.

2.1 THz Biosensing: Studying DNA

The analysis of deoxyribonucleic acid (DNA) macromolecules by means of THz spectroscopy was a very active research topic at the beginning of the 21st century. Several research groups focused their efforts on the THz regime searching for a

spectral evidence of DNA phonon resonances below infrared (IR) frequencies. The motivation of these studies was triggered by previous investigations on DNA macromolecules conducted at far/mid IR frequencies [11] and microwave regimes [12–14], devoted to either finding or refuting spectral fingerprints of DNA molecules in those regimes. In addition, although theoretical calculations predicted DNA phonon resonances at THz, the absence of an experimental evidence was an extra stimulus to inspect it in detail. In this context, two different experimental approaches were followed: Fourier Transform Interferometry (FTIR) spectroscopy and TDS-THz. FTIR offers broadband measurements and a well-stablished technology, borrowed from infrared. Nevertheless, with this technique, THz radiation is usually detected using bolometers which need cryogenic cooling for operation. On the contrary, TDS-THz is a more recent technology developed specifically for the THz band. It has narrower operation bandwidth than FTIR but a clear advantage is its capability to retrieve the magnitude and phase of the transmitted and reflected signals [15].

An example of FTIR characterization of commercial DNA chains, among other materials, between 0.3 and 0.75 THz can be found in Ref. [16]. Figure 2 shows the transmission derivative with respect to the frequency of 20 averaged spectra for herring and salmon DNA samples measured between 10 and 25 cm^{-1} (0.3 and 0.75 THz) obtained for identical orientation of the DNA chains. It can be observed that although many common resonance modes exist in the DNA of both species, there are also differences that can lead to species identification with the appropriate data post-processing. In fact, the same authors studied the applicability of artificial neural network in the quest of discrimination and recognition between different DNA molecules [17].

Another route for THz spectroscopy analysis of DNA biomolecules was investigated in the framework of TDS systems [18–21]. In these studies, label-free probing of the binding state of DNA molecules was pursued in contrast to traditional labelling techniques with fluorescent chromophores [19–21]. While in Ref. [19] the capability of THz techniques for discerning between hybridized (double

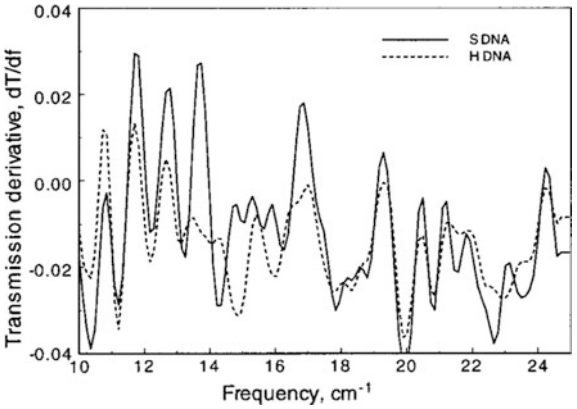

Fig. 2 Differential transmission averaged over 20 spectra for herring and salmon DNA samples. Reprinted from [16] with the permission of AIP Publishing

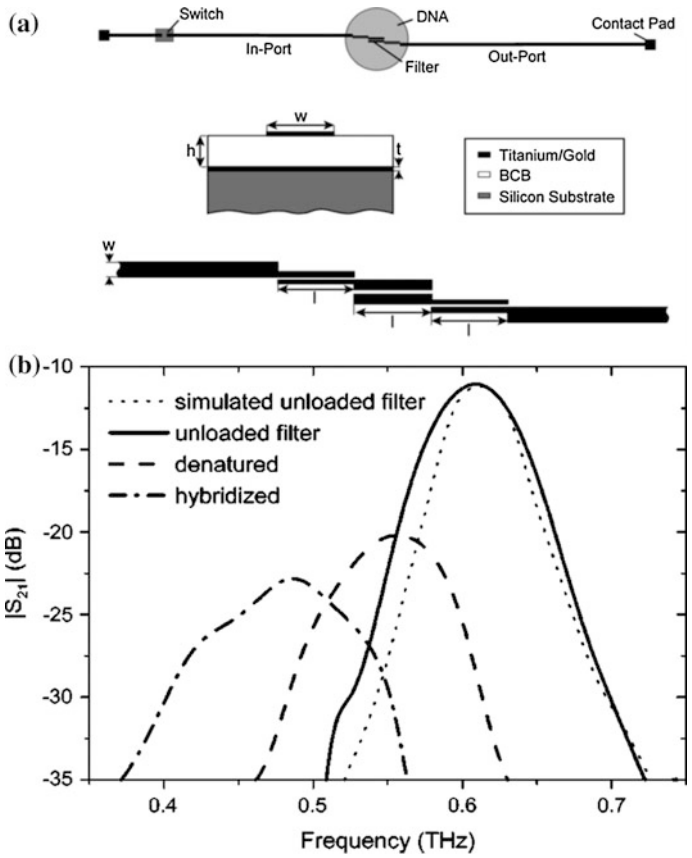

Fig. 3 **a** *Top* Bird's-eye view of the applied THz device structure. *Middle* Cross section of the thin-film microstrip line using gold for the signal lines and benzocyclobutene (BCB) as a low-*k* dielectric substrate. *Bottom* Bird's-eye view of the bandpass filter. **b** Magnitude of transmission parameter S_{21} of the band-pass filters unloaded and loaded with denatured or hybridized DNA films. Reprinted from [20] with the permission of AIP Publishing

stranded) and denatured (single stranded) hybridization states was demonstrated, in Refs. [20, 21] a passive THz resonator based on planar waveguide technology working as a transducer was proposed. Figure 3a shows a schematic of the sensor device and the response with and without a DNA sample with different binding states. In the spectrum of Fig. 3b, it can be observed a redshift and a reduction of the transmitted level when the DNA is present. Moreover, the redshift is larger for the hybridized DNA than for the denatured case, in concordance with the refractive indexes evaluated in Ref. [19]. However, it should be mentioned that Ref. [22] noted some skepticism about the results obtained in previous references. The main objections were related to the amount of sample (layer thickness) that was sufficient to be observed. However, additional experiments [23, 24] support the results of

Ref. [20]. In any case, these works are good examples to demonstrate the potential application of a resonant structure for sensing purposes.

Aside from DNA characterization, multiple examples of other kinds of biosensing applications can be found in the literature. For instance, two different strands of artificial ribonucleic acid (RNA) were characterized and identified via THz-TDS techniques [25]. In the same work, THz imaging was also applied for identification purposes. The spatial resolution obtainable with the THz-TDS system under free-space propagation and apertureless focusing of the THz beam was close to the diffraction limit. This limit could be overcome by applying confining techniques of the THz electric field. A thorough review on chemical spectroscopy and imaging with THz-TDS compiling the previous examples and other works can be found in a publication from the same authors [26].

2.2 THz Sensing for Security and Health Applications

Security and public health applications are very important for obvious reasons. Early detection of hazardous materials is crucial in crowded public areas, such as airports or railway stations. On the other hand, human rights of people in terms of privacy and healthcare must be preserved. In this way, non-invasive and non-ionizing radiation techniques are preferable for security scanners. THz radiation fulfils these requirements and hence it has been a very active application field since the beginning. A quite complete compilation of examples can be found in Ref. [7]. Here, only some relevant cases will be outlined.

THz-TDS and FTIR techniques were tested for THz security applications in [27]. There, a comparison between both approaches was made to ascertain the absorption features of the explosive 1,3,5-trinitro-s-triazine in the THz band working in transmission mode, with good agreement between both methods. However, it is important to note that transmission measurements have some limitations for characterizing bulky samples, as most of the energy might absorbed leaving only a tiny part at the detector and making the detection very challenging. For this and other reasons, working in the reflection mode is usually preferred, as was done in [28, 29] also for explosive material detection. THz radiation is also ideally suited for see-through-cloth imaging, able to detect weapons (knifes, guns, explosives, etc.) under several layers of clothing. This was analyzed in detail in [30, 31]. Finally, another application related with public healthcare issues where THz spectroscopy has been demonstrated to be promising, is the detection and identification of illicit drugs [32, 33]. For instance, a multispectral pattern analysis has been effectively applied to distinguish between methamphetamine, MMDA and aspirin samples concealed in mail envelopes [32].

In this section a concise overview of THz spectroscopy and imaging applications investigated during the last 20 years has been provided. Most of the mentioned examples relied on transmission, reflection, or imaging results of the bare substance to be detected or alternatively, mixed with other compounds in pellet forms.

Currently, some of the revolutionary ideas based on these principles are already implanted and working (e.g. 3D-THz scanners). THz for security and health application is thus very promising, but more research is still needed to achieve faster, cheaper and more sensitive sensor platforms. In the subsequent sections, THz sensors based on different technologies will be presented.

3 Sensing THz with Dielectric Waveguides (Fibres)

Throughout all this book, different fibres optics based sensor solutions have been proposed for a large number of applications in different ranges of the electromagnetic spectrum. In this chapter, we focus on the THz band. From an electromagnetic point of view, optical fibres are dielectric waveguides. As is well-known, the light confinement and guidance is due to the index contrast between the core and the cladding. Thanks to their geometry, they are flexible and bendable, which are highly desirable features for sensing applications since it permits to insert them in places difficult to reach. For instance, it is relatively easy to design an endoscope for medicine applications using optical fibres.

Due to the different operation regime, one can expect a very different behaviour of standard optical fibres at THz. To begin with, the materials that compose the fibres are dispersive (the constitutive parameters of any natural material change with frequency) and one can find that materials with low loss at optics have significant absorption peaks at THz. This implies that standard optical fibres are not directly applicable to THz and new strategies and materials must be found. Historically the first dielectric waveguides at THz were proposed in the early years of the 21st century by using sapphire and plastic ribbon materials [34, 35]. To date, photonic crystal fibres (PCF) [36, 37], subwavelength plastic fibres [38], low-index discontinuity fibres [39], anti-resonant pipe waveguides [40–42], ferroelectric cladding [43], micro-structured cladding with air core [44, 45] and porous core fibres solutions [46, 47] have been also investigated. From this succinct list, it is clear that THz guiding using solutions inspired by optical fibres is a quite active field of research in the field of communications. However, sensing applications have not received as much attention yet. In the following, we will present some examples of sensors based on dielectric waveguides at THz frequencies.

To begin with, biochemical sensing by means of photonic crystal waveguides (PCW) [48] and a coupled resonator optical waveguide (CROW) were investigated by Kurt et al. [48, 49]. In the former solution, the propagation characteristics of the PCW can be modified by introducing an analyte material inside the holes of the PCW. The CROW is the resonant version of the PCW and is achieved by including defect holes of different radii and filling them afterwards with the analyte material. Sensing is achieved by measuring the shift of the resonance frequency.

Another example that has been theoretically analysed as fibre-based THz sensing device for gases is an air-porous Teflon fibre coated with a ferroelectric polyvinylidene fluoride (PVDF) layer [50, 51]. The sensing principle here relies on

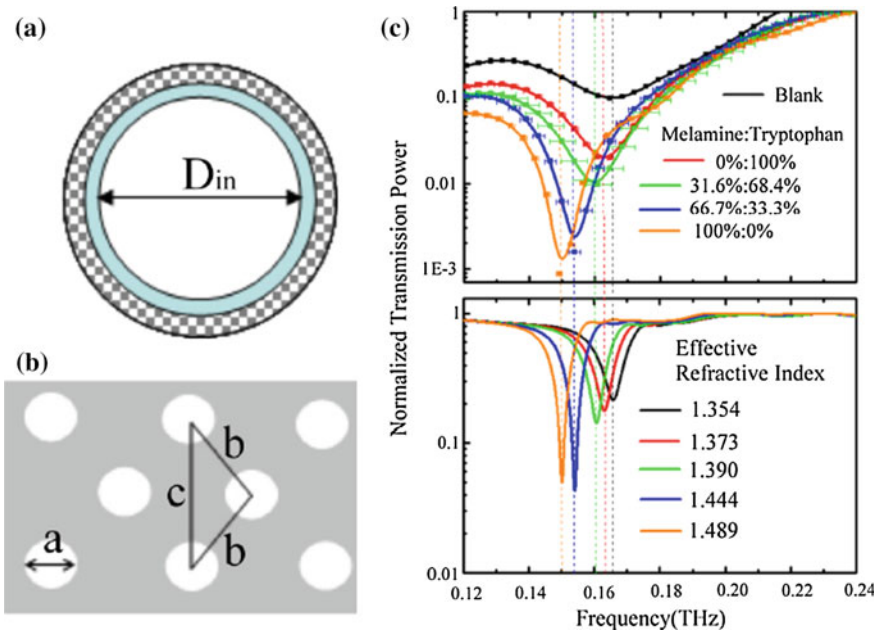

Fig. 4 **a** Cross section of a PP-pipe-waveguide sensor with an inner diameter D_{in} = 12 mm. **b** *Top view* of the porous PVC adsorber. Dimensions: a = 1.1 mm; b = 1.4 mm and c = 2.7 mm. **c** *Top* Measured spectral positions of 1st-order resonant waves for different adsorbed powders in the outer cladding. *Bottom* Simulated spectral positions of 1st-order resonant waves. Reprinted from [53] with permission of the Optical Society of America

a surface wave (plasmon) that is excited at the PVDF/air interface when a phase matching condition is satisfied. This condition is sensitive to changes of refractive index of the analyte and therefore can be used for sensing purposes.

An experimental demonstration of a sensor device based on an anti-resonant reflecting waveguide (ARRHW) can be found in Ref. [52]. The sensing device consists of a hollow polypropylene (PP) tube that allows sensing fluids by measuring the spectral variation of the resonance when the fluid is injected inside the tube. The same authors proposed another fibre-based dielectric pipe waveguide in which sensing can be done by loading the porous cladding with powder sample or by injecting a gas inside the hollow inner core [53]. The cross section of the dielectric pipe waveguide is shown in Fig. 4a. A bird's eye view of the porous cladding showing the hole diameter (a) and the dimensions of the triangular lattice (b and c), is presented in Fig. 4b. The dimensions can be found in the figure caption. Experimental and simulation results are shown in Fig. 4c. There, the normalized transmission power obtained for powder compositions of melamine and tryptophan with different concentrations are shown. The shift of the resonance varies depending on the effective refractive index with different melamine/tryptophan concentrations.

Simulation results with show a good agreement with the experiments, as it can be proven by comparing the upper and bottom plots of Fig. 4c.

Finally, another structure that was borrowed from optics and transferred to the THz regime, are filters based on Bragg gratings printed on a polymer fibre. They were developed at THz in Ref. [54] and used as sensing devices for paper quality monitoring and temperature distributed sensing [55, 56]. A stop-band is created by the Bragg grating which can be shifted in frequency when successive paper layers are added. It was observed that as the number of paper layers was increased, a larger frequency shift was obtained along with a reduction in the transmission level.

From the previous paragraphs, it can be concluded that devices based on fibres have an enormous potential for sensing applications within the THz range. As described above different sample forms can be sensed (powders, fluids and gases) with relatively simple architecture. This is the main advantage with respect to the metallic waveguide approaches that will be shown later. Fibres offer flexibility and conformability of the device which is a critical feature in medicine applications, for example.

4 THz Sensing with Frequency Selective Surfaces and Metasurfaces

In this section a review of different devices based on resonant structures for thin-film sensing THz applications is performed. Here the approach is radically different to fibre solutions. Instead of having a guided wave we work with waves travelling in free-space that hit an engineered screen producing a response (typically a resonance) that can be used for sensing. It is worth mentioning that this approach is currently one of the most active and popular fields of research for sensing applications at the THz regime. For this reason, we give it a great deal of attention in this chapter. Before getting into details, a short introduction about the fundamentals and brief history of these structures is presented. This introduction would be helpful for contextualize the growing relevance of this sensing solutions within the last few years.

The first group of structures treated here are the so-called Frequency Selective Surfaces (FSS). FSS are two-dimensional periodic resonant structures, usually composed of metallic elements (slots or patches), which can have band-pass or band-stop behaviour, and whose element dimensions are comparable with the resonant wavelength (typically about half or one wavelength). They have been classically used in radar systems since the 1970s as antenna hybrid radomes to deflect the frequencies out of the range of interest, reducing the radar cross section (RCS). Other classical applications for FSS are dichroic subreflectors (transparent at the operation frequency and opaque for other frequencies), circuit analog absorbers and meanderline polarizers [57]. All these examples have in common that a broadband operation is usually sought to optimize communication systems.

In sensing applications the peak or dip (depending on the character of the FSS, one can have either band-pass or notch response) that takes place at resonance is used as a reference. Ideally, the resonance frequency should be shifted when an analyte sample is placed near the structure. The performance on the sensor is customarily evaluated in terms of the maximum frequency shift and the linewidth of the resonance. Hence, for optimal sensing, narrowband FSS devices are preferred.

Metasurfaces are the second group of devices considered in this section. Metasurfaces evolve from metamaterials and can be considered the two dimensional version of them. Metamaterials are usually defined as manmade structures that exhibit exotic electromagnetic responses that cannot be observed in nature. They have received a great attention, becoming one of the most active fields of research since their advent at the beginning of 21st century, leading to important breakthroughs such as the experimental demonstration of negative refraction [58, 59] and invisibility cloaks [60, 61]. Metasurfaces are the ultimate hot topic in this field and are nowadays used for a variety of exotic applications like cloaking devices, polarizers, chiral structures, beam-steerers, analog computing and also for sensing [62–66]. In essence they are very similar to FSS, being the most substantial difference the element size. While in FSS the dimensions are comparable to the operation wavelength, for metasurfaces the dimensions are eminently subwavelength. In some occasions, the term metasurfaces and FSS are used interchangeably, given that both usually consist of a thin dielectric substrate with a metallic pattern printed on it.[1] Here we will ascribe to this trend and will not distinguish between metasurfaces and FSS in the upcoming sections. In favour of this decision is the fact that the application of FSS for sensing purposes is relatively new and has been boosted by metasurfaces research. Therefore, in the next lines, FSS and metasurface terms will be used depending on the references cited. The reader should just keep in mind that they are used equally as free-space and thin-film solutions for sensing applications.

Before going into an exhaustive description of the different FSS/metasurfaces sensing platforms we briefly define the parameters used to evaluate their performance. We will use the sensitivity, S, which in resonant systems is given by the frequency/wavelength shift of the resonance as a function of the sample index of refraction ($S = \Delta f/\Delta n = \Delta\lambda/\Delta n$). The units are [Hz/RIU] or [m/RIU] (RIU: refractive index unit). However, S, is also related to loosely-defined parameters such as the required "amount" of sample for operation. In this context, it can be the film thickness or the concentration of the chemical component to be detected [67]. Another important parameter of a sensor is the spectral linewidth. To enhance the selectivity of a sensor, narrowband resonances are required which is equivalent to having a small full wave at half maximum (FWHM) parameter or high Q-factor. A figure of merit (FoM) can be defined as the ratio (product) between S and $FWHM$ (Q). With the FoM the overall performance of the sensor can be evaluated in a single number.

[1]This definition is not general, as fully dielectric metasurfaces are also becoming very popular for THz and infrared applications.

4.1 FSS and Metasurfaces Based on Resonant Rings

Both FSS and metasurfaces are presented here as high sensitivity and free-space sensor solutions. In contrast with waveguide sensors, metasurfaces can lead to sensor implementations with sensing and the readout in different positions, a feature which is very convenient for disposable sensors in applications where contamination between samples is critical and must be avoided. One of the very first references devoted to FSS THz sensors came out in 2007 [68]. There, a two dimensional array whose elements were asymmetric double spring rings was proposed for thin-film sensing application. It was observed that the FSS resonance was redshifted in presence of a layer of biological material (simulated as an homogeneous layer with constant permittivity) placed on top of the patterned substrate. Additionally, a study of the position of the analyte was performed confirming that it should be within the area of high E-field confinement to effectively shift the resonance. In the case studied there, the E-field at resonance is strongly confined at the ring gaps. Figure 5 shows a summary of the main results. The shift of the resonance, denoted as dual resonance feature (DRF) is shown for two different scenarios: one with the

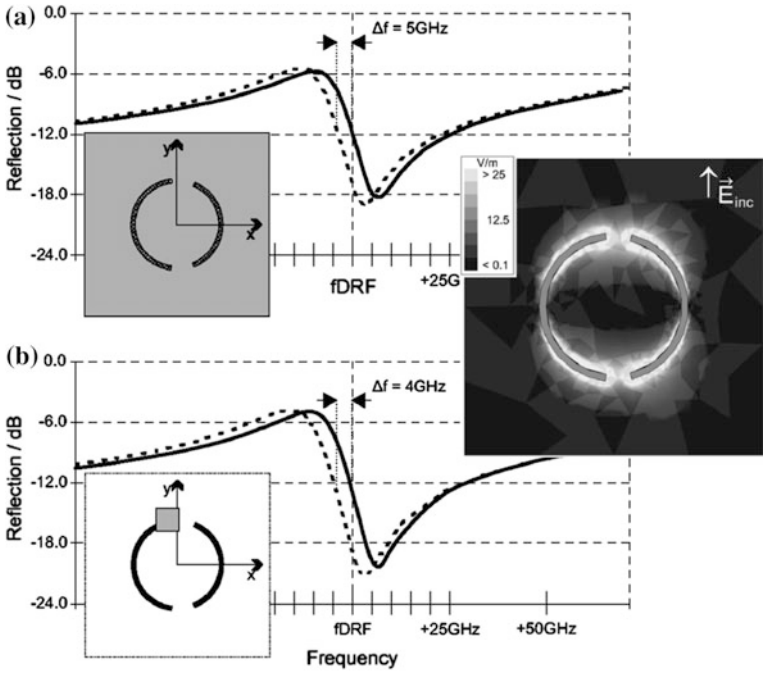

Fig. 5 DRF frequency shift upon dielectric loading ($\varepsilon_r = 3.2$) with a 10-nm-thick film. **a** Loading covers the complete surface. **b** Partial loading (27.5 × 27.5 μm^2 area) at the position of maximum *E*-field concentration. *Inset* The *E*-field in the resonator plane shows a strong concentration (white) at the ends of the arcs. Parameters: $f = 875$ GHz, amplitude of excitation 1 V/m. Reprinted from [68] with the permission of AIP Publishing

analyte covering the whole unit cell area (see Fig. 5a) and another with a small brick lying on top of the ring gaps (see Fig. 5b). Additionally, the field distribution at resonance is depicted in the inset confirming high concentration of E-field within the gaps of the rings.

This work paved the way for an intensive research on asymmetric periodic structures for sensing applications. Only a year later, thin-film sensors based on asymmetric rings were proposed in the microwave regime [69]. Recently, more advanced structures have been explored in the quest for high Q-factor sensing at THz, also based on asymmetric rings configurations [70–72].

Traditional split ring resonators (SRR) with a single axis of symmetry have been also investigated [73]. There, silicon (Si) nanospheres of 50 nm diameter (corresponding to 0.004λ at 1.2 THz) were spin-coated on a thin film SRR metasurface, producing a displacement of the resonance. In this case, it is important to highlight the reversibility of the system since the deposition can be removed to return to the original response of the SRR metasurface. Furthermore, other SRR based examples can be found for determination of solution concentration in aqueous solutions in the THz band [74]. In the context of SRR metasurfaces, it is worth mentioning a very interesting article by J. O'Hara et al, in which the strengths and limitations of this technique are discussed in detail [75]. There, for instance, a limit for the maximum analyte thickness to reach frequency shift saturation is given. This feature is connected with the maximum effective permittivity that permits to consider the substrate thickness of the FSS/metasurface semi-infinite at the operation frequency [57]. Additionally, the sensing limitation for analytes with small thicknesses is also described and compared to optical solutions. At difference with optical solutions, THz thin-film sensors are able to sense large changes of permittivity offering a great perspective for advanced sensor applications.

Aside from SRR, other ring shapes can be found in the literature for THz metasurface sensors. For instance, a metasurface composed of subwavelength metallic square rings with a capacitive gap in the middle was proposed for the detection of microorganisms [76]. Figure 6a shows a schematic of the metasurface with the microorganisms on top. An enhanced SEM-microscope image of the unit cell and a magnified image of the micro-gap are shown in Fig. 6b. The metasurface elements were designed to have gap dimensions of the order of the size the microorganisms deposited (penicillia, yeasts, etc.). The strong field concentration at resonance allowed for a detection of the microorganisms laying near the gap. A numerical study confirmed the dependence of the microorganism position on the detection capability. To improve the design and make it less sensitive to the exact analyte location, it could be proposed the enlargement of the area with strong field confinement by implementing more complex ring shapes. From the previous examples, it is beyond any doubt that this type of devices are a great step forward towards future high performance lab-on-a-chip biosensors. Although these are just the initial steps towards practical applications in areas as diverse as biological and chemical sensing, one can envision the future development of high-performance and advanced devices based on these ideas.

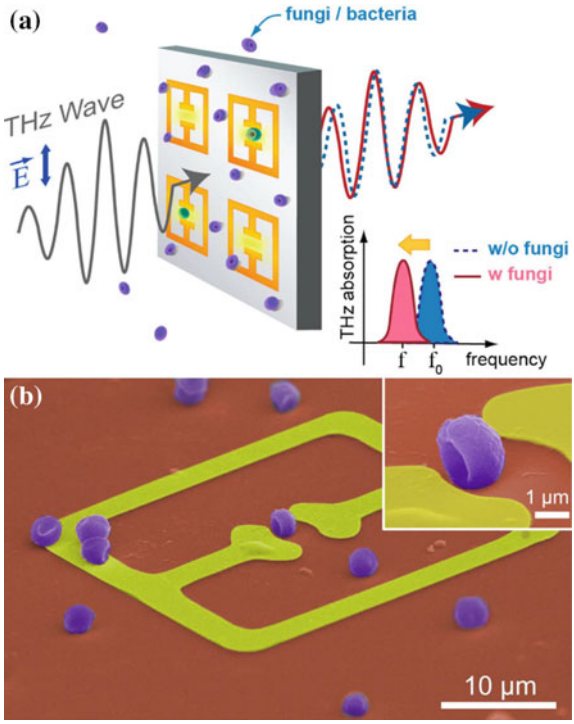

Fig. 6 **a** A schematic presentation of THz metamaterials sensing of microorganisms. **b** A color-enhanced SEM image of metamaterials coated by penicillia. (*Inset*) Magnified image of the fungi located in the micro-gap. Reprinted by permission from Macmillan Publishers Ltd: Scientific Reports [76], © (2014)

4.2 Classical Dipole FSS Based on Sensors

In the previous section, we have presented metasurface sensors based on ring elements with diverse geometries and features. In occasions the design of the rings entail very small details that may be difficult to fabricate due to tolerance errors. For these reasons, simpler FSS classical structures have been proposed as an alternative [77]. A popular example is the cross-dipole array. The design process is relatively straightforward as the resonance frequency occurs when the length of the cross arm is approximately equal to a half-wavelength. In addition, under normal incidence excitation, this structures is polarization independent, which might be advantageous in some cases where polarization of the wave cannot be controlled. Moreover, under oblique incidence the performance of the sensor can be enhanced thanks to the excitation of additional resonance dips which can be extremely narrow. Specifically, for transverse magnetic (TM) incidence a mode is excited leading to a small and narrow resonance, with high Q factor and hence high *FoM*. On the other hand, for transverse electric (TE) incidence this mode cannot be excited. Figure 7a, b show simulation results of a cross-dipole operating around 0.7 THz under oblique incidence TM and TE, respectively ($\theta = 45°$), designed for thin-film sensing, using as analyte a thin photoresitive layer of permittivity $\varepsilon_a \approx 2.855$ loss tangent $\tan\delta_a \approx$

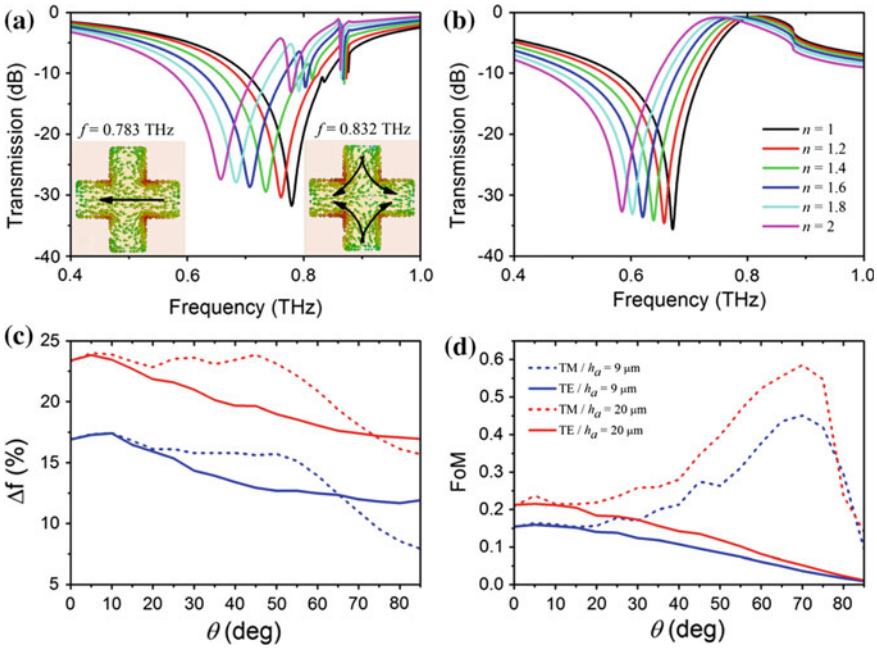

Fig. 7 **a** Simulated transmission results for the prototype with an analyte of thickness $h_a = 9$ μm and $\theta = 45°$ (TM polarization) *Insets* Simulated surface currents for the fundamental (*left*) and bend mode (*right*) resonances. **b** Same as (**a**) for TE incidence. **c** Maximum frequency shift versus angle of incidence for $h_a = 9$ and 20 μm under TE (*solid lines*) and TM (*dashed lines*) excitation. **d** Maximum *FoM* vs. angle of incidence for $h_a = 9$ and 20 μm under TE (*solid lines*) and TM (*dashed lines*). Reprinted from [77] with the permission of AIP Publishing

0.05 and two different thicknesses $h_a = 9$ and 20 μm. Figure 7c shows the frequency shift (Δf) for the dipole resonance (f_{res}) in percentage ($[\Delta f/f_{res}] \times 100$) versus the angle of incidence (θ). The maximum obtained *FoM* value versus θ is shown in Fig, 7d. As it can be seen, the maximum frequency shift (Δf) for the dipole resonance (f_{res}) is about 18 and 24 % for $h_a = 9$ and 20 μm respectively. It is remarkable the enhancement of the *FoM* value (up to 0.6 for $\theta = 70°$ and $h_a =$ 20 μm) under TM oblique incidence due to the appearance of the bent mode resonance (that occurs at $f = 0.832$ THz for a refractive index $n = 1$), as shown in Fig. 7a.

This is only an example of a classical FSS based on dipole arrays working at THz. It serves to put in context the potential of FSS structures to develop sensing platforms with a good performance and polarization independent features under normal incidence. Moreover, oblique incidence opens up new possibilities for sensing, due to the appearance of new resonances which might be narrower, giving as a result a better FoM.

4.3 Metallic Grid Meshes

Another set of FSS structures that can be found in the literature as sensing platforms are metallic meshes with holes. This kind of structures have their roots in the seminal works of Ulrich, published back in the 1960s [78, 79] and present a band-pass character. Metallic meshes were proposed for sensing by Miyamaru et al. some years ago [80, 81]. In [80] the sensing performance of a metallic hole array (MHA) working at 0.25 THz was demonstrated by placing clear and printed paper sheets on top of the device and measuring their response. It was demonstrated that printed paper could be identified by observing the transmission band redshift even though the ink thickness was approximately only 5 μm. In [81] a similar approach was used for protein detection. An electroformed nickel MHA was designed operating at 2.8 THz. Different concentrations of horseradish peroxidase protein were dissolved in water and printed on top of the MHA. It was observed that the shift of the transmission dip was larger at higher protein concentrations.

More recent works involving metallic-meshes for other THz biosensing applications such as the determination of molecular binding states at approximately 0.7 THz have been investigated by Hasebe et al. [82, 83]. In these studies a narrow dip that appears at the transmission band due to asymmetric modes excited under oblique illumination of the structure is exploited for detection. Figure 8 shows a schematic and some results extracted from Ref. [83]. There a metallic mesh with square holes was studied. A dielectric film of 125 μm of thickness was placed on top of the structure and its response was calculated by finite difference time domain (FDTD) simulations. A plot showing the relation between the refractive index of the analyte and the frequency shift of the dip is shown in Fig. 8d. In [84] similar devices were proposed operating at THz and far infrared (1, 10 and 40 THz).

As it can be seen, bandpass structures by means of metallic sheets with drilled holes can be used as free-space sensing devices. To date relatively thick metallic meshes have been used. However, the combination of a dielectric substrate with thin metallic plates could open new possibilities that could be investigated in the future for sensing applications.

4.4 Metasurfaces Based Absorbers for Sensing

Electromagnetic absorbers have been traditionally used at microwaves for different applications. Perhaps the most important ones are reducing the radar cross section (RCS) of objects as well as avoiding unwanted reflections in anechoic chambers for antenna testing. With the advent of metamaterials, this field has been revisited and new and more sophisticated absorber solutions have been proposed [85, 86].

In previous subsections, FSS/metasurfaces have been introduced as two dimensional arrays of metallic patches (or the complementary elements, slots on metallic sheets) patterned on a dielectric substrate. By backing the dielectric

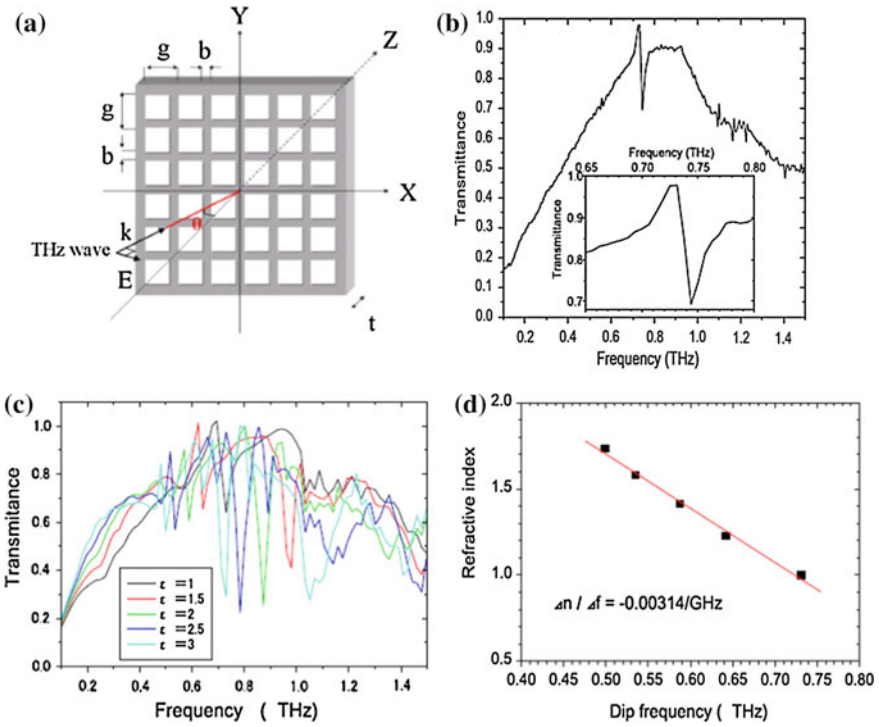

Fig. 8 **a** Schematic representation of the metallic mesh structure. **b** Transmission spectrum in the THz region of the metallic mesh with *g*, *b*, and *t* values of 302, 74, and 6 μm, respectively, for vertical polarization incidence. **c** Dependence on dielectric constant of the transmission spectrum of the metallic mesh attached to the dielectric film in FDTD simulations. **d** Dependence on refractive index of the frequency dip. Reprinted from [83] with the permission of AIP Publishing

substrate with a ground plane and choosing judiciously the substrate thickness, perfect absorption can be achieved at the resonance frequency. In these conditions, the reflection coefficient from the metasurface is ideally zero and the energy is dissipated by the losses of the metallic layer and the dielectric substrate. This response can be exploited for thin-film sensing, since the absorption peak is usually very narrow and sensitive to an analyte placed on top of the surface.

Cross dipole arrays absorbers, in both patch and slot versions, have been proposed for sensing at THz with very competitive *FoM* values with respect to ground-free metasurfaces [87]. The main drawback in this particular case is the bulkiness of the devices since the ground plane is printed on top of a Si substrate. Nevertheless, lately, this issue has been overcome by using thin flexible polymers and optical lithography. In this way, an ultrathin flexible absorber sensing device with multispectral response at the THz has been successfully demonstrated [88]. The unit cell elements are small metal strips surrounded by two additional C-shaped

strips with a mirror symmetry. Then, four resonances can be excited by a vertically polarized incident wave.

Absorber based solutions are very promising candidates for high-performance future free space sensors. Their design process is similar to FSS/metasurfaces working in transmission mode. In general this type of absorbers exhibit resonances which are spectrally narrow, a convenient feature for high selectivity sensing applications. The main drawback, if it can be considered so, is that they only can operate in reflection mode.

5 Surface Waves and Plamonics Oriented Solutions at THz Sensing Applications

Probably, after FSS/metasurfaces the next technology in terms of popularity are the sensors based on surface wave/plamonics. Plasmonics is the science branch that studies the propagation of surface plasmons. The drift of plasmonic community towards the THz regime responds to a natural phenomenon given its spectral proximity to the infrared and optical regime which are the regimes where the discipline originally developed. In this section sensing solutions based on surface wave excitation at THz will be treated. These structures often evolve from or are inspired by plasmonics. Although strictly speaking, surface plasmon polaritons (SPP) in a metal-dielectric interface only exist in the optical regime, other metallic structures can be proposed at THz to emulate the propagation of SPP at this frequency regime. The waves supported are usually called spoof-SPPs.

The first demonstration of SPP at THz frequencies was done in Ref. [89]. There, a TDS-THz system was used for generation and detection of THz waves. These waves impinged on a metal sheet coated with a thin dielectric layer by means of diffractive apertures in order to have tangent wave vector matching and launch the surface wave. Other strategies to excite surface waves are edge-diffraction and hump-coupling in metal polished plates and metal wires coated with thin dielectrics [90, 91]. In these works, the potential capability of this kind of technology in sensing applications was already highlighted. Nevertheless, the first investigations on surface wave excitation on the THz regime were devoted more towards waveguiding rather than to sensing applications.

Metal wires for surface wave propagation supposed a breakthrough, as these THz waveguides have both low loss and low dispersion [92]. Low loss appears due to the very small metal area, and the low dispersion is a consequence of the field distribution of the guided mode along the wire which resembles the TEM mode from coaxial line. Soon after these findings, a metal wire based solution for lactose powder spectroscopy was proposed [93]. There, the lactose powder was deposited along the wire and by measuring the THz pulse and comparing it with the case without the lactose, the absorption bands of lactose was identified.

More recent sensing solutions based on surface wave excitation on metal plates can be found in the works of Theuer et al. [94, 95]. In [94] a surface wave was launched on top of a metal surface via a modified parallel plate waveguide (PPW) against a metallic cylinder coated with the analyte material. By analysing the measured delay of the THz pulses the thickness of the analyte sample was determined. In [95] a similar mechanism was used for a two-cylinder waveguide sensor.

Recently, solutions inspired by plasmonics have been proposed for sensing applications. These are based on corrugated surfaces which is a classical solution for spoof-SPP excitation [96, 97]. In [96] a hybrid dielectric-metallic plasmonic waveguide was presented. While the surface wave/plasmon can be excited on the dielectric (i.e. a plastic ribbon) film the metallic grating creates transmission dips according to Bragg type resonances. Different plastic films and granular analytes were successfully identified by means of the spectral shifts recorded for the resonance dips.

The corrugated wave solution presented in [97] is particularly interesting. A thick layer of commercial photoresist material corrugated with subwavelength grooves was coated with a gold layer of 600 nm (almost 9 times the skin depth at the operation frequency). In order to couple the THz radiation to the corrugated surface, a classical Otto prism configuration was used. The grooves in the photoresist provide an adequate platform for analytes in liquid form. The liquid can be easily poured onto the sensor covering the grooves uniformly by volume occupation principle. In this way, various substances as gasoline, liquid paraffin, water, glycerine or nitrogen in liquid form were successfully sensed with high *FoM* values. Figure 9 shows the reflectivity spectra for different values of separation

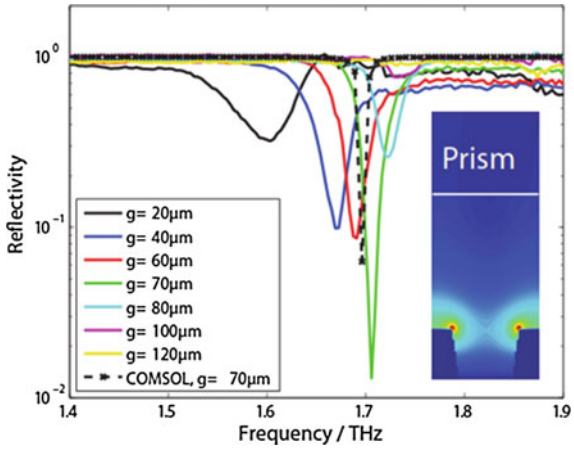

Fig. 9 Experimental reflectivity spectra for $g = 20$ μm (*black*), 40 μm(*blue*), 60 μm (*red*), 70 μm (*green*), 80 μm (*cyan*), 100 μm (*magenta*) and 120 μm (*yellow*). Simulated (*dashed-cross, black*) reflectivity spectrum at strongest spoof plasmon coupling point ($g = 70$ μm) is also shown for comparison. The fluid in the grooves is nitrogen. *Inset* Simulated field distribution at 1.70 THz for $g = 70$ μm. The *white line* demarcates the prism-coupling gap interface. Reprinted from [97] with permission from Wiley Company

distances (g) between the prism and the corrugated surface. In the case shown in the figure, the grooves were filled with nitrogen. The experimental results were in good agreement with simulations. This structure is a good example of THz sensing based on surface waves. The main drawback is the need of the prism coupler which complicates the integration within a final system.

6 Other Alternatives: Metallic Waveguides and Planar Technology

In this section alternative sensing solutions are discussed. These solutions rely on classical components used in the microwave regime such as waveguides and transmission lines [98]. Their translation to the THz band is not straightforward. Firstly, the dimensions of such devices at THz frequencies pushes the fabrication to the edge of the technology. In addition, losses due to finite conductivity in metals and absorption loss in dielectrics are much higher in the THz range in comparison with the microwave regime. Despite these drawbacks, many microwave concepts like filters and resonators integrated in waveguides and planar devices can be transferred to the THz for sensing purposes.

6.1 Metallic Waveguides

Metallic waveguides are classical components for wave propagation in the microwave regime. They are usually hollow metallic tubes in which the cross-section shape determines the electromagnetic modes than can be excited and actually propagate along the guide. Extrapolating classical waveguides used at microwaves to THz frequencies is very challenging because the dimensions of the guides are very small pushing standard fabrication techniques to the limit. Nevertheless, rectangular and circular THz waveguides were demonstrated by Gallot et al. back in 2000 [99].

A more practical waveguide in terms of fabrication is the classical parallel plate waveguide (PPWG). This guide consists of two conductor sheets and supports a transverse electromagnetic (TEM) mode which is ideally dispersion-free and exhibits low loss. The electric and magnetic field distribution of the TEM mode for a PPWG is shown in Fig. 10a. The separation between conductive sheets can be filled with a dielectric material (with relative permittivity, ε_r) for practical realization purposes. However, this has two direct effects: the cut-off frequency of the first evanescent mode is decreased by a factor of $\sqrt{\varepsilon_r}$, and the absorption losses are higher. At THz, usually this dielectric substrate is avoided by using plastic spacers at the edges of the PPWG. Its implementation at THz frequencies was demonstrated in 2001 [100]. This work opened the path and nowadays THz sensing based on metallic waveguides are mainly based on PPWG solutions. In this context, organic

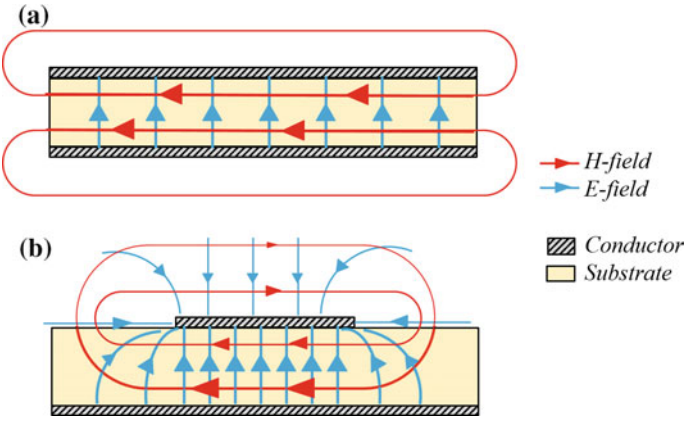

Fig. 10 *Top* Field distribution of the TEM mode of PPWG. *Bottom* Field distribution of the quasi-TEM mode of microstrip line. The number and size of *lines* and *arrows* denotes the field intensity in the area

materials, thin water layer contents and explosives have been successfully detected using this approach [101–103]. A thorough article that describes PPWG sensors and their application to the detection of explosives can be found in Ref. [104]. The main advantage of PPWG sensing systems is their long interaction length between THz waves and the analyte under test, which leads to an increased sensitivity, allowing ultimately for the detection of ultra-thin layers of material.

Other examples of PPWG sensors have also been proposed [24, 105]. In [24] the upper plate of the PPWG was corrugated to obtain a Bragg type filter. With this strategy, high-Q resonant modes can be excited. These modes are then redshifted in the presence of an analyte sample. In [105] a resonance was synthesized by machining a rectangular groove across one of the plates of the PPWG. In order to excite this groove, the TE_1 mode of the PPWG must be used instead of TEM mode. By filling the groove cavity with different materials a variation of the resonance frequency was observed.

6.2 Planar Technology

In this section a short review of sensor devices based on planar technology is done. Prior to sensing applications, planar technology has been crucial for the development of low-cost waveguides at microwaves. Planar technology is ubiquitous and is employed to produce cost-effective microwave components such as antennas, transitions, feeders, power dividers, filters, resonators, etc. The most popular planar technologies are microstrip, stripline, slotline and coplanar transmission lines [98].

A microstrip line consists of a conductive sheet and a strip separated by a dielectric substrate. While the sheet acts as a ground plane the strip serves as the

signal conductor. This transmission line supports a quasi-TEM mode where the electric field is strongly confined between the conductive strip and the ground plane and the magnetic field revolves around the strip. A sketch of the field distribution on the microstrip line is presented in Fig. 10b. Microstrip lines are by far less popular than FSS/metasurfaces for THz sensing. However, one can find in the literature some interesting sensors for vibrational absorption spectroscopy, polar liquids and biomolecular systems characterization [67, 106–108]. Further details and a compilation of examples regarding this topic can be found in Ref. [109].

The mentioned examples rely on direct deposition of the sample analyte on top of the microstrip line and the detection is done by comparing the response with and without sample. By inspecting Fig. 10b, it can be seen that the stronger field interaction in the microstrip line occurs within the substrate between the strip and the ground plane, and it vanishes in the air region. To improve the sensor performance one could think of other strategies beyond simple transmission lines such as implementing filters and/or resonators. In both cases, a high electric field concentration appears at resonance enhancing the detection. In fact, there are microstrip designs [110–112] similar to the sensing solutions based on integrated resonators already introduced in [20–22]. In [110] a set of different bandpass and stopband filters based on loops and meanders of the microstrip line were proposed for DNA sensing. In that work, effective sensing was numerically demonstrated even with much less amount of sample than previous solutions. Another set of solutions based on stopband stub filters were presented in [111, 112]. The main advantage in these works was the possibility of cascading several filters along the same microstrip line enhancing the integration and fabrication costs of the sensor. All in all, the main drawback of microstrip solutions are the high losses they present at THz waves. In fact, this kind of solutions have not been demonstrated beyond 1.2 THz yet.

7 Conclusions

To sum up, in this chapter we have presented the first approaches and latest advances towards the development of THz sensors. Given that this range is relatively new and unexplored, there is plenty of room for joint efforts from many different scientific communities, microwaves, plasmonics, infrared, optics, biology, chemistry, etc. This multidisciplinary character brings about a growing activity giving birth to a wide range of new applications in a very fast pace.

In this chapter, we have put the focus on sensing applications. Solutions ranging from fibre-oriented solutions to classical microwave components platforms have been outlined. From all of them, probably the solutions based on fibre, metasurfaces and surface-wave/plasmonics are the most promising in terms of performance and its future realization and integration in real-systems can be optimistically envisaged. Hence, if the research flow keeps on working with such intensity on sensing applications at THz frequencies one can foresee that the perspectives for advanced, label-free, low cost and efficient sensors are excellent.

References

1. Y.S. Lee, *Principles of Terahertz Science and Technology*, vol. 170 (Springer Science and Business, 2009)
2. P.H. Siegel, Terahertz Technology. IEEE Trans. Microw. Theo. Tech. **50**(3), 910–928 (2002)
3. D. Saeedkia, *Handbook of Terahertz Technology for Imaging, Sensing and Communications* (Woodhead, Oxford, 2013)
4. M.C. Gaidis, Space-based applications of far infrared systems, in *8th International Conference* on *Terahertz Electronics*, Darmstadt, Germany, 28–29 Sept. 2000, pp. 125–128
5. R. Piesiewicz, T. Kleine-Ostmann, N. Krumbholz, D. Mittleman, M. Koch, J. Schoebei, T. Kürner, Short-range ultra-broadband terahertz communications: concepts and perspectives. IEEE Antennas Propag. Mag. **49**(6), 24–39 (2007)
6. I.F. Akyildiz, J. Miquel, C. Han, Terahertz band: next frontier for wireless communications. Phys. Commun. **12**, 16–32 (2014)
7. H.-B. Liu, H. Zhong, N. Karpowicz, Y. Chen, X.-C. Zhang, Terahertz spectroscopy and imaging for defense and security applications. Proc. IEEE **95**(8), 1514–1527 (2007)
8. C.J. Strachan, T. Rades, D.A. Newnham, K.C. Gordon, M. Pepper, P.F. Taday, Using terahertz pulsed spectroscopy to study crystallinity of pharmaceutical materials. Chem. Phys. Lett. **390**(1–3), 20–24 (2004)
9. P.H. Siegel, Technology in biology and medicine. Instrumentation **52**(10), 0–3 (2004)
10. D.M. Mittleman, R.H. Jacobsen, M.C. Nuss, T-ray imaging. IEEE J. Sel. Top. Quantum Electron. **2**(3), 679–692 (1996)
11. H. Gousset, J. Liquier, E. Taillandier, Y.S. Sanghvi, D. Peoc'h, Conformational Study of DNA-RNA Duplexes Containing MMI Substituted Phosphodiester Linkages by FTIR Spectroscopy. J. Biomol. Struct. Dyn. **15**(5), 931–936 (1998)
12. G.S. Edwards, C.C. Davis, J.D. Saffer, M.L. Swicord, Resonant microwave absorption of selected DNA molecules. Phys. Rev. Lett. **53**(13), 1284 (1984)
13. D.L. Woolard, T. Koscica, D.L. Rhodes, H.L. Cui, R.A. Pastore, J.O. Jensen, J.L. Jensen, W. R. Loerop, R.H. Jacobsen, D. Mittleman, M.C. Nuss, Millimeter wave-induced vibrational modes in DNA as a possible alternative to animal tests to probe for carcinogenic mutations. J. Appl. Toxicol. **17**(4), 243–246 (1997)
14. C. Gabriel, E.H. Grant, R. Tata, P.R. Brown, B. Gestblom, E. Noreland, Microwave absorption in aqueous solutions of DNA. Nature **328**, 145–146 (1987)
15. D. Grischkowsky, S. Keiding, M.Van Exter, C. Fattinger, Far-infrared time-domain spectroscopy with terahertz beams of dielectrics and semiconductors. J. Opt. Soc. America B **7**(10), 2006 (1990)
16. T.R. Globus, D.L. Woolard, A.C. Samuels, B.L. Gelmont, J. Hesler, T.W. Crowe, M. Bykhovskaia, Submillimeter-wave Fourier transform spectroscopy of biological macromolecules. J. Appl. Phys. **91**(9), 6105–6113 (2002)
17. T. Globus, L. Dolmatova-Werbos, D. Woolard, A. Samuels, B. Gelmont, M. Bykhovskaia, Application of neural network analysis to submillimeter-wave vibrational spectroscopy of DNA macromolecules, in *International Symposium on Spectral Sensing Research Proceedings (ISSSR)* (2001), p. 439
18. A. Markelz, a Roitberg, E. Heilweil, Pulsed terahertz spectroscopy of DNA, bovine serum albumin and collagen between 0.1 and 2.0 THz. Chem. Phys. Lett. **320**(1–2), 42–48 (2000)
19. M. Brucherseifer, M. Nagel, P. Haring Bolivar, H. Kurz, A. Bosserhoff, R. Buttner, Label-free probing of the binding state of DNA by time-domain terahertz sensing. Appl. Phys. Lett. **77**(24), 4049–4051 (2000)
20. M. Nagel, P. Haring Bolivar, M. Brucherseifer, H. Kurz, A. Bosserhoff, R. Büttner, Integrated THz technology for label-free genetic diagnostics. Appl. Phys. Lett. **80**(1), 154–156 (2002)

21. M. Nagel, P.H. Bolivar, M. Brucherseifer, H. Kurz, A. Bosserhoff, R. Büttner, Integrated planar terahertz resonators for femtomolar sensitivity label-free detection of DNA hybridization. Appl. Opt. **41**(10), 2074–2078 (2002)
22. T. Baras, T. Kleine-Ostmann, M. Koch, On-chip THz detection of biomaterials: a numerical study. J. Biol. Phys. **29**(2–3), 187–194 (2003)
23. M. Nagel, F. Richter, P. Haring-Bolivar, H. Kurz, A functionalized THz sensor for marker-free DNA analysis. Phys. Med. Biol. **48**(22), 3625 (2003)
24. M. Nagel, H. Kurz, Corrugated waveguide based genomic biochip for marker-free THz read-out. Int. J. Infrared Millimeter Waves **27**(4), 517–529 (2006)
25. B. Fischer, M. Hoffmann, H. Helm, R. Wilk, F. Rutz, T. Kleine-Ostmann, P.U. Jepsen, Terahertz time-domain spectroscopy and imaging of artificial RNA. Opt. Express **13**(14), 5205–5215 (2005)
26. B.M. Fischer, H. Helm, P.U. Jepsen, Chemical recognition with broadband THZ spectroscopy. Proc. IEEE **95**(8), 1592–1604 (2007)
27. F. Huang, B. Schulkin, H. Altan, J.F. Federici, D. Gary, R. Barat, … D.B. Tanner, Terahertz study of 1,3,5-trinitro-s-triazine by time-domain and Fourier transform infrared spectroscopy. Appl. Phys. Lett. **85**(23), 5535–5537 (2004)
28. Y.C. Shen, T. Lo, P.F. Taday, B.E. Cole, W.R. Tribe, M.C. Kemp, Detection and identification of explosives using terahertz pulsed spectroscopic imaging. Appl. Phys. Lett. **86**(24), 1–3 (2005)
29. H. Liu, Y. Chen, G.J. Bastiaans, X. Zhang, Detection and identification of explosive RDX by THz diffuse reflection spectroscopy. Opt. Express **14**(1), 415–423 (2006)
30. D.M. Sheen, D.L. McMakin, T.E. Hall, Three-dimensional millimeter-wave imaging for concealed weapon detection. IEEE Trans. Microw. Theory Tech. **49**(9), 1581–1592 (2001)
31. C. Baker, T. Lo, W.R. Tribe, B.E. Cole, M.R. Hogbin, M.C. Kemp, Detection of concealed explosives at a distance using terahertz technology. Proc. IEEE **95**(8), 1559–1565 (2007)
32. K. Kawase, Y. Ogawa, Y. Watanabe, H. Inoue, Non-destructive terahertz imaging of illicit drugs using spectral fingerprints. Opt. Express **11**(20), 2549 (2003)
33. A.G. Davies, A.D. Burnett, W. Fan, E.H. Linfield, J.E. Cunningham, Terahertz spectroscopy of explosives and drugs. Mater. Today **11**(3), 18–26 (2008)
34. S.P. Jamison, R.W. McGowan, D. Grischkowsky, Single-mode waveguide propagation and reshaping of sub-ps terahertz pulses in sapphire fibres. Appl. Phys. Lett. **76**(15), 1987 (2000)
35. R. Mendis, D. Grischkowsky, Plastic ribbon THz waveguides. J. Appl. Phys. **88**(2000), 4449–4451 (2000)
36. H. Han, H. Park, M. Cho, J. Kim, Terahertz pulse propagation in a plastic photonic crystal fibre. Appl. Phys. Lett. **80**(15), 2634–2636 (2002)
37. A. Bingham, Y. Zhao, D. Grischkowsky, THz parallel plate photonic waveguides. Appl. Phys. Lett. **87**(5), 2003–2006 (2005)
38. L.-J. Chen, H.-W. Chen, T.-F. Kao, J.-Y. Lu, C.-K. Sun, Low-loss subwavelength plastic fibre for terahertz waveguiding. Opt. Lett. **31**(3), 308–310 (2006)
39. M. Nagel, A. Marchewka, H. Kurz, Low-index discontinuity terahertz waveguides. Opt. Express **14**(21), 9944–9954 (2006)
40. B. Bowden, J.A. Harrington, O. Mitrofanov, Silver/polystyrene-coated hollow glass waveguides for the transmission of terahertz radiation. Opt. Lett. **32**(20), 2945–2947 (2007)
41. C.-H. Lai, Y.-C. Hsueh, H.-W. Chen, Y. Huang, H. Chang, C.-K. Sun, Low-index terahertz pipe waveguides. Opt. Lett. **34**(21), 3457–3459 (2009)
42. C.-H. Lai, B. You, J.-Y. Lu, T.-A. Liu, J.-L. Peng, C.-K. Sun, H.-C. Chang, Modal characteristics of antiresonant reflecting pipe waveguides for terahertz waveguiding. Opt. Express **18**(1), 309–322 (2010)
43. T. Hidaka, H. Minamide, H. Ito, J.I. Nishizawa, K. Tamura, S. Ichikawa, Ferroelectric PVDF cladding terahertz waveguide. J. Lightwave Technol. **23**(8), 2469–2473 (2005)
44. R.J. Yu, B. Zhang, Y.Q. Zhang, C.Q. Wu, Z.G. Tian, X.Z. Bai, Proposal for ultralow loss hollow-core plastic Bragg fibre with cobweb-structured cladding for terahertz waveguiding. IEEE Photonics Technol. Lett. **19**(12), 910–912 (2007)

45. J.-Y. Lu, C.-P. Yu, H.-C. Chang, H.-W. Chen, Y.-T. Li, C.-L. Pan, C.-K. Sun, Terahertz air-core microstructure fibre. Appl. Phys. Lett. **92**(6), 064105 (2008)
46. S. Atakaramians, V.S. Afshar, B.M. Fischer, D. Abbott, T.M. Monro, Porous fibres: a novel approach to low loss THz waveguides. Opt. Express **16**(12), 8845–8854 (2008)
47. K. Nielsen, H.K. Rasmussen, A.J. Adam, P.C. Planken, O. Bang, P.U. Jepsen, Bendable, low-loss Topas fibres for the terahertz frequency range. Opt. Express **17**(10), 8592–8601 (2009)
48. H. Kurt, D.S. Citrin, Photonic crystals for biochemical sensing in the terahertz region. Appl. Phys. Lett. **87**(4) (2005)
49. H. Kurt, D.S. Citrin, Coupled-resonator optical waveguides for biochemical sensing of nanoliter volumes of analyte in the terahertz region. Appl. Phys. Lett. **87**(24), 1–3 (2005)
50. A. Hassani, A. Dupuis, M. Skorobogatiy, Surface-plasmon-resonance-like fibre-based sensor at terahertz frequencies. J. Opt. Soc. America B **25**(10), 1771 (2008)
51. A. Hassani, M. Skorobogatiy, Surface plasmon resonance-like integrated sensor at terahertz frequencies for gaseous analytes. Opt. Express **16**(25), 20206–20214 (2008)
52. B. You, J.-Y. Lu, J.-H. Liou, C.-P. Yu, H.-Z. Chen, T.-A. Liu, J.-L. Peng, Subwavelength film sensing based on terahertz anti-resonant reflecting hollow waveguides. Opt. Express **18** (18), 19353–19360 (2010)
53. B. You, J.Y. Lu, C.P. Yu, Ta Liu, J.L. Peng, Terahertz refractive index sensors using dielectric pipe waveguides. Opt. Express **20**(6), 2549–2554 (2012)
54. S.F. Zhou, L. Reekie, H.P. Chan, Y.T. Chow, P.S. Chung, K. Man Luk, Characterization and modeling of Bragg gratings written in polymer fibre for use as filters in the THz region. Opt. Express **20**(9), 9564 (2012)
55. G. Yan, A. Markov, Y. Chinifooroshan, S.M. Tripathi, W.J. Bock, M. Skorobogatiy, Resonant THz sensor for paper quality monitoring using THz fibre Bragg gratings. Opt. Lett. **38**(13), 2200–2202 (2013)
56. D. Uri, Z. Chen, G. Hefferman, Z. Chen, L. Yuan, G. Hefferman, T. Wei, THz fibre Bragg grating for distributed sensing THz fibre Bragg grating for distributed sensing **27**(10), 1084–1087 (2015)
57. B.A. Munk, *Frequency Selective Surfaces: Theory and Design* (2000)
58. V.G. Veselago, The electrodynamics of substances with simultaneously negative values of ε and μ. Soviet physics uspekhi **10**(4), 509 (1968)
59. D.R. Smith, J.B. Pendry, M.C. Wiltshire, Metamaterials and negative refractive index. Science **305**(5685), 788–792 (2004)
60. D. Schurig, J.J. Mock, B.J. Justice, S.A. Cummer, J.B. Pendry, A.F. Starr, D.R. Smith, Metamaterial electromagnetic cloak at microwave frequencies. Science **314**(5801), 977–980 (2006)
61. T. Ergin, N. Stenger, P. Brenner, J.B. Pendry, M. Wegener, Three-dimensional invisibility cloak at optical wavelengths. Science **328**(5976), 337–339 (2010)
62. P.Y. Chen, A. Alù, Mantle cloaking using thin patterned metasurfaces. Phys. Rev. B **84**(20), 205110 (2011)
63. B. Orazbayev, N.M. Estakhri, M. Beruete, A. Alù, Terahertz carpet cloak based on a ring resonator metasurface. Phys. Rev. B **91**(19), 195444 (2015)
64. N. Yu, F. Aieta, P. Genevet, M.A. Kats, Z. Gaburro, F. Capasso, A broadband, background-free quarter-wave plate based on plasmonic metasurfaces. Nano Lett. **12**(12), 6328–6333 (2012)
65. A. Pors, M.G. Nielsen, S.I. Bozhevolnyi, Analog computing using reflective plasmonic metasurfaces. Nano Lett. **15**(1), 791–797 (2014)
66. A.V. Kildishev, A. Boltasseva, V.M. Shalaev, Planar photonics with metasurfaces. Science **339**(6125), 1232009 (2013)
67. J.F. O'Hara, W. Withayachumnankul, I. Al-Naib, A review on thin-film sensing with terahertz waves. J. Infrared, Millimeter, Terahertz Waves **33**(3), 245–291 (2012)
68. C. Debus, P.H. Bolivar, Frequency selective surfaces for high sensitivity terahertz sensing. Appl. Phys. Lett. **91**(18), 2005–2008 (2007)

69. I.A.I. Al-Naib, C. Jansen, M. Koch, Thin-film sensing with planar asymmetric metamaterial resonators. Appl. Phys. Lett. **93**(8) (2008)
70. I. Al-Naib, C. Jansen, R. Singh, M. Walther, M. Koch, Novel THz metamaterial designs: From near- and far-field coupling to high-q resonances. IEEE Trans. Terahertz Sci. Technol. **3**(6), 772–782 (2013)
71. R. Singh, W. Cao, I. Al-Naib, L. Cong, W. Withayachumnankul, W. Zhang, Ultrasensitive terahertz sensing with high- Q Fano resonances in metasurfaces. Appl. Phys. Lett. **105**(17) (2014)
72. N. Born, I. Al-Naib, C. Jansen, R. Singh, J.V. Moloney, M. Scheller, M. Koch, Terahertz Metamaterials with Ultrahigh Angular Sensitivity. Adv. Opt. Materials **3**(5), 642–645 (2015)
73. T. Driscoll, G.O. Andreev, D.N. Basov, S. Palit, S.Y., Cho, N.M. Jokerst, D.R. Smith, Tuned permeability in terahertz split-ring resonators for devices and sensors. Appl. Phys. Lett. **91**(6) (2007)
74. X. Wu, X. Pan, B. Quan, X. Xu, C., Gu, L. Wang, Self-referenced sensing based on terahertz metamaterial for aqueous solutions. Appl. Phys. Lett. **102**(15) (2013)
75. J.F. O'Hara, R. Singh, I. Brener, E. Smirnova, J. Han, A.J. Taylor, W. Zhang, Thin-film sensing with planar terahertz metamaterials: sensitivity and limitations. Opt. Express **16**(3), 1786–1795 (2008)
76. S.J. Park, J.T. Hong, S.J. Choi, H.S. Kim, W.K. Park, S.T. Han, J.Y. Park, S. Lee, D.S. Kim, Y.H. Ahn, Detection of microorganisms using terahertz metamaterials. Sci. Rep. **4**, 4988 (2014)
77. P. Rodríguez-Ulibarri, S.A. Kuznetsov, M. Beruete, Wide angle terahertz sensing with a cross-dipole frequency selective surface. Appl. Phys. Lett. 111104 (2016)
78. R. Ulrich, K.F. Renk, L. Genzel, Tunable Submillimeter Interferometers of the Fabry-Perot Type. IEEE Trans. Microw. Theo. Tech. **11**(5), 363–371 (1963)
79. R. Ulrich, Far-infrared properties of metallic mesh and its complementary structure. Infrared Phys. **7**(1), 37–55 (1967)
80. F. Miyamaru, S. Hayashi, C. Otani, K. Kawase, Y. Ogawa, H. Yoshida, E. Kato, Terahertz surface-wave resonant sensor with a metal hole array. Opt. Lett. **31**(8), 1118–1120 (2006)
81. H. Yoshida, Y. Ogawa, Y. Kawai, S. Hayashi, A. Hayashi, C. Otani, E. Kato, F. Miyamaru, K. Kawase, Terahertz sensing method for protein detection using a thin metallic mesh. Appl. Phys. Lett. **91**(25), 2005–2008 (2007)
82. T. Hasebe, Y. Yamada, H. Tabata, Label-free THz sensing of living body-related molecular binding using a metallic mesh. Biochem. Biophys. Res. Commun. **414**(1), 192–198 (2011)
83. T. Hasebe, S. Kawabe, H. Matsui, H. Tabata, Metallic mesh-based terahertz biosensing of single- and double-stranded DNA. J. Appl. Phys. **112**(9) (2012)
84. T. Kondo, S. Kamba, K. Takigawa, T. Suzuki, Y. Ogawa, N. Kondo, Highly sensitive metal mesh sensors. Procedia Eng. **25**, 916–919 (2011)
85. N.I. Landy, S. Sajuyigbe, J.J. Mock, D.R. Smith, W.J. Padilla, Perfect metamaterial absorber. Phys. Rev. Lett. **100**(20), 207402 (2008)
86. C.M. Watts, X. Liu, W.J. Padilla, Metamaterial electromagnetic wave absorbers. Adv. Mater. **24**(23), OP98–120, OP181 (2012)
87. L. Cong, S. Tan, R. Yahiaoui, F. Yan, W. Zhang, R. Singh, Experimental demonstration of ultrasensitive sensing with terahertz metamaterial absorbers: a comparison with the metasurfaces. Appl. Phys. Lett. 106(3) (2015)
88. R. Yahiaoui, S. Tan, L. Cong, R. Singh, F. Yan, W. Zhang, Multispectral terahertz sensing with highly flexible ultrathin metamaterial absorber. J. Appl. Phys. **118**(8) (2015)
89. J. Saxler, J. Gómez Rivas, C. Janke, H.P.M. Pellemans, P. Haring Bolívar, H. Kurz, P. Bolívar, Time-domain measurements of surface plasmon polaritons in the terahertz frequency range. Phys. Rev. B **69**(15), 155427 (2004)
90. N.C.J. Van Der Valk, P.C.M. Planken, Effect of a dielectric coating on terahertz surface plasmon polaritons on metal wires. Appl. Phys. Lett. **87**(7) (2005)
91. J. O'Hara, R. Averitt, A. Taylor, Prism coupling to terahertz surface plasmon polaritons. Opt. Express **13**(16), 6117–6126 (2005)

92. K. Wang, D.M. Mittleman, Metal wires for terahertz wave guiding. Nature **432**(7015), 376–379 (2004)
93. M. Walther, M.R. Freeman, F.A. Hegmann, Metal-wire terahertz time-domain spectroscopy. Appl. Phys. Lett. **87**(26), 1–3 (2005)
94. M. Theuer, R. Beigang, D. Grischkowsky, Sensitivity increase for coating thickness determination using THz waveguides. Opt. Express **18**(11), 11456–11463 (2010)
95. M. Theuer, R. Beigang, D. Grischkowsky, Highly sensitive terahertz measurement of layer thickness using a two-cylinder waveguide sensor. Appl. Phys. Lett. **97**(7), 1–4 (2010). http://doi.org/10.1063/1.3481080
96. B. You, J. Lu, T. Liu, J. Peng, Hybrid terahertz plasmonic waveguide for sensing applications. Opt. Express **21**(18), 1786–1795 (2013)
97. B. Ng, J. Wu, S.M. Hanham, A.I. Fernández-Domínguez, N. Klein, Y.F. Liew, M.B.H. Breese, M. Hong, S.A. Maier, Spoof plasmon surfaces: a novel platform for THz sensing (Advanced Optical Materials 8/2013). Adv. Opt. Materials **1**(8), 537–537 (2013)
98. D.M. Pozar, Microwave Engineering, 3rd Ed
99. G. Gallot, S.P. Jamison, R.W. McGowan, D. Grischkowsky, Terahertz waveguides. JOSA B **17**(5), 851–863 (2000)
100. R. Mendis, D. Grischkowsky, THz interconnect with low-loss and low-group velocity dispersion. IEEE Microwave Wirel. Compon. Lett. **11**(11), 444–446 (2001)
101. J.S. Melinger, N. Laman, S.S. Harsha, S. Cheng, D. Grischkowsky, High-resolution waveguide terahertz spectroscopy of partially oriented organic polycrystalline films. J. Phys. Chem. A **111**(43), 10977–10987 (2007)
102. J. Zhang, D. Grischkowsky, Waveguide terahertz time-domain spectroscopy of nanometer water layers. Opt. Lett. **29**(14), 1617–1619 (2004)
103. J.S. Melinger, S.S. Harsha, N. Laman, D. Grischkowsky, Temperature dependent characterization of terahertz vibrations of explosives and related threat materials. Opt. Express **18**(26), 27238–27250 (2010)
104. J.S. Melinger, S.S. Harsha, N. Laman, D. Grischkowsky, Guided-wave terahertz spectroscopy of molecular solids [Invited]. J. Opt. Soc. America B **26**(9), A79 (2009)
105. R. Mendis, V. Astley, J. Liu, D.M. Mittleman, Terahertz microfluidic sensor based on a parallel-plate waveguide resonant cavity. Appl. Phys. Lett. **95**(17), 1–4 (2009)
106. M.B. Byrne, J. Cunningham, K. Tych, A.D. Burnett, M.R. Stringer, C.D. Wood, L. Dazhang, M. Lachab, E.H. Linfield, A.G. Davies, Terahertz vibrational absorption spectroscopy using microstrip-line waveguides. Appl. Phys. Lett. **93**(18) (2008)
107. T. Ohkubo, M. Onuma, J. Kitagawa, Y. Kadoya, Micro-strip-line-based sensing chips for characterization of polar liquids in terahertz regime. Appl. Phys. Lett. **88**(21), 86–89 (2006)
108. J. Kitagawa, T. Ohkubo, M. Onuma, Y. Kadoya, THz spectroscopic characterization of biomolecule/water systems by compact sensor chips. Appl. Phys. Lett. **89**(4), 1–4 (2006)
109. J. Cunningham, M.B. Byrne, C.D. Wood, L. Dazhang, On-chip terahertz systems for spectroscopy and imaging. Electron. Lett. **46**(26), s34–s37 (2010)
110. F. Stewing, T. Kleine-Ostmann, M. Koch, A new class of improved-efficiency THz filters for on-chip detection of biomaterials. Microw. Opt. Technol. Lett. **41**(2), 79–82 (2004)
111. J. Cunningham, C. Wood, A.G. Davies, I. Hunter, E.H. Linfield, H.E. Beere, Terahertz frequency range band-stop filters. Appl. Phys. Lett. **86**(21), 1–3 (2005)
112. C. Wood, J. Cunningham, I.C. Hunter, P. Tosch, E.H. Linfield, A.G. Davies, On-chip pulsed terahertz systems and their applications. Int. J. Infrared Millimeter Waves **27**(4), 557–569 (2006)

Multimode Interference Fiber Sensors for the Monitoring of Gasoline/Ethanol Blends

A.J. Rodriguez-Rodriguez, D.A. May-Arrioja, I. Hernandez-Romano and Ignacio R. Matías

Abstract Multimode interference (MMI) devices have attracted a great deal of interest due to their simplicity of fabrication. The MMI device is ready for testing after splicing a section of multimode fiber (MMF) between two single-mode fiber (SMF). In this chapter we provide an overview of the fundamentals behind the formation of self-images in MMI fiber devices, as well as the basic mechanisms for tuning their operational wavelength which is related with their application for sensing applications. The sensitivity enhancement of these MMI fiber sensors is also investigated by reducing the diameter of the MMF via wet chemical etching, as well as coating the MMF with a high refractive index overlay. The MMI fiber sensors are applied to the quality control of gasolines and in particular the real time monitoring of gasohol, mixtures of gasoline and ethanol, which is critical for the proper operation of flexible-fuel vehicles (FFV). The results demonstrate that MMI fiber sensors are well suited for such applications, as well as other applications were the binary mixture of liquids has to be controlled or monitored.

A.J. Rodriguez-Rodriguez (✉)
Universidad Autónoma de Tamaulipas, UAM Reynosa Rodhe,
88779 Reynosa, Tamaulipas, Mexico
e-mail: arodriguez@docentes.uat.edu.mx

D.A. May-Arrioja
Centro de Investigaciones en Optica, Aguascalientes, Ags. 20200, Mexico
e-mail: darrioja@cio.mx

I. Hernandez-Romano
CONACYT-Electronics Department, Sede Palo Blanco,
Universidad de Guanajuato, 36885 Salamanca, Guanajuato, Mexico
e-mail: heriromano@gmail.com

I.R. Matías
Depto. de Ing. Eléctrica y Electrónica, Universidad Pública de Navarra,
Campus Arrosadia, 31006 Pamplona, Spain
e-mail: natxo@unavarra.es

© Springer International Publishing Switzerland 2017

I.R. Matias et al. (eds.), *Fiber Optic Sensors*, Smart Sensors,
Measurement and Instrumentation 21, DOI 10.1007/978-3-319-42625-9_15

1 Introduction

Refractive index (RI) sensors based on different optical fiber configurations have been extensively studied in the past decade [1, 2]. Over these years, RI sensors have been developed using different fiber structures such as fiber Bragg gratings (FBG), long period gratings (LPG), in-fiber Fabry-Perot cavities, interferometric devices, and microfiber resonators [3–11]. A common feature in such RI sensors is that in order to fabricate the sensor they require either complex fabrication processes or rather expensive equipment. Additionally, although most of the RI sensors developed to date focus on large sensitivities for potential applications related to bio-sensing, there are several applications related to the real time monitoring of binary liquid mixtures where large sensitivities are not required. For instance, the real time monitoring of gasoline and ethanol blends is becoming increasingly important for flexible-fuel vehicle (FFV) which are designed to run on more than one fuel, usually gasoline blended with either ethanol or methanol fuel. Knowledge of the ethanol concentration in the gasohol blend allows modern FFV to adjust the fuel injection and spark timing according to the actual blend detected by a fuel composition sensor. Since the mixture of gasoline and ethanol involve liquids with a significant RI difference, a sensor with moderate sensitivity can be used to monitor the blend composition.

A particular fiber structure that has received a great deal of interest in the last 10 years is related to multimode interference (MMI) devices. The advantage of MMI devices relies on the fact that their fabrication is quite simple, since we only need to splice a section of multimode fiber (MMF) between two single-mode fibers (SMF), and they exhibit a band-pass spectral response with minimal transmission loss at the peak of the band. Such band-pass response is convenient for sensing applications since we can easily correlate either spectral shifts or intensity changes of the band-pass peak with the physical variable under measurement. This chapter provides an overview of the fundamentals behind the operation of MMI devices and their application to monitor gasolines and gasoline/ethanol blends.

2 Fundamentals of MMI Devices

MMI devices have been developed employing different platforms such as integrated optics (semiconductors, polymers, and plasmonics) and optical fibers. The versatility of MMI devices relies on the fact that we only need a multimode waveguide, which can have either a two or three dimensional geometry, in order to observe MMI effects. Since this requirement is easily achieved in optical fibers, the MMI structure has been widely investigated for the development of several optical fiber sensors.

2.1 Multimode Interference Effect

The basic structure to obtain a MMI device is shown in Fig. 1a. It consists of a MMF with a specific length, which is sandwiched between two SMF. The MMF must have a diameter that allows the propagation of more than three modes, which is easily achieved with any commercial MMF. The operation of the MMI device is quite simple. Light with a wavelength of λ_0 is coupled at the input SMF and when the fundamental mode reaches the SMF-MMF interface the radially symmetric modes supported by the MMF are excited. During the propagation of the modes along the MMF they interfere between each other and give rise to an interference carpet as the one shown in Fig. 1b. If we monitor the intensity of the interference carpet along the axis of the optical fibers, we can notice that there are certain positions where the light is being concentrated. Nevertheless, optimum light concentration with minimal insertion losses occur at the fourth concentration point, and repeats in a periodic fashion. At this particular position an exact image of the input field is formed and is known as self-image. The self-image position corresponds to the distance at which the phase difference between the propagating modes is the closest to an exact multiple of 2π.

Since MMI devices have been around for a while, the analysis to obtain an analytical expression to determine this self-image position can be found elsewhere [12]. The expression that correlates the MMF parameters and the wavelength of light with the self-imaging position is given by,

$$L_{MMF} = m\frac{n_{MMF}D_{MMF}^2}{\lambda_0} \quad with\, m = 0, 1, 2, \ldots, \tag{1}$$

where L_{MMF} is the physical length of the MMF, λ_0 is the free space wavelength, n_{MMF} and D_{MMF} are the effective RI and diameter of the fundamental mode of the MMF, respectively. The factor m is an indicative of the periodic nature of the imaging process

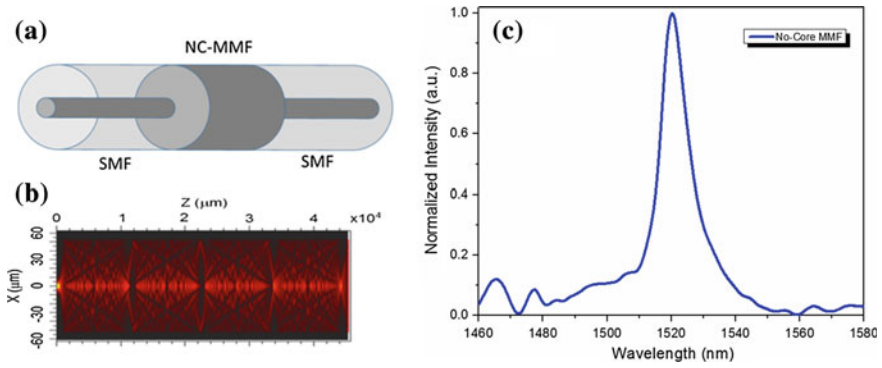

Fig. 1 **a** Fiber structure of the MMI device, **b** Intensity distribution of the light inside the MMF, and **c** MMI spectral response in air.

along the MMF. Therefore, at every fourth image ($m = 4, 8, 12, \ldots$.) we obtain the real self-image, and this is typically the position that we use for MMI applications. Any other self-image for other values of m correspond to pseudo-images where losses are significantly higher. The pseudo-images with higher losses are correlated with bigger phase errors between the propagating modes as compared to the required phase difference of 2π to reproduce the input field, and thus the intensity of the pseudo-image is reduced. Therefore, the MMF is cleaved such that its length is equal to L_{MMF} (with $m = 4$) and an output SMF is spliced at this end.

An interesting effect occurs when light with a wavelength different than λ_0 is transmitted through the MMI device. As dictated by Eq. (1), when light with a larger wavelength than λ_0 is coupled to the MMI device, the self-image will be formed before the output MMF-SMF interface and the intensity coupled to the output SMF will be reduced. A similar situation occurs for wavelengths shorter than λ_0, with a self-image formed beyond the output MMF-SMF interface and reduced coupled intensity to the output SMF. Therefore, when a light source with a wide wavelength range is coupled to the MMI device, the transmitted spectrum exhibits a band-pass response as shown in Fig. 1c. This type of response is adequate for sensing applications because any change induced to the optical properties of the MMF will modify either the peak spectral response or the transmitted intensity.

2.2 Fiber Sensors Based on MMI Devices

In order to use MMI devices for sensing applications, the physical variable of interest should be able to either modify the MMF parameters or interact with the propagating modes. Since the peak wavelength λ_0, as shown in Eq. (1), is directly related to the effective refractive index and diameter of the fundamental mode and inversely proportional to the MMF length, we can modify the MMI peak wavelength response in two ways. The simplest case is related to changes on the length of the MMF. Although this is not quite obvious, an approach to change the MMF length in real time involves using a liquid core multimode waveguides (LCMW). By filling a ferrule, with an inner diameter of 127 μm, with liquid having a higher RI than that of the ferrule we obtain a LCMW. Instead of splicing one of the SMF-MMF interfaces of the MMI device we insert the SMF into one end of the ferrule and the MMF on the other end. Therefore, the MMF of the MMI device is now formed by the solid MMF plus the length of the LCMW, and by changing the separation between the fibers inside the ferrule we effectively change the length of the composite MMF and the peak wavelength should be also modified. Using this principle a micro-displacement sensor [13] and different tunable fiber lasers have been demonstrated [14, 15].

Another scenario involves modifying the effective RI and diameter of the fundamental mode of the MMF, n_{MMF} and D_{MMF}, respectively. In fact, since both parameters are related with the RI value of core and cladding a simple option can be implemented. The key element is the use of a MMF without cladding known as No-Core MMF, i.e. air is the cladding, which allows that when the fiber becomes in

contact with a liquid both parameters will be affected. The only condition is that the RI of the liquid has to be less than that of the No-Core MMF to maintain waveguiding conditions. Therefore, different fiber sensors using a variety of liquids have been developed using this approach [16, 17]. Since the No-Core MMF is exposed to the environment some applications have been also developed to realize fiber biosensors that operate via the evanescent field [18].

3 MMI Refractometer

The spectral response of the MMI sensor based on the No-Core MMF under the influence of external liquids with different RI can be estimated using Eq. (1) with $m = 4$. In order to do this, we obtain the effective RI and diameter of the fundamental mode of the No-Core MMF when is surrounded by each liquid, and using Eq. (1) we can then estimate the resulting MMI peak wavelength. The effective RI and diameter are calculated using the finite element software COMSOL Multiphysics. The No-Core MMF parameters used in COMSOL consider a core RI of 1.444 and a No-Core MMF diameter of 125 μm, operating at a wavelength of 1540 nm. The effective diameter is taken at the position where the field of the fundamental mode has decreased to a value of $1/e^{-2} = 0.135$ times the maximum value. Using these values, and the air as the cladding, we then calculate using Eq. (1) the length of the No-Core MMF to exhibit a peak at 1540 nm. This provides a value of 58.60 mm, which will be used in the following calculations when we replace the air cladding by different liquids.

After we replace the air for a specific liquid we then recalculate the effective RI and diameter of the fundamental mode, and we use these values and the length of 58.60 mm to calculate the new MMI peak wavelength. The RI of the liquid used in the simulations is allowed to change from 1.318 to 1.420. As shown in Fig. 2, the MMI peak wavelength is shifted to longer wavelength as the RI of the liquid is increased. We can also notice that the wavelength shift is small for RI values smaller than that of the No-Core MMF, but is larger as the RI becomes closer to that of the No-Core MMF. The shape of Fig. 2 exhibits a quadratic behavior which is correlated with the diameter to the square of Eq. (1). In fact, this is correct since the effective RI barely changes and does not have a major effect in the MMI wavelength shift. By inspection of Fig. 2, we can estimate a sensitivity of 133.65 nm/RIU for the RI range from 1.318 to 1.373, and a sensitivity of 390.88 nm/RIU for the RI range from 1.373 to 1.420. Such sensitivity should be good enough for gasoline and ethanol blend identification.

The No-Core MMF was provided by the company Prime Optical Fiber Corporation. The MMI sensor was fabricated by cleaning the polymer cladding of the No-Core MMF and splicing one end to a SMF. The No-Core MMF is then cleaved to have a total length of 58.60 mm using a setup combining a micrometer and a cleaver. The cleaved end is spliced to another SMF and the MMI sensor is fabricated. The MMI sensor is immersed in a piranha solution (sulfuric acid and hydrogen peroxide) during 1 min to remove any organic residue, rinsed with

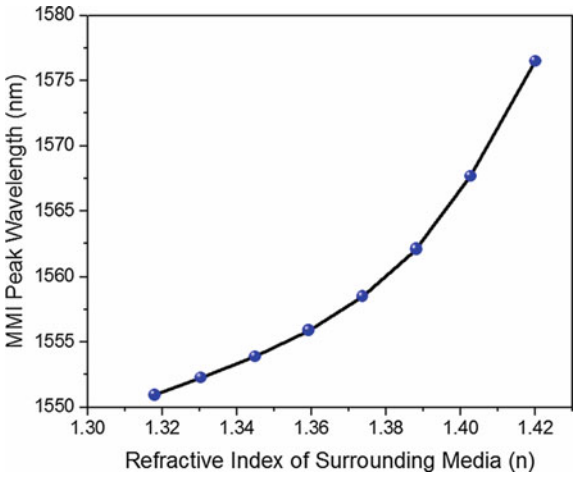

Fig. 2 MMI peak wavelength response as a function of the RI of the liquid around the No-Core MMF

deionized water and dried with nitrogen. The experimental setup for testing the MMI sensors is shown in Fig. 3. The optical source is a superluminescent diode (SLD) with a wavelength range from 1465 to 1650 nm. The SLD is connected to the input SMF of the device using FC/PC connectors, and the output SMF is then connected to an optical spectrum analyzer (OSA) Anritsu MS9740A to capture the transmitted spectrum.

As shown in Fig. 3, the MMI sensor was fixed into a liquid chamber engraved into a Delrin plate which was then covered by an acrylic plate and glued to the Delrin plate to seal the chamber. The chamber included liquid inlet and outlet plastic tubes to facilitate insertion and removal of the liquids. The measurements were performed at a controlled temperature of 23 °C and a humidity of 26 %. In order to evaluate the spectral response as a function of the external RI we prepared different mixtures of water and ethylene glycol (EG) at different volume proportions. Using these mixtures we can cover a RI ranging from n = 1.318 (water) to n = 1.420 (EG), this RI value was calculated by using the equations in Ref. [19], at a wavelength of 1550 nm.

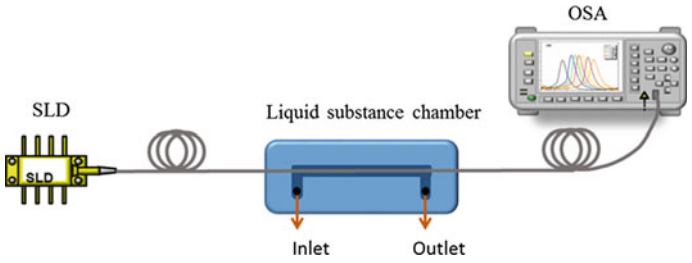

Fig. 3 Experimental setup for testing of the MMI sensors. The MMI sensor is fixed into a channel to facilitate insertion and removal of the liquids

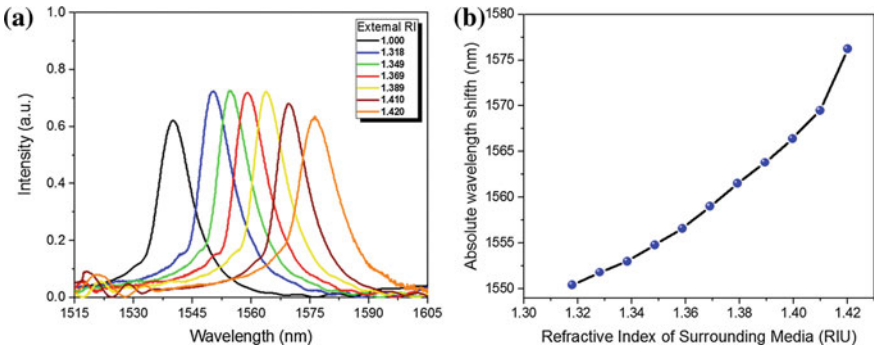

Fig. 4 **a** Spectral response of the MMI sensor for different external RI liquids and **b** MMI peak wavelength shift as a function of the RI of surrounding media

The spectral response of the MMI fiber sensor in air is shown in Fig. 4a. We can observe that the MMI peak wavelength is quite close to the design wavelength of 1540 nm. The mixtures of water/EG were inserted into the channel going from the lowest to the highest RI. As shown in Fig. 4a, we can observe that the spectral response of the MMI fiber sensor is shifted to longer wavelengths as the RI is increased, i.e. the amount of EG is increased in the water/EG mixture. We should mention that in Fig. 4a we only show the response of certain number of mixtures to better observe the shifting of the MMI spectral response. As shown in Fig. 4b, the MMI peak wavelength response is red shifted as the RI of the surrounding media is being increased, which is expected according to our simulations. We also observe quadratic behavior resulting from the diameter being the dominating factor. We can estimate from Fig. 5b sensitivities of 179.62 nm/RIU for RI range from 1.318 to 1.379 and 344.12 nm/RIU for a RI range from 1.379 to 1.420. Although such sensitivities are good enough for our application, in the next section we explore some options to increase the sensitivity of MMI fiber sensors.

4 Sensitivity Enhancement of MMI Sensors

As shown in the last section, the critical parameter that determines the sensitivity of a MMI fiber sensor is related to the effective diameter of the fundamental mode. Therefore, in order to enhance the sensitivity of MMI fiber sensors we need to either modify the MMF structure or incorporate a film that could increase the effective diameter of the mode. A simple way to achieve this is by tapering the MMF section [20]. However, this requires special equipment if we want to obtain reproducible results among fabricated devices. In this section we experimentally demonstrate two options to enhance the sensitivity of MMI sensors. Firstly, by reducing the diameter of the No Core MMF using a wet chemical etching process [21, 22], and secondly by incorporating a high RI thin film coating on the MMF section [23, 24].

4.1 MMI with Reduced Core

As we demonstrated in section three, when the liquid RI around the No-Core MMF is increased the effective diameter of the fundamental mode is also increased. Therefore, in order to increase the sensitivity of MMI devices we need to enhance this effect. A simple way to achieve this is by reducing the diameter of the No-Core MMF. When the diameter of the No-Core MMF is reduced the confinement of the fundamental mode is also reduced, which makes it more sensitive to external perturbations. In our particular situation, when the RI of the liquid is increased and approaches the RI of the core, the effective mode diameter will be increased as well and should be larger as compared to the No-Core MMF before reducing its diameter.

The diameter of the No-Core MMF was reduced using a buffered oxide etching (BOE) solution, which is a mixture of hydrofluoric acid and ammonium fluoride as the buffer agent. The advantage of BOE is that the etching rate is relatively slow (~130 nm/min), which allows us to have good control of the amount of removed material. In order to observe a self-image after the etching, we design the MMI fiber sensor using Eq. (1) for a wavelength of 1540 nm and a No-Core MMF diameter of 90 μm with a core RI of 1.444 at 1540 nm. This provides a No-Core MMF length of 30.38 mm. The MMI fiber sensor was fabricated as explained in section two, using a No-Core MMF length of 30.38 mm and was fixed inside a Delrin channel. When the transmitted spectrum is observed at the OSA we observe a random spectrum, since we are not at a self-image position, but we are able to locate a dominant peak to monitor during the etching. After the BOE is poured into the channel, we can observe that the selected peak is being shifted to shorter wavelengths because the diameter of the No-Core MMF is being reduced. After certain time we observe a well-defined peak, which corresponds to the self-image, on the long wavelength range of the transmitted spectrum. The No-Core MMF is left in the BOE until the MMI peak wavelength is located at 1540 nm when the fiber is in air.

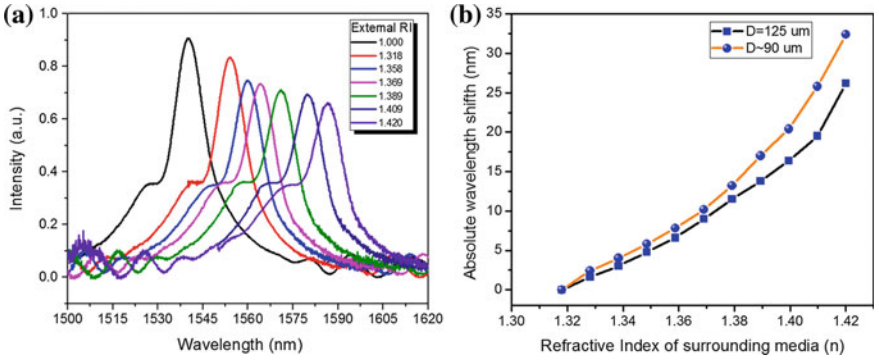

Fig. 5 **a** Spectral response of the MMI sensor with a MMF diameter of 90 μm for different external RI liquids and **b** MMI peak wavelength shift as a function of the liquid RI for different NC-MMF diameters

This corresponds to a No-Core MMF diameter of 90 μm, and a total etching time close to 135 min was employed. The spectral response of the MMI sensor in air is shown by the black line of Fig. 5a.

The reduced core MMI sensor was tested using the same liquid mixtures of water and EG of section three. As shown in Fig. 5a the MMI spectral response is shifted to longer wavelengths as expected. Again, only certain RI values were plotted to better observe the MMI peak wavelength shift. By plotting the peak MMI wavelength as a function of liquid RI we can compare the response to the MMI sensor with a diameter of 125 μm. We can observe that the sensitivity is slightly increased from 185.22 to 206.58 nm/RIU for the RI range from 1.318 to 1.379, and from 344.12 to 462.74 nm/RIU for the RI range from 1.379 to 1.420. Since the RI of gasoline is approximately 1.42 this enhancement should be beneficial for testing gasoline/ethanol blends.

4.2 ITO Coated MMI Devices

The application of an external coating in extrinsic fiber sensors have been mainly focused to perform the specific measurement of several physical variables such as temperature and humidity [24, 25], different gasses [26], pH [27], and chemical/biological materials [28, 29]. External coatings with high RI values, higher than that of the optical fiber, have been also used to enhance the evanescent field in optical fibers [30]. This is related to the fact that the sensitivity of extrinsic fiber sensors to external RI variations is enhanced as the evanescent field propagating in the fiber is also enhanced. Although different materials can be used as a high RI external coating [31, 32], Indium Tin Oxide (ITO) has been used in different fiber sensors because is a material that is electrochemically stable, compared to traditional materials, as well as the ease with which it can be deposited as a thin film [31]. The only drawback, since we are operating in the near infrared region (1550 nm), is related to the losses due to absorption of the ITO film in this region. Therefore, the thickness of the film has to be carefully controlled.

The fabrication process of the ITO coated MMI sensor is slightly different as our previous process. The cladding from an 80 mm long section of No-Core MMF is completely removed using acetone. The fiber is then cleaned using a Piranha solution, rinsed with deionized water and dried using nitrogen. The fiber is then attached to a rotation mechanism based on a DC motor which is adapted to clamp the fiber from one end and rotate the fiber throughout the whole deposition process. The ITO deposition process was performed using a sputtering system (K675XD Quorum Technologies Ldt.) operating with an Argon partial pressure between 6.1×10^{-3}–9.6×10^{-3} mbar and an applied current of 150 mA, which allowed us to achieve deposition rates of 0.3 nm/s [33]. Two No-Core MMF were coated with ITO with sputtering times of 1 and 2 min, which correspond to ITO film thickness of approximately 18 and 36 nm, respectively. After the sputtering process the ITO coated No-Core MMF is cleaved in one end and spliced to a SMF. Using a

micrometer system the ITO coated No-Core MMF is then cleaved with a length of 58.60 mm, which corresponds to a MMI peak wavelength of 1540 nm, and this end is also spliced to another SMF. During all the process care is taken to avoid contamination of the ITO surface. The optical properties of the ITO film were evaluated using an ellipsometer (UVISEL Horiba Jobin). The optical properties at 1550 nm provide a complex RI with a real value close to 2.13 and an imaginary value close to 2.

The spectral response of the ITO coated MMI sensor is obtained by using mixtures of water and glycerin to cover a RI range from 1.318 (water) to 1.408 (80 % Glycerin and 20 % water). Glycerin was used in these experiments because glycerin residues are easily removed from the MMI device surface. The response of a MMI sensor without ITO coating is shown in Fig. 6a, where a maximum spectral shift of 16.5 nm is observed when going from an external RI of 1.318–1.408. As shown in Fig. 6b, when the MMI sensor is coated with ~18 nm of ITO a maximum spectral shift of 27 nm is observed within the same RI range. This corresponds to an increment of more than 50 % from the original maximum spectral shift. We should

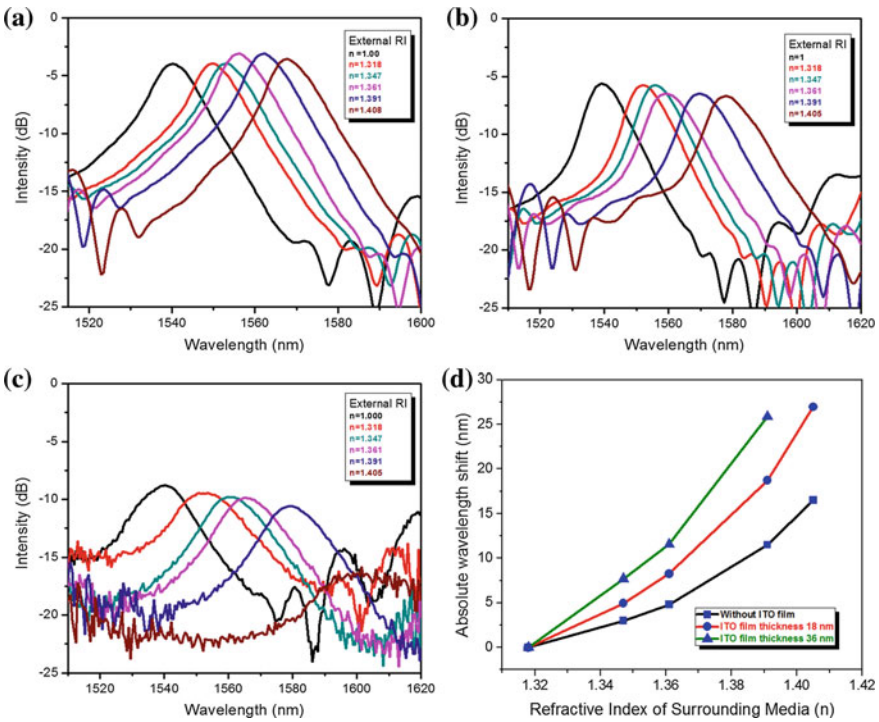

Fig. 6 Spectral response of the MMI refractometer for different RI liquids considering: **a** MMI ordinary structure, **b** MMI ITO coated structure (~18 nm), **c** MMI ITO coated structure (~36 nm); **d** MMI refractometer peak wavelength shift as a function of the water/glycerin blends RI for the MMI without ITO (*black*), MMI + ITO 18 nm (*red line*) and MMI + ITO 36 nm (*green line*)

also notice that the transmitted signal is reduced due to absorption losses from the ITO film. In the case of the MMI sensor coated with ~36 nm of ITO, we can observe that the transmitted signal is significantly reduced and it almost vanished for the RI of 1.408. Nevertheless, we can observe a spectral shift of 25.85 nm for the RI range from 1.318 to 1.391, which is a 124 % enhancement as compared to 11.5 nm spectral shift obtained with the MMI sensor without ITO. This corresponds to a sensitivity enhancement of 476.66 nm/RIU for the MMI coated with ~36 nm of ITO, as compared to 223.33 nm/RIU from the MMI sensor without ITO, for the RI range from 1.361 to 1.391, which is within the RI values for gasoline and ethanol. Therefore, the ITO coated MMI sensor should perform quite well for the discrimination of gasohol blends.

5 Monitoring of Gasohol Blends

Methanol and ethanol are typically used as fuel especially when they are mixed with gasoline. However, the use of methanol has been reduced because it is extremely volatile, highly toxic, and therefore increases the risk of fire or explosion [34]. Ethanol has become a choice as fuel in many countries like Brazil with the advantage that combustion is less polluting and highly oxygenated. This combustible comes typically from sugar cane and corn as well as cellulosic biomass, grass and trees. Ethanol is also employed as additive in gasoline to replace the Methyl Tert-Butyl Ether (MTBE), responsible for significant contamination of soil and groundwater. The resulting fuel mixture of gasoline and ethanol is called gasohol [35, 36]. Gasohol blends have "E" numbers to describe the percentage of ethanol fuel in the mixture by volume, for example, E85 is 85 % ethanol and 15 % gasoline, and so on. Gasohol has become very popular in several countries and modern flexible-fuel vehicles (FFV) are now designed to run on more than one fuel, usually gasoline blended with either ethanol or methanol fuel. Therefore, it is important to know the ethanol concentration in gasoline for modern FFV in order to adjust the fuel injection and spark timing according to the actual blend detected by the fuel composition sensor. Optical fiber sensors are an attractive option due to their inherent characteristics, and some approaches have been investigated using traditional optical fiber sensing techniques [37–41]. However, the main inconvenient in these systems is the need for a special preparation of the fiber or the deposition of a sensitive material. Since the mixture of gasoline and ethanol involve liquids with a significant RI difference, the MMI fiber sensor could be used to monitor the blend composition.

5.1 Octane Rating

The octane rating in fuels is related to their performance withstanding higher compression before ignition, i.e. the higher the octane rating the higher the

compression. In general, high octane gasolines are typically used in applications that require higher compression ratios such as high performance engines. For commercial applications, gasolines are offered to the public with different octane ratings depending on the particular country. For example, in the USA three different octane ratings are available from the company Exxon (octane rating of 87, 89, and 91–93), but in México two different octane ratings (87 and 92) are provided by the oil national company Petroleos Mexicanos (PEMEX). Knowing the octane rating is important because the use of a lower octane rating may lead to issues related with engine knocking [42]. Even more important is the fact of knowing that we are receiving the octane rating that we are buying. A common malpractice in some gasoline stations is related with the adulteration of gasolines to obtain a major profit by selling cheap gasoline instead of the advertised high octane rating. The adulteration is performed by receiving a lower octane rating than the high octane rating that is expected, mixture of gasolines with different octanes ratings, and even adding other products to the gasoline. Therefore a sensor to monitor in real time the octane rating should be highly beneficial for automotive vehicles.

The spectral response of the MMI fiber sensor for gasolines of 87 and 92 octanes is shown in Fig. 7a. These measurements were obtained using a No-Core MMF with a diameter of 90 μm. As shown in this figure a peak wavelength separation of 6 nm is clearly observed between the gasolines with 87 octanes (G87) and 92 octanes (G92), with the higher octane rating at longer wavelengths, which allow their identification using the MMI fiber sensor. We expect that it should be feasible to identify gasolines with higher octane content as the ones used in Europe and Asia using the MMI fiber sensor. In fact, a simple way to increase the octane content in gasolines is by adding gasoline additives (GA). There are other advantages associated with the use of GA. Oxygenated compounds such as methyl *tert*-butyl ether (MTBE), *tert*-amyl methyl ether (TAME) and Ethyl *tert*-butyl ether (ETBE), among others, are used as additives in replacement of tetraethyl lead that is highly pollutant. These oxygenated additives are added to gasoline providing greater

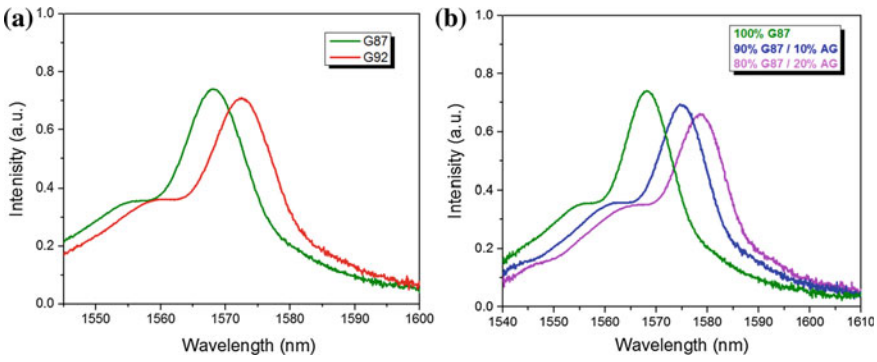

Fig. 7 Spectral response of MMI refractometer with reduced core (D ~ 90 μm): **a** identification of different octane gasoline (G87 and G92), **b** 87 octane gasoline (G87) and mixtures with a commercial gasoline additive (GA)

oxygenation, which directly provides a complete combustion and improved engine performance increasing the gasoline octane number, and providing more power to the engine using the same amount of gasoline.

We employed a commercial GA from the company AKRON which was added to the 87 octane gasoline. Mixtures of 90/10 and 80/20 % of gasoline/AKRON GA were prepared and measured using the same MMI fiber sensor. As shown in Fig. 7b when the mixture contains 10 % by volume of GA the MMI peak wavelength is red shifted by almost 7 nm as compared to pure G87 gasoline. This value is comparative to the G92 gasoline. The sample with 20 % of GA, as expected, exhibits a larger redshift since we have an even higher octane rating in the mixture. We should highlight that the redshift observed by adding GA to gasoline does not necessarily means that any higher octane mixtures will shift to longer wavelengths. This only means that the RI of the GA is higher than that of the gasoline and because of this the MMI peak wavelength shifts to longer wavelengths. As will be shown in the next section, the addition of ethanol to gasoline also increases the octane rating [43, 44], but because of its lower RI value the MMI sensor exhibits a blueshift in its spectral response when the gasohol mixture is measured.

5.2 *Gasohol Quality Control*

In this section we will evaluate the application of MMI fiber sensors for monitoring different gasohol blends. Before performing any gasohol measurement we first have to measure each separate compound. As shown in the inset of Fig. 8a when anhydrous ethanol (EtOH) is inserted in the channel we can observe a wavelength shift of 19.3 nm as compared to the sensor response in air. When the sensor is exposed to G87 gasoline the MMI peak wavelength is shifted another 20.3 nm with respect to the peak wavelength exhibited by the EtOH. This peak wavelength

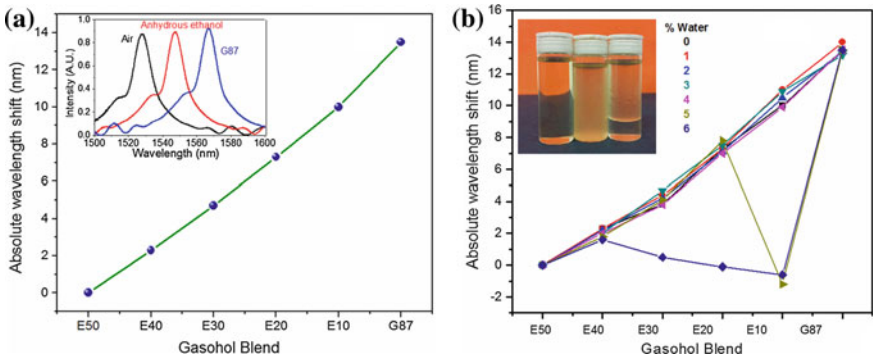

Fig. 8 **a** Absolute wavelength shift as a function of gasohol blends (*Inset* MMI spectral response for ethanol and gasoline), and **b** absolute wavelength response for different gasohol blends and different water percentages (*Inset* E10 Gasohol with water content of 1, 5, and 10 % going from *left* to *right*)

separation is wide enough to identify the different gasohol blends. It is important to notice that the peak wavelength of EtOH has a lower value than the G87 gasoline. This means that the addition of EtOH to the G87 gasoline should experience a blue wavelength shift, since the RI of the mixture will be reduced.

We prepared different mixtures of EtOH and G87 gasoline at different volume percentages going from E50 to pure G87 gasoline. After mixing, the gasohol was inserted into the channel and the spectral response of the MMI sensor was acquired with the OSA. As shown in Fig. 8a, we can observe that the MMI peak wavelength of the MMI sensor is shifted to longer wavelengths as the amount of EtOH is reduced from the gasohol blend. Such response is correlated with the fact that the G87 gasoline has a higher refractive index that the EtOH. We can also notice that the response is highly linear, which is related with fact that the RI change of the blends is very small.

A major effect in gasohol blends is related with the natural ability of ethanol to absorb water. There is an upper limit of 4 % of water that can be dissolved in ethanol in order to avoid phase separation between EtOH/water and gasoline. This effect is shown in the inset of Fig. 8b. The bottles are filled with E10 gasohol with water volumes in EtOH of 1, 5 and 10 % going from left to right. The bottles are shown after agitation and a settling time of 30 s. As we can see in the inset, the bottle with 1 % of water is well mixed with the gasoline. Nevertheless, the gasohol with 5 % of water is not homogeneously mixed and is very cloudy, which is indicative of a colloidal suspension. The gasohol sample with 10 % of water experience phase separation very rapidly, which can be observed by the gasoline on the top and the EtOH/water mixture at the bottom.

The key question is if the MMI fiber sensor should be capable of seeing such phase separation effects. Therefore, for each gasohol blend we prepared a set of samples with different contents of water from 0 to 6 % with 1 % increments relative to the total volume of EtOH. The samples were agitated before being inserted into the channel and the MMI spectrum is acquired with the OSA. As shown in Fig. 8b, all gasohol mixtures with water content from 0 to 4 % exhibit a similar response as compared to 0 % water content. However, in the case of the gasohol blends with 5 % of water we can observe a deviation of more than 10 nm for the E10 gasohol blend. As we raise the water content to 6 %, the deviation from the linear response is also observed for the E20 and E30 gasohol blends. This behavior can be explained due to the formation of droplets of gasoline and EtOH/water resulting from the phase separation which effectively reduces the RI of the gasohol.

The above results suggest that an ideal position for the MMI fiber sensor should be at the bottom of the gasohol container, because after phase separation it should be covered by the EtOH/water mixture and we should be able to detect exactly when phase separation occurs. We placed the MMI fiber sensor at the bottom of a container, and the E10 gasohol with 1 % of water concentration was agitated and poured into the container. A first measurement was acquired right after pouring the gasohol, and the second one after 60 s. As shown in Fig. 9a, the MMI peak wavelength remains the same at any time indicating that the mixture is well mixed without phase separation. When the E10 gasohol has a water volume at 5 %, the

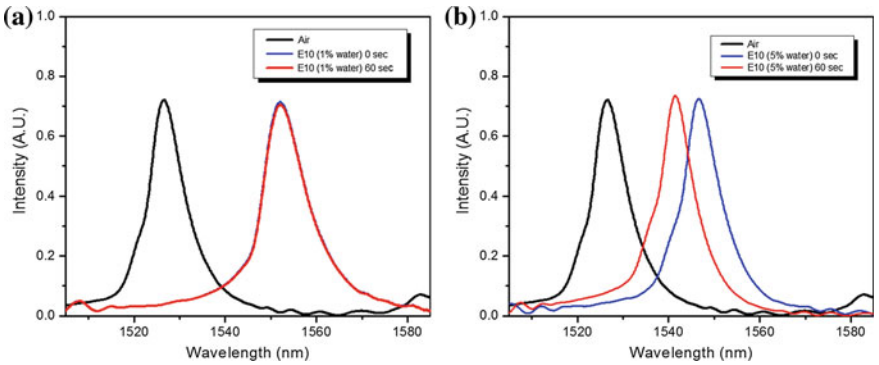

Fig. 9 MMI peak wavelength of the MMI sensor for E10 gasohol with water percentage of **a** 1 % and **b** 5 % acquired right after shaking and when the gasohol has been settled during 60 s

MMI peak wavelength does not reach the maximum value achieved when the water volume is 1 %. As shown in Fig. 9b, the MMI peak wavelength is shifted 5.4 nm to shorter wavelengths. This wavelength shift results from the effective RI index difference related to the droplet formation due to phase separation. After 60 s, phase separation can be observed in the container and the MMI peak wavelength has shifted another 5.2 nm to shorter wavelengths. This additional wavelength shift occurs because the MMI fiber sensor is completely immersed in an EtOH/water mixture and its refractive index is even lower than the gasohol right after agitation.

6 Conclusion

Some of the basic concepts behind the operation of MMI fiber devices, as well as an overview of the potential parameters that can be modified to achieve an MMI fiber sensor, have been investigated in this chapter. Two different schemes to enhance the sensitivity of MMI fiber sensors was also covered. We found that the ITO film provides the highest enhancement, but losses need to be tolerated. On the other hand, reducing the diameter provides a small improvement for lower external RI and a bit higher for higher external RI that are close to the RI of the MMF core. The MMI fiber sensors were successfully applied for the monitoring of gasohol blends, which includes the ability to detect when the upper limit of 4 % of water content in ethanol has been exceeded. This type of applications is very important for FFV, and should be very useful for the detection of adulterated fuels, either gasohol or gasolines.

References

1. S. Yin, P.B. Ruffin, F.T. Yu, *Fiber Optic Sensors* (Taylor & Francis Group, London, 2008)
2. I.R. Matias, F.J. Arregui, R.O. Claus, Optical fiber sensors. Encycl. Sens. **X**, 1–19 (2006)
3. W. Liang, Y. Huang, Y. Xu, R.K. Lee, A. Yariv, Highly sensitive fiber Bragg grating refractive index sensors. Appl. Phys. Lett. **86**(15), 151122 (2005)
4. S.M. Tripathi, W.J. Bock, A. Kumar, P. Mikulic, Temperature insensitive high-precision refractive-index sensor using two concatenated dual-resonance long-period gratings. Opt. Lett. **38**(10), 1666–1668 (2013)
5. T. Wei, Y. Han, Y. Li, H.L. Tsai, H. Xiao, Temperature-insensitive miniaturized fiber inline Fabry-Perot interferometer for highly sensitive refractive index measurement. Opt. Express **16** (8), 5764–5769 (2008)
6. Z.L. Ran, Y.J. Rao, W.J. Liu, X. Liao, K.S. Chiang, Laser-micromachined Fabry-Perot optical fiber tip sensor for high-resolution temperature-independent measurement of refractive index. Opt. Express **16**(3), 2252–2263 (2008)
7. Y.J. Rao, M. Deng, D.W. Duan, T. Zhu, In-line fiber Fabry-Perot refractive-index tip sensor based on endlessly photonic crystal fiber. Sens. Actuators A **148**(1), 33–38 (2008)
8. G. Salceda-Delgado, D. Monzon-Hernandez, A. Martinez-Rios, G.A. Cardenas-Sevilla, J. Villatoro, Optical microfiber mode interferometer for temperature-independent refractometric sensing. Opt. Lett. **37**(11), 1974–1976 (2012)
9. H. Luo, Q. Sun, Z. Xu, D. Liu, L. Zhang, Simultaneous measurement of refractive index and temperature using multimode microfiber-based dual Mach-Zehnder interferometer. Opt. Lett. **39**(13), 4049–4052 (2014)
10. G. Brambilla, F. Xu, Demonstration of a refractometric sensor based on optical microfiber coil resonator, in *Conference on Lasers and Electro-Optics* (Optical Society of America, 2008), p. CMJJ5
11. F. Xu, V. Pruneri, V. Finazzi, G. Brambilla, An embedded optical nanowire loop resonator refractometric sensor. Opt. Express **16**(2), 1062–1067 (2008)
12. W.S. Mohammed, P.W. Smith, X. Gu, All-fiber multimode interference bandpass filter. Opt. Lett. **31**(17), 2547–2549 (2006)
13. J.E. Antonio-Lopez, P. LiKamWa, J.J. Sanchez-Mondragon, D.A. May-Arrioja, All-fiber multimode interference micro-displacement sensor. Meas. Sci. Technol. **24**(5), 055104 (2013)
14. A. Castillo-Guzman, J.E. Antonio-Lopez, R. Selvas-Aguilar, D.A. May-Arrioja, J. Estudillo-Ayala, P. LiKamWa, Widely tunable erbium-doped fiber laser based on multimode interference effect. Opt. Express **18**(2), 591–597 (2010)
15. J.E. Antonio-Lopez, A. Castillo-Guzman, D.A. May-Arrioja, R. Selvas-Aguilar, P. LiKamWa, Tunable multimode-interference bandpass fiber filter. Opt. Lett. **35**(3), 324–326 (2010)
16. J.E. Antonio-Lopez, D.A. May-Arrioja, P. LiKamWa, Optofluidic tuning of multimode interference fiber filters, in *Proceedings of SPIE* vol. 7339 (2009), p. 73390D
17. Y. Chen, Q. Han, T. Liu, X. Lan, H. Xiao, Optical fiber magnetic field sensor based on single-mode–multimode–single-mode structure and magnetic fluid. Opt. Lett. **38**(20), 3999–4001 (2013)
18. J.G. Aguilar-Soto, M.A. Basurto-Pensado, P. Zhang, H.J. Cho, P. LiKamWa, D.A. May-Arrioja, Integrated fiber based multimode interference bio/chemical sensor, in *Frontiers in Optics* (Optical Society of America, 2009), p. FTuE1
19. E. Sani, A. Dell'Oro, Optical constants of ethylene glycol over an extremely wide spectral range. Opt. Mater. **37**, 36–41 (2014)
20. C.R. Biazoli, S. Silva, M.A. Franco, O. Frazão, C.M. Cordeiro, Multimode interference tapered fiber refractive index sensors. Appl. Opt. **51**(24), 5941–5945 (2012)
21. A.J. Rodríguez Rodríguez, D.G. Martínez Camacho, K. González Gutiérrez, D.A. May-Arrioja, R.F. Domínguez Cruz, I.R. Matías Maestro, C. Ruiz Zamarreño, Rum adulteration detection using an optical fiber sensor based on multimodal interference (MMI). Opt. Pura Appl. **46**(4), 345–352 (2013)

22. A.J. Rodríguez Rodríguez, O. Baldovino-Pantaleón, R.F.D. Cruz, C.R. Zamarreño, I.R. Matías Maestro, D.A. May-Arrioja, Gasohol quality control for real time applications by means of a multimode interference fiber sensor. Sensors **14**, 17817–17828 (2014)
23. A.B. Socorro, I. del Villar, J.M. Corres, F.J. Arregui, I.R. Matias, Mode transition in complex refractive index coated single-mode-multimode-single-mode-structure. Opt. Express, **21**(10) (2013)
24. H. Fukano, Y. Kushida, S. Taue, Multimode-interference-structure optical-fiber temperature sensor with high sensitivity. IEICE Electr. Express **10**(24) (2013)
25. H. Chen, Z. Gu, K. Gao, Humidity sensor based on cascaded chirped long-period fiber gratings coated with TiO_2/SnO_2 composite films. Sens. Actuators B: Chem. **196**, 18–22 (2014)
26. C. Elosúa, I. Vidondo, F.J. Arregui, C. Bariain, A. Luquin, M. Laguna, I.R. Matías, Lossy mode resonance optical fiber sensor to detect organic vapors. Sens. Actuators B: Chem. **187**, 65–71 (2013)
27. C.R. Zamarreño, M. Hernáez, I. Del Villar, I.R. Matías, F.J. Arregui, Optical fiber pH sensor based on lossy-mode resonances by means of thin polymeric coatings. Sens. Actuators B Chem. **155**(1), 290–297 (2011)
28. P. Pilla, A. Iadicicco, L. Contessa, S. Campopiano, A. Cutolo, M. Giordano, A. Cusano, Optical chemosensor based on long period fiber gratings coated with d form syndiotactic polystyrene. IEEE Photon. Technol. Lett. **17**(8), 1713–1715 (2005)
29. D.W. Kim, Y. Zhang, K.L. Cooper, A. Wang, Fibre-optic interferometric immuno-sensor using long period grating. Electron. Lett. **42**(6), 324–325 (2006)
30. S.K. Khijwania, K.L. Srinivasan, J.P. Singh, An evanescent-wave optical fiber relative humidity sensor with enhanced sensitivity. Sens. Actuators B: Chem. **104**(2), 217–222 (2005)
31. N. Paliwal, J. John, Lossy mode resonance (LMR) based fiber optic sensors: a review. Sens. J. IEEE **15**(10), 5361–5371 (2015)
32. S.K. Chauhan, N. Punjabi, D.K. Sharma, S. Mukherji, A silicon nitride coated LSPR based fiber-optic probe for possible continuous monitoring of sucrose content in fruit juices. Sens. Actuators B: Chem. **222**, 1240–1250 (2016)
33. S. López, C.R. Zamarreño, M. Hernaez, I. Del Villar, I.R. Matias, F.J. Arregui, Optical Fiber Refractometers with Response in the Visible Spectral Region by means of ITO Coatings. 7ª Reunión Española de Optoelectrónica, OPTOEL'11
34. United States Environmental Protection Agency, Aftermarket Retrofit Device Evaluation Program, Office of Mobile Sources - EPA 420 - B - 00 - 003 (2000)
35. W. Wigglesworth, MTBE—where do we go from here? Hydrocarbon processing (2000)
36. Frequently Asked Questions about Methanol, http://www.methanex.com/products/faqs.html. Accessed 25 May 2014
37. R. Falate, M. Müller, J.L. Fabris, H.J. Kalinowski, Long period gratings in standard telecommunication optical fibers for fuel quality control. Ann. Opt. **5**, 1–4 (2003)
38. V.V. Spirin, M.G. Shlyagin, S.V. Miridonov, F.M. Jiménez, R.L. Gutierrez, Fiber Bragg grating sensor for petroleum hydrocarbon leak detection. Opt. Lasers Eng. **32**(5), 497–503 (1999)
39. R.M. López, V.V. Spirin, S.V. Miridonov, M.G. Shlyagin, G. Beltrán, E.A. Kuzin, Sensor de fibra óptica distribuido para la localización de fugas de hidrocarburo basado en mediciones de transmisión/reflexión. Revista mexicana de física **48**(5), 457–462 (2002)
40. A. MacLean, C. Moran, W. Johnstone, B. Culshaw, D. Marsh, P. Parker, Detection of hydrocarbon fuel spills using a distributed fibre optic sensor. Sens. Actuators A **109**(1), 60–67 (2003)
41. A. Treviño Santoyo, M.G. Shlyagin, J. Mendieta, V.V. Spirin, L. Niño de Rivera, Variación del espectro de transmitancia de una fibra óptica con recubrimiento de polímero por influencia de hidrocarburos y cambios de temperatura. Revista mexicana de física **51**(6), 600–604 (2005)

42. W. Dabelstein, A. Reglitzky, A. Schütze, K. Reders, Automotive fuels, in *Ullmann's Encyclopedia of Industrial Chemistry* (Wiley-VCH, Weinheim, 2007). doi:10.1002/14356007.a16_719.pub2
43. The Royal Society Celebrating 350 years, "Sustainable biofuels: prospects and challenges", Policy document 01/08 (2008), https://royalsociety.org/~/media/Royal_Society_Content/policy/publications/2008/7980.pdf. ISBN 978 0 85403 662 2
44. Russian Biofuels Association, "What is bioethanol", http://www.biofuels.ru/bioethanol/What_bioethanol/

Fiber Optic Sensors Based on Multicore Structures

D.A. May-Arrioja and J.R. Guzman-Sepulveda

Abstract We present a review of the fundamentals and applications of fiber optic sensors based on multicore coupled structures. The fundamentals of these coupled structures are approached in general for arbitrary distributions of N cores on the foundations of coupled mode theory. The principle of operation of fiber optic sensors using this type of architectures is illustrated via numerical simulations of the simplest coupled structure—the two-core fiber. Illustrative experimental results using fiber optic sensors based on two- and seven-core multicore fibers are shown for a number of applications including temperature, curvature, and refractive index sensing. The main aspects of the performance of multicore fiber sensors are highlighted throughout this chapter and their characteristics, especially their sensitivity, are compared to those of other existing fiber sensing architectures such as fiber Bragg gratings, long period gratings, and photonic crystal fibers, among others.

1 Introduction

Fiber optic sensors (FOS) have numerous advantages as compared to conventional sensors such as their small size and light weight, multiplexing capabilities, long range operation, immunity to external electromagnetic interference, and the ability to operate in harsh environments. Because of these advantages they are unique for certain types of applications, especially where the deployment of conventional sensors is either difficult or quite challenging. Over the years, different configurations have been employed to develop FOS such as fiber Bragg gratings (FBG), long period gratings (LPG), tapered fibers, and multimode fibers. The aim for testing

D.A. May-Arrioja (✉)
Centro de Investigaciones en Optica, Aguascalientes, Ags. 20200, México
e-mail: darrioja@cio.mx

J.R. Guzman-Sepulveda
CREOL, The College of Optics and Photonics, University of Central Florida, Orlando, FL 32816, USA
e-mail: r.guzman@knights.ucf.edu

© Springer International Publishing Switzerland 2017

I.R. Matias et al. (eds.), *Fiber Optic Sensors*, Smart Sensors, Measurement and Instrumentation 21, DOI 10.1007/978-3-319-42625-9_16

different fiber devices is the need to achieve higher sensitivities. This triggered the use of specialty fibers with non-standard structures, such as D-shaped fibers, photonic crystal fibers (PCF), and microstructured optical fibers (MOF), which are specifically designed to achieve higher sensitivities for specific applications. The main features of these different fiber sensors are described throughout this chapter.

A particular configuration that can enhance the performance of FOS is related to the coupling of two or more cores within an optical fiber. Such configuration offers several advantages. First of all, due to the coupling between the cores they exhibit sinusoidal spectral response. This allows correlating the variable under measurement with either spectral shifts or intensity changes over the linear section of the sinusoidal. In addition, it is well known that optical couplers are highly sensitive to changes of the effective refractive index of the modes, which in turn affects the coupling coefficient. Therefore, FOS based on multicore fiber structures are being employed for sensing applications. This chapter provides an overview of the fundamentals behind the operation of multicore fibers, including different applications for measuring refractive index of liquid solutions, temperature, and curvature.

2 Fundamentals of Multicore Fibers

The linear interaction between the modes of N arbitrary, single-mode waveguides as they propagate can be described by the following dynamic equation according to the coupled mode theory [1]:

$$i\frac{d}{dz}\mathbf{A} = \overline{\mathbf{M}}\mathbf{A} \tag{1}$$

where $\mathbf{A} = [a_0 \quad a_1 \quad a_2 \quad \ldots \quad a_{N-1}]^T$ is a vector whose elements are the complex amplitudes of the electric field, at position z, for each core and $\mathbf{M}$ is the coupling matrix describing the interaction between pairs of cores. In its more general form, the coupling matrix $\mathbf{M}$ can be written as:

$$\overline{\mathbf{M}} = \begin{pmatrix} \beta_0 & \kappa_{01} & \kappa_{02} & \cdots & \kappa_{0(N-1)} \\ \kappa_{10} & \beta_1 & \kappa_{12} & \cdots & \kappa_{1(N-1)} \\ \kappa_{20} & \kappa_{21} & \beta_2 & \cdots & \kappa_{2(N-1)} \\ \vdots & \vdots & \vdots & \ddots & \vdots \\ \kappa_{(N-1)0} & \kappa_{(N-1)1} & \kappa_{(N-1)2} & \cdots & \beta_{(N-1)} \end{pmatrix} \tag{2}$$

where β_i is the propagation constant of the fundamental mode in the i-th waveguide and κ_{ij} is the coupling coefficient between the i-th and j-th cores. In the most general situation, all the modes in the independent waveguides have different propagation constant i.e. $\beta_i \neq \beta_j$, at the same time that all of them interact with one another i.e. $\kappa_{ij} \neq 0$ (Fig. 1).

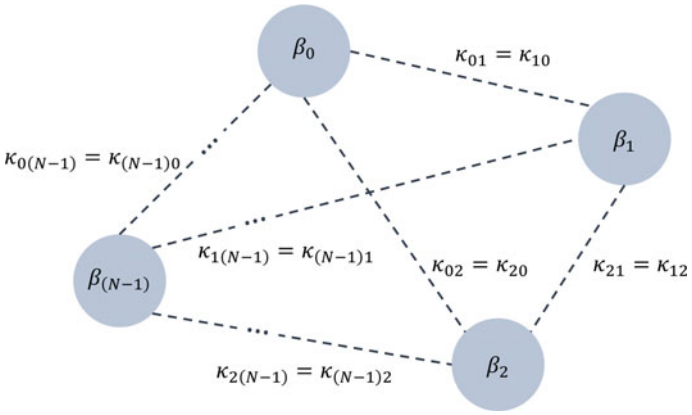

Fig. 1 General scheme of a linear coupled system consisting of N single-mode waveguides with different propagation constants and all the waveguides coupled to one another

The dynamic equation Eq. (1) can be solved if all the elements of the coupling matrix and the initial complex amplitudes of the electric field are known. The matrix **M** entirely describes the interaction between the waveguides for any given initial condition of the field amplitude in a pair-wise manner such that modeling an arbitrary coupled system can be reduced to the task of calculating the propagation constants of the modes in each waveguide, $\beta_i = (2\pi/\lambda_0) n_{eff,i}$, and the coupling coefficient between pairs of waveguides, $\kappa_{ij} = \kappa_{ji}$.

For calculating the coupling coefficient between the i-th and j-th waveguides, one could appeal to the rigorous definition in terms of the overlap integral [2]:

$$\kappa_{ij} = \kappa_{ji} = \frac{\omega\varepsilon_0 \int_{-\infty}^{+\infty}\int_{-\infty}^{+\infty} \left(n^2 - n_n^2\right) E_i^* \cdot E_j dxdy}{\int_{-\infty}^{+\infty}\int_{-\infty}^{+\infty} u_z \left(E_i^* \times H_i + E_i \times H_i^*\right) dxdy} \tag{3}$$

This is typically not the case and the calculation of both the propagation constant and the coupling coefficient for arbitrary configurations is usually performed by means of numerical approaches e.g. finite-element or finite-differences, or by using analytical approximations, or a combination of both. Commonly, the calculation of the coupling coefficient when the interacting waveguides have similar optical properties is performed in terms of the propagation constants of the even and odd coupled modes, β_{even} and β_{odd}, respectively [3]:

$$\kappa \approx \frac{\beta_{even} - \beta_{odd}}{2} = k_0 \left(n_{eff,even} - n_{eff,odd}\right) \tag{4}$$

where k_0 is the free-space wave vector, $k_0 = 2\pi/\lambda_0$, and $n_{eff,even}$ and $n_{eff,odd}$ are the effective refractive index of the coupled modes. Equation (4) is useful and

computationally cost-effective when the response of the system is to be evaluated at a single wavelength. However, if the spectral response of a coupled structure is to be studied, as it is the case when modeling spectrally operated fiber optics sensors, analytical models are preferred in order to evaluate a continuum of wavelengths within certain spectral window.

According to the formulation of the mutual light-wave interactions between two parallel single-mode waveguides in the weakly guiding approximation, the coupling coefficient κ for two similar cores can be approximated analytically by the following expression [4–7],

$$\kappa = \frac{\sqrt{2\Delta}}{a} \frac{U^2 K_0\left(\frac{sW}{a}\right)}{V^3 [K_1(W)]^2} \tag{5}$$

where $\boldsymbol{a}$ is the radius of the cores, $\boldsymbol{s}$ is the center to center separation distance between them, and $\boldsymbol{\Delta}$ is the relative refractive index difference. $\boldsymbol{K_0}$ and $\boldsymbol{K_1}$ are the modified Hankel functions of order 0 and 1, respectively. The normalized frequency $\boldsymbol{V}$, and the normalized transverse propagation constants of the LP_{01} mode in the core and cladding, $\boldsymbol{U}$ and $\boldsymbol{W}$, respectively, are defined as follows [2, 7]:

$$V = k_0 n_r a \sqrt{2\Delta} = \frac{2\pi}{\lambda_0} a \sqrt{n_r^2 - n_c^2} \tag{6}$$

$$U \approx 2.405 \exp\left[-\frac{(1-\sigma/2)}{V} \right] \quad , \quad \sigma = 1 - \left(\frac{n_c}{n_r}\right)^2 \tag{7}$$

$$W = \sqrt{V^2 - U^2} \tag{8}$$

Figure 2a shows the effective refractive index of the even and odd coupled modes for a two-core coupled structure, embedded into an infinite medium of uniform refractive index, as a function of the center-to-center separation distance between the cores at a single, fixed wavelength. For this particular example, the cores are 8.6 μm in diameter and the refractive index of the cores and the cladding is 1.448 and 1.443, respectively, at a free-space wavelength of 1550 nm. For this two-core coupled structure, the coupling constant calculated from numerical simulations (Eq. (4)) and the weakly-guiding analytical model (Eqs. (5)–(8)) is shown in Fig. 2b by the markers and the continuous line, respectively.

The interaction between the cores exponentially weakens with increasing separation distance due to a smaller overlap of the evanescent tails and eventually the structure decouples as can be seen from the zero-coupling asymptotic limit in Fig. 2b. In this particular example, in which the two cores have the same optical parameters, the effective refractive index of the coupled modes asymptotically reaches the same effective refractive index of the independent waveguides (see Fig. 2a).

It is clear that the closer the cores the stronger the interaction (see Fig. 2b), however, from Eq. (4) (see Fig. 2a) it can be seen that the stronger coupling is the

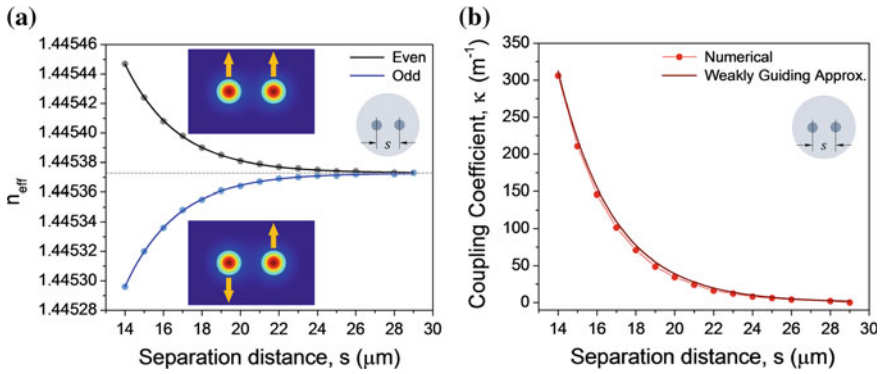

Fig. 2 Two-core coupled structure as a function of the separation distance between the cores (core diameter of 8.6 μm and indices of the core and the cladding of 1.448 and 1.443, respectively, at free-space wavelength of 1550 nm). **a** Effective refractive index of the even and odd coupled modes. **b** Coupling constant obtained from numerical simulations (Eq. (4)) and the weakly guiding approximation (Eq. (5))

result of a larger difference in the effective indices of the coupled modes. This leads to propagation constant mismatch that imposes some limit in the strength of the interaction in practical cases due to, for instance, the contrast reduction in the spectral response of the device, as it will be shown later in the experimental sections specially in the case of refractive index sensing.

From Eq. (4) and (5) one can readily note that any change in the optical and/or geometrical parameters will influence the effective refractive index of the coupled modes and therefore will lead to variations in the coupling coefficient. These variations will reflect in the changes in the overall response of the coupled system and can be used for sensing applications thanks to the underlying dependence of the coupling coefficient on the external parameters.

It is always convenient to have in hand analytical expressions for the coupling constant like Eq. (5) especially for modeling spectrally operated devices in which the response of coupled structures is evaluated for a continuum of wavelengths within certain spectral window. However, it is important to clarify the conditions in which these expressions can be safely used. In general, the weakly-guiding approximation is valid in situations where the refractive index contrast between the core and the cladding is 'low' such as it is typically the case in doped silica cores embedded in a silica cladding where the difference is on the order of $\Delta n = 5\ 10^{-3}$. Also, Eq. (5) assumes the interaction between circular cores with the same size and the same optical parameters. This is also commonly encountered in real structures. Typical conditions in which the weakly guiding approximation has proved valid can be found in the context of optoelectronic devices [5], communication structures [8], and sensing devices as the ones that will be discussed in the following sections.

3 Two- and Seven-Core Fibers

Here we will focus our attention to two particular multicore fibers (MCF) that have been exploited in a number of applications—the two-core and seven-core structures. The two-core fiber (TCF) is an asymmetrical design in which one of the cores is located at the center of the fiber while the other core is off-axis, while the seven-core fiber (SCF) consists of an array of 6 cores symmetrically disposed around a central core.

The TCF and SCF can be considered as part of a subset of MCFs consisting of a central core surrounded by N cores symmetrically disposed around it, as shown in Fig. 3.

For the case in which all the cores have the same size and they are symmetrically disposed around the central core such that there are only two characteristic coupling coefficients in the structure i.e. one for the coupling between external cores and another for the coupling between the central and external cores, the N-by-N system of coupled differential equations obtained from Eq. (1) reduces to two equations that can be solved analytically for the amplitude of the electric field in the central and (any of the) external cores [9]:

$$a(z) = e^{iCz}\left[a_0\left(\cos(qz) - \frac{iC}{q}\sin(qz)\right) + b_0\left(\frac{in\kappa}{q}\sin(qz)\right)\right] \tag{9}$$

$$b(z) = e^{iCz}\left[a_0\left(\frac{i\kappa}{q}\sin(qz)\right) + b_0\left(\cos(qz) + \frac{iC}{q}\sin(qz)\right)\right] \tag{10}$$

where $q = \sqrt{C^2 + nK^2}$ with n the number of cores around the central one, C and K are the coupling coefficients for the external-external and external-central interaction, respectively, and a_0 and b_0 are the initial i.e. at z = 0, amplitudes of the field in

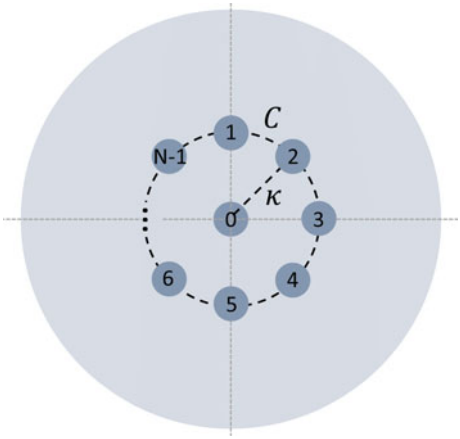

Fig. 3 N-core coupled structure consisting of (N-1) cores symmetrically disposed around a central core. For similar cores, two coupling constants characterize the entire system

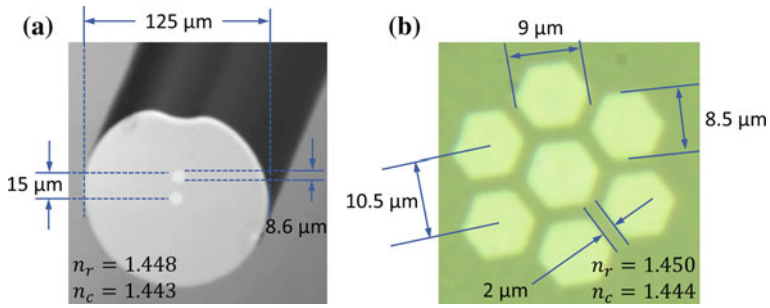

Fig. 4 Pictures of the cross sections of the two- (TCF) and the seven-core fiber (SCF)

the central and the external cores. In the typical experimental situation in which a section of MCF is spliced between two single-mode fibers (SMF) for sensor interrogation only the central core is excited at z = 0 i.e. $a_0 = 1$ and $b_0 = 0$. The usefulness of analytical expressions like Eq. (9) becomes evident when the spectral response of the coupled structure is to be modeled.

The experiments referred throughout this chapter were performed with a TCF and a SCF kindly provided by ACREO and the Microstructured Fibers and Devices Group at CREOL-UCF, respectively. Figure 4 shows pictures of the cross-sections of these fibers with the relevant dimensions indicated and the refractive index of the core and cladding, n_r and n_c, respectively, provided by the manufacturers at free-space wavelength of 1550 nm.

From the experimental standpoint MCFs having the structure of Fig. 3, such as TCF and SCF, have the advantage of having a core at the center of the structure. This permits direct splice to standard single-mode fibers e.g. SMF-28, which not only simplifies the fabrication and ensures the reproducibility of sensing devices but also allows for a direct interrogation of the interaction between the MCF and its surroundings via the external cores through the central one.

4 Refractive Index Sensing: Two-Core Fiber Refractometer

Refractive index (RI) sensors are useful in a number of applications ranging from quality control and industrial processing, mainly in the food industry and environmental contamination monitoring, to chemical and biological analysis, biomedical applications, and specimen detection [10, 11]. A general overview of the state of the art including the largest sensitivity reported for a variety of techniques using different types of fibers (not only MCF) can be found in Ref. [12].

More detailed reviews for the specific cases of fiber gratings and photonic crystal fibers can be found in Refs. [13–15].

Briefly, the main characteristics of the most common RI sensing architectures are highlighted below. RI sensors based on photonic crystal fibers (PCF) have been demonstrated in both transmission and reflection configurations. These sensors are capable of operating over a wide range of RI with linear response. The drawbacks are mainly the large interaction lengths required to achieve appreciable changes and the overall low sensitivity (190.9 nm/RIU and 6.67 nm/RIU for transmission and reflection configurations, respectively) [16, 17]. Grating-based RI sensors also exhibit low intrinsic sensitivity for both long-period (LPFG) and Bragg (FBG) fiber gratings. This sensitivity has been enhanced significantly by improving the coupling between the core and cladding modes by means of tilted gratings (340 nm/RIU) [18], and even more when these gratings are inscribed into PCFs (2000 nm/RIU) [19]. In terms of in-fiber interferometers for RI sensing, Michelson and Mach-Zehnder architectures are the most commonly exploited since the fabrication process can be done in a relatively simple way by abrupt tapering and micro-machining. In this sense, micro-machined cavities (9,300 nm/RIU) [20, 21] provide a sensitivity that is orders of magnitude larger than the one that can be achieved by tapering (30 nm/RIU) [22–24].

Other RI sensing schemes have been demonstrated by using liquid-core structures [25]. These techniques operate based on the changes observed in the propagating modes transmitted through the structure such that the RI of the liquids used to fill the capillaries has to be larger than the RI of the capillary tube. These sensors exhibit large sensitivity (3250 nm/RIU) but the main drawbacks are the long interaction length and the limited operation range for sensing. Overall, these architectures are suitable for high-index sensing but cannot be used in most biological applications where the RI of aqueous solutions is commonly measured.

A first attempt for sensing RI employing a MCF was reported using a twin-core fiber [26]. This sensing architecture has a central core and a side core, which are not coupled, with the side core exposed to the external medium via chemical etching. By properly splicing this twin-core fiber to a SMF a Michelson interferometer is realized with a sensitivity of 826.8 nm/RIU. In this section we demonstrate different RI sensing applications of the TCF shown in Fig. 4a, which demonstrate the advantage of the coupled multicore geometry.

4.1 Principle of Operation

The principle of operation of RI sensing with MCF is illustrated with the simplest coupled system—the two-core structure. Recall arbitrary coupled systems are described on a pair-wise basis so the principle of operation shown below can be extended to N cores.

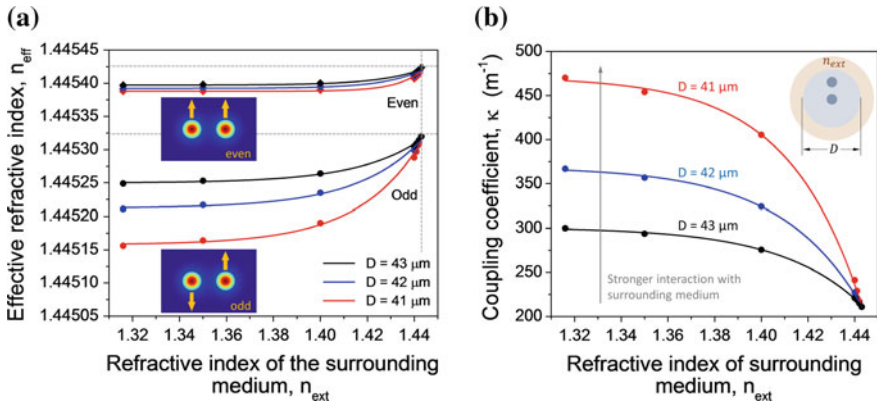

Fig. 5 Interaction between a two-core coupled system with finite-size cladding and an infinitely extended surrounding medium. **a** Effective refractive index of the even and odd coupled modes and **b** coupling coefficient, as a function of the refractive index of the surrounding media for different cladding diameters as indicated

Figure 5a shows the effective RI of the even and odd modes of a two-core coupled structure as it interacts with a surrounding medium of variable RI. The cores are embedded into a finite-size, circular cladding of diameter D and the whole coupled system i.e. cores and cladding, is surrounded by an infinite medium of uniform RI n_{ext} (see inset of Fig. 5b). In order to resemble realistic structures, one of the cores is located at the center of the cladding while the other is asymmetrically located off-axis. Similarly to how it was done previously, once the effective RI of the coupled modes are calculated, the coupling constant can be estimated by means of Eq. (4), as shown in Fig. 5b.

In this particular case, the cores are 8.6 μm in diameter and the refractive index of the cores and the cladding is 1.448 and 1.443, respectively, at a free-space wavelength of 1550 nm. The separation distance between the cores is kept fixed and only the RI of the external medium is allowed to vary. The plots show the effective indices and coupling constant for different diameters of the cladding as indicated. The dashed lines in Fig. 5a indicate the limit at which the RI of the surrounding media reaches the RI of the cladding.

From Fig. 5 it is important to realize that there is a maximum size for the cladding in order to interact with the surroundings. In other words, if the cladding it too thick the fiber does not 'see' the surrounding medium. Thus, the cores have to be exposed in order to induce this interaction. Naturally, with decreasing cladding diameter the strength of the interaction increased and larger changes in the coupling constant can be achieved.

From Fig. 5b, it is clear that the smaller the cladding the stronger the interaction with the surroundings. However, as it was shown before (see Fig. 2), the stronger interactions are the result of larger differences in the effective indices of the coupled modes. This produces a propagation constant mismatch whose effects are in complete analogy with the dephasing effects in standard directional couplers [2, 7].

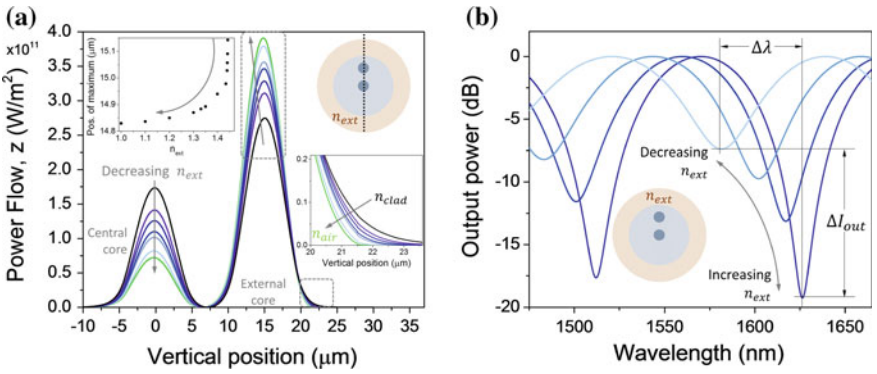

Fig. 6 **a** Power flow profile of the odd coupled mode, along the *dashed line* in the *inset*, for decreasing RI of the external medium. The *insets* show that the extent of the evanescent tail reduces and the position of maximum power flow moves towards the central core as the RI of the external core decreases. **b** In general, in RI sensing the spectral response of the coupled system exhibits both spectral shift associated to changes in the coupling constant and contrast variations due to mismatch between the propagation constants of the coupled modes

A more insightful explanation can be pursued in terms of the intensity or energy flow distribution in the coupled structure, as it is shown in Fig. 6a for the odd coupled mode of the above-described structure. Two main things happen when the RI of the external medium decreases. First, as the RI of the external medium decreases, both the extent of the evanescent tail above the off-axis core decreases and the position of the maximum power within the off-axis core slightly moves towards the central core, as shown in the insets of Fig. 6a. In other words, the field distribution of the coupled mode in the region of the off-axis core is 'pushed' towards the central core as the RI contrast increases thus producing a larger overlap in the region between the cores which results in a larger coupling coefficient. On the other hand, the power carried by each core dramatically unbalances due to the propagation constant mismatch.

Figure 6b shows the general spectral response of the two-core coupled system in RI sensing applications. The spectral response of this coupled system is expected to experience a red spectral shift as the RI of the external surrounding media increases. This shift is what is typically followed in spectrally operated RI sensors. Additionally, the contrast of the spectral response is expected to improve as the RI of the surrounding media increases. Again, this relates to the fact that the dephasing effects vanish in symmetric structures [2, 7].

The experimental setup employed for testing the performance of MCF-based spectrally operated RI sensors is schematically shown in Fig. 7. A fiber pigtailed broadband light source e.g. super luminescent diode (SLD), is used to spectrally interrogate the MCF sensor. After the optical signal propagates through the MCF sensor, the transmitted spectrum is acquired using a standard optical spectrum analyzer (OSA) (Anritsu MS9740A). This setup allows not only testing the sensors

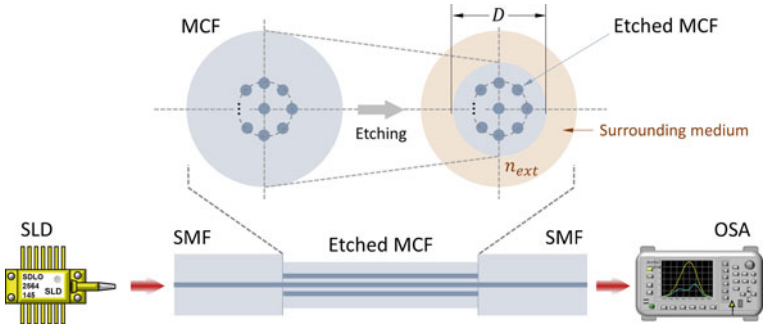

Fig. 7 Schematic of the experimental setup for spectrally operated refractive index multicore fiber sensors. The off-center cores of the MCF are exposed by etching material from the fiber cladding in order to induce the interaction with the surrounding medium. The sensitivity and contrast of the sensor response increase and decrease, respectively, with the etching depth

but also monitoring their response as the fiber cladding is being removed via chemical etching, which can be correlated with the amount of material being removed.

4.2 Binary Mixtures

A particular application where the ability to measure RI is important is related to binary mixtures. When two liquids are mixed the RI of the mixture has in general a RI that is different from that of the compunds and is related to the volume fraction of each constituent of the mixture. Therefore, by measuring the RI of the solution one could detect alterations in the composition and also control the mixture of two different liquids.

In order to test the performance of the TCF-based RI sensor to identify binary mixtures, we prepared a set of different solutions that gradually change from water to ethylene glycol. The water–ethylene glycol binary mixtures exhibit RI ranging from 1.331 (water) to 1.395 (ethylene glycol) at 1550 nm. The TCF-based RI sensor was slowly etched, and at different etching times we measured the transmitted spectrum for the set of binary mixtures. Figure 8a shows the net shift of the spectral response of the TCF-based RI sensor retrieved from the experiments. The net shift exhibits an exponential dependence on the refractive index of the external media. Net spectral shifts as large as 90 nm can be achieved for the deeper etching in this refractive index range, which is large enough to detect small changes in the binary mixture.

The sensor sensitivity can be tuned by means of the etching depth i.e. with the duration of the etching process, in order to optimize the free-spectral range of operation and avoid ambiguity in the measurements. Figure 8b shows the characterization of the sensitivity curve for different etching times. The characteristic

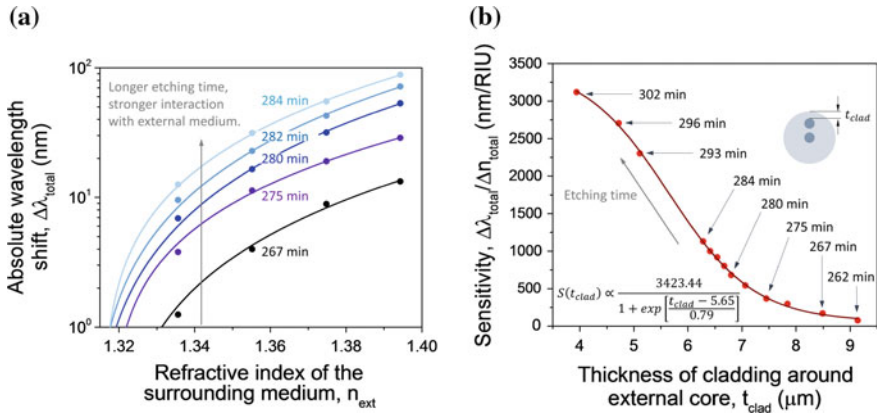

Fig. 8 Characterization of the TCF-based RI sensor. **a** Absolute wavelength shift, after different etching times, for sensing the refractive index of water-ethylene glycol binary mixtures. **b** Sensitivity curve as a function of the thickness of the cladding around the off-axis core (Data points from Ref. [12])

S-shape confirms that when the cladding is too thick the MCF does not interact with the surroundings. It also shows that the sensitivity saturates which is expected as the sensitivity will not further increase once the cladding is entirely removed. The largest sensitivity experimentally demonstrated for this asymmetrically etched TCF is 3119 nm/RIU for the RI range from 1.3160 to 1.3943. From the fitting of the sensitivity curve (Fig. 7b) an even larger sensitivity (>3480 nm/RIU) can be achieved in the limit where the cladding around the external core is removed completely. Other experimental details, such as the actual spectra measured in the experiments, can be found in Ref. [12].

4.3 Salinity

Conceptually, salinity is related to the quantity of dissolved salt content in water. Although this is a simple fact, there are two main areas where salinity sensors are needed. Firstly, earth scientists are required to constantly monitor the salinity of seawater because even small variations of the ocean surface salinity can have dramatic effects on the water cycle and ocean circulation. On the other hand, contamination of freshwater aquifers with saline seawater is a major issue in coastal areas, where the aquifer is the main resource of drinking water. In both situations, since the amount of dissolved salt will effectively change the RI of the water, fiber-based RI sensors have been used to measure salinity of water solutions.

The majority of fiber optic salinity sensors are based on FBG structures [27–29]. There are, however, some other reports using PCF [30], displacement and differential measurements [31, 32], in-fiber interferometers [33], and fiber resonators [34, 35],

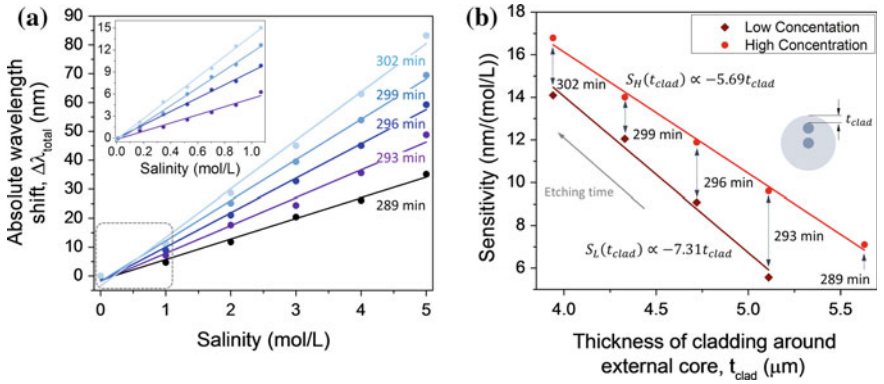

Fig. 9 **a** Absolute wavelength shift of the TCF sensor response for salinity sensing in the high concentration range up to 5 M. The *inset* shows the sensor response in the low-concentration regime highlighted by the *dashed rectangle*. **b** Sensitivity curve of the TCF salinity sensor as a function of the thickness of the cladding around the off-axis core in the high- and low-concentration regime. In both cases, the sensor sensitivity has a linear dependence on the thickness of the cladding and, similarly to the previous case, the sensor sensitivity can be tuned by means of the etching depth i.e. with the duration of the etching process (Data points from Ref. [36])

that have proved to be suitable for salinity sensing. Some of the drawbacks commonly encountered in these type of sensors is the low sensitivity, which of course can always be improved by using enhancing mechanisms e.g. polyamide coatings. One should exert care in choosing adequate materials to avoid degradation of the coatings when immersed in the saline solutions for long periods of time.

In order to evaluate the performance of our TCF-based RI sensor for salinity measurements, saline solutions with different salt concentrations were prepared in order to cover regimes of low (0–1 M) and high concentration (0–5 M). Figure 9a shows the experimental results for salinity sensing for different etching times as indicated. The main plot in Fig. 9a spans the salinity range up to typical values of sea water while the inset shows the performance in the low-concentration regime (dashed rectangle). In both scenarios the spectrum red-shifts with increasing salt content, and the spectral shift can be directly correlated to the solution concentration. It can also be noticed that the response is highly linear for both concentration ranges. We should also highlight that even in the low-concentration regime, which has smaller RI variations, an absolute wavelength shift of 15 nm for the largest etching time (302 min) can be observed and each saline solution in the low-concentration range can be clearly identified. Similar to the case of binary mixtures, the sensitivity is increased as the cladding thickness around the external core is reduced. As shown in Fig. 9b, the sensitivity as a function of the cladding thickness is also highly linear, achieving a maximum sensitivity of 16.7914 nm/(mol/L) for the high-concentration and 14.0917 nm/(mol/L) for the low-concentration measurements. The experiments demonstrate the capability of the TCF-based sensor to perform salinity measurements with high sensitivity over a wide range of concentrations. The highest

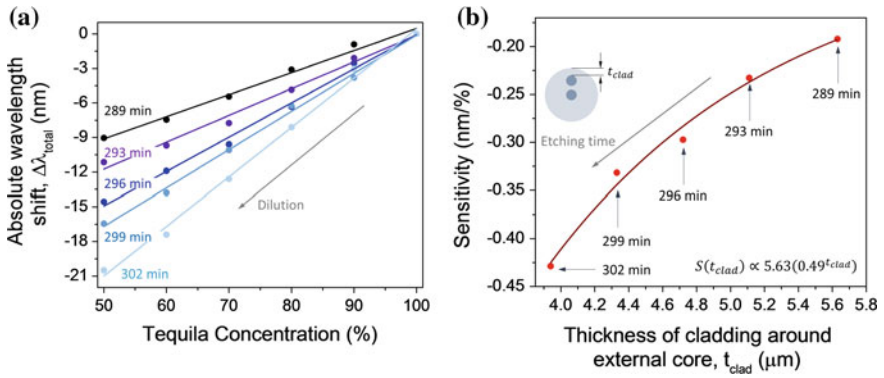

Fig. 10 **a** Absolute wavelength shift of the TCF sensor response for adulterated alcoholic beverages. **b** Sensitivity curve of the TCF sensor as a function of the thickness of the cladding around the off-axis core. In both cases, the sensor sensitivity has a linear dependence on the thickness of the cladding and, similarly to the previous case, the sensor sensitivity can be tuned by means of the etching depth i.e. with the duration of the etching process (Data points from Ref. [12])

sensitivity of 16.7914 nm/(mol/L) is more than 20 times larger than that recently reported for polyamide-coated PCF and polyamide-coated FBG. Other experimental details, such as the actual spectra measured in the experiments, can be found in Ref. [36].

4.4 Other Applications

Based on the previous results it is evident that the TCF-based RI sensor can be useful in other applications where measuring RI is critical. Other common applications of RI sensing of great interest in industrial environments include the detection of poisonous specimens e.g. ammonia [37], adulterated fuels e.g. gasoline [38], and altered commercial products e.g. alcoholic beverages [39].

The performance of the TCF-based RI sensor presented in the previous sections in the particular context of adulteration of alcoholic beverages is summarized in Fig. 10.

In order to test the TCF-based sensor for the detection of adulterated beverages, we prepared a set of solutions of Tequila diluted with water. The commercial tequila used in the experiments was Jose Cuervo Tradicional™, which was verified to be a certified tequila. The set of solutions ranges from pure tequila to a 50/50 volume percent diluted solution. Taking into account reported RI values for tequila, we estimate the RI of the tested solutions to be in the range from 1.3338 to 1.3518 at 1550 nm. The absolute wavelength shift of the TCF-based sensor as a function of the tequila concentration for different etching times is shown in Fig. 10a. We can observe that the response is highly linear, with a maximum sensitivity of

−0.42871 nm/% for an etching time of 302 min. As shown in Fig. 10b, this sensitivity is good enough to easily discriminate changes of 1 % of water adulteration, which can be critical if other adulterant such as ethanol or ethylene glycol is used instead of water. The experimental results and the sensor sensitivity show that these sensing platforms are feasible for developing adulteration-detection devices for law enforcement purposes. Other experimental details, such as the actual spectra measured in the experiments, can be found in Ref. [12].

5 Temperature Sensing

Spectrally operated fiber optics temperature sensors have been demonstrated using FBG and LPFG, specialty fibers such as D-shaped fibers and PCF, multimode fibers (MMF), and more recently MCF. A general overview of the state of the art including the largest sensitivity reported for a variety of techniques using different types of fibers can be found in Ref. [40].

A common feature in all these sensors, regardless of the sensing mechanisms and the type of fibers used, is their low sensitivity. Grating-based temperature sensors (FBGs and LPFGs) have sensitivities of only of a few tens of pm/°C (<100 pm/°C) in the low temperature regime for the case of bare gratings [41–43]. This sensitivity can be increased by inscribing chirped LPFGs (up to 150–300 pm/°C) [44] or by inscribing the grating on fibers with special doping such as boron-germanium (B-Ge) co-doped fibers (3.4 nm/°C) [45].

Interferometric techniques are well known for having high sensitivities and compact architectures in most applications. However, for temperature sensing applications using in-line schemes they have in general low sensitivity regardless of the configuration of the interferometer i.e., Fabry-Perot, Fizeau, and Mach-Zehnder, (<50 pm/°C up to 200 °C and about 100 pm/°C for higher temperatures) [46–50]. Similarly to grating-based sensors, the sensitivity can be enhanced by using special fibers e.g. highly birefringent fibers (0.25 nm/°C) [51]. The largest improvement for interferometric temperature sensing has been achieved by means of the interference of multiple modes (9.9 nm/°C) [52, 53].

Sensing structures based on PCFs also exhibit low sensitivity in spite of the implementation of sensitivity enhancement approaches such as tapering (<100 pm/°C) [54, 55]. In the particular case of PCF, there is also the drawback that long interaction lengths (on the order of tens of centimeters) are needed to induce appreciable changes in the spectral response. Temperature sensors based on MMFs permit compact sensing schemes but they also have low sensitivity (<50 pm/°C for low temperature and on the order of 100 pm/°C for high temperature) [56–60]. Similar sensitivities are obtained even if the interference is restricted to only a few modes by using graded-index MMF [57].

MCF are not the exception. The use of MCFs has also been demonstrated in high-temperature applications [61, 62] and similarly to the above-mentioned fiber optics sensors their sensitivity remains low (50 pm/°C) regardless of the number of

cores of the MCF. The reason why the vast majority of optical fiber temperature sensors, including those using 'bare' MCFs, exhibit low sensitivity regardless of the technique and the type of fiber is that they rely on the inherently low thermo-optic coefficient (TOC) of silica (1×10^{-5} °C^{-1}). Nevertheless, large temperature response i.e. high sensitivity, is desired especially in biological and medical applications in which a tight temperature control is mandatory and small temperature changes are to be detected [11, 63].

It has been recognized that this limitation can be overcome, and therefore the sensitivity can be increased dramatically, by involving other elements in the experimental setup with stronger temperature dependence in order for the optical signals to experience larger changes. For instance, by taking advantage of the large thermal expansion of metallic elements i.e. V-groove fiber holders, a Fabry-Perot configuration has been reported with sensitivity up to 260.7 nm/°C [64]. This is orders of magnitude larger than what is obtained when only the thermal properties of bare fibers come into play.

Other possibilities include using materials with large thermo-optic response instead. Significant enhancement of the sensitivity has been demonstrated using PCF-based temperature sensors infiltrated with alcohol and index matching liquids (up to 42.818 nm/°C) [65–68]. Large enhancements have also been reported for sensors based on MMI effects using polymer coatings (−3.195 nm/°C) [69], and liquid-core (up to 20 nm/°C) [40]. In the case of this liquid-core MMI device it was shown that the sensitivity for operating in a specific temperature range can be tuned by simply selecting the liquid in order to optimize the free-spectral range of the device.

Proof-of-concept experiments for temperature sensing were performed using a SCF. Figure 11 summarizes the results. In these experiments temperature sensing is

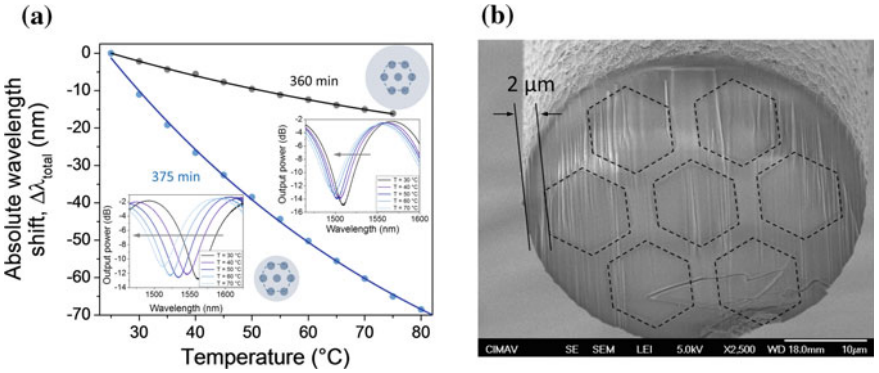

Fig. 11 **a** Absolute wavelength shift of the SCF temperature sensor for two different etching times. The experiments were performed using the setup from Fig. 7, using refractive index matching oil with large TOC as the surrounding medium. The *insets* show the actual spectral response obtained in the experiments for some of the measured temperatures. **b** SEM picture of the cross section of the SCF after 375 min of etching showing that the thickness of the cladding is of only 2 µm. The interaction between the etched SCF and the surroundings is strong due to the thin cladding

performed based on thermo-optic effects via the interaction of an etched SCF with a surrounding medium with large TOC i.e. the cores of the SCF are exposed by removing material from the cladding. These experiments were carried out by using the same setup shown in Fig. 7 for RI sensing but, unlike the asymmetric etching performed in the case of the TCF, here the SCF was uniformly etched. The surrounding medium used in the experiments was Cargille index matching liquid (Series AA, 1.452 at 653 nm and 25 °C, TOC -3.9×10^{-4} °C^{-1}).

As shown in the insets of Fig. 11a the spectrum is blue shifted as the temperature is increased, which is expected due to the negative value of the TOC. We can also notice that the sensitivity increases about four times, from −0.3 to −1.25 nm/°C, approximately, when the etching time is increased from 360 to 375 min.

Figure 11b shows a SEM picture of the cross section of the SCF after 375 min of etching. The SEM picture shows that the thickness of the cladding around the external cores is only 2 μm. It is worth highlighting that having tight control on the etching process is required to achieve this thickness since the etching rate dramatically increases close to the cores.

Although the maximum sensitivity achieved with the SCF sensor is not as large as compared to other temperature sensors, the sensitivity can be increased by simply using surrounding media with larger TOCs and the operation range can be pushed towards higher temperatures by using solid surrounding media e.g. polymer coatings. Nevertheless the sensitivity can be enhanced dramatically by inducing longer evanescent tails that result in a stronger interaction with the surrounding medium. This can be done by using high-index thin layers as it has been done in fiber devices based on multimode interference effects [70–73], or by using metal coatings as in the case of in-fiber plasmonic devices [74–77].

It is important to highlight that the above-mentioned sensitivities can be estimated in terms of RI units by simply taking the nominal TOC of the surrounding medium. For a TOC of 1×10^{-4} RIU/°C the sensitivities are estimated to be 3×10^{3} nm/RIU and 1.25×10^{4} nm/RIU for etching times 360 min to 375 min, respectively. The sensitivity value of 1.25×10^{4} nm/RIU, when the cladding around the cores is only 2 μm, is about three times larger than the maximum sensitivity achieved with the TCF (see Fig. 8b). With this sensitivity it can be estimated that in principle RI changes on the order of 10^{-5} could be detected with a lab scale OSA with resolution of 0.1 nm, which strongly suggests that MCF could be suitable for biological applications.

6 Curvature Sensing

Monitoring the structural health of buildings and bridges has gained wide acceptance in order to avoid catastrophic accidents. A simple way to do this is to measure the deformation of the structure, which can be transferred to a device attached to the structure and thus the deformation can be measured via the stress experienced by the attached device. In this respect, fiber optics sensors are being used to perform

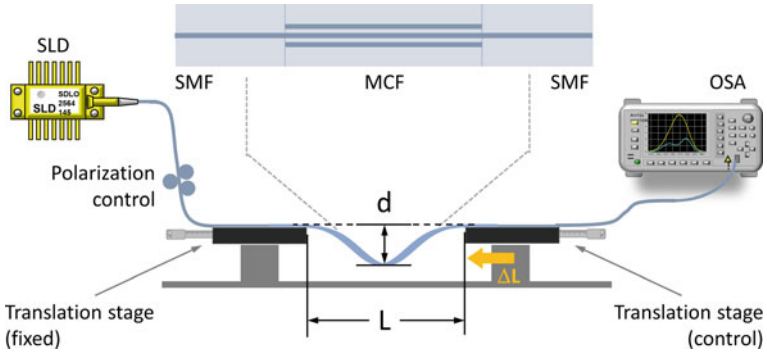

Fig. 12 Schematic experimental setup for curvature sensing using a fixed ends configuration for the evaluation of static states of curvature

this task. Stress-based fiber optics sensors including bending or curvature sensors are typically tested by isolating the section of fiber containing the responsive structure from the rest of the fiber and loading it in a controllable manner [78]. In the case of bending sensors there are a number of different configurations commonly used. For instance, in order to induce a pure bending stress, the fiber can be point-like supported at the extremes and loaded at the center [79–83]. Other configurations include inducing a constant radius of curvature by coiling the fiber [84–88] and bending the fiber in a beam-like fashion i.e. cantilever, for reflection configurations [89–91]. Nevertheless, the most common configuration consists on clamping both ends of the fiber to translation stages and displacing controllably one of these stages, in a step-like fashion, towards the other stage therefore bending the section of fiber containing the sensing region into a static configuration of known curvature [92–110]. The experimental results shown in this section refer to this particular configuration, which is schematically depicted in Fig. 12.

Figure 13 shows some experimental results regarding the performance of a TCF- and SCF-based curvature sensor. In these experiments the interaction length i.e. length of MCF, is 50 mm and 10 mm for the TCF and SCF, respectively. Further details on the experiments and modeling can be found in Ref. [106]. The results shown in Fig. 13 do not intent to directly compare between these two sensors as the interaction length is different in each case. Instead, these results show that different MCF can be used for optimum operation depending upon the curvature range, the sensitivity required for the measurement, and the size restrictions imposed by the conditions in which the sensor is to operate. In the particular case shown here, the TCF curvature sensor exhibits much larger sensitivity in the small-curvature regime at the expense of having longer interaction length while the more compact SCF sensor is capable to operate over a larger curvature range at the expense of exhibiting low sensitivity.

It is worth mentioning that, unlike other stress-related scenarios in bending there are several stress contributions in general e.g. axial compressive and bending

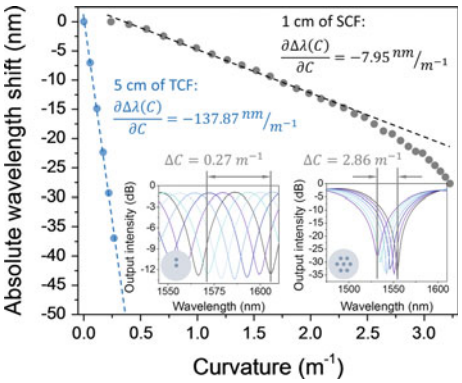

Fig. 13 Performance of TCF- and SCF-based curvature sensors with interaction length of 50 mm and 10 mm, respectively. The *insets* show the actual spectral response measured in the experiments. The free-spectral range of the curvature sensor can be optimized not only from the sensitivity perspective but also from the stand point of the interaction length such that compact and maximally sensitive sensors can be fabricated (Data points for the TCF from Ref. [106])

component. The net effect of these contributions depends not only on the actual curvature but also on the type of support at the ends e.g. point-like ends or fixed ends. In practically all the above-mentioned reports it has been recognized, not only for the numerical modeling and the derivation of theoretical expressions but also in the experiments, that when using MCFs in bending applications the situation dramatically complicates if the fiber is not limited to bend in a single plane and/or twisting is not completely avoided. Experimentally, when the fiber is allowed to bend in more than one plane, a plateau in the shift-curvature response curve appears at initial stages of the experiment i.e. small curvatures, until the bending component significantly dominates over the others [107, 109]. This unusual 'delay' in the sensor response is rather a detrimental effect for sensitive operation in the small-curvature regime [91, 106, 110]. To emphasize this point one can compare the experimental results from Fig. 12 with those from Ref. [107]. In both cases the same SCF was used and yet the sensitivity is more than 2 times larger when the fiber is carefully restricted to bend in a single plane. Together with the increase in sensitivity one can have spectral response with larger contrast (>20 dB) when the competition between the stress components is avoided i.e. single-plane bending, such that these MCF-based structures can be suitable in other applications such as bending-tuned band rejection filters. Some other aspects that are to be taken into account in MCF-based stress sensors involving bending components refer to the variations of the contrast in the spectral response as the experiment progresses. This includes the increase in the contrast of the spectral response with increasing curvature due to stress homogenization across the optical fiber. Further details on the stress homogenization mechanisms that drive the contrast characteristics in spectrally operated multicore fiber optic bending sensors can be found elsewhere [111].

7 Summary

Fiber optic sensors based on multicore coupled structures were reviewed in this chapter. The advantage of the coupled MCF is that the coupling mechanism is highly sensitive to small changes of the effective RI of the propagating mode. Therefore, their implementation to perform different sensing applications is widely investigated. As demonstrated in this chapter, they can be used to measure several physical variables, but there are some applications where multicore fibers offer certain advantages as compared to conventional fiber sensors. Currently, MCF sensors are based on symmetric configurations, i.e. same coupling constant between cores. However, future developments should incorporate asymmetric designs and also their combination with microstructured designs to provide more versatility to the MCF sensors.

Acknowledgments José Rafael Guzmán-Sepúlveda acknowledges CONACyT for their support through a Ph.D. scholarship. Also, J.R.G.S. gratefully acknowledges fruitful discussions with Armando Pérez-Leija. The TCF and SCF were kindly provided by ACREO (Sweden) and the Microstructured Fibers and Devices Group at CREOL-UCF (USA), respectively.

References

1. N. Kishi, E. Yamashita, A simple coupled-mode analysis method for multiple-core optical fiber and coupled dielectric waveguide structures, in *Microwave Symposium Digest, 1988, IEEE MTT-S International* (IEEE, 1988), pp. 739–742
2. K. Okamoto, *Fundamentals of Optical Waveguides*, 2nd edn. (Academic Press, Elsevier, 2006)
3. A. Hardy, W. Streifer, Coupled mode theory of parallel waveguides. J. Lightwave Technol. **LT-3**(5), 1135–1146 (1985)
4. W. Snyder, Coupled-mode theory for optical fibers. J. Opt. Soc. Am. **62**(11), 1267–1277 (1972)
5. H. Kogelnik, R.V. Schmidt, Switched directional couplers with alternating $\Delta\beta$. IEEE J. Quantum Electron. **12**(7), 396–401 (1976)
6. A.W. Snyder, P. Richmond, Effect of anomalous dispersion on visual photoreceptors. J. Opt. Soc. Am. **62**(11), 1278–1283 (1972)
7. Y. Murakami, S. Sudo, Coupling characteristics measurements between curved waveguides using a two-corefiber coupler. Appl. Opt. **20**(3), 417–422 (1981)
8. C. Xia, N. Bai, I. Ozdur, X. Zhou, G. Li, Supermodes for optical transmission. Opt. Express **19**(17), 16653–16664 (2011)
9. A. Perez-Leija, J.C. Hernandez-Herrejon, H. Moya-Cessa, A. Szameit, D.N. Christodoulides, Generating photon-encoded W states in multiport waveguide-array systems. Phys. Rev. A **87**(1), 013842 (2013)
10. S. Yin, C. Zhan, P. Ruffin, Fiber optic bio and chemical sensors, in *Fiber Optic Sensors*, ed. by S.S. Yin, P. Ruffin (Wiley, 2002)
11. M. Ben-David, I. Gannot, Optical fibers for biomedical applications, in *Specialty Optical Fibers Handbook*, ed. by A. Méndez, T.F. Morse (Academic Press, 2011)

12. J.R. Guzmán-Sepúlveda, R. Guzmán-Cabrera, M. Torres-Cisneros, J.J. Sánchez-Mondragón, D.A. May-Arrioja, A highly sensitive fiber optic sensor based on two-core fiber for refractive index measurement. Sensors **13**(10), 14200–14213 (2013)
13. L. Zhang, W. Zhang, I. Bennion, Ch. 4 "In-fiber grating optic sensors," in *Fiber optic sensors*, ed. by S.S. Yin, P. Ruffin (Wiley, 2002)
14. R. Kashyap, Ch. 10 "Principle of optical fiber grating sensors," in *Fiber Bragg gratings*, 2nd edn. (Academic Press, 2012)
15. S. Silva, P. Roriz, O. Frazão, Refractive index measurement of liquids based on microstructured optical fibers, in *Photonics,* vol. 1, No. 4 (Multidisciplinary Digital Publishing Institute, 2014), pp. 516–529
16. R. Jha, J. Villatoro, G. Badenes, V. Pruneri, Refractometry based on a photonic crystal fiber interferometer. Opt. Lett. **34**(5), 617–619 (2009)
17. J. Villatoro, M.P. Kreuzer, R. Jha, V.P. Minkovich, V. Finazzi, G. Badenes, V. Pruneri, Photonic crystal fiber interferometer for chemical vapor detection with high sensitivity. Opt. Express **17**(3), 1447–1453 (2009)
18. K. Zhou, L. Zhang, X. Chen, I. Bennion, Optic sensors of high refractive-index responsivity and low thermal cross sensitivity that use fiber Bragg gratings of > 80 tilted structures. Opt. Lett. **31**(9), 1193–1195 (2006)
19. Z. He, Y. Zhu, H. Du, Long-period gratings inscribed in air-and water-filled photonic crystal fiber for refractometric sensing of aqueous solution. Appl. Phys. Lett. **92**(4), 4105 (2008)
20. T. Wei, Y. Han, Y. Li, H.L. Tsai, H. Xiao, Temperature-insensitive miniaturized fiber inline Fabry-Perot interferometer for highly sensitive refractive index measurement. Opt. Express **16**(8), 5764–5769 (2008)
21. Y. Wang, M. Yang, D.N. Wang, S. Liu, P. Lu, Fiber in-line Mach-Zehnder interferometer fabricated by femtosecond laser micromachining for refractive index measurement with high sensitivity. JOSA B **27**(3), 370–374 (2010)
22. Z. Tian, S.S. Yam, H.P. Loock, Refractive index sensor based on an abrupt taper Michelson interferometer in a single-mode fiber. Opt. Lett. **33**(10), 1105–1107 (2008)
23. P. Lu, L. Men, K. Sooley, Q. Chen, Tapered fiber Mach-Zehnder interferometer for simultaneous measurement of refractive index and temperature. Appl. Phys. Lett. **94**(13), 131110 (2009)
24. Y. Li, L. Chen, E. Harris, X. Bao, Double-pass in-line fiber taper Mach-Zehnder interferometer sensor. Photonics Technol. Lett. IEEE **22**(23), 1750–1752 (2010)
25. H.W. Lee, M.A. Schmidt, P. Uebel, H. Tyagi, N.Y. Joly, M. Scharrer, P.S.J. Russell, Optofluidic refractive-index sensor in step-index fiber with parallel hollow micro-channel. Opt. Express **19**(9), 8200–8207 (2011)
26. A. Zhou, Y. Zhang, G. Li, J. Yang, Y. Wang, F. Tian, L. Yuan, Optical refractometer based on an asymmetrical twin-core fiber Michelson interferometer. Opt. Lett. **36**(16), 3221–3223 (2011)
27. L. Men, P. Lu, Q. Chen, A multiplexed fiber Bragg grating sensor for simultaneous salinity and temperature measurement. J. Appl. Phys. **103**(5), 053107 (2008)
28. L. Marrec, T. Bourgerette, E. Datin, N. Ferchaud, B. Pucel, L. Quetel, D. Tregoat, In-situ optical fibre sensors for temperature and salinity monitoring, in *Oceans 2005-Europe* vol. 2 (IEEE, 2005), pp. 1276–1278
29. J. Cong, X. Zhang, K. Chen, J. Xu, Fiber optic Bragg grating sensor based on hydrogels for measuring salinity. Sens. Actuators B: Chem. **87**(3), 487–490 (2002)
30. C. Wu, B.O. Guan, C. Lu, H.Y. Tam, Salinity sensor based on polyimide-coated photonic crystal fiber. Opt. Express **19**(21), 20003–20008 (2011)
31. H.A. Rahman, S.W. Harun, M. Yasin, H. Ahmad, Fiber-optic salinity sensor using fiber-optic displacement measurement with flat and concave mirror. IEEE J. Select. Topics Quantum Electr. **18**(5), 1529–1533 (2012)
32. Y. Zhao, X. Zhang, T. Zhao, B. Yuan, S. Zhang, Optical salinity sensor system based on fiber-optic array. Sens. J. IEEE **9**(9), 1148–1153 (2009)

33. L.V. Nguyen, M. Vasiliev, K. Alameh, Three-wave fiber Fabry-Pérot interferometer for simultaneous measurement of temperature and water salinity of seawater. Photonics Technol. Lett. IEEE **23**(7), 450–452 (2011)
34. S. Wang, J. Wang, G. Li, L. Tong, Modeling optical microfiber loops for seawater sensing. Appl. Opt. **51**(15), 3017–3023 (2012)
35. S. Robinson, R. Nakkeeran, Photonic crystal based sensor for sensing the salinity of seawater, in *2012 International Conference on Advances in Engineering, Science and Management (ICAESM)* (IEEE, 2012), pp. 495–499
36. J.R. Guzman-Sepulveda, V.I. Ruiz-Perez, M. Torres-Cisneros, J.J. Sanchez-Mondragon, D. A. May-Arrioja, Fiber optic sensor for high-sensitivity salinity measurement. Photonics Technol. Lett. IEEE **25**(23), 2323–2326 (2013)
37. A.J. Rodríguez, C.R. Zamarreño, I.R. Matías, F.J. Arregui, R.F.D. Cruz, D.A. May-Arrioja, A fiber optic ammonia sensor using a universal pH indicator. Sensors **14**(3), 4060–4073 (2014)
38. A.R. Rodríguez, D.M. Camacho, K.G. Gutiérrez, D.A. May-Arrioja, R.D. Cruz, I.R.M. Maestro, C.R. Zamarreño, Rum adulteration detection using an optical fiber sensor based on multimodal interference (MMI). Optica pura y aplicada **46**(4), 345–352 (2013)
39. A.J.R. Rodríguez, O. Baldovino-Pantaleón, R.F.D. Cruz, C.R. Zamarreño, I.R. Matías, D.A. May-Arrioja, Gasohol quality control for real time applications by means of a multimode interference fiber sensor. Sensors **14**(9), 17817–17828 (2014)
40. M.A. Fuentes-Fuentes, D.A. May-Arrioja, J.R. Guzman-Sepulveda, M. Torres-Cisneros, J. J. Sánchez-Mondragón, Highly sensitive liquid core temperature sensor based on multimode interference effects. Sensors **15**(10), 26929–26939 (2015)
41. J. Jung, H. Nam, B. Lee, J.O. Byun, N.S. Kim, Fiber Bragg grating temperature sensor with controllable sensitivity. Appl. Opt. **38**(13), 2752–2754 (1999)
42. K.H. Smith, B.L. Ipson, T.L. Lowder, A.R. Hawkins, R.H. Selfridge, S.M. Schultz, Surface-relief fiber Bragg gratings for sensing applications. Appl. Opt. **45**(8), 1669–1675 (2006)
43. V.R. Mamidi, S. Kamineni, L.S.P. Ravinuthala, S.S. Madhuvarasu, V.R. Thumu, V.R. Pachava, P. Kishore, Fiber Bragg Grating-based high temperature sensor and its low cost interrogation system with enhanced resolution. Optica Applicata **44**(2) (2014)
44. A.D. Kersey, M.A. Davis, H.J. Patrick, M. LeBlanc, K.P. Koo, C.G. Askins, M.A. Putnam, E.J. Friebele, Fiber grating sensors. J. Lightwave Technol. **15**(8), 1442–1463 (1997)
45. X. Shu, L. Zhang, I. Bennion, Sensitivity characteristics of long-period fiber gratings. J. Lightwave Technol. **20**(2), 255 (2002)
46. X. Chen, F. Shen, Z. Wang, Z. Huang, A. Wang, Micro-air-gap based intrinsic Fabry-Perot interferometric fiber-optic sensor. Appl. Opt. **45**(30), 7760–7766 (2006)
47. J. Zhang, Y. Zhang, W. Sun, L. Yuan, Multiplexing multimode fiber and Fizeau etalon: a simultaneous measurement scheme of temperature and strain. Meas. Sci. Technol. **20**(6), 065206 (2009)
48. Q. Li, C.H. Lin, P.Y. Tseng, H.P. Lee, Demonstration of high extinction ratio modal interference in a two-mode fiber and its applications for all-fiber comb filter and high-temperature sensor. Optics Commun. **250**(4), 280–285 (2005)
49. J. Ma, J. Ju, L. Jin, W. Jin, D. Wang, Fiber-tip micro-cavity for temperature and transverse load sensing. Opt. Express **19**(13), 12418–12426 (2011)
50. L. Jiang, J. Yang, S. Wang, B. Li, M. Wang, Fiber Mach-Zehnder interferometer based on microcavities for high-temperature sensing with high sensitivity. Opt. Lett. **36**(19), 3753–3755 (2011)
51. P. Hlubina, M. Kadulova, D. Ciprian, P. Mergo, Temperature sensing using the spectral interference of polarization modes in a highly birefringent fiber. Opt. Lasers Eng. **70**, 51–56 (2015)
52. P. Hu, Z. Chen, M. Yang, J. Yang, C. Zhong, Highly sensitive liquid-sealed multimode fiber interferometric temperature sensor. Sens. Actuators A **223**, 114–118 (2015)

53. G. Numata, N. Hayashi, M. Tabaru, Y. Mizuno, K. Nakamura, Strain and temperature sensing based on multimode interference in partially chlorinated polymer optical fibers. IEICE Electr. Express **12**(2), 20141173 (2015)
54. D. Monzón-Hernández, V.P. Minkovich, J. Villatoro, High-temperature sensing with tapers made of microstructured optical fiber. Photonics Technol. Lett. IEEE **18**(3), 511–513 (2006)
55. S.M. Nalawade, H.V. Thakur, Photonic crystal fiber strain-independent temperature sensing based on modal interferometer. Photonics Technol. Lett. IEEE **23**(21), 1600–1602 (2011)
56. E. Li, X.L. Wang, C. Zhang, Fiber-optic temperature sensor based on interference of selective higher-order modes (2006)
57. Y. Liu, L. Wei, Low-cost high-sensitivity strain and temperature sensing using graded-index multimode fibers. Appl. Opt. **46**(13), 2516–2519 (2007)
58. Q. Wu, Y. Semenova, A.M. Hatta, P. Wang, G. Farrell, Single-mode–multimode–single-mode fiber structures for simultaneous measurement of strain and temperature. Microwave Opt. Technol. Lett. **53**(9), 2181–2185 (2011)
59. J.G. Aguilar-Soto, J.E. Antonio-Lopez, J.J. Sanchez-Mondragon, D.A. May-Arrioja, Fiber optic temperature sensor based on multimode interference effects, in *Journal of Physics: Conference Series* vol. 274, No. 1 (IOP Publishing, 2011), p. 012011
60. L.V. Nguyen, D. Hwang, S. Moon, D.S. Moon, Y. Chung, High temperature fiber sensor with high sensitivity based on core diameter mismatch. Opt. Express **16**(15), 11369–11375 (2008)
61. P. Rugeland, W. Margulis, Revisiting twin-core fiber sensors for high-temperature measurements. Appl. Opt. **51**(25), 6227–6232 (2012)
62. J.E. Antonio-Lopez, Z.S. Eznaveh, P. LiKamWa, A. Schülzgen, R. Amezcua-Correa, Multicore fiber sensor for high-temperature applications up to 1000 C. Opt. Lett. **39**(15), 4309–4312 (2014)
63. Y.J. Rao, S. Huang, Ch. 10 "Applications of Fiber Optic Sensors," in *Fiber Optic Sensors*, ed. by S.S. Yin, P. Ruffin (Wiley, 2002)
64. X. Wen, T. Ning, Y. Bai, C. Li, J. Li, C. Zhang, Ultrasensitive temperature fiber sensor based on Fabry-Pérot interferometer assisted with iron V-groove. Opt. Express **23**(9), 11526–11536 (2015)
65. W. Qian, C.L. Zhao, S. He, X. Dong, S. Zhang, Z. Zhang, H. Wei, High-sensitivity temperature sensor based on an alcohol-filled photonic crystal fiber loop mirror. Optics Lett. **36**(9), 1548–1550 (2011)
66. H. Liang, W. Zhang, P. Geng, Y. Liu, Z. Wang, J. Guo, S. Yan, Simultaneous measurement of temperature and force with high sensitivities based on filling different index liquids into photonic crystal fiber. Optics Lett. **38**(7), 1071–1073 (2013)
67. W. Lin, Y. Miao, B. Song, H. Zhang, B. Liu, Y. Liu, D. Yan, Multimodal transmission property in a liquid-filled photonic crystal fiber. Optics Commun. **336**, 14–19 (2015)
68. W. Lin, B. Song, Y. Miao, H. Zhang, D. Yan, B. Liu, Y. Liu, Liquid-filled photonic-crystal-fiber-based multimodal interferometer for simultaneous measurement of temperature and force. Appl. Opt. **54**(6), 1309–1313 (2015)
69. E. Li, G.D. Peng, Wavelength-encoded fiber-optic temperature sensor with ultra-high sensitivity. Optics Commun. **281**(23), 5768–5770 (2008)
70. I. Del Villar, A.B. Socorro, J. Corres, F. Arregui, I. Matias, Optimization of sensors based on multimode interference in single-mode–multimode–single-mode structure. J. Lightwave Technol. **31**(22), 3460–3468 (2013)
71. I. Del Villar, A.B. Socorro, J.M. Corres, F.J. Arregui, I.R. Matias, Refractometric sensors based on multimode interference in a thin-film coated single-mode–multimode–single-mode structure with reflection configuration. Appl. Opt. **53**(18), 3913–3919 (2014)
72. A.J.R. Rodríguez, O. Baldovino-Pantaleón, R.F.D. Cruz, C.R. Zamarreño, I.R. Matías, D.A. May-Arrioja, Gasohol quality control for real time applications by means of a multimode interference fiber sensor. Sensors **14**(9), 17817–17828 (2014)

73. A.B. Socorro, I. Del Villar, J.M. Corres, F.J. Arregui, I.R. Matias, Sensitivity enhancement in a multimode interference-based SMS fibre structure coated with a thin-film: theoretical and experimental study. Sens. Actuators B: Chem. **190**, 363–369 (2014)
74. A.K. Sharma, R. Jha, B.D. Gupta, Fiber-optic sensors based on surface plasmon resonance: a comprehensive review. Sens. J. IEEE **7**(8), 1118–1129 (2007)
75. X. Yu, Y. Zhang, S. Pan, P. Shum, M. Yan, Y. Leviatan, C. Li, A selectively coated photonic crystal fiber based surface plasmon resonance sensor. J. Opt. **12**(1), 015005 (2009)
76. A. Dıez, M.V. Andres, J.L. Cruz, In-line fiber-optic sensors based on the excitation of surface plasma modes in metal-coated tapered fibers. Sens. Actuators B Chem. **73**(2), 95–99 (2001)
77. D. Monzón-Hernández, J. Villatoro, D. Talavera, D. Luna-Moreno, Optical-fiber surface-plasmon resonance sensor with multiple resonance peaks. Appl. Opt. **43**(6), 1216–1220 (2004)
78. S. Yin, P.B. Ruffin, F.T.S. Yu, *Fiber Optic Sensors*, 2nd edn. (CRC Press, by Taylor & Francis Group, 2008) (Ch. 4 In-Fiber Grating Optic Sensors. Section 4.5.3 "Optic Bend Sensors")
79. B.A.L. Gwandu, X.W. Shu, Y. Liu, W. Zhang, L. Zhang, I. Bennion, Simultaneous measurement of strain and curvature using superstructure fibre Bragg gratings. Sens. Actuators A **96**(2), 133–139 (2002)
80. Y.P. Wang, Y.J. Rao, A novel long period fiber grating sensor measuring curvature and determining bend-direction simultaneously. Sens. J. IEEE **5**(5), 839–843 (2005)
81. L.Y. Shao, A. Laronche, M. Smietana, P. Mikulic, W.J. Bock, J. Albert, Highly sensitive bend sensor with hybrid long-period and tilted fiber Bragg grating. Optics Commun. **283** (13), 2690–2694 (2010)
82. X. Chen, Y. Yu, X. Xu, Q. Huang, Z. Ou, J. Wang, C. Du, Temperature insensitive bending sensor based on in-line Mach-Zehnder interferometer. Photonic Sens. **4**(3), 193–197 (2014)
83. B. Sun, X.Y. Li, Y.Y. Yu, K.P. He, Design of a low cost and high sensitivity sensor for curve measurement. Optik-Int. J. Light Electr. Opt. **127**(1), 63–66 (2016)
84. L. Renqiang, F. Zhuang, Z. Yanzheng, C. Qixin, W. Shuguo, Operation principle of a bend enhanced curvature optical fiber sensor, in *2006 IEEE/RSJ International Conference on Intelligent Robots and Systems* (IEEE, 2006), pp. 1966–1971
85. Y. Fu, H. Di, R. Liu, Light intensity modulation fiber-optic sensor for curvature measurement. Opt. Laser Technol. **42**(4), 594–599 (2010)
86. Y. Fu, H. Di, Fiber-optic curvature sensor with optimized sensitive zone. Opt. Laser Technol. **43**(3), 586–591 (2011)
87. B. Sun, X.Y. Li, Y.Y. Yu, K.P. He, Design of a low cost and high sensitivity sensor for curve measurement. Optik-Int. J. Light Electr. Opt. **127**(1), 63–66 (2016)
88. H. Fu, N. Zhao, M. Shao, H. Li, H. Gao, Q. Liu, X. Qiao, High-sensitivity Mach–Zehnder interferometric curvature fiber sensor based on thin-core fiber. Sens. J. IEEE **15**(1), 520–525 (2015)
89. C.S. Shin, M.W. Lin, An optical fiber-based curvature sensor for endodontic files inside a tooth root canal. Sens. J. IEEE **10**(6), 1061–1065 (2010)
90. W. Liu, T. Guo, A.C.L. Wong, H.Y. Tam, S. He, Highly sensitive bending sensor based on Er 3 + -doped DBR fiber laser. Opt. Express **18**(17), 17834–17840 (2010)
91. J. Villatoro, A. Van Newkirk, E. Antonio-Lopez, J. Zubia, A. Schülzgen, R. Amezcua-Correa, Ultrasensitive vector bending sensor based on multicore optical fiber. Opt. Lett. **41**(4), 832–835 (2016)
92. J. Arkwright, P.L. Chu, T. Tjugiarto, Variable demultiplexing using a twin-core fiber Mach-Zehnder interferometer. Photonics Technol. Lett. IEEE **5**(10), 1216–1218 (1993)
93. J. Rathje, M. Svalgaard, J. Hubner, M. Kristensen, Sensitivity of a long-period optical fiber grating bend sensor, in *Optical Fiber Communication Conference and Exhibit, 1998. OFC'98, Technical Digest* (IEEE, 1998), pp. 238–239

94. M.J. Gander, W.N. MacPherson, R. McBride, J.D.C. Jones, L. Zhang, I. Bennion, A.H. Greenaway, Bend measurement using Bragg gratings in multicore fibre. Electr. Lett. **36**(2), 120–121 (2000)
95. Y. Liu, J.A.R. Williams, I. Bennion, Optical bend sensor based on measurement of resonance mode splitting of long-period fiber grating. Photonics Technol. Lett. IEEE **12**(5), 531–533 (2000)
96. C.K. Leung, Fiber optic sensors in concrete: the future? NDT E Int. **34**(2), 85–94 (2001)
97. K. Lee, D.S. Kwon, Wearable master device using optical fiber curvature sensors for the disabled, in *IEEE International Conference on Robotics and Automation, 2001. Proceedings 2001 ICRA*, vol. 1 (IEEE, 2001), pp. 892–896
98. C. Li, Y.M. Zhang, H. Liu, S. Wu, C.W. Huang, Distributed fiber-optic bi-directional strain–displacement sensor modulated by fiber bending loss. Sens. Actuators A **111**(2), 236–239 (2004)
99. H.N. Li, D.S. Li, G.B. Song, Recent applications of fiber optic sensors to health monitoring in civil engineering. Eng. Struct. **26**(11), 1647–1657 (2004)
100. H. Dobb, K. Kalli, D.J. Webb, Temperature insensitive long-period grating sensors in photonic crystal fiber, in *Photonics North* (International Society for Optics and Photonics, 2004), pp. 66–79
101. K.M. Tan, C.C. Chan, S.C. Tjin, X.Y. Dong, Embedded long-period fiber grating bending sensor. Sens. Actuators A **125**(2), 267–272 (2006)
102. C.Y. Huang, W.C. Wang, W.J. Wu, W.R. Ledoux, Composite optical bend loss sensor for pressure and shear measurement. Sens. J. IEEE **7**(11), 1554–1565 (2007)
103. Y.X. Jin, C.C. Chan, X.Y. Dong, Y.F. Zhang, Temperature-independent bending sensor with tilted fiber Bragg grating interacting with multimode fiber. Optics Commun. **282**(19), 3905–3907 (2009)
104. O. Frazão, S.F.O. Silva, J. Viegas, J.M. Baptista, J.L. Santos, J. Kobelke, K. Schuster, All fiber Mach-Zehnder interferometer based on suspended twin-core fiber. IEEE Photonics Technol. Lett. **17**(22), 1300–1302 (2010)
105. S. Zhang, W. Zhang, S. Gao, P. Geng, X. Xue, Fiber-optic bending vector sensor based on Mach-Zehnder interferometer exploiting lateral-offset and up-taper. Opt. Lett. **37**(21), 4480–4482 (2012)
106. J.R. Guzman-Sepulveda, D.A. May-Arrioja, In-fiber directional coupler for high-sensitivity curvature measurement. Opt. Express **21**(10), 11853–11861 (2013)
107. G. Salceda-Delgado, A. Van Newkirk, J.E. Antonio-Lopez, A. Martinez-Rios, A. Schülzgen, R. Amezcua Correa, Compact fiber-optic curvature sensor based on super-mode interference in a seven-core fiber. Opt. Lett. **40**(7), 1468–1471 (2015)
108. B. Sun, Y. Huang, S. Liu, C. Wang, J. He, C. Liao, J. Zhou, Asymmetrical in-fiber Mach-Zehnder interferometer for curvature measurement. Opt. Express **23**(11), 14596–14602 (2015)
109. A. Van Newkirk, J.E. Antonio-Lopez, A. Velazquez-Benitez, J. Albert, R. Amezcua-Correa, A. Schülzgen, Bending sensor combining multicore fiber with a mode-selective photonic lantern. Opt. Lett. **40**(22), 5188–5191 (2015)
110. Y. Yu, Y. Zhang, Z. Ou, X. Chen, Q. Huang, S. Ruan, Simultaneous measurement of one dimensional bending and temperature based on Mach-Zehnder interferometer. Photonic Sens. **5**(4), 376–384 (2015)
111. G. Capilla-Gonzalez et al., Stress homogenization in fiber optic bending sensors (submitted)

Index

A
Absorbers, 310, 318
Absorption coefficient, 227
Accelerometer, 189, 190
Acoustic emission, 191
Adiabatic, 275, 282
Adsorption mechanism, 11
Adulterated
  alcoholic beverage, 360
  beverage, 360
  fuels, 360
Advantages
  ALD, 100
  optical fiber sensors, 95
  plasma, 95, 106
  plasma modification, 102
Aerospace, 185
Air
  cavity, 279
  gap, 277, 284
  holes, 288
Alloy, 278, 284, 286, 289
Alumina (Al_2O_3), 21
Alzheimer, 118
Ammonia, 169, 176, 177, 180, 233
Ammonia sensors, 253
Amplitude, 275, 281
Angle, 34–37, 40, 41
Annealed samples of sapphire fiber tip, 23
Antibody, 77, 124, 132
  anti-Igg, 125, 133–137
  IgG, 125, 133–135
Antigen, 124, 132, 137
Antigen-antibody interaction, 85
Anti-interference capability, 8
Applications, 329–333, 340, 341–343
Artery, 126, 128, 141
Aromatic carboxylic acids, 256
ASE light source, 9
Atomic layer deposition (ALD), 100, 108
Attenuation bands, 283, 285, 288
Average humidity sensitivity, 16, 19, 27

B
Bandgap, 167, 168, 178
Band-pass response, 330–332
Beam, 275, 278, 281
Bending
  sensor, 364, 365
  stress, 364
Beverage quality, 262
Binary
  mixtures, 357–359
Biocompatible, 116, 128, 140
Biofunctionalization, 96, 102, 133
  amination, 102
  fluorination, 96, 102
  hydrogenation, 96
  PDMS, 102
Biological, 31, 34, 47
Biomaterials, 102
Biomedical engineering, 115, 116, 140
Biomolecular, 118, 132
Biomolecular sensor, 231
Biosensing, 304
Biosensor, 102, 109, 118–119, 131–141, 258
Birefringence, 276, 277
Blends, 329–330, 337–339, 341–343
Block theorem, 225
Bombarding, 98, 99, 101
Box-type vacuum coating system, 20
Bragg, 310, 319, 321
Bragg diffraction, 227, 228
Bragg fiber, 4, 168
Bragg grating, 1, 3, 196, 197, 274, 289
Bragg reflector, 224

© Springer International Publishing Switzerland 2017

I.R. Matias et al. (eds.), *Fiber Optic Sensors*, Smart Sensors,
Measurement and Instrumentation 21, DOI 10.1007/978-3-319-42625-9

Bragg structure, 104
Brillouin zone, 226, 227
Bruggeman equation, 11

C
Calixarene, 258
Capillary, 283, 286, 288, 294
Capillary condensation effect, 16
Capillary gas flow rate, 167
Capillary water condensation, 10
Carbon dioxide, 178
Cardiac, 118, 119, 128
Catheter, 115, 118, 126–128
Cerenkov, 157
CF_4, 101
Chemical, 31, 34, 45, 46
  etching, 354, 357
Chemical etching, 4
Chemical sensor, 231
Chemical vapor deposition (CVD), 96, 97, 99, 104, 106, 108, 109
  plasma enhanced CVD (PECVD), 104, 106, 108, 109
Chemisorption, 10
Civil infrastructure, 192
Civil structures, 197, 198
Cladding, 32, 167, 168, 225
Clothing, 118–122
CO_2 gas laser, 4
Coating, 96, 97, 99, 102, 103, 105–109, 284, 285, 290, 329, 335–337
Cobalt, 271, 281, 284, 285
Coil, 273, 276, 277
Columnar and porous structures, 11
Compact optical fiber humidity sensing system, 10
Condition assessment, 185
Conductor, 271, 275, 277
Conventional hydrogen sensors, 6
Conventional monitoring, 192
Core, 167–170, 225, 332, 333, 336–338, 340, 343
Corrugated, 320, 321
Coupled
  differential equations, 352
  modes, 349–351, 355, 356
  mode theory, 347, 348
  multicore structure, 354
  system, 349, 351, 354–356
Coupling
  coefficient, 348, 349, 351, 352, 355, 356
  constant, 350–352, 355, 356, 366
  matrix, 348
Coupling electrical energy, 99
  capacitive coupling (CCP), 99
  inductively coupled plasma (ICP), 99
Creatinine, 233
Critical structures, 187, 205
Cross-sensitivity to temperature, 15, 18, 19
Crystal lattice, 225
Crystalline structure, 228
Current, 269–272, 275–277, 284, 286, 293, 294
Curvature
  measurement, 364
  sensor, 364, 365

D
Damage classification, 185, 186
Damage detection, 185
Decibels (dB), 286
Deformation, 189, 190, 195, 198, 203, 204
Deposition, 95–97, 241, 245, 246, 249, 253–255, 264
Deposition rate, 13, 14, 21
Desorption of the chemisorbed layer, 11
Detection, 31, 36, 46, 47
Device, 115, 116–121, 128–131, 138–141, 329–332, 335–337, 343
Diagnostic methods, 69, 70
Diagnostics, 115, 116, 123, 141
Dielectric constant, 223, 224, 226, 231
Diodes, 271
Disease, 118, 123, 128, 140
Dispersion relation, 225
Dissociative mechanism, 10
Distributed fibre sensors, 199
DLC, 102, 106, 108
Dose rate, 151, 154, 156, 157, 159, 161
Dosimeter, 149–151, 153, 154, 156, 157, 160, 161
Dosimetry, 149, 150, 153, 154, 156, 157, 161

E
Earthquake, 185
e-beam evaporation, 4, 11, 13, 14, 19
Effect, 269–271, 273–275, 277, 284, 294
  Faraday effect, 270
  Hall effect, 269, 271, 273
  Josephson effect, 273
  Kerr effect, 273, 294
  magneto-optical effect, 269, 273, 274, 277, 284
Effective refractive index, 228
Electrical, 271, 274, 284, 288
Electrical sensors, 232
Electrochemical hydrogen sensors, 6
Electromagnetic, 290

Electromagnetic resonator, 228
Electron, 270, 273
ELISA, 124
Energy, 185, 191, 192
Energy band, 224
Escherichia coli, 69, 71, 75, 86, 88
Escherichia coli detection, 69
Etched or side-polished, 3
Etching, 95, 96, 100, 109, 117, 128, 134, 137, 225, 329, 335–337
  asymmetric, 363
  chemical, 354, 357
  rate, 363
Ethanol, 233, 329–330, 333, 337, 339, 341, 342, 343
Evaluation, 185, 202
Evanescent, 31, 34, 35, 38
Evanescent field, 3, 54, 59, 60, 71, 333, 337
Evanescent sensor, 7
Evanescent wave (EW), 69, 71, 72, 75, 77, 82, 85, 88
Evanescent wave interaction, 3
Evaporative deposition techniques, 20
Evolution of Plasmonics: A brief history, 51
Excitation of surface plasmons by light, 53
  Kretschmann-Raether configurations, 53
  Otto configuration, 53
Experimental set-up, 14, 15
Extinction coefficient, 103

F
Fabricate, 241, 246, 264
Fabry–perot, 117, 127
Fabry–Perot interferometer, 5, 10, 20
Fano resonance, 230, 235
Faraday, 270, 272
Femtosecond laser, 4
Femtosecond laser technique, 20
Ferromagnetic ferrites, 234
Fiber, 31, 32, 34, 37–39, 41, 43, 44, 46–48
  core, 332, 335, 340, 343
  diameter, 329–332, 335–337, 340, 343
  length, 331–331, 336–338
  multimode (MMF), 329–337, 340, 343, 347, 361
  sensors, 329–332, 335, 337, 343
  seven-core, 352, 353
  single mode, 353
  singlemode (SMF), 329–333, 337
  specialty, 348, 361
  twin-core, 354
Fiber Bragg grating (FBG), 1, 3, 4, 7, 195–197, 199, 201, 203
Fiber Bragg grating sensor, 7
Fiber interferometric sensors, 10
Fiber micro-machining, 4
Fiber optic, 198
  bending sensor, 365
  curvature Sensor, 364
  refractive Index Sensor, 353, 354, 356–360
  salinity sensor, 358
  sensors, 347, 366
  temperature Sensor, 361
Fiber optic sensor, 95–97, 99, 103, 105, 106, 108
  long period gratings, 106
  multilayers, 103
  multimode, 105
  photonic crystal, 108
  single-mode, 103, 108
Fiber optic sensors based on nano-films, 1, 2
Fiber Optic SPR Sensor, 59
Fibre
  bragg gratings, 117, 122, 126
  bundle, 124, 129–130
  fibre-optic, 115–141
  fibrescope, 115–118, 129–131
  long-period gratings (LPFG), 117, 136–138
  multimode, 117, 128
Figure of Merit (FoM), 311, 314, 315, 317, 319
Film, 280, 283, 294
Filter, 289, 290
Finite
  differences, 349
  element, 349
Fluids, 274, 275, 280, 282, 286, 288, 289, 291, 293, 294
  ferrofluids, 275
  magnetic fluid, 274, 280, 282, 286, 288, 289, 291, 293, 294
Fluorination, 102
Flux, 277
Focused ion beam, 167, 169
Forbidden band, 224
Force, 270–272, 290
Fourier Transform Interferometry (FTIR), 305, 307
Free-space, 310
Frequency Selective Surfaces (FSS), 310–313, 315, 316, 318, 322
Fresnel formula, 12
Full width at half maximum (FWHM), 288, 290
Functionalization, 75, 77, 78, 85, 86, 88, 89

G
Gamma radiation, 151, 152, 155, 157, 158
Gas, 95, 96

Gas concentration, 167–169, 180
Gas flow simulations, 174
Gasohol, 339, 341–343
Gasoline, 329–330, 333, 337, 339–343
Gas pressure, 231
Gas sensor, 167
Generator frequency, 95
Germanium-doped silica fiber, 3
Glass spheres, 226
Glow curve, 153
Glucose, 233
Gold
  coating, 124, 133–135
  nanoparticle, 133–137, 140
  nanorod, 133
  nanosphere, 133
Gold thin film coating, 78
Green theorem, 225
Ground-Penetrating Radar (GPR), 191
Grow rate, 97–99

H
Hazardous events, 187
Health, 115, 122, 140
Hetero-core optical fiber, 10
High temperature measurement, 24
High temperature measurement and characterization system, 21
High temperature sensor, 5, 20, 26
Hiperunifomly disordered, 224
Hole-assisted fiber, 4
Humidity, 37, 44, 46, 233
Humidity measurement and control, 10
Humidity response, 19
Hybrid fiber, 5
Hydrogel, 230
Hydrogenation, 102
Hydrogen characterization, 8, 9
Hydrogen sensitive film, 7, 9
Hydrogen sensor, 5–9
Hydroxyl group adsorbing, 10

I
Imaging, 191, 304, 307
Immobilization technique, 85
Immunocapture effect, 85, 87
Implantation, 96, 97, 102
Incidence angle, 227
Indium tin oxide (ITO), 34, 37–41, 43, 44, 46, 47, 337–339, 343
Indoor air quality, 261
Induction, 270–272
Infrared thermography, 192
Initial chemisorbed layer, 11
Inline optical filter, 3
Inorganic scintillators, 152, 160
Installation restrictions, 188
Integration of novel functional material with fiber optic components, 1, 27
Intensity, 275, 280, 281
Intensity measurement, 3
Interference, 117, 228, 230
Interference and masking, 3
Interferometers, 274, 275, 278–280, 282 , 294
  Fabry-Pèrot, 274, 278, 279, 294
  Mach-Zehnder, 274, 275, 280, 282
  modal interferometer, 274, 279, 282
Internal reflection, 225
Interrogation, 188, 199, 205
Intrinsic sensitive, 4
Inverse opal, 225, 233, 234
Ion-assisted deposition, 17, 18
Ionising radiation, 149, 150, 152, 160, 161
Iron, 271, 278, 285

J
Jacket, 281, 275

K
Kelvin equation, 11
k–extinction coefficient, 97, 103

L
Lab
  on-chip, 118, 124
  on-fibre, 119, 131
Laser, 168, 171–173, 176, 190
Laser Doppler Vibrometers, 190
Laser micromachining, 4
Latex, 227
Lattice constant, 232
Layer, 35–37, 39–41, 43, 44, 46, 47, 97, 100–103
Layer-by-layer deposition, 224
LbL technique, 249
Life line, 188
Light, 274, 275, 277, 278, 282, 284, 286, 288–290
  light source, 275, 277, 284, 286
Light amplification device, 26
Light confinement, 231
Light emitting diodes, 172, 177
Light propagation, 225
Linear, 276, 277, 288
Liquid Crystal (LC), 233
Localized surface plasmon resonance (LSPR), 71, 74, 75, 77, 80, 82, 84, 86, 88
Long period grating, 10, 241

Lorentz, 270, 272
Lossy mode resonance (LMR), 31–39, 41, 43–48, 105, 106, 133–141
Low-loss splice, 167
LPG, 106, 107
Luminescence, 152, 154, 157

M
Magnetic field, 269–275, 277, 279–289, 291–293, 294
Magnetic sensor, 232
Magnetite, 234
Magneto-optic Kerr Effect (MOKE), 274, 277, 284
Magnetostriction, 274, 278, 289, 294
Magnetron sputtering, 96, 98
Marine, 197
Materials, 31–33, 37, 38, 44, 45, 47
Maxwell equations, 225, 228
Measurement set-up, 75
Measuring accuracy, 187
Measuring scale, 187
Measuring speed, 187
Mechanical sensor, 232
Mechanical splicing, 179
Mechanical stability on tiny optical fibers, 2
Medicine, 115–131
MEMS, 189, 190
Mesurand, 223, 224, 232
Metal cations, 233
Metallic meshes, 316
Metasurfaces, 301, 304, 311, 318
Methane, 168
Micro, 288, 290, 292, 293
  endomicroscopy, 118
  mems/moems, 138
  micro-chip, 121, 138
  microfiber, 292, 293
  microfluidic, 124, 131, 138
  microorganism, 132
  microresonators, 290
  microstructured, 288
  microtechnologies, 138
Micro- and nano-fiber, 5
Micro-machined, 4, 5
Micromachining, 4
Micro-mirror, 3
Micro-mirror sensor, 7
Micro-mirror style, 3
Microspheres, 225, 234
Micro-structured fiber, 4
Microstructured optical fibers, 168
Microwave, 301, 302, 304, 305, 313, 321
Microwave radiation, 225
Mie scattering, 227, 228, 230
Miniature broadband tungsten halogen lamp TLS, 21
Miniature fiber spectrometer, 14, 16
Minimum of reflectance at resonance Surface Plasmon Resonance (SPR), 57
Mining, 188
Mobile
  application, 118–119, 124
  devices, 120–122
  phones, 120–122, 124
Mode, 32–35, 37–39, 42
  coupled, 347–351, 355, 356
  even, 349–351, 355
  fundamental, 348
  odd, 349–351, 355
Modification, 96, 102, 108, 109
Modulation, 277, 280
Modulation of the fibre, 242
Moisture sensitive material, 10
Molecular imprinting, 251, 252
Monitoring, 185–190, 329–330, 339, 341, 343
Monitoring of hydrogen concentration, 6
Morphology of film, 7, 14
Multicore
  fiber, 347, 348, 352, 357, 365, 366
  seven-core, 347, 352, 353
  structure, 347
Multimode, 282, 283, 286
  interference (MMI), 329–343
  no-core (NC-MMF), 332–333, 336–337, 340
Multimode fiber, 11, 13, 14, 20, 105

N
Nano-film deposition on fiber tip, 5
Nano-films, 1, 2, 5
Nanomaterials, 249
Nanorods, 75, 80, 88
Nanostructure, 100
Nano-structure technologies, 5
Nano thin films and coatings, 27
NH_2, 102
Nickel, 271, 281
Nitride, 98, 102
Nitrogen, 98, 102
Nm, 100, 107
Non-Destructive-Testing (NDT), 190
Non-linear hydrogen response, 9
Normalized total reflected intensity, 12
n–refractive index, 103, 104, 106
Nuclear, 149, 150

O
Octane, 339–341
OLED, 234
One Dimensional (1D), 224, 229, 230, 234, 235
Opal, 225, 228, 231, 233, 235
OPD versus temperature curve, 25
Operational performance, 186, 189
Optical, 269, 273–275, 277, 281–284, 286–288, 290, 292–294
  optical fiber, 269, 273–275, 277, 281, 284, 286–288, 290, 292–294
  optical path, 282
  optical spectrum, 283, 286
  optical structure, 282, 286
Optical biosensors, 70
Optic(al) sensor, 228, 233
Optical fiber, 32, 37, 44–47, 96, 97, 100, 102, 103, 225, 329–330, 333, 337, 339, 342–343
  high-temperature sensing, 20
  humidity sensing techniques, 10
  hydrogen sensors, 5–7, 9
  relative-humidity sensors, 10
  sensors, 5, 27
Optical fibre, 115–141, 149–151, 153–155, 157, 159–162
Optically stimulated luminescence, 154
Optical path deviation, 5
Optical path difference, 22, 27
Optical response, 224, 229, 233
Optical Sensing principle of SPR
  performance parameters, 58
  sensitivity, 58
  signal-to-noise ratio (SNR), 58
Optical setup, 81
Optical signal, 223, 230
Optical time domain reflectometry, 195, 199
Optimum deposition process, 13

P
Pd/Pt composite films, 7
Peak intensity, 7–9
PECVD, 96, 99, 104
PEGMA, 233
Permittivity, 313, 314, 320
pH, 37, 45, 46, 233
Phase, 276, 277, 280
  phase shift, 276, 277
Phase matching condition, 242, 243, 248
Phase matching curves, 243
Phase matching turning point (PMTP), 243
Phase transition, 234
Phenomenon, 33–35, 37, 38, 44, 45
Photodetector, 275, 280
Photogrammetric, 192
Photoisomerization, 235
Photolithography, 224
Photonic band gap, 225, 230, 231
Photonic bandgap fibers, 168
Photonic Band Structure (PBS), 225, 227, 229
Photonic Crystal (PhC), 223–225, 227, 228, 230–234, 308
Photonic Crystal Cavity (PCC), 231
Photonic crystal fiber, 4, 5, 20, 168, 172
Photonic Molecule (PM), 235
Physical, 31, 34
Physical vapor deposition (PVD), 97, 98
Physisorption, 10, 11
Planar, 306, 321
Plasma, 96–98, 100–102, 106, 107
  activation, 102
  cleaning, 96
  deposition, 98
  etching, 96, 100, 107
  implantation, 97, 102
  modification, 101, 102, 106
Plasmonic, 301, 319
Plasmons or Plasma oscillations, 52
Plastic optical fibre, 160, 161
Plastic scintillators, 152
PMMA, 86
POF, 71
POF probe, 83
POF sensor, 77
Point-by-point, 247, 248, 264
Polarization, 135, 274–276, 294
Polyamines, 256, 257
Polymer, 122, 132, 135, 136
Polymer swelling, 234
Polystyrene colloids, 233
Polyvinylidene fluoride (PVDF), 308
Porous oxide coating, 13, 19
Porous structure, 10, 16, 17
Portability, 188
Post-irradiation, 150, 153, 154
Power attenuation, 73
Power source, 230
Principle of detection, 70
Propagation, 274, 276
  constant, 348–350, 356
  constant mismatch, 351, 355
Properties, 99–101, 103, 105
  optical, 99–101, 103
  surface, 100, 105
Protocol, 77, 86, 87
Pseudogap, 227

Q
Quality, 97, 100, 102, 103, 106
  optical, 97, 100, 106
  thin films, 102, 103
Quasi crystalline, 224
Quick response rate, 9

R
Radar cross section (RCS), 310
Radiation, 149–151, 153–162, 223, 224, 228
Radiation-induced attenuation, 155, 156, 159, 160
Radioluminescence, 160
Radiotherapy, 157, 160
Raman, 189, 199, 201
Reactive magnetron sputtering, 96, 98
Red-shift, 16
Reflected interference fringes, 5
Reflection, 225, 228–230, 277, 290
Reflection surfaces, 11, 12
Refraction, 225
Refractive index (RI), 31, 34, 36, 38, 39, 43–46, 97, 99, 102, 103, 106, 107, 109, 224–228, 231–233, 274, 278, 283, 285, 287, 288, 291, 293, 329–339, 341–343
  effective, 348–351, 355
  sensor, 353, 354, 356–360
Refractive index change, 4, 10, 16
Refractometer, 44, 45, 47, 333, 338, 340
Relative humidity, 11, 15, 27
Reliability, 186, 192, 205
Remove surface contamination, 13, 20
Resonance, 31–36, 38, 43, 46, 47, 288, 292, 305, 309–315, 318, 321, 322
Resonance bands, 242, 243, 245, 255, 262
Resonant cavities, 235
Resonant frequency, 228
Resonant mode, 231
Response time, 234
Response time for hydrogen sensor, 9
Restrictions, 188
RFID, 190
RIE, 96, 101
RI sensing, 84
Road transport, 188
Rotation, 273–275, 294

S
Safety, 185, 186, 190, 191, 205
Salinity
  measurement, 358, 359
  monitoring, 358
  sensing, 359
  sensor, 358, 359
Sapphire fiber-based high-temperature sensors, 5, 20
Scatterer, 227
Scintillation, 152, 157
Scintillator, 152, 161
Selected significant works in the area of plasmonics-based fiber optic sensors, 61
Selectivity, 223
Self-assembly, 225
SEM image of the sensing head, 7
SEM micrographs of the section of the films, 17
Sensing, 31, 32, 34, 35, 37–41, 44–48, 224, 230, 231, 233
Sensing repeatability and consistency, 18
Sensing technology, 1, 5
Sensitive thin films or coatings, 5, 4
Sensitivity, 31, 36, 37, 43–46, 48, 241, 243, 245, 246, 248, 253, 254, 258, 261, 263, 269, 278, 281–284, 288, 290–292, 294, 312, 321, 329–330, 333–337, 339, 343
Sensor, 31, 32, 34, 37–39, 44, 45, 47, 48, 120–123, 125–128, 131–133, 138, 223, 224, 229, 231–234, 269, 271, 272, 274, 281, 283, 287–290, 293, 294, 329–335, 337, 339, 343
  curvature, 364, 365
  refractive index, 353, 354, 356–360
  temperature, 361–363
Seven-core
  fiber, 352, 353
  structure, 352
Shift of output spectra, 10
Side-polishing, 4
Silica, 234
Silica optical fibre, 153, 155, 160
Single-crystal sapphire, 20
Single mode, 108, 275, 278, 281, 286, 291
Single mode fiber, 7–9, 20
SiO_2 coating, 11
SiO_2 NPs, 249, 257, 258, 263
Smart
  fabric, 120
  phone, 115, 118, 119, 123–140
  shirt, 120–121
  tattoos, 121
  textiles, 122
  watch, 120
Snell's law, 225, 228
Spatial resolution, 187, 200, 203
Spectral response, 330–332, 334–335, 338, 340–341
Spectroscopy, 302–304, 307, 318, 322
Spin coating, 224

Splice, 172, 174, 179, 180
Split ring resonators (SRR), 313
Sputtering, 283, 284, 290
SRI, 36, 38, 40, 41, 44, 45, 125, 133, 134, 136, 140
Stem effect, 157
Sterilisation, 149, 157, 158
Strain, 187, 189, 199, 202
Strain gauge, 189, 233
Structural disorder, 231
Structural Health Monitoring (SHM), 185–192, 195, 201, 205
Structure fatigue, 187
Structure integrity, 187
Substance, 131, 132, 140
Superconducting Quantum Interference Devices (SQUID), 271, 273
Surface plasmon polariton (SPP), 304, 319
Surface plasmon resonance (SPR), 70, 74, 102, 105, 124–125, 126, 133–140
Surface plasmon resonance sensor, 7
Surface plasmons, 52
Surface waves, 304, 320
Surrounding medium, 33, 35–37, 44
Swan-Ganz, 128
System performance, 187

T
Tapered, 275, 282, 291, 292
Technology, 116–121, 124, 126, 131, 133–135, 138, 140, 141
Temperature, 230
  sensor, 234, 361–363
Temperature resolution, 25
Terahertz (THz), 301
Terfenol-D, 278, 289, 294
Theoretical simulation of interference fringe shift, 13
Thermal radiation, 22
Thermoluminescence, 153
Thermo-optic
  coefficient, 362
  effect, 363
Thermo-optic and elastic-optic effect, 22
Thickness, 31, 34, 36–39, 40, 41, 43–45, 47, 128, 135, 140
Thin film, 5, 32–34, 37–39, 41, 44–47, 96, 97, 99, 100, 102, 104–109, 117, 133–136, 140, 335, 337
  silicon nitride (SiN_x), 104, 106, 108, 109
  thickness, 97, 99, 100, 105–107
  titanium dioxide (TiO_2), 99, 104, 108
Thin film-based Fabry–Perot structure, 5
Three Dimensional (3D), 224, 225, 227–231, 233, 236
Tilted fiber Bragg's grating, 10
Time Domain Spectroscopy (TDS), 302, 305, 307
TiO_2 coatings, 11
Titania, 226
Titanium dioxide (TiO_2), 34, 44, 45–47
Total internal reflection (TIR), 72
Transducers, 269, 275, 293
Transformer, 269, 284, 286
Transmission, 34, 40, 43–45, 226, 228, 277, 283–285, 287, 289, 292
Transmission lines, 304, 321, 322
Transmission spectrum, 225, 226, 242, 243, 245, 246, 248, 250, 253, 256, 259
Transmittance, 226
Transmitted, 224, 225, 229, 230
Transverse electric (TE), 314
Transverse electromagnetic (TEM), 320–322
Transverse magnetic (TM), 314, 315
Tunable, 280, 288, 289
Two-core
  coupled structure, 350, 351
  fiber, 347, 352, 353
Two Dimensional (2D), 224, 225, 229, 230, 235
Typical reflection spectrum of the post-deposited probes, 22

U
Uniformity, 108
U-Shaped probe, 78, 82–85
U-Shaped sensor, 88

V
Vacuum, 98, 99
Vancomycin, 259
Variable, 118, 119, 123, 126, 140
Vein, 117, 126, 141
Verdet, 274, 277
VOCs, 258, 261
Voltage, 269, 271

W
Wave, 33, 34
Waveguide, 283, 290, 308–310, 312, 319, 321, 322
  anti-resonant reflecting (ARRHW), 309
  coupled resonator optical waveguide (CROW), 308
  dielectric, 308
  dielectric pipe, 309

metallic, 310
parallel plate, 319
photonic crystal, 308
plasmonic, 322
single-mode, 348–350
Wavelength, 31, 32, 34–38, 43, 44, 47, 223, 224, 228, 233, 234, 274, 278, 280, 282–286, 288, 289, 292
detection, 135, 141
shift, 132, 333, 335–336, 338, 341–342
Wavelength-specific reflector, 3
Wearable, 115, 120–122
Wet etching, 97, 101, 107
Winding, 276, 284, 286
WO_3 film, 7
WO_3-Pd-Pt multilayer, 7, 8
WO_3-Pd thin film, 6

X
X-ray diffraction, 227

Z
Zeeman effect, 272
Zirconium dioxide (ZrO_2), 21